



LECTURE NOTES IN GEOINFORMATION AND CARTOGRAPHY

LNG&C

Simon Jones · Karin Reinke (Eds.)

Innovations in Remote Sensing and Photogrammetry

 Springer

Lecture Notes in Geoinformation and Cartography

Series Editors: William Cartwright, Georg Gartner, Liqiu Meng,
Michael P. Peterson

Simon Jones · Karin Reinke
Editors

Innovations in Remote Sensing and Photogrammetry

 Springer

Editors

Prof. Simon Jones
RMIT University
Dept. Geospatial Science
Melbourne VIC 3001
Australia
simon.jones@rmit.edu.au

Dr. Karin Reinke
RMIT University
Dept. Geospatial Science
Melbourne VIC 3001
Australia
karin.reinke@rmit.edu.au

ISSN 1863-2246
ISBN 978-3-540-88265-7
DOI 10.1007/978-3-540-93962-7
Springer Heidelberg Dordrecht London New York

e-ISSN 1863-2351
e-ISBN 978-3-540-93962-7

Library of Congress Control Number: 2009933202

© Springer-Verlag Berlin Heidelberg 2009

This work is subject to copyright. All rights are reserved, whether the whole or part of the material is concerned, specifically the rights of translation, reprinting, reuse of illustrations, recitation, broadcasting, reproduction on microfilm or in any other way, and storage in data banks. Duplication of this publication or parts thereof is permitted only under the provisions of the German Copyright Law of September 9, 1965, in its current version, and permission for use must always be obtained from Springer. Violations are liable to prosecution under the German Copyright Law.

The use of general descriptive names, registered names, trademarks, etc. in this publication does not imply, even in the absence of a specific statement, that such names are exempt from the relevant protective laws and regulations and therefore free for general use.

Cover design: deblik, Berlin

Printed on acid-free paper

Springer is part of Springer Science+Business Media (www.springer.com)

Preface and Acknowledgements

This book has its origins in the Australasian Remote Sensing and Photogrammetry conference series. The theme for the book, Innovations in Remote Sensing and Photogrammetry, encompasses a broad range of topics in geoinformation and cartography presented over 36 papers. These are characterised in four sections: data fusion techniques and their applications in environmental monitoring; synoptic monitoring and data processing; terrestrial applications of remote sensing; and marine applications of remote sensing. Color figures are an important contribution to many of these papers. Readers are directed to the eBook version of this publication for access to full color reprints of the relevant papers.

The book begins with an introduction to spatial data visualization, with particular focus given to attribute uncertainty, as a critical step in enabling users to assess the suitability of the data for the intended application and to better understand the potential limitations of their data and subsequent outputs. This is important for policy-makers and natural resource managers whose decisions depend on spatial information. Consequences can be severe if data is unknowingly erroneous or misused. This paper provides a setting for the way in which we as spatial data providers and users need to think about, and share information. In addition it provides a linkage between this book and the book series, Lecture Notes in Geoinformation and Cartography, to which it belongs.

The first section begins with a series of papers on remote sensing data fusion techniques and their applications in environmental monitoring. Data synthesis and integration is critical to unlocking the full potential of earth observing sensors. In the context of landcover mapping, Ali et al. explore a method of combining both active and passive imagery. They conclude more accurate land cover mapping is attainable using object-level fusion than using the pixel-level supervised process. Bunting et al. present a technique that uses textural information, derived from image filters, to be used alongside hyperspectral data for the classification of broad forest types. Poon et al. discuss the potential for QuickBird as an effective method of extracting 3D information to be used for high accuracy ground feature determination. Lee et al. calibrate the ICESat laser data with airborne Lidar to generate new data products providing information about forest height and structure. Finally Sheffield et al. describe a native woody vegetation ground data collection protocol that attempts to

integrate the spatial resolution of several remotely sensed datasets and the spatial variation of vegetation into a common framework.

The second section presents an overview of the use of remote sensing as a synoptic monitoring tool. The importance of remote sensing in its capacity to monitor the Earth, often in near real time, requires advancing our understanding in sensor technology and in the methods we employ to obtain and use spatial monitoring information. The Landsat program and its data archive are reviewed by Arvidson et al. for its utility in the analysis of global climate and environmental change. Furby et al. and Wu et al. discuss Landsat alternatives and quantify the effects of using SPOT 4, CBERS and Landsat 7 SLC-off images instead of the current Landsat 5 images in the context of continuity in climate change monitoring. The potential of the PALSAR instrument to support the inventory, conservation and management of wetlands in different areas around the world is evaluated by Lowry et al. and a new classification procedure for mapping terrestrial carbon within an operational, satellite based, forest monitoring system is offered by O'Connell et al. Processing methods are overviewed by Broomhall et al. who propose an aerosol optical depth retrieval method to facilitate better atmospheric correction of remotely sensed data particularly at the synoptic resolution level. McAtee et al. present an improved near real time atmospheric correction for MODIS data and Goessmann et al. propose an algorithm for the detection of active fires using the MODIS sensor. Grant presents a paper on operational land surface monitoring, while Griersmith et al. review recent developments in meteorological remote sensing.

The third section on terrestrial applications of remote sensing provides an overview of several key application areas; woody vegetation, landcover, wildfire, agriculture and built environments. The variety presented in this section highlights the enormous breadth of applications afforded by remote sensing technologies. Barry et al. explore a remotely sensed technique with the potential for distinguishing eucalypt phenology (seasonal change) from leaf stress. Vescovo et al. assess the utility of vegetation indices for grassland mapping, whilst Ferwerda et al. assess a range of commonly used vegetation indices for detecting nitrogen status and crop growth/production of wheat under a range of nitrogen fertilizer and irrigation treatments. The paper by Handcock et al. asks 'how remotely-sensed observations of pastures in an intensively managed dairy system change in relation to intensive management practices?' and found the observed spectral response varied with the length of time since the paddock was grazed. An overview of the Pastures from Space program is given by Stovold et al. Hall et al. propose an algorithm to be used in identifying a set of vine pixels with the aim to achieve improved remote viticulture canopy mapping. Hempel et al. use a Generalised Additive Modelling approach to predict weed occurrence and Eustace et al. present a semi-automated method to map gully extent and volume using LiDAR. Land use and land cover mapping is addressed in papers by Schroers et al. and Schmidt et al., and Mauger et al. maps mineralogy using the three HyMap hyperspectral instruments. In contrast to the natural environment, Fulton et al. provide a description for the automated reconstruction of buildings using digital video imagery and photogrammetric techniques. The issue of remote sensing and wildfire is examined in four papers. Goessmann

et al. propose an algorithm for the detection of active fires using the MODIS sensor whilst Martin et al. present two papers on the theme of assessing grassland curing (or water content) for enhanced wildfire risk mapping. Cook et al. present a narrative of bushfire remote sensing from experience gained in NSW and the ACT, Australia, during the years 2001–2003.

The fourth section on marine applications of remote sensing begins with papers by Kutser et al. and Thankappan et al. which explore benthic mapping methodologies based on SAR, optical sensors and ancillary datasets. Majewski et al. evaluate methods for the monitoring the optical properties of marine water bodies, and Metsamaa et al. evaluate the performance of the new MERIS Level 2 products in retrieving marine chlorophyll metrics. Radliński et al. uses the diagnostic spectral features of oil to map oil slicks on the ocean.

In conclusion the editors wish to thank all the authors for their involvement and for enabling us to compile their work into this book. On behalf of the authors, the editors would also like to acknowledge and thank the generous contribution made by the many anonymous reviewers. Without this combined effort, this book would not have been realized.

Melbourne, Australia
23rd October 2008

Simon Jones
Karin Reinke

Contents

| | |
|--|------------|
| Introduction: Visualising Uncertainty in Environmental Data | xix |
| K.J. Reinke and S.D. Jones | |
| Part I Data Fusion Techniques and Their Applications in Environmental Monitoring | |
| A Comparison of Pixel- and Object-Level Data Fusion Using Lidar and High-Resolution Imagery for Enhanced Classification | 3 |
| S.S. Ali, P.M. Dare, and S.D. Jones | |
| Combining Texture and Hyperspectral Information for the Classification of Tree Species in Australian Savanna Woodlands | 19 |
| Peter Bunting, Wenda He, Reyer Zwiggelaar, and Richard Lucas | |
| High-Resolution Satellite Imaging in Remote Regions: A Case Study in Bhutan | 27 |
| J. Poon and C.S. Fraser | |
| A New Dataset for Forest Height Across Australia: Pilot Project to Calibrate ICESat Laser Data with Airborne LiDAR | 37 |
| Alex Lee, Peter Scarth, and Adam Gerrand | |
| Linking Biological Survey Information to Remote Sensing Datasets: A Case Study | 51 |
| K.J. Sheffield, S.D. Jones, J.G. Ferwerda, P. Gibbons, and A. Zerger | |
| Part II Synoptic Monitoring and Data Processing | |
| Characterizing the Landsat Global Long-Term Data Record | 65 |
| T. Arvidson, S.N. Goward, and D.L. Williams | |
| Evaluation of Alternative Sensors for a Landsat-Based Monitoring Program | 75 |
| S.L. Furby and X. Wu | |

| | |
|--|-----|
| Evaluation of CBERS Image Data: Geometric and Radiometric Aspects | 91 |
| X. Wu, J. Guo, J. Wallace, S.L. Furby, and P. Caccetta | |
| Mapping and Monitoring Wetlands Around the World Using ALOS PALSAR: The ALOS Kyoto and Carbon Initiative Wetlands Products | 105 |
| John Lowry, Laura Hess, and Ake Rosenqvist | |
| Testing of Alternate Classification Procedures Within an Operational, Satellite Based, Forest Monitoring System | 121 |
| Jared O'Connell and Peter Caccetta | |
| An Investigation of the Remote Sensing of Aerosols Based on MODIS Data for Western Australian Conditions | 133 |
| Mark Broomhall, Brendon McAtee, and Stefan Maier | |
| Improved Near-Real Time Atmospheric Correction of MODIS Data for Earth Observation Applications | 149 |
| Brendon McAtee and Stefan Maier | |
| Near-Real Time Satellite Products to Drive Australia-Wide Land Surface Monitoring and Modelling of Surface Water and Energy Balance | 161 |
| I.F. Grant | |
| Recent and Future Developments in Meteorological Remote Sensing | 173 |
| D.C. Griersmith, I.F. Grant, A.G. Rea, and M.C. Willmott | |
| Improved Spatial Resolution of Fire Detection with MODIS Using the 2.1 μm Channel | 183 |
| Florian Goessmann, Stefan W. Maier, and Mervyn J. Lynch | |
| Part III Terrestrial Applications of Remote Sensing | |
| Characterizing Eucalypt Leaf Phenology and Stress with Spectral Analysis | 193 |
| Karen Barry, Ross Corkrey, Christine Stone, and Caroline Mohammed | |
| Development of Satellite Vegetation Indices to Assess Grassland Curing Across Australia and New Zealand | 211 |
| Danielle Martin, Ian Grant, Simon Jones, and Stuart Anderson | |
| Assessment of Grassland Curing Using Field-Based Spectrometry and Satellite Imagery | 229 |
| Danielle Martin, Simon Jones, Ian Grant, and Stuart Anderson | |
| Airborne Fire Intelligence | 239 |
| R. Cook, A. Walker, and S. Wilkes | |

| | |
|--|------------|
| Give Me the Dirt: Detection of Gully Extent and Volume Using High-Resolution Lidar | 255 |
| Alisa Eustace, Matthew Pringle, and Christian Witte | |
| Integrating Mineralogical Interpretation of HyLogger Data with HyMap Mineral Mapping, Mount Painter, South Australia | 271 |
| A.J. Mauger and S. Hore | |
| A Preliminary Study of Mapping Biomass and Cover in NZ Grasslands Using Multispectral Narrow-Band Data | 281 |
| L. Vescovo, M. Tuohy, and D. Gianelle | |
| Comparing Common Hyperspectral Vegetation Indices for Their Ability to Estimate Seasonal Nitrogen and Other Variables in Winter Wheat Across a Growing Season | 291 |
| J.G. Ferwerda, S.D. Jones, G. O'Leary, R. Belford, and G.J. Fitzgerald | |
| The Spectral Response of Pastures in an Intensively Managed Dairy System | 309 |
| R.N. Handcock, G. Mata, G.E. Donald, A. Edirisinghe, D. Henry and S.G. Gherardi | |
| Using Pasture Growth Rate Data in a National Agricultural Drought Assessment Monitoring Tool | 323 |
| R.G.H. Stovold, M. Adams, S.W. Maier, G. Donald, S. Gherardi, and M. Broomhall | |
| Investigating the Potential for Mapping Fallow Management Practises Using MODIS Image Data | 331 |
| Ralf-D. Schroers, Robert Denham, and Christian Witte | |
| Spectral Mixture Analysis for Ground-Cover Mapping | 349 |
| Michael Schmidt and Peter Scarth | |
| Vineclipper: A Proximal Search Algorithm to Tie Gps Field Locations to High Resolution Grapevine Imagery | 361 |
| A. Hall and J. Louis | |
| Modelling Weed Distribution Across the Northern Australia Using Very Extensive Transects | 373 |
| C. Hempel, N. Preece, K. Harvey, and J.C.Z. Woinarski | |
| Automated Reconstruction of Buildings Using a Hand Held Video Camera | 393 |
| J.R. Fulton and C.S. Fraser | |

Part IV Marine Applications of Remote Sensing

| | |
|---|------------|
| Mapping Seagrass Biomass with Photo-Library Method | 407 |
| Tiit Kutser, Ele Vahtmäe, Chris Roelfsema, and Liisa Metsamaa | |
| A Comparison of Bathymetric Signatures Observed on ERS SAR and LANDSAT TM Images Over the Timor Sea | 417 |
| Medhavy Thankappan and Craig J.H. Smith | |
| Optical Properties of Water Bodies in the Torres Strait, Australia, from Above-Water Reflectance | 433 |
| L.J. Majewski, W.M. Klonowski, and M.M. Slivkoff | |
| Accordance of MERIS Standard Products over the Gulf of Finland to the Parameters Measured Under Regular Monitoring Program | 443 |
| L. Metsamaa, A. Reinart, K. Alikas, T. Kutser, and A. Jaanus | |
| Spectral Identification of Oil Slicks on the Ocean | 455 |
| A.P. Radliński | |

Contributors

M. Adams Landgate, Satellite Remote Sensing Services, Leeuwin Centre, Floreat, WA 6014, Australia

S.S. Ali School of Geography, Population and Environmental Management, Flinders University, Adelaide, SA, Australia, syed0009@flinders.edu.au

K. Alikas Tartu Observatory, Tõravere, Tartumaa 61602, Estonia, andres@sea.ee

Stuart Anderson School of Mathematical and Geospatial Sciences, RMIT, Melbourne; Bushfire Cooperative Research Centre, East Melbourne, VIC, Australia; Scion, Christchurch, New Zealand

T. Arvidson Lockheed Martin, Goddard Space Flight Center, Greenbelt, MD 20771, terry.arvidson@nasa.gov

Karen Barry School of Agricultural Science, University of Tasmania, Hobart, Tasmania, Australia

R. Belford Department of Primary Industries, Horsam, VIC 3402, Australia

Mark Broomhall Remote Sensing and Satellite Research Group, Department of Applied Physics, Curtin University of Technology, Bentley, WA, Australia 6102, M.broomhall@curtin.edu.au

Peter Bunting Aberystwyth University, Aberystwyth, SY23 3DB, UK

Peter Caccetta CSIRO Mathematical & Information Sciences, Wembley, WA 6913, Australia, peter.caccetta@csiro.au

R. Cook IAM Pty Ltd, Gungahlin, ACT 2912, Australia, rcook@iam.net.au

Ross Corkrey Tasmanian Institute of Agricultural Research (TIAR), University of Tasmania, Tasmania, Australia

P.M. Dare Spatial Scientific Technologies, Adelaide, SA, Australia, paul@spatialscientific.com

Robert Denham QLD Department of Natural Resources and Water, Indooroopilly, Qld Australia, robert.denham@nrw.qld.gov.au

G.E. Donald Commonwealth Scientific and Industrial Research Organization, Floreat, WA 6014, Australia

G. Donald CSIRO, Livestock Industries, Wembley, WA 6913, Australia, G.Donald@csiro.au

A. Edirisinghe Commonwealth Scientific and Industrial Research Organization, Floreat, WA 6014, Australia

Alisa Eustace Queensland Department of Natural Resources and Water, Remote Sensing Centre, Indooroopilly, QLD 4068, Australia, alisa.eustace@qld.gov.au

J.G. Ferwerda School of Mathematical and Geospatial Sciences, RMIT University, Melbourne, VIC, Australia, jelle.ferwerda@rmit.edu.au
jelle@bio-vision.nl

G.J. Fitzgerald Department of Primary Industries, Horsam, VIC 3402, Australia

C.S. Fraser Department of Geomatics, University of Melbourne, Melbourne, VIC 3010, Australia, c.fraser@unimelb.edu.au

J.R. Fulton Air Operations Division, Defence Science and Technology Organisation, Fishermans Bend, VIC 3207, Australia, John.Fulton@dsto.defence.gov.au

S.L. Furby CSIRO Mathematical and Information Sciences, Wembley 6913, WA, Australia

Adam Gerrand National Forest Inventory, Bureau of Rural Sciences, Canberra, ACT, Australia

S.G. Gherardi Commonwealth Scientific and Industrial Research Organization, Floreat, WA 6014, Australia

S. Gherardi CSIRO, Livestock Industries, Wembley, WA 6913, Australia

D. Gianelle Centre for Alpine Ecology, Viote del Monte Bondone, Trento 38040, Italy, gianelle@cealp.it

P. Gibbons Centre for Resource and Environmental Studies, The Australian National University, Canberra, ACT, Australia, pgibbons@cres10.anu.edu.au

Florian Goessmann Remote Sensing and Satellite Research Group, Department of Imaging and Applied Physics, Curtin University of Technology, Perth, WA 6845, Australia, Florian.Goessmann@postgrad.curtin.edu.au

S.N. Goward Department of Geography, University of Maryland, College Park, MD 20782, sgoward@umd.edu

I.F. Grant Space Based Observations Section, Bureau of Meteorology, Melbourne, VIC 3001, Australia, i.grant@bom.gov.au

Ian Grant Space Based Observations Section, Bureau of Meteorology, Melbourne; Bushfire Cooperative Research Centre, East Melbourne, VIC, Australia

D.C. Griersmith Space Based Observations Section, Bureau of Meteorology, Melbourne, VIC 3001, Australia, d.griersmith@bom.gov.au

J. Guo China Centre for Resources Satellite Data and Application (CRESDA), Beijing 100830, China

A. Hall National Wine and Grape Industry Centre, School of Environmental Sciences, Charles Sturt University, Wagga, NSW 2678; Cooperative Research Centre for Viticulture, Glen Osmond, SA 5064, Australia, ahall@csu.edu.au

R.N. Handcock Commonwealth Scientific and Industrial Research Organization, Floreat, WA 6014, Australia, Rebecca.Handcock@csiro.au

K. Harvey Department Of Defence, Australian Government, Campbell Park, ACT, Australia

Wenda He Aberystwyth University, Aberystwyth, SY23 3DB, UK

C. Hempel Environmental Protection Agency, Queensland Government, Queensland, QLD, Australia, craig.hempel@epa.qld.gov.au

D. Henry Commonwealth Scientific and Industrial Research Organization, Floreat, WA 6014, Australia

Laura Hess Institute for Computational Earth System Science, University of California, Santa Barbara, CA USA

S. Hore Curnamona Team, Geological Survey Branch, PIRSA, Adelaide, SA 5000, Australia, hore.stephen@saugov.sa.gov.au

A. Jaanus Tartu Observatory, Tõravere, Tartumaa 61602, Estonia, alikas@tu.ee

S.D. Jones School of Mathematics and Geospatial Science, RMIT University, Melbourne, VIC, Australia, simon.jones@rmit.edu.au

Simon Jones School of Mathematical and Geospatial Sciences, RMIT, Melbourne, VIC, Australia,

W.M. Klonowski Department of Imaging and Applied Physics, Curtin University of Technology, Perth, WA 6845, Australia

Tiit Kutser Estonian Marine Institute, Tartu University, Tallinn 12618, Estonia, tiit.kutser@sea.ee

T. Kutser Tartu Observatory, Tõravere, Tartumaa 61602, Estonia, reinart@aai.ee

Alex Lee Fenner School of Environment and Society, Defence Imagery and Geospatial Organisation, Australian National University, Canberra, ACT 0200, Australia, Alexander.Lee@defence.gov.au

J. Louis National Wine and Grape Industry Centre, Charles Sturt University, Wagga, NSW 2678; Cooperative Research Centre for Viticulture, Glen Osmond, SA 5064, Australia, jlouis@csu.edu.au

John Lowry Supervising Scientist Division, Department of the Environment, Water, Heritage and the Arts, Darwin, NT, Australia, john.lowry@environment.gov.au

Richard Lucas Aberystwyth University, Aberystwyth, SY23 3DB, UK

Mervyn J. Lynch Remote Sensing and Satellite Research Group, Department of Imaging and Applied Physics, Curtin University of Technology, Perth, WA 6845, Australia M.Lynch@curtin.edu.au

Stefan Maier Charles Darwin University, Casuarina, NT 0810; Satellite Remote Sensing Services, Landgate, Government of Western Australia, Wembley, WA 6913, Australia, Stefan.Maier@cdu.edu.au

Stefan W. Maier Government of Western Australia, Landgate Satellite Remote Sensing Services, Wembley, WA 6913, Australia, Stefan.Maier@landgate.wa.gov.au

S.W. Maier Landgate, Satellite Remote Sensing Services, Leeuwin Centre, Floreat, WA 6014, Australia

L.J. Majewski Department of Imaging and Applied Physics, Curtin University of Technology, Perth, WA 6845, Australia

Danielle Martin Space Based Observations Section, Bureau of Meteorology; School of Mathematical and Geospatial Sciences, RMIT; Bushfire Cooperative Research Centre, East Melbourne; Melbourne, VIC, Australia, Danielle.Martin@bom.gov.au

G. Mata Commonwealth Scientific and Industrial Research Organization, Floreat, WA 6014, Australia

A.J. Mauger CRCLEME, Geological Survey Branch, PIRSA, Adelaide, SA 5000, Australia, mauger.alan@saugov.sa.gov.au

Brendon McAtee Satellite Remote Sensing Services, Landgate, Government of Western Australia, Floreat, WA 6014, Australia, Brendon.Mcatee@landgate.wa.gov.au

Liisa Metsamaa Estonian Marine Institute, Tartu University, Tallinn 12618, Estonia, liisa.metsamaa@sea.ee

Caroline Mohammed School of Agricultural Science, University of Tasmania; Ensis, CRC Forestry, Hobart, Tasmania, Australia

Jared O'Connell CSIRO Mathematical & Information Sciences, Wembley, WA 6913, Australia, jared.oconnell@csiro.au

G. O’Leary Department of Primary Industries, Horsam, VIC 3402, Australia

J. Poon Department of Geomatics, University of Melbourne, Victoria 3010, Australia, jpoon@skm.com.au

N. Preece School for Environmental Research, Charles Darwin University, Darwin, NT, Australia

Matthew Pringle Queensland Department of Natural Resources and Water, Remote Sensing Centre, Indooroopilly, QLD 4068, Australia

A.P. Radliński Geoscience Australia, Canberra City, ACT, Australia, andrzej.radlinski@ga.gov.au

A.G. Rea Space Based Observations Section, Bureau of Meteorology, Melbourne, VIC 3001, Australia, a.rea@bom.gov.au

A. Reinart Tartu Observatory, Tõravere, Tartumaa 61602, Estonia, tiit.kutser@sea.ee

K.J. Reinke School of Mathematics and Geospatial Science, RMIT University, Melbourne, VIC, Australia, karin.reinke@rmit.edu.au

Chris Roelfsema Centre for Remote Sensing and Spatial Information Science, University of Queensland, Brisbane, QLD, 4072, Australia

Ake Rosenqvist European Commission – Joint Research Centre, Ispra, Italy

Peter Scarth Queensland Department of Natural Resources and Water, Remote Sensing Centre, Brisbane, QLD, Australia, Peter.Scarth@nrw.qld.gov.au

Michael Schmidt Department of Natural Resources and Water, Indooroopilly, QLD 4068, Australia, michael.schmidt@nrw.qld.gov.au

Ralf-D. Schroers Spatial Diversity Pty Ltd, Karalee, Qld 4306, Australia ralf@spatialdiversity.com.au

K.J. Sheffield School of Mathematical and Geospatial Sciences, RMIT University, Melbourne, VIC, Australia, s3102807@student.rmit.edu.au

M.M. Slivkoff Department of Imaging and Applied Physics, Curtin University of Technology, Perth, WA 6845; Australian Institute of Marine Science, Townsville, QLD 4810, Australia

Craig J.H. Smith Geospatial and Earth Monitoring Division, Geoscience Australia, Canberra, ACT 2601, Australia

Christine Stone Forest Resources Research, NSW Department of Primary Industries, Beecroft, NSW, Australia

R.G.H. Stovold Landgate, Satellite Remote Sensing Services, Leeuwin Centre, Floreat, WA 6014, Australia, Richard.Stovold@dli.wa.gov.au

Medhavy Thankappan Geospatial and Earth Monitoring Division, Geoscience Australia, Canberra, ACT 2601, Australia, medhavy.thankappan@ga.gov.au

M. Tuohy New Zealand Centre for Precision Agriculture, Massey University, Palmerston North, New Zealand, m.tuohy@massey.ac.nz

Ele Vahtmäe Estonian Marine Institute, Tartu University, Tallinn 12618, Estonia, ele.vahtmae@sea.ee

L. Vescovo Centre for Alpine Ecology, Viote del Monte Bondone, Trento 38040, Italy, vescovo@cealp.it

A. Walker ACT Emergency Services Agency, Curtin, ACT 2605, Australia, Alan.Walker@act.gov.au

J. Wallace CSIRO Mathematical and Information Sciences, Wembley 6913, Western Australia

S. Wilkes PyroLogica, Palmerston, ACT 2913, Australia, stephenw@tsn.cc

D.L. Williams NASA/ Goddard Space Flight Center, Greenbelt, MD 20771, darrel.l.williams@nasa.gov

M.C. Willmott Space Based Observations Section, Bureau of Meteorology, Melbourne, VIC 3001, Australia, m.willmott@bom.gov.au

Christian Witte Queensland Department of Natural Resources and Water, Remote Sensing Centre, Indooroopilly, QLD 4068, Australia

J.C.Z. Woinarski Natural Resources, Environment, The Arts and Sport, Northern Territory Government, Darwin, NT, Australia

X. Wu CSIRO Mathematical and Information Sciences, Wembley, 6913, Western Australia

A. Zerger CSIRO Sustainable Ecosystems, Canberra, ACT, Australia, Andre.Zerger@csiro.au

Reyer Zwiggelaar Aberystwyth University, Aberystwyth, SY23 3DB, UK

Introduction: Visualising Uncertainty in Environmental Data

K.J. Reinke and S.D. Jones

Abstract The ever-increasing use of spatial data in environmental applications and studies, coupled with the rapidly growing number of datasets available, the need for effective tools that enable users to manage issues of uncertainty is vital. This paper focuses on the visualisation of attribute uncertainty as a critical step in enabling users to assess the suitability of the data for the intended application and better understand the potential limitations of their data and subsequent outputs. For policy-makers and natural resource managers whose decisions depend on spatial information, the consequences can be severe if that data is erroneous or misused.

This paper explores some of the representation issues that exist with environmental data and reviews the different ways of describing and visualising uncertainty. The review progresses from examining standard visual variables through to more advanced, but common, static techniques such as the third dimension. The purpose of this paper is to identify and review some common representation and communication methods available for visualising spatial data uncertainty. Emphasis is directed to those examples that relate specifically to issues of uncertainty that commonly occur in environmental information and which have been sourced from imaging based technologies such as satellite remote sensing. This review is important, since it is needed to provide the link between attribute uncertainty and its implementation in software that will correctly communicate its meaning to users. Many methods exist for presenting spatial data quality and information to users. Traditionally this has usually been done using paper maps. However, the availability and development of new digital techniques has increased the ways in which such data can be portrayed. Such advances have allowed users to better explore their data and, hence, foster a better understanding of the problem at hand.

K.J. Reinke (✉)

School of Mathematics and Geospatial Science, RMIT University, Melbourne, VIC, Australia
e-mail: karin.reinke@rmit.edu.au

Introduction

Describing Uncertainty in Environmental Data

Attribute uncertainty refers specifically to the thematic content of the data and is fundamental to any type of environmental information. The thematic domain provides information about what occurs at different locations in the data. Often the attributes, which are the relevant properties of entities in the real world, are collected and organised into themes or layers. An attribute is usually considered to be a textual or numerical description of a defined location. The method by which environmental data are collected and/or represented plays an important role in understanding attribute uncertainty. In some instances, what is to be collected is relatively straightforward such as recording the spectral signature from remotely sensed imagery, the pH of a stream or the number of species per hectare. Yet, in many other situations it is defining what is to be collected and how these should be organised that is the source of uncertainty.

Most definitions of attribute uncertainty hinge around the notion of how closely the attribute data represents the truth, or what is accepted to be truth. In other words, the attribute in the dataset should correspond to what is found at the same location in the real world. However, this definition is considered too general when assigning visualisation techniques. Table 1 breaks down attribute uncertainty into five elements and meanings based on existing spatial data quality standards (ANZLIC 2007) and previous work by Beard (1997).

Attribute uncertainty in the data can be affected by each of the parameters described in Table 1. With some parameters, as in the case of resolution, completeness and accuracy, they may be strongly connected particularly in environmental data sourced from satellite remote sensing. Resolution clearly influences the level of accuracy and degree of completeness in the data.

The quality indicators and quality measures for attribute accuracy fall into two general groups, depending on the level of measurement of the attribute (Chrisman 1991). Attributes that use continuous measures (for example, interval/ratio) usually express accuracy by the standard deviation (σ) or the Root Mean Square Error (RMSE). Some attributes of this nature, such as elevation, can adopt the same accuracy tests used to determine positional accuracy (Chrisman 1991). The other group of attributes are those with non-quantitative or discrete values, such as categorical data. For this type of data it is difficult to calculate metric differences, although fuzzy set theory may give degrees of similarity. Sometimes as Woodcock and Gopal (2000) and others (e.g. Bordogna et al. 2006) explain, a linguistic rating system such as absolutely right, good answer, reasonable, understandable but wrong and absolutely wrong may be used to indicate accuracy. Yet generally the accuracy measurements assigned to categorical data include Percentage Correctly Classified (PCC), Overall Accuracy (OA), Kappa (κ), producer's accuracy and consumer's accuracy. Most of these indices are derived from a misclassification matrix (Veregin and Haragitai 1995) and are useful for assessing overall attribute accuracy (Veregin

Table 1 An overview of the quality parameters that affect the thematic domain in spatial information

| Parameter | Description |
|--------------|--|
| Accuracy | Attribute accuracy refers to the attribute in the dataset, and how closely the attribute corresponds to what is considered to be the truth at that location. |
| Resolution | Attribute resolution is dependent on the measurement scale of the attribute. For categorical data, resolution describes the fineness (or coarseness) of category definitions. For quantitative data, resolution is the precision of the measurements discernable in the data. |
| Consistency | Attribute consistency refers to the validity of the relationships between attributes. Attribute consistency can also describe the appropriateness of the logic associated with the attribute collection and definition method. Internal attribute consistency refers to the compliance of values with attribute codes and definitions and external attribute consistency refers to the logic and repeatability of attribute definitions and attribution methods. |
| Completeness | Attribute completeness describes the completeness to which the attributes collected match the intended model. It can include errors of omission where the attribute list does not account for all attributes, and commission where the attribute list contains attributes that do not belong. Completeness is affected by the sampling scheme, and in remote sensing by the atmospheric conditions in the scene (e.g. cloud cover). |
| Lineage | Attribute lineage provides a description on the attribute content of the data, who collected the data, the instruments used and the processes applied. Attribute lineage is not a true quality parameter because it is not an implicit characteristic of the data. |

1998). A measure produced by stochastic simulations (for example, Monte Carlo method) uses an error model to generate equally possible but simulated outcomes of the data. The measure is termed ‘realisations of the error model’ (Goodchild 1995) and is suitable for both continuous and discrete attributes.

Representing Environmental Data as a Source of Uncertainty

Research to date into attribute data uncertainty has concentrated primarily on the uncertainty generated from conversion between raster and vector structures, the misclassification of areal units and the uncertainty resulting from overlaying categorical datasets. Despite progress in these areas, the visualisation and communication of attribute uncertainty in environmental data is still of concern. Indeed, some of the sources of uncertainty stem from inappropriate methods of data representation, an issue that has been in existence since the creation of maps. The issue is more fundamental than the intentional or unintentional misuse of visualisation methods because it lies within the very nature of data itself. The problem surrounds the lack of commonly available categorical representations for entities that are ill-defined and not uniform in properties or type across that area. The same can also be applied to

how actual uncertainty measures associated with the data are visualised. The problem is compounded by human tendencies to generalise and classify the world into orderly and unnatural arrangements. There are, of course, entities that occur as crisp boundaries and/or homogenous units, many which can be found in the manufactured world, such as building footprints or road networks. Other discrete features are artificial constructs that do not exist in reality but exist in the social and digital realm such as the cadastre of a city, or a national park boundary. However, for those entities that do not fall naturally within easily defined spatial, temporal or thematic limits, they pose representational dilemmas.

Broadly, it is possible to define two types of representational uncertainty in environmental data of which many examples may be found in Wu et al. (2006), Hunsaker et al. (2001) and Couclelis (1996). The first may be termed category uncertainty (Edwards 1994) which is the degree of uniformity or purity of a feature's properties. The second may be termed as boundary uncertainty (Edwards 1994) which concerns the positioning and representation of ill-defined boundaries. Both are a function of scale (or resolution). If the scale is fine enough, then theoretically, diversity in the class should not occur and without diversity the cut-off between properties becomes discrete. However, to work at such a scale is simply impractical. In the same way that scale can eliminate the problem the reverse is also true. Some natural phenomena continue (for example, coastline) to vary spatially at all scales, as illustrated by work with fractals (Mandelbrot 1982 and Burrough 1986). It is not uncommon for diversity in class and boundary definitions to influence and exacerbate the problem in each other, as they are not always mutually exclusive.

Category Uncertainty

The definition and classification of environmental attributes, and how they are collected, can sometimes be vague or ambiguous. This issue is one of attribute accuracy; whether a location in the dataset has been allocated the correct properties. This is dependent on many factors including the intended use of a map, the mapping conventions adopted and the nature of the phenomenon itself (Aspinall and Pearson 1995). There is the underlying philosophical argument tied to scale because at some scale the meaning of an attribute can fall apart. For example, the concept of 'forest' can become meaningless at a sufficiently large scale. It becomes a case of not *seeing the forest for the trees*. Other class identification problems are based on how the group is defined. Unless stringent criteria are provided for each group, the allocation of space into each class may differ between people, or classes may appear ambiguous. It is not unusual for the observers or data collectors to disagree or produce different interpretations (Edwards 1994).

Categorical map units seldom represent homogenous areas, particularly for the classic example of soil polygons. It is more typical for an area to exhibit multiple characteristics of differing amounts rather than one uniform characteristic. Such data are considered to be internally heterogeneous (Aspinall and Pearson 1994). However, the degree to which the feature describes what is taken to be the truth in traditional GIS is either a definite yes or no. As an example, the vegetation type

is either open woodland or it is not. Categorical data suffer the most of all data types from this type of problem. Depending on the resolution of the classes used and on the data type, it can impact on the severity of this problem. While more general categories are likely to contain less attribute inaccuracy, they are more likely to be prone to heterogeneity within classes. The reverse also applies that whilst more specific classes are less prone to heterogeneity, they are more likely to contain attribute inaccuracy because the chance of correct classification has decreased. As described previously, there are methods of measuring this (for example, misclassification matrix) and whilst the information about the purity of the map or class units is often recorded in reports (Fisher 1991) it is rarely incorporated or stored with the digital data.

The question here, therefore, is how to represent this type of information? Methods are available for identifying the uncertainty in categorical coverages that arises from the purity of the classification and error models have been developed by applying stochastic processes to describe class membership and within-class inclusions (Wu et al. 2006, Hunsaker et al. 2001 and Goodchild 1992). Goovaerts (1997) believes that categorical uncertainty can be addressed using the indicator approach from geostatistics. But before these methods can become fully general and available to GIS users, Unwin (1995) believes that it will be necessary to be able to handle entities that are themselves fuzzy. The portrayal of category uncertainty has focussed on utilising animation techniques. Fisher (1993) used animation to visualise the uncertainty as multiple realisations were calculated. Little work has been done evaluating the effectiveness of such displays, and even fewer examples of static displays of category uncertainty can be found.

Boundary Uncertainty

The representation of feature boundaries attempts to delineate areas of different kinds. Representation is simple for sharply defined features, but how can the change between categories that are less exact be adequately represented? Where the transition zone between classes is abrupt it can be represented by a sharp line but where the transition zone is smooth, it is much more difficult to represent, particularly when the transition may not have a linear function of change. This is a commonly observed phenomenon within the natural world and such locations are formally described as ecotones or environmental gradients.

Representation of the transition zone depends on the adjacency behaviour or relationships between classes. For example, the change between Class A and Class B might be gradual over a small distance but between Class A and Class C, the change might be over a much larger distance. It could even favour a particular class so the change occurs more rapidly as Class A is approached. Burrough (1986) describes the transitions as being characterised by either sharp, large or trend-based changes. It requires knowledge about the spatial relationships shared between the attributes and how these can be stored as part of the database. Providing this type of information would assist in creating appropriate representations such as the use of transiograms (Li 2007).

Burrough (1986) defines three kinds of boundaries associated with soil mapping. These are abrupt boundaries, boundaries that divide a trend and boundaries resulting from sampling variation. Abrupt boundaries are where large changes in soil properties occur over short distances. Boundaries that divide a trend are used to group continuous data into discrete classes, and this is a common trait of choropleth maps. The final boundary type is created from sampling variation. It results from two similar observations being classified differently simply because they fall outside a certain class cut-off. This is a function of the binary nature of maps, which does not allow for the fuzzy nature characterised by some natural phenomena. In recognition of this, some researchers (for example, Chen 2002, Edwards and Lowell 1996 and Zhu 1996) have suggested the use of fuzzy logic to better describe boundaries between polygons.

Typically, boundary uncertainty has been represented by using the epsilon band and different distribution functions can be used to locate the boundary within the band (Aspinall and Pearson 1994). Edwards (1994) presents three different modes of presenting boundary uncertainty generated from a number of independent interpretations. The first provides all interpretations on the one map, the second presents a solid buffer for the full set of interpretations and the third uses a solid buffer plus a skeleton of the 'average' boundaries (Edwards 1994). Couclelis (1996) lists fuzzy boundaries, fractal boundaries, multiple boundaries, movable boundaries (animation), ad hoc boundaries, flashing boundaries, probability surfaces, buffer zones, bands, colour gradations, aural signals, textual warnings, multiple representations (multiple windows) as some of the available visualisation methods. However, the candidate stresses that there is a need for evaluating these types of displays against the different types of boundary uncertainty before they can be confidently applied.

Visualisation Methods

Methods for Visualising Environmental Uncertainty

The most common form of attribute uncertainty is attribute accuracy. It is the difference between the thematic value of data compared to that accepted as the truth or real world at the location at which the attribute was observed. Leitner and Battenfield (1997 and 2000) report attribute accuracy to be defined as the discrepancy in categorisation or the probability of misclassification. There are two main approaches to attribute accuracy: firstly, looking at the actual attribute accuracy measurements, and secondly, how the original values vary according to their attribute accuracy.

The application of the visual variables (Bertin 1967) to attribute accuracy has depended on mapping the visual variable to the scale of measurement (after Stevens 1946) for a particular attribute accuracy parameter. From this, it could be proposed that size and value are useful for portraying quantitative uncertainty values and orientation, shape, hue and texture useful for nominal uncertainty measurements. With

the exception of texture, MacEachren (1992) proposes the same visual variables of uncertainty visualisation. Van der Wel et al. (1994) specifically associates hue, size, texture, value and saturation for the display of attribute accuracy. Jaakkola (1996) suggests hue for qualitative data and saturation or intensity for quantitative data based on the theory of graphics. Clapham and Beard (1991) used size to increase the area of a symbol proportionately to the ratio measurement of the attribute accuracy and suggested discrete color variables to be used to represent nominal quality measurements. Buttenfield (2001) uses a more detailed definition that includes the data type of the attribute accuracy that links texture and saturation, hue and texture, and saturation and point gradients to discrete, categorical and continuous data respectively. Kurtener and Badenko (2001) and MacEachren (1992) employ color saturation as the most logical visual variable for portraying uncertainty where pure hue indicates high certainty and unsaturated hue is equated to low certainty. This is in contrast with Buttenfield and Beard (1994) who found that users had trouble associating color saturation with quality. With the exception of saturation, it appears that there is a consensus about the likely mapping of visual variables to attribute accuracy. However, empirical testing is required to validate these assumptions.

Empirical research has already been initiated in this area (for example, Aerts et al. 2003). In addition, Leitner and Buttenfield (1997 2000) investigated the degree to which value, saturation and texture when used to portray attribute accuracy influenced the confidence, correctness and timing in a decision making exercise. It was found that lighter values represented lower attribute accuracy measurement. Almost as effective in representing attribute accuracy was texture with finer textures being interpreted as low uncertainty and coarse textures as high uncertainty. It was concluded that these two variables were useful for assisting correct decisions whereas certainty maps that used saturation, where greater saturation implied greater certainty, improved decision response times. MacEachren et al. (1998) also found texture useful when embedded in a choropleth map that used value for representing attribute data. It was found that users were able to recognise unreliable (ratio) data and still perform map reading tasks associated with the actual data such as pattern recognition. This is in contradiction with what is expected from the accepted application of the visual variables but the experiment may have been limited to locating the attribute uncertainty.

Arising from investigations into the visualisation of uncertainty, and made possible through advancements in computer graphic technologies, MacEachren (1995) suggests further additions to Bertin's visual variables. They are essential variations in focus that MacEachren (1995) terms clarity and are useful methods for creating graphical ambiguity. It is suggested there are three states of clarity evolving from initial studies into focus by MacEachren (1992). They include:

- **Crispness.** This visual variable deals with the sharpness of map features. Details on the map may be de-focused by the spatial filtering of the edges (that is, contour crispness), internal fill (fill clarity) or both. The greater the visual fuzziness or fading of the feature, the greater the associated uncertainty. This can be applied

to all data types. McGranaghan (1993) believes crispness can portray qualitative, and most likely, quantitative information.

- Resolution. This visual variable shows change in spatial precision (for example, display size or grid size) and is concerned with the geometry of the object rather than its attributes. It is similar to texture and can produce the impression of zooming in and out.
- Transparency. This visual variable employs effects that are representative of fog or cloud. MacEachren et al. identified fog as having intuitive appeal for representing data reliability by obscuring uncertain map objects with fog. The degree of visual ambiguity is implied by the amount of fog present. Bastin et al. (1999) used tiny clouds to surround certain values in graphs to imply vagueness.

Plewe (1997) applied these new visual variables for portraying the uncertainty surrounding heterogeneous classes and uncertain class boundaries. Hansen (1998) used crispness to qualitatively display the fuzziness between non-discrete feature boundaries. Plewe (1997) Aspinall and Pearson (1994) and Edwards (1994) used resolution, specifically line thickness, to portray transitional boundaries between classes. Both methods suggest uncertainty about the boundary but provide no detail about the magnitude of that uncertainty or transitions in much the same way as dashed lines indicate inferred boundaries in geological maps.

Symbol presence or absence (McGranaghan 1993) has also been added to the list of visual variables. Its usefulness as a communication tool increases when driven by user interaction or thresholding (Reinke et al. 2006). In a fuzzy context, they serve as the extreme endpoints for the gradual degrading of features in applications of clarity. In other words, the object continually fades by varying the saturation of the background and symbols in the display until the object disappears from view. Clarke and Teague (2000) observe that fading is particularly suited to attribute uncertainty. The use of presence/absence as a visualisation technique relies on animation (McGranaghan 1993) and user interaction. Often the complete benefit of a single visual variable cannot be realised and it may prove fruitful where the variable is used in conjunction with another variable or display technique. For example, Leitner and Buttenfield (1997) found color saturation and focus useful for depicting uncertainty.

The visual variables that make up color are considered to be useful for bivariate mappings of uncertainty and spatial data. Hunter and Goodchild (1996) found hue (used to portray the data) and saturation (used to portray the uncertainty) to be a useful combination, usually with strong colors having high quality and pale colors having low quality. Color ramps that vary continuously or as discrete hues across transitional zones can also indicate ambiguity at boundaries (McGranaghan 1993). Clarke and Teague (2000) support this, finding brighter colors indicate less uncertainty. Color guidelines by Brewer (1999) have shown how color in bivariate mapping can be successfully applied. However, other empirical investigations have suggested that the use of color characteristics to simultaneously represent the data and the attribute accuracy generally caused users to have difficulty in distinguishing between them (MacEachren et al. 1998 and MacEachren 1995).

Digital imaging technology has enabled color transformations between red, green, blue (RGB) systems and their hue, value (or intensity) and saturation (HVS), hue, lightness and saturation (HLS), cyan, magenta and yellow (CMY) components. Hue is used to convey nominal data, together with value and/or saturation to convey quality information (Van der Wel et al. 1994). The quality information becomes embedded within the attribute information upon conversion from the HVS components back to RGB creating a bivariate map (for example, Jiang et al. 1995). Whilst Clarke and Teague (1998) and Jiang et al. (1995) both used HVS systems for representing uncertainty, the increase in complexity should not be overlooked (Van der Wel et al. 1994). In contrast, Schweizer and Goodchild (1992) observed no intuitive association between data quality and value. Once value and saturation have been re-transformed into the RGB system, there is no concept by the user of uncertainty as a linear progression

Other types of bivariate mapping exist apart from changing color characteristics. By applying line thickness to isolines, Beard and Mackaness (1993) were able to convey both actual data and reliability simultaneously. Another type of bivariate mapping employed hue to represent the actual data and opacity or size to depict the uncertainty (Drecki 1999, 2000). The first method uses low opacity to refer to low reliability and high opacity to refer to high reliability of a classified satellite image. The second method used the variable size to communicate the classification accuracy. Each pixel or cell was represented by a single square symbol (of a particular hue) its size being dependant upon the level of uncertainty. The maximum size was equal to pixel size and indicated no uncertainty. Smaller squares indicated poor quality. Thus, an area on the map that was of poor quality would be mostly absent of color and usually 'filled-in' with.

The use of the third dimension is another accepted method for portraying the magnitude of attribute uncertainty. It is particularly useful because when used in true 3D it allows the attribute component of the data to be shown in conjunction with the associated uncertainty. This method is well suited to continuous environmental data (e.g. temperature) as it allows the attribute component to be draped over the continuous landscape. Van der Wel et al. (1994) and Fisher (1992) use high *z* values to indicate areas that have high levels of uncertainty. Thus, plateaus indicate uniform accuracy, elevated peaks indicate areas of poor accuracy and low elevation indicate areas of good accuracy. Kraak (1994) contemplates both the positive and negative implications of allowing users to interactively exaggerate the uncertainty (*x*) axis as is available in many 3D modules of current GIS. Uncertainty relief maps can also be created using shading effects to achieve realistic 3D visualisations.

The use of perspective is not immune to interpretation problems because of distortion and obscurity problems associated with displaying a 3D image on a 2D screen. Thus, users can have trouble gathering useful information from them. To counteract this researchers (for example, Bastin et al. 1999) use linked plans and contour maps to preserve all information.

The methods used to visualise attribute accuracy are often a function of scale or resolution of the data. Visualising attribute accuracy specifically refers to the resolution of the data, whereas attribute accuracy can vary according the resolution

of the data. This is because of resolution requirements of the application. As such, attribute resolution is critical to map users. Attribute accuracy is only affected where the resolution is lower than the required scale. In such circumstances, this needs to be visualised appropriately. Attribute resolution refers to the smallest attribute unit, which can be observed. For discrete attributes, resolution refers to the number of categories, ranges or ranked classes. For continuous attributes, resolution is the equivalent of spatial resolution as resolution relates to the smallest unit able to be observed or represented and the precision of the measuring instrument. For remotely sensed data, this relates to the spectral and radiometric resolution of the sensor on board the satellite. In addition, to capture scale or resolution, the display scale will affect the size of the features (MacEachren 1995).

Traditionally, map scale was reported in one of three ways (Monmonier 1996). The first as a ratio scale (for example, 1:50,000), the second as a verbal scale (for example, one centimetre represents one kilometre) and the third as a graphic scale (for example, scale bars). The most effective method is the graphic scale because enlarging or reducing the map subsequently results in the graphic scale also being enlarged or reduced. However, with the advent of digital technologies, ratio and verbal scales are updated on the fly as the user zooms in or out of the display (for example, ArcGIS 9). The replacement or addition of a graphic scale would nevertheless be considered an improvement because of the ease of understanding they offer over ratio and verbal scales. This still only considers scale in terms of the display scale rather than providing information about the capture scale for the data. Source scale becomes important particularly where multiple datasets are being utilised. In a display context, ESRI's ArcGIS 9 product provides user control over the maximum and minimum scales a dataset may be shown. As a minimum, source scale information should be readily available to the user. In a sense, resolution is a part of the lineage accompanying the data. This merely emphasises the need for lineage to be an accessible adjunct to the data.

As stated previously, information often consists of multiresolution data. That is, the resolution of the data is not homogenous. To convey this variation, the presence/absence variable could be used such that when a user zooms in beyond a certain scale features visually disappear or appear as provided in the display thresholding of ArcGIS 9. Similarly, feature resolution or crispness (MacEachren 1995) for discrete objects could also be applied in conjunction with zooming facilities. Other display techniques could use multi-legends to illustrate the changes in source scale of the data. Because scale is a ratio, the visual variables of value but less so size because of the impact on the geometric resolution could be applied to depict differences in conjunction with a legend. An approach to show spatial variation in source scale for multinomial or continuous features would be to superimpose a grid where each grid cell size is representative of the source scale. Johnson (1995) introduced metapictures for satellite data as thumbnails of the data that communicated summary information including the resolution of the data. Part of an image is shown at full resolution as a thumbnail to convey resolution information.

Beard's (1997) definition of resolution separated discrete and continuous data into the number of classes and precision of the measuring instruments. It is possible

to extend this definition to include information about class homogeneity and, in the case of interpolated continuous values, the number of sites used during the interpolation process. Both additional examples can be considered a type of attribute resolution tied in closely to lineage (and subsequently accuracy). Most of this information may be documented within the lineage report; however, information such as site locations used in the interpolation may be more appropriately communicated to the user using map form to indicate spatial distribution. For example, Stephan (1995) provides an additional window to the display that shows the distribution of sampling stations in conjunction with the interpolated data. Likewise Beard and Mackaness (1993) showed the location of sample points as a simple method of visualising the reliability of the interpolated values allowing the user to toggle-on and toggle-off point locations. They further observe that it would be possible to graphically code the sample points according to lineage information providing the user with even more uncertainty information by which to assess the quality of the output interpolation.

Attribute resolution involves more than just the geometric scale at which the data was captured. It is equally as important to describe the details of the classifications and measurements. Many GIS provide the ability to interactively manipulate the range and classification of data. In other words, users may adjust the attribute resolution of data to coarser resolutions or classify continuous data. Increasing user control in data manipulation suggests that knowledge about the original attribute resolution would be useful for making classification decisions. In particular, attribute resolution, which is linked to class homogeneity, can be vital in assessing the fitness-for-use of data. Such an example can be found in soil data types where the type of inclusions and/or rate of change across the boundary that occur about a soil polygon is of the utmost importance. Attribute resolution is a way of assessing the suitability of a classification.

A variety of methods have been used to portray boundary and class accuracy when it is actually resolution that is being represented. Although, the distinction between resolution and accuracy is usually difficult to make as accuracy is partially a function of scale. There is considerable research dedicated to improving ways of recording and subsequently representing continuous or heterogeneous data. The most common approach to date appears to be fuzzy memberships. While this information can improve the fineness of classes, the attribute resolution information must still be available to the user. Where traditional discrete categories were relatively easy to report, fuzzy memberships may involve several values at the class or individual feature level. These are usually available in the form of matrices but alone do not provide information about their spatial distribution. In this sense, resolution may be considered internal class resolution (that is, homogeneity) and between class resolution (that is, boundary uncertainty). Hunter and Goodchild (1996) cite work whereby the description of homogeneity variation is communicated using variability diagrams. The value of these approaches is that resolution is shown implicitly rather than explicitly. As such the user is simultaneously viewing the data and its resolution.

Summary

This paper serves as a review by which to begin classifying visualisation techniques and assigning them to different uncertainty elements found in environmental data. It was suggested that key elements of attribute uncertainty should include accuracy, resolution, consistency, completeness and lineage. Although it was generally found that measures were supplied for attribute accuracy and resolution only. It also is apparent that the representation of the data itself could be a source of attribute uncertainty, particularly for features that had poorly defined boundaries and non-homogenous characteristics. How the data occurs as a natural phenomena, how this is arranged in a spatial framework and the levels of measurement for the attributes are all important considerations when choosing a representation for attribute uncertainty.

Different strategies may be used to assign different symbolisation and visualisation techniques to environmental data. Those employed vary depending on the phenomena being mapped and the level of measurement. Developments in computer graphics have improved ease of use and opened up new ways in which the traditional visual variables are used, as well as creating new visualisation methods entirely. This progress, coupled with advances in understanding the human cognitive and perceptual responses to these types of displays, will continue to promote the emergence of new types of representation of environmental data and information.

Acknowledgements This research was funded by the Australian Research Council under the supervision of Associate Professor Gary Hunter.

References

- Aerts, J. C. J. H., Clarke, K. C. and Keuper, A. D. (2003) Testing Popular Visualization Techniques for Representing Model Uncertainty. *Cartography and Geographic Information Science*, 30, 249–261.
- ANZLIC (2007) Metadata Profile Guidelines Version 1.0.
- Aspinall, R. J. and Pearson, D. M. (1994) A Method for Describing Data Quality for Categorical Maps in GIS. *Fifth European Conference on Geographic Information Systems*. Paris.
- Aspinall, R. J. and Pearson, D. M. (1995) Describing and Managing Uncertainty of Categorical Maps in GIS. In Fisher, P. (Ed.) *Innovations in GIS2*. London, Taylor and Francis.
- Bastin, L., Wood, J. and Fisher, P. F. (1999) Visualisation of Fuzzy Spatial Information in Spatial Decision Making. In Lowell, K. and Jaton, A. (Eds.) *Spatial Accuracy Assessment: Land Information Uncertainty in Natural Resources*. Michigan, Ann Arbor Press.
- Beard, K. (1997) Representations of Data Quality. In Craglia, M. and Couclelis, H. (Eds.) *Geographic Information Research: Bridging the Atlantic*. London, Taylor and Francis.
- Beard, K. and Mackaness, W. (1993) Visual Access to Data Quality in Geographic Information Systems. *Cartographica*, 30, 37–45.
- Bertin, J. (1967) *Semiology of Graphics: Diagrams, Networks, Maps*, Madison, The University of Wisconsin Press.
- Bordogna, G., Chiesa, S. and Geneletti, D. (2006) Linguistic Modeling of Imperfect Spatial Information as a Basis for Simplifying Spatial Analysis. *Information Sciences*, 176, 366–389.
- Brewer, C. A. (1999) Color Use Guidelines for Data Representation. *Section of Statistical Graphics, American Statistical Association*. Alexandria.

- Burrough, P. A. (1986) *Principles of Geographical Information Systems for Land Resources Assessment*, Oxford, Oxford University Press.
- Buttenfield, B. (2001) Mapping Ecological Uncertainty. In Hunsaker, C., Goodchild, M. F., Friedl, M. and Case, T. (Eds.) *Uncertainty in Spatial Data for Ecological Analysis*. New York, Springer-Verlag.
- Buttenfield, B. and Beard, K. M. (1994) Graphical and Geographical Components of Data Quality. In Hearnshaw, H. M. and Unwin, D. J. (Eds.) *Visualization in Geographical Information Systems*. Belhaven, Wiley and Sons.
- Chen, T. (2002) Fuzzy Objects: Their Changes and Uncertainties. *Journal of Photogrammetric Engineering and Remote Sensing*, 68, 41–49.
- Chrisman, N. (1991) The Error Component in Spatial Data. In Maguire, D. J., Goodchild, M. F. and Longman, D. W. (Eds.) *Geographical Information Systems: Principles and Applications*, 1, 165–174.
- Clapham, S. B. and Beard, K. (1991) The Development of an Initial Framework for the Visualization of Spatial Data Quality. *Proceedings of AUTO-CARTO 10*. Baltimore.
- Clarke, K. C. and Teague, P. D. (1998) Cartographic Symbolization of Uncertainty. *Proceedings of the 4th International Symposium on Spatial Accuracy Assessment in Natural Resources and Environmental Sciences*. Amsterdam, 109–116.
- Clarke, K. C. and Teague, P. D. (2000) Representation of Cartographic Uncertainty Using Virtual Environments. *Proceedings of the 4th International Symposium on Spatial Accuracy Assessment in Natural Resources and Environmental Sciences*. Amsterdam.
- Couclelis, H. (1996) Towards an Operational Typology of Geographic Entities with Ill-Defined Boundaries. In Burrough, P. A. and Frank, A. U. (Eds.) *Geographic Objects with Indeterminate Boundaries*. London, Taylor and Francis.
- Couclelis, H. (2003) The Certainty of Uncertainty. *Transactions in GIS*, 7, 165–175.
- Drecki, I. (1999) Visualization of Uncertainty in Geographic Data. *Proceedings of the International Symposium on Spatial Data Quality*. Hong Kong.
- Drecki, I. (2000) New Techniques in Visualizing Uncertainty. *Measure and Map*, 32–34.
- Edwards, G. (1994) Characterising and Maintaining Polygons with Fuzzy Boundaries in Geographic Systems. *Proceedings of the Sixth International Symposium on Spatial Data Handling*. Edinburgh, Taylor and Francis.
- Edwards, G. and Lowell, K. (1996) Modeling Uncertainty in Photointerpreted Boundaries. *Journal of Photogrammetric Engineering and Remote Sensing*, 62, 337–391.
- Fisher, P. (1991) Modeling Soil Map Inclusions by Monte Carlo Simulation. *International Journal of Geographic Information Systems*, 5, 193–208.
- Fisher, P. F. (1992) First Experiments in Viewshed Uncertainty: Simulating Fuzzy Viewsheds. *Journal of Photogrammetric Engineering and Remote Sensing*, 58, 345–352.
- Fisher, P. F. (1993) Visualizing Uncertainty in Soil Maps by Animation. *Cartographica*, 30(2), 20–27.
- Goodchild, M. F. (1992) Geographical Data Modeling. *Computers and Geosciences*, 18, 401–408.
- Goodchild, M. F. (1995) Attribute Accuracy. In Guptill, S. and Morrison, J. (Eds.) *Elements of Spatial Data Quality*. Oxford, Elsevier Science.
- Goovaerts, P. (1997) *Geostatistics for Natural Resources Evaluation*, New York, Oxford University Press.
- Hansen, D. T. (1998) Modeling Uncertainty in Spatial Location using ArcInfo. *Proceedings of the 18th Annual ESRI International User Conference*, San Diego, CD-ROM.
- Hunsaker, C. T., Goodchild, M. F., Friedl, M. and Case, T. (Eds.) (2001) *Spatial Uncertainty in Ecology: Implications for Remote Sensing and GIS Applications*, New York, Springer-Verlag.
- Hunter, G. J. and Goodchild, M. F. (1996) Communicating Uncertainty in Spatial Databases. *Transactions in GIS*, 1(1), 13–24.
- Jaakkola, O. (1996) Visualization of the Uncertainty of Land Cover Data. In Konecny, M. and Brno, M. *Conference Proceedings of GIS Frontiers in Business and Science*. Czech Republic, 33–47.

- Jiang, B., Brown, A. and Ormeling, F. J. (1995) Visualization of Uncertainty with a Fuzzy Color System. *Proceedings of the 17th International Cartographic Conference*. Barcelona.
- Johnson, D. B. (1995) Metapictures - Graphic Metadata Elements. *Australasian Urban and Regional Information Systems Association Incorporated*. Melbourne.
- Kraak, J. (1994) Interactive Modelling Environment for Three-Dimensional Maps: Functionality and Interface Issues. In Maceachren, M. and Taylor, D. R. F. (Eds.) *Visualisation in Modern Cartography*. Oxford, Elsevier.
- Kurtener, D. and Badenko, V. (2001) GIS Fuzzy Algorithm for Estimating the Quality of Soil Parameters: Evaluation of Attribute Data Quality. *GIM International*, March, Vol. 15, 76–79.
- Leitner, M. and Bittenfield, B. (1997) Cartographic Guidelines on the Visualization of Attribute Accuracy. *Proceedings of AUTO-CARTO 13*. Seattle.
- Leitner, M. and Bittenfield, B. P. (2000) Guidelines for the Display of Attribute Certainty. *Cartography and Geographic Information Science*, 27, 3–14.
- Li, W. (2007) Transiograms for Characterizing Spatial Variability of Soil Classes. *Soil Science Society of America Journal*, 71, 881–893.
- Maceachren, A. M. (1992) Visualizing Uncertain Information. *Cartographic Perspectives*, 13, 10–19.
- Maceachren, A. M. (1995) *How Maps Work: Representation, Visualization and Design*, New York, Guilford Press.
- Maceachren, A. M., Brewer, C. A. and Pickle, L. W. (1998) Visualizing Georeferenced Data: Representing Reliability of Health Statistics. *Environment and Planning A*, 30, 1547–1561.
- Maceachren, A. M., Robinson, A., Hopper, S., Gardner, S., Murray, R., Gahegan, M. and Hetzler, E. (2005) Visualizing Geospatial Information Uncertainty: What We Know and What We Need to Know. *Cartography and Geographic Information Science*, 32, 139–160.
- Mandelbrot, B. B. (1982) *The Fractal Geometry of Nature*, San Francisco, Freeman.
- Mcgranaghan, M. (1993) A Cartographic View of Spatial Data Quality. *Cartographica*, 30, 8–19.
- Monmonier, M. (1996) *How to Lie With Maps*, Chicago, University of Chicago Press.
- Plewe, B. (1997) The Cartographic Representation of Gradation: Fuzzy Maps from Fuzzy Data. *Proceedings of AUTO-CARTO 13*. Seattle.
- Reinke, K. J., Jones, S. D. and Hunter, G. J. (2006) Implementation of a Prototype Toolbox for Communicating Spatial Data Quality and Uncertainty Using a Wildfire Risk Example. In Riedl, A., Kainz, W. and Elmes, G. (Eds.) *Progress in Spatial Data Handling*. Berlin, Springer-Verlag.
- Stephan, E. M. (1995) Exploratory Data Visualization for Reliable Integration. *Proceedings of AUTO-CARTO 12*. Charlotte.
- Stevens, S. (1946) On the Theory of Scales of Measurement. *Science*, 103, 677–680.
- Unwin, D. J. (1995) Geographical Information Systems and the Problem of Error and Uncertainty. *Progress in Human Geography*, 19, 549–558.
- Veregin, H. (1998) Data Quality Measurement and Assessment.
- Veregin, H. and Hargitai, P. (1995) An Evaluation Matrix for Geographic Data Quality. In Guptill, S. and Morrison, J. (Eds.) *Elements of Spatial Data Quality*. Oxford, Elsevier Science.
- Van der Wel, F. J. M., Hootsman, R. M. and Ormeling, F. (1994) Visualization of Data Quality. In Maceachren, A. M. and Taylor, D. R. F. (Eds.) *Visualization in Modern Cartography*. Oxford, Elsevier.
- Woodcock, C. E. and Gopal, S. (2000) Fuzzy Set Theory and Thematic Maps: Accuracy Assessment and Area Estimation. *International Journal of Geographical Information Science*, 14, 153–172.
- Wu, J., Jones, B., Li, H. and Loucks, O. L. (Eds.) (2006) *Scaling and Uncertainty Analysis in Ecology: Methods and Applications*, New York, Springer-Verlag.
- Zhu, A. X. (1996) Generating an Uncertainty Map of Soil Spatial Information. *GIS/LIS Proceedings*. Bethesda.

A Comparison of Pixel- and Object-Level Data Fusion Using Lidar and High-Resolution Imagery for Enhanced Classification

S.S. Ali, P.M. Dare, and S.D. Jones

Abstract Fusion of multisource data is becoming a widely used procedure due to the availability of complementary yet dissimilar datasets. The combined use of high spatial resolution imagery and lidar (light detection and ranging) derived digital surface models (DSM) can reduce interclass confusion in the fusion process. However, pixel-level data fusion does not take spatial information into account. Pixels from multisource images are fused depending on their spectral values, regardless of their neighbour values. Object-level fusion overcomes this shortcoming by segmenting multisource images into meaningful objects and then performing fusion with the information imbedded into their topology. This paper compares the results of the pixel- and object-level fusion of a lidar derived DSM with colour aerial photography and multispectral imagery. The comparison is based on the assessment of the classification accuracy where reference information has been collected through field survey. Pixel-level fusion of the colour photography and the DSM exhibits better results than sole classification of colour photography. The same result is found for the multispectral imagery and the DSM. Object-level fusion achieves superior results compared to all pixel-level classification of tested categories. Object-level fusion of the colour photography and the DSM shows the highest classification accuracy (91%). Multispectral imagery and the lidar derived DSM achieve 90% classification accuracy. These results imply that the high spatial resolution of colour photography has a large influence on the fusion process perhaps greater than the spectral and radiometric resolution of the multispectral imagery.

Introduction

Airborne remote sensing provides valuable data in various forms and scales for mapping and monitoring land cover features. Its use has increased dramatically in recent years due to availability of high-density lidar and high spatial resolution

S.S. Ali (✉)

School of Geography, Population and Environmental Management, Flinders University, Adelaide, SA, Australia

e-mail: syed0009@flinders.edu.au

digital imagery. Hence, greater attention is now being given to the use of multisource data fusion and classification. The underlying assumption is that classification accuracy should improve if additional features are incorporated (Tso and Mather, 2001). Image fusion and subsequent classification can be performed at pixel-, object or feature- and decision-levels (Pohl and van-Genderen, 1998; Schistad-Solberg et al., 1994). Pixel level fusion operates at the lowest processing level, which refers to the merging of measured physical parameters. This fusion is very sensitive to geo-referencing and pixel spacing. The main drawback of this fusion is that a multi-dimensional feature space does not make use of any topological information in the imagery (Blaschke and Strobl, 2001). In the fusion process it is very likely that neighbouring pixels of the source images belong to the same land cover class due to spatial patterns of differing complexity or texture. Thus, the output from pixel-level processing algorithms may possess some uncertainty (Townshend et al., 2000). Object-level image fusion overcomes these difficulties by segmenting multisource images into meaningful multi-pixel objects of various sizes, based on both the spectral and spatial characteristics of groups of pixels. Then the segmented image objects are classified using expert knowledge within a fuzzy logic and hierarchical decision tree (Schiewe et al., 2001). In object-level fusion, a set of geo-referenced data from different sources defines the topology of image objects, and allows these different types of data to be brought together in a concrete local relation. An advantage of this process is that image objects can be extracted from one data layer, and subsequently in the image analysis step those image objects are able to take into account the attributes of the other data layers (Baatz and Schape, 2000). The application of pixel-level fusion and subsequent classification have been showing very unsatisfactory results when applied to high-resolution images (Blaschke et al., 2001; Rego and Koch, 2003). In high-resolution imagery each pixel is related not to the character of object or area as a whole, but to the components of the image. As a result, many more classes are often detected when a classification is performed (Smith et al., 2000).

The overall objective of this research, was to evaluate whether high resolution airborne optical imagery and/or small footprint lidar data could be used as tools, either singularly or in combination, for semi-urban landscape feature extraction. It focused on an agricultural-based semi-urban settlement in southern New South Wales (NSW), considered typical such settlements across large areas of Australia. The study aimed specifically to evaluate the results of the pixel- and object-level fusions used to integrate the information content of the colour aerial photograph with lidar derived DSM and multispectral imagery with lidar derived DSM. The comparison of these two approaches draws upon a quantitative assessment of the quality using statistical, visual and graphical analyses of the results.

Background

Although aerial photography has been used as a mapping tool for a century (Baltsavias, 1999), the fusion of aerial photography and lidar data has only been possible in the past few years due to advances in sensor design and data acquisition

and processing. The following sections therefore provide a brief overview of the different levels of image fusion as well as the different sensor fusion examples.

Imagery and Lidar Data Fusion

Lidar is a recent development in remote sensing with great potential for creating highly accurate DSMs. Three-dimensional point clouds describe the range (distance) of earth surfaces. Lidar provides very accurate position and height information, but less direct information on the object's geometrical shape. High spatial resolution imagery offers very detailed information on objects, including spectral reflectance, texture, and shape metrics. Combining these two kinds of complementary datasets is quite promising for improving land cover mapping (Tao and Yasuoka, 2002). There have been several attempts to fuse lidar and high-resolution imagery for mapping land cover in the past. The idea of exploiting the complementary properties of lidar and aerial imagery was first initiated by Schenk and Csatho (2002) to extract semantically meaningful information from the aggregated data for a more complete surface description. Haala and Brenner (1999) combine a lidar derived DSM with three colour spectral bands of aerial imagery. In this context, the most problematic task is to separate trees from buildings with low-resolution lidar data is greatly facilitated by the presence of a near-infrared band. Rottensteiner et al. (2004) use a lidar derived digital terrain model and the normalised difference vegetation index (NDVI) from multispectral image to detect buildings in densely built-up urban areas.

Pixel- and Object-Level Fusions

The most straightforward approach to deal with the pixel-level image fusion problem is simply to extend the dimension of the data vectors to include each source. This approach is known as the stacked-vector method (Tso and Mather, 2001). Each data vector can be used together as an input to any pixel-based classifier such as *unsupervised* or *supervised* classification. Unsupervised techniques detect clusters of pixels in feature space and categorize the pixels to the clusters based on the minimum distance criterion. Haala and Brenner (1999) apply unsupervised classification based on the ISODATA (Iterative Self-Organizing Data Analysis Technique) algorithm to the three bands of a CIR image and a normalised DSM. In this process, elevation data plays a role in separating different classes but automatic interpretation of the relevant classes is difficult. A rule-based classification scheme was applied to fuse lidar data and multispectral images (Rottensteiner et al., 2004). In this scheme Dempster-Shafer theory had been applied to delineate building regions, combining NDVI and the average relative heights to distinguish buildings from other objects. Mass (1999) applies a *supervised* maximum likelihood (ML) classifier on lidar derived DSM to extract different land cover features.

Object-level fusion starts with a grouping of neighbouring pixels into meaningful objects. Fusion is then achieved through utilising different rule-based classifications. Geneletti and Gorte (2003) developed a sequential application of object-based segmentation and classification for fusing Landsat TM data and aerial photographs. In this application they used a region-based segmentation technique to segment the aerial photographs. Then they employed a dedicated set of rules to classify the segmented image with a reference Landsat TM image. Hofmann (2001) put forward the idea of the object-level approach to detect buildings and roads from high resolution satellite imagery using additional elevation information. Object-level data fusion shows very promising results in recent years. Ali et al. (2005) applied an automated object-level technique to fuse high-resolution imagery and lidar data. In this process, a multi-resolution segmentation technique was used to segment multi-source images, after which a hierarchical decision tree was used to fuse segmented objects.

In the present study, a comparison of pixel- and object-level data fusion and subsequent classification of lidar and high-resolution imagery is discussed. Comparison is made using metrics of classification accuracy, and suggestions are made regarding the best land cover classification of the study site, the town of Mathoura, NSW.

Study Area and Materials

To evaluate the fusions of both optical imagery and the lidar data for classifying semi-urban structures, an area of 1×1 km in southern New South Wales was selected. The study area is situated in the small town of Mathoura, and comprises the central portion of the town and contains most typical semi-urban landscape classes. Buildings in this area have a very distinct shape and their sizes range from very large to small. This area has a mixture of vegetation, open space and road networks. This area was selected due to repeated coverage of a large data sets combine with aerial images and lidar data.

Lidar Data

The lidar data used for this project was acquired by AAMGeoScan (now AAMHatch) in May 2001. The lidar system used was the ALTM 1225, which operates with a sampling intensity of 11000 Hz at a wavelength of $1.047 \mu\text{m}$. Approximate flying height of this sensor, was 1100 m and the laser swath width was 800 m. Vertical accuracy was 0.15 m (1σ), the internal precision was 0.05 m, and the original laser footprint was 22 cm in diameter. The original lidar dataset was processed by AAMHatch and provided to the Victorian Department of Sustainability and Environment (DSE). The provided data were two separate files representing the first and last return point clouds. The original lidar data had point spacing in the order of 16 points per m^2 and was resampled to a 1 m grid.

Multispectral Imagery

The multispectral imagery was captured over the study area using an Ultracam-D with a calibrated focal length of 101.400 mm. Three colour (red, green and blue) and infrared (IR) band images were collected with a 28.125 μm pixel size. The radiometric resolution of the images was 16-bit. This enhanced radiometric range captures detailed information of the land cover features. As a result, in extreme bright and dark areas we still manage to get redundant information, which is beyond what is visible in images with lower radiometric resolution (Leberl and Gruber, 2005).

Colour Imagery

The colour image data, collected by AEROMETREX, was acquired using a Zeiss LMK 152 camera with a calibrated focal length of 152.261 mm. It was captured at an approximate flying height of 850 m above the ground level equating to an average scale of 1:5500, which was later scanned at 15 μm to provide a pixel size of 8.25 cm. The photographic images were orthorectified with the help of accompanying exterior orientation parameters (X_o , Y_o , Z_o , ω, ϕ, κ), which were captured using onboard GPS and IMU sensors.

Fieldwork carried out in the study area in July 2005 and April 2006 allowed the collection of ground data and the setting of a suitable land cover classes. The ERDAS Imagine 8.6 was used for image processing and pixel-level fusion, whereas eCognition Professional version 4.0 was used for the object-level fusion.

Methodology

Following data collection, the optical imagery and the lidar data were fused primarily to extract landscape features of the semi urban area, so that the comparative fusions could be better evaluated. The proposed comparative study of pixel- and object-level fusion is based on the use of high-resolution imagery and lidar derived DSM. The flowchart in Fig. 1, describes the major steps, which were performed through this data fusion project.

Geometric Corrections

The alignment of the supplied multispectral and colour imagery was not perfect. The lidar data was considered more stable in positional accuracy due to the availability of an accuracy report for the lidar mission. But the main constraint was that the lidar geometry couldn't be used to align the other images due to the imprecise shape and size of common visible features in both images. In this context, we used ground control points to align the optical images. An optimum number of ground

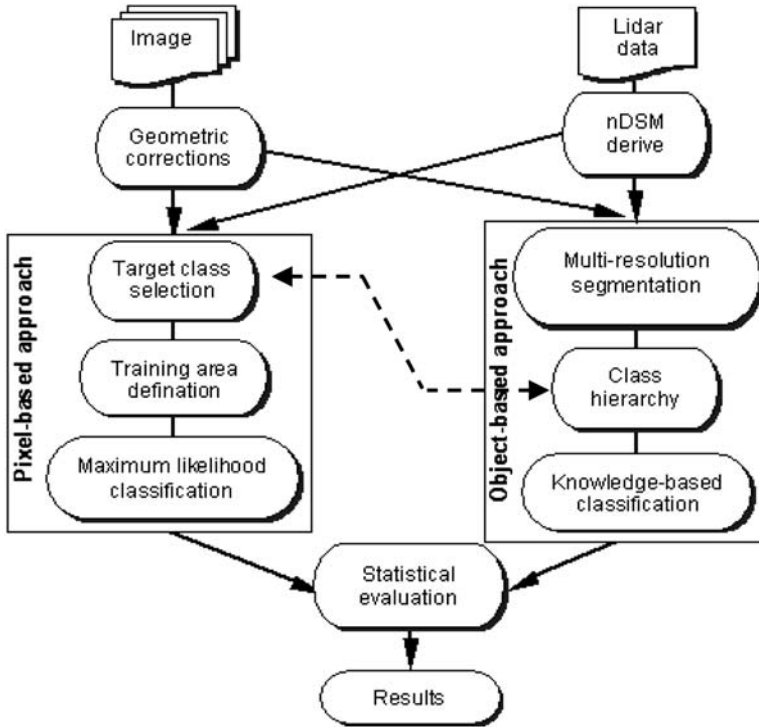


Fig. 1 The comparative approach of pixel- and object-level data fusion

control points were collected from the study area using differential GPS. The georectification of multispectral and colour imagery was independent from each other. Therefore, their accuracy level varied but consistently fell within the desirable limit. A third order polynomial transformation was applied to rectify the multispectral and colour imagery. The bilinear interpolation resampling technique was used to bring all the images to a common spatial resolution of 0.5 m.

Some temporal effects were expected in the data fusion process, due to the differences in acquisition time of the images. These were the only available images for this data fusion project; therefore we had to compromise on this issue. The study area is a slow growing regional town therefore within this time frame it had not seen many changes. However, some temporal effects were found, due mainly to moving objects, which is always a challenge in high-resolution data fusion.

Normalized Digital Surface Model (nDSM) Generation

Lidar first and last return height data were used to generate the normalized digital surface model for the study area. The last return of the lidar normally represents the digital terrain model (DTM) and the first return as the digital surface model (DSM).

A height difference between the DSM and DTM represents the absolute height of the features. A height threshold was applied to remove any features <2.0 m close to the terrain surface. This normalized DSM along with multispectral and colour images was used in the data fusion process.

Pixel-Level Fusion

A pixel-level approach was implemented to fuse the optical imagery and lidar derived nDSM. Two stacked-vector data sets were created, one nDSM with the three-band colour image and then the nDSM with the four-band multispectral image. An independent supervised classification procedure was then applied to them separately. First, a set of suitable target classes was established after careful analysis of the landuse maps and aerial photographs.

In particular the following eight land cover classes were identified: open-space/road, grey roof, grey roof shadow, colour roof, colour roof shadow, grass, tree and tree shadow. For each of these classes a set of ground data was collected, approximating to a stratified random criterion. The ground data plots covered nearly 5% of the total area to be classified. The ground data samples were then split into two subsets: the training data and the test data. The training data were used to create a spectral signature for each of the classes. Using the test data, accuracy assessment was performed on all classified images, calculating the relevant confusion matrix.

The training statistics show (Table 1) that the training areas contain an adequate number of pixels and they are separable in spectral bands and nDSM layer. This issue is important in supervised classification to avoid the misinterpretation of land cover features for similar spectral signatures. The degree of interclass spectral variability for each landscape class has been assessed through the computation of

Table 1 Derivation of training statistics used of 4-band multispectral image and nDSM data for maximum likelihood classification

| | Class | Tree | | Grass | Color roof | | Grey roof | | Roads |
|--------|-------------|--------|--------|--------|------------|------------------|-----------|-----------|---------|
| | | shadow | Tree | | shadow | Color roofshadow | Grey roof | Grey roof | |
| | Pixel count | 853 | 1091 | 2614 | 164 | 344 | 607 | 4778 | 10171 |
| Band 1 | Mean | 478.23 | 868.21 | 1325.6 | 650.78 | 1574.2 | 763.47 | 4152.6 | 2752.0 |
| | SD* | 140.97 | 170.65 | 294.51 | 165.50 | 593.44 | 190.82 | 1480.4 | 881.67 |
| Band 2 | Mean | 286.70 | 476.46 | 653.87 | 347.47 | 673.33 | 429.80 | 2057.5 | 1246.6 |
| | SD* | 60.97 | 74.01 | 86.18 | 77.60 | 199.99 | 91.344 | 727.89 | 348.01 |
| Band 3 | Mean | 312.06 | 364.22 | 444.59 | 370.31 | 605.23 | 415.99 | 1335.2 | 814.21 |
| | SD* | 32.87 | 31.24 | 38.44 | 69.71 | 153.62 | 54.06 | 457.12 | 168.07 |
| Band 4 | Mean | 806.84 | 2314.9 | 2335.2 | 1043.0 | 2323.8 | 933.23 | 2664.8 | 2014.1 |
| | SD* | 191.04 | 322.05 | 276.35 | 180.83 | 584.77 | 181.14 | 842.61 | 603.148 |
| nDSM | Mean | 0.15 | 5.36 | 0.07 | 0.80 | 3.73 | 0.32 | 3.96 | 0.00 |
| | SD* | 0.86 | 3.27 | 0.78 | 1.82 | 1.56 | 1.10 | 2.07 | 0.03 |

*SD = Standard deviation

training statistics as measured by spectral profiles. Table 1 summarises the training statistics of the sample classes. The mean and variance are the indicators of the spectral independence. The mean and variance of the training features for 4-band multispectral data indicated that the main groups such as roofs, and trees were better distinguished than the minor groups, such as different categories of shadows. Spectral independence was also examined by analysing spectral signatures for each of the candidate landcover classes. A scatter plot of the training signatures revealed that they were spectrally different from each other. Statistics were generated for the supervised classification of the integrated layers of colour imagery and nDSM data. The distance between signatures was assessed through both tests on their statistical separability and computation of contingency matrices (Richards, 1993). The classification was performed using a maximum likelihood classifier with equal prior probabilities.

Object-Level Fusion

Object-level data fusion requires the identification of meaningful objects over the multisource images and classifying them with class attributes. Therefore, the overall procedure consists of a sequential application of segmentation and classification. Object-level fusion was implemented on two sets of images, the multispectral image and nDSM and then the colour image and nDSM.

Image Segmentation

The basic processing units of object-level fusion are segments or image objects, and not single pixels. In the segmentation process, for each image object a meaningful statistic is calculated in an increased uncorrelated feature space using shape, texture and topological features. This information improves the value of the final classification and cannot be fulfilled by pixel-level approaches alone (Benz et al., 2004). Initially image-object primitives are created through multi-resolution segmentation. These objects are polygons of roughly equal size exhibiting interior homogeneity. In the segmentation process, the scale parameter determines the maximum allowed heterogeneity for the resulting image objects. The size of the image objects varies by modifying the value of the scale parameter. For homogeneity, the relative weight applies to spectral versus shape criteria to reduce heterogeneity. Here shape, smoothness and compactness criterion are applied in a mixed form to define homogeneity for the image objects (Table 2).

For multispectral and nDSM data fusion, equal weight was assigned to each of the multispectral bands. This emphasis was chosen because of the lack of colour homogeneity visually observed within the same features in the image. On the contrary, the lidar derived nDSM layer had more homogeneity in grey level; therefore

Table 2 Segmentation parameters for image and nDSM fusion

| Parameters | MS & nDSM fusion | Colour & nDSM |
|--------------|------------------|---------------|
| Scale factor | 25 | 25 |
| Shape factor | 0.75 | 0.15 |
| Compactness | 0.3 | 0.6 |
| Smoothness | 0.7 | 0.4 |

more weight was given to this layer. By visually interpreting different image segmentation results, a scale parameter of 25 was chosen to create local homogeneity and to keep global heterogeneity. The larger than 25 scale parameter had coarse segment size roughly equal to 40 pixels per feature. The large segment includes more detail within a feature and dilutes separability among the features. Therefore, appropriate feature extraction was not achieved with this segmentation. The same problem arose for the smaller than 25 scale parameters. Small segments only include part of a feature and may highlight noise within a feature. This segmentation behaves like a pixel-level approach and is not suitable for further fusion. Similarly on a trial and error basis, a ratio of smoothness to compactness weight was defined. Here, 3:7 was specified (Table 1), emphasizing the discrete, compact nature of building roofs. A higher smoothness emphasis would be used to define objects observed to have greater variability between features (Baatz et al., 2004). The compactness weight made it possible to separate objects that had quite different shapes but not necessarily a great deal of colour contrast, such as building roofs versus roads within the study area.

Class Hierarchy

The class hierarchy is the frame of object-level fusion used to create the knowledge base for the data fusion task. It contains all classes and is organized in a hierarchical structure (Baatz et al., 2004). The class hierarchy passes down class descriptions from parent classes (Level I) to their child classes (Level II). It reduces the redundancy and complexity in the class descriptions and creates a meaningful grouping of classes.

Figure 2 illustrates the class hierarchy of the object-level fusion, which was developed through utilizing similar legend of the pixel-level fusion. Class hierarchy is defined as an inheritance hierarchy, which refers to the physical relations between the classes. In Level I, *natural*, *manmade* and *obscure* features are the child class of whole segments and they become parent classes of *vegetation*, *infrastructure*, *house* and *shadow* classes (Fig. 2). Later in Level II, the *vegetation* class becomes a parent class with *grass* and *tree* child classes. Within this class-hierarchy each class is described either by one or more fuzzy-membership functions, a nearest neighbour classifier or by a combination of both. Membership functions are determined by the semantic import model, which is based on the expert knowledge of the features.

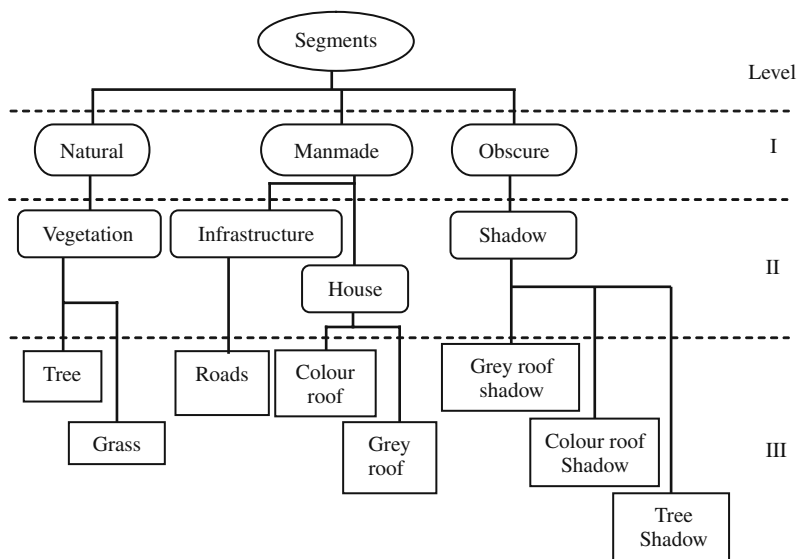


Fig. 2 The class hierarchy for the object-level fusion

A stepwise refinement of the class-hierarchy was achieved using the inheritance mechanism.

Fusion Based on Spectral Properties

Since the generated image objects hold more spectral information compared to pixels' digital numbers, the object-level fusion offers a huge variety of derivative spectral features (Hofmann, 2001). Brightness and spectral ratios of the image objects were calculated using all image layers. Textural features were calculated using standard deviations of layer values, spectral mean values of sub-objects, and average spectral differences of sub-objects. Contrast information were generated though spectral differences to neighbouring objects and super-objects. Context related features included mean spectral differences to a given class.

For the colour imagery, *natural* and *manmade* classes were separated by a fuzzy membership description of the mean and the ratio of the green spectral band. In contrast, the normalized difference vegetation index (NDVI) was utilised in the multispectral image.

Colour Surface' was the sub-class of the *manmade* class. This class was defined by the object's brightness and the ratio of the blue band. 'Grey Surface' was defined by the object's brightness and the ratio of the red band. *Shadow* was the subclass of *obscure* class and is defined by the brightness. An image object was a *shadow* if its brightness was less or equal to 70.

Fusion Based on nDSM Properties

In object-level data fusion, the nDSM property can be modelled by describing the difference in elevation to neighbouring objects. In this research, *houses* and *infrastructures* were discriminated by the mean difference of the nDSM layer. An image object was represented as *road* if its mean difference of nDSM was smaller or equal to 1.2 m. On the contrary, an image object was represented as *house* if its mean difference of nDSM was higher than 1.2 m. The *vegetation* class was further subdivided in *tree* and *grass* classes. The nDSM layer was utilised to discriminate *tree* and *grass* by their relative height difference.

Fusion Using Contextual Information

As shadows are typically created by elevated features, most of them can be detected and described by their source features. Additionally, shadow areas can be classified according to their spectral properties. Pixel-level classification using these properties showed unsatisfactory results (Dare, 2005). Thus it is useful to classify shadows by describing their contextual criteria and subsequently by their different spectral properties. Therefore, depending on the type, shadows may inherit their spectral properties from an appropriate super-class and then be identified by their surroundings. The logic applied for this was ‘if an object classified as shadow is surrounded sufficiently by objects classified as building, it should be classified as *building shadow*’. In this process, grey roof shadow was a subclass of shadow and the inherency was defined by the neighbour-object relation. A shadow object is classified as a grey roof shadow if its ‘border to neighbour-object relation’ for grey object is larger or equal to 0.025 m. A shadow object is classed as tree shadow if its ‘border to vegetation neighbour-object’ is larger or equal to 0.02 m.

Accuracy Assessment

The sample design of this project was extremely complex because it involved the assessment of eight different maps (pixel-level: colour, colour and nDSM, multispectral, multispectral and nDSM; object-level: colour, colour and nDSM, multispectral, multispectral and nDSM) and used two types of reference data (the 2006 aerial photos and field visits accomplished in 2005 and 2006). As a result, trade-offs between statistical rigor and practicality are apparent throughout this study. Existing aerial photography was used to design much of the sampling, including the selection of the appropriate sample unit and the methods used to select the sample units. Sample design for this project addressed two types of samples: (1) Samples from the 2006 aerial photo polygons for assessment of multispectral and fused multispectral and nDSM maps. (2) Samples from existing aerial photo polygons for field data collection and assessment of colour and fused colour and nDSM

maps. A total of 110 accuracy assessment sites were randomly selected from each of the classified maps and then collected the reference information from 2006 aerial photos and field survey data.

Fusions using lidar and optical imagery were evaluated using error matrices for each of the pixel- and object-level fusion algorithms. Overall fusion accuracy and the Kappa Coefficient were computed to provide measures of the success of the fusion process. Comparative values of Kappa were discussed in the following section and provide a relevant benchmark for comparison.

Results and Discussions

To provide summary information of the different fusion level, their accuracies were assessed using the field sample data. In the data fusion process, the evaluation of the results becomes relatively complex due to the involvement of different data sources. The different aspects of image acquisition of the various sensors have to be considered as well as the approach of the image fusion itself plays a role. In this analysis, both visual methods and statistical parameters were selected as the assessment criteria. From visually inspecting the results, the main difference between pixel- and object-level fusions is the sharpness of the classified feature. This is particularly evident when observing the open space and the building roofs in the pixel-level fusion. In the colour image classification results, 'pepper and salt' effect was prominent due to a large misclassification among the feature classes. Including DSM information reduced this 'pepper and salt' effect but the misclassification of the shadows was still present. The object-level approach improved the shadow classification by incorporating contextual information in this process.

In the pixel-level multispectral and nDSM fusion process, the high spectral depth of the multispectral image played a vital role. It reduced interclass confusion but the shape of the above ground features were not perfectly delineated due to the low spatial resolution of the images. Object-level classification of the single source image exhibited poor classification results for the abrupt spectral changes within the classes due to the sun illumination factor. From this observation, it can be said that additional elevation data can improve the classification results for the high-resolution imagery.

Based on the analysis outlined above, the use of both optical imagery and lidar data for semi-urban landscape mapping was evaluated. Accuracy assessment was performed for each of the classified images obtained through the pixel- and object-level fusion. To ensure consistency, the same sampling technique was employed for all of the classified images. For each of the classified images, the accuracy was assessed in an independent manner to reduce the systematic basis and defuse the temporal effect on the overall accuracy. The accuracy results, presented in Fig. 3, revealed that in most of the cases the object-level fusion exhibited higher accuracy level than the associated pixel-level fusion. Object-level fusion of colour and DSM data achieved highest (91%) accuracy with kappa value 0.90, which exhibited

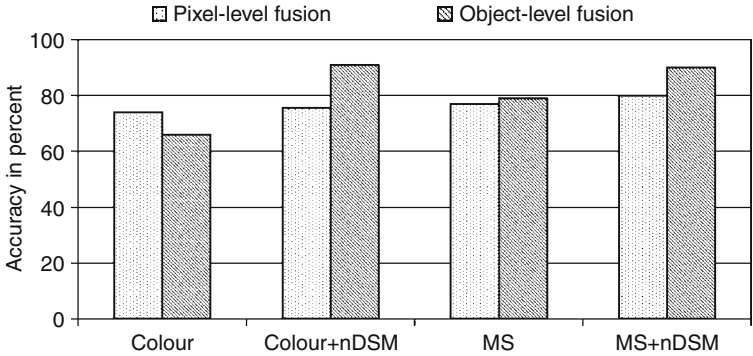


Fig. 3 Summary of the overall accuracy of the pixel- and object-level data fusion

better fusion technique than others. Whereas only colour image classification in this category had worst (66%) accuracy result.

As the kappa value approaches 1.0, it indicates perfect agreement between fused and reference maps. Table 3 and Fig. 3, shows the accuracy and kappa statistics were highly correlated further enhancing confidence of the results. In the pixel-level approaches, the highest accuracy (80%) was achieved through multispectral and DSM fusion with high kappa value 77%. On the contrary, object-level fusion of those images had accuracy 90% with kappa value 88.5%. In general, object-level fusion performed better than the pixel-level fusion for all combinations except solo colour image classification.

Fusion results for optical imagery and lidar data are shown in Table 3 indicate that at the 95% confidence level the standard normal deviate of the Kappa Coefficient is greater than 1.96 for both lidar and colour imagery fusion and the lidar and multispectral imagery fusion. A significant difference was detected between pixel- and object-level fusion algorithms with the object-level fusion providing the superior results for both cases.

Table 3 Comparison of pixel- and object-level fusion results at 95% confidence

| Fusion | Lidar and colour imagery fusion | | Lidar and multispectral imagery | |
|---------------------------|---------------------------------|--------------|---------------------------------|--------------|
| | Pixel-level | Object-level | Pixel-level | Object-level |
| Overall Accuracy (%) | 75.5 | 91.0 | 80.0 | 90.0 |
| Kappa $\hat{K}(\%)$ | 71.8 | 89.7 | 77.0 | 88.5 |
| $\hat{var}(\hat{K})$ | 0.002837 | 0.001063 | 0.002119 | 0.001216 |
| z | 13.4806 | 27.5094 | 16.7232 | 25.366795 |
| $z_{\hat{K}_1-\hat{K}_2}$ | 2.86 | | 1.99 | |
| Significance* | S | | S | |

*NS = not significant, S = significant

The main contributing factor to the observed difference between the pixel- and object-level fusions of the optical imagery and lidar data is the failure of the clustering process to recognize some classes. This problem was acute for the *Shadow* classes in pixel-level fusion, as it could not distinguish different shadow classes on the basis of spectral content alone. The object-level approach overcomes this problem by incorporating contextual information in the fusion process.

Conclusions

The goal of this study was to compare different data fusion techniques for classifying high-resolution imagery and lidar derived DSM data. A semi-urban image subset was analysed using two fusion techniques. Results suggest a more accurate land cover maps using object-level fusion than are attainable using the pixel-level supervised process. Shadow objects are particularly susceptible to misclassification when using only pixel-level spectra. Even so, object-level fusion has proven effective in correctly identifying the shadows where this is difficult using other methods. Although a very simple object-level approach was utilised to fuse imagery and lidar data, significant improvement over pixel-level fusion was obtained.

In this study, object-level fusion was found more flexible than the pixel-level supervised fusion. The improvement can be achieved with a relatively simple and unrefined application of the object-level approach. It allows data fusion in more meaningful ways with highly refined and specialized membership functions, which in a more complex case would probably lead to further improvements in accuracy. There is a great potential for further improving object-level fusion quality through refining the decision rule structure. In contrast, pixel-level supervised fusion offers very little potential for improvement, other than through a procedure that tries to imitate the object-level approach, and can be said to have reached the end of its paradigm.

Acknowledgement This work was supported by the Australian Research Council (ARC) under Discovery Project DP0450889. The Ultracam-D data set was provided by IFMS Germany (<http://www.arcforest.com/>).

References

- Tso B, Mather PM (2001) Multisource classification. In: Classification Methods for Remotely Sensed Data. Taylor & Francis, New York, pp. 271–298.
- Schistad-Solberg AH, Jain AK, Taxt T (1994) Multisource classification of remotely sensed data: fusion of Landsat TM and SAR image. IEEE Transactions on Geoscience and Remote Sensing 32:768–778.
- Pohl C, van-Genderen JL (1998) Multisensor image fusion in remote sensing: concepts, methods and applications. International Journal of Remote Sensing 19:823–854.
- Blaschke T, Strobl J (2001) What's wrong with pixels? Some recent developments interfacing remote sensing and GIS. In: GIS – Zeitschrift für Geoinformationssysteme 6/2001. Hüthig GmbH & Co. KG, Heidelberg, pp. 12–17.

- Townshend JRG, Huang C, Kalluri S, Deferies R, Liang S, Yang K (2000) Beware of per-pixel characterisation of land cover. *International Journal of Remote Sensing* 21:839–843.
- Schiewe J, Tufte L, Ehlers M (2001) Potential and problems of multi-scale segmentation methods in remote sensing. In: *GIS – Zeitschrift für Geoinformationssysteme* 6/2001. pp. 34–39.
- Baatz M, Schape A (2000) Multiresolution Segmentation-an optimization approach for high quality multi-scale image segmentation. In: Strobl J, Blaschke T (eds.) *Angewandte Geogr: Informationsverarbeitung XII*. Wichmann, Heidelberg, pp. 12–23.
- Rego F, Koch B (2003) Automatic classification of land cover with high resolution data of the Rio de Janeiro city Brazil comparison between pixel and object classification. In: Carstens J (ed.) *The International archives of the photogrammetry, remote sensing and spatial information sciences*. Regensburg, Germany.
- Blaschke T, Conradi M, Lang S (2001) Multi-scale image analysis for ecological monitoring of heterogeneous, small structured landscapes. In: *SPIE*. Toulouse, pp. 35–44.
- Smith GM, Fuller RM, Hoffmann A, Wicks T (2000) Parcel-based approaches to the analysis of remotely sensed data. In: *The Remote Sensing Society Conference, Adding value to remotely sensed data*. Remote sensing society, Nottingham, UK.
- Baltsavias EP (1999) A comparison between photogrammetry and laser scanning. *ISPRS Journal of Photogrammetry and Remote Sensing* 54:83–94.
- Tao G, Yasuoka Y (2002) Combining High Resolution Satellite Imagery and Airborne Laser Scanning Data for Generating bareland DEM in Urban Areas. In: *International Workshop on Visualization and Animation of Landscape*. International Archives of Photogrammetry, Remote Sensing and Spatial Information Science, Kunming, China.
- Schenk T, Csatho B (2002) Fusion of Lidar data and aerial imagery for a more complete surface description. *IAPRS XXXIV*:310–317.
- Haala N, Brenner C (1999) Extraction of buildings and trees in urban environments. *ISPRS Journal of Photogrammetry and Remote Sensing* 54:130–137.
- Rottensteiner F, Trinder J, Clode S, Kubik K (2004) Using the Dempster–Shafer method for the fusion of Lidar data and multi-spectral images for building detection. *Information Fusion* 6:283–300.
- Maas H-G (1999) Fast determination of parametric house models from dense airborne laser scanner data. *IAPRS XXXII(2W1)*:1–6.
- Geneletti D, Gorte BGH (2003) A method for object-oriented land cover classification combining Landsat TM data and aerial photographs. *International Journal of Remote Sensing* 24: 1273–1286.
- Hofmann P (2001) Detecting buildings and roads from IKONOS data using additional elevation information. In: *GIS – Zeitschrift für Geoinformationssysteme* 6/2001. Hüthig GmbH & Co. KG, Heidelberg, pp. 28–33.
- Ali SS, Dare P, Jones S (2005) Automatic classification of land cover features with high resolution imagery and lidar data: an object-oriented approach. In: *SSC2005 Spatial Intelligence, Innovation and Praxis: The national biennial Conference of the Spatial Sciences Institute*. Melbourne, Australia, pp. 512–522.
- Leberl F, Gruber M (2005) Ultracam-d: understanding some noteworthy capabilities. In: *Photogrammetric Week 2005*. Stuttgart, Germany.
- Richards JA (1993) *Remote Sensing Digital Image Analysis – An Introduction*. Springer-Verlag, Berlin.
- Benz UC, Hofmann P, Willhauck G, Lingenfelder I, Heynen M (2004) Multi-resolution, object-oriented fuzzy analysis of remote sensing data for GIS-ready information. *ISPRS Journal of Photogrammetry and Remote Sensing* 58:239–258.
- Baatz M, Benz U, Dehghani S, Heynen M (2004) *eCognition User Guide 4*. Definiens Imagine GmbH, Munchen, Germany.
- Dare P (2005) Shadow analysis in high-resolution satellite imagery of urban areas. *Photogrammetric Engineering & Remote Sensing* 71:169–177.

Combining Texture and Hyperspectral Information for the Classification of Tree Species in Australian Savanna Woodlands

Peter Bunting, Wenda He, Reyer Zwiggelaar, and Richard Lucas

Abstract This paper outlines research undertaken to assess the ability of textural information, from image filters, to be used alongside hyperspectral data for the classification of broad forest types. The study made use of 2.6 m hyperspectral HyMap data acquired over the Injune study area, Queensland, Australia, in September 2000. The HyMap data provided spectral data from the blue to shortwave infrared in 126 wavelengths, all of which were used for classification. A measure of texture was achieved using a set of 48 image filters including Laplacian of Gaussian and Gaussian smoothing, first and second order derivatives at different scale and where appropriate different rotations. Analysis took place using an air photo interpretation to provide regions of interest for areas dominated by *Angophora*, *Callitris*, and *Eucalyptus*, additionally areas of non-forest were also included. Classification of the resulting dataset was performed using Multiple Stepwise Discriminant Analysis where an accuracy of 60% was achieved using the combined reflectance and texture data compared to accuracies of 55 and 43% using only the reflectance and textural datasets, respectively.

Introduction

The delineation of woodlands into regions unique in terms of species and structure composition is important for many applications, including the provision of forest management units (Leckie et al., 2003), indicators of biodiversity (Bock et al., 2005) and the interpretation of other remotely sensed data.

The interpretation of aerial imagery is heavily scale dependent, where at high spatial resolutions interpretation has traditionally required experienced human interpreters and is mostly based on structure, context and texture, rather than spectral qualities (Held et al., 2003). Therefore, a number of studies (Cots-Floch et al., 2007; Buddenbaum et al., 2005; Coburn and Roberts, 2004; Franklin et al., 2000; Kushwaha et al., 1994) have started to introduce textural measures alongside the

P. Bunting (✉)
Aberystwyth University, Aberystwyth, SY23 3DB, UK

spectral values. Franklin et al., 2000, found the addition of textural information, in the form of homogeneity and entropy calculated through a moving window, increased the overall classification accuracy of forest stand types by 5–12%, providing overall accuracy in the order of 60–65%. While, Kushwaha et al., 1994 demonstrated an increase in classification accuracy from 69 to 80% when classifying stand age and levels of degradation when the textural measures entropy and the inverse difference moment were introduced alongside the spectral data.

Texture is the term used to describe information on the local variability of the image pixel values. Representation of texture can take a number of forms, one of the most common are the so called Haralick features (Haralick, 1979; Haralick et al., 1973) where the statistical properties of the pixels within a moving window are calculated, representing the homogeneity of the surrounding pixels. Although this method has demonstrated some success (e.g., Franklin et al., 2000), the results often vary with scale and application and have, therefore, not been widely adopted within the field of remote sensing where the pixel values (either reflectance or backscatter) have tended to be used in isolation. Another representation of texture is that of filter responses, where through the application of a number of image filters structures within the scene at different scales and rotations are identified and the composite of these filter responses forms the texture signature or texton (Leung and Malik, 2001, Varma, 2004). The texton is identified from the filter responses through a clustering stage (e.g., K-Means; Varma, 2004; He et al., 2008) where the resulting texton can be used for segmentation and classification.

Study Site and Datasets

The study was carried out using remote sensing and field data acquired over a 40×60 km area near the township of Injune (Lat $25^\circ 32'$, Long $147^\circ 32'$), located within the Southern Brigalow Belt, a biogeographic region of southeast central Queensland, Australia (Fig. 1). These woodlands contain forest communities

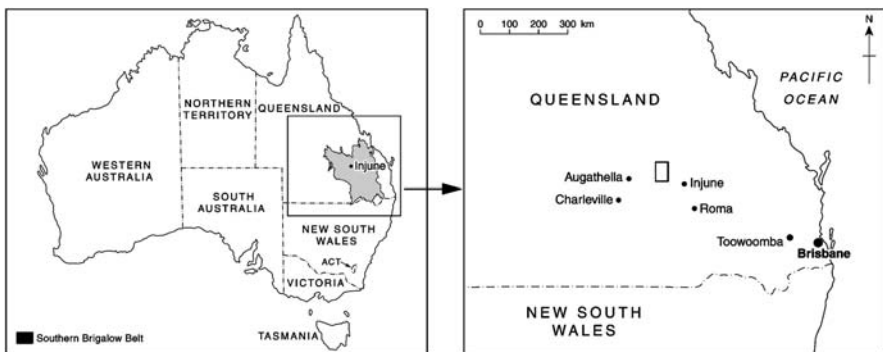


Fig. 1 The location of the Injune study area, southeast central Queensland, Australia. *The shaded area represents the Southern Brigalow Belt*

existing in varying states of degradation and regeneration as a result of prior disturbance (e.g., broad scale clearing, altered fire regimes and spread of exotic species) and are structurally similar to over 70% of those occurring in Australia. Many stands are dominated by *Callitris glaucophylla*, although selective harvesting has reduced the abundance of larger individuals, therefore, typically forming dense stands with a large number of small individuals (several trees per m²). *Eucalyptus* species are also common across the site with stands dominated by *Eucalyptus populnea* (Poplar Box), *Eucalyptus melanophloia* (Silver-leaved ironbark), *Eucalyptus microcarpa* (Grey Box), *Eucalyptus chloroclada* (Baradine gum), *Angophora leiocarpa* (Smoothed barked apple) and *Angophora floribunda* (Roughed barked apple). Additionally, *Eremophila mitchelli* and a number of *Acacia* species form dense understories. While *Acacia harpophylla* is commonly associated with duplex and cracking clay soils in the southeast of the study area, it is largely in the form of regrowth given previous clearing.

During July 2000, Large Scale (1:4000) stereo aerial photography (LSP) were acquired over a grid of one hundred and fifty 500 × 150 m Primary Sampling Units (PSUs), with each separated by 4 km in the north-south and east-west directions (Lucas et al., 2004). Across the site, 1 km wide strips of Hyperspectral Mapper (HyMap) data were acquired along six of the PSU columns, at 2.6 m spatial resolution with 126 bands in the VIS, NIR and SWIR parts of the electromagnetic spectrum. The HyMap data were subsequently atmospherically corrected and geo-referenced by HyVista Corporation (who acquired the data) using the HyCorr atmospheric correction software. The algorithm, developed by CSIRO as an extension to the ATREM atmospheric correction software (Gao and Goetz, 1990), retrieves information on atmospheric gases from wavebands operating in the water absorption regions and uses these to correct the image bands.

Methods

Airphoto Interpretation

Using the LSP, an aerial photography interpreter delineated the extent of broad forest communities and described each in terms of the dominant species (Tickle et al., 2006). It was observed that the woodlands were dominated by a number of broad forest communities that were often texturally different as much as they were spectrally different. *Angophora* dominated woodlands were distinct due to the large size of the trees where the textures presented were very coarse with large areas of ground and shadow being present between the crowns (Fig. 2aa). *Callitris* dominated stands were found to contain relatively smooth textures due to the dense number of stems and homogenous canopy cover (Fig. 2b). While *Eucalypts* (e.g., Silver-leaved Ironbark and Poplar Box) were often found to be only a few pixels (at a pixel resolution of 2.6 m) across but with small areas of soil and shadow visible between the crowns (Fig. 2c).

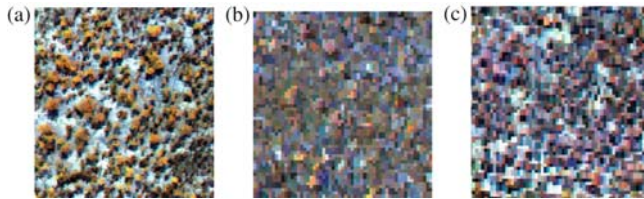


Fig. 2 Examples of the broad forest types (a) *Angophora*, (b) *Callitris*, and (c) *Eucalyptus*

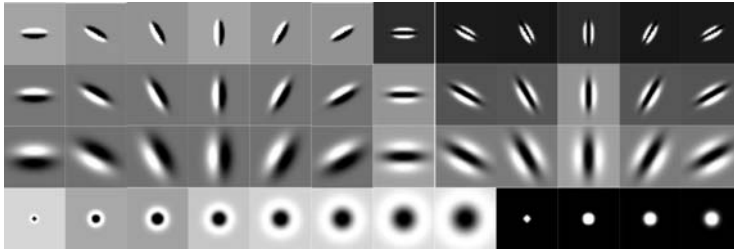


Fig. 3 The filter bank used to identify texture

Image Filtering

To identify the textures within the images a filtering technique similar to that of Varma (2004) was used where a series of image filters (Fig. 3) were applied to the image and the normalised filter responses were used to characterise the texture. For this study the Leung-Malik filter bank (Leung and Malik, 2001), consisting of 48 filters, including 8 Laplacian of Gaussian, 4 Gaussian smoothing filters and 6 Gaussian first and second order derivative filters at 3 scales, was used. For the Laplacian of Gaussian filters scales of $1, \sqrt{2}, 2, 2\sqrt{2}, 2, 3\sqrt{2}, 6$ and $6\sqrt{2}$ were used while the Gaussian smoothing used scales of $1, \sqrt{2}, 2$ and $2\sqrt{2}$. For the Gaussian first and second order derivative filters scales of $\sigma_x, \sigma_y, (1,3), (\sqrt{2}, 3\sqrt{2})$ and $(2,6)$ were used, where each scale was rotated by 0, 30, 60, 90, 120 and 150 degrees.

Remotely Sensed Data and Association to Forest Types

Filtering all 126 wavelengths available from the HyMap sensor would prove impractical due to the data size (48×126 output bands), therefore a subset of 3 bands was selected. The selected bands were in the blue channel (446.1 nm), on the red edge (716.2 nm) and the NIR (891.2 nm). These wavelengths were selected as they have been shown by Bunting and Lucas (2006) to provide the optimum visualisation of these woodlands for the differentiation of tree crowns and species.

Following the application of image filters to each of the image bands the polygons identified from the LSP by the airphoto interpreter were attributed with the

mean filter response for each of the 3 input bands along with the mean spectral response for each of the 126 bands.

Classification

Classification was performed on the data extracted for the LSP polygons using Multiple (stepwise) Discriminant Analysis (MDA), from within the SPSS software package. MDA was selected due to its success in the previous studies (Clark et al., 2005, Lucas et al., 2008), where hyperspectral data from individual crowns, from high resolution 1 m imagery, were extracted and classified to species, resulting in accuracies > 70% where 10 species were compared. The algorithm was parameterised such that the stepwise method was applied using the Rao’s V metric, with the probability of F being 0.05 for entry and 0.1 for removal of data bands in the forward and backward steps (Galvao et al., 2005).

Results

To test the method the polygons identified through the LSP interpretation for 4 of the 6 HyMap strips were select and attributed with the mean reflectance for each of the HyMap bands and mean filter responses providing 270 variables and 252 samples of the 4 ground cover types (Table 1).

To generate overall accuracy values for the 4 classes each set of samples was randomly split into training and testing datasets, using a Bernoulli distribution with a probability of 0.5. The split was made 25 times where for each split the results of the classification were recorded and the mean and standard deviations calculated. To test the significance of the texture and reflectance data the experiments were carried out individually on the reflectance and texture data as well as the combined data (Table 2).

Table 1 The number of samples for each ground cover type

| Species | Number of samples |
|-------------------------|-------------------|
| <i>Angophora</i> (ANG) | 10 |
| <i>Callitris</i> (CP-) | 82 |
| <i>Eucalyptus</i> (EUC) | 130 |
| Non Forest (NF) | 30 |

Table 2 Results for the experiments using both the datasets individual and in combination

| | Combined | | Reflectance only | | Texture only | |
|---------|----------|---------|------------------|---------|--------------|---------|
| | Training | Testing | Training | Testing | Training | Testing |
| Mean | 61.79 | 60.21 | 60.98 | 55.31 | 50.18 | 43.31 |
| Std Dev | 0.67 | 0.86 | 1.10 | 1.04 | 1.74 | 1.51 |

The results show a modest, 5%, improvement for the testing datasets when the combined data was used over the reflectance data while a significant, 17%, increase from the results using only the texture data. Also, by combining the reflectance and textural data the standard deviation of the classification results have been reduced, demonstrating a more robust classification, less sensitive to the training and testing samples used.

Discussion

From these initial results it is clear that the introduction of textural information has increased the classification accuracy and robustness to a similar extent as previous studies (e.g., Coburn and Roberts, 2004 and Franklin et al., 2000). The use of textural information at this scale is viewed as an important additional (Held et al., 2003) as it more closely corresponds with the methods used by human interpreters and allows the forestry environment to be more fully understood at this resolution. Alternative methods (Bunting and Lucas, 2009) have concentrated on the aggregation of high-resolution results, for example delineated tree crowns classified to species. These methods provide an advantage in that the resulting classification can be attributed with information from high-resolution analysis (e.g., crown area, number of individuals) useful for estimating attributes such as biomass and indicators of biodiversity (e.g., Shannon or Simpson indexes) but require significant effort in the production of intermediate data products to allow the analysis to take place. While the method outlined in this paper and those following on from this method, allow the regions to be directly selected from the imagery without intermediate products.

Limitations of the work mainly centered around the testing and training dataset, derived from the LSP, as although providing a good overview of the study area to guide further remote sensing acquisitions and field surveys, as originally intended, they do not accurately delineate the forest types leading to noise in the training and testing data. Additionally, the low number of *Angophora* samples has limited the reliability of the classification for this forest type which occurs in many parts of the imagery, although often outside the areas for which the LSP data was available, forms a very texturally distinct forest type. Therefore, further samples and more forest types (e.g., *Acacia*) and forest structures (e.g., regrowth, burnt) are to be selected for future study.

Future work on the algorithm will concentrate on data reduction methods to reduce the complexity of the input data, while allowing further variables (e.g., max response, min response and standard deviation) to be used alongside the mean filter responses. In addition, further classification methods (e.g., K-Means clustering, K-Nearest Neighbor and support vector machines) will be investigated with the possibility of further increasing the classification accuracy.

Conclusions

This research has demonstrated the use of a filter based texture measure in addition to spectral data for the classification of forest structural types from the 2.6 m HyMap data where the addition of the textural information contributed to a 5% increase in overall accuracy and robustness of the selected samples. Moving forward this study recommends the use of textural measures alongside reflectance data for studies of this type where large regions (> 1000 pixels) with significant spectral variation are of interest.

Acknowledgements The authors would like to thank the Queensland Herbarium and in particular Kerstin Jones for the interpretation of the aerial photography, while the Queensland Department of Natural Resources and Water and the Australian Research Council (ARC) are also thanked for their contributions to this research.

References

- Bock, M., Xofis, P., Mitchley, J., Rossner, G., and Wissen, M. 2005. Object-oriented methods for habitat mapping at multiple scales - case studies from northern Germany and Wyde downs, UK. *Journal for Nature Conservation*, 131:75–89.
- Buddenbaum, H., Schlerf, M., and Hill, J. 2005. Classification of coniferous tree species and age classes using hyperspectral data and geostatistical methods. *International Journal of Remote Sensing*, 26(24):5453–5465.
- Bunting, P. and Lucas, R. M. 2006. The delineation of tree crowns in Australian mixed species forests using hyperspectral Compact Airborne Spectrographic Imager (CASI) data. *Remote Sensing of Environment*, 101(2):230–248.
- Bunting, P. and Lucas R.M., 2009. Understanding the forest communities through the clustering of individual crown. *Remote Sensing of Environment*, Submitted Feb 2008.
- Clark, M. L., Roberts, D. A., and Clark, D. B. 2005. Hyperspectral discrimination of tropical rain forest tree species at leaf to crown scales. *Remote Sensing of Environment*, 96:375–398.
- Coburn, C. A. and Roberts, A. C. B. 2004. A multi-scale texture analysis procedure for improved forest stand classification. *International Journal of Remote Sensing*, 25(20): 4287–4308.
- Cots-Floch, R., Aitkenhead, M. J., and Martinez-Casasnovas, J. A. 2007. Mapping land cover from detailed aerial photography data using textural and neural network analysis. *International Journal of Remote Sensing*, 28(7):1625–1642.
- Franklin, S. E., Hall, J. R., Moskal, L. M., Maudie, A. J., and Lavigne, M. B. 2000. Incorporating texture into classification of forest species composition from airborne multiplespectral images. *International Journal of Remote Sensing*, 21(1):61–79.
- Galvao, L. S., Formaggio, A. R., and Tisot, D. A. 2005. Discrimination of sugarcane varieties in southeastern Brazil with EO-1 Hyperion data. *Remote Sensing of Environment*, 94(4):523–534.
- Gao, B. C. and Goetz, F. H. A. 1990. Column atmospheric water vapour and vegetation liquid water retrievals from airborne imaging spectrometer data. *Journal of Geophysical Research*, 95:3549–3564.
- Haralick, R. M., Shaumugam, K., and Dinstein, I. 1973. Texture features for image classification. *IEEE Transactions on Systems, Man and Cybernetics*, 3:610–621.
- Haralick, R. M. 1979. Statistical and structural approaches to texture. *Proceedings of the IEEE*, 67:786–804.

- He, W., Muhimmah, I., Denton, E.R.E. and Zwiggelaar, R. 2008 Mammographic segmentation based on texture modelling of Tabar mammographic building blocks. *Lecture Notes in Computer Science*, 5116, 17–24.
- Held, A., Ticehurst, C., Lymburner, L., and Williams, N. 2003. High resolution mapping of tropical mangrove ecosystems using hyperspectral and radar remote sensing. *International Journal of Remote Sensing*, 24(13):2739–2759.
- Kushwaha, S. P. S., Kuntz, S., and Oesten, G. 1994. Application of image texture in forest classification. *International Journal of Remote Sensing*, 15(11):2273–2284.
- Leckie, D. G., Gougeon, F. A., Walsworth, N., and Paradine, D. 2003. Stand delineation and composition estimation using semi-automated individual tree crown analysis. *Remote Sensing of Environment*, 85(355–369).
- Leung, T. and Malik, J. 2001. Representing and recognizing the visual appearance of materials using three-dimensional textons. *International Journal of Computer Vision*, 43(1):29–44.
- Lucas, R.M., Maghaddam, M., and Cornin, N. 2004. Microwave scattering from mixed species woodlands, Central Queensland, Australia. *IEEE Transactions on Geoscience and Remote Sensing*, 42(10):2142–2159.
- Lucas, R.M., Bunting, P., Paterson, M., and Chisholm, L. 2008. Classification of Australian forest communities using aerial photography, CASI and HyMap data. *Remote Sensing of Environment*.
- Tickle, P. K., Lee, A., Lucas, R.M., Austin, J., and Witte, C. 2006. Quantifying Australian forest and woodland structure and biomass using large scale photography and small footprint LiDAR. *Forest Ecology and Management*, 223(1–3):379–394.
- Varma, M. 2004. Statistical Approaches to texture classification. PhD thesis, Jesus College, University of Oxford.

High-Resolution Satellite Imaging in Remote Regions: A Case Study in Bhutan

J. Poon and C.S. Fraser

Abstract In remote developing countries, such as Bhutan, it is common for existing maps to be either out-of-date or to not exist. Featuring forest covered peaks and broad valleys with a 2000 m elevation range, the rugged mountainous and largely inaccessible landscape is not well suited to traditional topographic surveying and mapping. It does, however, provide a unique and challenging environment for the generation of image-based products. This paper demonstrates that even with limited ground control, satellite imagery has the potential to rectify the situation and vastly enhance mapping prospects in remote regions. By compensating exterior orientation biases inherent in the recorded sensor orientation data, the attainment of 1:5000 mapping scale ground measurement positions is possible with lowest cost QuickBird imagery. Two image matching algorithms were applied to produce DSM data. Firstly, intensity based matching procedure embodied in commercial software, and secondly a multi-photo, geometrically constrained (MPGC) image matching approach incorporating a hybrid matching algorithm. A third DSM generated by radar was also assessed and compared to the optically derived surfaces. The most accurate DSM generated (MPGC) was used to remove relief displacement, so that planimetric coordinates can be obtained from a single orthoimage to an accuracy of better than a metre. The results show that there is potential for QuickBird 'Basic' to be an effective and economically viable method of extracting 3D information to be used for high accuracy ground feature determination. The implications of using this imagery for precision geopositioning in remote areas include the generation of more accurate digital terrain models and cartographic maps and location data for incorporation into a GIS, providing useful information for development agencies and the wider community.

Keywords DSM · High-resolution satellite imagery · QuickBird · SRTM · Accuracy assessment · Remote regions

J. Poon (✉)

Department of Geomatics, University of Melbourne, Victoria 3010, Australia
e-mail: jpoon@skm.com.au

Introduction

It is without doubt that land is a precious resource. A country's economy relies either directly or indirectly on land information, and with sufficient land information, we can better monitor and manage our land resources. Topographic mapping is just one essential tool that is needed to accomplish this seemingly huge task. Developed countries with established mapping agencies focus on change detection and map updating and aided by incessant advances in technology, are spoilt with a range of data sources – electronic distance measurements, aerial imagery and radar to name a few, to complete such tasks.

The situation, however, is different in remote areas of the world, such as Bhutan, where it is common for existing maps to be either out-of-date or not exist. Therefore, we need to look towards information sources which can provide low cost and quick-delivery land information products, without compromising metric accuracy. Opportunities exist for access to low cost height models derived from Interferometric Synthetic Aperture Radar (InSAR) by way of the NASA/DLR Shuttle Radar Topography Mission (SRTM), which is freely available online.

Of greater application, high-resolution satellite imagery (HRSI) allows production of numerous spatial information products, such as geopositioning, surface models, orthoimages and visualisations. While HRSI can be costly, particularly when acquiring stereopairs, it does not assume existing infrastructure, such as equipment, mobilisation, or complex processing abilities.

Great Britain's National Mapping Agency (NMA) investigated QuickBird imagery for updating mid-scale, 1:25,000 and 1:50,000, and large scale 1:10,000, 1:2500 and 1:1250, mapping (Holland et al., 2006). The use of IKONOS imagery for mapping has been conducted by several European mapping agencies and institutions in the European Organisation for Experimental Photogrammetric Research (OEEPE). Findings were that rural regions can benefit from such imagery when mapping at 1:10,000 and 1:50,000 scales (Holland et al., 2003). Developing countries similarly consider IKONOS imagery for large scale map revision and conclude mapping at 1:2000–1:10,000 scales is theoretically feasible (Samadzadegan et al., 2003). Despite positive reinforcements about the geometric potential of HRSI, it seems the available technology has not yet made the transition to large scale topographic mapping in practice.

This paper investigates information sources for topographic mapping in remote areas, focusing on the application of HRSI in the Bhutan testfield. The testfield spans approximately 300 km², featuring forest covered peaks and broad valleys in the scene's west, overlooking the capital of Thimphu and extending northwards to the Dechenchoeling Palace. With an average terrain inclination of 27° and ground elevations from 2000 m and climbing as high as 4200 m, the scene provides a unique and challenging environment for the generation of image-based spatial information products. With limited ground control and lowest cost QuickBird imagery, we investigate geopositioning, and surface modelling from both commercial and independent algorithms, generate orthoimagery and explore the use of HRSI for visualisation.

QuickBird ‘Basic’ Imagery

The QuickBird satellite orbits the Earth at an altitude of approximately 450 km and travels at 7 km/s. With a field of view of 2.1° and focal length of 9 m, the pushbroom sensor captures submetre resolution for panchromatic (0.61–0.72 m) and 2.44–2.88 m multispectral imagery. Within the focal plane are 6 panchromatic arrays operating with time delay integration and 6 four-linear multispectral arrays imaging in 11 bits; all CCD lines are staggered (DigitalGlobe, 2006).

The satellite is agile such that oblique pointing is possible to 30° off-nadir. Along- and across-track stereo capability allows collection of same pass stereo pairs and therefore, the scene content, lighting conditions and satellite geometry are the same for the two images. After the initial forward image is acquired, the satellite is steered to point backwards to image the same scene with approximately 90% overlap. A stereo pair covers an approximate area of 21.2 × 21.2 km, totaling 450 km².

DigitalGlobe’s QuickBird products are provided at varying levels depending on their positional accuracy and degree of processing. Predictably, as the positioning accuracy is increased, the price of the product also increases (DigitalGlobe, 2006). The sensor corrected ‘Basic’ product with the least specified accuracy and lowest cost has been employed in this investigation.

Geopositioning

To facilitate high-precision geopositioning, a dozen precisely measured ground control points (GCPs) were acquired by GPS-survey conducted by Bhutan’s Department of Survey and Land Records. These largely constituted road markings in the Thimphu region, concentrated in the north-east of the scene.

An initial analysis of the satellite imagery utilising no GCPs and a Rational Polynomial Coefficient (RPC)-based approach resulted in absolute geopositioning accuracies of approximately 20 m. The positional biases in the DigitalGlobe generated RPCs are reflected by the large discrepancies, quantified in Table 1. These inherent biases can be accounted for by using a bias compensation method which incorporates corrections into the existing RPCs, without the need for additional correction parameters. A single GCP is all that is needed for this procedure (Fraser et al., 2006). The provision of GCPs enabled the geopositioning accuracy

Table 1 Geopositioning discrepancies in sensor orientation

| Orientation | GCPs | CKPs | RMSE discrepancies at CKPs [m] | | |
|----------------|------|------|--------------------------------|----------------|----------------|
| | | | S _E | S _N | S _H |
| QuickBird RPCs | 0 | 12 | 21.4 | 6.3 | 0.4 |
| Corrected RPCs | 4 | 12 | 0.6 | 0.7 | 0.4 |

to be significantly improved in the bias-compensated RPC bundle adjustments, where accuracy at 1-pixel level was obtained. Additionally, these bias-corrected RPCs were to be used as an additional control scenario to supplement the 12 measured GCPs for downstream generation of digital surface models (DSMs) and orthoimagery.

Height Modelling

DSM Generation

Elevation information and surface topography is important for a diverse range of applications such as hydrology, geomorphology and infrastructure planning. High costs associated with acquiring a dense elevation network often translate to limited and infrequent opportunities of DEM generation in developing countries. For instance, the existing DEM data for Bhutan is an old 1964 Survey of India scanned map; the contour interval is 200 m and contour lines are stated as only approximate. With the aid of optical stereo imagery and radar technologies, updated height information can be obtained and modelled at relatively low cost.

Two image matching algorithms were applied to produce DSM data from the optical imagery. The QuickBird along-track stereo pairs produce near simultaneous data capture resulting in consistent imaging conditions and reduced radiometric variation, conducive for image matching and DSM generation. First, an intensity based matching procedure embodied in Z/I Imaging's ImageStation Photogrammetry Suite 4.3 Image Station Automatic Elevations (ISAE) was applied; and second, a multi-photo, geometrically constrained (MPGC) image matching method incorporating a hybrid matching algorithm was used. A third approach to generating elevation information and an alternative to image matching, is utilising height models derived from low cost NASA/DLR SRTM InSAR DEMs.

ISAE

ISAE's commercially available automatic height generator uses bilinear finite elements to calculate differences in parallax of matched points within the limits of a user specified parallax bound and epipolar line distance. Matches are considered reliable once successful with similarity measures of correlation coefficient and interest value. A more detailed description of the ISAE mathematical model can be found in Z/I Imaging Corporation (2004).

Initially, it was anticipated that the bias-corrected RPCs would be used to orient the images to 1-pixel level accuracy. Unfortunately, this was not possible on the ImageStation due to Z/I Imaging QuickBird modules relying only on ephemeris, attitude and image metadata files, omitting the RPB files in triangulation. Without adaptive matching, the finest allowable post-spacing generated from the QuickBird scene was 15 m.

MPGC

The second image matching approach, MPGC, extracts matching candidates using a geometrically constrained cross-correlation method (Gruen, 1985). The procedure incorporates feature point matching, edge extraction and relational matching, where successfully matched features are further refined with a modified MPGC allowing potentially sub-pixel accuracy. Greater discussion of this process is provided in Zhang and Gruen (2006). The MPGC procedure allowed support from bias-corrected RPCs which ensured optimal object space accuracy and a DSM was generated with 5 m post-spacing.

SRTM

In February 2000, SRTM captured near-global height information by single-pass InSAR on two antenna pairs supporting C- and X-band wavelengths. The fixed antenna receiving shorter wavelength X-band pulses has a higher relative accuracy, ± 16 m absolute vertical and ± 6 m relative vertical accuracy (Rabus et al., 2003), although a narrower swath width of 50 km in comparison to the C-band data. C-band terrain model data is freely available over the internet at a 3 arcsec resolution world wide, and X-band data is available at 1 arcsec post spacings, although due to US Government restrictions, areas outside North America must be requested. The advantage of SRTM data over satellite imagery is that irrespective of time and seasonality, InSAR can acquire height information.

Here we concern ourselves with the X-band data for Bhutan, which was processed by DLR (Knöpfle et al., 1998) and made available for this study. As the X-band is a high energy wavelength, these height models represent the surface of the terrain (as opposed to 'bare earth'), similar to that of optical space imagery. The 1 arcsec resolution in this region translates to a DSM of 28 m post-spacing.

Accuracy Assessment

Given that orientation with bias-corrected RPCs can yield accuracy at the 1-pixel level, these RPCs were used as an additional control scenario to generate 33 CKPs from stereo measurements to supplement the 12 GPS-measured GCPs.

As a preliminary accuracy assessment of the DSMs, elevation comparisons were computed between the GPS- and stereo-derived CKPs and bilinearly interpolated heights for each of the DSMs. While the MPGC DSM had height discrepancies just under 2 m at the CKPs, the SRTM DSM had height discrepancies slightly over 13 m. The overall accuracy was reflected in the RMSE values, where the MPGC DSM had a height discrepancy of less than a metre, the ISAE image matching DSM a RMSE of 4 m, and the SRTM an error of 6 m. Averages of the discrepancies show that there is a mean shift in the ISAE and SRTM DSMs; the ISAE 1.5 m shifted below the true surface, and SRTM 3 m above the surface. Examining the MPGC DSM, there is no mean shift and the height discrepancy is pixel-level at the CKPs.

A statistical overview is given in Table 2; however, with only 40 or so CKPs over a 300 km² scene, these figures are unlikely to be representative of the entire test

Table 2 DSM Height discrepancies at GPS and stereo CKPs

| DSM and post spacing | Data source | Reference | Height discrepancy at CKPs | | | |
|-------------------------|----------------|--------------|----------------------------|----------|----------|-------------|
| | | | CKPs | RMSE [m] | Mean [m] | Abs Max [m] |
| ISAE 15 m | Image matching | GPS | 12 | 1.2 | −0.3 | 1.9 |
| MPGC 5 m | Image matching | GPS | 12 | 0.5 | −0.2 | 0.9 |
| SRTM 28 m | InSAR | GPS | 12 | 5.4 | 4.9 | 7.4 |
| ISAE 15 m | Image matching | GPS + Stereo | 43 | 3.7 | −1.5 | 10.8 |
| MPGC 5 m | Image matching | GPS + Stereo | 45 | 0.7 | −0.2 | 1.7 |
| SRTM 28 m | InSAR | GPS + Stereo | 38 | 6.2 | 3.1 | 13.3 |

region. In order to obtain a more representative overall heighting accuracy based on surface extraction results over a greater number of sample points and through variable relief and slope, the most accurate DSM available, the 5 m MPGC DSM, was utilised as a reference surface.

A comparison between the heights obtained in the ISAE matching method and bilinearly interpolated values in the reference MPGC DSM revealed a heighting RMSE of 10 m from over 1 million CKPs.

Although these divergences are partly attributed to sensor orientation differences and the image matching algorithms, it must be noted that blunders originating from image saturation were not excluded from assessment. There was no consideration given to the normal process of manual review and post-processing of the generated DSMs, although differences in height values over 25 m, which accounted for 18% of the offsets, were treated as blunders and disregarded in the analysis.

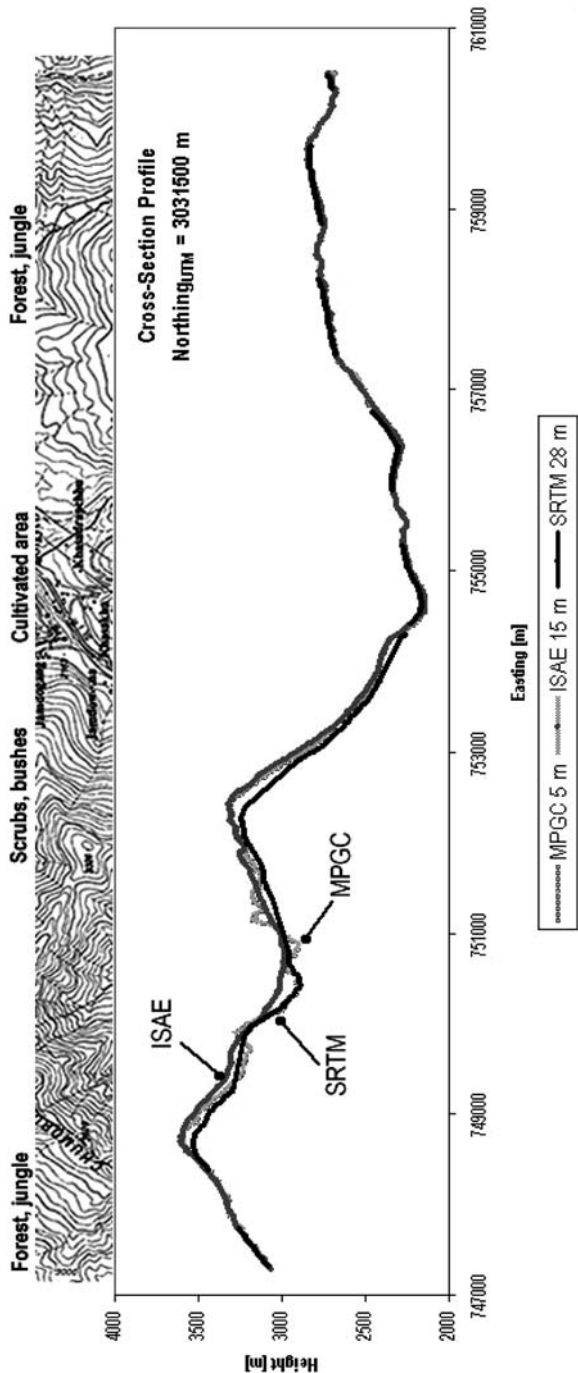
The same comparison procedure was carried out between the SRTM DSM and the reference MPGC DSM and summarized in Table 3. This resulted in a heighting RMSE of 13 m, where a third of the height discrepancies were deemed as blunders. This is not surprising, as the DLR height error map for the InSAR DSM indicated that well over half the test field was in error of 50–90 m.

The DSM evaluation assumes that errors are solely attributable to the source, i.e. aspects of the image matching or the InSAR acquisition; however, there are also other factors to consider when comparing multi-resolution DSMs, where interpolation errors may play a significant role. The differences in post spacing and its effect on modelling the surface can be seen when examining cross-section profiles, as shown in Fig. 1. Surface discontinuities are preserved in the MPGC 5 m

Table 3 DSM height discrepancies with MPGC 5 m reference

| DSM and post-spacing | Height discrepancy at CKPs | | | |
|-------------------------|----------------------------|--------------|----------|----------|
| | CKPs | Blunders (%) | RMSE (m) | Mean (m) |
| ISAE 15 m | 1,061,433 | 18 | 9.8 | 0.7 |
| SRTM 28 m | 246,009 | 32 | 12.7 | 1.0 |

Fig. 1 DSM height discrepancies with MPGC reference



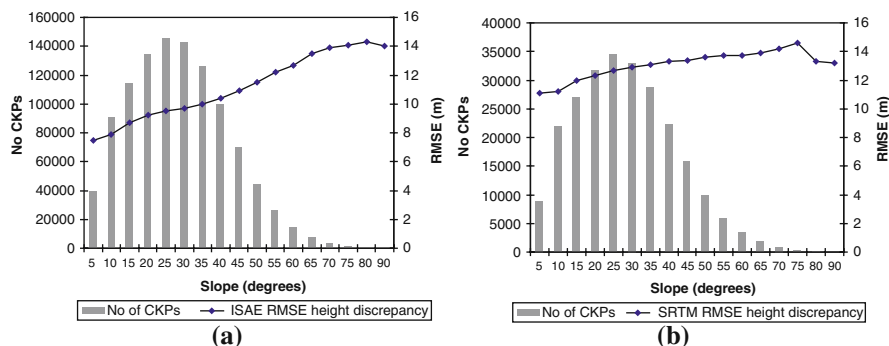


Fig. 2 Influence of slope on (a) ISAE and (b) SRTM height discrepancies with MPGC reference

post spacing DSM, whereas the ISAE 15 m DSM smoothed and generalised surface topography. Errors are most noticeable in the SRTM 28 m DSM in regions of variable relief, most likely due to the effects of radar foreshortening and layover susceptible in mountainous regions. There is a clear indication that slope plays a role in higher RMSE values, as shown in Fig. 2. As the terrain inclination increases, the height discrepancy also increases for both image matching and InSAR acquisition methods.

Data Integration: Orthorectification, Pansharpening and Visualisation

The QuickBird ‘Basic’ imagery has limited image processing, confined to corrections for radiometric and internal sensor geometry and optical and scan distortions. The panchromatic and the multispectral images are both in the satellite reference frame and preprocessing is required for geometric integration of all channels. In their raw form, the QuickBird pan and multispectral images are offset north and south to one another. As no georeferencing is applied, image-to-image registration must first be carried out before pansharpening can proceed.

The most accurate DSM generated (MPGC) was used to remove relief displacement, so that planimetric coordinates could be obtained from a single orthoimage to an accuracy of better than a metre. The metric results of this process are summarized in Table 4. The results show that high accuracy ground feature determination is possible with lowest cost QuickBird imagery.

Visual representation of the terrain can improve understanding of the landscape and has benefits in communicating information to a wider audience. The multispectral imagery was fused with the single band imagery to generate a pansharpened orthoimage and further, draped over the metrically accurate DSM, as shown in Fig. 3.

Table 4 Planimetric accuracy achieved with Orthoimagery

| Ortho imagery | CKPs | RMSE discrepancies at CKPs | |
|------------------|------|----------------------------|--------------------|
| | | S _E [m] | S _N [m] |
| Resampled to 1 m | 44 | 1.00 | 0.80 |

Fig. 3 Visualisation – orthorectified pansharpened image draped over DSM



Concluding Remarks

In remote areas such as Bhutan, it is common for existing maps to be either out-of-date or to not exist. Although picturesque, the rugged mountainous and largely inaccessible landscape is not well suited to traditional topographic surveying and mapping (e.g. there is only one airport in the country and only a few passenger aircraft). It has been shown here, that even with limited ground control, satellite imagery has the potential to rectify the situation and vastly enhance mapping prospects in such an environment.

By compensating exterior orientation biases inherent in the recorded sensor orientation data, the attainment of 1:5000 mapping scale ground measurement accuracy is possible with lowest cost QuickBird imagery. While low cost alternative data sources such as SRTM are available, the InSAR acquisition may not be suited to an undulating environment with an average terrain inclination of 27°, such as those experienced in Bhutan.

It has been shown that there is potential for QuickBird ‘Basic’ to be an effective and economically viable method of extracting 3D information to be used for high accuracy ground feature determination. The implications of using this imagery for precision geopositioning include the generation of more accurate digital terrain models and cartographic maps and location data for incorporation into a GIS, providing useful information for the wider community, especially in the case of a developing country with very limited resources for 3D spatial information generation.

Acknowledgements The authors are grateful to DLR for making the SRTM X-band DEM data available for this study and DigitalGlobe/SKM for the provision of imagery. We also acknowledge Dr Peter Reinartz of DLR and Dr Zhang Li for their contributions to the project.

References

- DigitalGlobe (2006) DigitalGlobe Basic imagery, Colorado, USA. http://www.digitalglobe.com/product/basic_imagery.shtml (accessed 21 Sep. 2006)
- Fraser CS, Dial G, Grodecki J (2006) Sensor Orientation via RPCs. *ISPRS J of Photogrammetry & Remote Sensing* 60(3): 182–194
- Gruen A (1985) Adaptive least squares correlation: a powerful image matching technique. *South African J of Photogrammetry, Remote Sensing and Cartography* 14(3): 175–187
- Holland D, Boyd DS, Marshall P (2006) Updating topographic mapping in Great Britain using imagery from high-resolution satellite sensors. *ISPRS J of Photogrammetry and Remote Sensing* 60(3): 212–223
- Holland D, Guilford R, Murray K (eds.) (2003) *Topographic Mapping from High Resolution Space Sensors*, OEEPE Official Publication No. 44.
- Knöpfle W, Strunz G, Roth A (1998) Mosaicking of digital elevation models derived by SAR interferometry. *International Archives of Photogrammetry and Remote Sensing*, Stuttgart, Germany 32(4): 306–313
- Rabus B, Eineder M, Roth A, Bamler R (2003) The shuttle radar topography mission – a new class of digital elevation models acquired by spaceborne radar. *ISPRS J of Photogrammetry and Remote Sensing* 57: 241–262
- Samadzadegan F, Hahn M, Bagherzadeh H, Haeri M (2003) On the geometric accuracy and information content of Ikonos high resolution imagery for map revision. *ISPRS Commission IV Joint workshop*, Sept 8–9, Stuttgart, Germany
- Z/I Imaging Corporation (2004) *ImageStation Automatic Elevations User's Guide*. Madison, AL, USA, pp. 59–68
- Zhang L, Gruen A (2006) Multi-image matching for DSM generation from IKONOS imagery. *ISPRS J of Photogrammetry & Remote Sensing*, 60(3): 195–211

A New Dataset for Forest Height Across Australia: Pilot Project to Calibrate ICESat Laser Data with Airborne LiDAR

Alex Lee, Peter Scarth, and Adam Gerrand

Abstract To better quantify and monitor the extent, structure and biomass of Australian forests, accurate cover and height information is required, yet only a small proportion of Australia's forests have reliable height information. The use of airborne laser survey using Light Detection and Ranging (LiDAR) data has rapidly developed and has demonstrated its effectiveness and high accuracy for forests height measurement. However it is expensive and data is not yet widely available for many areas. A recent source of height data is now available from the NASA ICESat satellite. The ICESat laser pulses give approximately 70 m diameter footprints, spaced at 170-m intervals along the Earth's surface. Tracks are spaced about 50 km wide, and since 2003 over 2 million points across Australia have been imaged. These could provide significant potential for improving vegetation structure assessment, and monitoring both natural and human induced change. A pilot project utilised three sites where coincident airborne LiDAR was available; in NE Victoria, south-central Queensland, and along the Brisbane River (Queensland). Ground elevation correspondence gave a mean difference < 2 m (ICESat higher than LiDAR), with woodlands recording a difference of 0.16 m. For forest structural attributes, ICESat gave reliable estimates (i.e. within 2 m for height and 10% for cover) in some cases, but the results were dependant on the density and height of the forest, and terrain slope within the footprint, thus making the extraction inconsistent between structural metrics. In sparser forests, ICESat tends to report foliage projective cover, whereas in dense forests, crown cover equivalent values are recorded. An apparent threshold of improved accuracy when cover was higher than 30% was observed. Further research is required to better define the thresholds where ICESat does not produce reliable results. Whilst ICESat appears to be unsuited to continental application for national reporting of both height and cover until further calibration across a greater range of forest environments is undertaken, however ongoing research efforts to improve the calibration are showing promise.

A. Lee (✉)

Fenner School of Environment and Society, Defence Imagery and Geospatial Organisation,
Australian National University, Canberra, ACT 0200, Australia
e-mail: Alexander.Lee@defence.gov.au

Introduction

To effectively respond to a changing climate, there is a need to improve forest and vegetation assessment methods, particularly as the dynamics (direction and magnitude) of potential change need to be identified as well as the current stock. In addition, such information is required by governments, industry, private landholders and the public to detect trends in commercial, biodiversity and greenhouse values, assess the performance of management practices and public policies, guide sustainable development, and forecast the future condition of these ecosystems (Henry et al. 2002, Brack 2007).

Undertaking comprehensive, consistent, and accurate assessments within Australia represents a significant challenge for two main reasons. First, Australia has an estimated 164 million hectares (ha) of native forests and woodlands, which are widely distributed, and generally located around the outer margins of the continent. Second, around 70% of these forests are under private management, with less than 10% in commercial public forest estates where traditionally the best information was collected. In the areas under private management, the information available on structure and condition is especially limited (National Forest Inventory (NFI) 2003). The development of efficient and cost-effective methods, such as that described for the proposed Continental Forest Monitoring Framework (CFMF) (Norman et al. 2003, Wood et al. 2006) from which this essential information may be retrieved, is therefore critical if national and international obligations are to be better fulfilled (Thackway et al. 2007).

The use of airborne laser survey using small footprint multiple (discrete) return and large footprint full waveform Light Detection and Ranging (LiDAR) data has rapidly developed, and has demonstrated an effectiveness and high accuracy for forest structure measurements (Reutebuch et al. 2005). Small footprint LiDAR is an active sensor that uses a laser beam in the near infrared spectral range directed towards the ground. For forest assessment purposes, small footprint LiDAR provides a commercially available, highly precise, point dataset of terrain and vegetation, and the high accuracies now makes it possible to 'image' and locate individual tree crowns (Suarez et al. 2005).

However, to date the extent of LiDAR use in Australia has been restricted to a small number of research sites (Lee and Lucas 2007). Therefore for nationwide sampling of forest height, satellite based measurements are currently the only feasible alternative. Whilst there are no satellite based laser altimetry systems presently dedicated to vegetation assessment, this limitation is being addressed to some extent by spaceborne LIDAR platforms used for monitoring changes in global ice volume. One such system is the Geoscience Laser Altimeter System (GLAS) on the current NASA Ice, Cloud, and land Elevation Satellite (ICESat). The full-waveform laser with an approximate ellipsoid footprint of 70 m diameter (variable between 50 m diameter circle to 60 × 120 m ellipse), which samples approximately every 170 m along track, and has a 183 day repeat cycle path. Investigations into forest height extraction have been initiated, and are currently ongoing (Lefsky et al. 2005a, Sun et al. 2008).

Research Design

The ICESat laser sensors provide a possible solution to the current lack of a height data source that is consistently collected across Australia. Therefore, to investigate the potential for ICESat data to meet this requirement, ICESat data were summarized and analysed in a number of steps, as described below. The full assessment is reported in (Lee et al. 2006).

1. The available data (version r26) were summarized across Australia to examine how the forest estate was represented, when compared to current NFI estimates. The main collection periods available in the r26 version were Oct-Nov 2003, March 2004, and Nov 2005.
2. Ground elevation comparisons were made from 132 footprints at three different locations where airborne LiDAR were available, with two sites in Queensland, and one site in NE Victoria utilising the CFMF pilot project data (Wood et al. 2006).
3. Vegetation assessment comparisons were made using CFMF data from NE Victoria. Here a total of 27 overlap locations within the LiDAR transects were found (Fig. 1). The locations span a wide range of broad ecological zones (ecozones), from floodplains, rolling foothills, to montane and subalpine sites. From the overlap sites, a total of 76 footprints were selected that were within the LiDAR swath and included forest. A detailed case study was undertaken

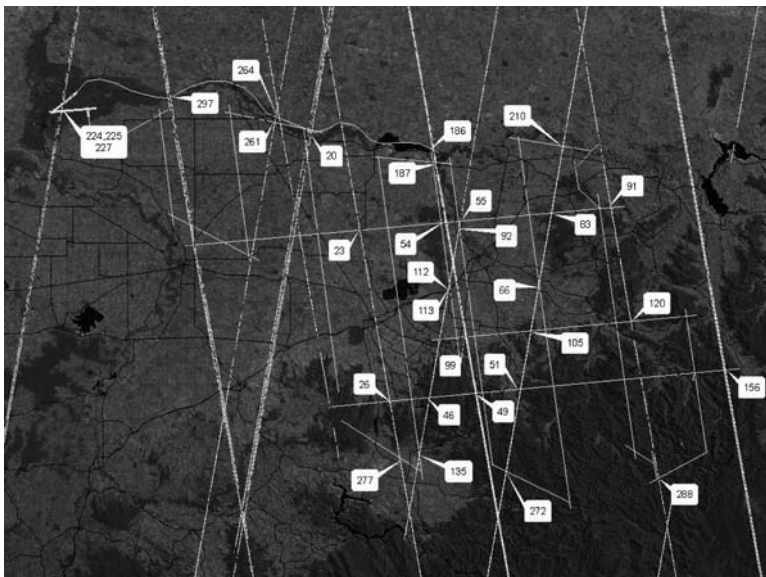


Fig. 1 ICESat transects (light diagonal points) with the airborne LiDAR transects (north-south & east-west lines) and numbered overlap locations across CFMF pilot region in NE Victoria. Darker areas are native forest; lighter areas are cropping and grazing. The image spans approximately 225 km across (east-west) and 170 km high (north-south)

with a subset of three footprints at one location that spanned a ridge, mid-slope and gully.

4. Subsequent to the r26 version analyses, the next version (r28) of ICESat data became available. This data were summarised at a continental scale and compared to the r26 results and current NFI data.

Analysis Methods

Detailed spatial comparisons of elevation and forest structure between ICESat and airborne LiDAR first calculated the approximate ICESat footprint size and shape, which were used to select the equivalent airborne LiDAR data. Then terrain and vegetation information were extracted from the LiDAR data from within the estimated footprint area (Lee et al. 2006). The footprint shape and size were accurately calculated, such that the selection of the associated airborne LiDAR data was as precise as possible. Standard elliptical formulae were utilised to model the bounding area of the ICESat footprint, using the parameters of azimuth, eccentricity and the major and minor axes (see Lee et al. 2006 for formulae and parameter description).

Different laser sensors on the satellite have been used since 2000, which has resulted in different footprint shapes being observed. Figure 2 illustrates one location with three footprints from different dates. The yellow crosses indicate the respective footprint centres, and the labels are the Julian day (number of days) since the sensor began recording (from 12 p.m., January 1st, 2000). The smallest (and most recent) footprint (purple) is approximately 50 m in diameter.

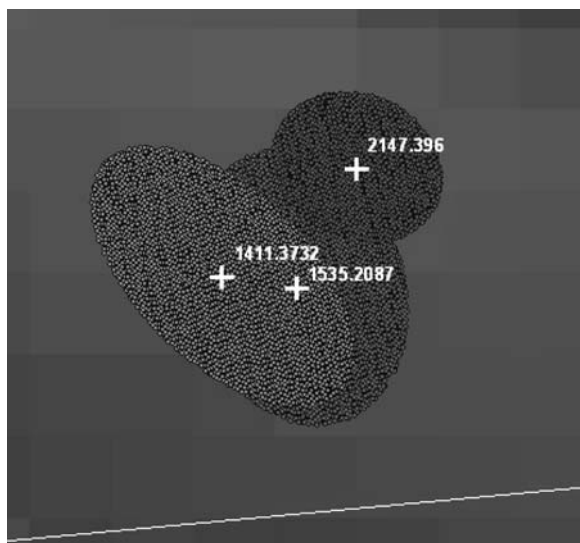


Fig. 2 Examples of airborne LiDAR selected within three ICESat footprints from different dates

The following parameters were extracted from the full waveform curve for comparison:

- Canopy cover (0–100%);
- Centroid height (distance from centre of the ground pulse to the centre of the highest vegetation pulse);
- Fit_height (the third parameter (β^A) in the weibull distribution used to fit the cumulative vegetation profile, calculated as $(\beta^A[1] \cdot \exp \beta^A[2] \cdot (\text{height}_{\beta^A} / f^A[\beta^A[4]))$;
- Veg_height (height on the curve where the cumulative FPC greater than 2 m crosses 95%);
- Height at 10% FPC (height where the cumulative FPC greater than 2 m crosses 10% (for r28 data only).

The forest structural attributes derived from the airborne LiDAR for comparison were:

- Maximum vegetation height (m);
- Predominant vegetation height, (m);
- Percent vegetation foliage cover (0.5 m+ height) (0–100%);
- Percent forest foliage cover (2 m+ height) (0–100%);
- Percent crown cover (0–100%).

See Lee et al. (2006) and Lee and Lucas (2007) for a detailed description of all the attributes.

Results

Initial Continental Summary

For the r26 version of the ICESat data, there were a total of 1,906,792 footprints across Australia, from which approximately 39.4% had height ≥ 2 m, and cover $\geq 10\%$ (i.e. forest) (Table 1). This contrasts with the NFI continental forest estimate of approximately 21.4%. In terms of structure class comparisons between ICESat and NFI, both medium and tall classes are within 3%, however all other height and cover classes differ by between 5.7 and 31.6%. The comparison in cover class estimates is especially disparate.

Ground Elevation Comparisons

For the North East Victorian sites, elevation extracted was within 2–3 m of airborne LiDAR data on average, within a mean range of ± 5 m ($n = 94$). For sites in central Queensland woodlands, the mean difference was approximately 20 cm, within a range of ± 2 m ($n = 18$). For the Brisbane river (south east Queensland) sites, the

Table 1 GLA v26 continental summary for height (centroid height) and cover, including the NFI estimate (2003–2007)

| % of records Height (m) | Cover (%) | | | | | NFI % |
|----------------------------|-----------|-------------------|------------------|--------|--------------|-------------------|
| | 0–10 | 10–30 | 30–70 | 70–100 | ICESat total | |
| 0–2 | 48.0 | 2.2 | 8.9 | 0.0 | 59.1 | 78.8 |
| 2–10 | 1.4 | 3.6 | 20.8 | 1.7 | 27.4 | 4.6 |
| 10–30 | 0.1 | 0.6 | 7.8 | 4.4 | 12.9 | 15.7 ^c |
| 30+ | 0.0 | 0.0 | 0.3 | 0.3 | 0.6 | 1.1 |
| ICESat total | 49.5 | 6.4 | 37.7 | 6.3 | 100.0 | 100.0 |
| NFI % | 78.8 | 14.6 ^a | 6.1 ^b | 0.6 | 100.0 | |

For NFI totals: ^aincludes 1.3% unknown cover; ^bincludes 0.2% plantations; ^cincludes 4.9% unknown height

mean difference was within 1–2 m, with a mean range of ± 5 m ($n = 20$). A more detailed description of the results is provided in (Lee et al. 2006).

Vegetation Comparisons in NE Victoria

Across all ecozones, ICESat FPC correspondence with LiDAR foliage-branch cover was very poor ($r^2 = 0.12$, $RSE = 18.26\%$, $y = 0.28115x + 20.486$), and crown cover ($r^2 = 0.14$, $RSE = 29.83\%$, $y = 0.5114x + 32.406$). When applying an arbitrary quality or utility assessment, ICESat gave a good result for foliage cover (i.e. within 10% cover) for 33% of footprints, whilst 41% gave poor results (i.e. a difference of greater than 20% cover). When examined by ecozone, 40% were good, and 20–40% were poor for floodplains and montane footprints. For footprints found in foothills sites, 21% were good whilst 50% were poor.

Forest height values extracted from ICESat had poor correspondence to the LiDAR heights, with r^2 values for the three different height parameters ranging from 0.2 to 0.45. The best initial correspondence was between ICESat parameter ‘veg_ht’ and LiDAR elevation range ($r^2 = 0.45$, $RSE = 13.47$ m; Fig. 3-left). ICESat gave a good result (i.e. within 5 m) for predominant canopy height for 54% of footprints, whereas 28% of footprints had a height difference greater than 10 m (i.e. poor). When assessed by ecozone, floodplains and montane footprints recorded 40% that were good, with 40% poor. For foothills sites, 75% were good and 10% were poor. The ICESat parameter ‘centroid_ht’ related best to LiDAR predominant height ($r^2 = 0.26$, $RSE = 8.13$ m; (Fig. 3-right)). When the comparison was further subdivided by ecozone, it is apparent that the floodplain sites have a higher number of poor comparison sites. The foothills and montane sites have most occurring within 5 m of the 1:1 line. There are some larger outliers where ICESat tends to report a lower height than the LiDAR, but further investigation is required to determine the

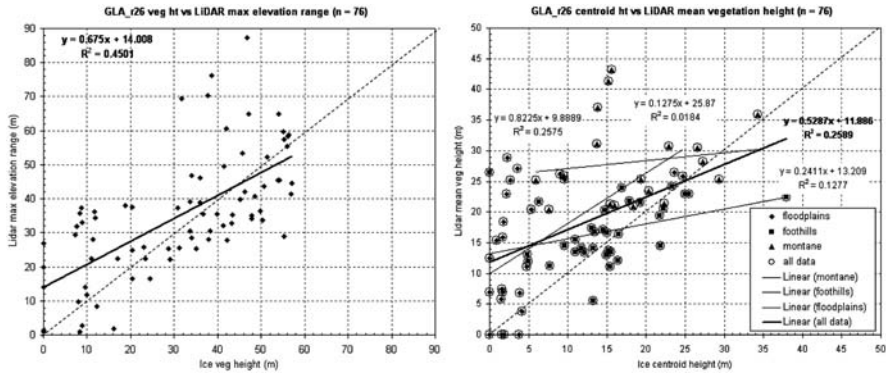


Fig. 3 (left) ICESat waveform ‘veg_ht’ versus LiDAR elevation range. (right) ICESat ‘centroid_ht’ related best to LiDAR predominant height

cause of the disparity. Additionally, it was noted from the results that ICESat data tended to give either a good result for height and poor for cover or vice versa.

ICESat Comparison Case Study in NE Victoria

The case study site examined three footprints (Fig. 4) in detail to assess the potential effects of slope, terrain position, and vegetation density on the extraction of ICESat height and cover attributes. In the riparian footprint, a close correspondence was observed for both ICESat ‘Fit_ht’ with LiDAR maximum height (~1 m difference), and ICESat ‘Centroid_ht’ with LiDAR predominant height (~2 m difference). This contrasts with the mid-slope and ridge top footprints, which recorded poorer height correspondences overall (differences in excess of 5 m). The exception was for mid-slope ICESat ‘Fit_ht’ and LiDAR maximum height, where the difference was < 1 m. The poorer correspondences observed for height and cover in the mid-slope and ridge top footprints were attributed to a combination of higher slope and relatively sparse vegetation within the respective footprints. The ICESat waveforms were extracted and compared to the airborne LiDAR return data for height and cover, and to compare between the apparent vertical profiles (Table 2).

For forest cover estimation at the case study site, the ridge-top footprint correctly estimates foliage-branch cover, whereas the riparian footprint correctly estimates crown cover. In the case study example the riparian stand has a higher LiDAR foliage-branch cover (43%), and the ICESat value extracted is closer to LiDAR crown cover (~70%), whereas the ridge-top LiDAR foliage-branch cover is lower (28%), with the corresponding ICESat cover value being similar to LiDAR foliage-branch cover. The mid-slope ICESat footprint cover estimate is much higher than either LiDAR foliage-branch cover or crown cover, with the combination of steeper slope (up to 13°) and lack of tree cover (LiDAR crown cover = 8%) as potential factors in the difference observed. See (Lee et al. 2006) for tabular results.

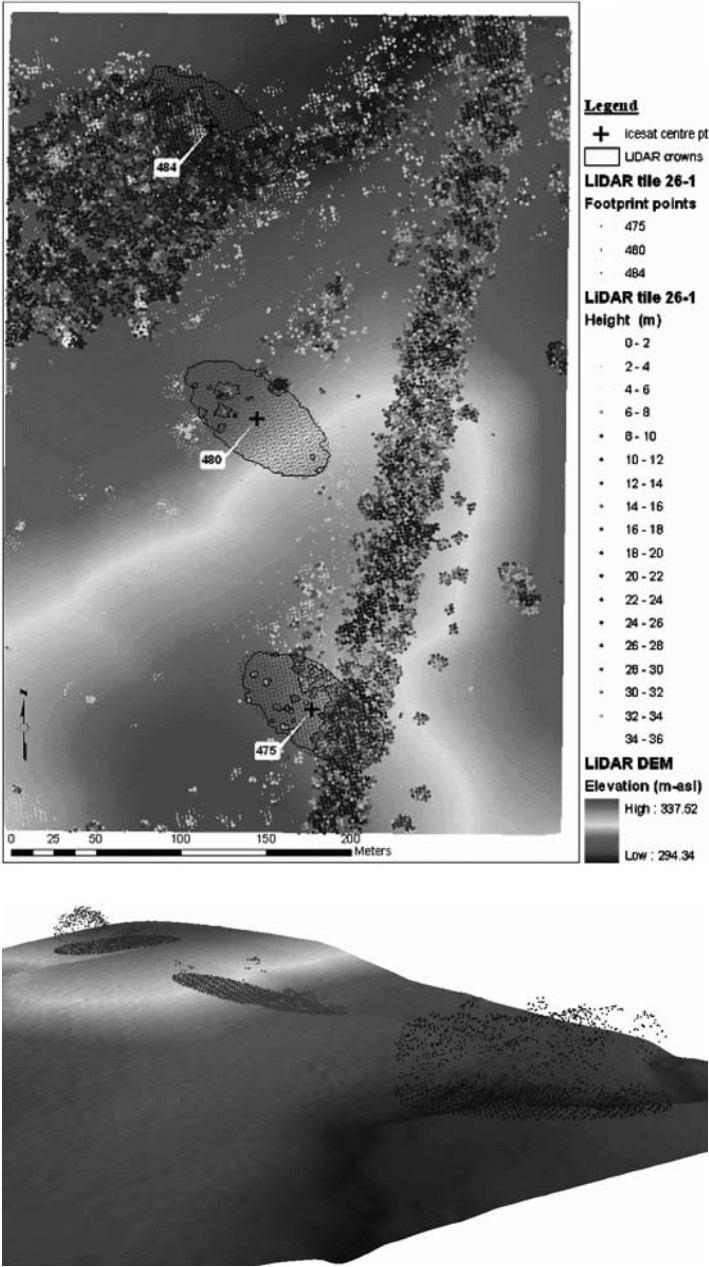


Fig. 4 Airborne LiDAR with three ICESat footprints displayed on a 1 m LiDAR derived DEM. (Upper) planimetric view showing footprints in relation to other vegetation, as represented by LiDAR returns. (Lower) LiDAR returns only within the ICESat footprints displayed in 3D

Table 2 ICESat case study footprints; description, full waveform, and LiDAR apparent vertical profiles (note: y-axis scales differ in range between LiDAR and ICESat)

| Case Study Footprint attributes | ICESat waveform profile | LiDAR apparent vertical profile |
|---------------------------------|-------------------------|---------------------------------|
| ICE-id: 484 | | |
| Collection date: 6-10-2003 | | |
| Major axis length: 89 m | | |
| Elevation: 304.9 m (asl) | | |
| No. of LiDAR returns: 1233 | | |
| Location (DD) | | |
| Latitude: -36.809288 | | |
| Longitude: 146.04567 | | |
| Site: gully riparian strip | | |

Table 2 (continued)

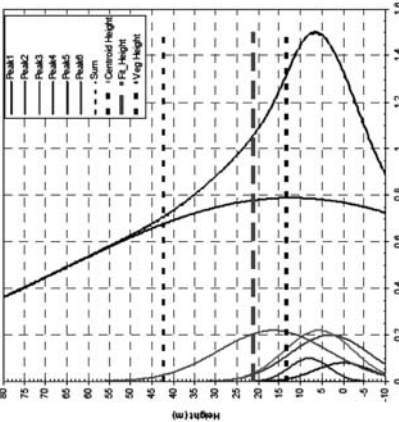
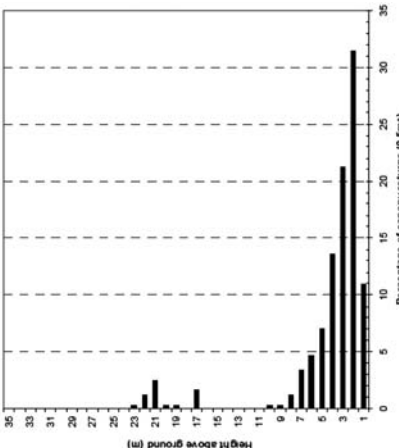
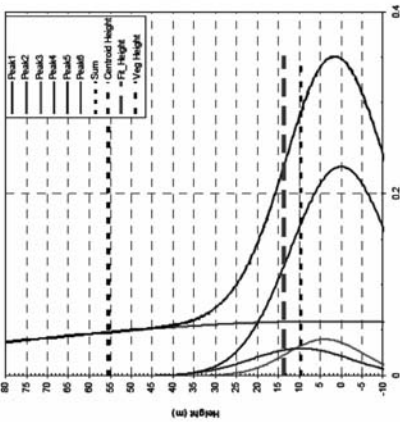
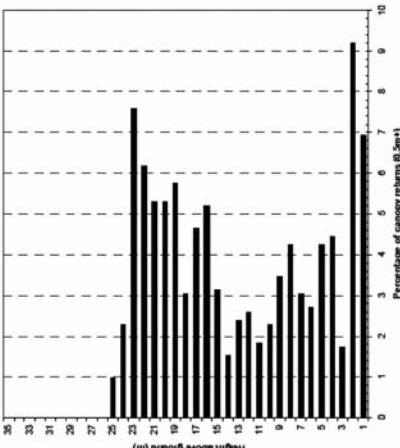
| Case Study Footprint attributes | ICESat waveform profile | LiDAR apparent vertical profile |
|--|---|--|
| <p>ICE-id: 480</p> <p>Collection date: 6-10-2003</p> <p>Major axis length: 89 m</p> <p>Elevation: 313.9 m (asl)</p> <p>No. of LiDAR returns: 413</p> <p>Location (DD)</p> <p>Latitude: -36.810833</p> <p>Longitude: 146.04591</p> <p>Site: mid-slope grazing area with scattered trees</p> |  |  |
| <p>ICE-id: 475</p> <p>Collection date: 6-10-2003</p> <p>Major axis length: 89 m</p> <p>Elevation: 328.8 m(asl)</p> <p>No. of LiDAR returns: 923</p> <p>Location (DD)</p> <p>Latitude: -36.81237</p> <p>Longitude: 146.0462</p> <p>Site: Ridge-top, bisecting a treed fence-line strip</p> |  |  |

Table 3 GLA v28 continental summary with NFI estimates (2003–2007)

| % of records Height (m) | Cover (%) | | | | | NFI % |
|----------------------------|-----------|-------------------|------------------|--------|--------------|-------------------|
| | 0–10 | 10–30 | 30–70 | 70–100 | ICESat total | |
| 0–2 | 80.8 | 0.0 | 0.0 | 0.0 | 80.8 | 78.8 |
| 2–10 | 0.4 | 0.1 | 1.1 | 0.0 | 1.7 | 4.6 |
| 10–30 | 1.9 | 1.5 | 8.7 | 2.3 | 14.3 | 15.7 ^c |
| 30+ | 0.1 | 0.2 | 1.9 | 1.0 | 3.2 | 1.1 |
| ICESat total | 83.1 | 1.8 | 11.8 | 3.3 | 100.0 | 100.0 |
| NFI % | 78.8 | 14.6 ^a | 6.1 ^b | 0.6 | 100.0 | |

NFI totals: ^aincludes 1.3% unknown cover; ^bincludes 0.2% plantations; ^cincludes 4.9% unknown height

Updated Continental Summary

For the r28 version of the ICESat data, there were a total of 2,579,278 records across Australia, from which approximately 16.9% were classed as forest, that is had height and cover attributes that were greater than or equal to 2 m and 10% respectively. The r28 data was significantly improved for national assessment when compared to the r26 version. The overall estimate of forest area is much closer to the NFI estimate (21.4%), differing by 4.5% (Table 3). The comparisons in height classes with NFI estimates are reasonably close, i.e. within 3%. The cover class comparisons are more variable, with large differences between the respective woodland and open forest class comparisons. This may reflect a threshold or limitation in the ability of ICESat to adequately resolve areas of scattered trees within the footprint area, particularly when cover is less than 20–30%.

Histograms of the height and cover distribution are shown in Fig. 5, and include the NFI structure class boundaries. Figure 6 illustrates the spatial distribution of ICESat footprints across the continent. Overall, the forest footprints appear in the same locations as have been mapped by the NFI, i.e. predominantly on the coastal margins of the eastern, south western and northern areas of the continent. Of note is the apparent forest recorded in northwest Western Australia and central Australia.

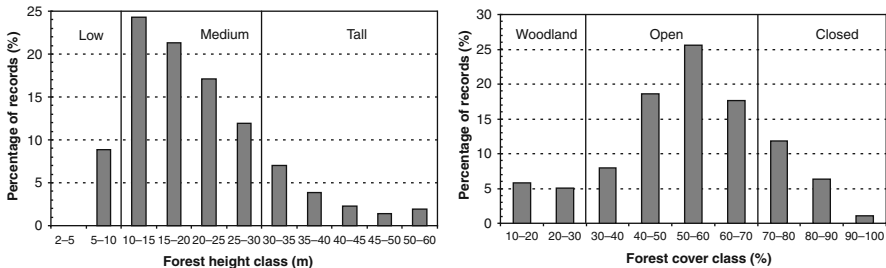


Fig. 5 ICESat GLA14r28 forest height and cover class distribution for Australia

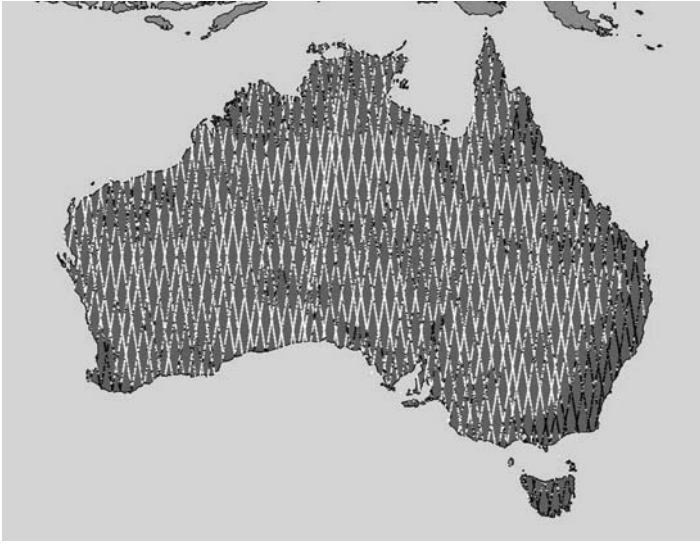


Fig. 6 ICESat GLA14r28 distribution across Australia (2006). Dark points are estimated forest (2 m+ height and 10%+ cover). Footprint point size representation is not to scale

Discussion

In terms of national level reporting and monitoring, the r28 version of ICESat shows promise for height assessment, though the cover estimates need improvement. The use of histograms for cover and height illustrate the advantage of the continuous measurement available with ICESat over the categorical classes used by the NFI. This provides an improved understanding of the actual distribution (assuming ICESat is an accurate sample) of forest height across the continent. However, improvements are required and currently ongoing. For example, with forest height the lowest value from the full waveform curve is 5.8 m ('height at 10% FPC' parameter). Therefore, to better match the NFI forest threshold of 2 m, more research is required to see if vegetation less than 5.8 m but greater than 2 m can be resolved from the waveform curves when using this parameter. This is especially relevant in the mallee and arid regions where much of the vegetation would be in the 2–5 m height range, and which is likely to be missed with the current parameter attribute extraction settings.

The three-footprint case study highlights several issues that combine to cause difficulties for attribute extraction and calibration. The case study has identified that ICESat (version r26) can extract attributes for height and cover that are similar to the LiDAR derived estimates, however the consistency of the extraction is variable. Issues that need to be further investigated, before consistent continental application can be undertaken, include an assessment of cloud cover at time of footprint collection (either with ICESat categorical attribute, or MODIS cloud opacity/depth

value for example), to determine if exclusion or additional calibration functions are required. This would assist in determining if there is any impact of smoke, high cloud, haze, and fog/mist on the ICESat response, especially in riparian areas, where these conditions may occur more frequently. Hazy conditions may result in greater scattering of the laser pulse, so resulting in less sensitivity to the vegetation, and incorrect assessment of height and cover.

Additionally, laser interactions with vegetation need more detailed investigation, as very sparse or clumped vegetation can violate many large footprint-processing assumptions, potentially resulting in incorrect results (Harding et al. 2001). Tall, dense, multi-layered forests can also present issues, especially when combined with steep slopes. Therefore likely error thresholds for height, cover, and strata need to be further investigated. This could include developing initial linear regression functions to improve height or cover using a range of ICESat attributes (e.g. elevation, slope, reflectance, intensity, footprint area, height, cover, time of day) to improve the attribute estimation. A combination of decision tree and/or series of calibration steps or functions stratified by ecozone will be required to optimise the extraction of height and cover from ICESat for all the major vegetation types across Australia.

Conclusions

Based on the comparisons undertaken for ground elevation, ICESat appears to be an effective calibration tool for continental terrain model validation. Whilst initial comparisons between ICESat and LiDAR forest structural metrics were variable and appeared to be dependant on the density of the forest and terrain slope within the footprint, ICESat did appear to extract reasonable estimates when compared to the LiDAR (especially with height), with an apparent threshold of improved accuracy when foliage-branch cover was higher than 30%. The differences observed in the case study were comparable (in terms of RSE for height) with those found in other pilot studies (e.g. Harding and Carabajal 2005, Sun et al. 2008), although more comparison sites are required to generate improved correlations and reliable continental application. It is encouraging to note the large improvement in national level statistics for forest structure with the r28 version over the r26 version, when compared to current National Forest Inventory estimates. This is especially so considering that height information is not consistently collected over the continent, and that not all forest area have been explicitly mapped or attributed with height and cover estimates.

References

- Brack, C. L., 2007. National forest inventories and biodiversity monitoring in Australia. *Plant Biosystems*, 141:104–112.
- Harding, D. J., Lefsky, M. A., Parker, G. G. and Blair, J. B., 2001. Laser altimeter canopy height profiles – Methods and validation for closed-canopy, broadleaf forests. *Remote Sensing of Environment*, 76:283–297.

- Harding, D. J. and Carabajal, C. C., 2005. ICESat waveform measurements of within-footprint topographic relief and vegetation vertical structure. *Geophysical Research Letters*, 32:L21S10.
- Henry, B. K., Danaher, T., McKeon, G. M. and Burrows, W., 2002. A review of the potential role of greenhouse gas abatement in native vegetation management in Queensland's rangelands. *Rangeland Journal* 24:112–132.
- Lee, A. C. and Lucas, R. M., 2007. A LiDAR-derived Canopy Density Model for Tree Stem and Crown Mapping in Australian Forests. *Remote Sensing of Environment*, 111:493–518.
- Lee, A. C., Scarth, P. and Gerrand, A., 2006. *ICESAT and airborne LiDAR calibration pilot project*. BRS internal technical report. Bureau of Rural Sciences, Canberra.
- Lefsky, M. A., Harding, D. J., Keller, M., Cohen, W. B., Carabajal, C. C., Del Bom Espirito-Santo, F., Hunter, M. O., de Oliveira, R. J. and de Camargo, P. B., 2005a. Estimates of forest canopy height and aboveground biomass using ICESat. *Geophysics Research Letters*, 32:L22S02.
- National Forest Inventory (NFI), 2003. *Australia's State of the Forests Report, 2003*. Canberra, Bureau of Rural Sciences.
- Norman, P., Wood, M. S. and Lee, A. C., 2003. *A Continental Forest Monitoring Framework for Australia – Background, concept and rationale*. Canberra, National Forest Inventory, Bureau of Rural Sciences.
- Reutebuch, S. E., Andersen, H.-E. and McGaughey, R. J., 2005. Light Detection and Ranging (LIDAR): An Emerging Tool for Multiple Resource Inventory. *Journal of Forestry*, 103: 286–292.
- Suarez, J. C., Ontiveros, C., Smith, S. and Snape, S., 2005. Use of airborne LiDAR and aerial photography in the estimation of individual tree heights in forestry. *Computers & Geosciences*, 31:253–262.
- Sun, G., Ranson, K. J., Kimes, D. S., Blair, J. B. and Kovacs, K., 2008. Forest vertical structure from GLAS: An evaluation using LVIS and SRTM data. *Remote Sensing of Environment*, 112:107–117.
- Thackway, R., Lee, A., Donohue, R., Keenan, R. J. and Wood, M., 2007. Vegetation information for improved natural resource management in Australia. *Landscape and Urban Planning*, 79: 127–136.
- Wood, M. S., Keightley, E. K., Lee, A. C. and Norman, P., 2006. *Continental Forest Monitoring Framework, Technical Report – Design and Pilot Study*. Canberra, National Forest Inventory, Bureau of Rural Sciences.

Linking Biological Survey Information to Remote Sensing Datasets: A Case Study

K.J. Sheffield, S.D. Jones, J.G. Ferwerda, P. Gibbons, and A. Zerger

Abstract Remote sensing is widely used as a tool to map and monitor environmental attributes, such as vegetation. This paper describes a native vegetation ground data collection protocol that attempts to integrate the spatial resolution of several remotely sensed datasets and the spatial variation of vegetation into a framework. A particular challenge of this study was to use pre-existing vegetation survey methodology and adapt this for use with a number of remote sensing satellite systems. The spatial properties of remotely sensed data were explored by calculating textural measures for images at progressively coarser spatial resolutions, allowing sources of remotely sensed data for this project to be evaluated, with respect to spatial scale. This study forms part of a larger project which investigates the potential use of remotely sensed data in the development of a vegetation assessment framework, providing linkages between variables at site, landscape, and regional scales.

Introduction

This paper presents an overview of the approach taken to develop a vegetation ground data collection protocol that provides relevant ground information for use with SPOT 5 and Ikonos imagery, and integrates currently operational ground-based methods for assessing vegetation attributes at a site scale. This case study takes established knowledge and techniques from remote sensing and ecological disciplines, and provides an applied example of how data requirements for two purposes can be integrated within the one approach. This work employs known concepts and issues relating to the collection of ground data for remote sensing studies and provides a practical application of this theory in the context of vegetation assessment for biodiversity conservation in south-eastern Australia.

K.J. Sheffield (✉)

School of Mathematical and Geospatial Sciences, RMIT University, Melbourne, VIC, Australia
e-mail: s3102807@student.rmit.edu.au

Multi-Spectral Remote Sensing of Vegetation

Imagery from multi-spectral satellite remote sensing platforms is frequently used for vegetation assessment. Remote sensing based vegetation measures range from highly detailed fine scale assessments, to regional and global applications (Thomlinson et al. 1999, Defries et al. 2000, Huang et al. 2001, Armston et al. 2004, Johansen et al. 2007). Satellite remotely sensed data provide an efficient method to measure stands of vegetation in a timely manner, particularly over larger tracts of vegetation (Coops and Culvenor 2000, Zawadzki et al. 2005).

The spectral response of vegetation is characterised by lower reflectance in the visible portion of the electromagnetic spectrum, and high reflectance of near infrared wavelengths. Key factors that affect the spectral reflectance characteristics of vegetation include leaf size and orientation, physical structure of the plant, species distribution, vegetation density, and the influence of other land covers (Bannari et al. 1995, Armitage et al. 2000, Nagendra 2001). The temporal influence on vegetation spectral response is also a key consideration as vegetation phenology (and consequently spectral reflectance) varies seasonally and at different plant growth stages (Jensen 2000, Nagendra 2001, McCoy 2005).

A common approach to the assessment of vegetation using multi-spectral remotely sensed data is the use of vegetation indices. Vegetation indices are radiometric functions that provide information about vegetation reflectance and biomass. Many different vegetation indices have been developed to provide information on a range of vegetation characteristics such as vegetation cover, leaf density or leaf water content. The Normalized Difference Vegetation Index (NDVI) is widely used to derive estimates of vegetation cover (Bannari et al. 1995, Defries et al. 2000, North 2002, Jiang et al. 2005, Carreiras et al. 2006, Liu et al. 2007). Other routinely used vegetation indices include the Soil Adjusted Vegetation Index (SAVI) and the Enhanced Vegetation Index (EVI) (Huete 1988, Bannari et al. 1995, Nagler et al. 2001, Huete et al. 2002).

The assessment of vegetation using multi-spectral remotely sensed data requires some form of ground data with which to compare products derived from remotely sensed data. The collection of ground or reference data for remote sensing studies is a well established, but often under-resourced process. There are, however, numerous issues that require consideration to produce a well-designed and flexible field that will allow appropriate ground data to be collected for a given study.

Ground Data Collection Issues

Ground data quality issues are an important consideration in any study involving geographic information, including remotely sensed data. Ground data, and specifically spatial data, quality elements identified within existing geographic data guidelines include what are termed the 'Big 5' issues: (1) positional accuracy, (2) attribute accuracy, (3) logical consistency, (4) data completeness, and (5) data lineage (Hunter et al. 2003a, Morrison 2005, Comber et al. 2006, Reinke and Jones







| | | |
|---|---|--|
| <p>Spatial Scale</p> <p></p> <p><i>Integrate ground data with spatial resolution of the imagery</i></p> | <p>Temporal Resolution</p> <p></p> <p><i>Synchronise ground data collection with image acquisition</i></p> | <p>Positional accuracy</p> <p></p> <p><i>Consider imagery and GPS accuracy when locating field sites</i></p> |
| <p>Ground Data Collection Issues</p> | | |
| <p>Homogeneity</p> <p></p> <p><i>Sample homogenous areas rather than boundary areas</i></p> | <p>Attributes</p> <p></p> <p><i>Measure attributes in a quantitative manner with appropriate accuracy</i></p> | <p>Data Legacy</p> <p></p> <p><i>Consider the future uses of the data and elements of data quality</i></p> |

Fig. 1 A summary of ground data quality issues considered in the development of this ground data sampling approach, based on issues identified in Guptill and Morrison (1995), Aspinall and Pearson (1996), Brogaard and Ólafsdóttir (1997), and Reinke and Jones (2006)

2006). While some issues are generic to all spatial data, such as lineage and attribute accuracy, others, such as spatial scale, temporal resolution, and site homogeneity, are particularly relevant to remote sensing applications.

Consideration of these data quality issues is required to improve the ability of existing vegetation field surveys to accommodate the needs of remote sensing applications (McCoy 2005, Reinke and Jones 2006), thus addressing the compatibility between remotely sensed data analysis and ground data requirements. Poor compatibility between ground data and remote sensing data will greatly impinge data analysis, and may undermine any identified relationships between the data (Congalton 1991, Defries et al. 2000, Liang 2004, Reinke and Jones 2006). Data quality issues that were considered in this study are summarised in Fig. 1.

Spatial scale and spatial resolution are key elements of remotely sensed data. The spatial resolution of a sensor is an important feature, as it determines the detail of the information that can be extracted from an image (Marceau et al. 1994). The spatial resolution of remotely sensed data is often considered as the pixel size of the imagery or in terms of the sensor’s ground sample area. Collection of ground data that corresponds with the spatial resolution of remotely sensed data enhances the utility of ground data, and is a key challenge for remote sensing studies (Brogaard and Ólafsdóttir 1997, McCoy 2005, Reinke and Jones 2006).

The spatial structure of remotely sensed data changes with image scale and resolution (Milne and Cohen 1999), which emphasises the need to carefully select appropriate remotely sensed data for specific studies, and is also an important consideration when collecting ground data for remote sensing projects. Semivariograms can be used to represent the spatial structure of remotely sensed imagery, and have been used to guide the selection of appropriate spatial resolutions for individual studies (Woodcock and Strahler 1987, Curran 1988, Woodcock et al. 1988a). This type of analysis can be particularly helpful when multiple spatial scales are considered simultaneously within a single study. Multi-scale analysis is becoming an increasingly important challenge, as recognition of the scale-dependent nature of ecological variation increases (White and Walker 1997, Hay et al. 2002, Fischer et al. 2004). Reconciling these considerations with remote sensing data requirements is a recognised issue.

In terms of temporal resolution, the synchronicity between ground and remotely sensed data acquisition is a key consideration. Where vegetation is the feature of interest in a study, temporal resolution is particularly important, as vegetation is a dynamic feature that varies temporally as well as spatially (White and Walker 1997, Landres et al. 1999, Jensen 2000, Nagendra 2001). The methods used to record ground data are a key issue given the variability of methods available to measure any given attribute. The use of continuous variables allows greater flexibility for future use of the data than variables recorded as categorical attributes, and allows the data to be manipulated for different purposes (Fassnacht et al. 2006, Reinke and Jones 2006). The methods used to record data also influence the accuracy and precision of the data, which can be an important consideration if it is then used to validate remotely sensed data.

A requirement of ground data for use in remote sensing applications is a known spatial relationship to the remotely sensed data. An important consideration of ground data collection planning is the estimation of potential positional inaccuracy sources and compensating for this within the ground sampling strategy (Treitz et al. 1992, Stehman and Czaplewski 1998, Means et al. 1999, McCoy 2005). To reduce the impact of positional errors on the estimate of variables from remotely sensed data, sampling strategies based on pixel clusters are often used in remote sensing studies. This strategy negates the need to locate single pixels accurately within an image.

The use of pixel clusters as sampling units can also assist in sampling the interior of an area, reducing the potential of sampling mixed pixels rather than homogenous ground areas. Incorporating a buffer around ground data collection sites also ensures a full pixel is sampled, rather than the edges of pixels (Thomlinson et al. 1999). Sampling in homogenous areas is advantageous since a given variable is evenly mixed, or distributed uniformly across an area (McCoy 2005).

Generally, for remote sensing studies, ground data collection sites are located within homogenous areas (Nusser and Klaas 2003, Armston et al. 2004, Gallo et al. 2005, Reinke and Jones 2006). While spatial heterogeneity of vegetation attributes is considered important from an ecological perspective (Turner 2005), homogenous

areas are often of more interest in terms of ground data collection for remote sensing studies. Large homogenous areas are less likely to be negatively affected by positional inaccuracy (Means et al. 1999, McCoy 2005).

There are many other data issues that influence the use of spatial data and the collection of ground data for remote sensing applications. In addition to those issues reviewed above, other important considerations include data lineage, data completeness, logical consistency, and the provision of appropriate metadata (Brassel et al. 1995, Hunter et al. 2003b, Lee et al. 2003, Reinke and Jones 2006).

Study Area

The case study was undertaken in southern New South Wales (NSW), Australia (Fig. 2). The study area covers approximately 120 km², and is located in the Murray Catchment Management Authority (CMA) area. The study area is dominated by agricultural land uses, predominately dryland grazing and cropping, with some areas of forestry plantations, remnant native vegetation and National Park.

The landscape has largely been cleared for agriculture, and consequently most remaining native vegetation is located along roadsides, in traveling stock reserves, along watercourses, and in small remnants on private land. The dominant vegetation types found in the area are Grassy Box Woodlands, Riverine Woodland Forest and Dry Foothill Forest (Murray CMA 2006). Dominant tree species found in this landscape include White Box (*Eucalyptus albens*), Western Grey Box (*E. microcarpa*), Yellow Box (*E. melliodora*), Blakely's Red Gum (*E. blakelyi*), and Silver Wattle (*Acacia dealbata*).

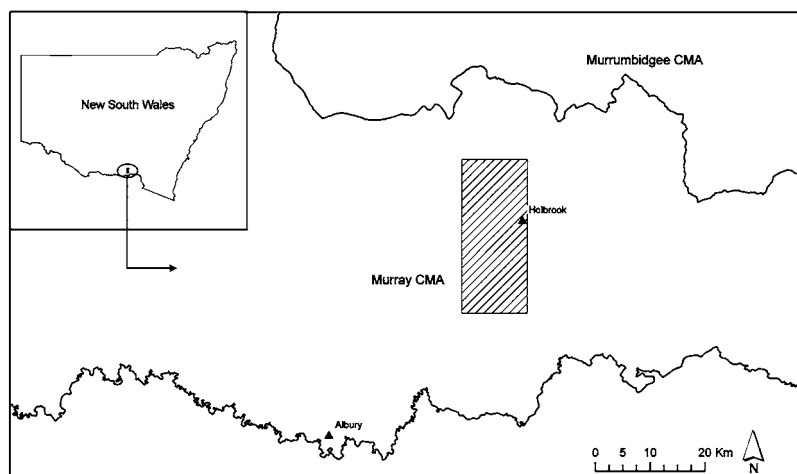


Fig. 2 Location and extent of study area within the Murray Catchment Management Authority area in southern New South Wales, Australia

Remotely Sensed Data

The choice of remotely sensed imagery used for this study was limited to two operational multi-spectral platforms: Ikonos and SPOT 5. These data were selected due to their availability and general use within the study area. Details of the spatial and spectral resolutions of the sensors are given in Table 1.

Table 1 Spatial and spectral (panchromatic (Pan) and multi-spectral (MS)) details of remote sensing platforms used in this study

| Platform | Mode | Spatial resolution | Spectral resolution |
|----------|------|--------------------|-------------------------|
| Ikonos | Pan | 1 m | 0.45–0.90 μm |
| | MS | 4 m | 0.45–0.52 μm |
| | | | 0.51–0.60 μm |
| | | | 0.63–0.70 μm |
| | | | 0.76–0.85 μm |
| SPOT 5 | Pan | 2.5 m | 0.48–0.71 μm |
| | MS | 10 m | 0.50–0.59 μm |
| | | | 0.61–0.68 μm |
| | | | 0.78–0.89 μm |
| | | 20 m | 1.58–1.75 μm |

Development of a Vegetation Ground Data Collection Protocol

The ability of remotely sensed data to provide measures of vegetation at landscape and regional scales that are consistent with those measured at a stand-level strongly depends on the sampling scheme used to collect ground data (Reinke and Jones 2006). The process outlined below was used to develop a vegetation ground data collection protocol that provides ground data relevant for use with SPOT 5 and Ikonos imagery, while integrating methods for assessing vegetation attributes at a site scale that are currently used within the study area. The development of this protocol considered three key areas:

1. Definition of an appropriate sampling unit, based of the spatial resolution of remotely sensed data,
2. Determination of a methodology to sample a suite of vegetation attributes within the defined sampling unit at an appropriate spatial scale, and
3. Consideration of key ground data collection issues considered relevant to this study.

Determining Field Site Dimensions

The field site structure was based on the spatial resolution of the imagery used in this project. Semivariograms and Moran's I spatial autocorrelation measured were used to examine the underlying spatial properties of the remotely sensed data. Semivariograms are a visual tool used to represent the spatial structure of remotely

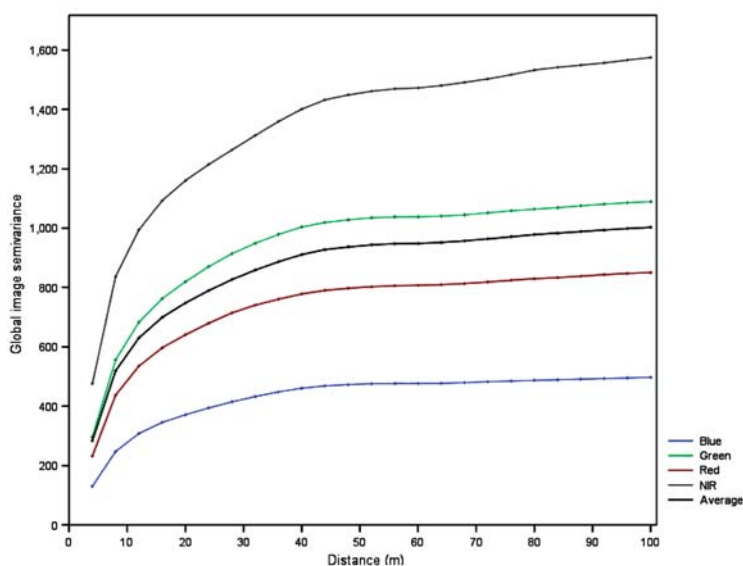


Fig. 3 Average and individual band semivariograms for Ikonos imagery (excluding urban areas) derived from global image semivariance calculations

sensed data, relating semivariance to distance (Curran 1988, Woodcock et al. 1988a, Tso and Mather 2001). Semivariograms derived from Ikonos imagery (both individual bands and an image average) are shown in Fig. 3. As vegetation was the primary interest in this study, urban land cover was excluded from the analysis.

Information regarding the spatial structure of remotely sensed data can be inferred from a number of semivariogram features. The sill is the value at which the maximum semivariance value is reached (Curran 1988, Woodcock et al. 1988a, Merino de Miguel 2000), and represents the amount of variation explained by the nugget effect and the spatial structure of the imagery (Zawadzki et al. 2005). The distance at which the sill is reached is known as the range (Woodcock et al. 1988b), and represents the spatial resolution above which image objects are considered spatially independent (Woodcock et al. 1988a). The range is related to the size of image objects as these contribute to the spatial structure of the image, and spatial dependence of pixel values (Woodcock et al. 1988a, Merino de Miguel 2000, Song and Woodcock 2002, Zawadzki et al. 2005).

Inspection of semivariograms derived from both Ikonos and SPOT 5 imagery, determined that a sill was approached at distances (range) of approximately 50 m. For all semivariograms, there was an initial rapid increase in semivariance below a distance of approximately 50 m, after which semivariance increased at a more gradual rate, suggesting larger variation in image object sizes at distances below 50 m (Woodcock et al. 1988b, Merino de Miguel 2000). A similar analysis was conducted using Moran's I, a measure of spatial autocorrelation (Emerson et al. 2005). The results of this analysis supported the conclusions established using semivariance values for the two images.

The ground data sampling protocol was therefore designed to target areas below 50×50 m, facilitating an analysis of spatial scale issues at distances where there is greater variability in image object size. A previous study conducted within the study area found that 34% of remnant native vegetation occurred in patches of less than 1 ha (Gibbons and Boak 2002), suggesting that using a field site of 50 m^2 was capable of capturing both information in small vegetation remnants within the landscape and variation within larger vegetation remnants.

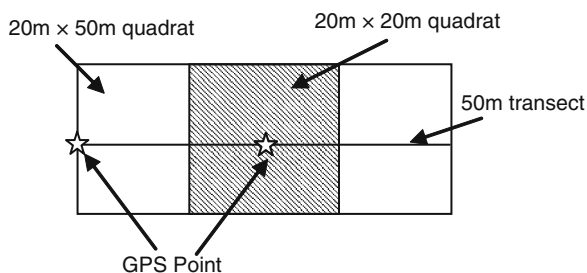
Due to the variable spatial resolution of the two sources of remotely sensed data, a nested sampling approach was used, following established ground data collection protocols such as the BigFoot calibration and validation program (Campbell et al. 1999). Pixel clusters, rather than individual pixels, were used to construct the nested field site design. The use of pixel clusters as sampling units is a common approach in remote sensing studies (Stehman and Czaplewski 1998, Lefsky et al. 1999, Means et al. 1999, Golevitch et al. 2002, Nusser and Klaas 2003).

Pixel clusters of 3×3 and 5×5 from both sensors were used to construct the nested field site design, which incorporated cluster dimensions ranging from 12 to 50 m^2 . The use of pixel clusters to sample remotely sensed data addresses two key spatial data issues identified previously: (1) the need to sample homogenous areas, and (2) the need to allow for potential positional inaccuracies. To ensure field sites were located in homogenous areas of vegetation and to reduce the potential influence of edge areas, the field sites a 20 m buffer was incorporated around sites.

Sampling Vegetation Variables Within the Field Site

Within the nested spatial arrangement of the field site, plots and transects were established to collect ground data measurements. The layout of plots and transects is shown in Fig. 4. This sampling design enabled assessment of vegetation at distances smaller than 50 m, corresponding to key spatial areas identified from the image semivariograms. Across each site, replicate areas were assessed to obtain a mean estimation of vegetation attributes within a given spatial area. Pilot studies were conducted to determine appropriate sampling intensities within the study area.

Fig. 4 Plot and transect arrangement used to sample vegetation attributes within a nested field site arrangement based on clusters of image pixels (adapted from Gibbons et al. 2005)



The structure and layout of each plot assessment is based on the BioMetric vegetation condition site assessment methodology (Gibbons et al. 2005). This approach to assessing stand-level vegetation attributes is widely used throughout NSW, Australia. Designing the ground data collection protocol for use with remotely sensed data, while also facilitating integration with existing vegetation survey work in the study area helps to explore how the two disciplines (ecology and remote sensing) can be incorporated into an effective vegetation assessment framework, an important area of work for natural resource management (Lee et al. 2003).

Vegetation attributes were measured using quantitative continuous measurements. Attribute measurement is a key ground data collection issue identified previously. The use of quantitative continuous measurements does not impose artificial restrictions on the data, allowing greater flexibility in the use and further analysis of that data (McCoy 2005, Fassnacht et al. 2006, Reinke and Jones 2006). By collecting ground data in this manner, the data could be re-scaled and compiled to yield information at different spatial scales and within different pixel cluster areas.

Conclusions

While the low cost, repeatability and synoptic overview provided by remotely sensed data means that it is a widely used technology to map and monitor environmental variables, linking these data with in-situ (or on-ground) observations is often difficult. This forms a central challenge of this work, through the design of a flexible ground data collection approach that is capable of providing ground data suitable for a suite of remotely sensed data.

A ground data collection protocol is presented that allows for: (1) the spatial resolution of the imagery utilized; and, (2) the spatial variation of the attribute being measured. An understanding of the spatial structure of remotely sensed data and the effect that spatial resolution has on classification and analysis of remotely sensed data has a significant influence on analysis results (Marceau et al. 1994). While the concepts behind this protocol are not new, it provides an example of how issues specific to re-mote sensing can be integrated in the design of a multi-purpose field campaign.

Identification of appropriate spatial resolutions for analyzing vegetation has important consequences for the choice and use of remotely sensed data. Outcomes from this project will be used to guide appropriate analysis and data use in the development of a vegetation assessment framework, which aims to provide data across a range of spatial scales (such as site, landscape and regional areas) incorporating a number of remotely sensed data sources.

Acknowledgements This work was supported by an ARC Linkage Grant (LP0455316) and by the NSW Department of Environment and Conservation.

References

- Armitage, R. P., R. E. Weaver, and M. Kent. 2000. Remote sensing of semi-natural upland vegetation: The relationship between species composition and spectral response. Pages 83–102. *In* R. Alexander and A. C. Millington, editors. *Vegetation Mapping: From Patch to Planet*. John Wiley & Sons, LTD, England.
- Armston, J. D., T. J. Danaher, and L. J. Collett. 2004. A regression approach to mapping woody foliage projective cover in Queensland with Landsat data. *In* Proceedings of the 12th Australasian Remote Sensing and Photogrammetry Conference, Fremantle, Australia.
- Aspinall, J., and D. Pearson. 1996. Data quality and spatial analysis: analytical use of GIS for ecological modelling. *In* M. F. Goodchild, L. Steyaert, and B. O. Parks, editors. *GIS and Environmental Modelling: Progress and Research Issues*. GIS World Books.
- Bannari, A., D. Morin, F. Bonn, and A. R. Huete. 1995. A review of vegetation indices. *Remote Sensing Reviews* **13**:95–120.
- Brassel, K., F. Bucher, E. Stephan, and A. Vckovski. 1995. Completeness. *In* S. C. Gupta and J. L. Morrison, editors. *Elements of Spatial Data Quality*. Elsevier Science, published on behalf of the International Cartographic Association, Oxford, UK.
- Brogaard, S., and R. Ólafsdóttir. 1997. Ground-truths or Ground-lies? Environmental sampling for remote sensing application exemplified by vegetation cover data. *Lund Electronic Reports in Physical Geography*. Department of Physical Geography, Lund University, Sweden.
- Campbell, J. L., S. Burrows, S. T. Gower, and W. B. Cohen. 1999. BigFoot. Characterizing Land Cover, LAI, and NPP at the Landscape Scale for EOS/MODIS Validation. Field Manual Version 2.1. Oak Ridge National Laboratory, Tennessee.
- Carreiras, J. M. B., J. M. C. Pereira, and J. S. Pereira. 2006. Estimation of tree canopy cover in evergreen oak woodlands using remote sensing. *Forest Ecology and Management* **223**: 45–53.
- Comber, A. J., P. F. Fisher, F. Harvey, M. Gahegan, and R. Wadsworth. 2006. Using metadata to link uncertainty and data quality assessments. *In* A. Riedl, W. Kainz, and G. A. Elmes, editors. *Progress in Spatial Data Handling*. 12th International Symposium of Spatial Data Handling. Springer, Berlin.
- Congalton, R. G. 1991. A review of assessing the accuracy of classifications of remotely sensed data. *Remote Sensing of Environment* **37**:35–46.
- Coops, N. C., and D. S. Culvenor. 2000. Utilizing local variance of simulated high spatial resolution imagery to predict spatial pattern of forest stands. *Remote Sensing of Environment* **71**: 248–260.
- Curran, P. J. 1988. The semivariogram in remote sensing: An introduction. *Remote Sensing of Environment* **24**:493–507.
- Defries, R. S., M. Hansen, J. R. G. Townshend, A. C. Janetos, and T. R. Loveland. 2000. A new global 1-km dataset of percentage tree cover derived from remote sensing. *Global Change Biology* **6**:247–254.
- Emerson, C. W., S. Lam, and D. A. Quattrochi. 2005. A comparison of local variance, fractal dimension, and Moran's I as aids to multispectral image classification. *International Journal of Remote Sensing* **26**:1575–1588.
- Fassnacht, K. S., W. B. Cohen, and T. A. Spies. 2006. Key issues in making and using satellite-based maps in ecology: A primer. *Forest Ecology and Management* **222**:167–181.
- Fischer, J., D. B. Lindenmayer, and A. Cowling. 2004. The challenge of managing multiple species at multiple scales: reptiles in an Australian grazing landscape. *Journal of Applied Ecology* **41**:32–44.
- Gallo, K., L. Ji, B. Reed, J. Eidenshink, and J. Dwyer. 2005. Multi-platform comparisons of MODIS and AVHRR normalized difference vegetation index data. *Remote Sensing of Environment* **99**:221–231.
- Gibbons, P., D. Ayers, J. Seddon, S. Doyle, and S. Briggs. 2005. BioMetric Version 1.8. A Terrestrial Biodiversity Assessment Tool for the NSW Property Vegetation Plan Developer. Operational Manual. NSW Department of Environment and Conservation, Canberra.

- Gibbons, P., and M. Boak. 2002. The value of paddock trees for regional conservation in an agricultural landscape. *Ecological Management and Restoration* **3**:205–210.
- Golevitch, B. M., T. J. Danaher, A. J. Stewart, D. P. Harris, and L. J. Lawrence. 2002. Mapping woody vegetation cover over the state of Queensland using Landsat TM and ETM+ Imagery. *In* Proceedings of the 11th Australasian Remote Sensing and Photogrammetry Conference, Brisbane, Australia.
- Guptill, S. C., and J. L. Morrison, editors. 1995. *Elements of Spatial Data Quality*. 1st edition. Elsevier Science, published on behalf of the International Cartographic Association, Oxford, UK.
- Hay, G. J., P. Dubé, A. Bouchard, and D. J. Marceau. 2002. A scale-space primer for exploring and quantifying complex landscape. *Ecological Modelling* **153**:27–49.
- Huang, C., L. Yang, and C. Homer. 2001. A strategy for estimating tree canopy density using Landsat 7 ETM+ and high resolution images over large areas. *In* Proceedings of the 3rd International Conference on Geospatial Information in Agriculture and Forestry, Denver, Colorado.
- Huete, A. R. 1988. A soil-adjusted vegetation index (SAVI). *Remote Sensing of Environment* **25**:295–309.
- Huete, A. R., K. Didan, R. Miura, E. P. Rodriguez, X. Gao, and L. G. Ferreira. 2002. Overview of the radiometric and biophysical performance of the MODIS vegetation indices. *Remote Sensing of Environment* **83**:195–213.
- Hunter, G. J., S. D. Jones, A. K. Bregt, and E. G. Masters. 2003a. Spatial data quality. *In* C. M. B. Medeiros, editor. *Advanced Geographic Information Systems. Encyclopaedia of Life Support Systems (EOLSS)*. Developed under the auspices of the UNESCO. EOLSS Publishers, Oxford, UK.
- Hunter, G. J., M. Wachowicz, and A. K. Bregt. 2003b. Understanding spatial data usability. *Data Science Journal (Spatial Data Usability Special Section)* **2**:79–89.
- Jensen, J. R. 2000. *Remote sensing of the environment: an earth resource perspective*. Prentice Hall, New Jersey.
- Jiang, J., S. Chen, S. Cao, H. Wu, L. Zhang, and H. Zhang. 2005. Leaf area index retrieval based on canopy reflectance and vegetation index in eastern China. *Journal of Geographical Sciences* **15**:247–254.
- Johansen, K., N. C. Coops, S. E. Gergel, and Y. Stange. 2007. Application of high spatial resolution satellite imagery for riparian and forest ecosystem classification. *Remote Sensing of Environment* **110**:29–44.
- Landres, P. B., P. Morgan, and F. J. Swanson. 1999. Overview of the use of natural variability concepts in managing ecological systems. *Ecological Applications* **9**:1179–1188.
- Lee, A., P. Norman, M. Wood, and S. Davey. 2003. Integrated sampling strategies – application at the regional and continental levels for monitoring sustainable forest management. *In* Proceedings Joint Australia and New Zealand Institute of Forestry Conference, Queenstown, New Zealand.
- Lefsky, M. A., W. B. Cohen, S. A. Acker, G. G. Parker, T. A. Spies, and D. Harding. 1999. Lidar remote sensing of the canopy structure and biophysical properties of douglas-fir western hemlock forests. *Remote Sensing of Environment* **70**:339–361.
- Liang, S. 2004. *Quantitative Remote Sensing of Land Surfaces*. John Wiley & Sons Inc., New Jersey, USA.
- Liu, Z., J. Huang, X. Wu, and Y. Dong. 2007. Comparison of vegetation indices and red-edge parameters for estimating grassland cover from canopy reflectance data. *Journal of Integrative Plant Biology* **49**:299–306.
- Marceau, D. J., P. J. Howarth, and D. J. Gratton. 1994. Remote sensing and the measurement of geographical entities in a forested environment. 1. The scale and spatial aggregation problem. *Remote Sensing of Environment* **49**:93–104.
- McCoy, R. M. 2005. *Field Methods in Remote Sensing*. The Guilford Press, New York.
- Means, J. E., S. A. Acker, D. J. Harding, J. B. Blair, M. A. Lefsky, W. B. Cohen, M. E. Harmon, and W. A. McKee. 1999. Use of Large-Footprint scanning airborne Lidar to estimate forest

- stand characteristics in the Western Cascades of Oregon. *Remote Sensing of Environment* **67**: 298–308.
- Merino de Miguel, S. 2000. Variograms of Real and Simulated High Resolution Images for Analysis of Forest Canopy Structure. Masters thesis. University College of London, London, UK.
- Milne, B. T., and W. B. Cohen. 1999. Multiscale assessment of binary and continuous land-cover variables for MODIS validation, mapping, and modeling applications. *Remote Sensing of Environment* **70**:82–98.
- Morrison, J. L. 2005. Spatial data quality. In S. C. Guptill and J. L. Morrison, editors. *Elements of Spatial Data Quality*. Elsevier Science, published on behalf of the International Cartographic Association, Oxford, UK.
- Murray CMA. 2006. Murray Catchment Action Plan. Murray Catchment Management Authority, Deniliquin, New South Wales.
- Nagendra, H. 2001. Using remote sensing to assess biodiversity. *International Journal of Remote Sensing* **22**:2377–2400.
- Nagler, P. L., E. P. Glenn, and A. R. Huete. 2001. Assessment of spectral vegetation indices for riparian vegetation in the Colorado River delta, Mexico. *Journal of Arid Environments* **49**: 91–110.
- North, P. R. J. 2002. Estimation of f_{APAR} , LAI, and vegetation fractional cover from ATSR-2 imagery. *Remote Sensing of Environment* **80**:114–121.
- Nusser, S. M., and E. E. Klaas. 2003. Survey methods for assessing land cover map accuracy. *Environmental and Ecological Statistics* **10**:309–331.
- Reinke, K., and S. Jones. 2006. Integrating vegetation field surveys with remotely sensed data. *Ecological Management and Restoration* **7**:S18–S23.
- Song, C., and C. E. Woodcock. 2002. The spatial manifestation of forest succession in optical imagery. The potential of multiresolution imagery. *Remote Sensing of Environment* **82**: 271–284.
- Stehman, S. V., and R. L. Czaplewski. 1998. Design and analysis for thematic map accuracy assessment: Fundamental principles. *Remote Sensing of Environment* **64**:331–344.
- Thomlinson, J. R., P. V. Bolstad, and W. B. Cohen. 1999. Coordinating methodologies for scaling landcover classification from site-specific to global: Steps toward validating global map products. *Remote Sensing of Environment* **70**:16–28.
- Treitz, P. M., P. J. Howerth, R. C. Shuffling, and P. Smith. 1992. Application of detailed ground information to vegetation mapping with high spatial resolution digital imagery. *Remote Sensing of Environment* **42**:65–82.
- Tso, B., and P. M. Mather. 2001. *Classification Methods for Remotely Sensed Data*. Taylor and Francis, New York.
- Turner, M. G. 2005. Landscape ecology: What is the state of the science? *Annual Review of Ecology, Evolution and Systematics* **36**:319–344.
- White, P. S., and J. L. Walker. 1997. Approximating nature's variation: selecting and using reference information in restoration ecology. *Restoration Ecology* **5**:338–349.
- Woodcock, C. E., and A. H. Strahler. 1987. The factor of scale in remote sensing. *Remote Sensing of Environment* **21**:311–332.
- Woodcock, C. E., A. H. Strahler, and D. Jupp, L. B. 1988a. The use of variograms in remote sensing: I scene models and simulated images. *Remote Sensing of Environment* **25**:323–348.
- Woodcock, C. E., A. H. Strahler, and D. Jupp, L. B. 1988b. The use of variograms in remote sensing: II real digital images. *Remote Sensing of Environment* **25**:349–379.
- Zawadzki, J., C. J. Cieszewski, M. Zasada, and R. C. Lowe. 2005. Applying geostatistics for investigations of forest ecosystems using remote sensing imagery. *Silva Fennica* **39**:599–618.

Characterizing the Landsat Global Long-Term Data Record

T. Arvidson, S.N. Goward, and D.L. Williams

Abstract The effects of global climate change are fast becoming politically, sociologically, and personally important: increasing storm frequency and intensity, lengthening cycles of drought and flood, expanding desertification and soil salinization. A vital asset in the analysis of climate change on a global basis is the 36-year record of Landsat imagery. In recognition of its increasing importance, a detailed analysis of the Landsat observation coverage within the US archive was commissioned. Results to date indicate some unexpected gaps in the US-held archive. Fortunately, throughout the Landsat program, data have been downlinked routinely to International Cooperator (IC) ground stations for archival, processing, and distribution. These IC data could be combined with the current US holdings to build a nearly global, annual observation record over this 36-year period. Today, we have inadequate information as to which scenes are available from which IC archives. Our best estimate is that there are over four million digital scenes in the IC archives, compared with the two million scenes held in the US archive. This vast pool of Landsat observations needs to be accurately documented, via metadata, to determine the existence of complementary scenes and to characterize the potential scope of the global Landsat observation record. Of course, knowing the extent and completeness of the data record is but the first step. It will be necessary to assure that the data record is easy to use, internally consistent in terms of calibration and data format, and fully accessible in order to fully realize its potential.

Introduction

Global climate change is rapidly becoming a common discussion point in the general populace, a rising concern for the scientific community, and a priority for policy and decision makers. Studies of the impact of climate change are conducted at many levels – global, regional, and local. Remotely sensed data at a moderate resolution – between 10 and 120 m (Green 2006) – play a critical role in addressing these

T. Arvidson (✉)

Lockheed Martin, Goddard Space Flight Center, Greenbelt, MD 20771

e-mail: terry.arvidson@nasa.gov

concerns. As the only systematic global archive of land scenes at a moderate resolution, the Landsat archive is key to the study of the changes being recognized in our global climate system.

Landsat has primarily been managed as a survey mission, concentrating on achieving global coverage at least annually. Thus a considerable archive of data has been gathered for the purpose of being available if needed in the future, as opposed to being acquired in response to a specific request. The exception to this is a period of commercialization ushered in by the *Land Remote Sensing Commercialization Act of 1984* (Public Law 98–365) and ended by the *1992 Land Remote Sensing Policy Act* (Public Law 102–555) (Green 2006). The commercial operator, EOSAT (later Space Imaging), concentrated on acquisitions based on user requests – data for which they had a buyer.

Additionally, Landsat data characteristics and calibration are generally well understood, enabling the goal of continuity from one spacecraft and sensor to the next. This also enables use of Landsat data with other sensor data. Recently, Geoscience Australia has studied, through a pilot project over Gwydir Catchment in Northern New South Wales, the value of Landsat archive data processed to consistent quality surface reflectance products, combined with Moderate Resolution Image Spectroradiometer (MODIS) time series data, to derive land cover information for tackling national issues such as water management, environmental responses to climate change, as well as provide data for national environment reporting. In this study, Lymburner et al. (2008) used MODIS data – 250 m spatial resolution and daily revisit frequency – with Landsat data – 30 m spatial resolution and 16-day revisit frequency – to identify irrigated versus rainfed crops, fallow periods, the number of crops per year, productivity, and yield trends from year-to-year. This type of information would support the accounting of water usage, interactions between surface water bodies and ground water, water allocation, and other water-related issues.

The first Landsat satellite was launched in 1972 and there has been continuous Landsat presence in orbit since then. Landsat 5 and Landsat 7 are currently operational, respectively adding a total of 6,000 and 9,000 scenes per month to the US archive.

An application of the Landsat long-term record is the National Carbon Accounting System (NCAS) of the Department of Climate Change in Australia (Australian Greenhouse Office 2005), which verifies compliance with the Kyoto Protocol. The NCAS monitors land clearing and revegetation and is vital to Australia's National Greenhouse Gas Inventory reporting. Using continental Landsat imagery maps with geometric and radiometric consistency, 15 sequences of land cover change from 1972 to 2004 have been generated and used to identify the sinks and sources of greenhouse gases and catalog those caused by human activity, including: fires, farming, land conservation, and forest management (Caccetta et al. 2007).

Given the importance of the 36-year Landsat archive to the science community, the US National Satellite Land Remote Sensing Data Archive (NSLRSDA) Advisory Committee commissioned an analysis of the state of the US Landsat holdings. This paper reports on the results-to-date of that analysis.

US Archive Status

Since 1972, the US has been accumulating Multispectral Scanner (MSS, from Landsats 1–5), Thematic Mapper (TM, from Landsats 4–5), and Enhanced Thematic Mapper Plus (ETM+, from Landsat 7) data in the US archive (Table 1). The archive is housed at the US Geological Survey’s (USGS) Center for Earth Observation and Science (EROS) in Sioux Falls, South Dakota.

Table 1 US archive holdings by sensor (as of 31 August 2008)

| Date range | Sensor source | No. of scenes |
|--------------|-------------------------------|---------------|
| 1972–1992 | Multispectral scanner | 649,423 |
| 1982–present | Thematic mapper | 760,437 |
| 1999–present | Enhanced thematic mapper plus | 840,364 |
| Total | | 2,250,224 |

EROS personnel are constantly assessing the physical state of the archive, refreshing the archive media, and recovering data from deteriorating media. For example, another 20,000 TM scenes were recently located during a transcription of tapes sent to the EROS by EOSAT.

In response to the NSLRSDA commission, we used metadata generated during the archival process to produce graphic representations of the annual and seasonal coverage for each Landsat sensor type in the archive. An example of each is shown in Figs. 1, 2, 3, 4, and 5. The full set of coverage graphics can be found at <http://edc.usgs.gov/archive/nslrda/geoCov.html>. An updated set of annual and seasonal coverage maps is in preparation at EROS, this time on a sensor/satellite/year basis rather than sensor/year. Additional statistics on the number of marketable

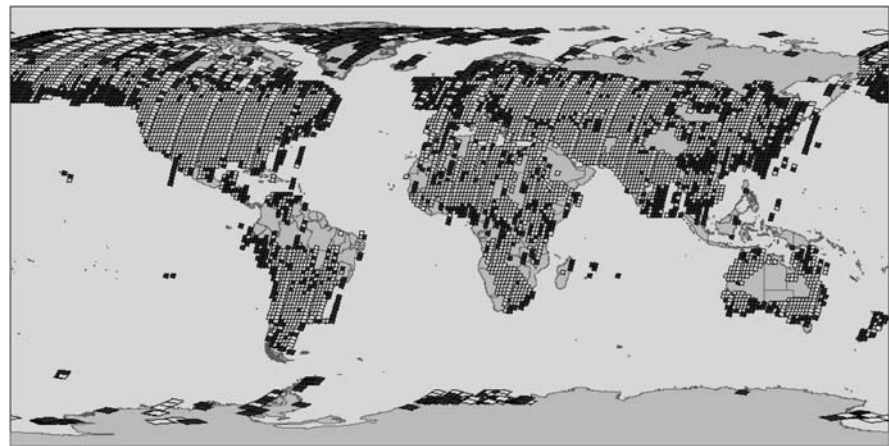


Fig. 1 MSS 1975 annual coverage in US archive. *Dark gray* tiles represent images that are ‘unusable’, with <5 quality rating (Goward et al. 2006) and > 30% cloud cover. *Light gray* tiles represent images having ≥5 quality rating and cloud cover ≤30%

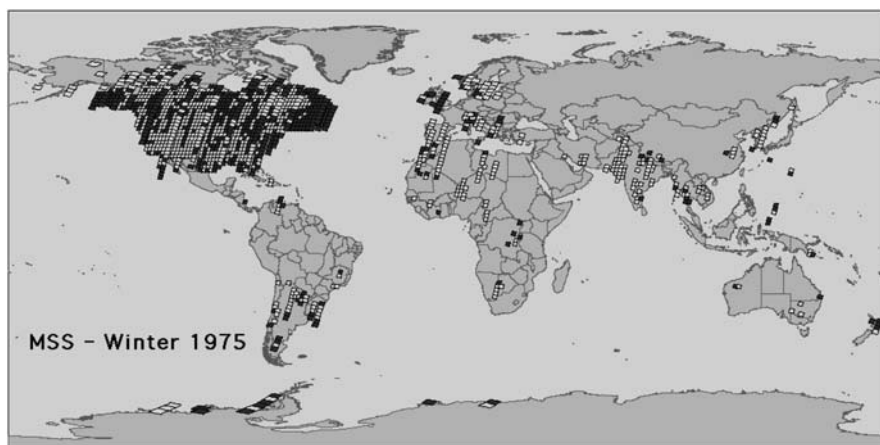


Fig. 2 MSS December 1974–February 1975 winter season

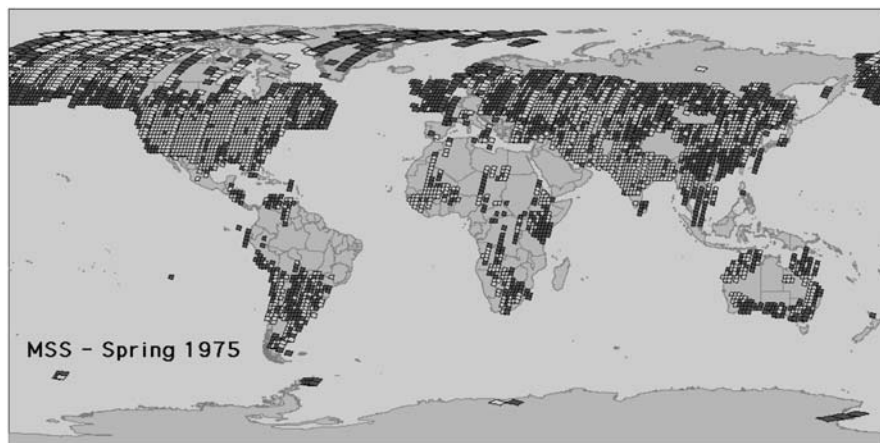


Fig. 3 MSS March–May 1975 spring season

scenes, the number of scenes with 30% cloud cover or less, and the depth of the archive will be provided for each map. These updated maps should be available in 2009.

Our subsequent analysis of the annual and seasonal maps revealed surprises. The global coverage was neither as consistent nor complete as we had expected. We went through historical documentation and interviewed Landsat personnel to discover why this was so. Table 2 summarizes the predominant reasons we have found for coverage gaps. Further details can be found in Goward et al. 2006. There are some gaps we have not yet been able to explain; for example, we suspect that, at times, data was routed directly to another government agency and never entered the EROS

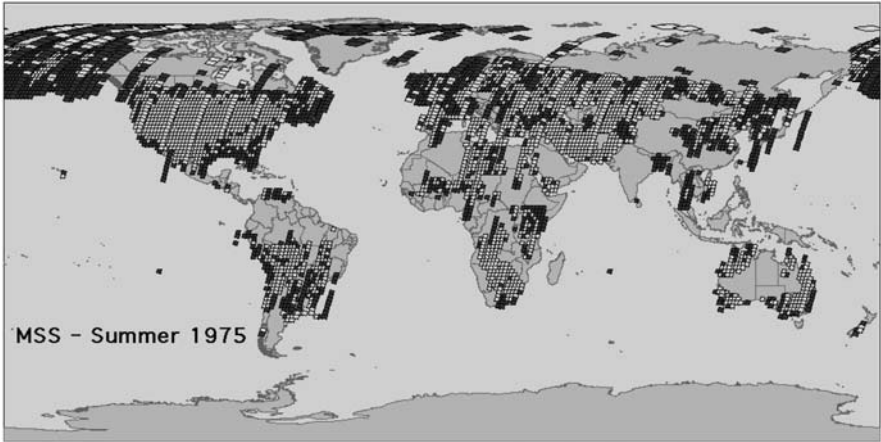


Fig. 4 MSS June–August 1975 summer season

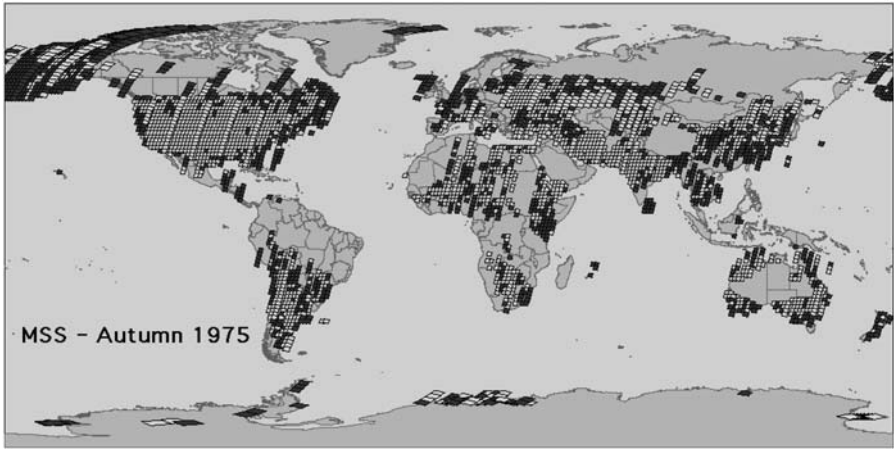


Fig. 5 MSS September–November 1975 autumn season

Table 2 Reasons for gaps in the US archive global coverage

| Category | Examples |
|---------------------------|---|
| Program management | Commercialization period with limited 4/5 coverage |
| Spacecraft problems | Ku-band failures on 4 and 5 Power problems on 4 Recorder problems on 1–3 |
| Sensor problems | MSS line start problems on 1–3 Scan-line corrector failure on 7 |
| Communication constraints | Late launch of TDRS-West, preventing western hemisphere coverage from 1982–1988 |
| Acquisition priorities | Reef campaign in 1981–1982 |

archives. Having discovered the extent of the gaps, our next concern is identifying data that might fill these gaps – perhaps from the international archives.

International Archive Status

From the onset of the Landsat program, participation of ground stations sponsored by other countries has been an important part of the mission, enhancing the global nature of the Landsat archive. This network of International Cooperator (IC) stations has been active since 1972, some since the beginning, others off and on, and some for short campaign periods only. The current complement of full-time US and IC stations is shown in Fig. 6. Those stations that operate on a campaign basis are not shown in that figure.

The IC stations are operated under a Memorandum of Understanding between the IC Government agency and the US operating agency for Landsat – currently this is the USGS. Some ICs comprise more than one station. The ICs are responsible for acquisition, archive, product generation, and distribution of the Landsat data that is downlinked to their stations. Each IC station receives a direct downlink of the land scenes within its acquisition circle at every viewing opportunity, subject to any scheduling constraints such as duty cycle or engineering activities. Thus there is a deep archive at each IC station from which gaps in the US holdings over their geographical areas could be filled. The requirements placed on the ICs, based on the MOU, include adherence to the Landsat data policies and retention of the Landsat data in an archive. If they make the decision to retire the archive, the IC must give the US first refusal on incorporating the IC archive holdings into the US archive.

Today for Landsat 7 and soon for Landsat 5, each IC must return metadata to the EROS detailing data entered into their archive. In the past, this policy was not as consistently applied nor was there consistent willingness on the part of the ICs to

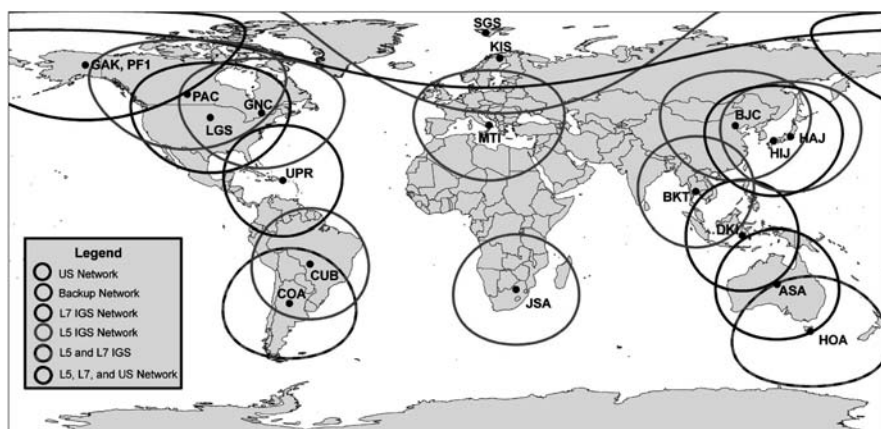


Fig. 6 Current network of Landsat stations

Table 3 Estimates of scenes held at IC archives (as of 31 March 2007)

| Countries involved | Years active | Holdings (scenes) |
|--|--------------|-------------------|
| Australia, Brazil, Canada, China, Europe, Indonesia, Japan, South Africa, Thailand | ≥ 20 | 4,205,038 |
| Argentina, Ecuador, India, Pakistan, Saudi Arabia, South Korea, Taiwan | < 20 | 260,224 |
| Antarctica, Dubai, Gabon, Iran, Kenya, Kyrgyzstan, Mongolia | Short-term | 21,042 |
| 23 countries, 30 stations | | 4,486,304 |

submit the metadata. Therefore, we do not have a clear picture as to what historical data are in the IC archives around the world. Based on the metadata that has been submitted over the years, we can estimate that there are two to three times more data in the IC archives than we have in the US archive (see Table 3). We have started efforts to remedy this lack of knowledge of the IC holdings; newly reported holdings numbers have raised the total to over 4.5 million scenes, with more stations yet to report.

Achieving a Global Archive

We have identified several steps toward achieving a more complete global Landsat archive that is useful and supportive of global climate change studies. These steps concentrate on the identification of IC holdings, establishing the status (or ‘state of health’) of the archived data, enabling access to the data through the implementation of standards, and enhancing utility of the data through improved calibration.

Metadata

The USGS and ICs have agreed upon a consistent metadata definition for Landsats 1–7, for all three sensors. The Landsat Metadata Definition Document (USGS/EROS 2008) describes a metadata format that is applicable to Landsats 1–5 and 7, as well as future Landsats. Once implemented at each IC, the ICs will submit to EROS metadata for the full set of Landsat holdings in their archives. This will be a gradual process in some cases, where older MSS data sets have yet to be incorporated into an online digital archive system. The US will ingest the metadata and establish a more complete global catalog of Landsat holdings. Each IC is being encouraged to submit the associated browse imagery with the new metadata.

Archive Maintenance

Maintaining an archive of digital data requires constant attention, and hence constant financial support. Data on older media need to be transcribed onto newer media. As time passes, this becomes more difficult to accomplish for data sets still

residing on wideband video tapes. Deterioration of the tape itself and scarcity of tape drives with which to read the tapes compound the problems. It is vital that we assure that archives are being maintained and media are being refreshed. The Landsat Ground Station Operators Working Group is compiling a list of tape drives and hardware experts available at each IC. The hope is that an IC with tape media issues may find a working tape drive at another station or an expert to assist with the repair of non-operational equipment.

Access Standards

Online catalog data and browse images ensure archive accessibility to researchers. For Landsat 7, an exchange product standard has been established and has proven its worth when data exchange has been necessary among the stations. This standard is currently being extended to Landsat 5; subsequent application to Landsats 1–4 should be the next step. An important part of the exchange product standard is USGS validation of the format generated by each station to assure compliance with the standard.

Data Utility

Once we have identified the global archive extent and enabled archive maintenance and data exchange, we need to address data utility. Calibration of the Landsat 7 data set is excellent (Markham et al. 2004) and efforts are underway to improve the calibration of Landsat 5 TM through cross-calibration with Landsat 7 ETM+ (Teillet et al. 2001). We have just started to address the calibration of the MSS. There are known artifacts and problems, and very little documentation on the calibration history of the sensor, but we are hopeful. Early results suggest that the MSS sensors were very stable over time (Helder, personal communications). Efforts are underway to gather whatever information might be available from the ICs on MSS algorithms and ancillary data sets.

Conclusions

Our analysis of the US-held Landsat archive has highlighted the importance of the IC-held assets in forming a more robust global Landsat archive with minimal coverage gaps. A standardized metadata format is essential to building a catalog of the Landsat archives held at IC stations, and this standard is now being implemented by the ICs.

The deterioration of the global Landsat archive is a major concern. Financial and technical support must be found within the Landsat stations, including that of the US, to maintain, document, and rescue, as necessary, the Landsat archives around the world.

Identifying and stabilizing the archives needs to be followed by enhancing the usability of the entire scope of archives, so that researchers can work as seamlessly as possible, from Landsat 1 MSS to Landsat 7 ETM+ data and the future Landsat Data Continuity Mission (Landsat 8) observations. Achieving this goal requires continual updating of data set calibration to maximize radiometric consistency, devising corrections for known image artifacts and sensor effects, and generation of orthorectified products at regular intervals – for example, every 2–3 years.

Knowing the extent and completeness of the data record is but the first step. Assuring that the data record is easy to use, internally consistent in terms of calibration and data format, and fully accessible is the ultimate requirement to arrive at a truly global and productive Landsat archive.

Acknowledgments The authors of this paper were supported with funds provided by the Earth Science program, Science Mission Directorate, NASA Headquarters and a US Geological Survey contract number 04CRFS0058, jointly funded by USGS and NASA.

References

- Australian Greenhouse Office (2005) Greenhouse gas emissions from land use change in Australia: results from the National Carbon Accounting System 1988–2003. <http://www.climatechange.gov.au/ncas/publications/index.html>. (accessed December 4, 2008)
- Caccetta P, Furby S, O'Connell J, Wallace J, Wu X (2007) Continental monitoring: 34 years of land cover change using Landsat imagery. Presented at the 32nd International Symposium on Remote Sensing of Environment (ISRSE). http://www.cmis.csiro.au/rsm/papers/Caccetta_et_al_ISRSE2007.pdf (accessed December 5, 2008)
- Goward SN, Arvidson TJ, Faundeen J, Williams DL, Irons J, Franks S (2006) Historical record of Landsat global coverage: Mission operations, NSLRSDA, and international cooperator stations. *Photogrammetric Engineering & Remote Sensing* 72(10):1155–1169
- Green K (2006) Landsat in context: the land remote sensing business model. *Photogrammetric Engineering & Remote Sensing* 72(10):1147–1153
- Lymburner L, Fuqin L, Tan P, Mueller N, Reddy S (2008) Dynamic landcover mapping from space. *AusGeo News* Dec 2008, issue 12. <http://www.ga.gov.au/ausgeonews200812/landcover.jsp> (accessed December 30, 2008)
- Markham BL, Thome KJ, Barsi JA, Kaita E, Helder DL, Barker JL, Scaramuzza P (2004) Landsat-7 ETM+ on-orbit reflective-band radiometric stability and absolute calibration. *IEEE Transactions on Geoscience and Remote Sensing* 42(12): 2810–2820
- Public Law 98–365 (1984) Land Remote Sensing Commercialization Act of 1984. July 17, 1984
- Public Law 102–555 (1992) Land Remote Sensing Policy Act. October 28, 1992
- Teillet PM, Barker JL, Markham BL, Irish RR, Fedosejevs G, Storey JC (2001) Radiometric cross-calibration of Landsat 5 Thematic Mapper and Landsat-7 Enhanced Thematic Mapper Plus based on tandem data sets. *Remote Sensing of Environment* 78(1–2):39–54
- USGS/EROS (2008) Landsat Metadata Definition Document (LMDD). LS-DIR-05. Version 5.0. July 2008. http://landsat.usgs.gov/tools_IGS_documents.php#4 (accessed December 5, 2008)

Evaluation of Alternative Sensors for a Landsat-Based Monitoring Program

S.L. Furby and X. Wu

Abstract In Australia, Landsat imagery is currently used in a number of regional and national monitoring projects to provide maps of the extent and change in area of perennial vegetation. They provide basic information for conservation, land management and for modelling carbon flux and water use. With the looming gap in Landsat data continuity it is timely to consider the issues involved in using data from other sensors to continue these monitoring programs. In the context of the Australian Department of Climate Change Land Cover Change Program, this paper describes the issues and quantifies the effects of using Spot 4 and Landsat 7 SLC-off images instead of the current Landsat 5 images. The data pre-processing issues investigated include ortho-rectification, calibration and terrain illumination correction. Overlapping sets of images from three different geographic regions were processed to assess logistical and technical issues. The ability to discriminate between classes of interest is considered in the context of the forest monitoring. The accuracy of the change products from mixed-sensor time series analysis is also discussed. Both the accuracy of the products from each step in the processing and the cost in terms of processing time and complexity are reviewed.

Introduction

In Australia, Landsat imagery is currently used in a number of regional and national monitoring projects. However, the future of Landsat imagery is not assured. Both Landsat 5 and Landsat 7 are estimated to run out of fuel around 2010. The Scan Line Corrector (SLC) failed on Landsat 7 in 2003 and only SLC-off products are now available. Landsat 5 has had problems with its Solar Array Drive which have affected data availability in 2006. A replacement Landsat or Landsat-like sensor from the Landsat Data Continuity Mission does not yet have a launch date, and so is unlikely before 2012.

S.L. Furby (✉)

CSIRO Mathematical and Information Sciences, Wembley 6913, Western Australia

With the looming gap in Landsat data continuity it is timely to consider the issues involved in using data from other sensors to continue these monitoring programs. This paper describes the issues and quantifies the effects of using Spot 4 and Landsat 7 SLC-off images in the Land Cover Change Program (LCCP) of the Australian Department of Climate Change (DCC) (<http://www.climatechange.gov.au/ncas>), instead of the current Landsat 5 images. Landsat 7 SLC-off images were also used in the 2006 update of the Land Monitor II Perennial Vegetation Monitoring program (<http://www.landmonitor.wa.gov.au>). Experiences with the Land Monitor data are also included in this paper. Other Landsat-like data that are being evaluated are from the China-Brazil Earth Resources Satellites (CBERS) (Wu et al. 2006) and the Indian Remote Sensing satellites (IRS) (Furby and Wu 2007).

All aspects of the forest cover mapping program are considered; including scene selection, ortho-rectification, calibration, mosaicking and thresholding to produce forest cover maps. Unless indicated otherwise in the text, all processing was performed according to the standard methodology for the LCCP (Furby 2002, 2006). Full details of the results summarised here can be found in Furby and Wu 2006 and Furby et al. 2006.

Test Areas

Overlapping sets of images from three different geographic regions were processed to assess logistical and technical issues. The test areas are in New South Wales (NSW), Tasmania (Tas) and Western Australia (WA) as shown in Fig. 1. Specific scenes are listed in Tables 1 and 2.

The NSW test area (red in Fig. 1) was selected to include a black soil stratification zone so that forest/non-forest discrimination can be evaluated in one of the most challenging environments encountered in Australia. It also includes a region

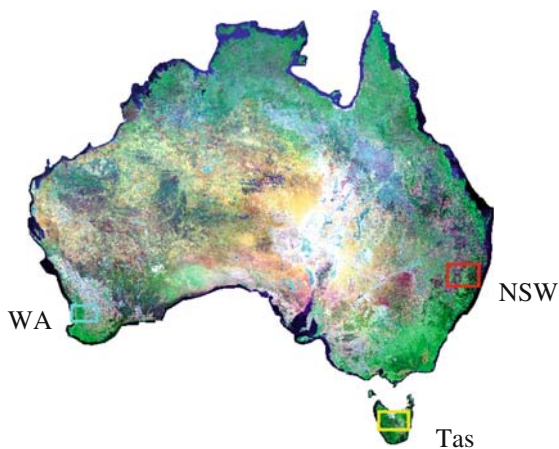


Fig. 1 Approximate location of the test areas

Table 1 SPOT 4 images

| Path/Row | Date | Cloud | Inc. angle |
|----------|------------|--------------|------------|
| WA | | | |
| 317/416 | 26/01/2006 | Partly | −13.8 |
| 318/416 | 05/02/2006 | Clear | +3.2 |
| 319/416 | 21/01/2006 | Clear | −13.8 |
| 319/415 | 10/02/2006 | Clear | +13.4 |
| Tas | | | |
| 384/434 | 06/01/2006 | Little cloud | +7.7 |
| 385/434 | 06/01/2006 | Some cloud | +10.7 |
| 386/434 | 17/02/2006 | Some cloud | −26.5 |
| 387/434 | 06/01/2006 | Clear | −13.1 |
| NSW | | | |
| 387/410 | 22/12/2005 | Hazy | −1.2 |
| 388/410 | 10/03/2006 | Clear | −30.4 |
| 389/410 | 01/02/2006 | Little cloud | +25.8 |
| 390/410 | 22/12/2005 | Little cloud | −24.4 |

Table 2 Landsat 7 ETM+ SLC-off images

| Path/Row | Date | Cloud | Purpose |
|-------------------|------------|-------|---------|
| NSW | | | |
| 89/81 | 15/03/2006 | Clear | Primary |
| 89/81 | 31/03/2006 | 5% | Fill |
| 90/81 | 07/04/2006 | Clear | Primary |
| 90/81 | 10/02/2006 | 40% | Fill |
| Tas | | | |
| 90/89 | 23/04/2006 | 55% | Primary |
| 90/89 | 07/04/2006 | 50% | Fill |
| 91/89 | 24/01/2006 | 40% | Primary |
| WA (LCCP) | | | |
| 111/83 | 21/01/2006 | 25% | Primary |
| 111/83 | 06/02/2006 | 25% | Fill |
| 112/83 | 17/03/2006 | Clear | Primary |
| 112/83 | 13/02/2006 | 25% | Fill |
| WA (Land Monitor) | | | |
| 113/82–84 | 03/03/2006 | 10% | Primary |
| 113/82–84 | 19/03/2006 | 10% | Fill |

with significant terrain effects to allow evaluation of registration, bi-directional reflectance distribution function (BRDF) and terrain illumination correction issues in an ‘extreme’ environment. The Tas test area (yellow) was selected to include mountainous areas as well as an agricultural environment where discrimination between cropped paddocks and plantations can be difficult. The WA test area (blue) was chosen to include a significant region of new plantations as well as some of the wheat belt tree cover that is close to the 20% canopy cover cut-off used in the forest

definition. This test area is relatively flat. Additional imagery for WA was available from the Land Monitor project.

Image Data and Scene Selection

Images from the SPOT 4 satellite have been acquired in archive mode since approximately December 2005. Acquisitions from the most recent SPOT satellite, SPOT 5, must be pre-ordered, making the SPOT 4 archive a more practical alternative to Landsat TM data when circumstances preclude ordering data in advance of the required acquisition interval.

Unlike the Landsat series of satellites, the SPOT satellites can point to the left and right of nadir. The SPOT 4 overpasses which have been archived have a variety of pointing angles. Variation in acquisition angle results in shifts in scene location and varying BRDF effects. In some cases there are gaps between nominally adjacent images in the archive. Near-nadir acquisition cloud-free imagery is desirable and, for this evaluation, an east-west row of four scenes was considered ideal. In practice scene selection against these criteria from the existing archive proved difficult. The image archive was searched for several path/rows surrounding those eventually selected to obtain the best possible sequences of test data. For the broader areas searched, most archived images had extensive cloud cover and/or significant missing data. Generally there was at most one suitable image, not a choice of dates. Operationally, scene selection specifications would need to consider these issues. The images selected for this study are listed in the Table 1. Due to their smaller spatial extent, at least six SPOT 4 images are required to cover the extent of a Landsat TM image.

To evaluate the Landsat SLC-off data both individual path-oriented images and the composite products produced by the Australian Centre for Remote Sensing (ACRES) were obtained to allow investigation of the compositing process as well as issues with using the individual scenes directly. The composite product is created by merging multiple Landsat 7 SLC-off images to fill the gaps in any one image. The standard scene selection criteria were applied to select the 'primary', or main, image for each path/row. The criteria for selecting the 'fill' image were closeness to the primary image acquisition date and low cloud cover. A slightly increased cloud cover was considered better than a longer time between acquisitions.

At least two images are required for each path/row, a primary image and at least one fill image. Although some gaps remain after compositing two images, three relatively cloud-free images were very rare due to extensive cloud cover during the 2006 summer. In Tasmania only one relatively cloud-free image for path 91 row 81 could be obtained. The images used are listed in Table 2. The ACRES composites were formed using the same primary and fill images. The composites were provided as ACRES standard ortho-rectified products.

Table 3 shows the remaining 'gap' area after compositing for the NSW test area. As discussed in section (Mosaicking Issues), cloud is masked from the individual

Table 3 Proportion of Landsat 7 image area filled by compositing

| Image | Date | Percentage of 89/91 composite | Percentage of 90/81 composite |
|-------|------------|-------------------------------|-------------------------------|
| 89/81 | 15/03/2006 | 78.82 | 0.52 |
| 89/81 | 31/03/2006 | 11.79 | 0 |
| 90/81 | 07/04/2006 | 2.29 | 80.72 |
| 90/81 | 10/02/2006 | 1.07 | 18.10 |

images before compositing. The percentage of the composite remaining unfilled includes cloud-masked areas. Cloud is a minor component in the filled NSW data but a major component in the other test areas; hence the results are presented for NSW only. In the overlap region between adjacent paths, data from all four images are included in the composite. The 89/81 images are an example where the gaps are largely coincident in the two images. This would represent a near ‘worst case’ scenario when only two images are used. The 90/81 images are an example from the opposite extreme. Even with a higher proportion of cloud in the ‘fill’ image, the coverage is almost complete.

At the time of writing this paper, a new Landsat 7 SLC-off ‘interpolated’ product was being released by the United States Geological Survey. The product is created from a single Landsat 7 SLC-off image. The gaps are filled by interpolation from the adjacent data in the same ‘region’. Regions are identified by segmentation of an earlier complete Landsat 5 or Landsat 7 image. This product is not suitable for our application as the size of the missing data is larger than the area of change that we need to be able to detect (0.2 hectares). The interpolated product is suitable only when the area of change to be detected is larger than the amount of data missing. Hence examples of this product were not sought for evaluation.

Landsat 5 TM imagery was acquired for the test areas for comparison. The images are listed in Table 4.

Table 4 Landsat 5 TM image dates

| Path/Row | Date | Cloud |
|----------|------------|--------------|
| 89/81 | 08/04/2006 | 10% cloud |
| 90/81 | 14/03/2006 | Mostly clear |
| 111/83 | 08/04/2006 | 30% cloud |
| 112/83 | 14/03/2006 | Mostly clear |
| 90/89 | 26/02/2006 | 40% cloud |

Raw Image Quality Issues

With the exception of the missing data, the image quality of the individual Landsat 7 SLC-off path-oriented image products is as expected for Landsat TM data. The gaps are approximately one swathe wide at the edge of the images and disappear towards

the centre of the image. Along the edges of the gaps there are occasional pixels for which the data for only some of the image bands are missing, e.g., bands 1, 2 and 3 may contain zeros, while bands 4, 5 and 7 contain non-zero data. In the composites from ACRES, these pixels end up having intensity values from both images. In the composites we formed, such pixels were excluded.

The raw SPOT 4 images appeared noisier than path level Landsat TM images. The images appear to have some geometric patterns. The variation in intensity values within the forest is generally small compared to the differences between forest and non-forest cover. There should be little overall effect on forest/not forest discrimination, but there may be some effects at the edge of forest blocks and in areas with forest density around the 20% canopy cover cut-off. It should be noted, however, that this noise effect is not obvious visually in the ortho-rectified image data.

The order of the image bands in the supplied imagery was XS3, XS2, XS1, SWIR (i.e. 3, 2, 1, 4). The image bands were reordered prior to processing.

Ortho-rectification Issues

The individual path-oriented Landsat 7 SLC-off images were ortho-rectified using the standard processing sequence for Landsat 7 imagery. The satellite orbital model (Toutin, 1994) in the PCI OrthoEngineTM software was used for ortho-rectification, however an issue was encountered with the resampling algorithm. The algorithm places a zero in the output image any time its resampling window includes a zero from the input image. Effectively all gaps in the SLC-off images are grown by the size of the resampling window (8 pixels square for the 8 pt sin/x kernel used) causing an unacceptable loss of data. Within PCI, the only options are to use alternative resampling algorithms with smaller resampling windows such as cubic convolution or nearest neighbour. The alternative considered was to 'fill' the gaps with data that will produce a sensible resampled pixel value. The gaps were filled by interpolating the data above and below the gap. An indicator image tracking the location of the interpolated data was created. The image with the interpolated data was ortho-rectified in PCI using the usual resampling algorithm. The indicator image was ortho-rectified separately using the same ground control points (GCPs) and nearest neighbour resampling. The indicator image is then used to mask the extra data from the ortho-rectified overpass image.

The interpolation strategy provided the best ortho-rectified imagery. Equivalent registration accuracy was obtained as for unaffected Landsat 7 imagery. The modified procedures are all automated rather than manual, providing only a very minor 'per image' increment to the ortho-rectification effort.

In order to composite (merge) two or more images, they must be registered to each other. To create their Landsat 7 SLC-off composite product ACRES ortho-rectifies each image, applying their normal processing sequence using standard GCP chips with known coordinates. (The images are ortho-rectified to an ACRES base

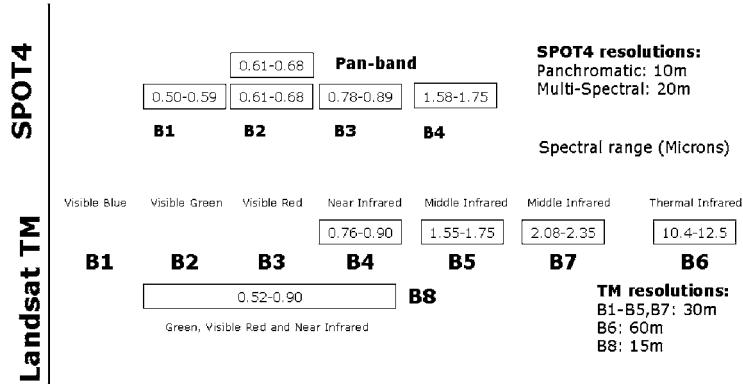


Fig. 2 Comparison of SPOT 4 and Landsat TM image bands

rather than the LCCP base, the correspondence of which has not been systematically investigated.) In the test data, for some areas the registration to the LCCP base is good, but in other areas, such as the 89/81 composite image in NSW, a clear shift between the two images of up to two pixels (50 m) can be seen. The LCCP base and images registered to it match the terrain features in the NSW state digital elevation model (DEM). The position of ridges and valley floors in the ACRES composite are displaced from the DEM leading to artefacts in the terrain illumination correction.

In one of the ACRES Landsat 7 SLC-off composite image supplied for the Land Monitor project there was a displacement of between 8 and 12 pixels (200–300 m) between the two images being composited. ACRES investigated the problem and reported that it was caused by the failure to automatically locate sufficient GCPs. A combination of the missing data and cloud cover meant that GCPs were not correctly located. As a result of the review of all composite imagery provided, ACRES reprocessed the 91/89 imagery to correct a similar but much smaller deficiency.

These registration issues require that if Landsat 7 SLC-off data is going to be used in the LCCP, the individual images must be obtained rather than the ACRES composite, even though it means more processing.

The SPOT 4 images were initially ortho-rectified using the standard procedures applied to the Landsat data used in the LCCP, i.e. using the merged Australian Land Information Group (AUSLIG) 3 and 9 second DEMs.

Landsat TM band 7 is typically used in the correlation matching calculations to locate Master GCP features in the overlap images. As an equivalent spectral band is not available in the SPOT imagery (see Fig. 2), matching SPOT band 4 to Landsat TM band 5 and SPOT band 2 to Landsat TM band 3 were both evaluated. Equivalent results both in numbers of GCPs matched and GCP locations were obtained.

Twenty seven GCPs spread uniformly across the image area are considered sufficient to adequately register the Landsat images. The Master GCP files typically deliver between sixty and one hundred well matched GCPs for each (single) Landsat TM image. However, the SPOT images cover only about one sixth of a Landsat TM

image. Only ten to fifteen well matched GCPs were obtained over the test images. Comparisons showed that better registration to the base was obtained by adding GCPs so that a minimum of twenty five to thirty GCPs were used in the model fit. Operationally, during the first epoch for which SPOT imagery is used the Master GCP and Master Check GCP files will need to be revised for most areas, requiring a small 'per image' increase in effort for the ortho-rectification processing.

The biggest issue encountered during the ortho-rectification process was poor registration in areas of terrain, particularly for images with large incidence angles. The effect was largest for the NSW images. Even with extra GCPs, errors up to 100 m in the registration in some valleys could not be corrected. Using the NSW state DEM in place of the usual merged AUSLIG DEM produced an image with improved registration. Many problem regions were resolved completely using the higher-resolution DEM and the remaining shifts were limited to around 25 m. These results are consistent with the SPOT Image Technical Information (SPOT Image, 2008) that states that ortho-rectification locational accuracy is 15–30 m depending on DEM quality. Smaller shifts were observed in the Tasmanian images using the AUSLIG DEM (no more than 25–50 m). Again the registration was visibly improved by using a higher resolution DEM. Testing with the NSW images showed that the results using the NASA Shuttle Radar Topography Mission-DEM were almost identical to those from the state DEMs. It appears that the ortho-rectification is more sensitive to terrain issues and that the registration of SPOT 4 imagery to the base may not be quite as good as can be obtained for Landsat imagery.

Calibration

The standard calibration process consists of three distinct steps:

1. top-of-atmosphere and BRDF corrections (Danaher et al. 2001);
2. invariant target atmospheric check/correction (Furby and Campbell 2001); and
3. terrain-illumination correction (Wu et al. 2004), if required.

Each of these steps is discussed for both image types. In addition, a calibration step is part of the process for creating the ACRES Landsat 7 SLC-off products. The effect of this calibration on the composite image is also discussed.

There are no issues in applying the top-of-atmosphere and BRDF corrections to the individual ortho-rectified Landsat 7 SLC-off images. The invariant target check/correction is hampered by some of the targets being located in gaps in the SLC-off images. Over these test areas the number of targets in gaps was sufficient to compromise the gain and offsets calculated. Typically more targets in one of the dark, mid-range or bright intensity ranges were omitted than the others causing the targets to be unbalanced. Targets had to be manually updated for each image separately, not just for each path/row, which would add a substantial 'per image' amount to the calibration effort.

However, particularly with Landsat 7 imagery, the invariant target calculations are performed as a check of the processing rather than an automatic correction.

Corrections are applied only in very rare circumstances when very seasonally atypical images are used and it can be clearly demonstrated that the image is more similar to adjacent images with the correction than without it. The invariant target correction was not needed for any of the test imagery. Potentially this step could be omitted for the primary Landsat 7 SLC-off imagery with no consequences for thresholding accuracy. Systematically subsampled pixels from the overlapping image area were used to estimate a whole-scene correction of the fill image(s) directly to the primary image rather than trying to calibrate image each to the calibration base independently.

In the standard processing sequence terrain illumination correction is performed after the images have been mosaicked into map sheet units. Image date boundaries are used to derive and apply an individual correction to each constituent image as the individual sun-angles differ. The coefficients for each correction are estimated from the image data using a woody cover mask. If the Landsat 7 SLC-off images are composited before terrain illumination correction there are too few woody pixels remaining from the 'fill' image for reliable coefficient estimation. Instead, the corrections must be calculated and applied before the images are composited, i.e. before the mosaicking stage. This change to the processing order does not change the overall level of effort involved.

ACRES perform a calibration of the fill image to the primary image as part of their compositing process. As the images are merged, a local calibration is performed for each fill pixel. A local gain and offset is estimated to calibrate the intensity values for the 'fill' image to the intensity values in the primary image using data in a small local window centred on the pixel being inserted. The result in all of the images provided by ACRES is a seamless visual product. Numerical processing of such images is valid only if ground cover reflectances have not changed between the two images. However, even with images acquired sixteen days apart it is rarely true that there is no change anywhere in the image.

In the extreme, clear pixels in the fill image are 'calibrated' to look like the cloud in the primary image. Cloud-covered pixels in a fill image are also 'calibrated' to the underlying cover in the primary image. The Land Monitor images were acquired 16 days apart. The earlier image, acquired shortly after significant rains, shows residual effects of flooding. In the later image much of the surface water is gone and the wetness and greenness of many paddocks has changed. The ACRES composite image is visually pleasing, but for mapping and monitoring land cover change it is of concern that water in the fill image appears like dry land in the final merged image. Other undesirable changes are likely to be present, although perhaps not always as obvious.

The top-of-atmosphere/BRDF correction software relies on reading satellite gain and offset and sun-angle information from ancillary 'report' files normally provided with path-oriented image data. These files were not part of the composite product.

For this evaluation the composite images were corrected as if they were a single image using report files from the individual primary image; however the values used were incorrect for the fill image. There were no complications in performing the invariant target check, but again no correction was deemed necessary. The

terrain illumination correction was performed on the composite image (again using parameters from the primary image only) in a straightforward manner, but a comparison of the corrected individual images with the composite for the 89/81 image in NSW highlighted a consequence of the registration issues noted earlier. Terrain effects remain in the corrected composite image. This is not actually due to any inherent fault in the terrain illumination correction process, simply that the image is slightly displaced from the DEM. Incorrect slopes and aspects are applied near apparent ridgelines and streamlines in the image data.

The intensity values in the SPOT 4 images are observed to have a much greater dynamic range than Landsat data (2–3 times in the visible bands). A new calibration strategy is required to avoid compressing the intensity range of the SPOT image data, with subsequent loss of discrimination, if it were adopted operationally. For the tests conducted here the data were rescaled to the full 0–255 data range at each step in the calibration process.

The viewing geometry of the SPOT 4 images is such that new BRDF kernels as well as coefficients may well be required. The BRDF kernels used for Landsat data are not the optimal choices for SPOT 4 data due to the viewing geometry differences (SPOT 4 has a wider field of view compared to Landsat and, usually, a non-zero satellite incidence angle). The test data were insufficient for testing the validity of the current kernels and coefficients. The current Landsat kernels were applied and coefficients were estimated scene-by-scene by matching directly to the Landsat calibration base image using sites in forested areas. This approach is a short-term solution for the study areas, but is not recommended for large scale operational processing.

As with the Master GCPs, the invariant targets are distributed over the Landsat TM scene area (and rarely uniformly). There are too few, if any, targets located in most of the SPOT 4 test images. New targets were selected for all of the test images; however most of the good bright pseudo-invariant targets are saturated in the first two SPOT 4 image bands. A common gain and offset (usually estimated from pooled data) was used to align the data for each test area with the (scaled) base.

If SPOT 4 imagery is to be used operationally, a much more detailed investigation of calibration issues needs to be conducted using significantly more image data than considered here, of the order of a good portion of at least one state. However, once this research establishes the appropriate corrections and parameters, the operational processing effort will only increase by the ‘per image’ amount necessary for the selection of new invariant targets.

Mosaicking

For the individual Landsat 7 SLC-off ‘path’ images, mosaicking can be considered to consist of two activities:

- compositing two or more images from the same path/row (to fill the gaps); and
- mosaicking images from adjoining path/rows to form map sheet units.

Operationally, both activities would be performed simultaneously. Overlay order (primary and fill images) would be stipulated for the compositing activity; otherwise the standard overlay order rules apply.

Although not part of the mosaicking stage of the current LCCP processing sequence, it is more efficient to cloud mask Landsat 7 SLC-off images before compositing/mosaicking rather than as the first step in the thresholding process. In the individual image each cloud or patch of cloud is digitised as a single polygon. After compositing, many cloud-affected areas will appear as stripes in the composited image. Either separate polygons are required for every stripe or stripes of clear data will be masked. This will result in additional mosaicking effort, but the extra effort will be matched by a reduction of effort during the thresholding stage.

Vector image date boundaries are created during the current mosaicking sequence. The vector polygons allow separate thresholds to be applied to each image date and the tracking of the image acquisition dates of each change area during the carbon modelling phase of the DCC program. Vector polygons are simple and efficient when there is only a single image per path/row, but are inefficient for tracking the areas of primary and fill images in a composite. Raster images are more efficient and are easily created during the mosaicking process.

No difficulties arise in the mosaicking stage of the processing for SPOT 4 or ACRES Landsat 7 SLC-off composite imagery.

Thresholding Issues

Due to the local calibration issues identified for the ACRES Landsat 7 SLC-off composite products, they were not considered in the thresholding evaluation.

The standard thresholding procedures were applied to the mosaicked individual Landsat 7 SLC-off images to derive a single-date forest cover probability image. For each stratification sub-zone, image matching was applied to derive thresholds independently for the mosaicked image and the individual primary and fill images that form the mosaic for this evaluation. The final thresholds produced by the matching program for each input image for a particular sub-zone varied slightly, particularly between the values estimated from the full 'fill' image compared to the primary image or the mosaic (about 80% primary image). However, the resulting probability images were virtually identical. All of the fill images are visually very similar to their primary image for the NSW test area and separate thresholds were not needed within a composite image. Larger differences are apparent in the WA test area, however only one sub-zone showed some slight stripes in the probability image formed from the mosaic. Even then the difference in probability between the 'stripes' was slight and the subsequent multi-temporal processing corrected the problem so that the effect is not observed in the outputs.

The wet/dry image pair from the Land Monitor project provided the best opportunity to evaluate the thresholding process when the individual Landsat 7 SLC-off images forming the mosaic are very different. Thresholds were estimated separately

for each sub-zone for the individual images and the mosaic image. Stripes were observed in the forest cover probability image derived from the mosaic. Most of the stripes are commission errors with the wetter image stripes being assigned a higher probability of forest cover using thresholds derived from the mostly dry mosaic image. When thresholds are derived directly from the wet image, the commission errors are reduced and fewer stripes appear in the probability mosaic. Image pairs (or triples) where such stripes occur in the composites will be identified at the calibration stage in the LCCP processing. It is recommended that the individual images are provided for thresholding in such situations and the probabilities are mosaicked. Operationally, this should be a rare occurrence.

For the NSW and Tasmanian test areas, each set of indices for discriminating between forest and non-forest cover in each stratification zone includes at least one index using Landsat TM bands 1 or 7. As is shown in the comparison of SPOT 4 and Landsat TM image bands in Fig. 2, there are no SPOT equivalents to these image bands. New indices were derived from the SPOT data for such stratification zones using the standard discrimination analysis procedures.

As well as deriving the required SPOT indices for each zone, TM-equivalent indices were compared to new optimal SPOT-specific indices to determine whether better indices could be derived. For some zones, TM-equivalent indices remained optimal. In other zones, small increases in discrimination were observed for SPOT indices. The improvements tended to involve masking non-forest paddocks which were spectrally different from forest rather than separating spectrally similar forest and non-forest regions.

Image matching was applied to derive thresholds. Matching was successful for all but one sub-zone in NSW. Manual thresholds were used for this sub-zone in the 'black soil' stratification zone. Discriminating between forest and non-forest cover is observed to be very difficult in this zone, regardless of the source of the image data. More omission and commission errors are made in black soil zones than are typically observed in other zones. The overall correspondence with the base forest cover probability image was broadly as would be expected from Landsat data. The same levels of omission and commission errors appear in the black soil sub-zones, although the particular cover types causing confusion were a little different.

Landsat TM bands 1 and 7 are not used in the indices for the WA test area. The overall correspondence with the base forest cover probability image was broadly as would be expected from Landsat data, suggesting that deriving new indices is not essential. Using the SPOT 4 imagery one sub-zone showed slightly higher probabilities on some non-forest cover than expected, however the multi-temporal processing corrected the probabilities.

If SPOT 4 data is to be used operationally, new indices will have to be derived for many stratification zones. Thresholds are derived for each sub-zone created by the intersection of the image date and stratification zone boundaries. Once indices have been established, the overall thresholding effort is increased compared to Landsat data as there are approximately six SPOT 4 images for every Landsat TM image.

Comparison of Time Series Results

Forest cover probability images were created for the 2006 epoch using Landsat 7 SLC-off, SPOT 4 and Landsat 5 data. Each of the forest cover probability images was added to the existing sequence of probability images from 1972 to 2005 for multi-temporal processing using standard error rates tables (Caccetta 1997). Forest extent and change maps were created from the outputs of the multi-temporal processing according to the usual procedures.

Figure 3 compares the forest cover products and imagery for a region in the black soil stratification zone in the NSW test area. Forest cover extent maps derived from Landsat 5, Landsat 7 SLC-off and SPOT 4 are displayed together in red, green and blue respectively in the top right of Fig. 3. Where these products coincide, the display appears white (forest) or black (non-forest). Colours indicate that the area is labelled as forest by only one or two of the products. In particular, yellow shows where the products from Landsat 5 and Landsat 7 SLC-off images are identical, but the product from the SPOT 4 images differs. Red, green or blue indicate that the area is labelled as forest in only the Landsat 5, Landsat 7 or SPOT 4 product respectively. The image in the bottom right of Fig. 3 compares the 2005–2006 clearing layers from the three products. Again the Landsat 5 derived product is in red, Landsat 7 SLC-off in green and SPOT 4 in blue.

The extensive yellow regions in Fig. 3 show the results from the Landsat 5 and Landsat 7 SLC-off images are consistent but differ from SPOT 4 results. These areas are mapped as ‘cleared’ in the change products derived from SPOT 4 (blue regions in the bottom-right image in Fig. 3). Green regions can be observed in the

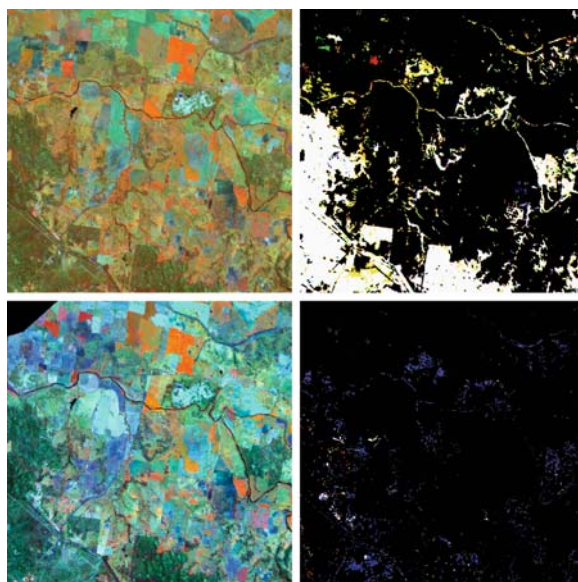


Fig. 3 *Top Left:* 2006 Landsat 5 TM image, bands 3, 5, 4 in BGR. *Bottom Left:* 2006 SPOT 4 image, bands 2, 4, 3 in BGR. *Top Right:* Overlay of forest extent maps for 2006 for Landsat 5 (red), Landsat 7 (green) and SPOT 4 (blue). *Bottom Right:* Overlay of 2005–2006 clearing maps for Landsat 5 (red), Landsat 7 (green) and SPOT 4 (blue)

Table 5 Forest extent comparison for the NSW test area

| Epoch | Landsat 5 forest extent (ha) | Landsat 7 forest extent (ha) | SPOT 4 forest extent (ha) |
|-------|------------------------------|------------------------------|---------------------------|
| 2000 | 901,612.9 | 901,554.2 | 901,303.5 |
| 2002 | 903,661.7 | 903,371.4 | 903,129.6 |
| 2004 | 905,869.4 | 905,343.1 | 904,437.8 |
| 2005 | 912,433.2 | 912,809.1 | 909,352.4 |
| 2006 | 914,660.2 | 916,070.6 | 910,981.1 |

Table 6 Area of vegetation loss (clearing layer) comparison for the NSW test area

| Interval | Landsat 5 clearing (ha) | Landsat 7 clearing (ha) | SPOT 4 clearing (ha) |
|-----------|-------------------------|-------------------------|----------------------|
| 2000–2002 | 11,961.8 | 12,230.8 | 11,922.4 |
| 2002–2004 | 9223.0 | 8992.2 | 9054.2 |
| 2004–2005 | 11,597.5 | 12,210.6 | 12,388.1 |
| 2005–2006 | 7270.3 | 6633.9 | 9970.6 |

combined forest cover image in Fig. 3. These tend to be narrow linear features or along the edge of regions mapped as forest in the Landsat 5 product. As has been observed with the Landsat 7 data used in the 2000 and 2002 epochs, forest/non-forest discrimination is slightly better in Landsat 7 than Landsat 5 imagery allowing such features to be mapped. They cannot be excluded without under-estimating the extent of forest cover compared to Landsat 5. The same trends were observed in the other test areas.

Tables 5, 6, and 7 show the area of forest and change for the NSW test area calculated from the three products for the more recent epochs. The observation that the 2006 forest extent is similar for the two Landsat products is confirmed, with the forest extent slightly larger from the Landsat 7 product. The SPOT 4 product shows a different 2006 forest extent and both higher clearing and revegetation rates in the 2005–2006 interval. Most of the extra revegetation in the SPOT 4 product appears along the edges of forest areas, particularly in the more mountainous regions. Some of it seems due to the registration not being quite as good when extreme satellite pointing angles are combined with mountainous terrain.

It should be noted that all regions of land cover change observed in the test area were detected in all three products. The regions in which the SPOT and Landsat

Table 7 Area of vegetation gain (revegetation layer) comparison for the NSW test area

| Interval | Landsat 5 regrowth (ha) | Landsat 7 regrowth (ha) | SPOT 4 regrowth (ha) |
|-----------|-------------------------|-------------------------|----------------------|
| 2000–2002 | 14,010.6 | 14,048.0 | 13,748.4 |
| 2002–2004 | 11,440.6 | 10,964.0 | 10,362.4 |
| 2004–2005 | 18,161.3 | 19,676.7 | 17,302.8 |
| 2005–2006 | 9497.4 | 9895.4 | 11,599.3 |

products differ tend to be edge pixels, narrow features and the least dense forest cover. It is only possible to say which is most consistent rather than most accurate for the areas that differ. For change detection, consistency is an important consideration.

One consequence of using Landsat 7 SLC-off imagery should be noted. There was extensive cloud cover in the Western Australian test area. As cloud was masked, some stripes of missing data remain in the mosaicked image. The multi-temporal processing infers the cover in such gaps using the data from the surrounding epochs. In the case of the 2006 epoch, the cover is assumed to be unchanged from 2005. In this test area stripes of missing data appear within areas of forest that were cleared between 2005 and 2006. Above and below the missing data, the cover is correctly mapped as non-forest and hence as cleared in the 2005–2006 clearing map. In the gap, the cover is extrapolated from the 2005 forest cover and is not mapped as change, resulting in stripes in the forest extent and change maps.

Conclusions

The SPOT 4 images cannot be as accurately registered to the rectification base as the Landsat 7 SLC-off images, particularly in mountainous areas when the images have large incidence angles. Calibration of the SPOT 4 imagery requires further study. New BRDF kernels will need to be derived as well as new model coefficients. Once appropriate methodologies have been established the operational registration and calibration processing effort should only increase by a small ‘per image’ amount for both SPOT 4 and Landsat 7 SLC-off imagery. However, at least six Spot images and two (or occasionally three) Landsat 7 SLC-off images are required for every current Landsat path/row.

Using Landsat 7 SLC-off imagery will require a reordering of the mosaicking, terrain illumination correction and cloud masking steps in the processing, however the overall effort is not increased. No changes are required when using SPOT 4 imagery.

New indices will have to be derived for many stratification zones when using SPOT 4 imagery. This may take up to two weeks of effort for each of thirty seven 1:1,000,000 map sheets. Ideally indices are derived by considering two or more image dates to ensure they are robust through time rather than tailored to particular conditions in a single image. All indices derived for the first epoch using SPOT 4 data should be reviewed when a second epoch is available. Once indices have been established, the overall thresholding effort is increased compared to Landsat TM data, in the worst case by the number of extra scenes required for complete coverage.

For the Landsat 7 SLC-off data, if there is no significant change between the images being composited, the thresholding can be performed treating each composite as a single path/row image. In the event that differences have been flagged between images to be composited, thresholds should be derived from the individual

images and the probability images mosaicked. There may be a slight increase in thresholding effort.

The forest cover extent and change products from SPOT 4 are not as consistent with prior results as those obtained from Landsat 5 or Landsat 7 SLC-off data. The mapped forest extent is smaller and the rates of change correspondingly larger in all of these test areas.

Of these two alternatives, the Landsat 7 SLC-off data would be preferred as a replacement to Landsat 5 as it provides greater consistency and less overall increase in processing effort. However, as noted in the introduction, the Landsat 7 satellite is unlikely to be available to bridge the full gap until a new Landsat sensor is launched. Investigations into the data from other sensors are ongoing.

Acknowledgements This work was supported by DCC Land Cover Change program.

References

- Caccetta PA (1997) Remote Sensing, Geographical Information Systems (GIS) and Bayesian Knowledge-Based Methods for Monitoring Land Condition. PhD Thesis, Curtin University of Technology, Australia.
- Danaher T, Wu X and Campbell NA (2001) Bidirectional Reflectance Distribution Function Approaches to Radiometric Calibration of Landsat TM Imagery. IGARSS 2001 Conference proceedings, Sydney, Australia, July 2001.
- Furby SL (2002) Land Cover Change: Specification for Remote Sensing Analysis. Australian Greenhouse Office Technical Report 9.
- Furby SL (2006) Documentation for the 2005 Update of the Forest Cover Mapping for the Australian Greenhouse Office Land Use Change Program, CSIRO Mathematical and Information Sciences Technical Report 06/43.
- Furby SL and Campbell NA (2001) Calibrating images from different dates to 'like value' digital counts. *Remote Sensing of Environment*, 77:186–196.
- Furby SL and Wu X (2006) Evaluation of Landsat 7 SLC-off Image Data for Forest Cover Mapping. CSIRO Mathematical and Information Sciences Technical Report 06/154.
- Furby SL and Wu X (2007) Evaluation of IRS P6 LISS-III and AWiFS Image Data for Forest Cover Mapping. CSIRO Mathematical and Information Sciences Technical Report 06/199.
- Furby SL, Wu X and O'Connell J (2006) Evaluation of SPOT 4 Image Data for Forest Cover Mapping. CSIRO Mathematical and Information Sciences Technical Report 06/155.
- SPOT Image (2008) SPOT Image Technical Information [Internet documents cited April 2008]. Available from <http://www.spotimage.fr/web/en/224-technical-information.php>.
- Toutin Th (1994) Rigorous geometric processing of airborne and spaceborne data. Proceedings of EUROPTO Symposium on Image and Signal Processing for Remote Sensing, Rome, Italy, Vol SPIE 2315, 825–832.
- Wu X, Furby SL and Wallace J F (2004) An Approach for Terrain Illumination Correction. The 12th Australasian Remote Sensing and Photogrammetry Conference Proceedings, Fremantle, Western Australia, 18–22 October
- Wu X, Guo J, Wallace J, Furby SL and Caccetta P (2006) Evaluation of CBERS Image Data: Geometric and Radiometric Aspects. Proceedings of the 13 Australasian Remote Sensing and Photogrammetry Conference, Canberra, Australia.

Evaluation of CBERS Image Data: Geometric and Radiometric Aspects

X. Wu, J. Guo, J. Wallace, S.L. Furby, and P. Caccetta

Abstract In Australia, Landsat imagery is currently used in a number of regional and national monitoring projects. However, the future of Landsat imagery is not assured. Both Landsat 5 and Landsat 7 are estimated to run out of fuel around 2010. With the looming gap in Landsat data continuity it is timely to consider the issues involved in using data from other sensors to continue these monitoring programs. In the context of the Australian Greenhouse Office (AGO) Land Cover Change Program (LCCP) (<http://www.climatechange.gov.au/ncas>), this paper describes the issues on CBERS geometric and radiometric aspects, and quantifies the effects of using CBERS images to produce forest cover maps. Other alternatives to Landsat data that are being considered by AGO are SPOT 4 and Landsat 7 SLC-off images (Furby and Wu 2006a) and the Indian Remote Sensing satellites (IRS) (Furby and Wu 2006b).

Introduction

Most important aspects of the forest cover mapping program were considered during various evaluation stages, including ortho-rectification, radiometric calibration and thresholding to produce forest cover maps. Unless indicated otherwise in the text, all processing was performed according to the standard methodology for the Land Cover Change Program as described in (Furby 2002, 2006).

The structure of this paper is organized as follows: Section ‘CBERS Background’ gives a brief introduction of CBERS series. Section ‘CBERS Image Datasets’ describes the CBERS datasets obtained and used for evaluation. In sections ‘CBERS Otho-Rectification’ and ‘CBERS Radiometric Calibration’, various aspects and problems of geometric rectification and radiometric calibration of CBERS data will be discussed, a new approach for CBERS radiometric calibration is described and results are presented. Results of thresholding to produce forest cover maps are given in section ‘Thresholding Issues’. Finally,

X. Wu (✉)

CSIRO Mathematical and Information Sciences, Wembley 6913, Western Australia

section ‘Conclusion’ presents some findings and recommendations for using CBERS data for monitoring the extent and change in area of perennial vegetation.

CBERS Background

China has joined forces with the Brazilian government to develop a series of earth-observing satellites launched by Long March rockets from China. Their program goes by the name of CBERS (China-Brazil Earth Resources Satellites); CBERS series is called ZY—1 (ZY is abbreviated from Zi Yuan, which means resources) series in China. CBERS 01, the first in CBERS series, was launched on October 14, 1999 and CBERS 02 was launched on October 21, 2003. CBERS 02 is still operational, although exceeding its design life. A replacement satellite, called CBERS 02B, has been launched on September 27, 2007. CBERS 03 and 04 are to be launched in the near future. The CBERS series demonstrates China’s capability of developing earth resources satellite and satellite application products. The more than 280,000 images received are concentrated mainly over China and Brazil, and are not generally available to other nations.

CBERS 02 is technically identical to CBERS 01. The first two CBERS satellites carry on-board a multi-sensor payload with different spatial resolutions. The three sensors are: (1) Wide Field Imager (WFI) (900 km swath; 258 m resolution; 2 bands); (2) Infrared MSS (IRMSS) (120 km swath; 78 m resolution; 4 bands including thermal); and (3) Charge Coupled Device (CCD) (120 km swath; 19.5 m resolution; 5 bands). Figure 1 shows the detailed sensor comparison between CBERS and Landsat TM.

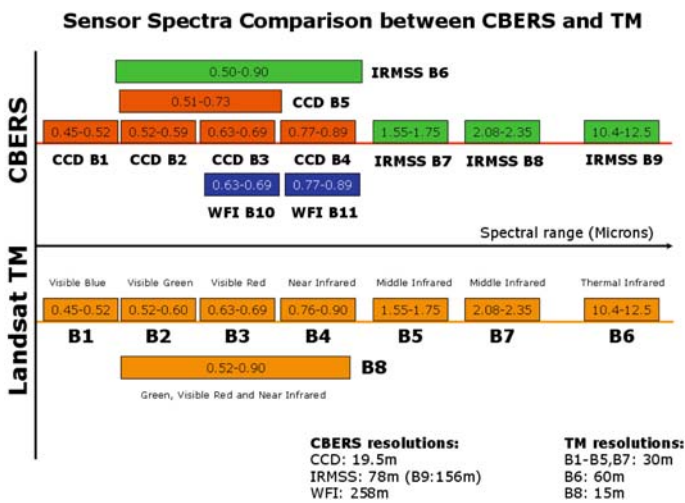


Fig. 1 Sensor bandwidth comparison between CBERS and Landsat TM

CBERS Image Datasets

CBERS Guangzhou Dataset

A CBERS scene was provided by CRESDA (unless indicated otherwise in the text, CBERS refer to CBERS 02 CCD image). This dataset covers the surrounding area of Guangzhou, China, and contains 5-band images from CCD sensor and 4-band image from IRMSS sensor. Figures 2 and 3 show the composed images from CCD and IRMSS sensors, respectively.

Fig. 2 CBERS scene of path 372 row 74, acquired on December 1, 2004, Guangzhou, China. The scene data contains 5 CCD bands; however the above picture only shows bands 4, 3 and 2, represented by *red*, *green* and *blue* colours, respectively

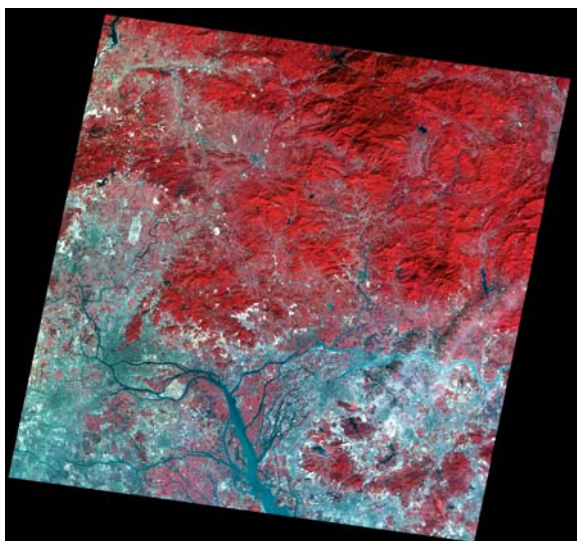
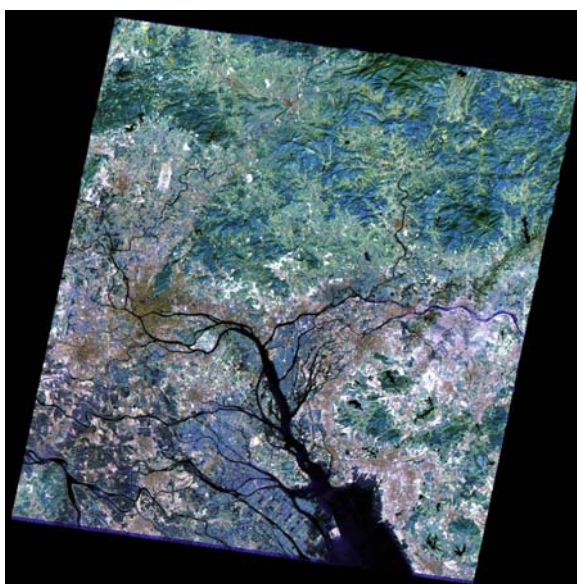


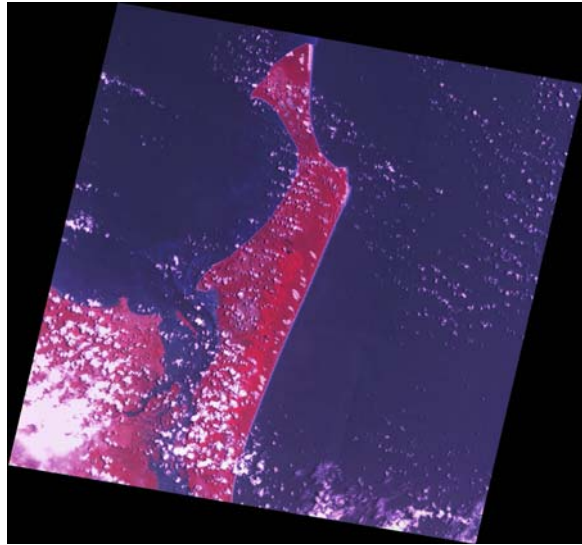
Fig. 3 CBERS scene of path 372 row 74, acquired on December 1, 2004, Guangzhou, China. The scene data contains 4 IRMSS bands; however, the above picture only shows bands 3, 2 and 1, represented by *red*, *green* and *blue* colours, respectively



CBERS QLD Dataset

In late 2004, CRESDA planned a special mission to acquire some CBERS data for Australia. To our knowledge, the CBERS 02 scene of path 319 row 128 (Fraser Island, Queensland), provided by CRESDA, was the first CBERS dataset for Australia. It was acquired on December 3, 2004 (see Fig. 4). Due to the on-board data storage limitations, the scene only contains CCD bands 4, 3 and 2. Unfortunately, this scene was heavily covered by clouds at the acquisition time and therefore was not considered for our evaluation purpose.

Fig. 4 CBERS scene of path 319 row 128 (Fraser Island, Queensland), acquired on December 3, 2004. The scene contains CCD bands 4, 3 and 2 (represented by *red*, *green* and *blue* colours, respectively)



CBERS WA Dataset

1. In January 2005, through negotiation with CSIRO, CRESDA planned the second mission to acquire some CBERS data in Western Australia, for part of the region covered by the Land Monitor project (<http://www.landmonitor.wa.gov.au>). Four consecutive CBERS scenes from row 132 to row 135 in path 358 were acquired on February 7, 2005. Due to the on-board data storage issue, this dataset only contains CCD bands 4, 3 and 2 (represented by red, green and blue colours in Fig. 5, respectively). The row 132 and row 133 scenes are nearly cloud-free (shown in Fig. 5) while row 134 and row 135 were heavily covered by clouds and therefore were not considered for evaluation purpose.

Fig. 5 CBERS WA dataset (combined two scenes of row 132 and row 133 at path 358), acquired on February 7, 2005, in the Land Monitor project region, Western Australia. The scene contains CCD bands 4, 3 and 2 (represented by red, green and blue colours, respectively)



CBERS Ortho-Rectification

CBERS WA Dataset

The CBERS WA dataset provided by CRESDA is map-oriented (images have been rotated to align with the map grid) which makes it difficult to apply orbital modelling techniques in order to establish the rigorous geometric relationship between provided images and the ground truth. Therefore the Rational Polynomial Function (RPF) (Grodecki 2001) model was used for ortho-rectification instead of using the rigorous orbital modelling method.

The 2005 Land Monitor data was used as the base image to collect the ground control points (GCP) and match to the CBERS images. The base image used was mosaicked mainly from two Landsat 5 TM scenes: Mullewa (path 113, row 80) and Moora (path 113, row 81). By a coincidence, these two Landsat TM scenes were acquired on February 9, 2005, only 2 days after the CBERS scenes. The Digital Elevation Model (DEM) from the Land Monitor project was used for image ortho-rectification.

Table 1 RMS errors of RPF model fitting for CBERS scenes (unit: pixel, CCD pixel size is 19.5 m)

| CBESR scene | GCP | RMS X (m) | RMS Y (m) |
|-------------|-----|-----------|-----------|
| Mullewa | 104 | 21 | 12 |
| Moora | 113 | 21 | 10 |

More than 100 well distributed GCPs were collected for each CBERS scene and the RPF model fitting results for each scene show a good agreement. The RMS (root mean squares) errors are less than 25 m for both the easting and northing directions (Table 1).

Statistical analysis between the ortho-rectified CBERS image and the Landsat 5 TM base image was carried out using correlation matching to locate 29 check GCPs in these two images. RMS errors for best 90% of 29 check GCPs with correlation coefficients larger than 0.85 are 23 m in the easting direction and 11 m in the northing direction, which is less than one pixel of the Landsat 5 TM base image. This is of the same order of magnitude as obtained for Landsat TM to Landsat TM ortho-rectifications.

A visual inspection was conducted by manually checking overlays of the two images (TM image Band 4 as the red channel and CBERS band 4 as the green channel). The yellow colour should be dominant if both images are matched perfectly, while red or green colour indicates there are some misalignments between ortho-rectified CBERS and TM base images. The misalignment is less than one pixel (25 m) over most of the area. Figure 6(a), (b) and (c) show the good alignment

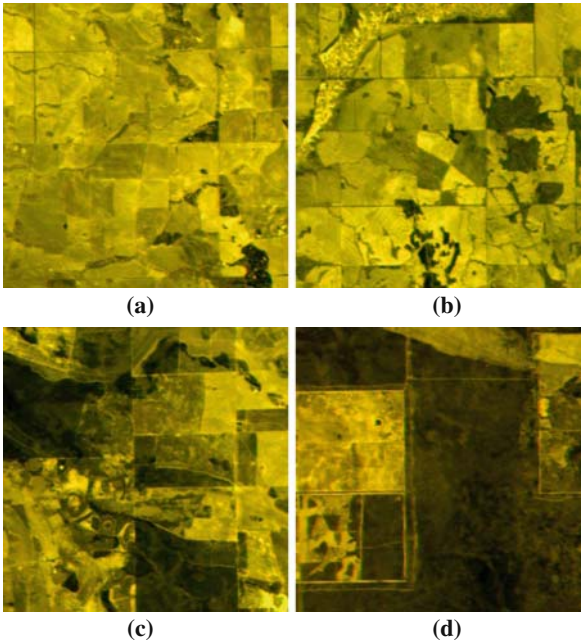


Fig. 6 Four zoomed areas on the composed image (TM image Band 4 as the *red* channel and CBERS band 4 as the *green* channel). (a), (b) and (c) show the good alignment on the composed image in three enlarged areas (see *boxes A, B and C* in Fig. 5), while (d) shows the mis-registration of around two pixels

on the composed image in three enlarged areas (see boxes A, B and C in Fig. 5). However, the misalignment in some areas exceeds the limits set by both Land Monitor and AGO projects (normally less than 25 m). For example, Fig. 6(d) shows the mis-registration is around two pixels (50 m).

Further improvement could be made if the path-oriented (orbital) images are provided and the rigorous orbital model techniques are applied.

CBERS Guangzhou Dataset

The purpose of CBERS Guangzhou dataset evaluation is to investigate the alignment issue of CBERS data between its CCD bands and its IRMSS bands. Registration process was carried out in two steps:

1. The CCD image was registered and ortho-rectified to a reference image, and
2. The IRMSS image was registered and ortho-rectified to the ortho-rectified CCD image.

The reference image in Step 1 is an ortho-rectified Landsat 7 ETM+ image which was downloaded from the Global Land Cover Facility (GLCF) web-site (<http://glcf.umd.edu/data/>). The reference image was acquired on September 14, 2000 and can be identified by path 122 and row 44. The DEM used for ortho-rectification is the Shuttle Radar Topography Mission (SRTM) DEM (<http://seamless.usgs.gov/>) with post-processing applied by the authors. Both datasets are freely available.

The CBERS Guangzhou dataset provided by CRESDA is also map-oriented which makes it difficult to apply orbital modelling techniques. RPF model was used for ortho-rectification.

Forty-one well distributed GCPs were collected from the CCD image and matched to the reference image. Fifty three well distributed GCPs were collected from the IRMSS image and matched to the ortho-rectified CCD image. The RPF model fitting residual errors for both CCD and IRMSS images are listed in Table 2.

Statistical analysis between the ortho-rectified CCD image and the ortho-rectified IRMSS image was carried out using correlation matching to locate 63 check GCPs in these two images. RMS errors for best 90% of 63 check GCPs with correlation coefficients larger than 0.85 are 42 m in the easting direction and 37 m in the northing direction, which is about two third of an IRMSS pixel size.

Table 2 RMS errors of RPF model fitting for CBERS sensors (unit: pixel, CCD pixel size is 19.5 m, IRMSS pixel size is 78 m)

| CBESR sensor | GCP | RMS X (m) | RMS Y (m) |
|--------------|-----|-----------|-----------|
| CCD | 41 | 33 | 25 |
| IRMSS | 53 | 31 | 23 |

Fig. 7 Zoomed area on the composed image (CCD image Band 3 as the *red* channel and IRMSS band 2 as the *green* channel. IRMSS image pixel resolution was resampled from 75 into 25 m)



Visual inspection confirms the statistical analysis results in majority of areas. Figure 7 shows a zoomed region on the composed image (CCD and IRMSS combined image). However, it is unknown how this amount of shift affects forest cover maps if the combined data (CCD with IRMSS) is tried.

CBERS Radiometric Calibration

The standard calibration process for both the Land Monitor project and AGO LCCP consists of three distinct steps:

- top-of-atmosphere and Bi-directional Reflectance Distribution Function (BRDF) corrections;
- invariant target atmospheric check/correction; and
- terrain-illumination correction, if required.

CRESDA provides the necessary parameters for applying the top-of-atmosphere corrections to the CBERS images using the current procedure with slight modifications. However, a new approach is required in applying the BRDF corrections to the CBERS images.

CBERS WA dataset was chosen for radiometric calibration evaluation. Terrain-illumination correction is not applied to the South West region of WA in either the Land Monitor project or the AGO LCCP as the area is relatively flat. Only top-of-atmosphere and BRDF corrections were applied for CBERS WA dataset.

CBERS Radiometric Calibration Approach

Given a base image (ortho-rectified and radiometrically calibrated) and an ortho-rectified CBERS image, a new BRDF calibration model is proposed from an early model developed by Wu (2006). Assuming there are enough overlapping regions between the base image and a CBERS image, the BRDF calibration model can be written as:

$$v = a_0 + k_1 a_1 + k_2 a_2 - (s \cdot g - g_b) \quad (5.1)$$

where

k_1, k_2 are the two BRDF kernels for the CBERS image, which can be calculated once necessary kernel parameters are provided,
 a_0 is the offset and a_1, a_2 are the kernel coefficients for the CBERS image,
 g is the CBERS image's band value, s is the scaling factor of g , g_b is the base image's corresponding band value, and
 v is the fitting residuals for observation.

Some commonly used BRDF kernels considered are Ross Thick, Ross Thin, Roujean, Li Sparse and Li Dense. Image geometric view angles need to be calculated in order to apply these BRDF kernels. Most BRDF kernels are the functions of image geometric view angles related to the centres of the imaging sensor and solar direction (Vermote et al. 1994). A detailed description of the relationship between image and space, and the procedures to calculate image view angles are provided by Wu (2006).

Once enough samples (usually in the order of tens of thousands) are collected, this model can be fitted in different ways such as the least squares techniques. A robust S-estimate technique was employed to estimate the kernel coefficients and the scaling factor (Campbell et al. 1998).

It is worth mentioning that though this model is applied to CBERS images, it can be easily modified to applicable to other satellite images and aerial images. For example, SPOT 4 images were BRDF calibrated to Landsat TM base images using this model (Furby and Wu 2006a).

The practical approach consists of three consecutive steps as follows:

1. Due to the nature of CBERS CCD sensor imaging (push-broom scanning), each scanline has its own solar zenith and azimuth angles and view zenith and azimuth angles. These angles are accurately calculated using the photogrammetric method which utilises: (i) satellite positions at different scanlines; (ii) each pixel's location (longitude and latitude) and; (iii) time, date and orbital data;
2. Several kernel models (one kernel mode or a combination of two kernels mode) can be chosen and modelled using samples taken within the vegetation and bush areas. The linear coefficients of these models are estimated using a robust S-estimate technique (Campbell et al. 1998); and
3. CBERS images are then corrected using the kernel coefficients.

CBERS Calibration Results

In the CBERS BRDF calibration experiment, the forest/non-forest masks are available and the samples are collected within the forest areas only. Roujean and Li Dense were chosen as the two kernels. Histogram comparison shows there are significant improvements (matched to the base image) after applying BRDF calibration to the CBERS image (Fig. 8). However, there is more work required to assess the BRDF calibration, more adjacent CBERS images are required to further analyse the BRDF calibration model for CBERS data.

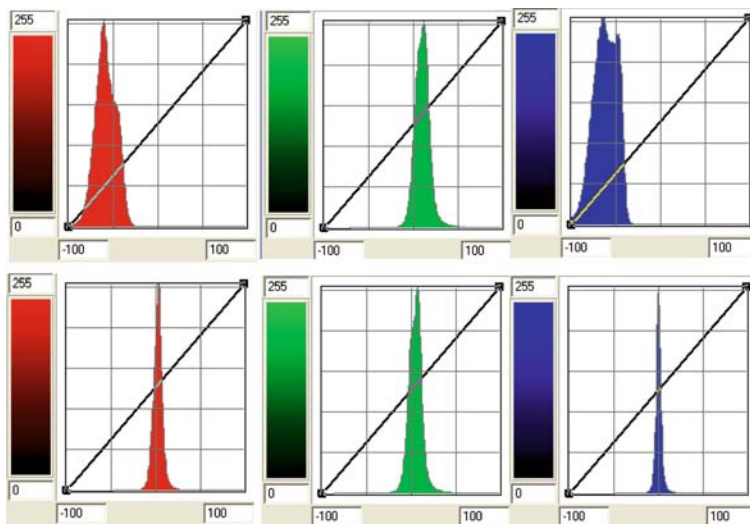


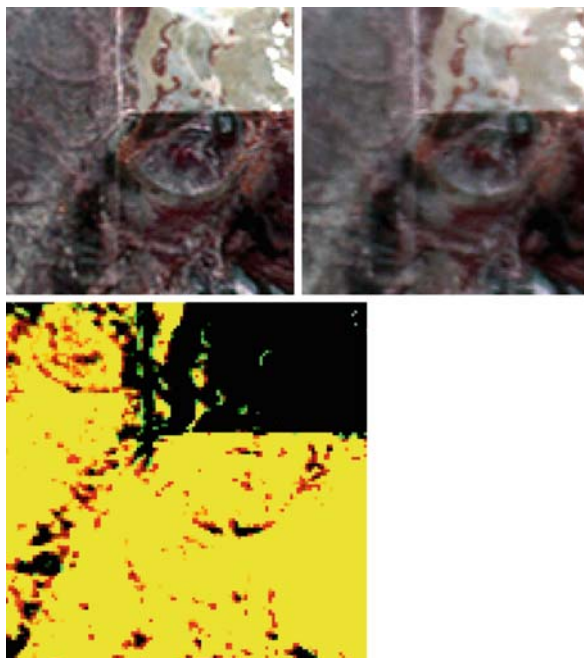
Fig. 8 Histograms of the subtracted image (the base image is subtracted by the CBERS image) before and after applying the BRDF calibration to the CBERS WA dataset. The first row shows the histograms of the subtracted image before applying the BRDF calibration to the CBERS image. The second row shows the histograms of the subtracted image after applying the BRDF calibration to the CBERS image. Subtracted bands 4, 3 and 2 (Landsat TM equivalent) are represented by *red*, *green* and *blue* colours, respectively

Thresholding Issues

CBERS WA Dataset

Forest cover probability images were created using the index-threshold methods of AGO LCCP (Furby 2002). The index derivation is based on discriminant analysis procedures applied to training sites selected from existing forest cover masks. Here these were applied to the TM image (6 bands), the CBERS image in which only

Fig. 9 *Top Left:* Landsat 5 TM image, bands 4, 3, 2 in RGB. *Top Right:* CBERS image, bands 4, 3, 2 in RGB (equivalent to TM bands 432). *Bottom row:* Overlay of forest extent maps for Landsat 5 TM (red) and CBERS (green)



3 bands are available and to the 3 CBERS-equivalent bands from the TM image. After conducting the same AGO classification procedure, as expected, reduction of TM bands from 6 to 3 reduces overall discrimination and discrimination forest vs non-forest ‘contrasts’. LCCP indices for this region include Landsat TM band 5 or 7 for this reason. Site ordination plots showed similar patterns for CBERS and equivalent 3-band TM data; forest and non-forest sites are generally separable, but some sites which are well separated using 6 TM bands, are in an ‘overlap region’ using the three bands. These evidences are mainly based on expert’s photo-interpretation using forest cover probability images. Despite its nominal 19.5 m resolution, the CBERS image is ‘blurry’ in comparison with the same Landsat bands (Fig. 9), indicating a coarser effective resolution.

Figure 9 compares the forest cover products and imagery for a small sample in the CBERS WA dataset area, produced derived common indices and comparable thresholds. This area was chosen as it is relatively challenging, having thin perennial vegetation (below the LCCP threshold) and fine spatial features. Forest cover extent maps derived from Landsat 5 TM and CBERS are displayed together in green and red respectively in the bottom row of Fig. 9. Where these products coincide, the display appears yellow (forest) or black (non-forest). Red and green shows where the CBERS and 3-band TM derived forest maps disagree. The red areas appear largely to be a result of the coarser effective resolution of CBERS.

Conclusions

This paper explores some potentials of using CBERS data, mainly from the geometric rectification and radiometric calibration aspects. The preliminary results from experiments using the CBERS WA and Guangzhou datasets are encouraging. However, there are more aspects need to be investigated for the CBERS data if it is to be used in Land Monitoring project and AGO LCCP.

The CBERS WA dataset demonstrates that map-oriented CBERS CCD images can be registered to the base image (Landsat 5 TM), with apparently satisfactory RMS error. However, in some areas, mis-registration error is greater than Land Monitor or LCCP standards. It is likely that orbital models applied to path-oriented image CBERS data will improve the registration, and this should be investigated. In conjunction with the proposed BRDF calibrated model, CBERS WA dataset can be radiometrically calibrated to the Landsat 5 TM base, and the thresholding analysis shows that the forest cover map derived using limited CBERS bands is comparable to the forest cover map derived using Landsat 5 TM equivalent bands. The coarser effective spatial resolution would create some issues if CBERS products are used to extend existing Landsat TM monitoring programs.

The registration results from the CBERS Guangzhou dataset show that it is possible to register the CBERS CCD image and its companion IRMSS image (both IRMSS and CCD images were acquired simultaneously). The misalignment errors are 42 m in the easting direction and 37 m in the northing direction, which is about two thirds of an IRMSS pixel size.

During both CBERS WA and Guangzhou datasets ortho-rectification experiments, only the RPF model was applied due to the CBERS images provided being map-oriented. Further improvement could be expected if the path-oriented images are provided and the rigorous orbital model techniques are applied.

In the context of monitoring programs, accurate registration is critical. IRMSS data was not available for the Australian study area, and the potential and effect of its additional spectral bands have not yet been evaluated. This should be carried out following examination of results from orbital modelling registration.

The following areas are recommended for CBERS further investigation:

- Evaluate more CBERS images from ortho-rectification and terrain illumination aspects, particularly in mountainous areas,
- further study the issues surrounding the fusion between CCD and IRMSS data, including the forest cover maps derived from combined CCD and IRMSS bands,
- Apply the rigorous orbital model techniques to CBERS path-oriented images from CCD and IRMSS,
- further study on the proposed BRDF calibration model, especially the optimal kernel's choice, and
- The accuracy of the change products from 'mixed' sensor time series analysis (e.g. CBERS and Landsat TM).

Acknowledgements The authors would like to thank Mr Pinxiong Liu (Chinese National Space Administration) for his assistance of providing the important CBERS contacts in China. The authors also would like to thank USGS and NASA for making the SRTM DEM and the GLCF Landsat data available for public use.

References

- Campbell NA, Lopuhaa HP and Rousseeuw PJ (1998) On the calculation of a robust S-estimator of a covariance matrix. *Statistics in Medicine* 17:2685–2695
- Furby SL (2002) Land Cover Change: Specification for Remote Sensing Analysis, National Carbon Accounting System – Technical Report No. 9. Department of Climate Change, Australia, <http://climatechange.gov.au/ncas/reports/tech09.html>
- Furby SL (2006) Documentation for the 2005 Update of the Forest Cover Mapping for the Australian Greenhouse Office Land Use Change Program. CSIRO Mathematical and Information Sciences Technical Report 06/43
- Furby SL and Wu X (2006a) Evaluation of Alternative Sensors for a “Landsat-based” Monitoring Program. Proceedings of the 13 Australasian Remote Sensing and Photogrammetry Conference, Canberra Australia
- Furby SL and Wu X (2006b) Evaluation of IRS P6 LISS-III and AWiFS Image Data for Forest Cover Mapping. CSIRO Mathematical and Information Sciences Technical Report 06/199
- Grodecki J (2001) IKONOS stereo feature extraction—RPC approach. Proc. ASPRS Annual Conference, St. Louis, 23–27 April. American Society of Photogrammetry & Remote Sensing
- Vermote EF, Tanré D, Deuzé JL, Herman M and Morcrette JJ (1994) Second Simulation of the Satellite Signal in the Solar Spectrum (6S). 6S User Guide Version 0
- Wu X (2006) Radiometric Calibration of Aerial Digital Imagery. Proceedings of the 13 Australasian Remote Sensing and Photogrammetry Conference. Canberra, Australia

Mapping and Monitoring Wetlands Around the World Using ALOS PALSAR: The ALOS Kyoto and Carbon Initiative Wetlands Products

John Lowry, Laura Hess, and Ake Rosenqvist

Abstract Climate change and the conservation of the environment are extremely significant and topical global issues. The ALOS Kyoto and Carbon (K&C) Initiative is a global, multi-disciplinary research initiative of the Japanese Aerospace Exploration Agency (JAXA), aiming to produce remote sensing products which can support international conservation conventions, carbon cycle science, and conservation of the environment. The objective of the Initiative is to define, develop and validate products derived primarily from the PALSAR (Phased Array L-Band Synthetic Aperture Radar) sensor on-board the ALOS (Advanced Land Observing Satellite). The ALOS-PALSAR instrument provides a range of enhancements, including full polarimetry, variable off-nadir viewing, ScanSAR mode, and improved radiometric and geometric performance, compared to the earlier Japan Earth Resources Satellite (JERS-1) SAR. Data are being developed on a thematic basis, relating to global biomes, including forest, desert and wetlands. In this paper, which is a summary of the wetlands parts of the ALOS K&C Science Plan, we describe a range of tools and products that are being developed to utilize the advantages of the PALSAR instrument to support the inventory, conservation and management of wetlands in different areas around the world. These include products which will specifically enhance information on the extent and characteristics of global wetlands; and products for seasonal monitoring of tropical/sub-tropical wetlands; mapping and monitoring of key wetland types, including mangroves, peat swamp forests, and lakes, including northern Australia and south-east Asia. We highlight and compare the relative strengths of the PALSAR sensor, such as the ability to detect wetland environments in areas of the world which are regularly obscured by clouds, smoke or dense vegetation, with other SAR and optical sensors. Importantly this information will be used to support the Ramsar Convention on wetlands, and other conservation initiatives aimed at protecting and enhancing wetland management.

J. Lowry (✉)

Supervising Scientist Division, Department of the Environment, Water, Heritage and the Arts,
Darwin, NT, Australia

e-mail: john.lowry@environment.gov.au

Introduction

The Kyoto and Carbon (K&C) Initiative was initiated by the Japanese Aerospace Exploration Agency (JAXA) Earth Observation Research and Applications Center (EORC) in 2000 (Rosenqvist et al. 2003), and is based on the conviction that Earth Observation technology has the potential to play a more significant role than it does today, in supporting international conservation Conventions, Carbon cycle science and natural Conservation (referred to hereafter as CCC), with information that cannot be obtained in a feasible manner by any other means. It is recognised that close integration with in situ information and analytical models is fundamental in this context.

The objective of the K&C Initiative is to define, develop and validate products derived primarily from the PALSAR (Phased Array L-Band Synthetic Aperture Radar) sensor on-board the ALOS (Advanced Land Observing Satellite). The ALOS-PALSAR instrument provides a range of enhancements, including full polarimetry, variable off-nadir viewing, ScanSAR mode, and improved radiometric and geometric performance, compared to the earlier Japan Earth Resources Satellite (JERS-1) SAR. Specifically, the K&C Initiative aims to support the CCC through the provision of (1) systematic global observations and consistent data archives, and (2) derived and verified thematic products.

Thematically, the Initiative is structured around three main thematic areas (Forest, Wetlands and Desert and Water) that each relate uniquely to one or more of the CCC drivers of the project.

The Forest Theme is focused to support the UNFCCC Kyoto Protocol and the part of the carbon research community concerned with CO₂ fluxes from terrestrial sinks and sources. Key areas considered include land cover (forest) mapping, forest change mapping and biomass and structure.

The Wetlands Theme aims to serve information needs posed by the Ramsar Wetlands Convention and the Convention on Biological Diversity, as well as the significance of wetlands as sources of tropospheric carbon. Key areas considered include regional wetland inventories, seasonal inundation monitoring and specific inventories of mangroves and peat swamp forests.

The Desert and Water Theme addresses issues relevant to water supply and land degradation in arid and semi-arid areas. Key areas considered include freshwater supply and desertification.

In this paper, we explain the significance of PALSAR data for wetland applications, and highlight the specific products developed for wetland applications in the ALOS K&C Science Plan (Rosenqvist et al. 2008), as they apply to the Asia-Pacific region (including Australia).

PALSAR

The PALSAR sensor is an enhanced version of the Synthetic Aperture Radar on JERS-1 (L-band; HH-polarisation; 35° off-nadir angle). PALSAR is a fully polarimetric instrument, operating at L-band with 1270 MHz (23.6 cm) centre

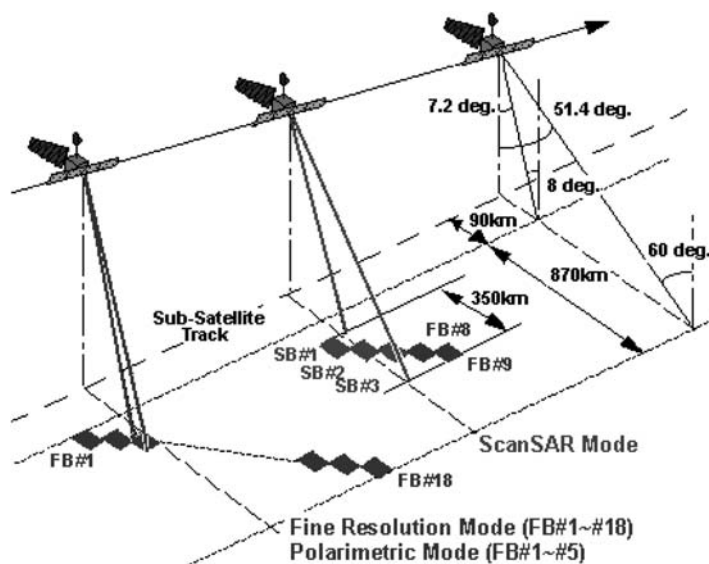


Fig. 1 PALSAR observation characteristics

frequency, and 28 MHz, alternatively 14 MHz, bandwidth. The antenna consists of 80 transmit/receive (T/R) modules on four panel segments, with a total size of 3.1 by 8.9 m.

PALSAR features four main modes of operations (Fig. 1):

- Fine resolution beam mode
- Polarimetric mode
- ScanSAR mode
- Direct transmission mode

The Fine resolution Beam (FB) mode, features 18 beam selections between 9.9 and 50.8° off-nadir angle, each with 4 alternative polarisations: single polarisation HH or VV, and dual polarisation HH+HV or VV+VH. The bandwidth is 28 MHz in single polarisation and 14 MHz in the dual polarisation mode. The data recording rate in FB mode is 240 Mbps, thus requiring data downlink via the DRTS.

Out of the 72 alternative FB modes available, two have been selected for operational use: [HH pol.; 34.3° off-nadir] and [HH+HV pol.; 34.3° off-nadir]. These modes yield 70 km swath width and 10×10 and 10×20 m ground resolution in HH and HH+HV polarisation, respectively. The 34.3° off-nadir angle corresponds to an incidence angle range of 36.6 and 40.9° from near- to far range. PALSAR is operated in near zero-Doppler yaw steering mode to improve processing efficiency and geometric accuracy.

The Polarimetric mode provides the full quad-pol (HH+HV+VH+VV) scattering matrix with 12 alternative off-nadir angles between 9.7 and 26.2°. The default off-nadir angle for polarimetric acquisitions is 21.5° (22.8–25.2° incidence range), resulting in 30 km swath width and 30×10 m ground resolution.

The wide-swath ScanSAR mode is available at single polarisation (HH or VV) and can be operated with 3, 4 or 5 sub-beams transmitted in either short (14 MHz bandwidth) or long bursts (28 MHz). Out of the 12 ScanSAR modes available, the short-burst, HH polarisation, 5-beam mode has been selected for operations. It features a 360 km swath width with an incidence angle range varying from 18.0 to 43.0° (the off-nadir angles for each of the 5 beams are 20.1, 26.1, 30.6, 34.1 and 36.5°).

Wetland Theme

The increasing recognition of the importance of wetland ecosystems to both the economic and environmental health of human communities has stimulated renewed interest in mapping the distribution of wetlands around the world (Darras et al. 1999, Finlayson and Rea 1999). However, the broad definition of what constitutes a wetland and disagreements on definition have led to a wide range of mapping techniques and inconsistencies in their application. Indeed, one of the major handicaps facing wetland inventory is the lack of a universally understood classification system to describe wetland environments (Finlayson and van der Valk 1995). As a result, estimates of wetland extent vary widely. The establishment of globally acceptable definitions of wetlands and wetland types is therefore fundamental if appropriate mapping techniques are to be implemented. Furthermore, the provision of a spatially consistent data source to which the mapping techniques can be applied is also fundamental. Remote sensing does provide such a dataset but even so, standardising procedures for mapping regionally, let alone globally, remains a significant challenge.

Remote sensing data have, for some time, provided opportunities for identifying, describing and mapping the distribution of wetlands at a range of scales from local to global and certainly recent advances in remote sensing instruments and spatial analysis techniques have only increased their potential (Phinn et al. 1999, Sahagian and Melack 1996). However, few studies have been undertaken with the explicit aim of presenting the spatial distribution of wetlands on a global or even continental scale. Further, the methods by which wetland environments are identified or classified from existing global datasets vary considerably (Sahagian and Melack 1996, Darras et al. 1999) and the results of mapping are often inconsistent. For example, Lowry and Finlayson (2004) analysed ten different datasets representing wetland distribution across northern Australian and found considerable differences in the areal estimates of wetland extent. Mapping has proved difficult in many areas because of the lack of temporally and spatially consistent datasets and also because many areas are inaccessible, remote or temporally dynamic. The accuracy of many of these approaches has rarely been tested (Sahagian and Melack 1996) with many assessments relating to specific environments, without providing an overall indication of the areal extent of all wetlands types in the area of interest.

The Wetlands Theme of the K&C Initiative focuses on the provision of remote sensing datasets that can be used to assist the global mapping and monitoring of wetlands and identifying and quantifying the threats to which these are exposed.

Specifically, it aims to develop a suite of products which may be used to improve the understanding of carbon cycle science, assist the implementation of conservation and management strategies and support national and international obligations to multi-national conventions.

In terms of carbon cycles, the boreal wetlands, tropical peat swamps, paddy rice and mangroves are of particular relevance. Specifically, boreal wetlands and tropical peat swamps contain significant amount of carbon which may be released as a result of climate change and anthropogenic activities (e.g., deforestation and disturbance) (e.g. Weller and Holmgren 1993, Shaver et al. 1990, Chapin et al. 1995). Significant amounts of methane are released through rice cultivation practices. The clearance of mangroves is another significant (but poorly recognised) means by which carbon may be released into the environment. Mangrove forests often contain more carbon per unit area than tropical forests.

The most basic requirement for modelling regional to global methane or carbon dioxide emissions from wetlands is a digital wetlands map with appropriate scale and classification scheme. While several global wetlands datasets exist (e.g., Matthews and Fung 1987, Lehner and Döll 2004) these datasets possess a number of limitations, reflecting the methods/processes used to generate these datasets. Specifically, these have been compiled from a variety of map sources generated using a range of methods and to varying degrees of accuracy. Many of these sources use class names (e.g., swamp, fen and bog) that may overlap or vary in meaning and seasonal and permanent wetlands may not be distinguished. For these reasons, such classification schemes cannot usually be directly incorporated into physical models. Working groups of the International Geosphere-Biosphere Program (IGBP) (Sahagian and Melack 1996) have addressed this concern and concluded that there is a need to characterize wetlands in terms of their functional characteristics rather than based on traditional regional terminology or on criteria such as phytosociology.

Wetland ecosystems fulfil a vital role in maintaining the ecological and economic health of many regions. As well as providing a wealth of resources or services, including products used for fuel, construction, fishing, paper, medicines, textiles and leather, and food items, these ecosystems also influence ground water recharge, retain nutrients and sediment and stabilise shorelines (Saenger 1994, Blasco et al. 1996, Finlayson and D'Cruz 2005). Mangrove ecosystems, for example, are an integrated component of the coastal environment in that they are important contributors to primary production (Bandaranayake 1994), act as nursery sites for many commercial fish and crustacean species and are a seasonal base for many migratory species (Finlayson and D'Cruz 2005). The Sumatra tsunami disaster in December 2004 furthermore made evident the importance of mangroves as protective buffers to reduce the impacts from natural hazards. From a conservation perspective, wetland habitats contain many of the world's most endangered species of fauna and flora, many of which are unique, or endemic to specific wetland habitats.

Long-term preservation and sustainable use of these resources is therefore critical for the economic and social well being of current and future generations. Key requirements include the establishment of regional and temporal datasets of wetland

Table 1 Community information needs and wetland theme products (Groups I to IV)

| Carbon cycle | Conservation | Conventions | |
|---|---|---|-----------------------|
| Global areas of basic wetland physiognomic types | Establishing baseline datasets of wetland extent and characteristics | Global wetlands mapping in support of Ramsar database | |
| Seasonal changes in inundated area: effect on CH ₄ and CO ₂ emissions | Identify areas subject to disturbance and quantify rates of change | Capability for periodic updating of wetlands mapping for disturbance monitoring | |
| Freeze-thaw dynamics of boreal region | Inventory and monitoring of critical habitat for fish, amphibians, birds, and mammals | Wetlands products to assist Ramsar signatories in completing national inventories | |
| Assessment of carbon stocks in wetland vegetation | Mapping to support location of bioreserves | Seasonal inundation monitoring for Ramsar-supported wetland management projects | |
| Effects of water management on methane emissions from paddy rice | Identification of wetlands performing critical ecosystem services | Ensure accessibility of information to contracted parties | |
| Group I | Group II | Group III | Group IV |
| Global Wetland Extent and Properties | Seasonal monitoring of major wetland regions | Mapping and Assessment of Major Wetland Functional Types | Product dissemination |
| – Tropical | – Tropical | – Mangroves | – Dissemination Plan |
| – Temperate | – Temperate | – Tropical Peatlands | |
| – Boreal | – Boreal | – Paddy Rice | |
| | | – Lakes | |

extent and condition which incorporate an understanding of the inundation dynamics of an area and spatially quantifiable measures of both anthropogenic and natural pressures and threats to wetland communities.

The requirement for wetland information range from the reporting requirements of signatory members of international conventions such as the Ramsar convention, to the requirements of government and non-government organisations involved in the conservation of wetlands and study of the carbon cycle. The key requirements of these organisations, and the products that will be developed to address these issues are summarised in Table 1.

Application of ALOS-PALSAR to Wetland Applications

Over the past few decades, numerous studies have established the theoretical basis and practical application of mapping wetland extent, vegetation structure, and inundation status using active microwave SAR systems (Hess et al. 1995, Costa

et al. 2002, Costa 2004). All SAR instruments share the advantages of day-night operability (as active sensors), cloud penetration, and the ability to calibrate without performing atmospheric corrections. The longer L-band (~ 23.5 cm) SAR wavelength, and to a certain extent also C-band (~ 5.5 cm), have the ability to penetrate vegetation canopies to various degrees depending on vegetation density and height, dielectric constant (primarily a function of water content), and SAR incidence angle. Variations in backscattering allow discrimination among non-vegetated areas (very low to low returns), herbaceous vegetation (low to moderate returns), and forest (moderate to high returns), and to some degree among different forest structures and regrowth stages. Where water is present beneath a forest canopy, enhanced returns caused by specular “double bounce” scattering between water surface and tree trunks makes it possible to distinguish between flooded and non-flooded forest.

Wetland Theme Products

As identified in the preceding sections, carbon cycle, conservation, and multi-national conventions have a range of information requirements relating to wetland inventory, mapping and monitoring. To address these issues and requirements, three key components of the wetlands theme have been identified, through which product development will be undertaken using ALOS PALSAR data (alone, or in conjunction with complementary datasets) (Table 2).

Table 2 Components and products of the wetlands theme

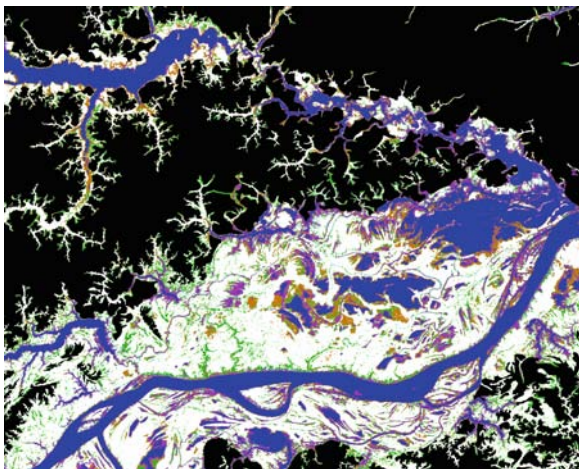
| Component | Product |
|--|---|
| I. Global wetland extent and properties | 1. Tropical wetland extent and properties 2. Boreal wetland extent and properties |
| II. Seasonal monitoring of major wetland regions | 3. Seasonal monitoring of major tropical/sub-tropical wetlands 4. Wetland extent, flood inundation patterns and vegetation change in the Greater Mekong River Basin 5. Seasonal dynamics of the Pantanal ecosystem 6. Seasonal monitoring of major boreal wetlands |
| III. Mapping and monitoring of key wetland types | 7. Global mangrove extent and properties 8. Tropical peat lands extent and properties 9. Pan-Asian mapping and monitoring of rice paddies 10. Global lakes census |

Selected examples of the proposed products for each component, as they relate to the Asia-Pacific region and northern Australia are described below. More information on each product may be found in the Kyoto and Carbon Initiative Science Plan (Rosenqvist et al. 2008).

Tropical Wetland Extent and Properties

It is estimated that wetlands emit about 20% of the methane entering the atmosphere each year, but large uncertainties exist owing to lack of accurate estimates of total wetland area. Since the global warming potential of methane as a greenhouse gas is 4–35 times that of carbon dioxide, improved knowledge of wetland extent and properties are a high priority in order to understand the global methane budget and to predict how changes in climate could alter net emissions of methane. Further, wetland ecosystems in tropical regions of the world are experiencing increasing pressures and disturbances, including clearance and conversion, rising sea levels, extreme climate events, and sediment deposition. These degrade ecosystem services provided by these ecosystems, such as erosion control, fisheries conservation, and wildlife habitat. However, many tropical regions lack regional baseline information on the temporal extent, distribution and character of wetlands which could be used to conserve and protect wetlands. The K&C Initiative is aiming to produce maps of wetland extent, that could be used to document, monitor, and understand the regional biodiversity, habitats, vegetation and ecological dynamics of the tropical wetlands. River basins in South America (the Amazon, Orinoco and Parana basins) and northern Australia, have been selected for developing these products in the first instance. An example of an output product is shown in Fig. 2.

Fig. 2 Classified high-water JERS-1 mosaic for the Cabaliana floodplain along the Solimões river, Amazonas, Brazil. Classes are open water (*blue*), flooded forest (*white*), flooded herbaceous (floating meadows; *magenta*), flooded woodland (*tan*), non-flooded forest (*green*), and non-wetland (*black*). and (S) shrubland. (Courtesy of L. Hess)



Wetland Extent, Inundation Patterns and Vegetation Change in the Greater Mekong River Basin

Within the K&C Initiative, PALSAR observations in ScanSAR mode will be undertaken over a large number of selected river basins of global significance – including the Amazon, Orinocco, Paraguay, Paraná, Yukon, Mackenzie, Congo,

Niger, Zambesi, Okavango, Darling, Mekong, Irrawaddy, Yangtze, Yellow river, Ob, Lena and Yenisey – on a 46-day repeat basis 8–9 times during 1-year time windows, to enable flood duration mapping of unprecedented extents and details. The timing of the acquisition windows vary between the areas, as they have been individually adapted to fully capture the local inundation seasonality.

The need for adequate monitoring and management of environmental resources in order to meet the food, water and energy needs of the population of the Greater Mekong Basin as well as to minimise the deleterious impacts of economic development on the environment are major challenges facing all member governments (Thailand, Lao PDR, Cambodia and Vietnam) who are signatories to the “Agreement on the Cooperation for the Sustainable Development of the Mekong River Basin” signed in 1995, and for international agencies working to promote sustainable development, utilisation, management and conservation of water related resources in the Mekong River including the United Nations Development Program (UNDP), United Nations Environment Program (UNEP), Mekong River Commission (MRC) and the Ramsar Convention on Wetlands.

PALSAR data will be used specifically to produce maps of wetland distribution, flood extent and seasonal water recession patterns, and maps of spatial changes in land cover including that of critical wetlands, natural forests, agricultural land, and human settlements for the Greater Mekong River Basin.

These will be used to determine the spatial pattern of vegetation classes in freshwater wetlands and the associated sequence of floodplain draining and drying that accompanies flood events. This is an important first step in assessing the hydrologic, geomorphic and ecological processes operating in flooded ecosystems. It is also a necessary pre-requisite to the formulation of management plans relating to the sustainable use, conservation and rehabilitation of such environments. PALSAR derived data products from this study will then be integrated with SRTM and other topographic data to produce flood height maps for use in identifying flood prone areas and for predicting the magnitude of flood inundation events for selected study sites within the Mekong Basin. These products will also be used to investigate and understand the flood dynamics and hydrologic exchange mechanisms within the Mekong River network, adjacent floodplains and wetlands (Fig. 3).

Global Mangrove Extent and Properties

Mangroves are a floristically diverse assemblage of salt-tolerant plants, widespread throughout the tropics and subtropics, and also extending to more temperate zones in both the northern and southern hemispheres (32° N and 38° S respectively). They are most extensive in the tropics, where more than 10 million hectares occur, although their combined area represents less than 3% of the world’s tropical forest (Spalding et al. 1997). Mangroves are an important component of coastal ecosystems and are recognized as important contributors to primary production and nutrient cycling in estuarine systems (Bandaranayake 1994), as providing nursery

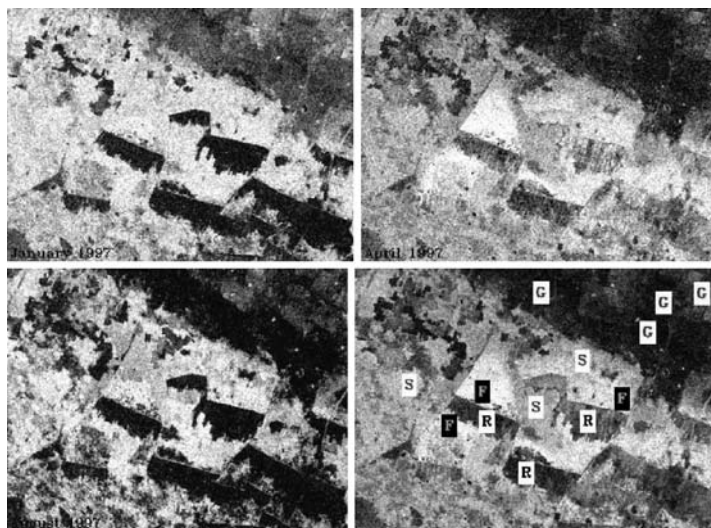


Fig. 3 Composite change image (*left*) derived from the January, April and August (1997) JERS-1 images (*above*). The changing level of irrigation water stored up-slope under scrubland vegetation (F) leading to higher backscatter is clearly evident in all images. Other landcover types are (B) bare ground (G), rice fields (R) and (S) shrubland. (Courtesy of A. Milne. Image copyright JAXA/METI)

grounds for many commercial fish and crustacean species and as a seasonal base for a variety of migratory species. As mangroves occur at the land-sea interface, they also create shoreline buffer zones that protect the coast from erosion and flooding and contribute to groundwater recharge, nutrient and sediment retention and shoreline stabilisation (Blasco et al. 1994, Saenger 1994). Products will include datasets derived from JERS-1 SAR and ALOS PALSAR and will be used to map and monitor the changing extent of mangrove communities subject to both natural and anthropogenic change (including cyclones, tsunami damage, sea level rise, and changing sediment patterns). The key focus areas will include northern Australia, Indonesia, South America, and west Africa. Figure 4 illustrates a potential application.

Tropical Peat Swamp Forests and Properties

Thick deposits of peat underneath peat swamp forests are among the world's largest reservoirs of carbon. Although they occupy only about 0.3% of the global land surface, they could contain as much as 20% of the global soil carbon stock. More than half of this area is located in Indonesia (MacDicken 2002, Rieley and Setiadi 1997). Peat systems appear fragile and sensitive to hydrological disturbance. Drainage through canalisation has frequently severely disrupted water table level dynamics,



Fig. 4 Conversion of coastal mangroves for firewood and aquaculture in Perak, Malaysia, as observed using a multi-annual time series of JERS-1 SAR data (R:1992; G:1995; B:1998). Clearings which occurred between 1992–1995 and 1995–1998 appear in green and blue, respectively, regenerating areas since 1992 in orange. Image reproduced from Rosenqvist et al. 2007. Image copyright JAXA/METI

causing the peat layers to dry out and trees to collapse over large areas. Besides resulting in CO₂ emissions due to oxidation this process makes them particularly vulnerable to fire, especially during ‘El-Niño’ years. In addition to their significance to the carbon cycle, peat swamps are particularly significant to the conservation and maintenance of species diversity. For example, of the 57 mammal and 237 bird species recorded in peat swamp forests to date, 51 and 27% respectively are listed as globally threatened species (Sebastian 2002). The relationship between spatial and temporal dynamics of peat swamp forest hydrology, carbon content and forest health needs further study. Such understanding would not only support the conservation of peat swamp forest, but also the rehabilitation of degraded peat areas, which may significantly reduce carbon emission and fire risk.

Temporal dynamics in flooding intensity can be related to the hydrology of ombrogenous peat swamp forests and, indirectly, to peat depth. The blue areas visible in the multi-temporal JERS-1 SAR image in Fig. 5-B (Mawas, Indonesia) are flooded parts of the relatively flat tops of a complex of two peat domes, with a river originating from a central depression (red spot). In the lower left corner a blue arch shows the relative flat and wet fringe of a dry peat dome.

In the humid tropical regions optical remote sensing systems largely fail because of persistent cloud cover. Conversely, spaceborne radar observation is not hindered by adverse atmospheric conditions (such as clouds, smoke and haze) and can be made frequently and repetitively, including during the wet season. Moreover, radar signals are sensitive to forest structure and biomass level (Hoekman and Quiñones

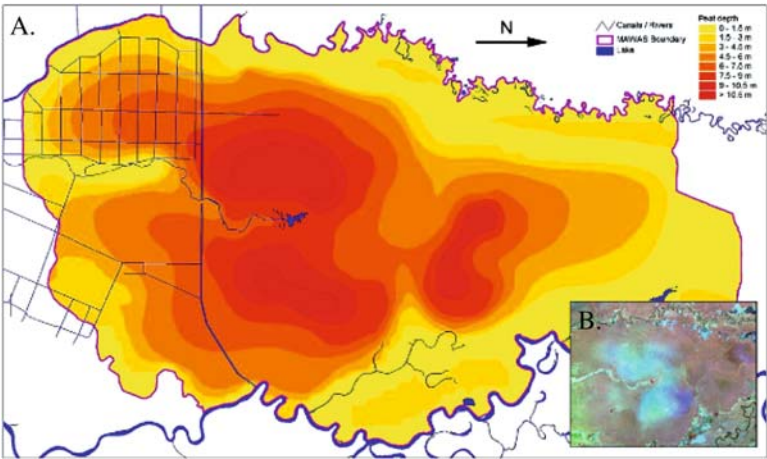


Fig. 5 A: Peat depth map derived from flooding dynamics, visible on JERS-1 time series, and peat depth sampling. In this 300,000 ha section of Mawas, Central Kalimantan, peat depth varies from 2–15 m. (Courtesy of D. Hoekman). B: JERS-1 Multi-temporal composite of a peat dome, Mawas, Central Kalimantan; (Red 940907; Green 950712; Blue 960104). (Image copyright JAXA/METI)

Table 3 Benefits of using ALOS PALSAR for mapping and monitoring peat swamp environments

| |
|--|
| All weather observation capability |
| High temporal capture – good for monitoring disturbance |
| Assessment of hydrological cycles |
| Ability to monitor biomass, and forest structure (and thus health/condition of wetlands) |
| Ability to assess susceptibility to forest fires |

2000, 2002, Le Toan 2002). This offers unique opportunities for applications such as peat swamp forest health and fire susceptibility monitoring as well as fast illegal logging response monitoring. The advantages of ALOS PALSAR for mapping and monitoring peat swamps are summarised in Table 3.

ALOS PALSAR will be used to produce maps of tropical peat swamp forests in Indonesia, focussing on the islands of Borneo, Sumatra and New Guinea, derived from a complete annual cycle of 8 consecutive PALSAR ScanSAR observations, showing location, vegetation type, inundation characteristics, degree of disturbance and estimated peat depth (Fig. 5). These will be used to assist with peat swamp forest management, protection, risk assessment (assessment of excessive drainage conditions), hydrological modelling, restoration, more accurate and updated assessment of carbon stocks.

Pan-Asian Mapping and Monitoring of Rice Paddies

Demand for rice in Asia is projected to increase by 70% over the next 30 years (IRRI 2002, Hossain 1997). At the same time, population increase and intensification of economic development will lead to significant land use conversion (e.g., Seto et al. 2000). Paddy rice cropland distributions and management intensity (fertilizer use, cultivars, water management, multi-cropping) will have to change over the coming decades. As water resources become scarcer (Vörösmarty et al. 2000), rapidly expanding urban areas will compete with agriculture for available water. In Asia, agriculture currently accounts for 86% of total annual water withdrawal (IRRI 2002). Urban demand for water will generally have greater financial and political resources than agricultural demand for water, and for some regions water availability to agriculture may decline significantly over the next few decades. Rising water costs will force all agriculture to improve its water-use efficiency. As this occurs, the practice of midseason draining of rice paddies, which requires less water than continual flooding, is likely to increase throughout many parts of Asia.

In order to assess regional rice production and methane emission in conjunction with in situ, climatic data and ecological modelling, a range of K&C products are being developed (Fig. 6). These include algorithms for regional mapping and

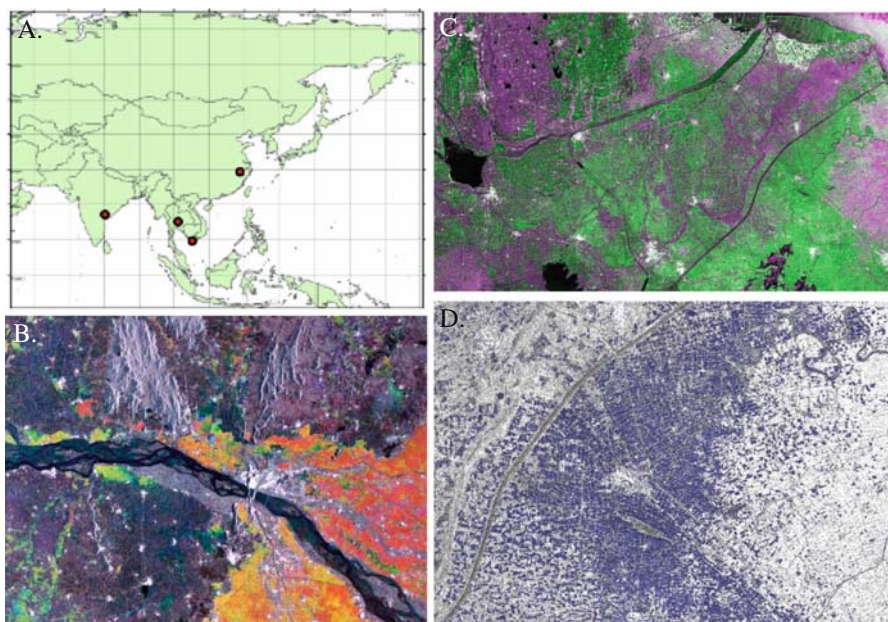


Fig. 6 **A** – Location of algorithm development sites in India, Thailand, Vietnam and China. **B** – Multi-temporal JERS data for mapping rice paddy extent and cropping cycles in Vijayawada, India. Map of early (*red* areas) and late (*orange*) Kharif rice. **C** – Mapping of regional irrigated paddy fields in the Jiangsu province, China, as exemplified by the results using multi-temporal ENVISAT ASAR WideSwath data. **D** – The paddy field map is based on the temporal change of the SAR backscatter. (Courtesy of B. Salas. Image copyright JAXA/METI)

monitoring of rice production with PALSAR Scansar; a regional map of irrigated paddy field (single crop and multiple crop per year) derived from multi-temporal PALSAR Scansar data; algorithms for mapping rice paddy inundation dynamics with multi-temporal PALSAR Scansar data; and maps of inundation periods will be developed using multi-temporal PALSAR Scansar data. The key areas for these products include China, India, Mainland South-East Asia, and Luzon Philippines.

Conclusions

In summary, L-band SAR systems are the single best option for fine spatial - resolution remote sensing of wetland extent and characteristics over large regions because they operate regardless of cloud cover, can distinguish basic vegetation structure, and provide superior canopy penetration and water surface discrimination relative to C-band. A dual-polarisation L-band system such as ALOS PALSAR will furthermore provide improved accuracy in discriminating between rough water surfaces and bare ground, and improved mapping of vegetation structural characteristics. The characteristics of the PALSAR sensor combine to provide products which can be utilised to assist with the assessment and monitoring of the diverse range of wetland environments found in the Asia-Pacific region.

References

- Bandaranayake WM (1994) Phyto-chemical constituents and pigments in mangrove species and mangal associates of Northern Australia. *Australian Institute of Marine Science (AIMS) Report* 19:1–21, AIMS, Townsville, Australia.
- Blasco F, Saenger P, and Janodet E (1996) Mangroves as indicators of coastal change. *Catena* 27:167–178.
- Chapin FS, Shaver GR, Giblin AE, Nadelhoffer KJ and Laundre JA (1995) Responses of arctic tundra to experimental and observed changes in climate. *Ecology* 76:694–711.
- Costa M (2004) Use of SAR satellites for mapping zonation of vegetation communities in the Amazon floodplain. *International Journal of Remote Sensing* 25(10):1817–1835.
- Costa M, Niemann O, Novo E, Ahern F, Mantovani J (2002). Biophysical Properties and mapping of aquatic vegetation during the hydrological cycle of the Amazon floodplain using JERS-1 and RADARSAT. *International Journal of Remote Sensing* 23(7):1401–1260
- Darras S, Michou M, Sarrat C (1999) *IGBP-DIS Wetland Data Initiative – A first step towards identifying a global delineation of wetlands*, IGBP-DIS Working Paper Number 19, France.
- Finlayson CM, D’Cruz R (2005) Millennium ecosystem assessment report on inland waters – in prep for publication end of March 2005 – Chapter 20 Inland Water Systems.
- Finlayson CM, Rea N (1999) Reasons for the loss and degradation of Australian wetlands. *Wetlands Ecology and Management* 7:1–11.
- Finlayson CM, van der Valk AG (1995) Classification and inventory of the world’s wetlands; a summary. In: Finlayson CM, van der Valk AG (eds.) *Classification and Inventory of the World’s Wetlands*, Advances in Vegetation Science 16, Kluwer Academic Press, Dordrecht, The Netherlands.
- Hess LL, Melack JM, Filoso S, Wang Y (1995). Delineation of inundated area and vegetation along the Amazon Floodplain with SIR-C synthetic aperture radar. *IEEE Transaction on Geoscience and Remote Sensing* 33(4):896–903.

- Hoekman DH, Quiñones MJ (2002) Biophysical forest type characterization in the Colombian Amazon by airborne polarimetric SAR. *IEEE Transactions on Geoscience and Remote Sensing* 40(6), 1288–1300.
- Hoekman DH, Quiñones MJ (2000) Land cover type and biomass classification using AirSAR data for evaluation of monitoring scenarios in the Colombian Amazon. *IEEE Transactions on Geoscience and Remote Sensing* 38(2):685–696.
- Hossain M (1997). Rice supply and demand in Asia: a socioeconomic and biophysical analysis. In Teng PS, Kropff MJ, ten Berge HFM, Dent JB, Lansigan FP, van Laar HH, (eds.) *Applications of Systems Approaches at the Farm and Regional Levels*. Academic Publ. Dordrecht, The Netherlands.
- IRRI (2002) Riceweb, <http://www.riceweb.org/>, produced by International Rice Research Institute (IRRI), West Africa Rice Development Association (WARDA), and Centro Internacional de Agricultura Tropical (CIAT).
- Le Toan T, Ribbes F, Wang L, Floury N, Ding K, Kong JA, Fujita M, Kurosu T (1997) Rice crop mapping and monitoring using ERS-1 data based on experiment and modeling results. *IEEE Transactions on Geoscience and Remote Sensing* 35:41–56.
- Lehner B, Döll P (2004) Development and validation of a global database of lakes, reservoirs and wetlands. *Journal of Hydrology* 296(1–4):1–22
- Lowry J, Finlayson CM (2004). *A Review of Spatial Datasets for Wetland Inventory in Northern Australia*. Supervising Scientist Report 178, Supervising Scientist, Darwin NT.
- MacDicken KG (2002) Cash for tropical peat: land use change and forestry projects for climate change mitigation. In: Rieley JO, Page SE, Setiadi B (eds.) *Peatlands for people: natural resource functions and sustainable management*. Proceedings of the International Symposium on Tropical Peatland, 22–23 August 2001, Jakarta, Indonesia. BPPT and Indonesian Peat association, 272 pp.
- Matthews E, Fung I (1987). Methane emission from natural wetlands: global distribution, area, and environmental characteristics of sources. *Global Biochemical Cycles* 1:61–86.
- Phinn S, Hess L, Finlayson CM (1999). An assessment of the usefulness of remote sensing for wetland monitoring and inventory in Australia. In: Finlayson CM, Spiers AG (eds.) *Techniques for Enhanced Wetland Inventory, Assessment and Monitoring*. Supervising Scientist Report 147, Supervising Scientist Group, Canberra, pp 44–82.
- Rieley JO, Setiadi B (1997) Role of tropical peatlands in the global carbon balance: preliminary findings from the high peats of Central Kalimantan, Indonesia. *Alami* 2(1):52–56.
- Rosenqvist A, Lucas R, Lowry J, Hess L, Chapman B, Paillou P, Shimada M. (eds.) (2008) *The ALOS Kyoto & Carbon Initiative, Science Plan v.3.1. Japan Aerospace Exploration Agency, Earth Observation Research Center*. (http://www.eorc.jaxa.jp/ALOS/kyoto/KC-Science-Plan_v3.1.pdf).
- Rosenqvist A, Finlayson M, Lowry J, Taylor D (2007) The potential of long wavelength satellite borne radar to support implementation of the Ramsar Wetlands Convention. *Journal of Aquatic Conservation; Marine and Freshwater Ecosystems* 17: 229–244.
- Rosenqvist A, Milne T, Lucas R, Imhoff M, Dobson C (2003). A review of remote sensing technology in support of the Kyoto Protocol. *Environmental Science & Policy* 6(5): 441–455.
- Saenger PE (1994). Mangroves and Saltmarshes. In: Hammond L, Synnot RN (eds.) *Marine Biology*. Addison Wesley Longman, Australia.
- Sahagian D, Melack J (eds.) (1996). Global Wetland Distribution and functional Characterization: Trace Gases and the Hydrologic Cycle. Report from the Joint IGBP-GAIM-DIS-BAHC-IGAC-LUCC wetlands workshop, Santa Barbara, USA, May 1996. IGBP/GAIM, University of New Hampshire, USA.
- Sebastian A (2002) Globally threatened mammal and bird species in Malayan peat swamp forests. In: Rieley JO, Page SE, Setiadi B (eds.) *Peatlands for people: natural resource functions and sustainable & management*. Proceedings of the International Symposium on Tropical Peatland, 22–23 August 2001, Jakarta, Indonesia. BPPT and Indonesian Peat association, 272 pp.

- Seto KC, Kaufman RK, Woodcock CE (2000) Landsat reveals China's farmland reserves, but they're vanishing fast. *Nature* 406:121.
- Shaver GR, Nadelhoffer KJ, Giblin AE (1990) Biogeochemical diversity and element transport in a heterogeneous landscape, the North Slope of Alaska. In: Turner MG, Gardner RH (eds.) *Quantitative Methods in Landscape Ecology*. Springer, Berlin, Heidelberg, New York, pp. 105–126.
- Spalding MDF, Blasco, F and Field CD. (eds) (1997) World Mangrove Atlas. International Society for Mangrove Ecosystems. Okinawa (Japan) 903-01: 178 pp.
- Vörösmarty CJ, Green P, Salisbury J, Lammers R (2000). Global water resources: Vulnerability from climate change and population growth. *Science* 289:284–288.
- Weller G, Holmgren B (1993) The microclimates of the Arctic tundra. *Journal of Applied Meteorology* 13:854–862.

Testing of Alternate Classification Procedures Within an Operational, Satellite Based, Forest Monitoring System

Jared O'Connell and Peter Caccetta

Abstract In Australia, continental mapping and monitoring of the extent and change in perennial vegetation using Landsat satellite imagery is routinely performed as part of the National Carbon Accounting System - Land Cover Change Project (NCAS-LCCP). Since its original inception, the methods within the operational LCCP system have been progressively developed by the CSIRO Mathematical and Information Sciences division in collaboration with the Australian Greenhouse Office (AGO). Under a framework of contracts and Quality Assurance (QA) procedures, commercial companies apply these methods to the growing archive of Landsat images to produce time-series continental coverages of the presence and absence of perennial vegetation cover at a pixel resolution of 25 m. The raw data archive currently consists of approximately 5000 Landsat images having an approximate data volume of 2×10^{12} bytes (2 terabytes), which is transformed into information products having similar data volumes. Given the above operating environment, accuracy, interpretability (for outsourcing and QA), computational efficiency, the ability to incorporate 'better' algorithms, and reliability when applied through space and time, are important aspects for consideration during methodology development. In this paper, we examine the potential benefits and costs associated with using several popular classification techniques within (as subcomponents) the operational classifier. Our key criteria for benefit/cost comparisons are classification accuracy versus computational requirements and interpretability. Our main findings are: that the current operational subcomponent is within 2.5% on average of the benchmark (the classification obtained with the most sophisticated technique used); adopting the benchmark may allow the earlier identification of new plantations, at the expense of an order of magnitude computation; the choice of method for the subcomponent has less effect than choices made elsewhere in the process.

J. O'Connell (✉)

CSIRO Mathematical & Information Sciences, Wembley, WA 6913, Australia
e-mail: jared.oconnell@csiro.au

Background

In Australia, time-series remotely sensed Landsat TM data is routinely used for mapping and monitoring the change in extent of woody perennial vegetation. The satellite imagery and ground information is used to form multi-temporal classifications of presence/absence of woody cover, typically for state-based management and reporting of clearing. More recently, there has been increased interest from land use changes associated with agriculture and forestry which are a significant component of Australia's carbon budget. To quantify the amount, the NCAS-LCCP has developed the capability for continental monitoring of land cover changes using Landsat data. The project uses some 5000 Landsat MSS, TM and ETM+ images to map the presence/absence of perennial vegetation at 25 m resolution for fifteen time periods since 1972, and is being expanded to quantify the extent and changes in other land cover classes such as sparse perennial and urban environments.

For monitoring of forest presence/absence, the current operational system includes the following components:

1. registration of time-series Landsat data to a common spatial reference,
2. calibration of Landsat data to a common spectral reference,
3. (if required) processing of the calibrated data to adjust for viewing geometry including differential terrain illumination,
4. stratification of the data into 'zones', where landcover types within a zone have similar spectral properties,
5. processing of the calibrated data to remove 'corrupted' data, which include dropouts, data affected by fire, smoke and cloud,
6. analysis of ground and satellite spectral data to determine a single-date classifier and its parameters,
7. specification of a joint model for multi-temporal classification
8. validation of the classifications to quantify their accuracy.

In this paper, we compare the operational classifier used in step 6 (described in section, referred to as 'Matching, Random Forests and Other Classifiers') to several popular techniques; Random Forests (RF), CART (Breiman et al., 1984), Linear Discriminant Analysis (LDA) (Ripley, 1996) and logistic regression (LR) (McCullagh and Nelder, 1983). R (R Development Core Team, 2004) implementations of each classifier (excluding Matching) were used. Random Forests is considered a 'state of the art' classifier, on a par with other techniques such as Neural Networks and Support Vector Machines (SVM) (Breiman, 2001). We view the classification accuracy obtained from Random Forests as an upper bound on the accuracies possible in step 6, a benchmark to compare other methods to. We consider the difference between this upper bound and our current technique as a guide for possible benefit (improved classification accuracy) versus costs (computational requirements, interpretability) associated with more sophisticated classification methods.

In the section 'Methodology', we give a description of our current single date classifier for estimating land-cover change as well as a brief overview of the Random

Forests algorithm, the data analysed and our rationale for comparison. In section ‘Results’ we present comparisons of single date classifications and also their effect on accuracy when incorporated into the spatial-temporal model from step 8. Section ‘Discussion and Conclusion’ provides some discussion and possible further work in this area.

Methodology

Matching, Random Forests and Other Classifiers

The operational classifier (Fig. 1, left) used in step 6 is constructed in two steps;

1. the derivation of linear combinations of spectral bands, ‘indices’, that give the ‘best’ separation of classes using Canonical Variate Analysis (Campbell and Atchley, 1981). Typically two or three indices are used.
2. specification of decision boundaries (thresholds) on these indices to map the spectral space into classes (here forest or non-forest)

Following (Caccetta and Bryant, 2002), we assume a reference or ‘base’ image is already available to be used as our response variable. Given a new image to classify, we estimate thresholds by minimising the objective function,

$$\sum_{i=1}^n |\hat{p}_i - p_i|$$

where p_i are the class probabilities for pixel i from the base image and \hat{p}_i are the estimated probabilities for the new image. This function is minimised using the Simplex

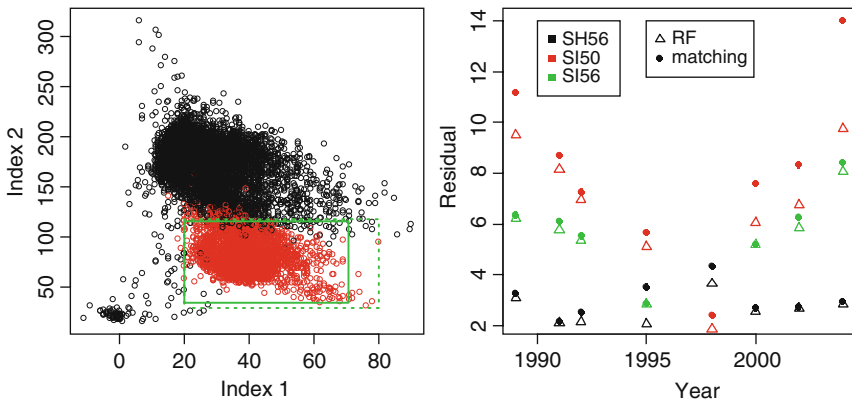


Fig. 1 *Left.* A typical ‘matching’ example. Certain (*solid*) and uncertain (*dashed*) boundaries applied to two linear thresholds. *Right.* Comparison of residuals for RF and Matching. *Black* is SH56, *red* is SI50 and *green* is SI56. *Circles* are Matching results and *triangles* are RF. RF generally outperforms Matching by a small amount

algorithm (Nelder and Mead, 1965). The nature of this model is conducive to manual fine tuning, a user can simply adjust the thresholds in the case of a poor fitting model. Poor fits do occur operationally with some frequency. There were several reasons why this relatively simple classifier was chosen for operational work;

- Initial pilot studies demonstrated that forest/non-forest classes were typically separable using two or three linear discriminants (Wallace and Furby, 1994).
- The nature of the classifier allows for manual intervention in the fitting of models (via image processing software).
- The simplicity of the classifier meant we were confident in its ability to extrapolate well.
- Computational issues, a typical training region may be of the order of $2000 \times 2000 = 4,000,000$ observations (pixels) and it is useful in an operational setting to perform classification on desktop PC's.

We compared Matching with Random Forests, a tree ensemble classifier which we describe briefly. Many decision trees are grown, each tree 'votes' for a class, the class with the majority vote is the predicted value. Each tree is grown using a bootstrap sample with a random selection of predictor variables used to choose a split at each node. The primary advantages of using Random Forests over other sophisticated classifiers are that they can handle large data sets and require minimal fine tuning, which are both beneficial for this application. We briefly examine the performance of some older but popular classifiers; LDA, and logistic regression and CART. These techniques have similar computational requirements to Matching.

Data

Temporal sequences (between 1989 and 2004) of Landsat 5 and 7 satellite imagery processed up to and including step 3 were analysed. For each map-sheet, the 'base' images used as responses were output from spatial-temporal models (used in previous AGO work) which are more accurate than single-date classifications. Three training sites (from the standard AUSLIG 1:1,000,000 mapsheets) were selected to compare the performance of the classifiers described in the previous section;

1. SI50 (SW Western Australia) presents a challenge for several reasons, the region has seen a large amount of change in forest cover (largely increased cover as the result of tree planting), atmospheric haze resulting in increased calibration error and green flushes in some summer scenes.
2. SH56 (NE New South Wales) is generally considered a difficult area to classify due to the presence of dark soils. Vegetation in this area is relatively static.
3. SI56 (SE New South Wales) is difficult to analyse for similar reasons to SH56 and also has static vegetation.

The size of the training regions had to be limited to allow testing in R, specifically for $n > 1,000,000$ it was difficult to fit a reasonable number of trees with RF.

Comparison Rationale

Probability images were briefly viewed to ensure the output was reasonable. We then thoroughly examined years where there was a large difference in misclassification rates between the classifiers. We also look at a measure of similarity between two classified images, calculating the proportion of pixels assigned a different class for a given year. This was performed because it is conceivable (although unlikely) that two different classifiers achieve similar residuals but these residuals occur on a very different set of pixels.

Due to the differing dates of the base image and our new image, the residual differences are comprised of both genuine error (misclassification) and real change in vegetation. For this reason, the values of residuals alone are not always a sufficient measure to judge which classifier is more accurate. However, we consider the vegetation SH56 and SI56 to be largely static, in which case residuals are likely to be a sufficient measure of classifier performance. SI50 was examined since we wish to assess the ability of a classifier to track change, but because of this, change residuals need to be regarded cautiously.

Results

Single Date Classification

The results for areas 1, 2 and 3 are summarised in Tables 1, 2 and 3 respectively. The majority of the time, Matching outperformed CART, LDA and logistic regression

Table 1 Summary of residual differences for SH56 NW, Zone 4

| Method | Year | | | | | | | | Mean |
|----------|------|------|------|------|------|------|------|------|------|
| | 1989 | 1991 | 1992 | 1995 | 1998 | 2000 | 2002 | 2004 | |
| LR | 3.51 | 2.24 | 2.36 | 2.86 | 4.13 | 2.75 | 2.78 | 3.17 | 2.97 |
| LDA | 4.93 | 3.24 | 3.56 | 4.15 | 4.75 | 3.07 | 3.65 | 4.09 | 3.93 |
| CART | 3.34 | 2.54 | 2.88 | 3.05 | 4.1 | 3.01 | 3.23 | 3.6 | 3.22 |
| Matching | 3.27 | 2.16 | 2.53 | 3.52 | 4.34 | 2.7 | 2.74 | 2.95 | 3.02 |
| RF | 3.12 | 2.13 | 2.16 | 2.07 | 3.66 | 2.56 | 2.69 | 2.84 | 2.65 |

Table 2 Summary of residual differences for SI56 SW, Zone 4

| | Year | | | | | | | |
|----------|------|------|------|------|------|------|------|------|
| Method | 1989 | 1991 | 1992 | 1995 | 2000 | 2002 | 2004 | Mean |
| LR | 6.63 | 6.23 | 6.15 | 3.44 | 5.76 | 6.33 | 9.16 | 6.24 |
| LDA | 6.47 | 6.04 | 5.79 | 3.58 | 5.73 | 6.64 | 8.53 | 6.11 |
| CART | 7.6 | 7.33 | 6.09 | 3.68 | 6.22 | 6.75 | 9.89 | 6.8 |
| Matching | 6.36 | 6.11 | 5.54 | 2.8 | 5.21 | 6.29 | 8.39 | 5.82 |
| RF | 6.21 | 5.78 | 5.34 | 2.87 | 5.2 | 5.84 | 8.07 | 5.62 |

Table 3 Summary of residual differences for SI50SE, Zone 11

| Method | Year | | | | | | | | Mean |
|----------|-------|-------|------|------|------|------|------|-------|------|
| | 1989 | 1991 | 1992 | 1995 | 1998 | 2000 | 2002 | 2004 | |
| LR | 11.23 | 10.33 | 9.18 | 7.24 | 5.18 | 9.33 | 11.1 | 15.5 | 9.89 |
| LDA | 10.97 | 10.35 | 8.71 | 7.56 | 4.37 | 8.41 | 9.48 | 14.06 | 9.24 |
| CART | 10.25 | 8.94 | 7.4 | 5.8 | 2.69 | 7.99 | 8.48 | 14.46 | 8.25 |
| Matching | 11.15 | 8.71 | 7.26 | 5.64 | 2.4 | 7.58 | 8.32 | 14 | 8.13 |
| RF | 9.49 | 8.16 | 6.95 | 5.1 | 1.87 | 6.04 | 6.77 | 9.74 | 6.77 |

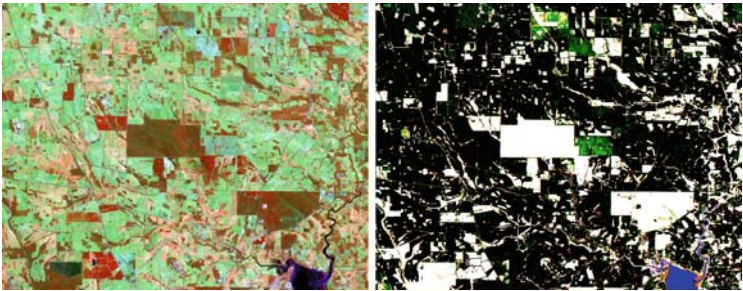


Fig. 2 *Left:* SI50 2000, Bands 4,5,2 (in RGB). *Right:* Comparison of RF (*green*), Matching (*red*) and LR (*blue*). RF has identified some early plantations (beneficial) and logistic regression has classified a large body of water as forest vegetation (a serious commission error)

(Tables 1, 2, 3). When one of these classifiers did outperform Matching, it was by a small margin. In addition, the errors committed by the linear classifiers were serious (and systematic) as can be seen in Fig. 2. For this reason we did not go into any further analysis of these classifiers and focus on the differences between Matching and RF. We can see in Fig. 1 (right) that Random Forests consistently achieved lower residuals than our operational classifier with one exception, Matching did slightly better for SI56 in 1995. The classifiers typically only differ by a small margin, particularly for the SH56 and SI56 map-sheets (Fig. 1, right). For these two map-sheets, large differences were only observed in the presence of a scene boundaries (Fig. 8) or haze (Fig. 3), which represent atypical data. In operational circumstances, different scenes are assigned different strata and smoke/haze covered areas are masked. So RF was capable of adjusting to data that should have been stratified or removed (when using Matching). This could be useful in regions where haze is persistently present or where manual stratification is not a practical option.

The residuals for the SI50 scene were generally higher than the other test areas due to the large amount of real change in this region (primarily new plantations). Some very large disparities between RF and Matching were observed here. In particular, for the years 2000, 2002 and 2004, RF achieved a much closer match to the base (Table 3). On inspection, we observed that RF had failed to identify much of the new growth from plantations in these years (Fig. 4) meaning RF had performed worse than Matching. We believe that this was due to the different spectral signature of the new growth and the fact that all of this growth was labelled as ‘non-forest’ in

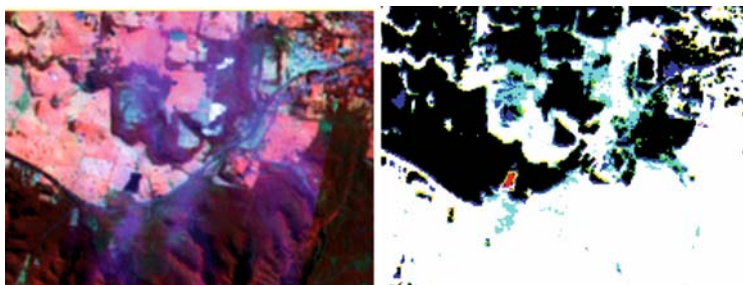


Fig. 3 *Left:* SH56 1995, Bands 4,5,2 (in RGB). *Right:* Comparison of Random Forests (*green*) and Matching (*red*). Random Forests can handle the scene boundary while our simpler classifier cannot

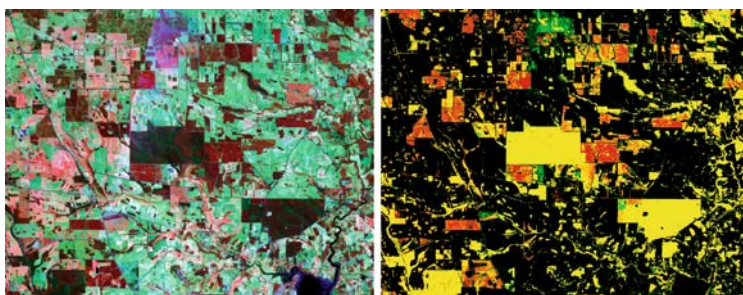


Fig. 4 *Left:* SI50SE 2004, Bands 4,5,2 (in RGB). *Right:* Comparison of Random Forests (*green*) and Matching (*red*). Compared to matching, RF does poorly at identifying new growth. Matching seems unaffected by the presence of a scene boundary in this example

our base probability image. So this was not a case of over-fitting in the conventional sense, there was genuine discrimination between new and old growth. This highlights one of the major challenges in classifying this data, there are systematically mislabelled observations. It should be noted that while Matching did outperform RF, the Matching results for 2000 and 2002 would still have been unacceptable operationally. For example, we can see in Fig. 5 that matching has also failed to classify some new growth.

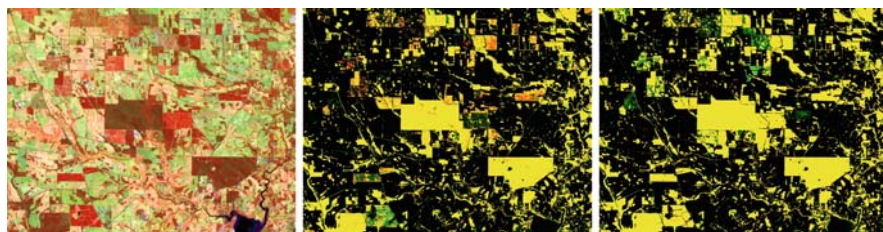


Fig. 5 *Left:* SI50SE 2002, Bands 4,5,2 (in RGB). *Centre:* Comparison of Random Forests (*green*) and Matching (*red*) using a 1998 base; both classifiers have failed to identify new growth but in different locations. *Right:* Results when using a 2004 (propagating) base. Results for the propagating base were preferable for both classifiers

Table 4 SI50 classification differences when propagating the base image backwards through time

| Year | 1989 | 1991 | 1992 | 1995 | 1998 | 2000 | 2002 | 2004 | Mean |
|-------------|------|------|------|------|------|------|------|------|------|
| M=1, RF=0 | 2.35 | 0.78 | 0.43 | 0.58 | 0.62 | 1.36 | 0.56 | 1.14 | 0.98 |
| M=0, RF=1 | 2.53 | 0.86 | 0.54 | 1.25 | 1.48 | 2.07 | 1.71 | 1.69 | 1.52 |
| % different | 4.88 | 1.65 | 0.97 | 1.84 | 2.1 | 3.43 | 2.27 | 2.83 | 2.5 |

Effect of Altering Base Image

While Matching did perform significantly better than RF for the years 2000, 2002 and 2004, both classifiers produced results for 2000 and 2002 that would have been unacceptable operationally (Fig. 5, centre). To circumvent this problem in practice, an operator would have set the thresholds manually or perhaps considered a different year to use as the base. To compare the two algorithms, we took the latter approach.

Several different choices of base year image were informally compared. It is not possible to generate a quantitative measure for which base image was ‘best’, but a trained operator can make a reasonable judgement on whether a classification accurately represents the real land cover. Better results (as measured by human judgement) were achieved by using a 2004 probability image as a response for 2002 data and then propagating the predicted classes as responses backwards through the time-steps.

The results for both Matching and RF were better than those which used a static (1998) base as can be seen in Fig. 5 (right). However we could no longer directly compare the misclassification rates for each technique as we were using different responses (except for 2002). Instead, we look at the number of pixels assigned a different class by each method for each year (Table 4).

The results in Table 4 indicate that RF tended to classify a greater number of pixels as ‘Forest’ compared to Matching. This was not surprising since the majority of vegetation change in this region is due to new plantations (increase in forest cover) and RF was capable of classifying these plantations at earlier stages, examples such as the one shown in Fig. 6 were typical. When the new plantations were present in

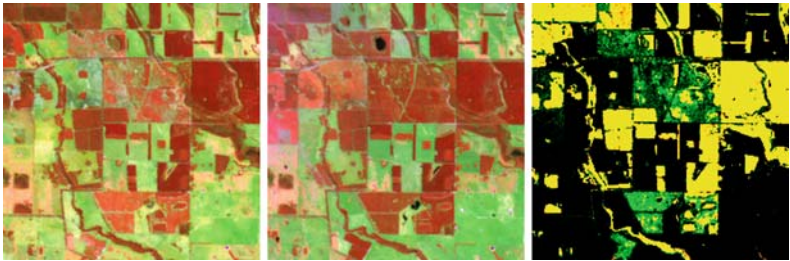


Fig. 6 Left: SI50 2002. Centre: SI50 2004, Bands 4,5,2 (in RGB). Right: Comparison of Random Forests (green) and Matching (red) for 2002. RF was capable of identifying the early stages of new growth

the response, RF accurately classified this new spectral class while Matching did not. When using the propagating base technique, the results from RF were consistently better than those from Matching, albeit marginally. This was mainly due to the ability of RF to classify plantations at earlier stages.

Effect of Classifier on Results After Spatial-Temporal Processing (Step 8)

The use of spatial-temporal models greatly increases the accuracy of land-cover estimates when a time-series of images is available (Caccetta, 1997). In operational circumstances, we first classify images from each year independently and then apply a spatial-temporal model to improve accuracy. While we are interested in improving single-date classification, from an operational perspective, it is also of interest to assess the difference in accuracy after spatial-temporal processing. We test this by applying a spatial-temporal model to the single-date classifications described in the previous section. We face a similar situation to the SI50 classifications with a propagating base here, in that classifications do not share a common response so no reasonable measurement of error can be obtained to compare the two classifiers. Although we do know that change in SH56 and SI56 should be close to zero and there should be significant change in SI50 in some years.

For the purposes of carbon accounting, identification of landcover change is the goal, so we compare the estimates of change from each classifier here. We can see in Figs. 7 and 8 that spatial-temporal processing consistently reduces the estimated land-cover change, this is due to the removal of false change. While the amount of change estimated by each classifier varies somewhat, the trends are very similar. Random Forest change estimates are reduced by a larger amount by the spatial-temporal model suggesting RF has slightly less consistency than matching. Random Forests estimates slightly less change for SI56 and SH56, these images have little, if any, change so RF has performed marginally better.

A good example of spatial-temporal modelling's worth can be seen from the SH56 data. A scene boundary was present in 1995 (Fig. 8), causing a large amount of commission in Matching, this also occurred in RF to a lesser extent. The large spike in the Fig. 9 change graph is false change caused by this scene boundary. Spatial temporal modelling has removed most of this error and the classifiers were in far greater agreement after this process. This was also quite clear from the probability image. (Fig. 8). While this was an extreme case that would not occur operationally, it does demonstrate the spatial-temporal model's ability to remove errors in single date classifications.

Discussion and Conclusion

Matching generally compared favourably with RF, with both classifiers achieving similar results for the majority of data tested. There were some notable exceptions, where RF could operate accurately for atypical data such as haze or early growth,

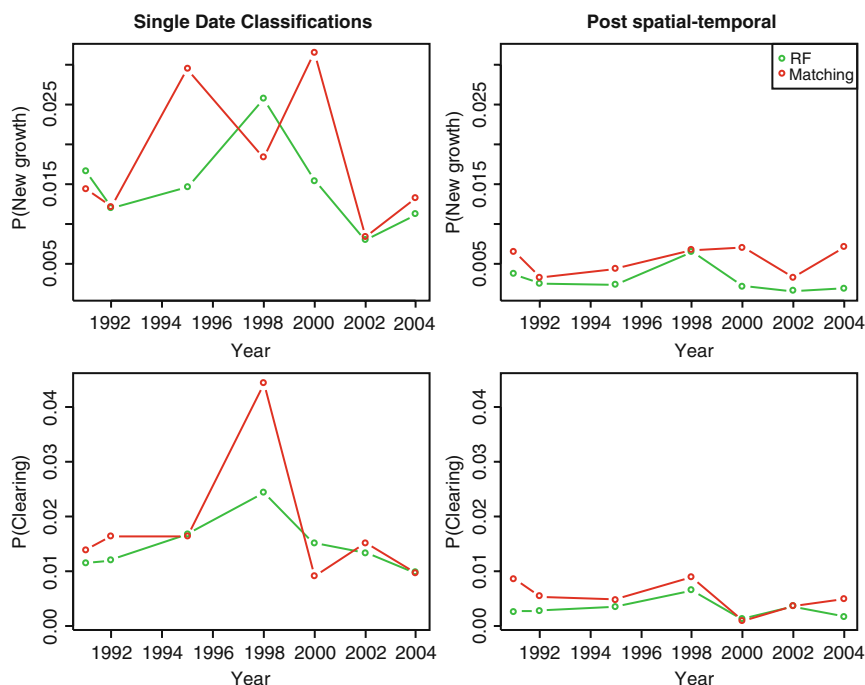


Fig. 7 Comparison of estimated change for the SI50 mapsheet

and was inaccurate when a poor ‘base image’ was chosen, while Matching was somewhat more robust. Indeed, it was found that the choice of base image was far more influential on estimates than the choice of classifier.

We face some difficult challenges with data of this nature. An obvious problem is size, few classification techniques are aimed at data sets where $n > 1,000,000$, this is largely an implementational issue. Another (more difficult) challenge is the nature of our response variable, when change occurs, we have mislabelled pixels in our response. If these mislabelled observations were randomly distributed throughout the data, this would not be a serious issue. Unfortunately, as was seen in the later years for the SI50 mapsheet, this is not the case. The new growth was spectrally different to older growth and this caused problems for RF and Matching. However, Matching was more robust to this problem than RF and this speaks strongly for parsimony in modelling. In the SI50 example, this difficulty was circumvented via the propagation of the base image. The most interesting results were from the SI50 example, due to the large amount of land cover change in this area. In the SI56 and SH56 map-sheets, where vegetation is relatively static, only relatively small differences between the classifiers were observed (disregarding examples with smoke/cloud or scene boundaries) and while RF performed better here, it did not yield any massive improvements in accuracy. The SI50 example revealed both the advantages and disadvantages of using RF classifier instead of Matching.

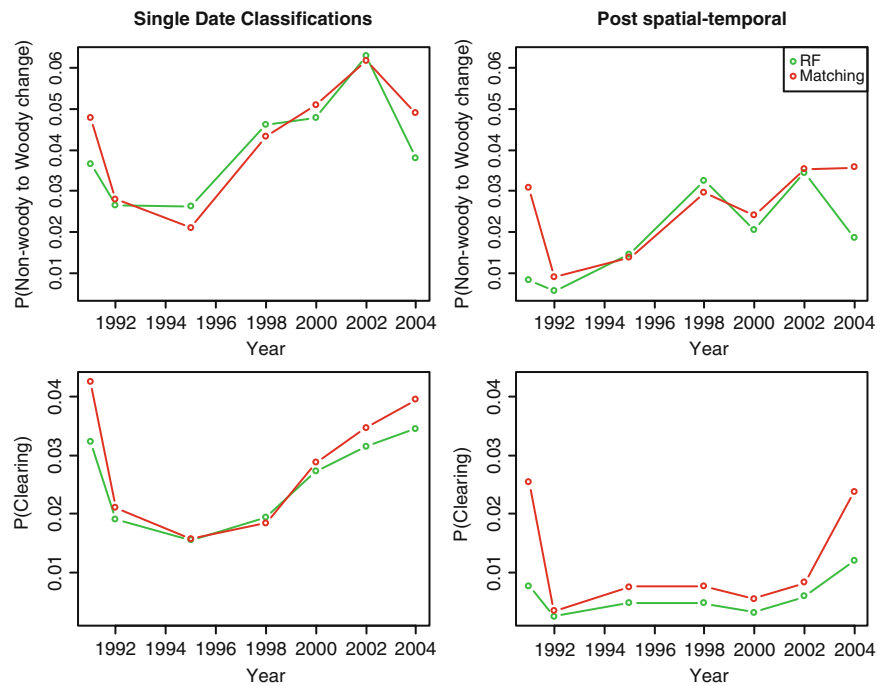


Fig. 8 *Left:* SH56 1995, Bands 4,5,2 (in RGB). *Centre:* Comparison of Random Forests (green) and Matching (red) for single data classifications. *Right:* Classification comparison post spatial temporal processing. The spatial-temporal model has improved the inconsistent scene boundary for the Matching classification

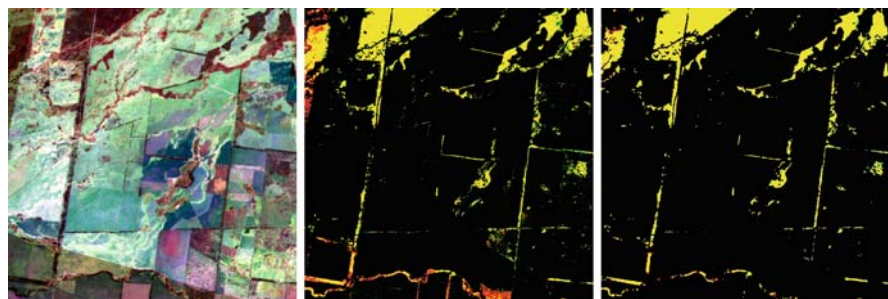


Fig. 9 Comparison of estimated change for the SH56 map-sheet

- The cases where RF was performed better were;
1. the identification of plantations in early stages of growth (when a later base image is available)
 2. accurate classification in the presence of haze or smoke
 3. accurate classification in the presence of a scene boundary (this is largely a superficial benefit, as it would be avoided in operational circumstances)

The benefits of Matching were;

1. computationally cheap (an order of magnitude less than RF)
2. more robust to large amounts of change (but not immune)
3. models can be fitted manually using standard image processing software (interpretability)

If we take our final estimates of land-cover using Random Forests to be our 'optimal' benchmark, then our current Matching methodology was (at worst) within 2.5% of optimal in all cases (typically much less). In reality, some of the differences in classification cannot be reliably identified as correct or incorrect. Our operational classifier compares favorably with Random Forests, a technique that is generally considered state of the art.

References

- Breiman, L., 2001. Random forests. *Machine Learning* 45(1), 5–32.
- Breiman, L., Friedman, J. H., Olshen, R. A. and Stone, C. J., 1984. *Classification and Regression Trees*. Wadsworth Statistics/Probability Series, Wadsworth Advanced Books and Software, Belmont, CA.
- Caccetta, P. A., 1997. *Remote Sensing, GIS and Bayesian Knowledge-Based Methods for Monitoring Land Condition*. PhD thesis, School of Computing, Curtin University of Technology.
- Caccetta, P. and Bryant, G., 2002. Notes on the Automatic Determination of Index Thresholds for Classification of Perennial Vegetation Change. Technical Report 247, CSIRO Mathematical & Information Sciences.
- Campbell, N. and Atchley, W., 1981. The geometry of canonical variate analysis. *Systematic Zoology* 30(3), 268–280.
- McCullagh, P. and Nelder, J. A., 1983. *Generalized linear models*. Monographs on Statistics and Applied Probability, Chapman & Hall, London.
- Nelder, J. A. and Mead, R., 1965. A simplex algorithm for function minimization. *Computer Journal* 7, 308–313.
- R Development Core Team, 2004. *R: A language and environment for statistical computing*. R Foundation for Statistical Computing, Vienna, Austria. ISBN 3-900051-00-3.
- Ripley, B. D., 1996. *Pattern Recognition and Neural Networks*. Cambridge University Press, Cambridge.
- Wallace, J. and Furby, S., 1994. Assessment of change in remnant vegetation area and condition. Technical report, CSIRO Division of Mathematical and Information Sciences.

An Investigation of the Remote Sensing of Aerosols Based on MODIS Data for Western Australian Conditions

Mark Broomhall, Brendon McAtee, and Stefan Maier

Abstract Landgate Satellite Remote Sensing Services (SRSS) operates a MODerate resolution Imaging Spectroradiometer (MODIS) direct broadcast read-out producing surface reflectance in near real-time using atmospheric correction from the Simple Method for Atmospheric Correction (SMAC) code using a single fixed value for Aerosol Optical Depth (AOD). The project which inspired this paper aims to retrieve AOD for inclusion in the SMAC process, replacing the single, static AOD value with spatially and temporally dynamic AOD input. Three methods of AOD retrieval will be investigated for accuracy and suitability for the surface conditions found in Western Australia. Two of these methods are NASA produced institutional algorithms, denoted MOD04 and MOD09, and the final method is under development by SRSS and Curtin University.

The first two methods are used within MODIS institutional algorithms developed by NASA for global applications. The MOD04 and MOD09 algorithms use an empirical relationship based on surface reflectance in the near infrared to infer surface reflectance for blue and red wavelengths which leads to the production of AOD and aerosol properties. The third method is being developed in house by SRSS and Curtin University and is driven by a reflectance change determination based on time-series Bidirectional Reflectance Function (BRF) data. This compares the most current SMAC corrected observation with a predicted surface reflectance derived from the BRDF time-series. The difference or change between the two reflectance values can then be attributed to a change in the atmospheric aerosol.

The AOD output from the MODIS institutional algorithms is compared to in-situ Western Australian sun photometer data to ascertain the accuracy of the retrieval methods. The suitability of these algorithms for use in the Near Real-Time (NRT) atmospheric correction process can be determined from an examination of the spatial coverage of the algorithm output. The reflectance change method will in future

M. Broomhall (✉)

Remote Sensing and Satellite Research Group, Department of Applied Physics, Curtin University of Technology, Bentley, WA, Australia 6102
e-mail: M.broomhall@curtin.edu.au

be investigated for suitability through radiative transfer modelling and sensitivity analysis.

These results will be presented and their implication for NRT atmospheric correction will be discussed.

Introduction

The accurate measurement of atmospheric aerosol is important for (i) the study of the radiative forcing of the atmosphere where aerosols have a net cooling effect (Kaufman and Tanre, 1998), and (ii) atmospheric correction to produce surface reflectance products (Liang et al., 2006). The project which inspired this paper aims to improve the current retrieval methods for aerosol data over Australia for use in an atmospheric correction process. The MODerate resolution Imaging Spectroradiometer (MODIS) instrument on-board the Terra and Aqua satellites is an ideal platform for daily monitoring of atmospheric and surface parameters on a global scale, with some locations having up to four overpasses per day during daylight hours. There are two institutional algorithms employed by NASA which retrieve aerosol properties, designated MOD04 and MOD09. MOD04-derived aerosol products are used principally for the study of aerosol radiative forcing, aerosol transport and for the development of aerosol climatology (Remer et al., 2005). MOD04 is also designed to retrieve aerosol products over both land and the ocean. MOD09 is principally designed to retrieve land surface reflectance. This algorithm retrieves aerosol information as part of the atmospheric correction process where MODIS Bottom of Atmosphere (BOA) reflectances are derived from Top of Atmosphere (TOA) radiance values (Vermote and Vermeulen, 1999). Both algorithms use band ratio techniques to derive surface reflectance in visible bands. This technique is referred to as the 'dark target' approach and makes use of the low surface reflectance of dense dark vegetation so that surface and atmospheric reflectance signals can be separated. In the MOD04 and MOD09 algorithms, this technique has been extended to include brighter surfaces to improve the spatial coverage. This study will investigate the success of the MODIS institutional algorithms in areas where there is little or no dense dark vegetation and the surface reflectance is considered to be high. It will concentrate on Western Australia in general and specifically on our test site in Merredin, approximately 270 km east of the Western Australian capital city, Perth.

This paper will also discuss a possible new method of separating the surface and atmospheric signals using a reflectance change process based on time-series BRF information.

MOD04 and MOD09 Aerosol Retrieval Algorithms

Atmospheric correction of satellite data is based largely on radiative transfer modelling, either directly or by the use of pre-computed look-up tables. Radiative transfer modelling is based on a radiative transfer equation which describes the

path and interaction of solar radiation from the sun, through the atmosphere to the surface, and from the surface back through the atmosphere, before finally being received by a satellite based sensor. This type of equation can be used to retrieve information about any part of the radiative transfer process provided information is obtained for the other parts of the process. The radiative transfer equation for a Lambertian surface can be expressed as (Vermote et al., 1997);

$$\rho_{TOA}(\theta_s, \theta_v, \phi_s - \phi_v) = T_g(\theta_s, \theta_v) \left[\rho_{R+A} + T_{\downarrow}(\theta_s) T_{\uparrow}(\theta_v) \frac{\rho_{sur}}{1 - S \rho_{sur}} \right] \quad (1)$$

where ρ_{TOA} and ρ_{R+A} are the sensor perceived and atmospheric path equivalent reflectances respectively. Equivalent reflectance is given by, $\rho = \pi L / \mu_s E_s$, with L being the measured radiance, E_s is the solar flux above the atmosphere, and $\mu_s = \cos(\theta_s)$, where θ_s is the solar zenith angle. Of the other angles, θ_v refers to the satellite view angle, and $\phi_s - \phi_v$ is the relative azimuth between the satellite and the sun. The surface reflectance is represented by ρ_{sur} , S is the spherical albedo of the atmosphere, $T_{\downarrow}, T_{\uparrow}$ are the total transmission of the atmosphere from the sun to the surface and from the surface to the sun, and T_g is the gaseous transmission.

ρ_{R+A} is the equivalent reflectance due to the path radiance. This is the signal that would be received at the satellite if the surface had a reflectance of 0. This signal is due to Rayleigh scattering (ρ_R) which is almost totally a result of gaseous molecules in the atmosphere, and Mie scattering, which is caused mainly by aerosols (ρ_A).

In order to retrieve the signal due to atmospheric aerosols, all other parts of the radiative transfer equation must somehow be determined. It is possible to determine almost all of the radiative components from atmospheric data such as pressure, water vapour content and ozone concentration. The surface reflectance and aerosol content are not as easily determined.

The MOD04 and MOD09 algorithms use the same basic premise as the first step in the retrieval of aerosol optical depth (AOD). The surface reflectance in two visible bands, 0.49 μm ($\rho_{0.49}$) and 0.66 μm ($\rho_{0.66}$) is determined using the relationships (Kaufman et al., 1997);

$$\begin{aligned} \rho_{0.49} &= \frac{\rho_{2.1}}{4} \\ \rho_{0.66} &= \frac{\rho_{2.1}}{2} \end{aligned} \quad (2)$$

The atmospheric signal due to aerosol scattering in the 2.1 μm band is assumed to be negligible so the TOA 2.1 μm is used to infer the surface reflectance in the visible bands. This relationship is only valid when the surface reflectance is low, such as over a dense forested area.

The signal due to the atmospheric aerosol can now be determined using the pre-computed look-up tables. These look-up tables are designed so that a multitude of TOA radiance or satellite received values (L_{TOA}) are listed for a range of values of all of the other atmospheric parameters (water vapour, surface pressure, ozone

concentration, etc) and the surface reflectance. The look-up tables are searched for all of the known parameters. When these are found then the corresponding value for AOD is retrieved.

Both MOD04 and MOD09 produce AOD values in three bands. MOD04, as mentioned above, retrieves AOD values in the 0.49 μm and 0.66 μm bands. It also provides values for the 0.55 μm band as this band is used in many atmospheric correction models and is often used in global climate modelling (Remer et al., 2005). As there is no direct relationship between the 2.1 μm band and the surface reflectance in the 0.55 μm band, the AOD is inferred from the retrieved bands using an Angstrom relationship. This states that the AOD is a function of wavelength and can be expressed as (Teillet et al., 1994);

$$\tau(\lambda) = A\lambda^{-\alpha} \quad (3)$$

where τ is the AOD, λ is the wavelength, A is the turbidity coefficient, and α is the angstrom exponent.

Given AOD at two or more wavelengths it is possible to linearise equation 3 using the logarithms of the AOD and corresponding wavelength to produce the angstrom exponent as (Schuster et al., 2006),

$$\alpha = \frac{\ln A - \ln \tau(\lambda_i)}{\ln \lambda_i} \quad (4)$$

where λ_i represents different wavelengths.

The relationship of $\ln \tau$ to $\ln \lambda$ is not actually linear so the angstrom exponent changes depending on wavelength. A better fit can be achieved using a second-order polynomial such that (Schuster et al., 2006);

$$\ln \tau(\lambda_i) = a_0 + a_1 \lambda_i + a_2 (\ln \lambda_i)^2 \quad (5)$$

This is evident in Fig. 1 which shows the comparison of a linear and second-order polynomial fit to $\log(\text{AOD})$ vs $\log(\text{wavelength})$ data from Merredin Aerosol Robotic Network (AERONET) data in March, 2006 (<http://aeronet.gsfc.nasa.gov/>). The raw data for the graph in Fig. 1 was retrieved by the photometer between 2 and 4 air masses in the afternoon. If the sun was directly overhead and a sample was taken then this sample would have been done through 1 air mass. As the sun get further from nadir a larger amount of atmosphere is between the sun and the sensor. The convention is to describe the amount of atmosphere in terms of the ratio to a single air mass. Two to four air masses occur when the sun is approximately 60–80° from nadir and last for about 1 hour.

Figure 1 and Eq. 5 show that when using two AOD values at different wavelengths to estimate a third, these wavelengths need to be as close together as possible and the wavelength of the value to be estimated should lay between the other two. If this isn't the case then the risk is run that the linear estimation will be too far from the actual curve and the estimation of AOD will be of less use.

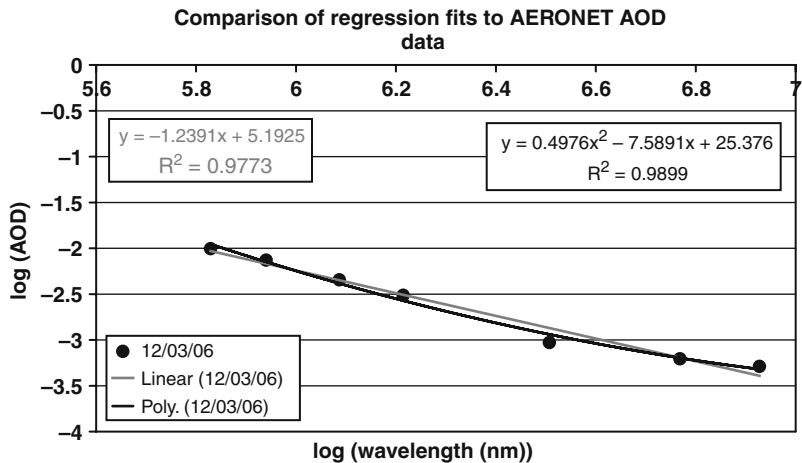


Fig. 1 This figure shows the difference between a linear and second-order polynomial fit to a log/log plot of AOD vs wavelength

AOD is retrieved up to a maximum $2.1 \mu\text{m}$ TOA reflectance value of 0.4. This upper limit requires that the view zenith angle be large enough so that there is a significant path radiance contribution to the TOA signal (Remer et al., 2005). The retrievals are considered to be ‘very good’ within the range $0.001 \leq \rho_{2.1} \leq 0.25$ (Remer et al., 2005).

Evaluation of AOD Retrieval by MOD04 and MOD09

This evaluation will investigate the spatial coverage of AOD retrievals for both MOD04 and MOD09, and the validity of the retrievals. It will also compare AERONET AOD figures with MODIS AOD retrievals for all days in March, 2006 when there were concurrent MODIS and AERONET retrievals.

Spatial Coverage and Retrieval Validity

The following images show composite AOD values for various months over the state of Western Australia. The AOD values are scaled to produce the clearest representation, so it is not indicative of the lowest or highest values. In each image, the same scale is applied to all bands. Each image is an 8-bit RGB. In the MOD04 images the $0.49 \mu\text{m}$ band (MODIS band3) is displayed as blue, the $0.55 \mu\text{m}$ band (MODIS band 4) as green, and the $0.66 \mu\text{m}$ band (MODIS band 1) as red. In the MOD09 images the $0.41 \mu\text{m}$ band (MODIS band 8) is displayed as blue, the $0.49 \mu\text{m}$ as green and the $0.66 \mu\text{m}$ band as red.

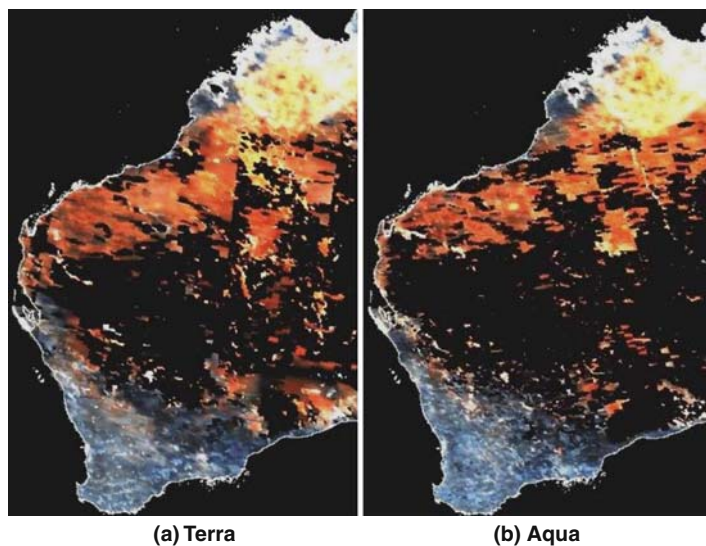


Fig. 2 MOD04 AOD composites for Western Australia, August 2005. These images are RGB representations of the AOD amounts for band 1, band 4 and band 3 respectively

Figures 2 and 3 are monthly composites of AOD for MOD04 where, at some time within the composite period, there were clear conditions over the entire state allowing data to be collected. These images show where the MOD04 algorithm will retrieve AOD. Figure 4 shows MOD09 retrievals over a 2 week period in

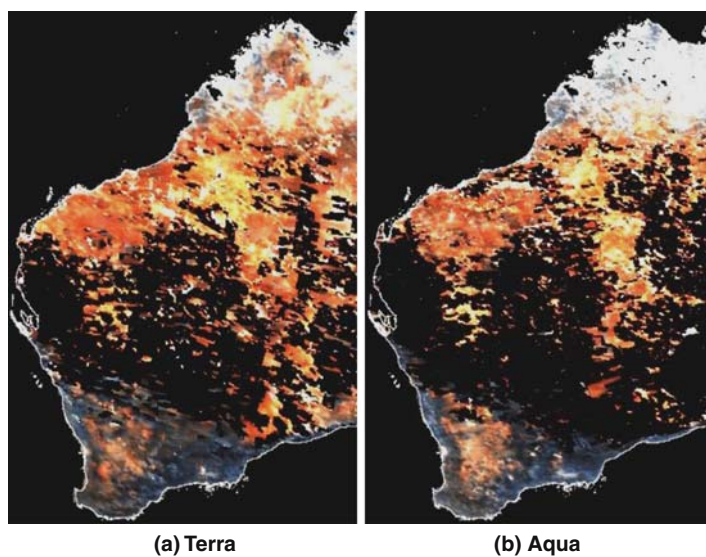


Fig. 3 MOD04 AOD composites for Western Australia, March 2006. These images are RGB representations of the AOD amounts for band 1, band 4 and band 3 respectively

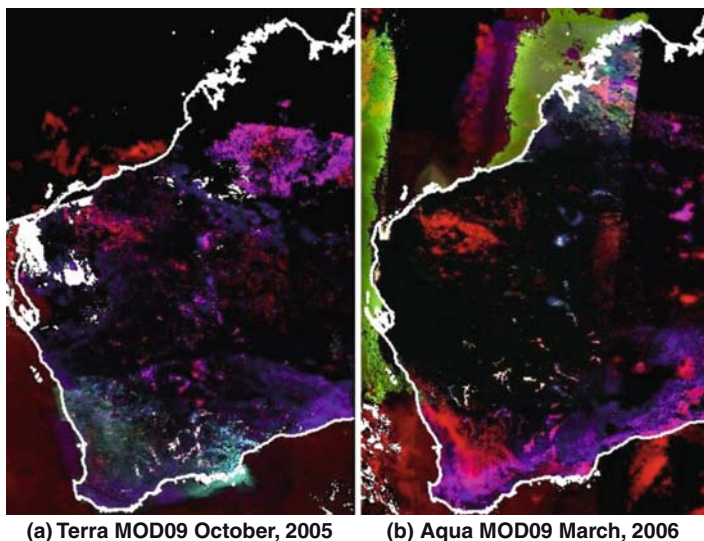


Fig. 4 MOD09 AOD composites for Western Australia. The images are RGB representations of the AOD amounts for band 1, band 3 and band 8 respectively. The predominantly white areas in the north-west in (a) indicate that there were no cloud-free pixels in this area over the composite period

October, 2005 and a 1 week period in March, 2006. The images in Fig. 4 show where cloud was present and there were no subsequent retrievals. This comprises a very small part of the land surface and thus gives a good estimation of where retrieval is possible.

Figures 2, 3 and 4 show that the AOD retrieval over Western Australia is not comprehensive. The composites show that up to a third of the state (or approximately $835 \times 10^3 \text{ km}^2$) has no AOD retrieved from MODIS. On a day to day basis this can extend to well over half of the state.

The angstrom exponent from theory and observation is known to be positive. This means that AOD must be larger at lower wavelengths. The difference between AOD at different wavelengths is a result of the composition of the atmospheric aerosol. Larger aerosol particles such as dust show less difference between AOD values whereas smaller aerosol particles show larger differences. AOD figures from AERONET for the Cimel sun photometer at Merredin verify these equations. The equations and fit residuals are displayed on the graph from Fig. 1. This means that the AOD plots should be blue not red.

There is seasonality shown in the images with the south west corner of the state predominantly blue in the winter month of August with the red becoming more dominant in early autumn month of March. The red colour in March closely matches the geographical extents of the wheat belt region of Western Australia. This trend is reversed in the Kimberley region in the north of the state with the blue colour dominating in March and the red in August. This is consistent with the theory of the algorithms which are designed to work over dense vegetation. The seasonality

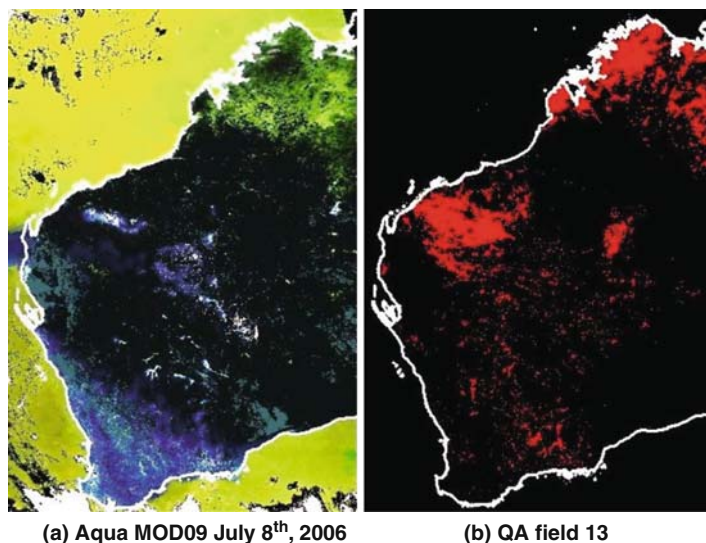


Fig. 5 (a) MOD09 AOD output from Aqua on the 8th of July, 2006. (b) Output from the QA flag from MOD09 which indicates where the retrieved AOD amounts in band 1 exceed the amounts retrieved for band 3

shown by the AOD retrievals follows the wet and dry seasons for these regions. The vegetation density is greatest in the Kimberly in March and in the south-west in August, following the annual rainfall patterns.

The unrealistic sign of the AOD dependence on wavelength, the seasonal control by vegetation density and the visible difference between high density and low density vegetated areas indicate that the MOD04 and MOD09 are suspect over Western Australia. This shows that surface reflectance has not been well determined.

The MOD09 algorithm provides quality assurance information on the data produced. The AOD retrieval process provides information on where the band 1 AOD exceeds that of band 3. This provides clear evidence where using band ratio techniques is likely to produce erroneous results. This is shown in Fig. 5.

Comparisons with sun photometer data at the Merredin test site, shown in Fig. 6, have also shown conclusive evidence of erroneous retrievals by the MOD04 algorithm. The AERONET figures are inferred from Eq. 5 as the Cimel sun photometer does not take readings at the same wavelength as MODIS bands 1, 3 and 4. A comparison is done only if the AERONET and MODIS measurements are within 10 minutes of each other. No comparison is shown here for MOD09 as, at the time of writing, only 2 points were available that satisfied the comparison guidelines.

The erroneous retrievals are largely due to the band ratio technique used to infer surface reflectance in band 1 and band 3. If the actual reflectance ratio is greater than the theoretical value then TOA signal attributed to the surface will be under estimated. This will cause an over estimation of the contribution from the atmosphere and thus AOD estimates will be far larger than the true value.

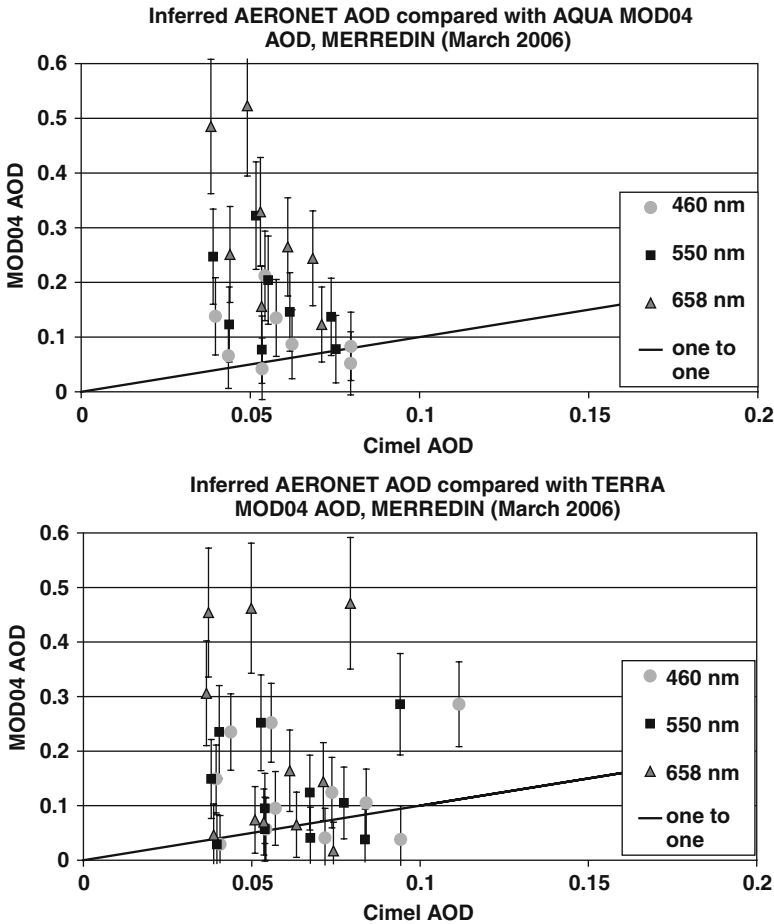


Fig. 6 Comparison of AOD figures from MOD04 with Cielmel AERONET AOD figures showing the expected MOD04 uncertainty of $\Delta\tau = \pm 0.05 \pm 0.15\tau$

Figure 7 shows values for the reflectance ratios from Eq. 2 from measurements made with an Analytical Spectral Devices spectrophotometer (ASD), at Merredin, in March 2006. Data was taken at 200 m spacing with measurements made at nadir, 30 and 60°. At Each successive line of the grid the off-nadir measurements were alternated between forward-scatter (sun in the northern sky and the ASD pointed north) and back-scatter directions (sun in the northern sky and the ASD pointed south). The spectral readings have been band averaged over the MODIS spectral response function for each band. The data have then been spatially averaged to a pixel size of 600 m.

The plots in Fig. 7 show that at nadir the reflectance ratios are very close to the MODIS-assumed theoretical value but when the off-nadir values are included the reflectance ratios increase rather dramatically. As this reflectance ratio is assumed

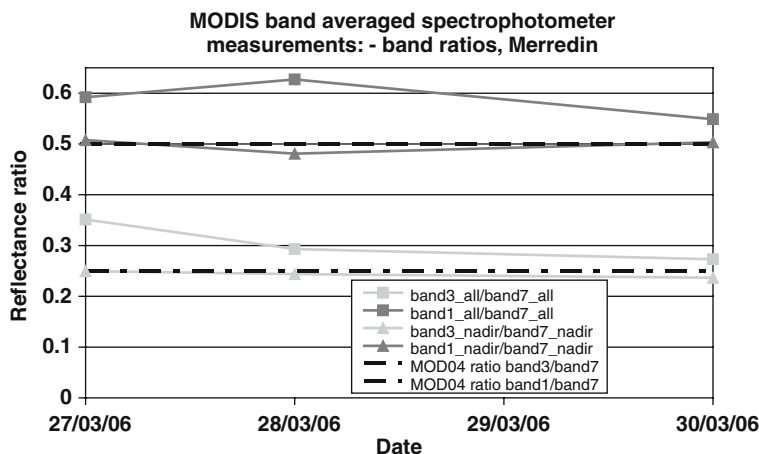


Fig. 7 This figure shows a comparison of the critical reflectance ratios used to infer surface reflectance with the NASA MODIS aerosol algorithms (see Eq. 2). These figures in these plots are generated by band averaged data that is spatially averaged over the Merredin field site

to be fixed by the MOD04 and MOD09 algorithms, any samples taken off-nadir would under-estimate the surface reflectance in band 1 and band 4. As a result the AOD would be over-estimated.

Reflectance Change from Time-Series BRF

Atmospheric correction of satellite data requires that the surface and atmospheric signals can be separated from each other. The atmospheric signal is due to scattering by the constituents of the atmosphere. Of these constituents, aerosols are by far the most variable, spatially, temporally and in constitution. The surface, and thus the contribution to the TOA, may vary but the time period of this change is long compared to the change in the atmospheric signal. Exceptions to this are events such as burning, snow and crop harvesting. These can generally be spotted by examination all of the MODIS reflectance bands.

SRSS, as part of the processing routine, perform a reflectance change determination using time-series BRF information. The BRF is a mathematical expression of the apparent change in reflectance due to the changes in geometry between the illumination and viewing directions over a surface. The MODIS instrument on-board both Terra and Aqua, which have a 16-day repeat cycle, will experience at least 15 changes in this geometry for each point on the Earth's surface over this 16-day period. In order to get a geometrically-independent indication of the reflectance of a point or pixel on the surface a normalisation for BRF is required.

The BRF process involves fitting observational data to a model. Semi-empirical models are a popular choice as they combine computational ease with underlying physical meaning. SRSS uses a model similar to that developed by (Roujean et al., 1992),

$$\rho(\theta_s, \theta_v, \phi) = k_0 + k_1 f_1(\theta_s, \theta_v, \phi) + k_2 f_2(\theta_s, \theta_v, \phi) \quad (6)$$

where, $\rho(\theta_s, \theta_v, \phi)$ is the bidirectional reflectance at the specific sun zenith (θ_s), view zenith (θ_v) and relative azimuth (ϕ) angles. The first term represents isotropic reflectance, the second term represents geometric scattering, the third term represents volumetric scattering. The forms of terms 2 and 3 are determined by f_1 and f_2 while the contribution of each term is determined by the coefficients k_0, k_1, k_2 . f_1 and f_2 are analytical functions of the view and illumination geometry, whereas the functions k_0, k_1, k_2 are based on a physical representation of the surface conditions. The coefficients are determined by linear regression of Eq. 6 using multiple observations.

In practice the data fitted to the BRF model should be atmospherically corrected although if the fit period is long enough then atmospheric variations will average out.

It is possible to exploit this averaging process to examine both surface and atmospheric changes. The BRF determination performed by SRSS provides a forward predicted reflectance for the next observations view and illumination geometry. If there is a change on the surface, such as a fire, then comparing the forward predicted reflectance with the actual observation will show there is a reflectance change or anomaly. This method is used operationally at SRSS to detect fire scars.

AOD Retrieval from Time-Series BRF

If the BRF process was to be used with data that was atmospherically corrected using a single AOD value for all observation, then comparing the forward predicted reflectance from the model with the actual observation should show where there is a change due to a variation in aerosol. This can be seen in Fig. 8. The images in Fig. 8 show a small amount of reflectance change even when it is unlikely that any such change occurred. This is more evident at longer wavelengths. The uncertainty in the BRDF is larger at longer wavelengths and often the predicted surface reflectance can be higher or lower than the true value. This corrupts the reflectance change data as a result.

Such a process could be used to measure changes in AOD. The reflectance change will stem from changes around an average value. This will be for average aerosol conditions. As the reflectance change varies, it provides information on the radiative properties of the atmosphere due to aerosols. These radiative properties when fitted to an appropriate aerosol model could produce AOD and other useful parameters. This approach could use the inversion procedures from the MODIS AOD algorithms given that the reflectance change procedure would provide path radiance and surface contributions for the bands. The major difference is that it does not require any sort of band ratio technique to derive the surface and path radiances.

Figure 9 shows the result of the reflectance change determination over the Merredin test site for January and February, 2006. The presence of clouds can be seen from the large increases in the bands, particularly band 3. The samples from the 5th of February show a large decrease in band 7 (2.13 μm) and band 5 (1.24 μm).

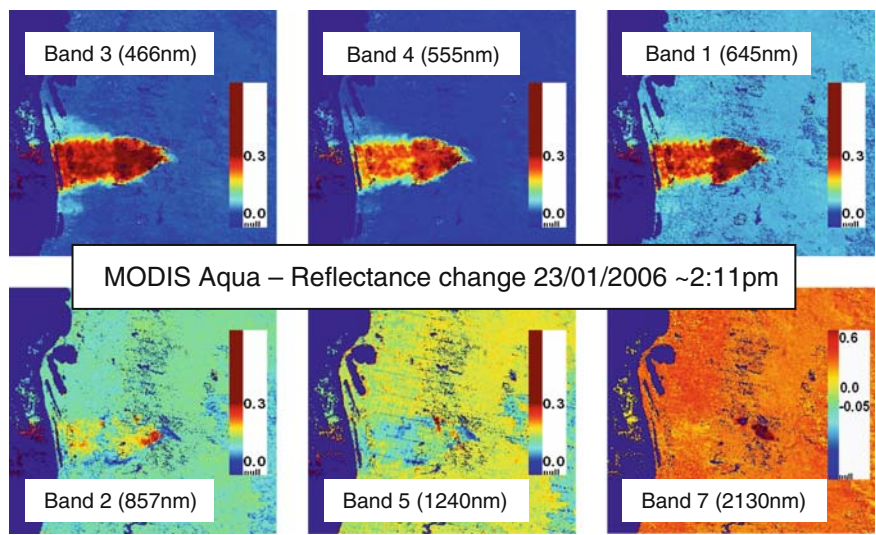


Fig. 8 Example of the ability of the BRF reflectance change determination to identify atmospheric aerosol. This figure shows the change in reflectance from the predicted value for MODIS land bands

This is due to a registration issue as all of the bands have been re-projected to 250 m pixels. In this case the band 5 and 7 pixels are in a cloud shadow and the other pixels are sitting on the cloud. In the case where pixels are contaminated by cloud, they would be excluded from any AOD retrieval process. The other samples provide a good indication of what reflectance change due to the atmospheric contents looks

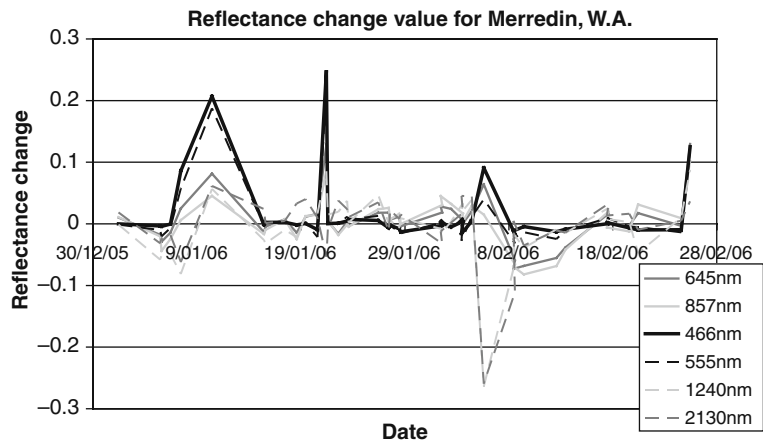


Fig. 9 This figure shows the reflectance change values for the 250 m MODIS pixel in each band located over the Merredin field site

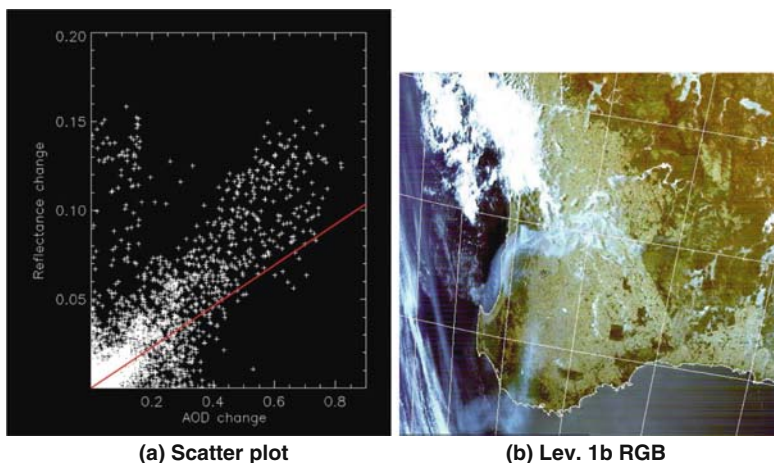


Fig. 10 (a) This shows a scatter plot of MOD04 derived band 3 AOD increase from an average value for the scene shown by (b). (b) This shows a large smoke plume in the south-west of Western Australia

like, as there was very little change to the surface conditions over the test site over this period. The samples shown in the plots in Fig. 9 have only been atmospherically corrected using a single value for many of the key atmospheric parameters. The reflectance change in the plots therefore cannot be directly attributed to changes in AOD but changes in atmospheric aerosols do produce the greatest change in path radiance.

A rough comparison of the reflectance change determination and AOD change can be seen in Fig. 10(a). This comparison was done primarily over the south-west corner of Western Australia, using products derived from Terra. This area was affected by smoke from a fire in the forest east of Perth. The smoke had been blown out to sea, then blown south, before being blown north, back over land. A very crude scaling technique was used to change the 250 m resolution reflectance change data to a 10 km resolution for comparison with the MOD04 data. The AOD change was determined by taking the difference between an averaged composite of AOD data from the 6/01/2005 to the 11/01/2005 and the swath AOD data for the 17/01/2005.

Figure 10(a) shows a correlation between the two sets of data. This correlation shows the possibility of using reflectance change data to infer a comparative change in AOD. The regression line (shown as red in Fig. 10(a)), which was produced using a modified least-squares technique, is skewed by the lower values. The group of points which show a large increase in reflectance without a corresponding increase in AOD (those points above 0.05 reflectance change and close to the y-axis) are due to cloud affected pixels included in the reflectance change scaling process.

While there is no definitive way to judge the validity of the comparison in Fig. 10(a), the MOD04 retrieval in the area examined is under favourable conditions. The area in question is the south-west corner of Western Australia, which is the most heavily forested area of the state. The AOD is quite high due to the presence of the

smoke, which means that the path radiance will increase in relation to the surface signal. This retrieval is at the edge of the swath which means that there is a large slant path. A larger slant path means that the path radiance increases in relation to the surface signal. These factors provide confidence in the MOD04 retrieved AOD.

Conclusion and Further Work

The results of this work have shown that the spatial coverage of the AOD retrievals from the MOD04 and MOD09 algorithms over Western Australia is not comprehensive. Vast areas of the state do not have AOD figures retrieved at all and in some areas there are only sporadic retrievals. In areas where the RGB representations of the AOD in three bands show a predominately red colouration, it indicates that the AOD retrieved in band 1 exceeds the other 2 bands, invalidating the retrieval in this band and casting doubt on the accuracy of the data for the other bands. Comparisons with sun photometer data in the Western Australian wheat belt in March, 2006 have shown that the MOD04 data, in general, largely over estimates the AOD. Spectrophotometer data have shown that the reflectance ratios used by the MODIS algorithms over the test site will become larger as the reflectance is measured further from nadir. This will lead to an over estimation of the contribution from the atmosphere to the TOA signal and result in over-estimation of the AOD.

It should be noted here that MOD09 is designed to retrieve surface reflectance and the AOD produced by the algorithm is a purely internal product. If the AOD figures fail one of the internal quality assessment tests then the figures are not used in the atmospheric correction process.

It should also be noted that this evaluation is based on collection-4 data. The ATBD for MOD04 collection-5 shows that the next generation of the MOD04 algorithm will, among other things, account for the aerosol effect in the 2.1 μm channel, employ angular information and surface types when determining the reflectance ratios, and adjust the algorithm to account for differences in Rayleigh scattering due to surface height (Remer et al., 2006).

The reflectance change determination using time-series BRF information provides information on the change of state of the surface and the atmosphere. It can be shown that it detects the change in atmospheric aerosols. The rough comparison of the change in atmospheric aerosol derived from MOD04 data, with the reflectance change, shows that it may be feasible to use reflectance change to measure the magnitude of AOD change, and thus give AOD data. This does not require the use of a band ratio technique to separate the path and surface radiance. It is also hoped that this approach will allow retrievals over brighter targets where MOD04 and MOD09 do not work effectively.

The project which inspired this paper aims to develop a method to retrieve AOD over areas of Western Australia and Australia where the dark target methods used in MOD04 and MOD09 fail. The problems with these algorithms stem from the methods used to determine surface reflectance, namely the band ratio techniques.

Reflectance change offers a way to separate path and surface radiance directly from the MODIS spectral data. Modelling this process using radiative transfer simulations will be the next step in developing an AOD retrieval algorithm based on reflectance change. This will also allow the sensitivity of such a process to be examined.

An examination of the data produced by the new algorithms from collection 5 will also be done, when the data used for this study are re-processed by the new algorithm.

Once a suitable AOD retrieval method is developed and included in the atmospheric correction process, the impact of the change will be examined to ensure it improves the current products.

Acknowledgments This work is part of the CRC for Spatial Information project 4.1, with project participants, Landgate, Curtin University of Technology, Geoscience Australia and Sinclair Knight Merz. The Authors would like to thank the staff at SRSS and the Merredin Drylands Research Institute, Department of Agriculture and Food, Western Australia.

References

- Kaufman, Y. and Tanre, D., 1998. Algorithm for remote sensing of tropospheric aerosols from MODIS, MODIS algorithm theoretical basis document: MOD04 (URL: <http://modis.gsfc.nasa.gov/data/atbd/>).
- Kaufman, Y. et al., 1997. The MODIS 2.1- μ m channel – correlation with visible reflectance for use in remote sensing of aerosols. *IEEE Transactions on Geoscience and Remote Sensing*, 35(5): 1286–1298.
- Liang, S., Zhong, B. and Fang, H., 2006. Improved estimation of aerosol optical depth from MODIS imagery over land surfaces. *Remote Sensing of Environment*, 104(4): 416–425.
- Remer, L. et al., 2005. The MODIS aerosol algorithm, Products and validation. *Journal of Atmospheric Sciences*, 62(4): 947–973.
- Remer, L., Tanre, D. and Kaufman, Y., 2006. Algorithm for remote sensing of tropospheric aerosols from MODIS: Collection 5, MODIS algorithm theoretical basis document: MOD04 (URL: <http://modis.gsfc.nasa.gov/data/atbd/>).
- Roujean, J., Leroy, M. and Deschanps, P., 1992. A bidirectional reflectance model of the Earth's surface for the correction of remote sensing data. *Journal of Geophysical Research*, 97(D18): 20455–20468.
- Schuster, G., Dubovik, O. and Holben, B., 2006. Angstrom exponent and bimodal aerosol size distributions. *Journal of Geophysical Research*, 111, D07207.
- Teillet, P., Fedosejevs, G., Ahern, F. and Gauthier, R., 1994. Sensitivity of surface reflectance retrieval to uncertainties in aerosol optical properties. *Applied Optics*, 33(18): 3933–3940.
- Vermote, E., Tanre, D., Deuze, J., Herman, M. and Morcette, J., 1997. Second simulation of the satellite signal in the solar spectrum, 6S: An overview. *IEEE Transactions on Geoscience and Remote Sensing*, 35(3): 675–685.
- Vermote, E. and Vermeulen, A., 1999. Atmospheric Correction Algorithm: Spectral Reflectances (MOD09), MODIS Algorithm Technical Background Document (URL: <http://modis.gsfc.nasa.gov/data/atbd/>).

Improved Near-Real Time Atmospheric Correction of MODIS Data for Earth Observation Applications

Brendon McAtee and Stefan Maier

Abstract Current operational satellite-based sensors designed for Earth observation such as the MODerate Resolution Imaging Spectroradiometer (MODIS) possess the capability to provide remotely sensed land surface information in Near-Real Time (NRT). This means that vegetation parameters, measures of land cover change, pasture and crop yield, and a range of environmental indicators may be available within an hour of the satellite overpass for areas up to regional scale.

Such land surface parameters are based on surface reflectance data acquired from MODIS. To produce remotely sensed surface reflectance data of the highest quality the atmospheric component of the signal received at the satellite sensor must be removed. This step requires that the amount of water vapour, ozone and aerosols in the atmosphere be accurately determined so that their contributions to the measured signal may be evaluated and removed. For optimum results, these ancillary data should be obtained coincidentally with reflectance information from the satellite sensor. The MODIS sensor was designed as an operational NRT sensor for just such a purpose, possessing the necessary spectral coverage to retrieve the required atmospheric parameters.

This paper will describe the development of an operational system for the atmospheric correction of reflectance data from the MODIS sensor. It discusses the sensitivity of the atmospheric correction process to the accuracy of the input ancillary data with a focus on the validation of results to date. This Cooperative Research Centre for Spatial Information project serves as a foundation for future NRT processing of remotely sensed data in Australia.

Introduction

The Satellite Remote Sensing Services (SRSS) section of Landgate, Western Australia, runs an operational system for the processing of remotely sensed data from the MODIS satellite-based sensor in NRT (see Maier et al. (2006) for further

B. McAtee (✉)

Satellite Remote Sensing Services, Landgate, Government of Western Australia, Wembley, WA 6913, Australia

e-mail: Brendon.Mcatee@landgate.wa.gov.au

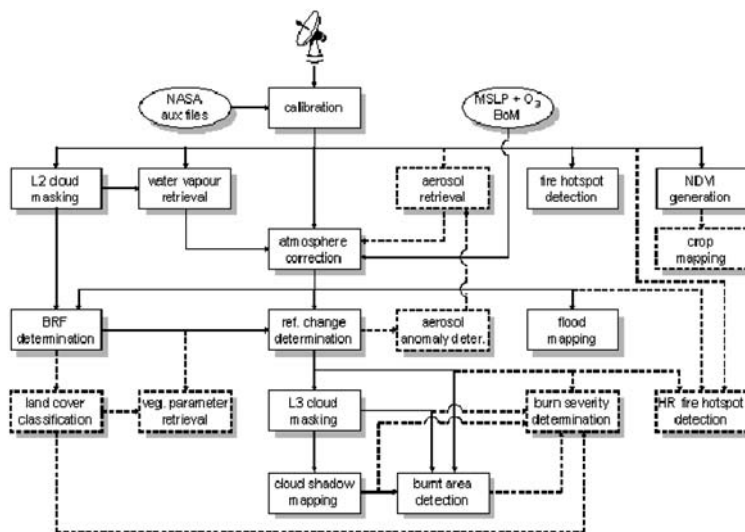


Fig. 1 Flow diagram showing the operational processing system described in Maier et al. (2006). *Solid boxes* show existing components of the system. *Dashed boxes* show components under development. *Ovals* contain external inputs to the processing system. Taken from Maier et al. (2006)

discussion of this operational system). Figure 1 (taken from Maier et al. (2006)) describes the processing sequence for MODIS data at SRSS. It may be seen from this figure that the atmospheric correction process is fundamental to deriving remotely sensed products from MODIS data for a range of applications.

Under Project 4.1 of the Co-operative Research Centre for Spatial Information (CRC-SI), two approaches to the atmospheric correction of MODIS data are being implemented. SRSS is implementing the Simple Method of Atmospheric Correction (SMAC) (Rahman and Dedieu 1994) algorithm for atmospheric correction, utilising NRT data sources for all the necessary ancillary inputs to the algorithm. This allows the atmospheric correction of MODIS data to be optimised for continental Australian conditions. In parallel with the SMAC development, at Geoscience Australia the National Aeronautics and Space Administration (NASA) algorithm for atmospheric correction of MODIS data, referred to as MOD09 (Vermote and Vermeulen 1999), has also been implemented.

This paper summarises the development of these algorithms for atmospheric correction of MODIS data and presents the results from the validation analyses undertaken to date.

Methodology

Algorithm Development

The atmospheric correction algorithm for MODIS is complex and has many data dependencies. It is best described by Fig. 5 in the MOD09 Algorithm Theoretical

Basis Document (ATBD) (Vermote and Vermeulen, 1999). The reader is directed to the MOD09 ATBD for a more detailed description of its workings as the architecture of the MOD09 algorithm is not the focus of this paper. In summary, the radiative properties of the atmosphere must be well-characterised in order to separate the atmosphere and surface-derived components of the signal measured by the satellite sensor. Clearly, when the atmospheric component of the at-sensor signal is estimated and removed, the remainder is the contribution from the surface. This surface contribution is the quantity of interest for most of SRSS' current applications.

The important atmospheric parameters which need to be known in order to accurately characterise the atmosphere are water vapour, ozone concentration and aerosol optical depth. The vertical pressure gradient within the atmosphere also influences the radiative properties observed. Each of these parameters are ancillary inputs into the atmospheric correction algorithm.

For the MOD09 algorithm, surface pressure and water vapour information are sourced from Global Data Assimilation System (GDAS) files. The necessary ozone information is sourced from Total Ozone Analysis using SUBV/2 and TOVS (TOAST) files, which are also global data sets. These data files may be obtained from archives such as that maintained by the Space Science and Engineering Centre at the University of Wisconsin-Madison (<ftp://aqua.ssec.wisc.edu.au/pub/terra/ancillary>). GDAS files are updated 6-hourly while TOAST files are updated on a daily basis. For the SMAC algorithm, the necessary ancillary data are sourced from a number of locations, all in NRT.

Surface pressure and ozone data are acquired from the Bureau of Meteorology (BoM), while the water vapour data are produced from MODIS at SRSS in NRT using the algorithm developed by Albert et al. (2005).

By far the most problematic of the required ancillary inputs to the basic atmospheric correction algorithm is the Aerosol Optical Depth (AOD). This parameter describes the concentration of particulate matter in the atmosphere such as dust, smoke or other photochemicals. It is a particularly important parameter as the accuracy with which the radiative contribution of aerosols may be estimated is the limiting factor on the accuracy of the atmospheric correction process in the visible part of the electromagnetic spectrum (section "Sensitivity Study" discusses the importance of accurate AOD estimation in more detail).

As AOD is a difficult parameter to measure accurately, a dedicated AOD retrieval algorithm exists for MODIS (MOD04, Kaufman and Tanrè (1998)), and an algorithm for AOD retrieval based upon similar physical principles is included within the MOD09 algorithm. However, as the work of Broomhall et al. (2006) shows, the results from the MOD04 and MOD09 AOD retrieval algorithms are patchy at best under Australian conditions. The need for an improved source of AOD data for the purpose of atmospheric correction under Australian conditions to feed into the NRT SMAC-based atmospheric correction algorithm provides the motivation for the work of Broomhall et al. (2006) in developing an alternative AOD retrieval methodology for MODIS, more suited to continental Australian conditions.

As noted above, the atmosphere and surface-derived contributions are coupled together within the signal measured at the sensor, and are required to be separated.

A further complication exists in that the surface contribution is also dependant upon the satellite viewing geometry of the surface and the relative solar position. The description of the change in measured surface reflectance due solely to sensor-solar geometry is frequently termed the Bi-Directional Reflectance Distribution Function (BRDF, Roujean et al. (1992)). Knowledge of the BRDF is a critical input for optimising the results from the atmospheric correction process (Vermote and Vermeulen 1999). The BRDF is also important to the validation of results from the atmospheric correction procedure, as will be shown later in sections ‘The Role of Validation’ and ‘Validation of the MOD09 Algorithm’.

Sensitivity Study

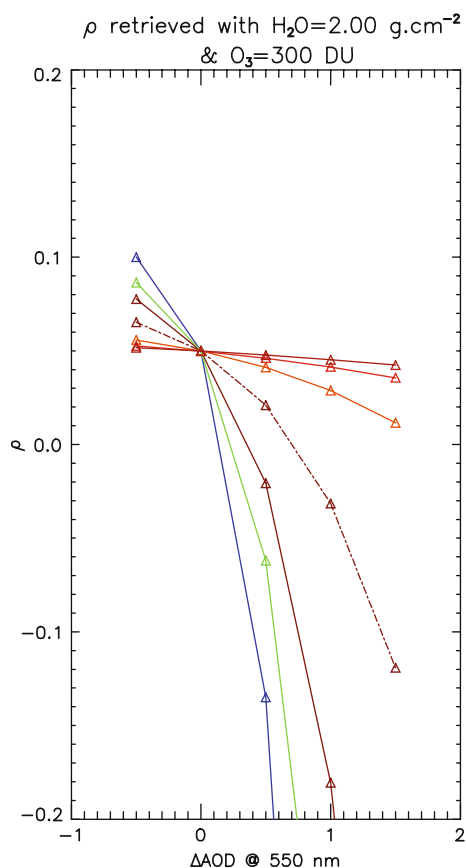
As part of the incorporation of NRT atmospheric parameters into the SMAC atmospheric correction methodology, a sensitivity study was initiated to determine how sensitive the atmospherically corrected surface reflectance is to the accuracy with which each of the important atmospheric parameters is known. This study was undertaken using the MODTRAN atmospheric radiative transfer model (Berk, Bernstein 1989). In the model, the land surface was given reflectances of 0.05, 0.5 and 1.0 to encompass the full range of possible values encountered over the spectral range of MODIS bands 1 to 7 for surface types typical of continental Australia. The values of the water vapour, ozone concentration and AOD in the model were iterated over typical ranges of their values for continental Australian conditions, for each of the set of surface reflectance values. Information on the sensitivity of the surface reflectance retrieved through the atmospheric correction process to the accuracy of the atmospheric parameters was gleaned through characterising the difference between the simulated surface reflectance that would be measured by MODIS, for the predefined set of atmospheric parameters, and the surface reflectance set in the MODTRAN model. The difference between the predefined surface reflectance and the retrieved surface reflectance for MODIS simulated using the model changes as the values of the atmospheric parameters used in the model are varied. The magnitude of this change defines the sensitivity of the retrieved surface reflectance to each of the atmospheric parameters. Results from this study are presented in Fig. 2.

The Role of Validation

Motivation for the development of an accurate atmospheric correction methodology arises from the need to optimise the quality of the downstream products based on atmospherically corrected surface reflectance data (see Fig. 1 for a full list of these). As such, validation of the results flowing from the atmospheric correction process is a critical quality control measure.

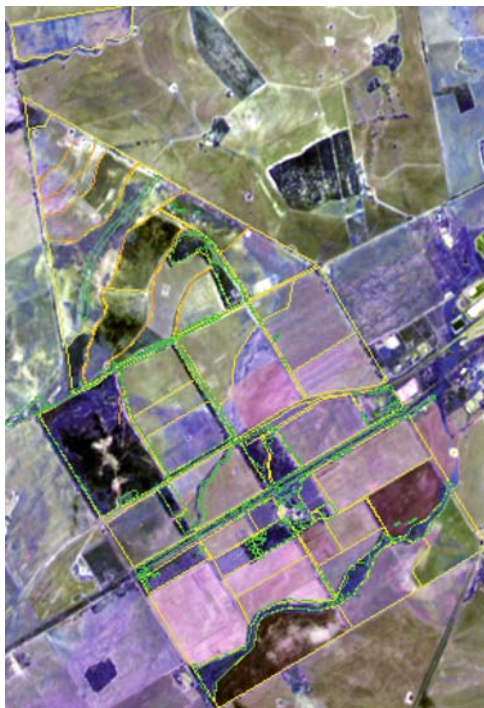
To this end, a field site for validation of atmospherically corrected surface reflectance data derived from MODIS has been set up within the DryLands Research Institute run by the Department of Agriculture and Food, Western Australia

Fig. 2 Sensitivity of atmospherically corrected surface reflectance to accuracy of AOD estimate. From the top of the figure in an anticlockwise direction the order of MODIS bands is 3 (469 nm), 4 (555 nm), 1 (645 nm), 2 (858 nm), 5 (1240 nm), 6 (1640 nm), 7 (2130 nm)



(DAFWA), near the town of Merredin, 270 km east of Perth (see Fig. 3). Grids have been laid out in different paddocks of the site with spacings ranging from 10 to 200 m so as to characterise the surface properties of the site at a range of spatial scales applicable to different satellite-based sensors. Instrumentation for measuring the AOD has also been installed at the site (Broomhall et al. 2006) as the aerosol component of the atmospheric correction methodology has been identified as being critical to the quality of results obtained (see section “Surface Reflection Sensitivity”) and is the subject of intensive investigation within this project (Broomhall et al. 2006). Figure 3 shows an Advanced Spaceborne Thermal Emission and Reflection Radiometer (ASTER) image of the field site with the boundaries of paddocks overlaid. The false colour image of the field site suggests that different areas of the site have different spectral properties. This illustrates that it is important to characterise such variability of the site up to the spatial scale of MODIS pixels (250–500 m) in order to correctly validate results from the atmospheric correction algorithms (see section “Field Site Characterisation”).

Fig. 3 ASTER image of the Merredin field site



The current component of the validation program focuses on results from the MOD09 algorithm as the necessary components of the NRT SMAC methodology continue to be integrated (e.g. the AOD component (Broomhall et al. 2006)). To characterise the spectral properties of the site and validate the results from the MOD09 algorithm spectral measurements were made with an ASD Hyperspectral Spectroradiometer at defined grid points covering the field site. The ASD instrument covers the spectral range of MODIS bands 1 to 7 and MODIS surface reflectances were simulated from these ground measurements by applying the respective relative response functions for each MODIS band to the spectral surface reflectance data acquired using the ASD instrument.

Results and Discussion

Surface Reflectance Sensitivity

Results from the sensitivity study show that the accuracy of the AOD estimate has the largest impact on the surface reflectance retrieved through the atmospheric correction process, particularly in MODIS bands with shorter wavelength. Figure 2

shows the sensitivity of the retrieved surface reflectance to errors in the AOD estimate for bands 1 to 7 of MODIS for a predefined surface reflectance of 0.05. The water vapour concentration is 2 g cm^{-2} and the ozone concentration is 300 DU. The accuracy of the AOD estimate at 550 nm is shown on the x-axis. At a value of zero on the x-axis the AOD estimate used in the atmospheric correction process is exactly correct. To the left of this point the AOD value used is too low by the amount given on the x-axis, while to the right it is too large. The simulated surface reflectance estimated-through the MODTRAN model is given on the y-axis. The figure illustrates that even small errors in AOD can have a large effects on the surface reflectance estimated by the MOD09 and SMAC algorithms.

The impacts of errors in water vapour and ozone concentrations on the atmospherically corrected surface reflectance are less significant than for the AOD. McAtee, Maier (2006) have quantified the accuracy of NRT water vapour retrieval using the Albert et al.(2005) algorithm to be $\pm 0.6 \text{ g cm}^{-2}$. The current sensitivity study confirmed that this result only translates to a 5% error at most in the atmospherically corrected surface reflectance for satellite viewing angles approaching 60° in the longer wavelength bands (MODIS bands 5–7). In other bands the impact is generally much smaller than this. The MODIS spectral bands, except for band 4 located at 555 nm (see Fig. 3b from Vermote and Vermeulen (1999)), remain relatively unaffected by errors in the estimation of atmospheric ozone concentration. Even in band 4, which is located near an atmospheric ozone absorption feature, the impact of errors in ozone estimation is negligible in most cases.

Field Site Characterisation

From Fig. 3 it is apparent that there are some spectral differences between different areas within the field site. It is unlikely that a given MODIS field-of-view (FOV) will fall completely within one of the distinct areas depicted in the ASTER image of Fig. 3. As such it is necessary to characterise the homogeneity of the field site at spatial scales up to the MODIS pixel size to ensure that any differences between the ground and satellite-derived surface reflectance measurements can be said to originate from the MOD09 algorithm rather than surface variability.

The field survey grid is spaced at 200 m intervals over the field site, and includes several smaller $100 \times 100 \text{ m}$ grids with a grid spacing of 10 m. The combination of these grid spacings allows spectral reflectance measurements made using the ASD instrument to be averaged over different spatial scales. A representative result of this process for the field site is shown in Fig. 4.

At the shorter wavelengths (MODIS bands 3 and 4) the site appears homogenous across all spatial scales. At the longer wavelengths the mean surface reflectance appears to decrease at the larger spatial scales. For these longer wavelengths the variability about the mean value over all spatial scales approaches 7% of the mean value. In the absence of any atmospheric contribution this value of will be the limiting accuracy for the validation of the atmospherically corrected surface reflectances from the MOD09 algorithm.

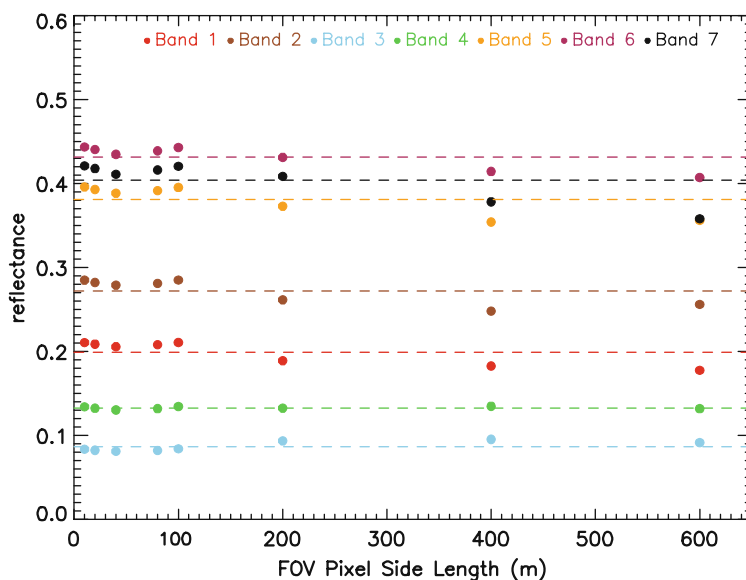


Fig. 4 Spectral variability of the Merredin field site at different spatial scales

To achieve the best validation results between the ground measurements and satellite-derived surface reflectances it is also important to consider any BRDF effects which may impact the comparisons, i.e. the solar-sensor geometry at which the ground measurements are made compared to the solar-sensor geometry of the satellite. For this work, the survey grids were laid out in a north-south orientation. As such, there were two main solar-sensor geometries in the field measurements – into the sun when heading north, and away from the sun when heading south. These directions equate to the forward and backscatter directions for solar radiation from the Earth’s surface.

The results from the ground measurements presented in Fig. 5 show that as the angle of view from the ASD instrument to the surface increased definite BRDF effects began to emerge in the reflectance data. The measurements were taken at nadir (Fig. 5a), 30° (Fig. 5b) and 60° (Fig. 5c) on a grid with 10 m spacing. Figure 5 is for Band 2 of MODIS, but similar structure is also apparent in the equivalent contour plots at other wavelengths. It is clearly evident from these figures that at larger zenith angles backscatter dominates over forward scatter from the land surface of the field site. As a result, the measured surface reflectance is higher in the south-facing direction than in the north-facing direction by between 5 and 10% due to BRDF effects. The high and low contours of reflectance shown in the figure are aligned north-south and match the forward and backscatter directions noted above. This is an important result as there are two MODIS instruments, one on the TERRA platform which follows a north-south orbit, while the second on the AQUA platform follows a south-north path. As such, when these sensors view the field site at large

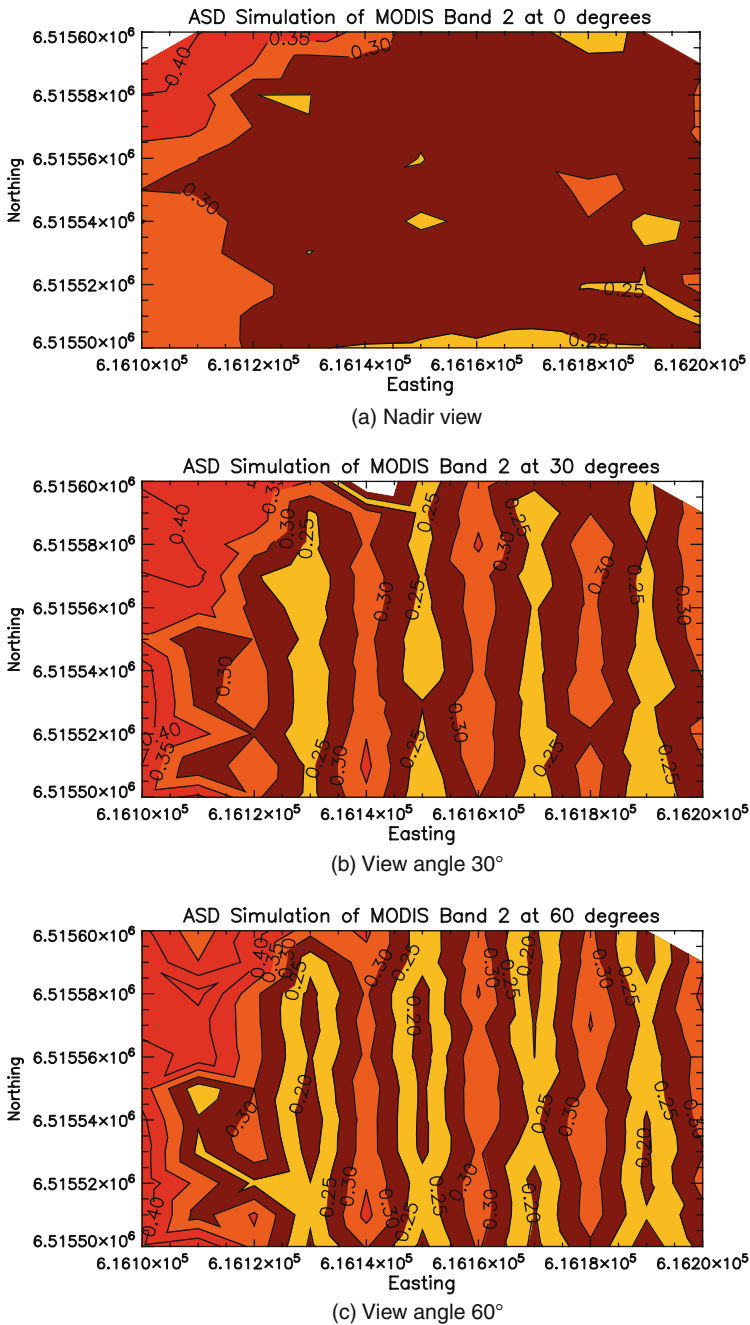


Fig. 5 Contour plots of surface reflectance measured using the ASD instrument illustrating the BRDF effects which emerge as the viewing angle increases. North is towards the top of the page

zenith angles it will be important to validate these results against ground measurements made at matching solar-sensor orientations in order to minimise the impact of BRDF effects on the validation of the atmospheric correction algorithm.

Validation of the MOD09 Algorithm

Over the 26th, 27th, 28th and 30th of March 2006 a field experiment was undertaken at the Merredin field site to provide preliminary validation of the MOD09 surface reflectance product supplied by Geoscience Australia. For each day of the experiment the pixel in the MOD09 image from the MODIS sensor aboard the Terra platform closest to the grid locations at which ASD ground measurements were made during a period of the day close to the MODIS overpass time was selected. A spatially averaged surface reflectance for each of MODIS bands 1 to 7 was calculated from the ground measurements over a 600 by 600 m area as close to coincident as possible with the MODIS measurements. Figure 6 shows the comparison between the ground measurements of surface reflectance made using the ASD instrument and the atmospherically corrected surface reflectance from the MOD09 algorithm.

The figure shows that the MOD09 algorithm generally over estimates the surface reflectance measured on the ground. In the figure, the colour of each symbol (as noted in the figure) signifies the MODIS band for which the comparison was made. The different symbols represent the days on which the comparisons were made.

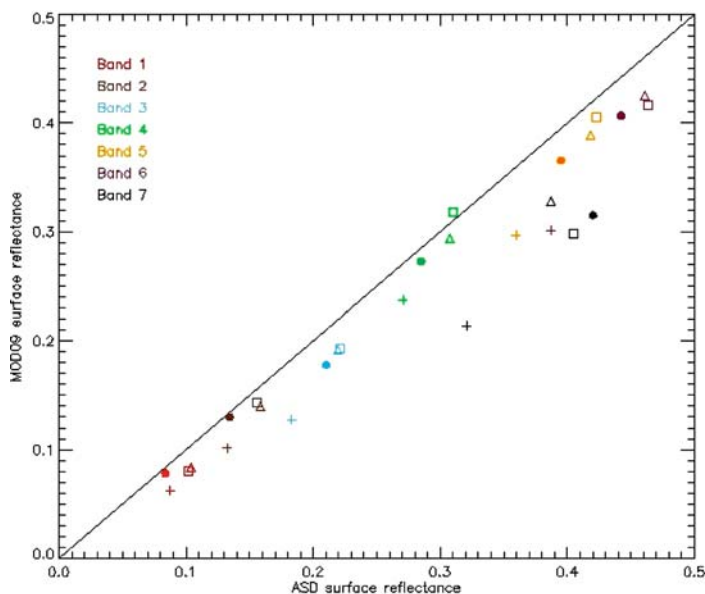


Fig. 6 Validation of results from the MOD09 algorithm against the ground measurements made during the Merredin validation experiment

Table 1 Comparison between the theoretical accuracy of the MOD09 algorithm and results from the Merredin validation experiment

| Band | MOD09 ATBD (%) | Merredin experiment (%) |
|------|----------------|-------------------------|
| 1 | 10–33 | 5 |
| 2 | 3–6 | 2 |
| 3 | 50–80 | 6 |
| 4 | 5–12 | 4 |
| 5 | 3–7 | 3 |
| 6 | 2–8 | 4 |
| 7 | 2–8 | 8 |

The filled circles are for March 26, the “plus” signs for March 27, the triangles for March 28 and the squares for March 30. The comparisons are best for bands 1, 2 and 4, while the comparisons do not appear as good for the bands at longer wavelengths (bands 5, 6 and 7). Overall the comparison shows an RMS error of approximately 0.05 about a bias of 0.03.

When the validation results are examined individually by spectral band the outcome agrees well with the theoretical accuracy of the algorithm described in the ATBD for MOD09, authored by Vermote and Vermeulen (1999). This comparison is presented in Table 1.

Conclusions and Future Work

Deriving accurate atmospherically corrected surface reflectance from satellite-based sensors is a complex task. However, this work has shown that the MOD09 algorithm is currently producing good quality results in agreement with its theoretical limitations. This is a promising result from this preliminary analysis for a number of reasons; (1) more rigour may be added to the present validation analysis to further refine the estimates of accuracy presented based on incorporation of BRDF information into the validation analysis, and; (2) there is a large scope for improvement to the accuracy of the ancillary atmospheric parameters which are input into the MOD09 and SMAC algorithms for atmospheric correction. In particular, the AOD estimation methodology being developed by Broomhall et al. (2006) will markedly improve AOD estimation for continental Australian conditions. Inclusion of this algorithm into the suite of algorithms for MODIS processing will serve to deliver further improvements to remotely sensed data for Earth observation applications in the future.

Acknowledgements The authors would like to thank the Co-operative Research Centre for Spatial Information for continued support of this project and Geoscience Australia for supplying the MOD09 data used in the validation analysis.

References

- Albert, P., R. Bennartz, et al. (2005) "Remote sensing of atmospheric water vapor using the moderate resolution imaging spectroradiometer (MODIS)." *Journal of Atmospheric and Oceanic Technology* **22**: 309–314.
- Berk, A., L. S. Bernstein, et al. (1989) "MODTRAN: a moderate resolution model for Lowtran-7." Technical Report, Spectral Sciences Inc., GL-TR-89-0122, Burlington, Massachusetts, USA.
- Broomhall, M., B. McAtee, et al. (2006) "An investigation of the remote sensing of aerosols based on MODIS data for Western Australian conditions." *Proceedings of the 13th Australasian Remote Sensing and Photogrammetry Conference*, Canberra, Australia.
- Justice, C. O., E. Vermote, et al. (1998) "The moderate resolution imaging spectroradiometer (MODIS): land remote sensing for global change research." *IEEE Transactions on Geoscience and Remote Sensing* **36**: 1228–1249.
- Kaufman, Y. and D. Tanrè (1998) "Algorithm for remote sensing of tropospheric aerosols from MODIS." *MODIS algorithm theoretical basis document: MOD04*, NASA Goddard Space Flight Center, Greenbelt, MD 20771, USA.
- Maier, S. W., J. Adams, et al. (2006) "The MODIS near-real time processing system at satellite remote sensing services." *Proceedings of the 13th Australasian Remote Sensing and Photogrammetry Conference*, Canberra, Australia.
- McAtee, B. K. and S. W. Maier (2006) "A Comparison of algorithms for near-real time water vapour retrieval from MODIS." *International Journal of Remote Sensing* **27**(23): 5145–5163.
- Roujean, J., M. Leroy, et al. (1992) "A bidirectional reflectance model of the Earth's surface for the correction of remote sensing data." *Journal of Geophysical Research* **97**(D18): 20455–20468.
- Rahman, H. and G. Dedieu (1994) "SMAC: A simplified method for the atmospheric correction of satellite measurements in the solar spectrum." *International Journal of Remote Sensing* **15**: 123–143.
- Vermote, E. F., N. Z. el Saleous, et al. (2002) "Atmospheric correction of MODIS data in the visible to middle infrared: first results." *Remote Sensing of Environment* **83**: 97–111.
- Vermote, E. and A. Vermeulen (1999) "Atmospheric correction algorithm: Spectral reflectances (MOD09)." *MODIS Algorithm Technical Background Document Version 4.0*. Department of Geography, University of Maryland, USA.

Near-Real Time Satellite Products to Drive Australia-Wide Land Surface Monitoring and Modelling of Surface Water and Energy Balance

I.F. Grant

Abstract The Bureau of Meteorology continuously acquires low resolution multi-spectral image data, with continental coverage of Australia in near-real time, from both the Advanced Very High Resolution Radiometer (AVHRR) on the US National Oceanic and Atmospheric Administration (NOAA) polar orbiting satellites and from the geostationary imagers on Japan's MTSAT-1R and China's Fengyun-2C satellites. The Bureau routinely derives several products from these satellites which can serve as continuous data streams that can contribute to operational land surface monitoring, either directly or as inputs (drivers or constraints) to land surface models. Solar radiation, in the form of fields of integrated daily solar horizontal exposure, is produced daily from MTSAT-1R visible-band data. A 17-year climatology of daily solar radiation has recently been produced by processing archived satellite data from 1990 to 2006, and will find application in agriculture, solar energy planning, building design, and surface energy balance studies. The Bureau is implementing operational production of Normalised Difference Vegetation Index (NDVI) and land surface temperature (LST) from AVHRR data using the Common AVHRR Processing System (CAPS) software developed by CSIRO, for use in applications that require national monitoring of vegetation condition. All of these products are produced on a 0.05° national grid: at least once per day for LST, daily for solar exposure, and weekly for NDVI. The AVHRR data products and solar exposure can together serve as near-real time continental inputs to systems for the assessment of surface moisture status across Australia, based either on simple surface energy balance models or more complex land surface models. The Australian Water Availability Project, a collaboration between the Bureau of Rural Sciences, CSIRO and the Bureau of Meteorology, is using such an approach with the data streams described to establish national monitoring of land surface water availability.

I.F. Grant (✉)

Space Based Observations Section, Bureau of Meteorology, Melbourne, VIC 3001, Australia
e-mail: i.grant@bom.gov.au

Introduction

The Bureau of Meteorology (the Bureau) maintains a network of satellite receiving stations which continuously acquires low resolution multispectral image data, with continental coverage of Australia, from polar orbiting and geostationary satellites. Data reception currently includes the Advanced Very High Resolution Radiometer (AVHRR) on board the US National Oceanic and Atmospheric Administration (NOAA) polar orbiting satellites and the imagers on Japan's MTSAT-1R and China's Fengyun-2C geostationary satellites. Several of the near-real time products that the Bureau derives from these satellites can serve as continuous data streams that can contribute to operational land surface monitoring, either directly or as inputs (drivers or constraints) to land surface models.

The Australian Water Availability Project (AWAP) is a collaboration of the Bureau of Rural Sciences, the Bureau of Meteorology and CSIRO which aims to establish a national capability for the monitoring of soil moisture and other components of the surface water balance. A better understanding of water availability will improve the management of natural resources, farms, water supply and ecosystems. The first phase of AWAP, which was conducted in 2004 and 2005, developed historical remote sensing and meteorological datasets with national coverage, and used these with a land surface water balance model to demonstrate the feasibility of monitoring water availability at the basin scale. The second phase of AWAP, being conducted over 2006 and 2007, is establishing a near real-time national water availability monitoring system. AWAP is working towards using the model within an assimilation scheme in order to make optimal use of the data. The contribution of the Bureau of Meteorology will include the establishment of near real-time satellite products: solar radiation from geostationary satellite data; and Normalised Difference Vegetation Index (NDVI) and land surface temperature from AVHRR.

This paper describes implementation details of these near-real time streams of satellite data products.

Solar Radiation

The Bureau produces daily fields of solar radiation on a 0.05° grid covering Australia, from geostationary satellite visible-band imager data. Specifically, the parameter is daily integrated global solar exposure, at the land surface, for a horizontal surface and over the full solar spectrum. Figure 1 shows an example. Production of each day's field is completed each evening. Applications include agriculture, solar energy planning, building design, and surface energy balance studies.

The primary data input for solar radiation is the hourly visible-band imagery from the MTSAT-1R geostationary satellite which is stationed over the equator at longitude 140° E and operated by the Japan Meteorological Agency (JMA). The data is received by the Bureau at Crib Point near Melbourne. The images have 1.25-km resolution at nadir. They are geolocated and calibrated using the information placed into the header of each image by JMA, then regridded to 0.01° and averaged to the final 0.05° grid.

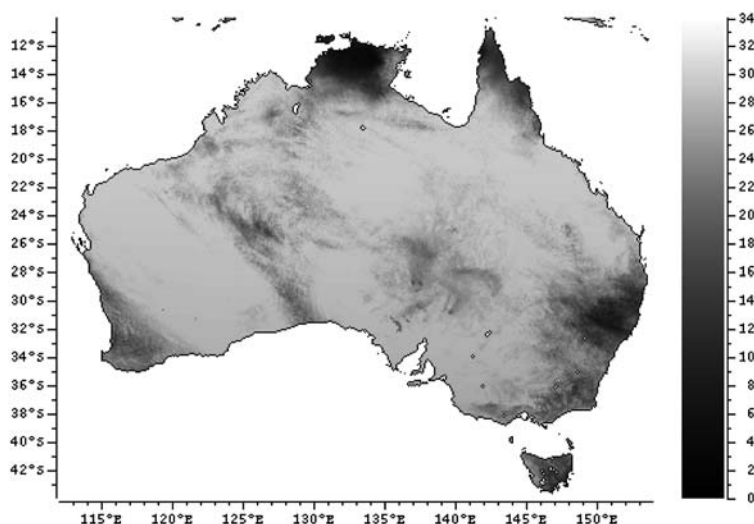


Fig. 1 Daily solar exposure derived from the MTSAT-1R visible band imager, in MJ m^{-2}

Instantaneous surface solar radiation (irradiance) is calculated for the time of each satellite image with a physical model that parameterises the important aspects of the atmospheric radiative transfer in two spectral bands, in the visible and near-infrared (Weymouth and Le Marshall 1999, 2001). The physical parameterisations are adapted to the spectral response characteristics of the MTSAT-1R imager. The model uses ancillary data on atmospheric composition. Total column water vapour amount is taken from the forecast field of the Bureau's numerical weather prediction model LAPS. Total column ozone amount is taken as a fixed function of latitude. The strongest factor controlling the surface radiation, after the solar zenith angle, is the cloudiness. At clear-sky locations, the satellite data is used to estimate the surface reflectance and this is used together with the atmospheric data to calculate the surface radiation. At cloudy locations, the satellite data are used to estimate the cloud-top reflectance, from which the cloud transmission is inferred. The cloud optical properties are used with the atmospheric data and the surface reflectance to calculate the surface radiation. The surface reflectance is estimated from preceding clear-sky conditions by compositing the calculated surface reflectances of the previous two months: at each grid point and each hour, the day at the twentieth percentile in brightness is selected as being cloud-free. The hourly surface irradiance estimates for each day are integrated to give a daily solar exposure value at each grid point. The accuracy of the satellite product is assessed, and biases removed, with surface-based observations from the Bureau's network of radiation sites, as described in more detail below.

The Bureau has produced a solar radiation product since 1990. The original software was in FORTRAN and stored results as McIDAS format files over 36 regions with varying resolutions. To improve the software flexibility and maintainability, and to enable the reprocessing of archived data, most of the software was recently

rewritten to use the NAP extension to the Tcl language, which was developed by CSIRO to manipulate gridded data (see <http://tcl-nap.sourceforge.net/>, Davies 2002). Product files are now a single grid in netCDF format.

The archive of the near-real time product that had been produced since 1990 constituted a historical solar radiation record that had large gaps and non-uniform quality due to the need to upgrade software when satellites changed and the associated delays. Therefore, a new 17-year record of daily solar radiation has recently been produced by reprocessing archived raw satellite data from 1990 to 2006 with the new software. The satellites used were, in sequence, GMS-4 and GMS-5, operated by JMA, GOES-9, operated by NOAA, and MTSAT-1R, operated by JMA. The model was adapted to the respective spectral response function of each satellite. The calibration derived by the International Satellite Cloud Climatology Project (ISCCP) was adopted, except for MTSAT-1R for which the prelaunch calibration was adopted. Total column water vapour amount was taken from the European (European Centre for Medium-Range Weather Forecasts, ECMWF, ERA-40) and US (National Centers for Environmental Prediction/National Center for Atmospheric Research, NCEP/NCAR, after August 2002) numerical weather reanalysis datasets. The resulting daily solar exposure values were compared with high quality surface observations, the majority coming from the Bureau's network of radiation sites since 1993. This permits the estimation of biases that result, for instance, from uncertainties in the satellite calibration and total water vapour amount. Each month of exposure grids was debiased by a single linear function of exposure, derived from the observations at all surface sites for all days in the month. Figure 2 compares the satellite and surface values for a typical month, before and after bias removal. For each month, the mean modulus of the daily difference from the surface observations was, after bias removal, generally in the range $0.8\text{--}1.5\text{ MJ m}^{-2}$. This is comparable with the value of 1.4 MJ m^{-2} quoted by

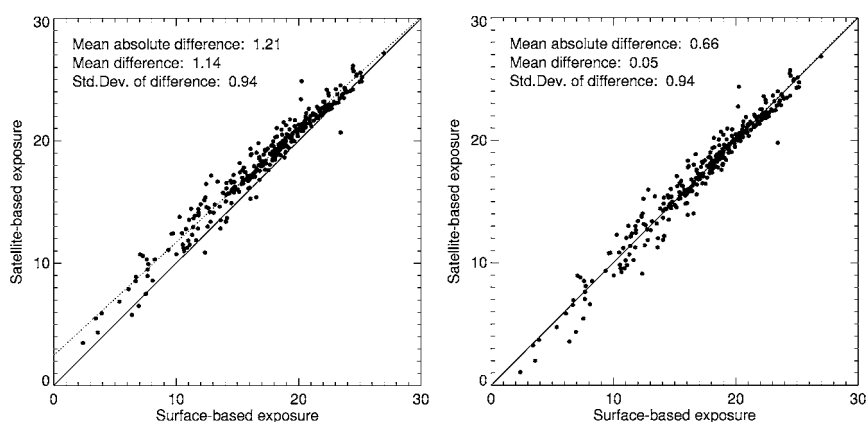


Fig. 2 Comparison of daily solar exposure derived from MTSAT-1R with surface observations, in MJ m^{-2} , before bias removal (*left*) and after (*right*)

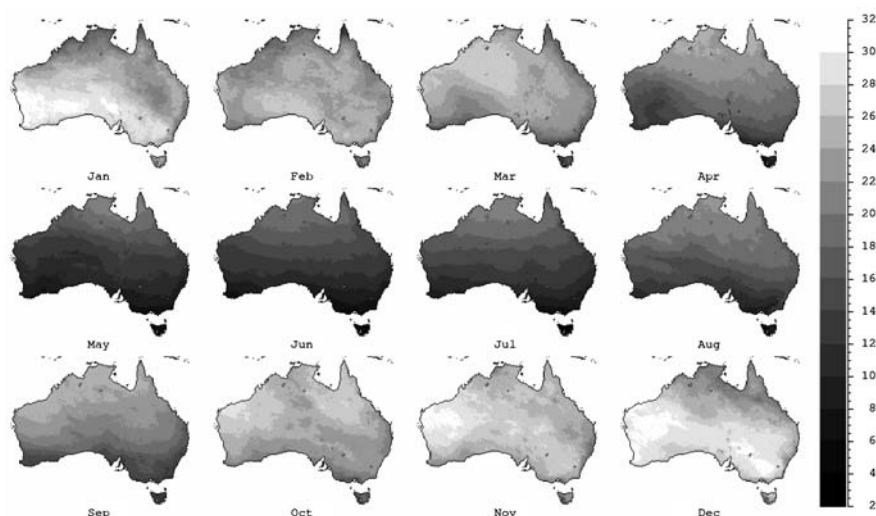


Fig. 3 Monthly means of daily solar exposure for 1997, in MJ m^{-2}

Weymouth and Le Marshall (2001) for the accuracy of the solar radiation system when they established it for GMS-5. Compared to the old record, the new record is more complete, is at a uniform resolution on a single grid, and is of more uniform quality, to the extent permitted by the raw data.

The long timeseries of daily exposure over the Australian continent is a resource for investigation of the climatology of solar exposure over the Australian continent. Figure 3 shows the twelve monthly means for 1997. While latitudinal effects dominate the spatial variation, and seasonal solar declination effects dominate the temporal variation, other features are evident, such as the low values in northern Australia during the monsoon (summer) period, and low values in Tasmania and along the eastern and south-eastern coast at some times of the year. Interannual variation may also be explored, with Fig. 4 showing that over 16 years there is marked variation between January means.

AVHRR Products

In addition to solar radiation, the AWAP requires streams of near-real time products derived from AVHRR satellite data. Within the AWAP, CSIRO is developing a Hydrological and Terrestrial-Biosphere Data Assimilation System (HTBDAS) to assimilate timeseries of NDVI (normalised difference vegetation index, a measure of vegetation greenness) and land surface temperature (LST). NDVI is derived from land surface reflectances in the red and near-infrared spectral bands that are measured by AVHRR as channels 1 and 2 respectively. LST may be estimated using the thermal window bands of AVHRR (channels 4 and 5).

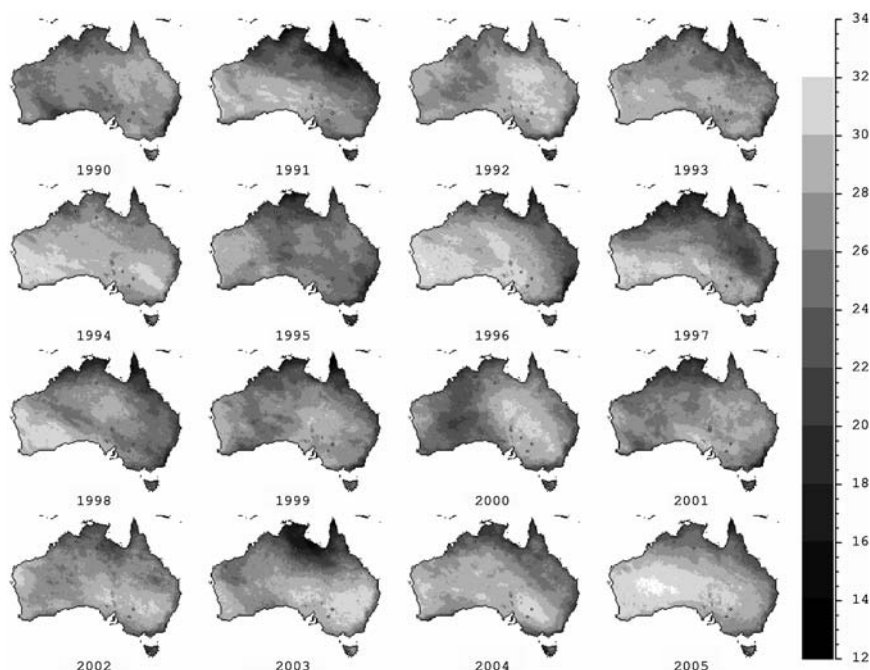


Fig. 4 Monthly mean of daily exposure for all Januaries from 1990 to 2005, in MJ m^{-2}

The Bureau of Meteorology acquires AVHRR data with national coverage daily, and is establishing the production of national fields of NDVI weekly, and LST at least daily. The following sections describe the details of the implementation.

Data Acquisition

The Bureau acquires raw AVHRR data in High Resolution Picture Transmission (HRPT) format from reception stations in Perth, Darwin and Alice Springs and near Melbourne. Data from all four stations is transferred in near-real time to the Bureau's Head Office in Melbourne, arriving within one hour of the satellite pass. Thus the Bureau maintains complete and timely national daily coverage by AVHRR. The next section describes the data processing common to all of the AVHRR products. Subsequent sections describe product-specific processing.

Generic Processing

The Bureau processes raw AVHRR data to the higher level products required by the AWAP with the Common AVHRR Processing System (CAPS) software developed by CSIRO and based on NAP (see <http://www.eoc.csiro.au/cats/caps/>, King 2003).

CSIRO used CAPS software to process its AVHRR archive into the CSIRO AVHRR Time Series (CATS) dataset, a version of which was used in the first phase of the AWAP.

Image geolocation is done by CAPS, using near-real time satellite orbital parameters generated by CSIRO in Hobart which are automatically downloaded hourly. The CAPS navigation has a demonstrated accuracy of better than 1 km.

Calibration is applied using CAPS. The calibration of the thermal channels (channels 3a, 4 and 5) derives from the on-board calibration measurements that are included in the HRPT data stream. The calibration coefficients for the reflective channels (channels 1 and 2) are taken from the monthly bulletins released by the National Environmental Satellite, Data, and Information Service (NESDIS) of the National Oceanic and Atmospheric Administration (NOAA) in the US.

The cloud mask implemented in CAPS, which is a modification of the CLAVR algorithm (Stowe et al. 1998), is being used initially. Each pass is gridded to a 0.01° latitude-longitude grid and sea masked.

AVHRR Reflectance Products

Reflectance measurements derived from AVHRR channels 1 and 2 are the basis for calculating NDVI. They can also form the basis for estimating surface albedo, a measure of land surface reflectance that considers the radiation in all incoming and outgoing directions, and McVicar and Jupp (2002) used channel 1 and 2 reflectances to estimate vegetation fractional cover. At present, only NDVI is produced, and it is calculated straightforwardly from top-of-atmosphere channel 1 and 2 reflectances ρ_1 and ρ_2 as

$$\text{NDVI} = (\rho_2 - \rho_1)/(\rho_2 + \rho_1). \quad (1)$$

A national NDVI grid is updated weekly by compositing the set of cloud-masked, gridded NDVI images for all passes within the previous 30 days by the maximum value composite method (Fig. 5).

Land Surface Temperature

Calibrated data from AVHRR channels 4 and 5 may be expressed as effective blackbody temperatures of the Earth scene, commonly referred to as brightness temperatures. CSIRO has adopted the algorithm of Sobrino and Raissouni (2000) to estimate LST as a function of channel 4 and 5 brightness temperatures and NDVI. For each daytime NOAA orbit, the Bureau will supply LST at the time of the overpass, calculated from the Sobrino algorithm. The LST map in Fig. 6 demonstrates the spatial coverage of a single NOAA orbit.

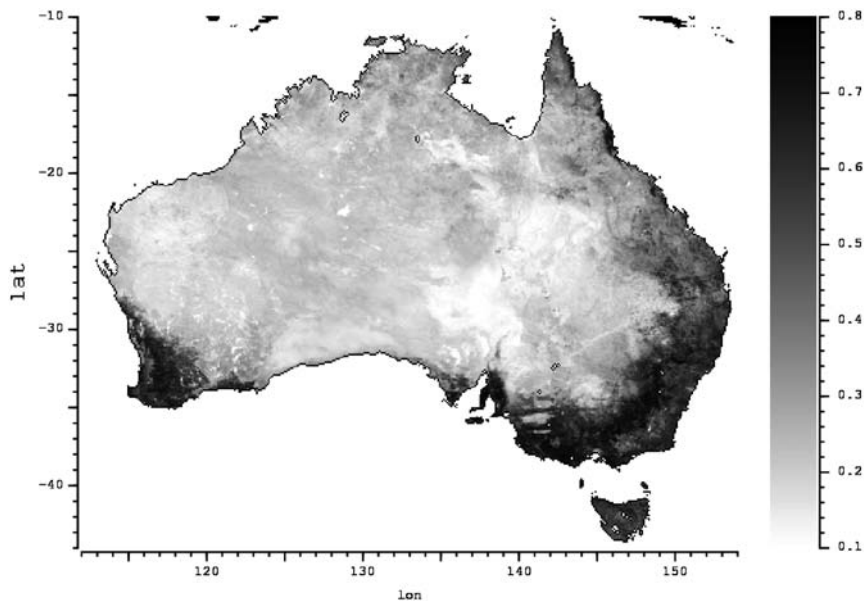


Fig. 5 30-day maximum value composite NDVI for September 2007, derived from NOAA-18

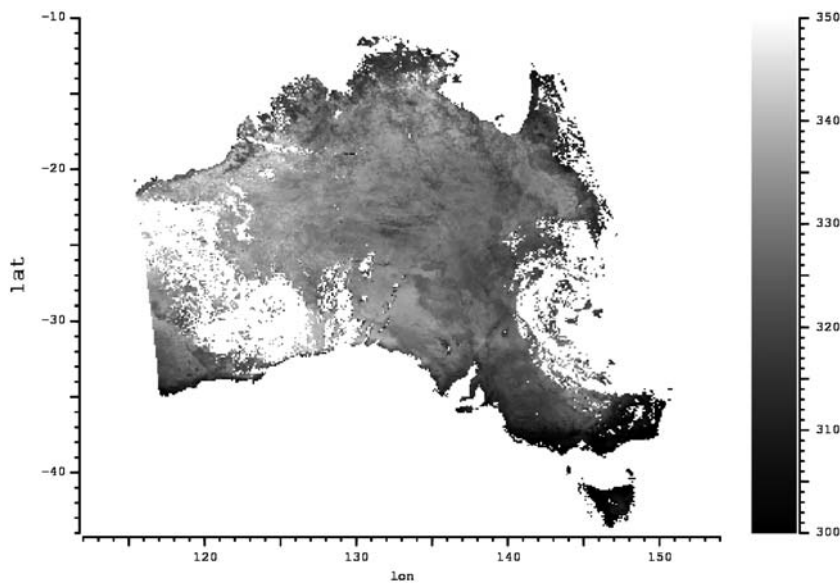


Fig. 6 Cloud-masked AVHRR LST from a NOAA-18 afternoon pass on 24 September 2007 at 0455 UTC, in K

Planned Improvements

CAPS aims to realise the consensus best processing practice of the Australian AVHRR supplier community. Research to improve the processing of moderate resolution polar orbiting sensors continues around the world, including for the venerable AVHRR, particularly because of its uniquely long data record. Once the baseline processing system described above is implemented, several potential improvements can be investigated.

On-orbit calibration of the AVHRR reflective bands is a difficult problem with a long history of research, much of it summarised several years ago in the CalWatch report by CSIRO (Mitchell 1999), which recommended preferred calibration methods and coefficients. Many methods have been developed and all have drawbacks. The NOAA/NESDIS monthly updates rely on the approach of Rao and Chen (1999) by assuming the invariance of a particular desert target – an assumption which has been shown to be invalid for some deserts at some times – and take about one year to establish for a new satellite. Thus new methods to calibrate channels 1 and 2 independently of the monthly updates from NOAA/NESDIS will be examined for possible implementation. Projects are being developed overseas to continuously intercalibrate AVHRR against other satellite instruments (for example, Minnis et al. 2002), and the results from these will be considered for operational use once they mature.

Land surface measurement from satellites requires effective cloud screening. Development of AVHRR cloud detection has continued since Stowe et al. (1998) introduced the CLAVR algorithm, and more recent alternatives will be investigated. A recent innovative approach is the CLAVR-X method, under development by NOAA/NESDIS (Heidinger et al. 2002), which sets spatially and temporally varying detection thresholds based on timely albedo measurements from satellites and surface temperature from a numerical weather prediction model.

However, the ultimate goal is to maximize the consistency of the reflectance products by applying a correction for the effect of the atmosphere, and normalising for the variation of land surface reflectance with sun and view directions. This will reduce the channel 1 and 2 measurements to land surface reflectance values that are, to first order, intrinsically characteristic of the land surface and independent of the atmospheric conditions and the satellite measurement process. The atmospheric effect depends on the amounts of water vapour and aerosol in the atmosphere, and the nature of the aerosol, all of which vary in space and time. The reflectance anisotropy of the surface depends on the land cover characteristics and may be characterised by an angular model with a small number of parameters, which vary spatially and temporally.

Surface reflectance for channels 1 and 2, corrected for atmospheric and angular effects, can be calculated using the existing CAPS software. An atmospheric correction is implemented in CAPS, based on the parameterisation of atmospheric radiative transfer developed by Mitchell and O'Brien (1993), and implemented in a fast form using look up tables by Dilley et al. (2000). The atmospheric correction

requires as inputs estimates of the amounts of water vapour and aerosol in the atmosphere. The total column water vapour at the time of the satellite pass will be taken from the Bureau's regional numerical weather prediction model (currently LAPS). The aerosol type and seasonally varying amount will be taken from the Global Aerosol Data Set (GADS) climatology (Koepke et al. 1997) that is built into CAPS. For the angular anisotropy model the Bureau will initially adopt the same seasonal climatology that CSIRO used, namely the one that has been implemented in CAPS and is based on data collected by the POLDER-1 satellite mission in 1996 and 1997.

The angular correction factors can differ from unity by tens of percent. Their interannual variation, for a particular AVHRR channel in a particular month, can exceed 10%, although the variation is less for NDVI. To improve the normalisation of reflectance anisotropy, a dynamic angular model can be derived by inverting an angular model (a model of the bidirectional reflectance distribution function, BRDF) against the AVHRR data within a sliding temporal window, following the methodology developed for the Moderate Resolution Imaging Spectroradiometer (MODIS) BRDF and albedo product MOD43 (Schaaf et al. 2002). An accurate albedo may also be efficiently derived from a dynamic angular model, again following the MODIS methodology, and using the conversion of (Liang et al. 1999) for AVHRR to convert channel 1 and 2 albedos to solar broadband albedos.

Grassland Curing Index (GCI) for southeastern Australia will also be produced for operational use in fire danger assessment and fire management planning. This will be derived from NDVI by the algorithm that was developed by CSIRO in collaboration with the Victorian Country Fire Authority (Barber 1989; Paltridge and Barber 1988) and implemented in the software system (Dilley and Edwards 1998) that the Bureau adopted in 2001 for operational production of GCI. The Bureau is a partner in a Bushfire Cooperative Research Centre Project to improve the satellite based assessment of curing and extend it, robustly and validated, throughout Australia and New Zealand.

AVHRR stands out among low resolution multispectral sensors as providing a record of over twenty years that can be used to calibrate land surface models and provide context for current observations. However, several advanced polar orbiting research sensors that have operated over the last several years, such as MODIS, AATSR, SeaWiFS and SPOT-VGT have more spectral bands, bands that are better positioned to avoid atmospheric contamination, and better calibration. Therefore, these sensors offer more accurate and consistent products, such as NDVI (Huete et al. 2002; Brown et al. 2005; Miura et al. 2006) and LST (Wan et al. 2004), than does AVHRR. Moreover, the multiplicity of overpass times of several of these sensors taken together offers more frequent temporal sampling through the strong diurnal cycle of LST. CSIRO has begun implementation of these diverse sources of LST in the development of its modelling system, and the Bureau will begin generating MODIS products in parallel with its AVHRR products when its real-time MODIS reception network is established.

Conclusions

The Bureau of Meteorology is developing several near-real time continental data products from its streams of AVHRR and geostationary data that will be useful for rapid national land monitoring. These are daily solar radiation and land surface temperature, and weekly NDVI. The Australian Water Availability Project has motivated the establishment of these product streams, and will use these, together with streams of meteorological data supplied by the Bureau, with a land surface model to enable national monitoring of water availability. Besides their synergistic use in AWAP, the satellite land products can serve other environmental management applications.

There is potential to enhance these products further in future. Solar radiation and LST at sub-diurnal resolution are potentially available, after some development, from geostationary data. The Bureau is rolling out an X-band reception network, with mainland stations near Darwin and Melbourne, that with the existing Western Australian Satellite Technology and Applications Consortium (WASTAC) station in Perth will give the Bureau access to near-real time data from MODIS and other advanced imagers. This offers the prospect of improving the quality of the NDVI and LST products, and developing new products.

References

- Barber J (1989) Remote sensing strategies for monitoring grassland fire fuels. Ph.D. thesis, University of Melbourne
- Brown ME, Pinzon JE, Morisette JT, Didan K, Tucker CJ (2005) Evaluation of the consistency of long-term NDVI time series derived from AVHRR, SPOT-Vegetation, SeaWiFS, MODIS, and Landsat ETM+ sensors. *IEEE Trans Geosci Remote Sens* 44:1787–1793
- Davies HL (2002) The NAP (N-Dimensional Array Processor) extension to Tcl. In: Ninth Annual Tcl/Tk Conference, http://tcl-nap.sourceforge.net/nap_paper2002.pdf
- Dilley AC, Edwards M (1998) The automatic processing of ASDA format NOAA HRPT data at CSIRO DAR. Internal Paper 6, CSIRO Division of Atmospheric Research, Aspendale, Australia
- Dilley AC, Edwards M, O'Brien DM, Mitchell RM (2000) Operational AVHRR processing modules: Atmospheric correction, cloud masking and BRDF compensation. Internal Paper 14, CSIRO Division of Atmospheric Research, Aspendale, Australia
- Heidinger AK, Venkata RA, Dean C (2002) Using MODIS to estimate cloud contamination of the AVHRR record. *J Atmos Ocean Technol* 19:586–601
- Huete AR, Didan K, Muiira T, Rodriguez EP, Gao X, Ferreira LG (2002) Overview of the radiometric and biophysical performance of the MODIS vegetation indices. *Remote Sens Environ* 83:195–213
- King EA (2003) The Australian AVHRR data set at CSIRO/EOC: Origins, processes, holdings and prospects. Report 2003/32, CSIRO Atmospheric Research, Canberra, Australia
- Koepke P, Hess M, Schult I, Shettle EP (1997) Global aerosol data set. Report 243, Max-Planck Institut für Meteorologie, Hamburg, Germany
- Liang S, Strahler AH, Walthall C (1999) Retrieval of land surface albedo from satellite observations: A simulation study. *J Appl Meteor* 38:712–725
- McVicar TR, Jupp DLB (2002) Using covariates to spatially interpolate moisture availability in the Murray-Darling basin: A novel use of remotely sensed data. *Remote Sens Environ* 79:199–212

- Minnis P, Nguyen L, Doelling DR, Young DF, Miller WF, Kratz DP (2002) Rapid calibration of operational and research meteorological satellite imagers. Part I: Evaluation of research satellite visible channels as references. *J Atmos Ocean Technol* 19:1233–1249
- Mitchell RM (1999) Calibration status of the NOAA AVHRR solar reflectance channels: CalWatch revision 1. Technical paper 42, CSIRO Atmospheric Research, Aspendale, Australia
- Mitchell RM, O'Brien DM (1993) Correction of AVHRR shortwave channels for the effects of atmospheric scattering and absorption. *Remote Sens Environ* 46:129–145
- Miura T, Huete A, Yoshioka H (2006) An empirical investigation of cross-sensor relationships of NDVI and red/near-infrared reflectance using EO-1 hyperion data. *Remote Sens Environ* 100:223–236
- Paltridge GW, Barber J (1988) Monitoring grassland dryness and fire potential in Australia with NOAA/AVHRR data. *Remote Sens Environ* 25:381–394
- Rao CRN, Chen J (1999) Revised post-launch calibration of the visible and near-infrared channels of the Advanced Very High Resolution Radiometer (AVHRR) on the NOAA-14 spacecraft. *Int J Remote Sensing* 20:3485–3491
- Schaaf CB et al. (2002) First operational BRDF, albedo and nadir reflectance products from MODIS. *Remote Sens Environ* 83:135–148
- Sobrino JA, Rassouni N (2000) Toward remote sensing methods for land cover dynamic monitoring: Application to Morocco. *Int J Remote Sensing* 21:353–366
- Stowe LL, David PA, McClain EP (1998) Scientific basis and initial evaluation of the CLAVR-1 global clear/cloud classification algorithm for the Advanced Very High Resolution Radiometer. *J Atmos Ocean Technol* 16:656–681
- Wan Z, Zhang Y, Zhang Q, Li Z-L (2004) Quality assessment and validation of the MODIS global land-surface temperature. *Int J Remote Sensing* 25:261–274
- Weymouth GT, Le Marshall JF (1999) An operational system to estimate global solar exposure over the Australian region from satellite observations 1. Method and the initial climatotomy. *Aust Meteor Mag* 48:181–195
- Weymouth GT, Le Marshall JF (2001) Estimation of daily surface solar exposure using GMS-5 stretched-VISSR observations: The system and basic results. *Aust Meteor Mag* 50:263–278

Recent and Future Developments in Meteorological Remote Sensing

D.C. Griersmith, I.F. Grant, A.G. Rea, and M.C. Willmott

Abstract Satellite-based remote sensing for meteorological and climate applications is a global enterprise, and is on the threshold of a generational increase in the capability and data volumes of sensors on polar orbiting meteorological satellites. This paper will describe, in the global context, the recent achievements and plans of the Australian Bureau of Meteorology (the Bureau) to continue to develop its capability to acquire and process near-real time satellite data for the Australian region, complementing its surface based observing system.

The Bureau continues to acquire data with national coverage from the polar orbiting US National Oceanic and Atmospheric Administration (NOAA) satellites, distributing both imagery and derived products from the Advanced Very High Resolution Radiometer (AVHRR) and the Advanced TIROS Operational Vertical Sounder (ATOVS) sensor suite for atmospheric sounding. The Bureau is rolling out a network of X-band receiving stations to complement the existing Australian stations in preparation for the new generation of sensors on the US National Polar-orbiting Operational Environmental Satellite System (NPOESS), NPOESS Preparatory Project (NPP) and European MetOp satellites.

The recent successful launches of Japan's MTSAT-1R and MTSAT-2 and China's Fengyun-2C and Fengyun-2D geostationary satellites have secured the supply of hourly multispectral imagery in Australia's region. In addition to the continuing production of satellite-derived solar radiation and atmospheric motion vectors, work is underway to characterise the calibration of these sensors and to derive new, high temporal resolution products including sea surface temperature and fog.

There is an emerging global trend towards rapid exchange of regional data for assimilation into numerical weather forecasting systems. The Bureau coordinates, and has been an early participant in, the Asia-Pacific Regional ATOVS Retransmission Service (AP-RARS) which enables routine rapid exchange over the internet of ATOVS atmospheric sounding information between centres in the Asia-Pacific region. The European forerunner of RARS, EARS, has expanded to include

D.C. Griersmith (✉)

Space Based Observations Section, Bureau of Meteorology, Melbourne, VIC 3001, Australia
e-mail: d.griersmith@bom.gov.au

other datasets, and to include regional dissemination by satellite broadcast, and such enhancements are being considered for RARS.

The Bureau increasingly collaborates with other Australian agencies in the provision of satellite-based services. Examples are the planned provision of Bureau data layers to the *Sentinel* fire management website hosted by Geoscience Australia, the Bureau's supply of satellite-based sea surface temperature to the BLUElink collaboration between the Bureau, Australia's Commonwealth Scientific and Industrial Research Organisation (CSIRO) and the Royal Australian Navy, and the exchange and shared development of CSIRO's Common AVHRR Processing Software (CAPS) software for processing satellite data.

Introduction

The Australian Bureau of Meteorology (the Bureau) acquires a range of satellite data, from both local and indirect reception, in support of its services to the Australian public. Other national meteorological and hydrological services (NMHSs) around the world have similar requirements for satellite data to support similar services. Because the weather and climate system is intrinsically global in nature, there are well established international systems to coordinate the reception, processing and exchange of satellite data products. These arrangements are evolving rapidly to accommodate the impending generational increase in the capability and data volumes of sensors on polar orbiting meteorological satellites. This paper will describe the current international trends in usage of satellite data for meteorological purposes, highlighting the activity at the Australian Bureau of Meteorology. These trends, described in the remainder of this section, suggest a possible future paradigm for the utilisation of near-real time continental scale satellite data in the Australian region for all applications.

The trends are:

Transition from L-band to X-band: Satellites downlinking at L-band are being phased out and replaced by X-band advanced satellites which can transmit at higher data rates. The most important polar orbiting L-band meteorological satellite system, namely the US NOAA (National Oceanic and Atmospheric Administration) series, is being replaced with the MetOp system and the upcoming National Polar-orbiting Operational Environmental Satellite System (NPOESS). MetOp is the European polar orbiting meteorological satellite system, with transmission at six times conventional data rates. The first MetOp satellite was launched in October 2006 but its direct broadcast capability failed shortly after. NPOESS is the US equivalent which merges two hitherto separate satellite series, namely NOAA civilian polar orbiters and the US Department of Defense DMSP (Defense Meteorological Satellite Program) polar orbiters. The precursor NPP (NPOESS Preparatory Project) satellite is planned to be launched in 2009. In addition, China's Fengyun-1 polar orbiters are being replaced by an advanced Fengyun-3 series at X-band, the first of which was launched in 2008. Overall, for the next decade there will be a transition period with both L-band and X-band systems, with a shift towards direct transmission only at X-band.

Synergy of multiple sensors: Increasingly, satellite data assimilation and processing is being done synergistically by integrated processing of data combined from multiple sensors. For many years, the capability to assimilate satellite data has been central to state-of-the-art numerical weather prediction (NWP) systems. More recently, it has become apparent that far better impact and product quality from advanced satellite data is now being obtained by processing data from multiple sensors synergistically. For example, rather than process Advanced Infrared Sounder (AIRS) atmospheric sounder data on its own, processing suites now combine AIRS data with that from the Moderate Resolution Imaging Spectroradiometer (MODIS) plus the Advanced Microwave Sounding Unit (AMSU), an advanced humidity sounder, all of which are on board the Aqua platform. In this way, data usage is improved, especially in partly cloudy and cloudy areas. Also, the better spatial resolution of MODIS (0.25–1 km) compared with AIRS (14 km) allows far better cloud clearing, leading to higher quality radiances for NWP assimilation. The whole is greater than the sum of the parts.

Composite observing systems: There is a growing trend towards better integration of multiple observing technologies, enabling the creation of composite observing systems which are cost effective, provide redundancy and which are more adaptive and flexible in meeting the needs of NMHSs. An example is the use of advanced satellite sounder data to complement radiosonde, surface-based wind profiler and aircraft data. It is now commonly recognised that the greatest positive impact of data on NWP comes from considering and managing multiple data types as an integrated, composite whole. Those data types include multiple advanced satellite sensor data, complementary ground-based conventional data (for example, from radiosonde, aircraft or ships), and new satellite data types such as MODIS polar winds, Global Positioning System (GPS) total precipitable water, and GPS Occultation soundings.

Rapid data exchange: The need of NWP models, including regional models, for non-local data has motivated the recent establishment of systems for the rapid exchange of meteorological satellite products across each of the European, North American and Asia-Pacific regions. These are initially using surface telecommunication networks, and will eventually transition to satellite rebroadcast.

The following sections describe current and planned satellite activity at the Bureau in the context of these trends.

Polar Orbiting Satellite Data

The Bureau of Meteorology continues to acquire data with national coverage from the polar orbiting NOAA satellites, distributing both imagery and derived products from the AVHRR (Advanced Very High Resolution Radiometer) and the ATOVS (Advanced TIROS Operational Vertical Sounder) sensor suite for atmospheric sounding. Data from China's Fengyun-1 is also received routinely.

NOAA and Fengyun-1 data is received via a network of L-band receiving stations across the continent (Melbourne, Darwin, Perth and Alice Springs) and in Antarctica. Data received on the mainland is transmitted to Head Office (Melbourne)

immediately after completion of reception of the pass. Transfers are conducted using the Bureau's dedicated communications network, WeatherNet. Once a full pass is received in Melbourne, it is processed into products for use in operations.

AVHRR data is distributed as cloud imagery, and processed into products including fog and low cloud, volcanic ash, sea surface temperature, Normalised Difference Vegetation Index (NDVI), and Grassland Curing Index (GCI).

ATOVS Atmospheric Sounder

Modern weather forecasting relies heavily on global and regional computer-based modelling of the atmosphere system driven by observations: numerical weather prediction (NWP). A key data source for the Bureau's weather services is ATOVS data from the NOAA satellites, which carries information on the vertical profiles of temperature and humidity through the atmosphere and is assimilated into the Bureau's NWP models. Timeliness is critical to meet the cut-off times of NWP model runs.

The ATOVS data are extracted from the High Resolution Picture Transmission (HRPT) full pass data from the NOAA satellites that is transferred to head office in near-real time for processing with the internationally standard ATOVS and AVHRR Pre-processing Package (AAPP). Fig. 1 shows the regional coverage of ATOVS

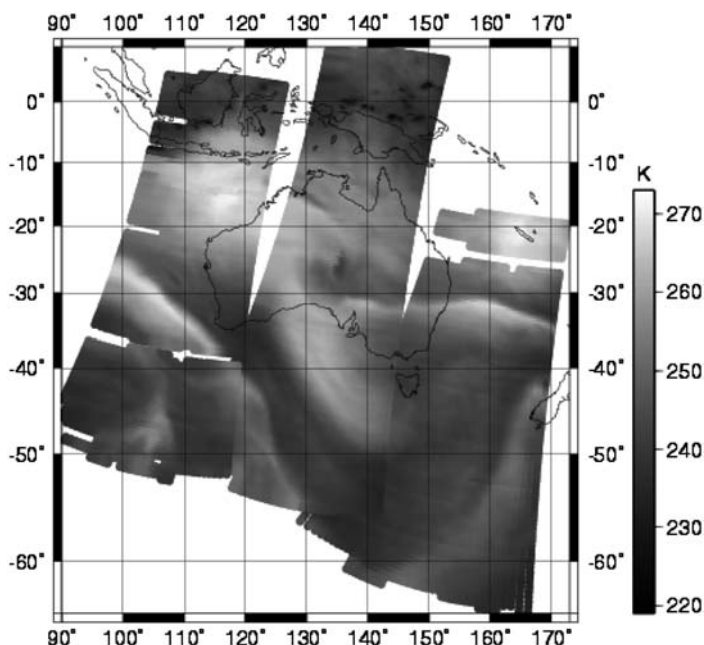


Fig. 1 HIRS channel 1 brightness temperatures for the NOAA-17 orbits received at Melbourne, Darwin and Perth during the daytime on 11 May 2007

data afforded by the Bureau's network, as illustrated by one channel of the High Resolution InfraRed Sounder (HIRS) instrument of the ATOVS suite.

The transfer of a pass from Darwin to Melbourne takes 15 min, on average, with 90% of passes received within 16 min. From Perth, the average transfer time is 13 min, with 90% of passes received within 17 min. Processing through AAPP typically takes another five minutes.

X-Band Network

The Bureau is currently rolling out a network of X-band receiving stations to complement the existing Australian stations in preparation for the new generation of NPP, NPOESS and Fengyun-3 satellites. The Bureau is part of the Western Australian Satellite Technology and Applications Consortium (WASTAC) which already operates an X-band station in Perth. A Bureau station near Melbourne commenced operation on a test basis in late 2008. Installation of two further Bureau stations, near Darwin and at Casey, Antarctica, is planned for completion in early 2009. The coverage of the complete network is shown in Fig. 2.

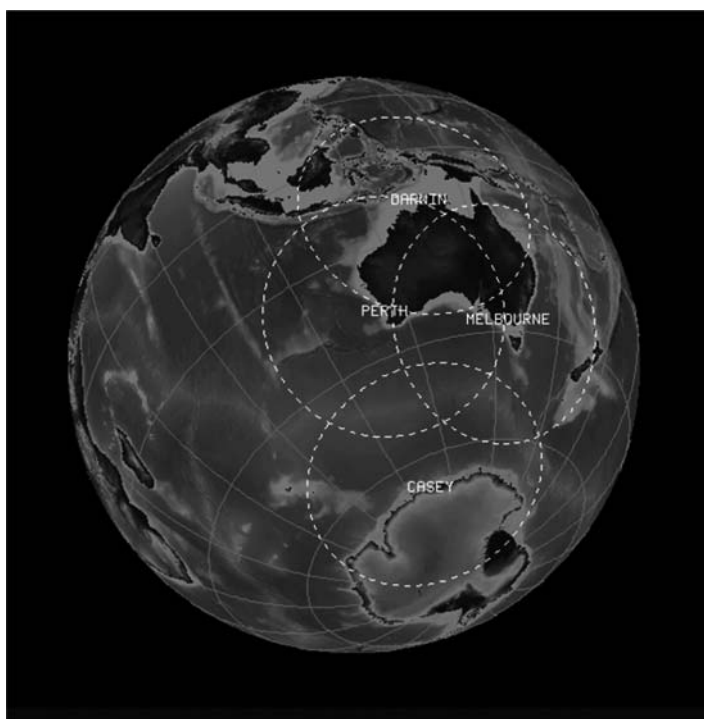


Fig. 2 Coverage from the Bureau's planned X-band network, including the WASTAC consortium station in Perth

A key output from the Bureau's X-band reception will be the delivery of MODIS products to the Bureau's regional forecasting offices: true colour imagery, false colour images created from bands that emphasise atmospheric features of interest, and level 2 products such as atmospheric stability indices, total water vapour and cloud properties. To optimise timeliness and minimise data transfer volumes, each reception site includes a MODIS data processing system to generate high-level products for rapid distribution.

Advanced Atmospheric Sounders

Over the next two years, as the Bureau upgrades its NWP systems under the Australian Community Climate and Earth System Simulator (ACCESS) project, there will be a requirement for more satellite data, both from local reception and indirect sources. Key locally received data sources will be the advanced sounders carried by the new generation of polar orbiters, initially AIRS on Aqua and the Infrared Atmospheric Sounding Interferometer (IASI) on MetOp, which provide vertical profiles of temperature and moisture and many other geophysical parameters.

The first advanced sounder to provide data was AIRS on board NASA's Aqua satellite, which was launched in 2002. While HIRS on the NOAA satellites makes measurements in 19 spectral bands, AIRS measures radiation in 2378 bands which, whilst individually still a broad layer measurement, may be combined to provide significantly higher vertical resolution. Temperature profiles from the AIRS instrument have errors around 1 K in a 1 km layer, and moisture errors are about 10–20% in layers 2 km thick, while water vapour profiles have better than 10% rms errors under clear and partially cloudy conditions. By comparison, radiosondes have temperature errors around 1 K and moisture errors around 5%.

While satellite data like that from AIRS is becoming comparable to radiosonde data in terms of uncertainties, the satellite data spatial and temporal coverage is orders of magnitude better than what is possible with any radiosonde or ground-based network. It has been demonstrated that the skill of numerical weather prediction models is very significantly improved by the introduction of AIRS data.

The advanced sounders that follow AIRS include the 8000-channel IASI on MetOp, launched in 2006, the Cross-track Infrared Sounder (CrIS) hyperspectral sounder on NPP and NPOESS, and China's suite of infrared and microwave sounding instruments on the FY-3 series, starting in 2008.

Geostationary Satellite Data

The imagers on the geostationary meteorological satellites stationed over the equator supply high temporal resolution multispectral imagery of Australia's region. The Bureau of Meteorology directly receives data from Japan's MTSAT-1R (at 140°

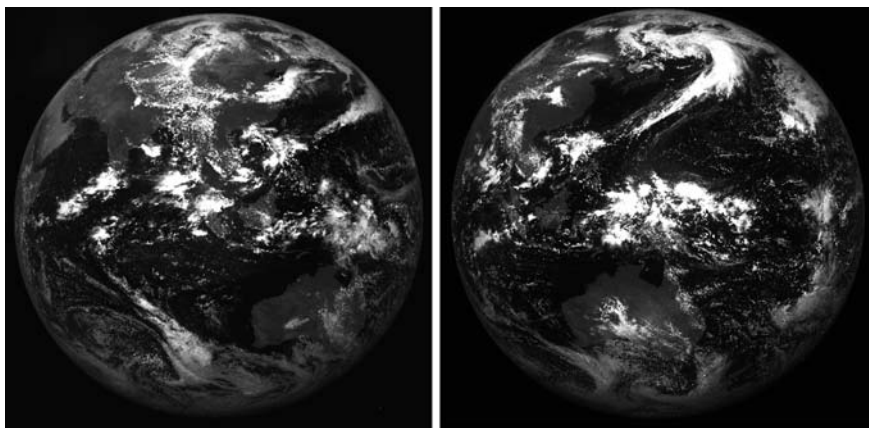


Fig. 3 Visible-band whole Earth disk images from the geostationary satellites Fengyun-2C at longitude 105°E (*left*) and MTSAT-1R at 140°E (*right*)

East) and China's Fengyun-2C and -2D (at 105° East and 86.5° East, respectively), both of which provide images at least hourly (Fig. 3). For the purposes of redundancy and to reduce communications costs, geostationary reception systems are located in Melbourne, Darwin, Perth and Sydney. These stations all receive data from MTSAT-1R. Data from Fengyun-2C and -2D is received in Melbourne. Due to its position over the eastern Indian Ocean, Fengyun-2C is very useful for forecasts and warnings in Western Australia. MTSAT-2 is now in orbit to provide standby back-up to the MTSAT-1R imager.

Both MTSAT-1R and Fengyun-2C have five channels: visible (0.63 μm), mid-infrared (3.7 μm), water vapour (6.8 μm) and thermal split window (11 μm and 12 μm). Data from both satellites is used as imagery in forecasting operations, and for the generation of derived products such as atmospheric motion vectors – estimated from the automatic tracking of clouds between images – and daily insolation. The Bureau has developed products with sub-diurnal resolution from MTSAT-1R, such as sea surface temperature in collaboration with NOAA, and fog and low cloud, the mapping of which is critical for aviation efficiency. The Bureau is working to better characterise the calibration of these sensors.

Data Exchange

Regional ATOVS Retransmission Service

There is a global trend towards rapid exchange of regional data for assimilation into numerical weather forecasting systems. The European ATOVS Retransmission Service (EARS) was initially established to exchange ATOVS products for the

European region in near-real time over surface telecommunications networks, but has grown rapidly and evolved considerably:

- it has expanded its data scope to delivering AVHRR data on an operational basis within 10 min using line-by-line processing at multiple HRPT stations. Data from multiple stations is combined, with the stitched product sent to users being comprised of the lines most rapidly received at the uplink central processing station; and
- it is supporting Advanced Scatterometer (ASCAT) and IASI data from MetOp on a pilot basis; and
- it is now using secondary satellite broadcast by uplinking products to a communications satellite which then rebroadcasts to a broad user region.

The Asia-Pacific Regional ATOVS Retransmission Service (AP-RARS) has been established, under coordination by the Bureau of Meteorology, to implement the EARS concept in a region that includes Australia. The Bureau routinely sends processed ATOVS data from its Perth, Darwin, Melbourne and Davis (Antarctica) stations, as well as from Townsville, Singapore and New Zealand, to Japan, where it has been successfully assimilated into NWP models with positive impact. Data originating from China, Hong Kong, Japan and South Korea has been received in Melbourne via Japan.

Advanced Dissemination Methods

While AP-RARS currently uses the meteorological Global Telecommunications System, in the future telecommunications satellite broadcast of data is planned. China leads the provision of C-band Digital Video Broadcasting – Satellite (DVB-S) broadcast services over the Asia-Pacific Region with its FengyunCast system. This dissemination concept, which was pioneered by EUMETCast in Europe, has the potential to revolutionise the rapid distribution of satellite products. It promises users near-real time access to a large range of raw data and derived products from numerous satellites by means of modest-sized fixed antennas.

Interagency Collaboration

The Bureau of Meteorology increasingly collaborates with other Australian agencies in the provision of satellite-based services. This section describes several examples.

The Bureau supplies satellite-based sea surface temperature (SST), from both local and overseas reception, to the BLUElink collaboration between the Bureau, Australia's Commonwealth Scientific and Industrial Research Organisation (CSIRO) and the Royal Australian Navy. BLUElink is developing an ocean

forecasting system, and SST is a key input to the underpinning oceanographic model. Work is underway to blend the SST the Bureau produces from locally received AVHRR data with externally sourced global SST products from AVHRR, the Advanced Along-Track Scanning Radiometer (AATSR) and the Advanced Microwave Scanning Radiometer for EOS (AMSR-E, on Aqua), in order to produce a blended SST that benefits from the strengths of each dataset. Geostationary satellites can resolve the diurnal variation of sea surface temperature, and in 2007 the Bureau, in collaboration with NOAA, established a system to derive sea surface temperature from MTSAT-1R data.

The Australian Water Availability Project is a collaboration between the Bureau of Rural Sciences (BRS), the Bureau of Meteorology and CSIRO to establish a national capability to monitor soil moisture and other components of the land surface water balance. Historical datasets have been generated, and a prototype operational monitoring system has been running since 2007. The Bureau contributes historical and near-real time streams of meteorological data and satellite-derived products, CSIRO the modelling and historical satellite data, and BRS the coordination, end product delivery and interface with users. The satellite streams from the Bureau of Meteorology include daily solar radiation derived from geostationary satellites, and weekly NDVI and per-orbit land surface temperature from AVHRR.

The Bureau works with other agencies in supporting bushfire management. Mapping the annual curing (senescence and drying) of grassland is critical for fire danger rating and fire management planning, and the Bureau, CSIRO and RMIT University are partnered, through a Bushfire Cooperative Research Centre project, to develop a robust and validated satellite-based assessment of grassland curing applicable across Australia and New Zealand. The Bureau provides meteorological data layers to the Sentinel fire management website, which was created by CSIRO and is now hosted and developed by Geoscience Australia.

These examples demonstrate that in many cases satellite data delivers value to users not directly through derived satellite products but as input to a system that delivers the information the user needs.

The Bureau has also contributed to the CSIRO's development of the Common AVHRR Processing Software (CAPS) package, notably CAPS code which is under development to dynamically derive a reflectance anisotropy (bidirectional reflectance distribution function, BRDF) model from AVHRR data.

Conclusions

The Australian Bureau of Meteorology continues to develop its systems for the reception and processing of polar orbiter and geostationary satellite data in support of its weather, climate and other services. The Bureau is currently developing a capability to deliver products from MODIS and advanced sounders. In many cases, the value of new satellite data and products will be delivered to end users in partnership with, or through the higher level data systems of, other agencies.

National meteorological services in the Asia-Pacific region are working towards a regional system, under the auspices of the World Meteorological Organisation, for coordinated:

- direct reception, such as at X-band;
- processing, such as calibration and navigation, and archive;
- applications;
- distribution and on-line access;
- research, development and training; and
- rapid data exchange, as is being pioneered by RARS.

The Bureau will contribute as a supplier and distributor of low-level data and higher level products. In servicing the satellite data requirements of the Bureau's programs, the balance between local reception and regional and global access will be driven by user needs, security of access, satellite constraints (Direct Broadcast versus onboard storage), and operator constraints (availability of near-real time products).

The EARS and RARS systems, in conjunction with local reception, address time-liness issues for NWP by enabling satellite data to be available for assimilation within model cutoff times. It is important to remember, however, that the mere existence of this retransmission concept and its manifestation and success in Europe and North America is evidence that local reception is needed to meet many user needs, such as those of advanced NMHSs such as the Bureau. The RARS concept is a significant innovation that points to a possible future in which a large range of near-real time satellite data and products is accessible to users with modest receiving infrastructure.

Improved Spatial Resolution of Fire Detection with MODIS Using the 2.1 μm Channel

Florian Goessmann, Stefan W. Maier, and Mervyn J. Lynch

Abstract Since the first Moderate Resolution Imaging Spectroradiometer (MODIS) instrument on board the Terra satellite started collecting data in February 2000, the detection of active fires was one of the initial applications. The algorithms used to detect active fires with MODIS that are used in production (Giglio et al., 2003a; Kaufman and Justice, 1998; Kaufman et al., 1998) are based on algorithms developed for Advanced Very High Resolution Radiometer (AVHRR) and the Visible and Infrared Scanner (VIRS) (Flasse and Ceccato, 1996; Giglio et al., 1999; Giglio et al., 2003b; Giglio et al., 2000; Justice et al., 1996; Lee and Tag, 1990; Li et al., 2000) that exploit the difference in spectral response of a hot target in the middle (MIR) and thermal (TIR) infrared.

The MODIS channels typically used for this task, out of the 36 channels MODIS provides, are the 3.7 μm channel, which is available as a high gain channel (21) and low gain channel (22) to cover the MIR and the 11 μm channel (31) in the TIR range. Both these channels have a native spatial resolution of 1 km.

In this work, we will give an overview of the possibilities in regards to improving the spatial resolution of fire detection from MODIS data by utilizing the 2.1 μm channel (7), which is available at 500 m resolution. This channel has been mentioned in the literature (Chuvieco, 1999; Kaufman and Justice, 1998) as being potentially useful for the detection of fires, but its application has not been further investigated before.

Introduction and Method

According to Wien's Displacement Law,

$$\lambda_{\text{max}} = \frac{2.898 \times 10^{-13} k \cdot m}{T} \quad (1)$$

F. Goessmann (✉)

Remote Sensing and Satellite Research Group, Department of Imaging and Applied Physics, Curtin University of Technology, Perth, WA 6845, Australia
e-mail: Florian.Goessmann@Postgrad.curtin.edu.au

where:

λ^{\max} = wavelength of maximum radiation, m

T = temperature of blackbody, K

blackbodies of typical wildfire temperatures ranging from 600 K for smoldering fires to about 1200 K for flaming fires (Kaufman and Justice, 1998; Wooster et al., 2003) have an emission maxima at 4.8 and 2.4 μm respectively. The 2.1 μm channel of MODIS is therefore well placed to observe actively flaming fires but has only very limited capabilities to locate smoldering fires. Kaufman and Justice (1998) attest the 2.1 μm channel to be very sensitive to fires of 1000 K and above.

Fire detection using the 2.1 μm channel of MODIS is based on a high change in observed reflectance compared to the expected reflectance for each pixel, as shown in Fig.1. An overview of all channels used in the proposed methodology can be found in Table 1.

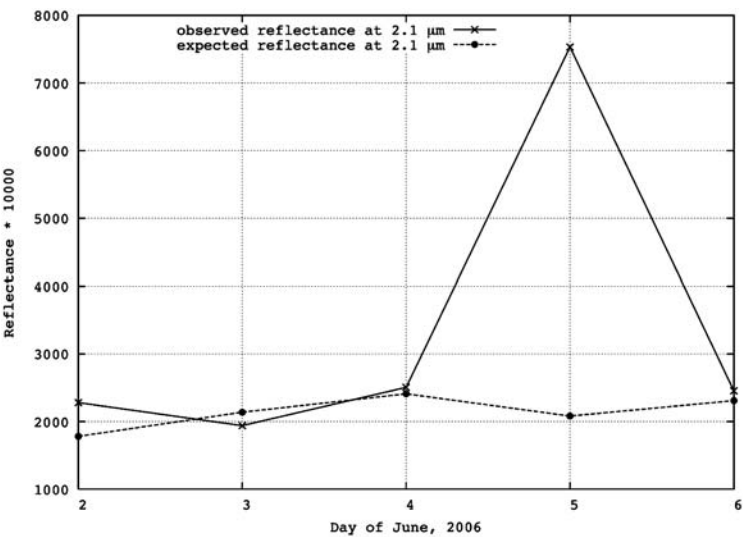


Fig. 1 Observed and expected reflectance of the 2.1 μm channel of MODIS for a pixel centered at 127.841° east and -20.176° north before, during and after a fire from June 2 to 6 2006

Table 1 MODIS channels used in fire detection

| Channel number | Centre wavelength (μm) | Purpose |
|----------------|-------------------------------------|-----------------------|
| 1 | 0.65 | Cloud masking |
| 2 | 0.86 | Cloud masking |
| 5 | 1.24 | False alarm rejection |
| 7 | 2.1 | Active fire detection |
| 31 | 11.0 | Cloud masking |

Apparent Reflectance

As reflectance values are calculated from the radiances measured by the sensor, the retrieved reflectance value of a pixel containing an active fire is not its spectral reflectance $\rho(\lambda)$ as defined by

$$\rho(\lambda) = \frac{L_R(\lambda)}{E^0(\lambda)\pi} \times 100 \quad (2)$$

where:

$E^0(\lambda)$ = irradiance at object

$L_R(\lambda)$ = reflected radiance,

but the apparent reflectance $\rho_a(\lambda)$ defined as,

$$\rho_a(\lambda) = \frac{L_R(\lambda) + L_F(\lambda)}{E^0(\lambda)/\pi} \times 100 \quad (3)$$

where: $L_F(\lambda)$ = fire emitted radiance.

Equation (3) shows that a fire will lead to reflectance values higher than they should be for a particular pixel as the radiance measured by the sensor is not only the radiance caused by reflection but also the radiance caused by the fire.

Properties of Detectable Fires

In order to be detectable, a fire's $L_F(\lambda)$ has to be big enough to raise the pixel's $\rho_a(\lambda)$ significantly above the pixel's expected reflectance. The two main contributors to $L_F(\lambda)$ are the fire's average temperature (a fire within a pixel will not be homogenous) and its size.

According to Kaufman and Justice (1998), the 2.1 μm channel saturates at a reflectance of 0.8. Observation however suggest that the 2.1 μm channel saturates at a reflectance value of 0.98 which corresponds to a fire of a 1000 K covering 0.09% of the area of a pixel with a highly reflective background of 0.18 reflectance. Following the sensitivity studies of Kaufman and Justice (1998) and Wien's Displacement Law, a fire of 900 K and above is expected to be able to produce a $L_F(\lambda)$ big enough to be significant and will be used as the prototype temperature for a detectable fire. Such a fire with a background of 0.18 reflectance would saturate the 2.1 μm channel if it fractionally covered 0.192% or greater of a pixel.

It is more difficult to determine the size of the fire necessary to produce a big enough $L_F(\lambda)$. We expect a fire to significantly add to the effective reflectance if the reflectance caused by the fire equals or exceeds the spectral reflectance of the background. With a high reflective background of 0.18, a 900 K fire has to cover 0.06% of a pixel to satisfy this condition. With a background of a lower reflectance

Table 2 Sample combinations of fire size and temperature that satisfy the conditions of the smallest detectable fire

| Fire temperature (K) | Burning fraction | Size (m ² , 500 m Pixel) |
|----------------------|------------------|-------------------------------------|
| 600 | 0.2141 | 53525 |
| 700 | 0.0424 | 10600 |
| 800 | 0.0126 | 3150 |
| 900 | 0.005 | 1250 |
| 1000 | 0.0023 | 575 |
| 1100 | 0.0012 | 300 |

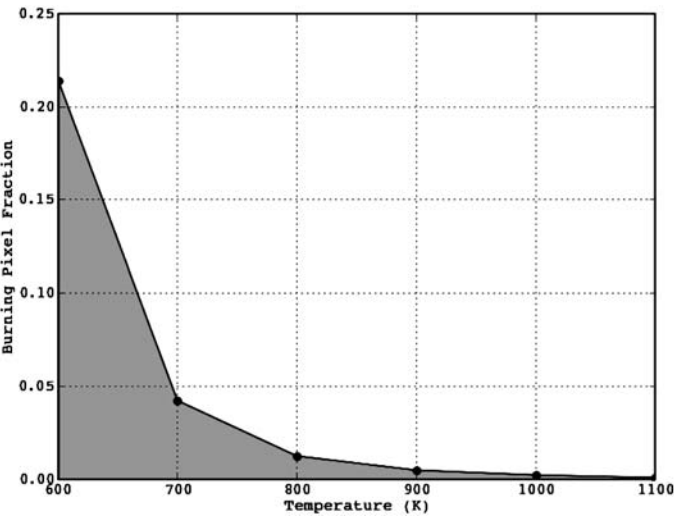


Fig. 2 Combinations of burning fraction and fire temperature that satisfy the requirements for the smallest detectable fire

of 0.13 the fire has to cover only 0.045% to fulfill the requirement. For present purposes we set the size of the prototype for the detectable fire to 0.005 (0.5%) of the pixel size.

This prototype fire corresponds to a fire-caused reflectance change of 0.25. This reflectance change can be caused by an infinite number of combinations of average fire temperature and fire fraction. Table 2 shows the values for a number of valid combinations. These combinations are indicated by the grey area in Fig. 2.

Determination of Background Reflectance and Change

The required estimation of the reflectance of an observed pixel without the presence of a fire is derived from a multi-temporal bidirectional reflectance distribution function (BRDF) (Roujean et al., 1992) model developed by Maier (2006).

This model calculated the expected reflectance of a pixel from previous BRDF and atmospherically corrected observations of the same pixel. At least 7 cloud free observations not more than 21 days old are required to derive the expected reflectance (Maier 2006) (ρ_{Ex} , x being the centre wavelength of the channel) of a pixel. It further provides the difference between the observed reflectance (ρ_x) and ρ_{Ex} (reflectance change, $\Delta\rho_x$) and the standard deviation of the differences between the modeled and observed reflectances ($\sigma\rho_x$).

Cloud Masking

Apart from active fires, clouds can also cause a high reflectance change in the 2.1 μm channel. Cloud masking is performed using a technique based on the one proposed by Stroppiana et al. (2000) for the AVHRR instruments.

The cloud mask uses the reflectances of channels 1 and 2, denoted $\rho_{0.65}$ and $\rho_{0.86}$ and the blackbody brightness temperature of channel 31 denoted T_{11} . A pixel is classified as contaminated by clouds if it satisfies:

$$\rho_{0.65} + \rho_{0.86} > 0.55 \quad (4)$$

or

$$T_{11} < 275 \text{ K}. \quad (5)$$

Pixels classified as cloud are excluded from further examination.

Identification of Fire Pixels

All pixels that have not been identified as cloud contaminated are tested if they satisfy:

$$\Delta\rho_{2.1} > 0.25 \quad (6)$$

and

$$\frac{\Delta\rho_{2.1}}{\sigma\rho_{2.1}} > 3 \quad (7)$$

and

$$\rho_{1.24} < \rho_{2.1} \quad (8)$$

Equation (6) tests if the reflectance change of the pixel is greater than the reflectance change caused by the prototype of a detectable fire as defined above. The

test in Eq. (7) checks if the reflectance change is bigger than three times the standard deviation of the modeled expected reflectance to ensure that the reflectance change was not likely to be caused by normal variations in reflectance. Equation (8) eliminates false alarms caused by unmasked clouds or other highly reflective objects.

If a pixel satisfies all three tests, it is classified as containing an active fire.

Results

Figure 3 shows the comparison of three different fire detection approaches applied to a large fire complex. The high resolution detection of 30 m is derived from data from the Advanced Spaceborne Thermal Emission and Reflection Radiometer (ASTER) that shares its platform Terra with one of the MODIS instruments. It shows how the fire detection based on the 2.1 μm channel is capable of providing more precise location information of intense fires compared to MOD14 which is based on the MIR and TIR bands of MODIS.

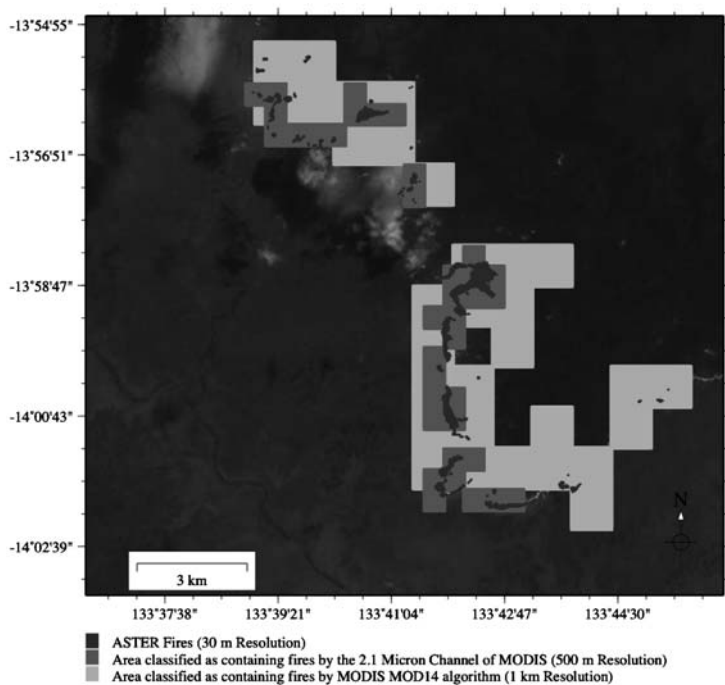


Fig. 3 Fire complex as detected at three different resolutions

Conclusions

Due to its insensitivity to smoldering fires as well as the unavailability of data from the 2.1 μm channel for night time observations, the proposed methodology to detect active fires from MODIS using its 2.1 μm channel cannot be a replacement for the algorithms based on the MIR and NIR channels.

However, it has shown its ability to provide more accurate spatial information on flaming fire fronts than provided current fire detection algorithms and could be deployed together with existing fire detection methodologies to provide an overall improved fire detection framework.

The methodology presented further shows that fire detection possibilities using current satellites have not yet been fully exploited.

References

- Chuvieco E (1999) *Remote Sensing of Large Wildfires*, Springer, Berlin
- Flasse SP, Ceccato P (1996) A contextual algorithm for AVHRR fire detection. *International Journal of Remote Sensing* 17:419–424
- Giglio L, Descloitres J, Justice CO, Kaufman YJ (2003a) An Enhanced Contextual Fire Detection Algorithm for MODIS. *Remote Sensing of Environment* 87:273–282
- Giglio L, Kendall JD, Justice CO (1999) Evaluation of global fire detection algorithms using simulated AVHRR infrared data. *International Journal of Remote Sensing* 20:1947–1985
- Giglio L, Kendall JD, Mack R (2003b) A multi-year active fire dataset for the tropics derived from the TRMM VIRS. *International Journal of Remote Sensing* 24:4505–4525
- Giglio L, Kendall JD, Tucker CJ (2000) Remote sensing of fires with the TRMM VIRS. *International Journal of Remote Sensing* 21:203–207
- Justice CO, Kendall JD, Dowty PR, Scholes RJ (1996) Satellite remote sensing of fires during the SAFARI campaign using NOAA-AVHRR data. *Journal of Geophysical Research* 101: 23851–23863
- Kaufman Y, Justice C (1998) *Algorithm Technical Background Document - MODIS FIRE PRODUCTS*.
- Kaufman YJ, Justice C, Flynn L, Kendall J, Prins E, Giglio L, Ward DE, Menzel P, Setzer A (1998) Potential Global Fire Monitoring from EOS-MODIS. *Journal of Geophysical Research* 103:32215–32238
- Lee TF, Tag PM (1990) Improved detection of hotspots using the AVHRR 3.7 μm channel. *Bulletin of The American Meteorological Society* 71:1722–2730
- Li Z, Kaufman YJ, Ichoku C, Fraser R, Trishchenko A, Giglio L, Jin J, Yu X (2000) A Review of AVHRR-based Active Fire Detection Algorithms: Principles, Limitations, and Recommendations.
- Maier SW (2006) Using the predictive power of a kernel driven BRDF model to map clouds and burnt areas. 4th International Workshop on Multiangular Measurements and Models, 20–14 March. Sydney, Australia
- Roujean J-L, Leroy M, Deschamps P-Y. (1992) A Bidirectional Reflectance Model of the Earth's Surface for the Correction of Remote Sensing Data. *Journal of Geophysical Research* 97:20455–20468
- Stroppiana D, Pincock S, Gregoire J-M (2000) The Global Fire Product: daily fire occurrence from April 1992 to December 1993 derived from NOAA AVHRR data. *International Journal of Remote Sensing* 21:1279–1288
- Wooster MJ, Zhukov B, Oertel D (2003) Fire radiative energy for quantitative study of biomass burning: derivation from the BIRD experimental satellite and comparison to MODIS fire products. *Remote Sensing of Environment* 83:83–10

Characterizing Eucalypt Leaf Phenology and Stress with Spectral Analysis

Karen Barry, Ross Corkrey, Christine Stone, and Caroline Mohammed

Abstract Detection of stress with remote sensing in any vegetation type relies on development of methods that highlight properties associated with stress which are discernable from background variation, such as phenological changes. Therefore the nature (and timing) of phenological foliar change needs to be systematically compared to foliar stress symptoms with physical, biochemical and optical analyses. Two such case studies with eucalypt species are presented here, including *Eucalyptus globulus* and *Eucalyptus pilularis*. Studies with both eucalypt species have shown that different leaf ages can be associated with alterations in pigments and properties that are as pronounced as those occurring for well-developed stress responses (potassium deficiency for *E. globulus* and low nutrient and cold exposure in *E. pilularis*). Chlorophyll, carotenoid and anthocyanin content were analysed, as well as specific leaf area and water content. Significant differences between leaf ages were detected for many of these leaf pigments and properties, but the significant differences between healthy and stressed leaves were usually of greater magnitude. Only carotenoid content was not significantly different with leaf age for *E. globulus*, but was significantly different with potassium-deficiency. This is a basis to further investigate the potential of carotenoids to discern stressed leaves from phenological changes. Preliminary data shown here provides a background for ongoing spectral research on this theme for eucalyptus.

Introduction

Remote Sensing of Canopy Health in Eucalypt Forests

Eucalyptus represents the most commonly planted broad-leaved tree genus worldwide, with almost 18 million ha in 2000, approximately half the amount represented by the *Pinus* spp. (Palmberg-Lerche et al. 2002). Despite this extent, remote sensing of eucalypt plantations is only in the initial stages: the industry is dominated

K. Barry (✉)

School of Agricultural Science, University of Tasmania, Hobart, Tasmania, Australia

by relatively new plantation estates, the majority of which are in South America and Asia where use of remote sensing is not as common as in Europe or Northern America. Australia has a growing eucalypt plantation estate (740,000 ha in 2005) of which over half is represented by *Eucalyptus globulus* (Parsons et al. 2006) and the potential of remote sensing is being explored. Remote sensing of native or plantation forests can offer a variety of uses, including assessment of productivity (Asner et al. 2003; Smith et al. 2002) and detection of stress due to a range of causes (Pontius et al. 2005a; Sampson et al. 2000; Stone et al. 2004; Wulder et al. 2006). In fast-growing, intensively-managed plantations such as *Eucalyptus globulus* this spatially-explicit information can aid management decisions and ultimately increase productivity.

Detecting the Difference Between a Stress Response and Changes Due to Normal Leaf Aging

A range of abiotic and biotic stressors may be experienced during the rotation length of a eucalypt plantation, which result in various foliage symptoms (Abbott et al. 1999; Carnegie et al. 1998; Coops et al. 2004; Snowdon 2000; Stone et al. 1998) and cause various impacts on growth. Response to many stressors is typically revealed at both the leaf and crown level; stressed eucalypts can develop contracted crowns and prematurely shed leaves and the foliar symptoms may include chlorosis, necrosis or reddening. Detection of stress with remote sensing may be possible for eucalypt plantations if the symptoms can be reliably correlated with spectral data and this requires a good understanding of symptom development and the chemical, physiological and structural basis of those symptoms. In terms of foliar chemistry, chlorophyll content has been widely regarded as a generic indicator of stress and a range of vegetation indices can be correlated to it (le Maire et al. 2004). There has also been some focus on carotenoids (Gamon and Surfus 1999; Gitelson et al. 2002) and development of vegetation indices which relate to photosynthetic functioning, such as the photochemical reflectance index (Gamon et al. 1990).

Methods to assess chlorophyll content with remote sensing in eucalypts have been tested with hyperspectral imaging and leaf scale studies (Coops et al. 2003; Datt 1998; Datt 1999a). Chlorophyll content can vary widely with leaf age in many plant species, including eucalypts (Choinski Jr et al. 2003; Stone et al. 2005). Anthocyanins are frequently produced in eucalypts as a response to both abiotic and biotic stress (Close and Beadle 2003; Stone et al. 2005). Anthocyanins can be detected using spectral reflectance wavelengths in the UV-VIS region (Gamon and Surfus 1999) and have been investigated in eucalypt forests to a limited extent. While some research has been conducted into changes in chlorophyll content with leaf age and stress in eucalypts (Datt 2000; Stone et al. 2005), corresponding data including anthocyanin content is not available. Carotenoid dynamics have been characterized in stressed plantation eucalypt species (Close and Beadle 2005; Close et al. 2003) but the relationship between total carotenoids and spectral indices has not been well explored for eucalypts (Datt 1998).

Characterization of leaf pigments in visible wavelengths has dominated studies of stress indicators, but changes in water content and leaf dry mass may also contribute to characterizing some stress types, with spectral changes particularly in the near- and middle-infrared wavelengths (Baret and Fourty 1997; Datt 1999b; Peñuelas and Inoue 1999; Tucker 1980). During leaf expansion and aging, water content and specific leaf area (SLA) decrease, and reflectance in the near-infrared (NIR) also tends to decrease (Roberts et al. 1998; Stone et al. 2005) although may increase (Gausman et al. 1973). Damaged adult eucalypt leaves have reduced reflectance in the NIR compared to healthy (Stone et al. 2005), but internal collapse of cells associated with senescence has been related to increased reflectance in the NIR (Sinclair et al. 1971).

A range of vegetation indices can be used to explore spectral differences between foliage types, especially when particular traits are of interest (e.g. chlorophyll). However, when attempting to characterize spectral variation that may be specific to a certain foliage or stress type, an exploration of the whole spectral range is beneficial and may enable identification of key spectral regions or wavelengths. Large, non-normal hyperspectral data sets require effective methods, which is suited to non-parametric analyses. Examples used in stress detection include, logistic regression (Delalieux et al. 2007), partial least squares (Delalieux et al. 2007; Pontius et al. 2005b), regularized regression (Renzullo et al. 2006), tree-based modeling (Delalieux et al. 2007) and neural networks (Wang et al. 2008). We chose to explore regularized regression, in a discriminant analysis framework to identify key spectral regions in stressed *E. pilularis* leaves. Ridge regression and the least absolute shrinkage and selection operator (lasso) are methods of regularized regression that can handle the high dimensionality of spectral data and give stable estimates of discriminant variable coefficients (Renzullo et al. 2006). Lasso is powerful because only wavelengths that exhibit the strongest effect in separating treatment groups are considered (other wavelengths are given zero values), while the ridge regression (or penalized discriminant analysis) can have problems with overfitting, as estimates of the discriminant variable coefficients is more variable.

In this chapter, we explore leaf pigments (chlorophyll a and b, total carotenoids and anthocyanins), water content and SLA of leaves from two eucalypt species, comprising studies of leaf age and stress effects. In this case stress symptoms were the result of abiotic factors, primarily nutritional. With spectral studies we correlated these leaf properties with some published indices. In addition we have utilized multivariate data analysis for one data set to determine key wavelengths which may indicate better methods for discrimination of stress effects. *E. globulus* (blue gum) is a widely grown species in Australia and other countries while *Eucalyptus pilularis* (black butt) is a minor species grown in sub-tropical areas of Australia. For *E. globulus* symptoms induced by a potassium deficiency were studied, while in *E. pilularis* (black butt) fertiliser was withheld and plants were exposed to cold. While nutrient deficiencies were involved in both these cases, our aim was not to detect foliar nutrient content but rather the symptoms exhibited by their deficiency. Chlorosis, necrosis and reddening are common symptoms of a range of stressful condition and we treat the data here as case studies.

Materials and Methods

Eucalyptus Globulus

Studies of leaf age were conducted with healthy pot-grown *E. globulus* (German Town, North-eastern Tasmania seed stock) plants which were approximately 1 m in height when sampled. Three categories of leaf age were used; (1) recently expanded, >1 month old (2) fully expanded, current season's growth, 2–3 months old (3) last season's growth, >6 months old. Three leaf pairs (six leaves) from each class were sampled from five plants, resulting in thirty leaves per class per tree. These leaves were labelled, pooled for reflectance measurements and then one leaf of each pair was immediately placed in a freezer for later chlorophyll and carotenoid analysis, while the other leaves were used for SLA determination and then frozen for later anthocyanin extraction.

Leaves with potassium deficiency symptoms were collected from an experimental planting of *E. globulus* in SE Tasmania when trees were approx. 2.5 years. Full site details are available (O'Grady et al. 2005). Three trees with symptoms (patchy necrosis and red discolouration, particularly around the leaf margin) and three apparently healthy trees were sampled. From each tree, 24 leaves were removed in total, including four leaves from node 4 and 5 of each of six branches around the lower crown (0.5–1.5 m above ground level). All leaves were placed on ice and returned to the laboratory within 2 hours, reflectance measurements were made and leaves processed as above. The cause of the symptoms was verified by analyzing foliar K with a second set of leaf samples from the same field-trees as above. A total of 18 leaves with K-deficient symptoms were sampled and 18 leaves with healthy appearance, comprising six leaves from each of three trees in each case. Leaves were dried at 70°C for a minimum of 48 h and ground in a Wiley mill. Samples (150–200 mg) were digested with sulphuric acid and hydrogen peroxide, following a standard method (Lowther 1980). On average, there was $4.7 (\pm 0.3) \text{ mg g DW}^{-1}$ of potassium in the leaves with K-deficient symptoms and $9.9 (\pm 0.3) \text{ mg g DW}^{-1}$ in the healthy leaves. Previous studies of young *E. globulus* have concluded that amounts of 3–7 mg g DW^{-1} K are deficient, while 8–15 mg g DW^{-1} is adequate (Dell et al. 2002), therefore amounts detected in this study are commensurate with a K deficiency.

For both studies, spectral reflectance (400–1000 nm) was obtained of fresh leaves placed on a black background using a UniSpec-DC spectroradiometer (PP Systems, USA). Leaves were arranged in stacks six layers deep, based on studies by O'Neill et al. (1990) who found the maximum reflectance of eucalypt leaves occurred when stacks were 5–7 layers deep, representing infinite reflectance. Leaf stacks were shuffled between repeated measurements to obtain an average for each sample and the spectroradiometer was calibrated against a SpectralonTM standard. Mean reflectance was determined by averaging the spectra each time the leaf stack was reshuffled.

Three spectral indices were applied using wavelengths in the visible region for pigment content. All major leaf pigments have overlapping absorption ranges

(Gitelson et al. 2006; Lichtenthaler 1987) and indices utilize wavelengths to quantify specific pigments with reduced influence of the others. These included an index developed by Datt (1999a) to estimate chlorophyll content in eucalypt leaves, the anthocyanin reflectance index (Gitelson et al. 2001) and the photochemical reflectance index (Gamon et al. 1990) which is well correlated to carotenoid content (Blanchfield et al. 2006; Gamon et al. 1997). The carotenoid reflectance index (Gitelson et al. 2002) was tested with our data (K. Barry, unpublished) but results were poor, possibly because use of the index has only been successful in anthocyanin-free samples (Gitelson et al. 2006; Merzlyak et al. 2003). This needs to be explored further in eucalyptus.

The point of the maximum slope of the spectrum between the red and NIR wavelengths (red edge position, REP) was determined using the Lagrangian interpolation method (Dawson and Curran 1998; Demetriades-Shah et al. 1990). Lagrangian interpolation is applied to the first derivative transformation of the spectrum in the red edge region, then a second-order polynomial curve is fitted using 3 bands centre around the maximum slope position (in this case 692.9, 702.7 and 712.4 nm were used). A second derivative is then performed on the Lagrangian equation to determine the maximum slope position (resolved when the second derivative is zero).

While areas of the spectrum most influenced by water content and specific leaf area are above 1300 nm (Baret and Fourty 1997) one absorption feature of water occurs at 970 nm (Curran 1989) and a water index using a ratio of 900 and 970 nm was tested here (Peñuelas and Inoue 1999). Details of the indices mentioned here are provided in Table 1.

Leaves were destructively analysed for content of chlorophyll, carotenoids and anthocyanin using standard extraction methods and quantification with a Cary UV-VIS spectrophotometer (Barry et al. 2008; Close et al. 2001; Lichtenthaler 1987). Specific leaf area (SLA) was determined by measuring leaf area, drying the leaves in an oven at 65°C for 3 days and then obtaining dry weight.

Table 1 Six narrowband vegetation indices, where ρ is the reflectance at a given wavelength (nm)

| Index | Name | Equation | Reference |
|----------|---------------------------------|--|--|
| REP | Red edge position | Determined using Lagrangian interpolation | Demetriades-Shah et al. (1990), Dawson and Curran (1998) |
| Datt '99 | Chlorophyll index | $(\rho_{850} - \rho_{710}) / (\rho_{850} - \rho_{680})$ | Datt (1999a) |
| ARI | Anthocyanin Reflectance Index | $(\rho_{550}^{-1}) / (\rho_{700}^{-1})$ | Gitelson et al. (2001) |
| CRI | Carotenoid Reflectance Index | $a = (\rho_{510}^{-1}) / (\rho_{550}^{-1})$ $b = (\rho_{510}^{-1}) / (\rho_{700}^{-1})$ | Gitelson et al. (2002) |
| PRI | Photochemical Reflectance Index | $(\rho_{531} - \rho_{570}) / (\rho_{531} + \rho_{570})$ | Gamon et al. (1990) |
| WI | Water Index | P_{900} / ρ_{970} | Peñuelas and Inoue (1999) |

Eucalyptus Pilularis

Clonal plants of *E. pilularis* (Queens Lake provenance, clone A) were prepared from cuttings and maintained in a glasshouse with adequate fertiliser. Leaf development was monitored when the plants were 14 months old, over a 4-week period from the time of expansion. The reflectance of each leaf (in the same position) was successively measured each week in a non-destructive manner. Newly-expanded *E. pilularis* leaves were soft and pink in colour and visible green colouration developed in the second and third week. By week 4 all leaves appeared more than 95% green. For this non-destructive study of leaf development a SPAD chlorophyll meter (Minolta) was used to estimate relative chlorophyll content. Replicate leaves were used to determine SLA at the first and last measurement time point.

Different pot-grown *E. pilularis* plants (Queens Lake provenance, clone B) were used for a stress experiment where five plants were subjected to cold (outdoor winter temperatures, minimum 7–8°C) and nutrient deprivation, while another five were maintained in a glasshouse environment and given adequate fertiliser. At one time point (3 weeks after the stress treatment was begun), five leaves from each plant were removed from the plants and destructively sampled. For the stress study, leaf pigments and SLA were analysed as for *E. globulus*.

For both *E. pilularis* studies an ASD Handheld FieldSpec UV/VNIR (Analytical Spectral Devices, Boulder CO, USA) with contact probe was used. Spectra were obtained with a white SpectralonTM surface behind the leaf; therefore a component of transmittance is added to the reflectance spectra and data needs to be interpreted with this in mind. While the leaf stack approach with a black background would involve an element of transmittance also, the two data sets here cannot be directly compared. Both *E. pilularis* data sets presented here are comparable to each other, but not directly to similar studies using a black background. For all data sets here, spectra are termed as ‘apparent reflectance’ to signify this. Transmittance back towards the sensor can occur commonly in the natural environment due to a range of reflective surfaces being behind leaves (e.g. lower leaves in a crown, under storey vegetation or bright soil). Leaf level studies with a range of species showed that background changes resulted in very small effects in the UV and visible spectra (with the exception of the green reflectance peak) and greater effects in the NIR between 750 and 1300 nm (Noble and Crowe 2001). Crown-level studies with eucalypts have shown that some of those indices used here (e.g. REP, ARI and Datt index) were not significantly affected by background when black canvas and bright soil were compared (Barry et al. 2008).

Spectral indices were calculated as described for *E. globulus* and in addition two different multivariate methods of spectral discrimination were applied to the data set for stressed and healthy *E. pilularis* leaves. These methods included a penalized discriminant analysis method (Hastie et al. 1995) and lasso regression (Tibshirani 1996) as have been applied by Renzullo et al. (2006) to reflectance data to identify wavelengths which are most sensitive to different treatment groups. The penalized regression function is executed using the lars function in the lars R package (Hastie and Efron 2004) in R (R Development Core Team 2006). Tuning parameters were

selected to minimize validation and training errors for the penalized analysis, while for the lasso analysis tuning was set to result in only one coefficient being selected (hence one wavelength is identified).

Results and Discussion

Eucalyptus Globulus

Average reflectance spectra of juvenile *E. globulus* leaves of three different ages showed a progressive decrease in reflectance in the visible wavelengths as leaves aged (Fig. 1a). Reflectance in the NIR wavelengths was significantly lower in leaves which grew in the previous season compared to the two younger categories of leaves, as found for older compared to young adult eucalyptus leaves (Stone et al. 2005). Comparison of average spectra of leaves with potassium-deficient symptoms and those of healthy appearance revealed little difference in the visible wavelengths but a progressive divergence in the NIR region, as stressed leaves had higher reflectance

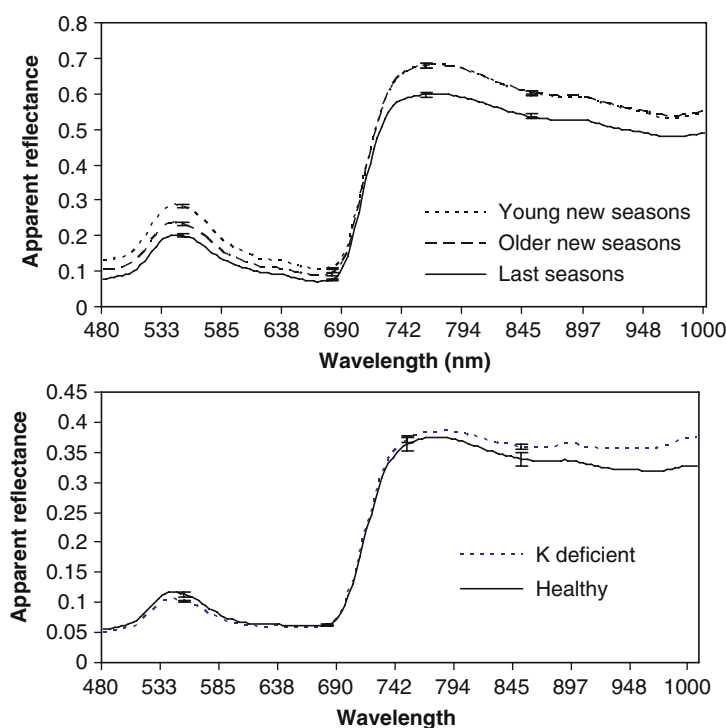


Fig. 1 Mean reflectance spectra of juvenile *E. globulus* leaves, (a) three different age classes, (b) healthy and those with symptoms of potassium deficiency. Error bars are SE

than healthy leaves at 850 nm (Fig. 1b) which may be related to changes in internal cell structure in the necrotic regions of the leaf.

Anthocyanin content was significantly greater in the oldest leaf class which was detectable by application of the ARI to the spectral data (Table 2). Chlorophyll content was significantly higher for the intermediate class (Table 1) but this difference was not detected with use of the Datt index for chlorophyll content and the REP changed little with leaf age in the study (Table 2). Carotenoid content did not differ significantly between age classes based on destructive analysis. Leaves of the older two classes were significantly tougher (lower SLA) and drier than the youngest leaf class which are common changes during leaf aging (Roberts et al. 1998) and this was detected by the WI (Table 2).

Anthocyanin content was significantly increased in potassium deficient *E. globulus* leaves compared to healthy leaves (Table 2) while chlorophyll content was significantly decreased. Application of the Datt index for chlorophyll did not detect these differences between healthy and symptomatic leaves. The ARI was significantly different between healthy and potassium-deficient leaves and was well correlated to anthocyanin content ($r^2=0.72$). Total carotenoids, SLA and water content were also significantly different between healthy and potassium-deficient leaves (Table 2).

In conclusion, total carotenoids were the only variable that was significantly different between the stressed and healthy leaves but not changed with the three leaf ages used here.

Eucalyptus Pilularis

Non-destructive determination of reflectance of leaves during the first four weeks after expansion showed that the average spectrum from the first week was of a very different profile in the visible wavelengths compared to the following three weeks (Fig. 2a). In the NIR region the reflectance of leaves at week 2 was significantly reduced compared to the other weeks (Fig. 2a). *E. pilularis* plants which were subjected to cold and nutrient stress developed leaves which were chlorotic and red in colour. Reflectance spectra (Fig. 2b) revealed very prominent differences in the visible wavelengths; stressed leaves had inverse reflectance trends in the green peak and chlorophyll well regions compared to the healthy leaves. There was little apparent difference in the NIR region (Fig. 2b).

New leaves of healthy *E. pilularis* plants became tougher (SLA decreased significantly over time), drier and SPAD values indicated that chlorophyll content increased significantly over time (Table 3). The position of the maximum reflectance of red edge peak, derived from the first derivative spectra, was shifted to higher wavelengths (up to 4 nm shift) as the leaves aged (Table 3). Also, the red edge peak area was increased as leaves aged. Both these trends are characteristic of what was found for the expansion of purple foliage into new green leaves for a range of *Eucalyptus* species (Datt 2000). Significant changes in the values determined using

Table 2 Average values of leaf properties and a range of spectral analyses for three studies of juvenile leaves of *E. globulus*

| <i>E. globulus</i> | Leaf material | Leaf properties | | | | Spectral analysis (with black background) | | | | | |
|--------------------|---------------|--------------------------------------|------------------------------------|---------------------------------------|-------------------|---|--------------------|-------------------|--------------------|-------------------|-------------------|
| | | Chl a+b ($\mu\text{g cm}^{-2}$) | Antho. (nmol cm^{-2}) | T carot. ($\mu\text{g cm}^{-2}$) | Water (% DW) | SLA ($\text{cm}^2 \text{g}^{-1}$) | REP (nm) | Datt '99 | ARI | PRI $\times 1000$ | WI |
| Age | Class 1 | 18.7 ^a | 2.5 ^a | 4.4 ^a | 63.8 ^a | 120.8 ^a | 704.4 ^a | 0.43 ^a | -0.51 ^a | 98.9 ^a | 1.11 ^a |
| | Class 2 | 22.5 ^b | 4.1 ^a | 4.2 ^a | 56.1 ^b | 97.4 ^b | 704.6 ^a | 0.43 ^a | -0.02 ^b | 95.7 ^a | 1.10 ^b |
| | Class 3 | 17.6 ^a | 14.4 ^b | 4.4 ^a | 56.1 ^b | 92.5 ^b | 703.3 ^a | 0.38 ^a | 0.44 ^c | 82.6 ^b | 1.09 ^b |
| K-def. | Stressed | 29.8 ^a | 20.1 ^a | 5.9 ^a | 52.5 ^a | 70.9 ^a | 709.1 ^a | 0.60 ^a | 0.84 ^a | 61.5 ^a | 1.02 ^a |
| | Healthy | 45.4 ^b | 5.2 ^b | 7.9 ^b | 59.4 ^b | 100.2 ^b | 709.5 ^a | 0.58 ^a | -0.19 ^b | 62.7 ^a | 1.05 ^b |

^{a b c} values within the same column section followed by different letters are significantly different (P<0.05). NA, not available.

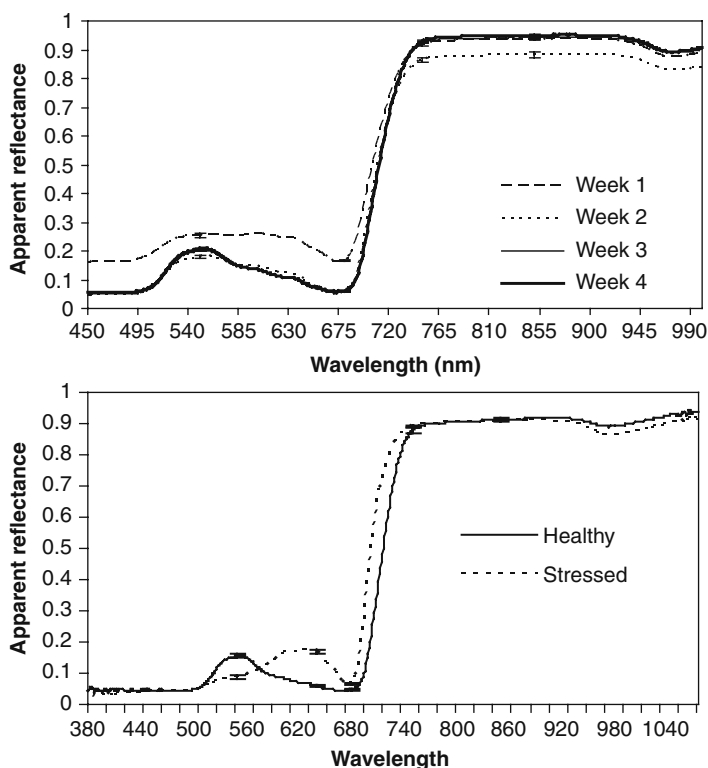


Fig. 2 Mean reflectance of young *E. pilularis* leaves, (a) healthy leaf development over a four week period with non-destructive assessments, (b) healthy and those exposed to cold and nutrient deprived. Error bars are SE

the Datt index were the same as for chlorophyll content (Table 3). The initial red discolouration was visibly reduced over time and while the extent of reduction in anthocyanin content is unknown, the ARI suggested that anthocyanin content was progressively and significantly reduced at each measurement time as leaves aged (Table 3).

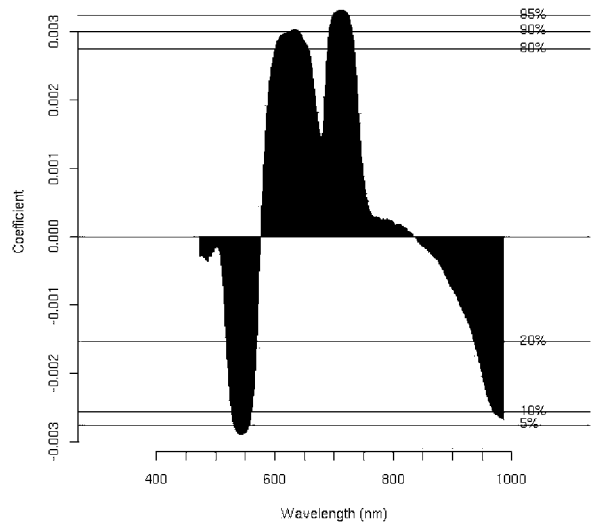
Differences in chlorophyll and anthocyanin content were large (6-fold reduced and 3.7-fold increased respectively) and significant between leaves from plants that were subjected to cold and nutrient deprivation and those which were maintained in favourable growth conditions (Table 3). Results of the Datt index and ARI mirrored these pigment difference, as did a very large shift (approx. 13 nm) in the position of the maximum slope of the red edge. Associated with leaf development and the stress treatment, large and significant differences in water content and SLA were also detected (Table 3). The WI detected significant differences between leaf ages and between the healthy and stressed leaves in these studies. Total carotenoid content was over 3-fold reduced in leaves of stressed plants and was well correlated

Table 3 Average values of leaf properties and a range of spectral analyses for two studies of pot-grown *E. pilularis*

| <i>E. pilularis</i> | Leaf material | Leaf analysis | | | Spectral analysis (with white background) | | | | | | |
|---------------------|---------------|--------------------------------------|--------------------------------------|---------------------------------------|---|-------------------------------------|--------------------|-------------------|-------------------|---------------------|-------------------|
| | | Chl a+b ($\mu\text{g cm}^{-2}$) | Antho. (nmoles cm^{-2}) | T carot. ($\mu\text{g cm}^{-2}$) | Water (% DW) | SLA ($\text{cm}^2 \text{g}^{-1}$) | REP | Datt '99 | ARI | PRI $\times 1000$ | WI |
| Age | Week 1 | 19.5 ^{a*} | NA | NA | 68.6 ^a | 137.1 ^a | 702.5 ^a | 0.45 ^a | 3.71 ^a | -21.9 ^a | 1.07 ^a |
| | Week 2 | 20.5 ^{a*} | NA | NA | NA | NA | 702.6 ^a | 0.45 ^a | 2.77 ^b | -28.9 ^a | 1.06 ^b |
| | Week 3 | 23.6 ^{b*} | NA | NA | NA | NA | 705.5 ^b | 0.51 ^b | 1.36 ^c | -7.7 ^b | 1.05 ^c |
| | Week 4 | 25.8 ^{c*} | NA | NA | 63.6 ^b | 117.3 ^b | 706.7 ^b | 0.53 ^c | 1.05 ^d | 1.5 ^c | 1.06 ^b |
| Cold/no F | Stressed | 5.4 ^a | 51.6 ^a | 1.9 ^a | 63.1 ^a | 109.8 ^a | 696.5 ^a | 0.31 ^a | 9.81 ^a | -147.2 ^a | 1.05 ^a |
| | Healthy | 39.2 ^b | 13.9 ^b | 6.4 ^b | 73.8 ^b | 258.6 ^b | 710.2 ^b | 0.62 ^b | 0.95 ^b | 18.4 ^b | 1.03 ^b |

* Relative chlorophyll content derived from SPAD (unitless); ^{a b c} values within the same column section followed by different letters are significantly different (P < 0.05). NA, not available.

Fig. 3 Coefficient values for the penalized discriminant analysis of reflectance spectra for healthy and stressed (cold and low fertilizer) *E. pilularis* leaves. Quantiles are marked



with the PRI ($r^2=0.79$) which has been shown in numerous studies (Blanchfield et al. 2006; Gamon and Surfus 1999).

Multivariate analysis revealed that a range of wavelengths are important in discriminating the reflectance spectra of the healthy and stressed *E. pilularis* leaves, as shown by the coefficient values for each wavelength (displayed for the penalized analysis in Fig.3, detailed for both analyses in Table 4). Both methods selected similar wavelengths as the most important (712 and 709 nm) which are also similar to the REP (710 nm, Table 3) of the spectra determined from healthy leaves.

Table 4 Important wavelengths to discriminate the healthy and stressed *E. pilularis* reflectance data

| | Wavelength ranges (nm) |
|--------------------|------------------------|
| Penalised analysis | |
| Quantiles | |
| Max | 712 |
| 95% | 699–724 |
| 90% | 627–638; 692–731 |
| 80% | 600–656; 689–734 |
| 20% | 518–569; 937–987 |
| 10% | 527–561; 971–987 |
| 5% | 531–556 |
| Min | 541 |
| Lasso analysis | 709 |

An Approach to Detect Stress in Eucalypt Plantations

Studies with both eucalypt species have shown that different leaf ages can be associated with alterations in pigments and properties which are as pronounced as those occurring for a well-developed stress response. For *E. globulus*, changes in anthocyanins and SLA were most pronounced with the longer-term leaf aging (with less change in chlorophyll and no significant changes in carotenoids), while all pigments and properties were significantly altered when leaves were low in potassium. This study highlights carotenoids as a possible basis to discern healthy leaves from stressed leaves (with less difference between ages) and spectral methods to detect carotenoids in eucalypt leaves need to be improved to explore this further. The PRI has a well demonstrated relationship with carotenoid to chlorophyll ratio and xanthophyll pigments and this is currently being explored further in *Eucalyptus globulus* with a study integrating leaf age and multiple stress types (K. Barry, unpublished).

For *E. pilularis*, vegetation indices suggested that changes during the early stages of leaf growth were substantial for chlorophyll, anthocyanins and water, but probably not to the extent of the changes for plants subjected to cold and nutrient stress. However, the stress imposed was particularly pronounced and may not occur to this extent in a field situation. While carotenoid content could not be determined, the PRI suggests that alterations in carotenoids probably occur within the four week timeframe of leaf development studies here. Vegetation indices tested here showed general correlation with leaf properties data, but statistically significant differences were not detected for the *E. globulus* study, which may be a function of the leaf stack approach, compared to the individual leaf spectra obtained for *E. pilularis*. The penalized discriminant analysis and lasso regression identified similar wavelengths in the *E. pilularis* stress reflectance data set which were close to the REP. This is a useful tool to explore the full spectrum for differences between treatments and may be particularly useful to discern the key wavelengths when a range of symptoms are apparent together.

Spectral methods used in these two studies include an element of transmittance data and therefore represent apparent reflectance. This gives us a preliminary understanding of the relationship between spectral data and pigments and physical properties of eucalypt foliage. While transmittance is always part of the optical signal of vegetation, ideally it is minimized in leaf-level reflectance studies. To obtain reflectance with no or minimal transmittance, a black background with single leaves is preferable. An integrating sphere should be used to separate reflectance from transmittance and data can then be incorporated into leaf and crown radiative transfer models. Our ongoing studies are using this approach. Disadvantages of using integrating spheres is that foliage must be removed, which does not allow repeated spectral studies of leaves during development, as conducted here. Ideally, obtaining a spectrum using a black and then white background with a contact probe (such as the ASD instrument used here) would allow repeated spectral studies of attached leaves and an ability to separate reflectance from transmittance (Noble and Crowe 2001).

Leaf-level studies are the basis for our understanding of vegetation detection with remote sensing, but an understanding of the distribution and normal phenology of leaves is also needed at the crown and canopy scale. For example, the distinct changes occurring as leaves initially develop (seen here in *E. pilularis*) usually occur across a short growing season (known as the 'red flush' or 'spring flush' for eucalypts). Changes in red edge or anthocyanin indices occurring at other times of the year may more reliably signify a stress event, but may be difficult to distinguish from a 'spring flush' if occurring at that time. Leaf distribution within the crown is also important and leaves from last years growth (as seen in the *E. globulus* study) will occupy a smaller proportion of the outer leaf layers than the current seasons growth which contribute more towards the whole-tree or whole-canopy spectrum. This can only be fully understood by light interception modeling for the species of interest and the growing environment. In a closed canopy, effective photon penetration depth (EPPD) is 1–2 layers of foliage in the visible through to short wave infrared wavelengths (Asner 2008), therefore only the younger age classes may contribute to this range of the spectra, where the influence of pigments dominates. It follows that stress symptoms which primarily affect older, lower foliage in a crown may be difficult to detect. In crown studies of *E. globulus*, defoliation of the lower crown was difficult to detect with reflectance spectra (Barry et al. 2008). Therefore an understanding of the distribution of symptomatic foliage is equally important in the detection of stress with remote sensing and ideally for key eucalypt species a good understanding of EPPD should be developed with field measurements and canopy radiative transfer models (Asner 1998). Along with changes in foliage quality, crown responses to stress are an important factor in the detection of stress by remote sensing, including reduced leaf area index due to production of smaller leaves or loss of leaves.

The current studies show that a similar range of properties alter with eucalypt leaf age or when they become stressed. While separation of these effects is challenging, there is a basis to further explore carotenoid content and dynamics. Development of strategies to detect stress in eucalypt plantations need to consider the magnitude of the symptoms at the leaf- and crown-level, time of year and how they contrast with normal changes in leaf development. A range of vegetation indices should ideally be used together to detect symptoms of stress. A combination of approaches may be useful for separating stress and phenology in time and space, for example a time-series approach (e.g. MODIS) could be used to track phenological changes and then a higher spectral and spatial resolution approach could target areas of forest that do not follow the local trends.

Acknowledgements This research was supported with funding from the Australian Research Council and five industry partners (Forestry Tasmania, Forests and Forest Industries Council of Tasmania, Forests NSW, Gunns Ltd. and WAPRES).

References

- Abbott I, Wills A, Burbidge T (1999) The impact of canopy development on arthropod faunas in recently established *Eucalyptus globulus* plantations in Western Australia. For Ecol Manage 121: 147–158.

- Asner G (2008) Hyperspectral remote sensing of canopy chemistry, physiology and biodiversity in tropical rainforests. In: M Kalacska and GA Sanchez-Azofeifa (eds) Hyperspectral remote sensing of tropical and subtropical forests. CRC Pr I Llc, Lafayette, LA.
- Asner GP (1998) Biophysical and biochemical sources of variability in canopy reflectance. *Remote Sens Environ* 64: 234–253.
- Asner GP, Scurlock JMO, Hicke JA (2003) Global synthesis of leaf area index observations: implications for ecological and remote sensing studies. *Global Ecol Biogeogr* 12: 191–205.
- Baret F, Fourty T (1997) Estimation of leaf water content and specific leaf weight from reflectance and transmittance measurements. *Agronomie* 17: 455–464.
- Barry KM, Stone C, Mohammed CL (2008) Crown-scale evaluation of spectral indices for defoliated and discoloured eucalypts. *Int J Remote Sens* 29: 47–69.
- Blanchfield AL, Robinson SA, Renzullo LJ, Powell KS (2006) Phylloxera-infested grapevines have reduced chlorophyll and increased photoprotective pigment content – can leaf pigment composition aid pest detection? *Funct Plant Biol* 33: 507–514.
- Carnegie AJ, Ades PK, Keane PJ, Smith IW (1998) *Mycosphaerella* diseases of juvenile foliage in a eucalypt species and provenance trial in Victoria, Australia. *Aust For* 61: 190–194.
- Choinski Jr JS, Ralph P, Eamus D (2003) Changes in photosynthesis during leaf expansion in *Corymbia gummifera*. *Aust J Bot* 51: 111–118.
- Close DC, Davies NW, Beadle CL (2001) Temporal variation of tannins (galloylglucoses), flavonols and anthocyanins in leaves of *Eucalyptus nitens* seedlings: implications for light attenuation and antioxidant activities. *Aust J Plant Physiol* 28: 269–278.
- Close DC, Beadle CL (2003) The ecophysiology of foliar anthocyanin. *Bot Rev* 69: 149–161.
- Close DC, Beadle CL, Hovenden MJ (2003) Interactive effects of nitrogen and irradiance on sustained xanthophyll cycle engagement in *Eucalyptus nitens* leaves during winter. *Oecologia* 134: 32–36.
- Close DC, Beadle CL (2005) Xanthophyll-cycle dynamics and rapid induction of anthocyanin synthesis in *Eucalyptus nitens* seedlings transferred to photoinhibitory conditions. *J Plant Physiol* 162: 37–46.
- Coops NC, Stone C, Culvenor DS, Chisholm L, Merton R (2003) Chlorophyll content in eucalypt vegetation at the leaf and canopy scales as derived from high resolution spectral data. *Tree Physiol* 23: 23–31.
- Coops NC, Stone C, Culvenor DS, Chisholm L (2004) Assessment of crown condition in eucalypt vegetation by remotely sensed optical indices. *J Environ Qual* 33: 956–964.
- Curran PJ (1989) Remote sensing of foliar chemistry. *Remote Sens Environ* 30: 271–278.
- Datt B (1998) Remote sensing of chlorophyll *a*, chlorophyll *b*, chlorophyll *a + b* and total carotenoid content in eucalyptus leaves. *Remote Sens Environ* 66: 111–121.
- Datt B (1999a) Visible/near infrared reflectance and chlorophyll content in *Eucalyptus* leaves. *Int J Remote Sens* 20: 2741–2759.
- Datt B (1999b) Remote sensing of water content in *Eucalyptus* leaves. *Aust J Bot* 47: 909–923.
- Datt B (2000) Red edge shifts for detecting phenologic change and stress symptoms in evergreen eucalyptus forests. In: 10th Australasian Remote Sensing and Photogrammetry Conference, Adelaide, Australia. Casual Productions. pp. 863–874
- Dawson TP, Curran PJ (1998) A new technique for interpolating the reflectance red edge position. *Int J Remote Sens* 19: 2133–2139.
- Delalieux S, van Aardt J, Keulemans W, Schrevens E, Coppin P (2007) Detection of biotic stress (*Venturia inaequalis*) in apple trees using hyperspectral data: Non-parametric statistical approaches and physiological implications. *Europ J Agronomy* 27: 130–143.
- Dell B, Malajczuk N, Xu D, Grove TS (2002) Nutrient disorders in plantation eucalypts. ACIAR, Canberra, 188p.
- Demetriades-Shah TH, Steven MD, Clark JA (1990) High resolution derivative spectra in remote sensing. *Remote Sens Environ* 33: 55–64.
- Gamon JA, Field CB, Björkman O, Fredeen AL, Peñuelas J (1990) Remote sensing of the xanthophyll cycle and chlorophyll fluorescence in sunflower leaves and canopies. *Oecologia* 85: 1–7.

- Gamon JA, Serrano L, Surfus JS (1997) The photochemical reflectance index: an optical indicator of photosynthetic radiation use efficiency across species, functional types and nutrient levels. *Oecologia* 112: 492–501.
- Gamon JA, Surfus JS (1999) Assessing leaf pigment content and activity with a reflectometer. *New Phytol* 143: 105–117.
- Gausman HW, Allen WA, Cardenas R, Richardson AJ (1973) Reflectance discrimination of cotton and corn at four growth stages. *Agron J* 65: 194–198.
- Gitelson AA, Merzlyak MN, Chivkunova OB (2001) Optical properties and nondestructive estimation of anthocyanin content in plant leaves. *Photochem Photobiol* 74: 38–45.
- Gitelson AA, Zur Y, Chivkunova OB, Merzlyak MN (2002) Assessing carotenoid content in plant leaves with reflectance spectroscopy. *Photochem Photobiol* 75: 272–281.
- Gitelson AA, Keydan GP, Merzlyak MN (2006) Three-band model for noninvasive estimation of chlorophyll, carotenoids, and anthocyanin contents in higher plant leaves. *Geophys Res Lett* 33: L11402.
- Hastie T, Buja A, Tibshirani R (1995) Penalized discriminant analysis. *Ann Stat* 23: 73–102.
- Hastie T, Efron B (2004) lars: Least Angle Regression, Lasso and Forward Stagewise. <http://www-stat.stanford.edu/~hastie/Papers/LARS/>, accessed 11.07.07
- le Maire G, François C, Dufrêne E (2004) Towards universal broad leaf chlorophyll indices using PROSPECT simulated database and hyperspectral reflectance measurements. *Remote Sens Environ* 89: 1–28.
- Lichtenthaler HK (1987) Chlorophylls and carotenoids: pigments of photosynthetic biomembranes. *Methods Enzymol* 148: 350–382.
- Lowther JR (1980) Use of a single acid-hydrogen peroxide digest for the analysis of *Pinus radiata* needles. *Commun Soil Plant Anal* 11: 175–188.
- Merzlyak MN, Solovchenko AE, Gitelson AA (2003) Reflectance spectral features and non-destructive estimation of chlorophyll, carotenoid and anthocyanin content in apple fruit. *Postharvest Biol Tech* 27: 197–211.
- Noble SD, Crowe TG (2001) Background effects on apparent leaf reflectance. In: ASAE Annual Meeting, St. Joseph, Michigan, USA. American Society of Agriculture and Biological Engineers.
- O'Grady AP, Worledge D, Battaglia M (2005) Temporal and spatial changes in fine root distributions in a young *Eucalyptus globulus* stand in southern Tasmania. *For Ecol Manage* 214: 373–383.
- O'Neill AL, Hardy S, Fraser SJ, McCloy KR (1990) Leaf morphology and the spectral reflectance of some Australian plant species. In: 5th Australasian Remote Sensing Conference, Perth, Australia. Remote Sensing and Photogrammetry Association of Australia. pp. 1096–1103
- Palmberg-Lerche C, Aarup Iversen P, Sigaud P (2002) Forest Genetic Resources. <http://www.fao.org/docrep/004/y2316e/y2316e0b.htm>, accessed 20.10.07
- Parsons M, Gavran M, Davidson J (2006) Australia's plantations 2006. Commonwealth of Australia, National Plantation Inventory
- Peñuelas J, Inoue Y (1999) Reflectance indices indicative of changes in water and pigment contents of peanut and wheat leaves. *Photosynthetica* 36: 355–360.
- Pontius J, Hallett RA, Martin ME (2005a) Using AVIRIS to assess hemlock abundance and early decline in the Catskills, New York. *Remote Sens Environ* 97: 163–173.
- Pontius J, Hallett RA, Martin ME (2005b) Assessing hemlock decline using visible and near-infrared spectroscopy: indices comparison and algorithm development. *Appl Spectrosc* 59: 836–843.
- R Development Core Team (2006) A language and environment for statistical computing. R Foundation for Statistical Computing, Vienna, Austria
- Renzullo LJ, Blanchfield AL, Powell KS (2006) A method of wavelength selection and spectral discrimination of hyperspectral reflectance spectrometry. *IEEE T Geosci Remote* 44: 1986–1994.

- Roberts DA, Nelson BW, Adams JB, Palmer F (1998) Spectral changes with leaf aging in Amazon caatinga. *Trees* 12: 315–325.
- Sampson PH, Mohammed GH, Zarco-Tejada PJ, Miller JR, Noland TL, Irving D, Treitz PM, Colombo SJ, Freemantle J (2000) The bioindicators of forest condition project: a physiological, remote sensing approach. *Forest Chron* 76: 941–951.
- Sinclair TR, Hoffer RM, Schreiber MM (1971) Reflectance and internal structure of leaves from several crops during a growing season. *Agron J* 63: 864–868.
- Smith M, Ollinger SV, Martin ME, Aber JD, Hallett RA, Goodale CL (2002) Direct estimation of aboveground forest productivity through hyperspectral remote sensing of canopy nitrogen. *Ecol Appl* 12: 1286–1302.
- Snowdon P (2000) Nutritional disorders and other abiotic stresses of eucalypts. In: PJ Keane, GA Kile, FD Podger and BN Brown (eds) *Diseases and Pathogens of Eucalypts*. CSIRO Publishing, Collingwood, Victoria pp. 385–410
- Stone C, Simpson JA, Eldridge RH (1998) Insect and fungal damage to young eucalypt trial plantings in northern New South Wales. *Aust For* 61: 7–20.
- Stone C, Coops NC, Sims NC, Ryan PJ, Stanford M, Goodwin N (2004) Remote assessment of pine plantation condition: A handbook describing the use of multi-spectral imagery to measure impacts from three damaging agents of *Pinus radiata*. CSIRO and State Forests New South Wales, CSIRO Client Report (Report to Forestry and Wood Products Research and Development Corporation PNO2. 1906,1480)
- Stone C, Chisholm L, McDonald S (2005) Effects of leaf age and psyllid damage on the spectral reflectance properties of *Eucalyptus saligna* foliage. *Aust J Bot* 53: 45–54.
- Tibshirani R (1996) Regression shrinkage and selection via the lasso. *J Royal Statist Soc B* 58: 267–288.
- Tucker CJ (1980) Remote sensing of leaf water content in the near infrared. *Remote Sens Environ* 10: 23–32.
- Wang X, Zhang M, Zhu J, Geng S (2008) Spectral prediction of *Phytophthora infestans* infection on tomatoes using artificial neural network (ANN). *Int J Remote Sens* 29: 1693–1706.
- Wulder MA, Dymond CC, White JC, Leckie DG, Carroll AL (2006) Surveying mountain pine beetle damage of forests: A review of remote sensing opportunities. *For Ecol Manage* 221: 27–41.

Development of Satellite Vegetation Indices to Assess Grassland Curing Across Australia and New Zealand

Danielle Martin, Ian Grant, Simon Jones, and Stuart Anderson

Abstract Grasslands, including woodlands, grass and scrub mixes, cover nearly 75% of Australia and constitute 70% of vegetation cover in New Zealand. Grass characteristics such as water content and degree of curing (senescence), determine the vulnerability of grasses to propagate and carry fire. This work is part of a Bushfire Cooperative Research Centre (CRC) project that aims to improve the assessment and prediction of grassland curing across Australia and New Zealand. This will be carried out with the use of two satellite remote sensors. NOAA AVHRR has been used operationally to produce a satellite curing index since the 1980s across southeastern Australia. In the near future, the use of this sensor will be extended across the continent on the basis of extensive field data collected by the CRC. The EOS MODIS sensor, can provide more detailed assessments of vegetation than AVHRR, and has the potential to provide better curing estimates due to its greater number of spectral bands. The aim of this project is to develop a satellite-based method for curing assessment that is robust and can be validated across Australia and New Zealand. This paper covers the background research of satellite remote sensing on grassland curing, and presents preliminary methods and results using field data and MODIS-derived vegetation indices.

Introduction

Motivation

Fires are a major socio-economic and natural hazard in Australia, affecting over 25,000 km² of land annually. This figure remains uncertain, owing to the difficulty in distinguishing between wildfires and agricultural/cultural burning-off in northern

D. Martin (✉)

Space Based Observations Section, Bureau of Meteorology; School of Mathematical and Geospatial Sciences, RMIT; Bushfire Cooperative Research Centre, East Melbourne; Melbourne, VIC, Australia

e-mail: Danielle.Martin@bom.gov.au

Australia. For example, in 1992, 74,000 km² of land was burnt in the Northern Territory; the proportion burnt by wildfires is unknown (Cheney and Sullivan, 1997). In addition, the area of burnt land can easily rise in a severe fire season such as the summer of 1982/83 when the Ash Wednesday fires took 71 lives and destroyed 2000 homes in Victoria and South Australia (Jones et al., 2004). Currently the Bureau of Meteorology distributes grassland curing maps for south-eastern Australia which are derived from remotely sensed satellite data, using an algorithm developed by the Commonwealth Scientific and Industrial Research Organisation and Victoria's Country Fire Authority (Barber and Paltridge, 1986). The research described here is part of a Bushfire Cooperative Research Centre (CRC) project (Project A1.4: Improved methods for assessment and prediction of grassland curing). Bushfire CRC research covers a wide range of social and environmental issues, and emphasises that fire management should be underpinned by reliable prediction tools which are research-based. This part of the project aims to develop remote sensing methods to assess grassland curing across Australia and New Zealand. Information produced from this project will provide fire management agencies with access to accurate and reliable maps of grassland curing during fire seasons for planning and input into grassland fire danger rating and fire behaviour models. Outputs from these models provide input into a range of fire management strategies and decisions, such as implementation of prescribed burning programs, determining fire preparedness levels, imposition of fire restrictions, safe fire fighting actions, and public warning. This research aims to make the best use of emerging technology, so that the usefulness of the results will continue in future years.

Aims

Current grassland curing assessment is based on visually assessed field data and AVHRR (Advanced Very High Resolution Radiometer) satellite data. Visual assessment of curing has inherent problems and has led to inaccurate assessment of grassland curing (Anderson et al., 2005). In order to produce a better satellite-based grassland curing index, this research will establish algorithms to estimate grassland curing routinely across Australia and New Zealand using field techniques such as destructive sampling and the Levy rod method, and using vegetation indices from MODIS (MODerate resolution Imaging Spectroradiometer) satellite data. This research will be advanced through the use of MODIS due to its higher number of spectral bands than AVHRR. The research questions to be addressed are:

- What is the accuracy of the current satellite curing estimates?
- How may satellite measurements in several spectral bands be best combined to quantitatively estimate the degree of grassland curing?
- How do factors such as grassland type, soil type, topography and amount of tree cover influence the algorithm?
- Do very cloudy regions/seasons require a modification to the algorithm to accommodate less frequent satellite views?

This paper presents the past research on satellite remote sensing of grassland curing, and compares results from past studies to preliminary results from the current study.

Background

Grasslands

Within Australia, there are four main vegetation classes; forests and woodlands, covering 34% of the continent (NLWRA, 2001), shrublands, covering 13% (NLWRA, 2001) and grasslands (Moore, 1970). Including mixes of woodlands and scrublands, grasslands cover nearly 75% of Australia (Cheney and Sullivan, 1997), consisting of hundreds of grass species, which have been classified into; crops and pastures, tussock, hummock, coastal and sub-humid grasslands (Groves, 1994). In New Zealand, the steep and divided relief of the country provides a dramatic variation in climate and vegetation cover across the land. New Zealand is covered mainly by forests, grasslands (including pasture/croplands), scrublands, and mixes of these vegetation types. Grasslands include both native (such as tussock) and pasture grasses. Native and exotic forests cover less than 20 and 6% of the land respectively, and 'pure' grasslands as well as mixes of grass/forest/scrub cover approximately 70% (Newsome, 1987).

Grassland Curing

Grassland curing is defined as the progressive senescence and drying out of a grass after flowering (annual) or in response to drought (perennial). The degree of curing is the fraction of dead material in the grass sward expressed as a percentage (Cheney and Sullivan, 1997). At the time of year when all of the grass is dead, the grass is said to be 100% cured (Fig. 1). Luke and McArthur (1978) state that when leaves and stems die, roots cease drawing moisture from the soil, causing plants to dry out (Barber, 1979) and become cured.

Grassfires

In comparison to forest fuels, grass fuels are relatively simple in structure (Cheney and Sullivan, 1997). Grasslands consist of fine fuels, which respond very quickly to changes in weather conditions and are capable of supporting fires, which develop and spread rapidly (McArthur, 1966). Grassland fire fuels have an annual life cycle of germination, growth, maturity and curing (senescence). Depending on the stage of this life cycle, certain characteristics determine the vulnerability of grass to ignite

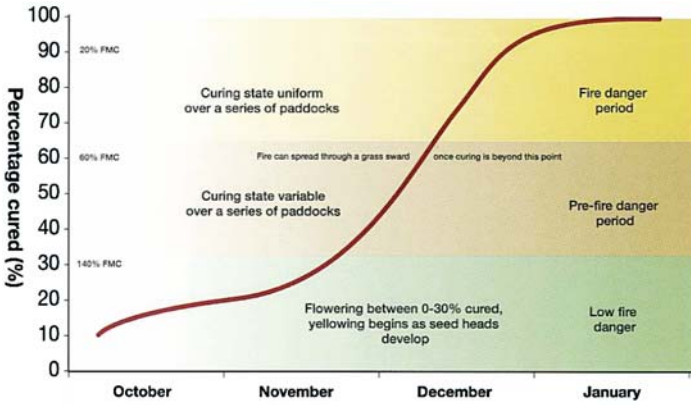


Fig. 1 The life cycle of annual grasses in southeastern Australia. Grasses experience a period of growth (in Spring) until reaching a stage where they lose their ability to draw up moisture from the soil. Source: (Garvey and Millie, 2001, p. 3, Copyright CFA, 2006)

and allow fire to spread (Barber, 1992). Grasslands are also unlikely to carry fire when the curing is less than 50% (Cheney et al., 1998).

Fuel Moisture Content

Fuel is a key ingredient for fire. Along with the fuel's variability of quantity and arrangement, the most important aspect is the Fuel Moisture Content (FMC) (Foley, 1947). As the degree of curing represents the percentage of dead material in vegetation, the (FMC) refers to the percentage of water in vegetation,

$$FMC (\%) = ((W_w - W_d) / W_d) \times 100 \quad (1)$$

which is calculated from the wet weight W_w and dry weight W_d of a sample (Chuvieco et al., 2004). Using data supplied by McArthur (1966), Barber (1990) established a relationship between field-derived FMC and a Grassland Curing Index (GCI), based on visual estimates. This relationship converts the FMC to GCI, where FMC (oven dried weight %) is represented by x .

$$y = (-0.000006295x^3) + (0.0044x^2) - (1.0721x) + 109.68 \quad (2)$$

This relationship has been used in several studies (Dilley and Edwards, 1998; Dilley et al., 2004), and the use of this relationship avoids the uncertainties that would arise if the GCI was estimated by visual observations (Dilley and Edwards, 1998), which tend to underestimate the curing value, particularly when

secondary growth occurs (Anderson and Pearce, 2003; Hosking, 1990; Millie and Adams, 1999).

Fuel moisture has a significant impact on the combustibility of fuel as the greater the FMC the higher the specific heat and thermal conductivity of the fuel, requiring more absorbed heat for the surface layer of the fuel to reach ignition temperature (Chandler et al., 1983). This required amount of heat is very high for wet fuel, so its risk of burning is usually quite low (Foley, 1947). The FMC of grasslands is controlled by temperature and rainfall patterns on a long-term scale, and also by temperature and relative humidity on a daily basis. However, once the grasses have reached a certain stage of curing, generally when the FMC has declined to 40%, it becomes irreversible despite even a major rainfall (McArthur, 1966).

Vegetation Indices

Unlike traditional methods of vegetation assessment, satellite remote sensing provides a non-destructive and instantaneous monitoring approach at various landscape scales (Davidson et al., 2005). As plant pigments absorb visible light, vegetation usually has a low visible reflectance. On the other hand, plants have a high reflectance in the near-infrared (NIR) to mid-infrared (MIR) part of the spectrum (Gausman, 1977). Vegetation indices (VIs), based on values of reflectance, are formed from a combination of spectral bands whose values are divided, multiplied or added together to obtain a single value that indicates the amount of vegetation cover (Campbell, 2002; Wiegand et al., 1991). VIs are the most widely used tools for making quantitative estimates of properties of vegetation (Alexander and Millington, 2000), as they tell us how densely or sparsely vegetated a region is, and how much electromagnetic radiation that could be used for photosynthesis is being absorbed by vegetation. With the use of multispectral remotely sensed data, different indices have been developed. As well as measuring vegetation cover across the Earth's surface, these indices can quantify the structure of vegetation, as well as stem/leaf density and distribution, moisture content, mineral deficiencies, parasitic attacks and stand age (Liang, 2004). Various indices have been used to monitor vegetation cover from a number of different satellite sensors (Paltridge and Barber, 1988). The range of available indices to assess curing in grasslands will depend on the spectral bands offered by the operational sensors. Three selected indices produced from MODIS suitable for curing assessment include, NDVI, EVI and NDWI (Table 1).

Satellite Remote Sensors

Two satellite sensors will be utilised for this research, namely AVHRR (to be used in the near future) and MODIS, as summarised in Table 2.

Table 1 Vegetation indices

| Index | Formula | Measurement | Reference |
|---|--|--|----------------------|
| NDVI Normalised Difference Vegetation Index | $NDVI = (NIR - Red) / (NIR + Red)$ | Global vegetation changes | (Tucker, 1979) |
| EVI Enhanced Vegetation Index | $EVI = 2.5 \cdot ((NIR - Red) / (NIR + (6 \cdot Red) - (7.5 \cdot Blue) + 1))$ | Vegetation changes in regions of high biomass | (Huete et al., 2002) |
| NDWI Normalised Difference Water Index | $NDWI = (NIR - MIR) / (NIR + MIR)$ | Leaf water content | (Gao, 1996) |

Table 2 General characteristics of MODIS and AVHRR

| Satellite | EOS-TERRA | NOAA |
|---------------------|--------------------|-------------------|
| Sensor | MODIS | AVHRR |
| No. bands | 36 | 5 |
| Spectral range | 0.62–14.38 μ m | 0.58–12.5 μ m |
| Temporal resolution | Daily | Daily |
| Spatial resolution | 250, 500, 1000 m | 1000 m |

AVHRR has been used since the mid 1980s to estimate grassland curing in southeastern Australia (Anderson et al., 2005). To assess curing across the whole continent and also New Zealand, an extension to other regions of Australia and New Zealand requires validation against field data representative of the grassland types in those regions. The newer MODIS sensor, from which data can be collected free of charge (from National Aeronautics and Space Administration), can monitor vegetation more precisely than AVHRR (Campbell, 2002), and has the potential to provide better curing estimates due to its modern design and greater number of spectral bands. MODIS has the advantages over AVHRR that its spectral bands are less affected by the atmosphere (Campbell, 2002) and are calibrated on board the satellite. MODIS, however, is a research sensor, and so does not have the same security of data continuity as an operational sensor series. Thus an AVHRR-based curing system should be maintained as a backup, in case of MODIS failure, until a future sensor, VIIRS (Visible Infrared Imager/Radiometer Suite) is in operation, which is due to be launched on the NPOESS (National Polar-Orbiting Operational Environmental Satellite System) and NPP (NPOESS Preparatory Project) satellites from 2009. For this research, three MODIS products (datasets generated from a particular algorithm) will be utilised to assess the vegetation indices of selected sites. Internationally standard software packages are available to enable local satellite reception stations to process raw MODIS data in near-real-time into products such

as MOD09 (surface reflectance – 8 day composite), MOD13 (vegetation indices – 16 day composite), and MOD43 (BRDF/Albedo – 16 day composite), where BRDF is the Bidirectional Reflectance Distribution Function. These products, which have all been corrected for atmospheric effects, are suitable for use as they avoid any difficulties that may arise when using raw satellite data, for example, atmospheric disturbance. The MOD09 product (consisting of the first seven MODIS bands), has a higher temporal resolution than MOD13 and MOD43, and all products are projected to a convenient coordinate system. In any case, it is recognised that GIS compatibility is a very desirable characteristic for modern operational fire products, and this will be kept in mind as these research results are moved into operation.

Remote Sensing of Grassland Curing

Remote sensing methods have endeavoured to produce a Grassland Curing Index (GCI) that is equivalent to field measured curing values. The NDVI-GCI relationship has been investigated in few studies (Allan et al., 2003; Dilley and Edwards, 1998), which have shown differing results due to dissimilar methods and regional characteristics. In Victoria, Dilley and Edwards (1998) found that the satellite-derived GCI decreases exponentially with the satellite-derived NDVI. Similarly, researchers in Northern Australia found the same exponential decline between visual-curing values and NDVI over red soils; however, the negative relationship was linear over black soils (Allan et al., 2003). Alongside the effects of seasonal change, the contrasting soils limited the accuracy of these results. It has also been suggested that there is a direct relationship between FMC and NDVI (Dilley et al., 2004). For example, Paltridge and Barber (1988) correlated field-based FMC estimates with satellite-derived NDVI values to find a positive linear relationship. The current operational method converts NDVI to FMC using the relationship of Paltridge and Barber (1988), and then converts FMC to GCI using Barber's (1990) relationship (derived from a graph supplied by McArthur (1966)) shown in Fig. 2.

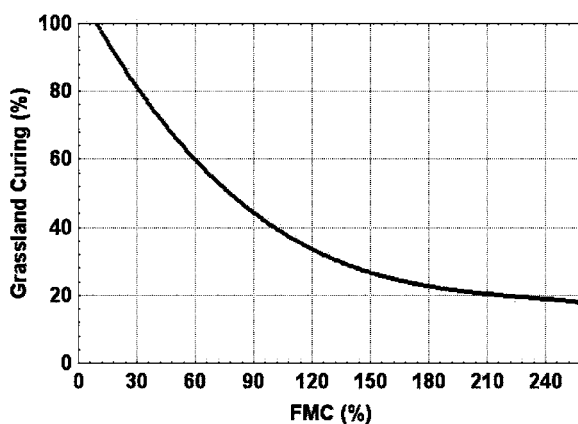


Fig. 2 The mathematical relationship between GCI and FMC, derived by Barber (1990). Source: (Garvey and Millie, 2001, p. 4, Copyright CFA, 2006)

The use of the GCI-FMC relationship, investigated in several studies (Dilley and Edwards, 1998; Dilley et al., 2004), avoids the uncertainties that arise from visual curing observations, which are significantly less accurate than destructive sampling (Dilley and Edwards, 1998). However, the GCI-FMC relationship may be species specific (Gill, 2006).

Methods

To assess grassland curing across Australia and New Zealand, MODIS-derived vegetation indices were investigated and compared to field data collected by fellow Bushfire CRC researchers. Field data were collected from a number of selected grassland sites (Fig. 3), which cover a variety of climate, topography and grass types.

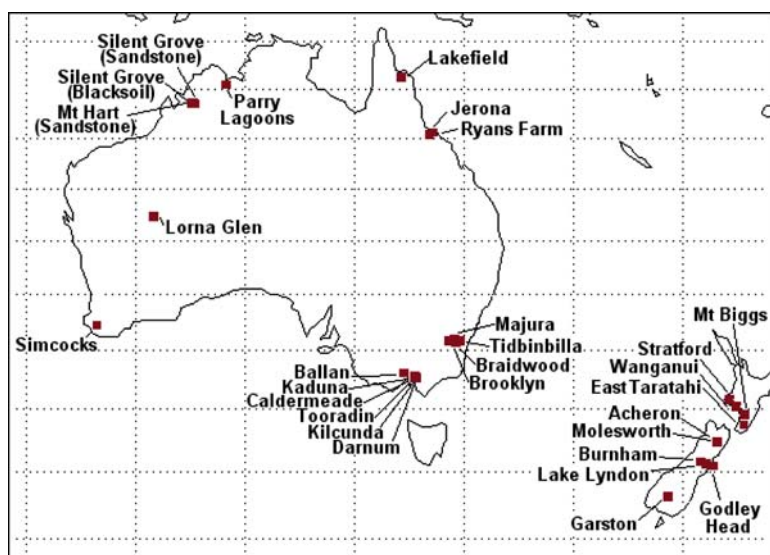


Fig. 3 Locations of grassland study sites in Australia and New Zealand

The majority of Australian sites presented in this paper have also been summarised in Table 3, to show the climatic differences and variability in grass type between sites.

Field Data

Various field methods have been used in past studies to measure grassland curing and FMC (Dilley et al., 2004). FMC has been estimated using the destructive sampling technique (Barber, 1979). This method entails collecting grass samples from random sites, weighing, oven-drying for 48 hours (105–110°C), then reweighing.

Table 3 Grass species, and annual rainfall of sites in Australia

| Site | | Grass Species | Mean Annual Rainfall (mm)* |
|------|--------------------------|---|----------------------------|
| ACT | Majura | Tall Spear grass, Tall fescue, Wall Fescue, Common Wheat grass | 611 |
| | Tidbinbilla | Fringed Fescue, Tall fescue, Phalaris, Weeping grass | 862 |
| NSW | Braidwood | Wall Fescue, Kangaroo grass | 706 |
| VIC | Caldermeade | Rye grass | 855 |
| | Kaduna | Rye grass | 855 |
| QLD | Jerona | Salt Couch, Black Spear grass | 907 |
| | Lakefield | Black Spear grass, Kangaroo grass, Paspalum, Love Grass | 1146 |
| WA | Ryans Farm | Black Spear grass, Urochloa grass | 907 |
| | Silent Grove [Blacksoil] | Spear grass, Buffel Grass, Mintbush, Golden Beard grass | 932 |
| | Silent Grove [Sandstone] | Spear grass, Spinifex, Golden Beard grass | 932 |
| | Parry Lagoons | Three-awned Spear grass, Native Annual Sorghum, Sand grass, Wanderrie grass | 754 |
| | Lorna Glen | Wanderrie grass, Love grass, Spinifex, Curry flower | 230 |

* Rainfall data collected from the Bureau of Meteorology, 2007.

Grassland curing has been estimated in the past by visual observations, using a photo guide. These observations generally underestimate the curing value, particularly when secondary growth occurs (Anderson and Pearce, 2003; Hosking, 1990; Millie and Adams, 1999).

Field data have been collected by Bushfire CRC researchers throughout Australia and New Zealand. Only a portion of these data however, are presented in this paper. The three methods used to estimate curing were destructive sampling, visual observations and Levy rod sampling. Destructive sampling of curing involved collecting grass samples in the field and sorting them into live and dead material in the laboratory, then oven-drying and weighing these live and dead components to calculate the proportion of dead fuel. Visual assessments were made by observers in the field, estimating the proportion of dead grass present. The Levy rod method is a modification of that proposed by Levy and Madden (1933), and entailed counting live and dead grasses that come in contact with a thin steel rod placed vertically into the ground at several points along a transect (Anderson et al., 2005). As the visual assessments of grassland curing have shown to be least accurate in a CRC study (Anderson et al., 2006), data derived from the destructive sampling and Levy rod methods are presented in this paper. Dead and combined (live and dead) fuel moisture samples were also collected from most sample sites.

Satellite Data

For each MODIS tile (geographic areas in which MODIS products are distributed), 68 MOD09 images (12 July 2005–27 December 2006), and 32 MOD13 images (from ACT) (26 June 2005–10 October 2006) were collected from the Land Processes Distributed Active Archive Center (<http://edcdaac.usgs.gov/datapool/datapool.asp>). The two Collection 4 MODIS products are as follows:

- MOD09A1: 8-day 500-m surface reflectance.
- MOD13A1: 16-day 500-m vegetation indices.

To reduce uncertainty in the results, the 500 m-resolution data were averaged over a 3×3 pixel area for each site, which was required to be uniform in grassland cover for accurate satellite-surface comparisons.

Results and Discussion

NDVI-time series (2005–2008) were generated from MOD09 at each field site and supplied from MOD13 for sites in the ACT. For each site across Australia and New Zealand, this process will be repeated for MOD09 over the next year. Using MOD09 data, the NDVI is plotted (Fig. 4) from August 2005 to February 2008 in Queensland and northern Western Australia. The NDVI generally peaks in autumn, mainly due to heavy monsoonal rains in summer. High variation is found between the sites, particularly throughout the curing period (in the winter months).

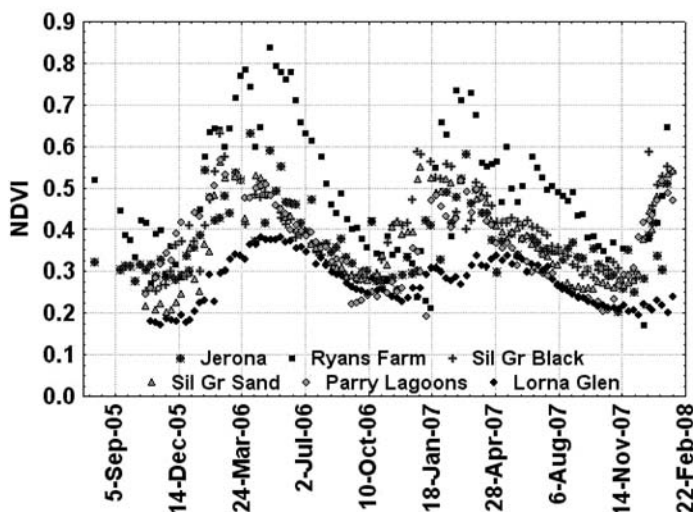


Fig. 4 Northern Australia NDVI Time series. Mean MOD09-derived NDVI, 500 m-resolution (3×3 pixel window) from two sites in Queensland (Jerona, Ryans Farm), and four sites in northern WA (Silent Grove [Blacksoil], Silent Grove [Sandstone], Parry Lagoons, Lorna Glen), 2005–2008

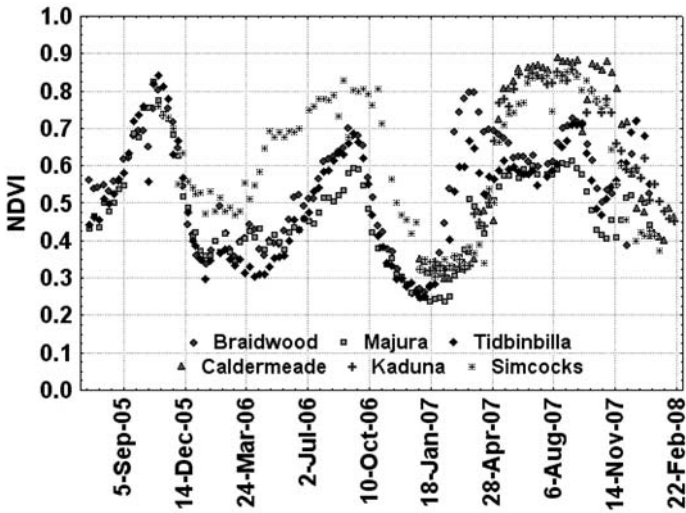


Fig. 5 Southern Australia NDVI Time series. Mean MOD09-derived NDVI, 500 m- resolution (3×3 pixel window) from two sites in the ACT (Majura, Tidbinbilla), one site in NSW (Braidwood), two in VIC (Caldermeade, Kaduna) and one site in southern WA (Simcocks), 2005–2008

In contrast, the NDVI in sites from southern Australia (from July 2005 to February 2008) generally shows spring to be the ‘greenest’ season of each year (Fig. 5).

The maximum NDVIs in southern Australia were much lower in 2006 than in 2005 and 2007. As the summer period approaches, the NDVI declines as grasslands are likely to cure. The variations between sites are large, and differences between the sites were observed in the timing of senescence. Peaks are also observed (particularly in Braidwood) throughout later summer to autumn (2006), due to secondary growth following rain. The annual cycle of NDVI is expected to vary throughout Australia and New Zealand due to different soil and grass types, and climatic and topographic variability. Throughout northern Australia, for example, NDVI is expected to decline throughout winter. In contrast, the NDVI in southern Australia decreases in summer.

The MOD09 time-series from Majura (ACT) is also presented in Fig. 6 for comparison with the MOD13 NDVI time-series, which uses a different compositing algorithm.

There is very little variation between the two MODIS products (root mean square difference of 0.033); however, MOD09 has an advantage with an enhanced 8-day temporal resolution, compared to 16 days for MOD13. In agricultural regions (consisting of grasslands and cereal crops, including wheat, maize, and mainly rice) of Southern China, Cheng (2006) found that MOD13 NDVI had a slightly closer correlation with ground data than MOD09 NDVI. Similarly, over selected cotton fields in the southwestern part of USA, McKellip et al., (2005) found less noise for the

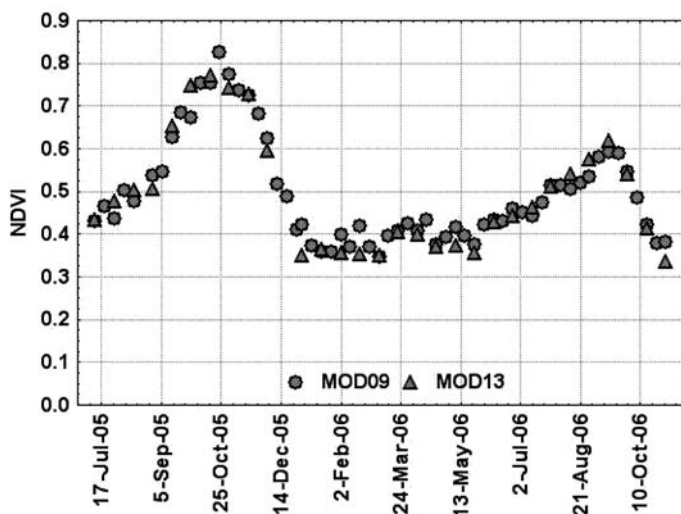


Fig. 6 MOD09 and MOD13 NDVI. MOD09 and MOD13-derived NDVI in Majura (ACT) from July 2005 to November 2006

MOD13 NDVI time-series than that of MOD09. In this current study, MOD13 and MOD09 NDVI were closely related, yet slight variability was found between the two products. These differences will be examined in future; for now it is fair to suggest that both products deliver similar information. As Cheng (2006) and McKellip et al. (2005) suggested good data was retrieved from MOD13-derived NDVI, they found that MOD09 had an advantage with its higher temporal resolution. Therefore, MOD09 NDVI has been compared, for this study, with field measurements.

The period in which NDVI decreases, is generally the period in which grassland curing occurs. As illustrated in Fig. 4, the NDVI in northern Australia decreases from May to October, which is the expected time for grasslands to cure in this region. As shown in Fig. 7a, the NDVI of three sites in northern WA has shown to decrease, while curing increases (Fig. 7b).

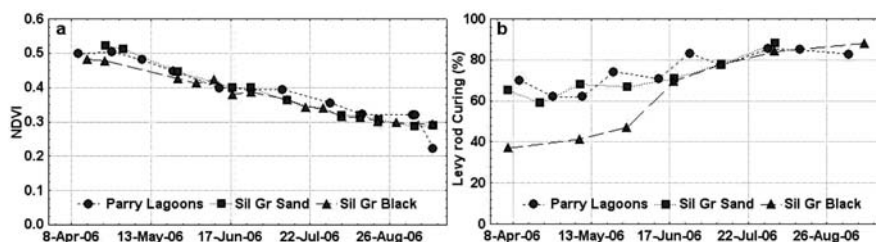
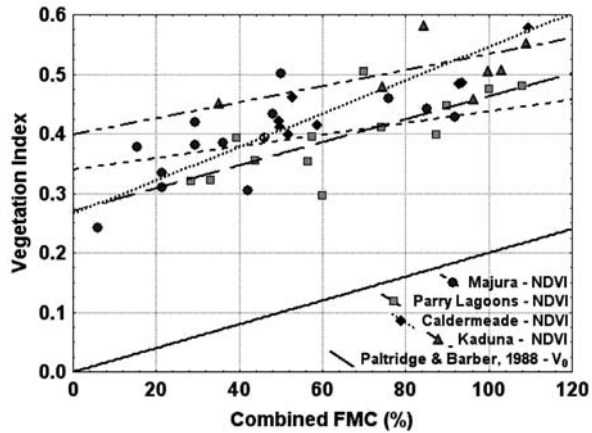


Fig. 7 Time series of (a) MOD09-derived NDVI, and (b) Levy rod curing, during the 2006 curing period in Parry Lagoons, Silent Grove [Sandstone], and Silent Grove [Blacksoil] (northern WA)

Fig. 8 FMC and NDVI. Field-derived FMC (destructive sampling) and MOD09-derived NDVI. From Majura (ACT), Parry Lagoons (northern WA), Caldermeade and Kaduna (Victoria), 2005–2008, with the FMC- V_0 relationship from Paltridge and Barber (1988)



The relation between NDVI and curing will be discussed later in this paper. Firstly, Paltridge and Barber (1988) correlated a full cover Vegetation Index

$$V_0 = (NIR - 1.2 \cdot Red) / (NIR + Red) \quad (3)$$

with FMC in Victoria. This index uses the coefficient of 1.2; the best-fit line for non-vegetated surfaces, calculated from plotting the red against the NIR radiance (Paltridge and Barber, 1988). A positive linear relationship was found between V_0 and FMC until the FMC reaches 250%. Above this percentage, the grass does not appear any greener. Therefore the V_0 will not continue to increase. A similar relationship was found between field-derived FMC and MOD09-derived NDVI in Majura (ACT), Parry Lagoons (northern WA), Caldermeade and Kaduna (Victoria) from 2005 to 2008 (Fig. 8). The four field sites show a similar NDVI-FMC relationship, even though they are of differing grass type (Table 3), in contrasting soils and in different climate zones. Compared to Paltridge and Barber's (1988) FMC- V_0 relationship, however, the NDVI from both sites does not decrease to 0 with 0% FMC.

According to Barber (1990), FMC has a cubic relationship with grassland curing (Fig. 2). The results obtained from Braidwood (NSW), displayed such a relationship (Fig. 9). As the visual observations are less accurate, only the Levy rod and destructive sampling methods were considered, and are presented with the FMC-curing curve from Fig. 2. Further data collection is obviously required, and the relationship may also vary between sites. So far, the FMC-destructive curing relation, roughly follows the curve derived from Barber (1990), with an offset of about 10%.

The Levy rod method has generally been found to be accurate when used in grasslands in Eastern Australia and New Zealand, as demonstrated by its agreement with the destructive curing estimates (Anderson et al., 2006). In this case, however, the FMC-Levy rod curing relation differs from Barber's (1990) curve and the

Fig. 9 FMC and Grassland Curing. The correlation derived by Barber (1990), with the FMC-Curing relationship from 2005 to 2006 field measurements in Parry Lagoons (WA) (using two methods)

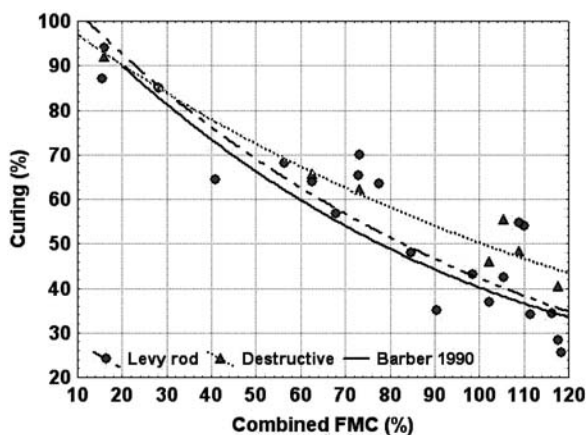
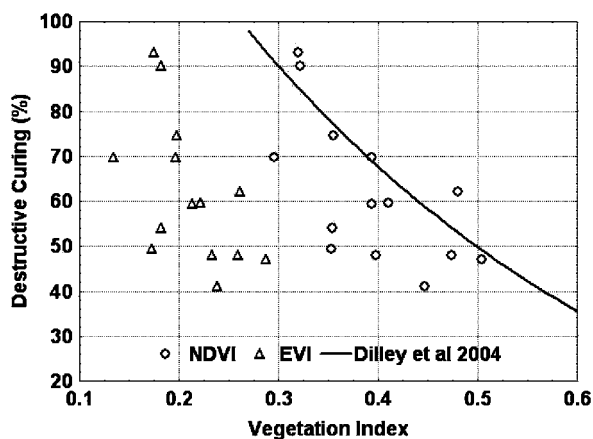


Fig. 10 Destructive Curing, against MOD09-derived NDVI and EVI in Parry Lagoons, (WA) 2005–2008, with the NDVI-GCI curve from (Dilley et al., 2004)



FMC-destructive curing curve by up to 20%. Therefore, destructive curing has been correlated with EVI and NDVI (Fig. 10).

The relation between these indices and grassland curing (ranging from 40 to 100%; the critical range of medium to high fire danger) is similar to the relation between NDVI and grassland curing found in several past studies (Allan et al., 2003; Dilley and Edwards, 1998), which are based on AVHRR-derived NDVI and visually assessed curing values. The exponential curves of best fit (not shown) for each method do not support strong correlations; however, data are limited.

Various vegetation indices will be analysed to identify which index correlates best with curing measurements. At this stage, it is uncertain which index will be the most appropriate to assess grassland curing across Australia and New Zealand, or whether the vegetation index – curing relationship will vary regionally.

Conclusions

To support bushfire management, this research aims to deliver a satellite based curing assessment method that is applicable across Australia and New Zealand. In summary, the NDVI annual cycle has illustrated definite differences between sites from northern and southern Australia due to climatic differences. Results have also shown that grassland curing occurs in the period of time when NDVI decreases. Current results, which compared MOD09-derived NDVI with field-derived curing measurements, show similar trends to the findings from past studies; however, these past studies either cover southeastern Australia only, or are based overseas. Therefore, variation in results between this project and past research is expected. The information produced from this project will lead to improved assessments of the degree of curing in grasslands across Australia and New Zealand, thereby providing sound science to support fire management in protecting life and property from grassfires, as well as using fire safely and effectively.

Acknowledgements This study is a part of the Bushfire CRC Project A1.4 'Improved Methods for the Assessment and Prediction of Grasslands Curing'. D. Martin acknowledges financial support from a Bushfire CRC Postgraduate Scholarship, and also acknowledges Dr Wendy Anderson and Dr Elizabeth Botha for assisting with the manuscript.

References

- Alexander, R. and Millington, A.C., (2000) Vegetation Mapping. John Wiley & Sons, Ltd, England.
- Allan, G., Johnson, A., Cridland, S. and Fitzgerald, N., (2003) Application of NDVI for predicting fuel curing at landscape scales in northern Australia: can remotely sensed data help schedule fire management operations? *International Journal of Wildland Fire*, 12: 299–308.
- Anderson, S.A.J., Anderson, W.R., Douglas, K.L. and Hollis, J., (2006). Development of a field method for assessment of degree of curing in grasslands. Poster presented at AFAC/IFCAA/Bushfire CRC Conference, 10–12 August 2006, Melbourne.
- Anderson, S.A.J., Anderson, W.R., Hines, F. and Fountain, A., (2005). Determination of field sampling methods for the assessment of curing levels in grasslands, Bushfire CRC Report (unpublished).
- Anderson, S.A.J. and Pearce, H.G., (2003) Improved methods for the assessment of grassland curing, 3rd International Wildland Conference, Sydney, Australia.
- Barber, J., (1990) Monitoring the Curing of Grassland Fire Fuels in Victoria, Australia with sensors in satellites and aircraft. A Country Fire Authority study in Remote Sensing. CFA, Melbourne.
- Barber, J., (1992) Monitoring grassland fire fuels with satellites. *Journal of the Australian Institute of Agricultural Science*, 5(1): 44–47.
- Barber, J. and Paltridge, G.W., (1986) Fuel Moisture Content of Vegetation from AVHRR – An Operational Fire Potential Monitoring System., 1st Australian AVHRR Conference. Communications Group, CSIRO, Perth, WA.
- Barber, J.R., (1979) Remote Sensing in Fire Prevention Planning: monitoring the curing of grasslands by means of sensors in satellites and aircraft. MEnvSc Thesis, Monash University, Clayton.
- Campbell, J.B., (2002) Introduction to Remote Sensing – Third Edition. The Guilford Press, New York.

- Chandler, C., Cheney, P., Thomas, P., Trabaud, L. and Williams, D., (1983) Vol 1, Forest Fire Behaviour and Effects, Fire in Forestry. John Wiley and Sons, New York.
- Cheney, P., Gould, J.S. and Catchpole, W.R., (1998) Prediction of fire spread in grasslands. *International Journal of Wildland Fire*, 8(1): 1–13.
- Cheney, P. and Sullivan, A., (1997) Grassfires: Fuel, Weather and Fire Behaviour. CSIRO Publishing, Melbourne.
- Cheng, Q., (2006) Multisensor comparisons for validating of MODIS vegetation indices. *Pedosphere*, 16(3): 362–370.
- Chuvieco, E., Cocero, D., Aguado, I., Palacios, A. and Prado, E., (2004) Improving burning efficiency estimates through satellite assessment of fuel moisture content. *Journal of Geophysical Research*, 109: 1–8.
- Davidson, A., Wang, S. and Wilmshurst, J., (2005) Remote sensing of grassland-shrubland vegetation water content in the shortwave domain. *International Journal of Applied Earth Observation and Geoinformation*, 8(44): 225–236.
- Dilley, A. and Edwards, M., (1998) Satellite – Based monitoring of grassland curing in Victoria, Australia. *Journal of the Australian Map Circle*, 47: 10–15.
- Dilley, A., Millie, S., O'Brien, D. and Edwards, M., (2004) The relation between normalized difference vegetation index and vegetation moisture content at three grassland locations in Victoria, Australia. *International Journal of Remote Sensing*, 25(19): 3913–3928.
- Foley, J.C., (1947) A Study of Meteorological Conditions associated with Bush Fire and Grass Fires and Fire Protection Strategy in Australia., Bureau of Meteorology, Melbourne.
- Gao, B.-C., (1996) NDWI a normalized difference water index for remote sensing of vegetation liquid water from space. *Remote Sensing of Environment*, 58: 257–266.
- Garvey, M. and Millie, S., (2001) Grassland Curing Guide. Country Fire Authority, Victoria.
- Gausman, H.W., (1977) Reflectance of leaf components. *Remote Sensing of Environment*, 6(1): 1–9.
- Gill, M.A., (2006) Grass Curing: A Fire-Oriented Review – ‘Curing’ and the moisture content of grasses, (Unpublished), Melbourne.
- Groves, R.H., (1994) Australian Vegetation. Cambridge University Press, U.K.
- Hosking, R., (1990) Grassland Curing Index – a district model that allows forecasting of curing. *Mathematical and Computer Modelling*, 13(12): 73–82.
- Huete, A.R., Didan, K., Miura, T., Rodriguez, E.P., Gao, X. and Ferreira, L.G., (2002) Overview of the radiometric and biophysical performance of the MODIS vegetation indices. *Remote Sensing of Environment*, 83(1–2): 195–213.
- Jones, S.D., Garvey, M.F. and Hunter, G.J., (2004) Where's the fire? Quantifying uncertainty in a wildfire threat model. *International Journal of Wildland Fire*, 13(1): 17–25.
- Levy, E.B. and Madden, E.A., (1933) The point method of pasture analysis. *New England Journal of Agriculture*, 46: 267–279.
- Liang, S., (2004) Quantitative Remote Sensing of Land Surfaces. John Wiley & Sons, Inc., New York.
- Luke, R.H. and McArthur, A.G., (1978) Bushfires in Australia. Australian Government Publishing Service, ACT.
- McArthur, A.G., (1966) Weather and grassland fire behaviour. No. 100, Commonwealth of Australia, Department of National Development, Forestry and Timber Bureau, Forestry Research Institute.
- McKellip R., Ryan R.E. and Blonski, S. (1995) Crop surveillance demonstration using a near-daily MODIS derived vegetation index time series. *International Workshop on the Analysis of Multi-Temporal Remote Sensing Images*, pp. 54–58.
- Millie, S. and Adams, R., (1999) Measures of Grassland Curing: a comparison of destructive sampling with visual and satellite estimates, Australian Bushfire Conference. School of Ecology and Environment, Deakin University, Rusden, Albury, pp. 1–8.
- Moore, R.M., (1970) Australian Grasslands. Australian National University Press, ACT.

- Newsome, P.F.J., (1987) The Vegetative cover of New Zealand. Ministry of Works and Development, Water and Soil Directorate, Wellington, New Zealand.
- NLWRA, (2001) Australian Native Vegetation Assessment. National Land and Water Resources Audit, Commonwealth Government, ACT.
- Paltridge, G.W. and Barber, J., (1988) Monitoring Grassland Dryness and Fire Potential in Australia with NOAA/AVHRR Data. *Remote Sensing of Environment*, 25(3): 381–394.
- Tucker, C.T., (1979) Red and Photographic Infrared Linear Combinations for Monitoring Vegetation. *Remote Sensing of Environment*, 8: 127–150.
- Wiegand, C.L., Richardson, A.J., Escobar, D.E. and Gerbermann, A.H., (1991) Vegetation Indices in Crop Assessment. *Remote Sensing of Environment*, 35: 105–119.

Assessment of Grassland Curing Using Field-Based Spectrometry and Satellite Imagery

Danielle Martin, Simon Jones, Ian Grant, and Stuart Anderson

Abstract Depending on a grass's growth stage, certain curing characteristics determine the vulnerability of grass to ignite or to propagate a fire. The current curing input into fire behaviour models and fire danger rating systems in Australia and New Zealand is generally based on visual estimates, which are widely recognised by both researchers and end-users as being inaccurate and thus causing uncertainty in system outputs. This Bushfire Cooperative Research Centre (CRC) project aims to develop improved methods to assess grassland curing across Australia and New Zealand. This paper reports on one component of the CRC project, which has focused initially on vegetation indices derived from EOS MODIS (MODerate resolution Imaging Spectroradiometer) satellite data. Results suggest a positive correlation between these satellite data and field data for curing assessment. Methods include destructive sampling, visual observations and Levy rod sampling. More comprehensive field data collection has been conducted in Victoria, entailing measurements of spectral reflectance signatures of grasslands using an ASD Fieldspec Spectroradiometer covering the wavelength range 350–2500 nm. These measurements identify which regions of the visible to mid-infrared spectrum best correlate with field data collected for curing assessment. The information produced from this project will lead to improved assessments of the degree of curing in grasslands across Australia and New Zealand, thereby providing sound science to support fire management in protecting life and property from grassfires, as well as using fire safely and effectively.

Background

The degree of curing, defined as the drying out and dying of grasses, reflects the proportion of dead material in a grassland fuel complex (as a percentage), and has

D. Martin (✉)

Space Based Observations Section, Bureau of Meteorology; School of Mathematical and Geospatial Sciences, RMIT, Melbourne; Bushfire Cooperative Research Centre, East Melbourne, VIC, Australia

e-mail: Danielle.Martin@bom.gov.au

a strong influence on the ability of fire to develop and spread, and the rate at which it spreads (Cheney and Sullivan 1997). The current curing input into fire behaviour models and fire danger rating systems in Australia and New Zealand is generally based on visually assessed field data and AVHRR (Advanced Very High Resolution Radiometer) satellite data. Both of these techniques have inherent problems and have lead to inaccurate assessment of grassland curing (Anderson et al. 2005). This can have major implications for fire management, particularly in terms of fire prevention and control, as well as the effective use of fire in prescribed burning programs. The accurate assessment of grassland curing has been the subject of past research throughout Australia (Allan et al. 2003, Barber 1979, Barber 1989, Dilley et al. 2004, Hosking 1990, Millie and Adams 1999, Paltridge and Barber 1988), mainly in the south-eastern corner of the continent. In south-eastern Australia, curing generally commences around late spring (see Fig. 1, Martin et al. this volume). However, in drought – affected areas, the onset of this process can occur much earlier (Barber 1989).

Vegetation characteristics that can be assessed via satellite remote sensing include Fuel Moisture Content (FMC) and curing percentage (chlorophyll content and colour of vegetation) (Barber 1992). Moisture content can be estimated using a number of spectral wavelengths centred on 970, 1200, 1450, 1950, and 2250 nm (Sims and Gamon 2003, Danson and Bowyer 2004, Davidson et al. 2005). Chlorophyll content is dependent on grass-species, leaf-age, phenological stage and leaf-health, as well as site specific factors such as shading. The main chlorophyll absorption bands are located in the blue and red bands, located 375–495 nm and 600–700 nm (Knipling 1970, Daughtry and Biehl 1985). Assessing either FMC or chlorophyll content, past studies have monitored, mostly using vegetation indices, pastures and crops in Victoria (Paltridge and Mitchell 1990, Paltridge and Barber 1988, Dilley et al. 2004, Dilley and Edwards 1998), tropical savannas in northern Australia (Allan et al. 2003), grasslands and shrublands in Spain (Chuvieco et al. 2004), grasslands and cereal crops in China (Cheng 2006) and cotton fields in the USA (McKellip et al. 2005). A number of different large area satellite sensors, such as AVHRR (Advanced Very High Resolution Radiometer) and MODIS have been widely used in past studies. This paper explores which MODIS bands correlate well with curing, via collection of spectral signatures from two Victorian sites, Caldermeade and Kaduna, for comparison with the MODIS measurements. These spectral readings are then utilised to identify which regions of the visible to mid-infrared spectrum best correlate with field data collected for curing assessment.

Methods

Throughout Australia and New Zealand, the Bushfire CRC has collected in situ curing measurements from 46 grassland sites. After assessing the representativeness and data quality of these sites 29 were selected for comparison with EOS MODIS (see Fig. 3, Martin et al this volume). From November 17th 2007 to February

18th 2008, two of these sites (Caldermeade and Kaduna) also included in situ spectral measurements using an ASD Fieldspec Spectroradiometer (350–2500 nm). Caldermeade and Kaduna are located 70 and 50 km southeast of Melbourne respectively, and both sites (used for cattle grazing) consist of improved pastures, with rye grass (*Lolium perenne*) being the dominant species.

Grassland curing was assessed at Caldermeade and Kaduna using three methods; visual observations, destructive sampling and Levy rod curing. For a full description of this method please see Martin et al. this volume. As visual assessments of curing have shown to be least accurate in past research (Anderson et al. 2006), and the destructive sampling technique was used less frequently in this study, data derived from the Levy rod method have been presented in this paper. The satellite data generated from MODIS are arranged into various sets of products. The product used for this study (MOD09A1) provides an estimate of surface spectral reflectance, at a 500 m resolution, corrected for atmospheric scattering and absorption, to provide an 8 – day temporal composite. Out of 36 MODIS bands, MOD09A1 provides the first seven, which are listed in table 1. These bands are located in the visible (380–720 nm), Near Infrared – NIR (720–1300 nm) and Mid Infrared – MIR (1300–3000 nm) regions of the spectrum (Campbell 2002). In the wider context of the CRC curing research, these bands are used to calculate various vegetation indices. To identify which of these bands offer maximum utility in curing research, this paper compared each MOD09A1 band with the in situ curing measurements.

Table 1 MODIS surface reflectance bands (NASA 2004)

| Band | Spectral region | Wavelength (nm) |
|------|---------------------|-----------------|
| 1 | Red | 645 |
| 2 | Near Infrared – NIR | 857 |
| 3 | Blue | 466 |
| 4 | Green | 554 |
| 5 | Near Infrared – NIR | 1242 |
| 6 | Mid Infrared – MIR | 1629 |
| 7 | Mid Infrared – MIR | 2114 |

To obtain satellite data for the two Victorian sites, MOD09A1 images were gathered from one MODIS tile (a geographic area in which MODIS products are distributed). Thirteen of these images (all from Collection 5) were collected from the Land Processes Distributed Active Archive Center (<http://edcdaac.usgs.gov/datapool/datapool.asp>). To reduce uncertainty in the results, the 500 m resolution data were averaged over a 3×3 pixel area for each site for accurate satellite-surface comparisons. These averaged values were produced from each 8 – day composite, which have been compiled throughout the curing sampling period. On each day of curing sampling, field spectroscopy was utilised to investigate the changes in spectral reflectance of grass, as curing progresses. An ASD Fieldspec Spectroradiometer was used, covering the spectral range between 350 and 2500 nm. With measurements taken at nadir, the spectroradiometer 8° lens was mounted on

a tripod 108 cm from the surface, resulting in a field of view diameter of 30.4 cm. To account for spectral variability across the site, these spectral measurements were collected every 2 metres along a 20 m transect. This process was repeated along a second transect located perpendicular to the original. At every 2 m interval, a minimum of 15 readings were taken. To calibrate for changing illumination geometry and to convert readings into reflectance factors, a white reference Spectralon panel was used, and held 15 cm below the 8° lens. The frequency of use was dependent on weather conditions, but as a minimum, one spectralon sample was collected at each sample point.

Results and Discussion

MODIS data were correlated simultaneously with in situ curing measurements for all sites around Australia and New Zealand. In this paper, preliminary results are presented from the Caldermeade and Kaduna sites in Victoria, from November 17th 2007 to February 18th 2008. In addition to curing and MODIS data comparisons, these measurements have been compared with in situ spectral measurements. To understand the changes in spectral reflectance as grassland curing progresses, Fig. 1 represents the spectral signatures of grassland produced by an ASD Spectroradiometer.

Each curve is the reflectance spectrum on a particular day, and is coloured according to the (Levy rod) curing value on that or the nearest day. To follow on from these ASD – derived reflectance spectra, the reflectance spectra illustrated in Fig. 2 were generated from MODIS bands 1 to 7 (Table 1) (after the approach of Zarco-Tejada et al., (2003)), again, coloured according to curing values. Since these reflectance

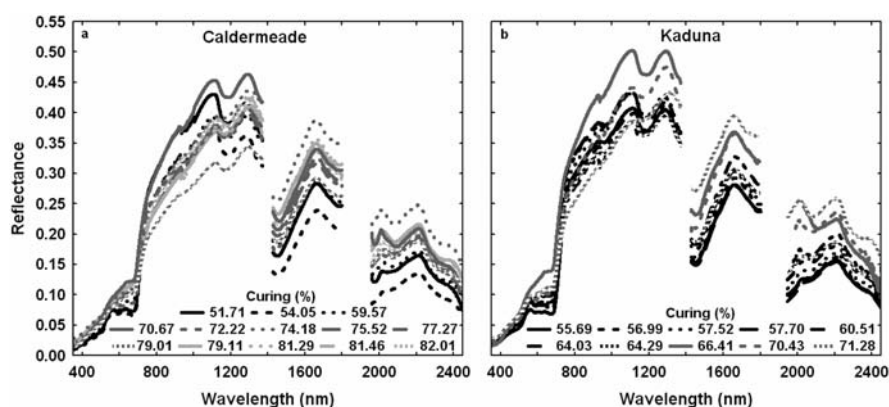


Fig. 1 Spectral signatures derived from an ASD Spectroradiometer at (a) Caldermeade (30-11-07–22-01-08) and (b) Kaduna (28-12-07–19-02-08). Areas with gross atmospheric scattering have been removed, resulting in a gap between 1800 and 1960 nm

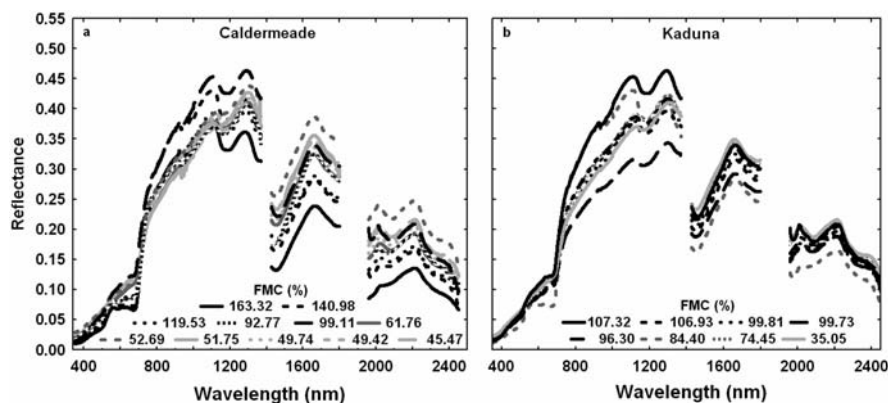


Fig. 2 Spectral signatures of grasslands generated from MOD09's seven bands at (a) Caldermeade (30-11-07–19-02-08) and (b) Kaduna (18-12-07–19-02-08)

signatures have only seven reflectance values the water and chlorophyll absorption features are less prominent than those presented in Fig. 1.

Vegetation spectral signatures are characterised by low reflectance in the visible and MIR (controlled by pigment and water absorption features) and high reflectance in the NIR (dominated by cell structure) (Cheng et al. 2006, Daughtry and Biehl 1985, Knipling 1970). The low reflectance in the visible spectrum is due to leaf pigments, primarily chlorophylls, although, carotenoids, xanthophylls and anthocyanins also have an effect (Knipling 1970). As leaves grow and mature, chlorophyll concentrations are suggested to increase (Gates and Tantraporn 1952), creating high absorption in the red and blue wavelengths (MODIS bands 1 and 3 respectively). This is shown in Figs. 1 and 2. As leaves senesce (cure), chlorophyll levels decline (Gates and Tantraporn 1952). In the NIR, there is little or no electromagnetic radiation absorption by leaf pigments (Gausman 1977, Knipling 1970), resulting in a region of high reflectance from 750 to 1300 nm (illustrated clearly in Fig. 1), known as the NIR plateau (Belward and Lambin 1990). As curing commences, lack of moisture causes the internal leaf volume to decline and the number of cell interfaces to increase, resulting in a rise in NIR scattering and hence reflectance (Rock et al. 1988, Knipling 1970). Figure 1b illustrated a minor trough for green grass at 970 nm, owing to a water absorption band, which does not feature in the coarse MODIS spectra (Fig. 2). This trough tends to vanish from the spectrum when vegetation loses its moisture (Rahman et al. 2003). As well as two minor water absorption bands (970 and 1200 nm) located in the NIR, water content generally controls the reflectance spectra in the MIR wavelengths at 1450, a major trough shown in Fig. 1, and also at 1950 and 2250 nm (Davidson et al. 2005, Danson and Bowyer 2004, Sims and Gamon 2003). Leaf reflectance in the MIR is therefore inversely related to water content (Gates and Tantraporn 1952, Belward and Lambin 1990). However, the sensitivity of reflectance to change in water content is wavelength dependent (Danson and Bowyer 2004). Both Figs. 1 and 2 show that

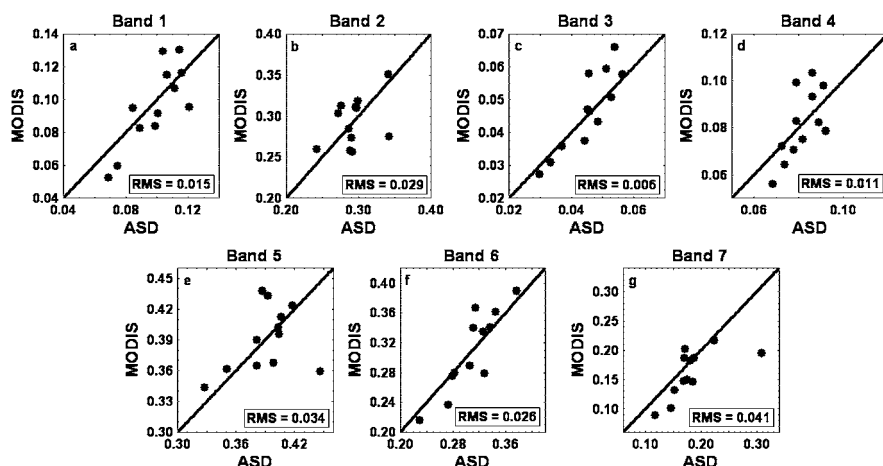


Fig. 3 Comparisons between MOD09 and ASD simulated reflectance values at Caldermeade

even though both sites received similar amounts of rainfall during the study period (located 20 km apart), and also consist of the same grass type and land-use intensity, Caldermeade reached a higher degree of curing than Kaduna. Resembling past studies of vegetation water content (Danson and Bowyer 2004, Pu et al. 2003), both figures indicate that as grasses cure, the surface reflectance tends to increase in the visible, decrease in the NIR, and increase in the MIR. Similarly, a study in central Spain compared the reflectance spectra of Mediterranean grasslands with different FMC values. Even though Yebra et al. (2008) found a lower FMC to result in a slightly lower reflectance in the visible, the spectra demonstrated a lower and higher reflectance in the NIR and MIR respectively, similar to the spectral responses shown in Figs. 1 and 2.

To validate the MODIS surface reflectance using field spectroscopy, all seven MOD09 bands were then compared with the seven simulated MOD09 bands generated from the ASD spectroradiometer at the Caldermeade site (Fig. 3). In order to synchronise the MODIS data with the field data, the spectral measurements were matched with the closest date of MODIS data. Even though the field data cannot be entirely coincident with the time of over-flight, the field data collection should generally bracket the satellite overpass time (McCoy 2005), hence, fall within the 8-day composite. Therefore, to match up these data, some data points were removed.

Each ASD reflectance spectrum (in Fig.3), was multiplied by the relative spectral response curve of each MODIS band (Jupp 2003) and summed to give seven simulated MODIS reflectance values. These comparisons in Fig. 3 demonstrate that for all bands, the MOD09 and ASD simulated values agree well with little bias, as shown by the closeness of the points to the one-to-one line. Excepting band 7 with an outlier resulting in a higher Root Mean Square (RMS) (Fig. 3 g), the scatter is generally small. This agreement demonstrates that the MOD09 product, which is the result of an atmospheric correction, provides accurate surface reflectance values,

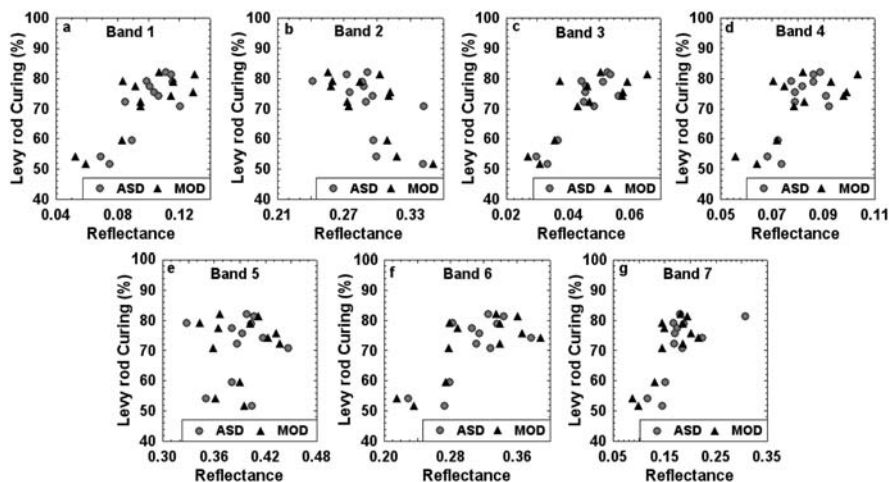


Fig. 4 Relationship between Levy rod curing (%) and each MODIS Band (derived from MOD09 'MOD', and from ASD field spectroscopy 'ASD') at Caldermeade

at least at the Caldermeade site. It also gives confidence that the field locations and sampling methodology of the spectroscopy yield values that are representative of the MODIS scale. By implication, the Levy rod measurements are representative of the MODIS scale because they are sampled on the same transect as the spectroscopy. Therefore, assuming from Fig. 3 that both the MOD09 and ASD spectral data have the same relationship with curing, the band sensitivity to curing was then examined. Figure 4 compares, for each band, the MODIS and ASD simulated reflectance with Levy rod curing (ranging from 52 to 83%) at Caldermeade.

Referring to Figs. 1a and 2a, the reflectance spectra at Caldermeade had changed as curing progressed, particularly in the water and chlorophyll absorption bands. One of the minor water absorption bands, at 1200 nm, is located adjacent to Band 5 (1242 nm) on the spectrum. Past studies have used this band, as well as Bands 2 and 6, to estimate vegetation water content (Zarco-Tejada et al. 2003, Cheng et al. 2006), and as water content (in this case FMC) relates with curing (Dilley and Edwards 1998, Barber 1979, Dilley et al. 2004, Millie and Adams 1999), the Levy rod curing estimates were expected to show a spectral response at this wavelength (Fig. 4e). Reasons for such a poor relationship between Band 5 and curing remain uncertain, however, spectral reflectance had changed with curing for the other 6 MOD09 bands.

Conclusions

In summary, the reflectance spectra of grasslands at both Victorian sites illustrated definite differences between green and cured grass due to the affects in the water and chlorophyll absorption bands. In situ observations of curing using the Levy Rod

method were found to correlate well with MOD09A1 spectral responses and be broadly representative of the monitored sites. The relationships found between curing estimates, MODIS data, and ASD field spectroscopy will help identify which vegetation indices are most useful for curing assessment, and will assist in creating a possible new index. The information produced from this project will lead to improved assessments of the degree of curing in grasslands across Australia and New Zealand, thereby providing sound science to support fire management in protecting life and property from grassfires, as well providing for the safe and effective use of fire.

Acknowledgements This study is a part of the Bushfire CRC Project A1.4 'Improved Methods for the Assessment and Prediction of Grasslands Curing'. D. Martin acknowledges financial support from a Bushfire CRC Postgraduate Scholarship.

References

- Allan, G., Fitzgerald, N. (2003) Application of NDVI for predicting fuel curing at landscape scales in northern Australia: can remotely sensed data help schedule fire management operations? *International Journal of Wildland Fire*, 12, 299–308.
- Anderson, S. A. J., Anderson, W. R., Douglas, K. L. and Hollis, J. (2006) Development of a field method for assessment of degree of curing in grasslands. Poster presented at AFAC/IFCAA/Bushfire CRC Conference, 10–12 August 2006, Melbourne.
- Anderson, S. A. J., Anderson, W. R., Hines, F. and Fountain, A. (2005) Determination of field sampling methods for the assessment of curing levels in grasslands. Bushfire CRC Report (unpublished).
- Barber, J. R. (1979) Remote Sensing in Fire Prevention Planning: monitoring the curing of grasslands by means of sensors in satellites and aircraft. Environmental Science. Clayton, Monash University</pub>.
- Barber, J. R. (1989) Remote Sensing Strategies for monitoring grassland fire fuels. Melbourne, The University of Melbourne.
- Barber, J. R. (1992) Monitoring Grassland Fire Fuels with Satellites. *Journal of the Australian Institute of Agricultural Science*, 5, 44–47.
- Belward, A. S. and Lambin, E. (1990) Limitations to the identification of spatial structures from AVHRR data. *International Journal of Remote Sensing*, 11, 921–927.
- Campbell, J. B. (2002) Introduction to Remote Sensing – Third Edition, New York, The Guilford Press.
- Cheney, P. and Sullivan, A. (1997) Grassfires: fuel, weather and fire behaviour, Melbourne, CSIRO Publishing.
- Cheng, Q. (2006) Multisensor comparisons for validating of MODIS vegetation indices. *Pedosphere*, 16, 362–370.
- Cheng, Y., Zarco-Tejada, P. J., Riano, D., Rueda, C. A. and Ustin, S. L. (2006) Estimating vegetation water content with hyperspectral data for different canopy scenarios: Relationships between AVIRIS and MODIS indexes. *Remote Sensing of Environment*, 105, 354–366.
- Chuvieco, E., Cocero, D., Riano, D., Martin, P., Martinez-Vega, J., Riva, J. and Perez, F. (2004) Combining NDVI and Surface Temperature for the Estimation of live Fuel Moisture Content in Forest Fire Danger Rating. *Remote Sensing of Environment*, 92, 322–331.
- Danson, F. M. and Bowyer, P. (2004) Estimating live Fuel Moisture Content from Remotely Sensed Reflectance. *Remote Sensing of Environment*, 92, 309–321.
- Daughtry, C. S. T. and Biehl, L. L. (1985) Changes in spectral properties of detached birch leaves. *Remote Sensing of Environment*, 17, 281–289.

- Davidson, A., Wang, S. and Wilmshurst, J. (2005) Remote sensing of grassland-shrubland vegetation water content in the shortwave domain. *International Journal of Applied Earth Observation and Geoinformation*, 8(44): 225–236.
- Dilley, A. and Edwards, M. (1998) Satellite – Based Monitoring of Grassland Curing in Victoria, Australia. *Journal of the Australian Map Circle*, 47, 10–15.
- Dilley, A., Millie, S., O'Brien, D. and Edwards, M. (2004) The Relation between Normalized Difference Vegetation Index and Vegetation Moisture Content at three grassland locations in Victoria, Australia. *International Journal of Remote Sensing*, 25, 3913–3928.
- Gates, D. N. and Tantraporn, W. (1952) The Reflectivity of Deciduous Trees in the Infrared to 25 microns. *Science*, 115, 613–616.
- Gausman, H. W. (1977) Reflectance of Leaf Components. *Remote Sensing of Environment*, 6, 1–9.
- Hosking, R. (1990) Grassland Curing Index – a district model that allows forecasting of curing. *Mathematical and Computer Modelling*, 13, 73–82.
- Jupp, D. L. B. (2003) Earth Observation Centre – MODIS Tools. <http://www.eoc.csiro.au/>. Accessed 23.05.08., Commonwealth Scientific and Industrial Research Organisation.
- Knipling, E. B. (1970) Physical and physiological basis for the reflectance of visible and near-infrared radiation from vegetation. *Remote Sensing of Environment*, 1, 155–159.
- McCoy, R. M. (2005) *Field Methods in Remote Sensing*, New York, The Guilford Press.
- McKellip, R., Ryan, R. E., Blonski, S. and Prados, D. (2005) Crop Surveillance Demonstration Using a Near-Daily MODIS Derived Vegetation Index Time Series. NASA, USA.
- Millie, S. and Adams, R. (1999) Measures of Grassland Curing: a comparison of destructive sampling with visual and satellite estimates. Australian Bushfire Conference. Albury, School of Ecology and Environment, Deakin University, Rusden.
- NASA (2004) EOS Data Products Handbook Volume 1. King, M.D.; Closs, J.; Spangler, S.; Greenstone, R.; Wharton, S.; Myers, M. (Eds.). Maryland, NASA Goddard Space Flight Center.
- Paltridge, G. W. and Barber, J. (1988) Monitoring Grassland Dryness and Fire Potential in Australia with NOAA/AVHRR Data. *Remote Sensing of Environment*, 25, 381–394.
- Paltridge, G. W. and Mitchell, R. M. (1990) Atmospheric and Viewing Angle Correction of Vegetation Indices and Grassland Fuel Moisture Content Derived from NOAA/AVHRR. *Remote Sensing of Environment*, 31, 121–135.
- Pu, R., Ge, S., Kelly, N. M. and Gong, P. (2003) Spectral absorption features as indicators of water status in coast live oak (*Quercus agrifolia*) leaves. *International Journal of Remote Sensing*, 24, 1799–1810.
- Rahman, A. F., Gamon, J. A., Sims, D. A. and Schmidts, M. (2003) Optimum pixel size for hyperspectral studies of ecosystem function in southern California chaparral and grassland. *Remote Sensing of Environment*, 84, 192–207.
- Rock, B. N., Hoshizaki, T. and Miller, J. R. (1988) Comparison of in situ and airborne spectral measurements of the blue shift associated with forest decline. *Remote Sensing of Environment*, 24, 109–127.
- Sims, D. A. and Gamon, J. A. (2003) Estimation of vegetation water content and photosynthetic tissue area from spectral reflectance: a comparison of indices based on liquid water and chlorophyll absorption features. *Remote Sensing of Environment*, 84, 526–537.
- Yebra, M., Chuvieco, E. and Riano, D. (2008) Estimation of live fuel moisture content from MODIS images for fire risk assessment. *Agricultural and Forest Meteorology*, 148, 523–536.
- Zarco-Tejada, P., Rueda, C. and Ustin, S. (2003) Water Content estimation in vegetation with MODIS reflectance data and model inversion methods. *Remote Sensing of Environment*, 85, 109–124.

Airborne Fire Intelligence

R. Cook, A. Walker, and S. Wilkes

Abstract A bushfire is part of the Australian summer landscape. Over the past two decades there has been an increasing use of aircraft, both fixed and rotary wing, for water bombing and the gathering of fire intelligence. In Australia prior to 2001, the gathering of airborne fire intelligence was mostly catered for by the use of paper maps that were subject to considerable operator error, delays and risk getting the information to the incident management team. The delay and risk factors were generally caused by airborne drops over pre-determined zones, or the aircraft needing to land to supply paper maps with hand drawn fire activity information, or by verbal passing of intelligence over congested radio frequencies.

Recent years have seen an increasing use of computer based airborne mapping systems, line scanners and infrared devices and cameras. These systems can be complex to operate and require careful coordination on a state-wide basis to ensure that the various incident management teams receive timely, readily understandable and useful information. These new systems, however, enabled the relevant authorities from 2001 on to make soundly based and timely fire fighting decisions with otherwise limited resources.

This paper is based on bushfire experience gained in NSW and the ACT during the years 2001–2003. It looks at the aircraft based fire intelligence systems used and the coordination of these systems together with fire weather, predictive fire behaviour, assets under threat and local knowledge perspectives. Hopefully the work that has been undertaken will stimulate discussions as to what is best practice to fully utilise these limited and expensive tools in fire management.

Introduction

Traditionally, bushfire incident management teams needing spatial coordination and planning data relied on the use of 1:25,000 scale topographic maps that were often considerably out of date; some not printed since the change to metric maps in 1966.

R. Cook (✉)
IAM Pty Ltd, Gungahlin, ACT 2912, Australia
e-mail: rcook@iam.net.au

In the late 1980s and early 1990s, digital data derived from these sources was being increasingly made available for the use of emergency services staff for incident and operational management.

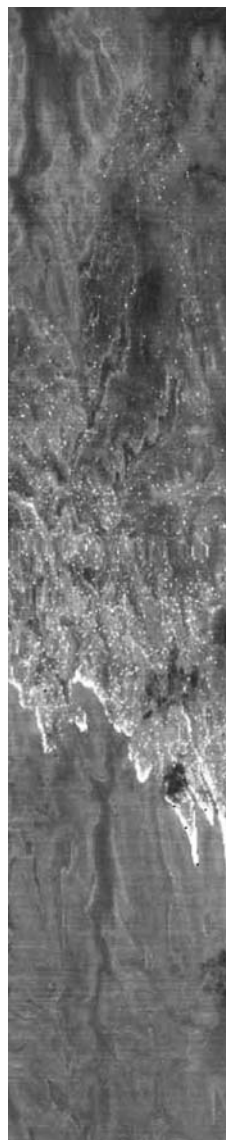
At the local grass roots level, some emergency managers were already aware or became aware of the short comings of basic data for incident management. Some local regions developed and operated various configurations of 'community mapping' to improve the data and keep it current and accurate (McRae and Walker, 2001). Community mapping, as the name implies, is a local consortium of land managers, response agencies and volunteers who undertake data collection and upkeep in an agreed manner. The use of simple Geographical Information Systems (GIS) together with this enhanced community gathered data enabled local emergency managers to rapidly locate the incident, check its authenticity, and dispatch appropriate resources. In most cases, local areas achieved considerable cost savings as a result of better utilisation of their scarce resources.

The NSW Rural Fire Service (NSW RFS) for the years up to 2001 mainly relied on fire information collected from the fire ground (or from aircraft when these were available) and drawn on paper maps. In many cases the information gathering was a slow process (the aircraft had to land or the vehicle had to be driven back to the incident control centre and the data transcribed on to a map) and was often of poor quality due to many factors. Up to this time many in incident management teams thought that airborne fire intelligence gathering sorties were expensive exercises in futility. Concurrent with this at times of extreme State-wide fire activity, data from an airborne Daedalus line scanner (a multispectral system with 12 bands ranging from the visible, through the near infrared, shortwave infrared to the thermal infrared wavelengths) system (Air Affairs Australia Pty Ltd (AAA)) was flown only at night using the thermal infrared channel (Fig. 1). Incident management teams usually found them difficult to relate to their particular fire incident as the results were often hours old, could not be rapidly geolocated or easily interpreted. Also, as this product was not rectified, it could not be overlain by topographic or other data (such as cadastre and property information) in a GIS.

In October 2001, the NSW RFS obtained the services of Image Analysis & Mapping Pty Ltd (IAM) to provide a review of and recommendations for the use of this airborne scanner system. Most of this work was carried out in northern NSW during an actual fire situation early in the fire season of 2001. The review centred on the requirement of fire incident operations staff to transfer fire front data from the scanner imagery on to the NSW RFS's standard incident management 1:25,000 scale map backgrounds. A further requirement was to provide the digital data in a form that could be easily understood by the incident management teams.

Local GIS platforms facilitated the rapid exchange of data particularly during emergency incidents. Fire mapping software such as 'PyroMap'TM and 'Incident Management Tools' developed during 2002 (PyroLogicaTM) increased the power of GIS. Also, community sourced GIS data enabled the rapid mapping of emergency incidents, both on the ground and from airborne platforms such as helicopters. Recently, due to the 'Cinderella factor' nature of these developments, many vested interests attempted to push various inappropriate and insufficiently evaluated

Fig. 1 Raw Daedalus night TIR fire image north of post Macquarie, October 2001



technologies for these purposes at the local level. As an example, there are some very good and very poor instances of this situation in web enabled systems that are in use in various States and Territories throughout Australia.

The ability to collect very accurate information and produce maps using the best possible information at the local level ensures the best possible safety for emergency workers. The Canberra fires of 2003 (where the methods described were used) clearly demonstrated this and could be the most comprehensively mapped bushfires

in the long history of fire in the landscape of Australia. This ability at the local level to produce such accurate maps and enable the information to be transmitted between locations meant that it could also be rapidly transmitted in digital form to regional offices and headquarters enabling better planning of emergency resources. The digital data supplied enabled a planned approach to all incidents on a state wide basis and improved the efficiency of the intelligence capture process. This becomes particularly important during post-incident coronial enquiries.

The discussion describes the processes developed and employed by the NSW RFS between 2001 and 2003 to improve the operational management of bushfires.

Fire Intelligence

Good coordination results from the supply of accurate and timely information. The forward deployment of Geographical Information Systems at the district (fire, local government, etc) level increased the supply of accurate and timely information to many fires across the state. At NSW RFS headquarters the information could be made up of satellite (NOAA AVHRR) data identified hotspots (thermally hot areas), lightning strikes and current and forecast weather conditions (BOM) over the fire ground. Headquarters could then readily see those incidents that required additional management. In these cases, the Daedalus airborne scanner was tasked to fly a carefully planned flight pattern over fires to obtain data on which to base the increased deployment of resources. The efficient fighting of fires is becoming an expensive exercise, in part due to the increased use of aircraft and in particular of water bombing aircraft. This is a cost that will more than likely continue to increase with changing climatic conditions that may well lead to not just more bushfires but to more serious (intense) bushfires. This will increase requirements for and demands on ground and airborne reconnaissance systems.

To improve such systems, further research is required for fire management coordination, communication systems, aircraft instrument scanning and other instrument systems use and to deliver overall reductions in the cost of fire fighting operations. An example of cost reductions would be by way of a decrease or at least a better use of water bombing aircraft provided for by the more cost effective use of airborne scanner and other fire intelligence data. Possible research examples are the filtering techniques used for lightning strike data to improve its accuracy for those strikes most likely to start a fire, and post-fire research to investigate and analyse airborne data acquired during fire incidents. Another technology the NSW RFS has been using is a thermal infrared camera (FireSearch Pty Ltd) that is mounted on a fixed wing aircraft for mapping hotspots near to the fire edge and particularly for mopping up operations.

Coordinating resources across a large area such as NSW requires accurate and timely intelligence on bushfire situations across the State. Bushfire suppression and property protection is most critical when fire conditions are extreme. When this is the case, available resources are stretched to the limit and assistance is often sought

from other jurisdictions. Unbiased, accurate and consistently collected information obtained across the range of situations is needed quickly to ensure the resources are deployed safely where they are most efficiently used. This requires confidence in the decisions made which can only be achieved by having confidence in the data provided. This can be achieved, at least in part, by having standardised GIS mapping methods, attributes (metadata) and depiction (appearance), plus personnel trained to understand not only what the data shows but also the limitations of such data and derived information.

During the bushfire seasons of 2001–2003, a system of intelligence gathering using various techniques was established and supplied the NSW RFS and other stakeholders with accurate, timely and highly relevant information to enable coordination of fire management across the state.

Daedalus Airborne Scanner

Up to the 2000–2001 fire season, the Daedalus airborne line scanner did not have an attitude correction system installed to enable the scanner data to be geographically located. Figure 1 (above) is an example of the type of basic raw data product that was used up to this time. In the night time TIR example given, the fire front appears white with the area burnt from behind the fire front and up the image having a speckled appearance. Some cloud is also evident. As can be seen, such an image is not particularly useful in this form.

IAM's review of the scanner system highlighted the need (to AAA and NSW RFS) for the scanner to have an attitude correction system installed.

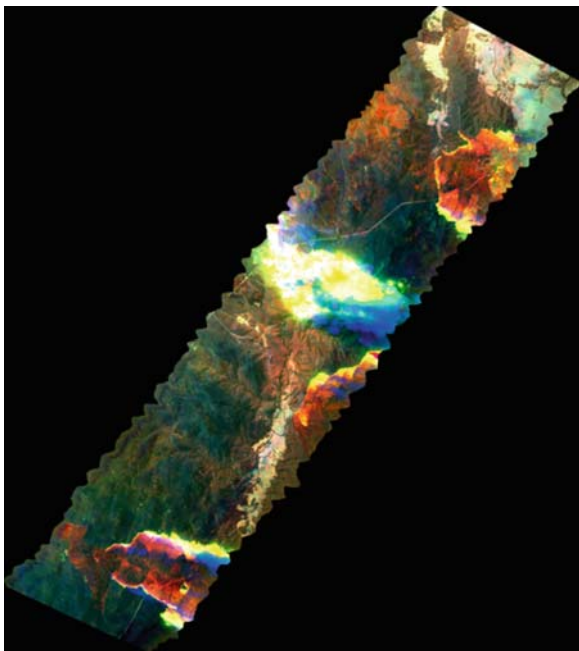
Four of IAM's recommendations included:

1. An upgrade to the AAA scanner to provide accurate geographic location of the data.
2. That the RFS install an air-to-ground data down link system.
3. That the RFS set up a permanent spatial data group for rapid response processing of the airborne data.
4. That with the above systems in place, the scanner also be used for day time monitoring of fires using multispectral bands as well as night time with thermal infrared (TIR) data only.

By mid 2002, AAA had upgraded their airborne scanner with an attitude correction system that allows the scanner data to be geo-rectified. Further to this, IAM had software developed that uses the scanner attitude correction system data (providing X, Y, Z, roll, pitch and yaw locations for each line scanned) to rectify the scanner data.

During the 2002–2003 bushfire season, the NSW RFS made full use of the upgraded Daedalus scanner system with fire activity images produced shortly after the data was received and dispatched to the GIS unit at operations headquarters,

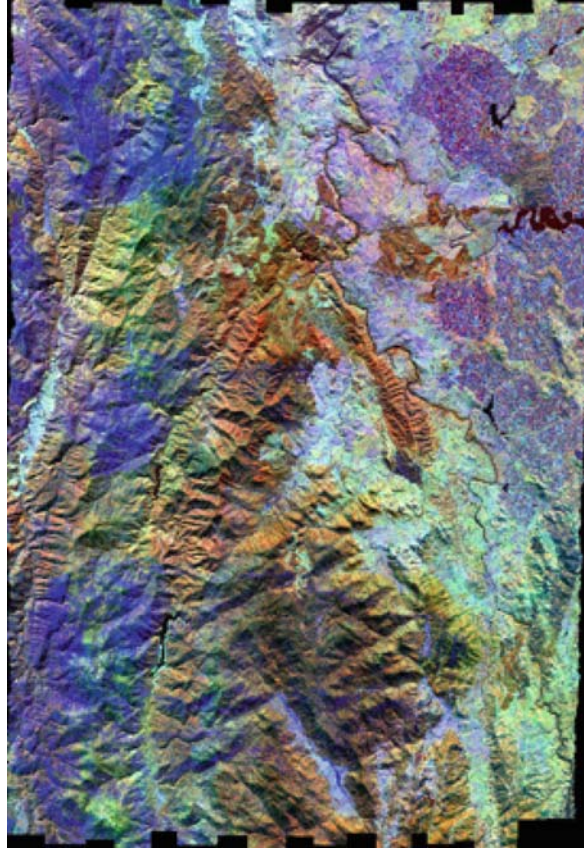
Fig. 2 Rectified and processed Daedalus data showing bushfire intensity



regional offices and other authorities such as the NSW NPWS, NSW State Forests, metropolitan brigades and police. This data was very well received by all who understood what the data provided. Figure 2 (below) is an example of the type of output from this upgraded system. This particular example with a spatial resolution of 8 m is of the Canberra bushfires of January 2003 and is located to the west of Canberra. Brindabella Valley can be seen in the southern half of the image. After rectification and with appropriate image processing, nearly all of the cloud and smoke is removed providing images that not only show the status (intensity, volatility), locations and directions of fire fronts and spot fires but also of varying fire intensity and existing and potential property and environmental damage. The white to yellow area of fire in the centre of the image indicates that the fire is very intense and taking a run. The red areas indicate less intense fire and where the fire has already burnt through. The blue areas are of very dense smoke that includes ash and other debris. Daedalus data in this form is a considerable improvement over the raw TIR night time data as shown in Fig. 1 and is invaluable to fire operation management teams as it allows them to accurately assess fire conditions, where to send available resources and plan further fire fighting activities.

The Daedalus system has also been flown over post-bushfire areas throughout NSW and the ACT and provides a very effective means of mapping the final fire extent and of determining fire severity. This is of particular importance where property damage has occurred. An example of this is provided in Fig. 3 that is a mosaic of 19 runs of orthorectified data at 3 m spatial resolution over the Canberra bushfire affected region of 2003 (data acquired April/May 2003).

Fig. 3 Daedalus post fire data of the Canberra area bushfires of January 2003. This mosaiced image comprises 19 runs of data at 3 m spatial resolution



This and other such data has been extensively used by various authorities to help determine fire severity and the consequential impact on property and the natural environment and can be used as evidence in post-fire Coronial inquiries.

In 2004 in collaboration with the NSW RFS, AAA installed a downlink system that allows rapid response quick-look images of fire activity to be downloaded to operations staff on the ground.

Digital Air Observers

Bushfire air observers have been providing intelligence data on fire behaviour and location for many years using well accepted paper mapping techniques that has provided a basic set of data. GPS (Global Positioning System) technology progressed from large transportable units (early 1980s) to the palm of one's hand with a significant increase in accuracy to the present day.

From about 1996, land managers started using a GPS connected to a laptop computer to capture a fire plot and fax it back to a single location using a modem card and mobile phone. This consisted of a black line with grid squares for locating on a topographic map. This fax was copied to clear overlay and placed on the planning map showing where the fire was within minutes of finishing a mission. Soon came the ‘What if?’ questions. ‘What if we could collect all the data needed to enable acceptable spread predictions at the same time?’ What if we could have more types of lines and symbols and annotations? What if we could attach images? What if. . .?

During the period 2000–2002, GPS logger software was no longer meeting the challenge and so GPS was coupled with GIS opening up a wide range of possibilities. As digital vector data was not of sufficient quality to use as a background base for quality control, raster versions of topographic maps were used. These were overlaid with digital data such as that provided by community mapping exercises or of aviation and other features of concern such as power lines. It was now possible to collect as many line and symbol styles as necessary and have the ability to attribute the data and increase the amount of data being captured.

This process steadily evolved on various platforms such as pen tablets and PDAs (Personal Digital Assistants). Due to technological advances it is now possible to collect in near real-time, fire characteristics and weather data and attach georeferenced digital oblique stills, video and TIR images capturing a number of important features to assist incident planning. The automation of the system and in flight transmission enables many missions to be completed in one trip. This data is digitally transmitted to a number of end users at the completion of the data capture as a finished incident map. The next mission is often commenced in minutes flying time from the last, saving a 1 h round trip to deliver the data. A typical map product emailed back to control centres and State operations concurrently are shown in Fig. 4 (above). The image inset at the lower left is a georeferenced photograph



Fig. 4 Screen shot of a PyroMap fire plot that has a hot-linked digital hand-held camera photo (Bottom left) to indicate fire behaviour

taken at the location of the small black arrow. It shows a benign backing fire working slowly downhill. GPS data capture and attribution can occur on foot, in a vehicle or helicopter, depending on access to and behaviour of the fire.

These products were used directly as GIS layers, as PDF maps or projected onto a screen to report the situation to the incident team meeting. The system has evolved again to another level of efficiency. As the use of these systems and methodologies increased, more time was available for the capturing of higher quality and quantity of data that led to an increase and overall improvement in thoroughness, quality control and safety. Also, the increased volume of data collected greatly improved the efficiency of operations.

GPS mapping produced at control centres would typically involve an early morning and early evening (last light) flight. This allows planners to assess whether the fire's overnight travel was likely to compromise the planned strategies or to check the efficacy of the day's operation and determine a last light perimeter plot. When placed on field crew maps, the crew would be able to assess the fire's progress they met in the morning and develop a feel for the fire's behaviour. In this way, the most recent intelligence was presented to the planning meetings to assist in decision making.

This data collection strategy was put in place to free available aircraft for other duties such as water bombing during the peak period and allows the observer time to attend to land based duties. It also enabled critical information pertaining to the relevance of the daily planned strategies reaching the planning team so that contingencies could be put in place to address any change in the fire situation. Intelligence missions increased coincident with heightened risk and to confirm conflicting field reports. Although field reports are an important source of fire ground information that lack the perspective offered by other methods, digital air observing gives the field crew an elevated perspective while they focus on the frontline tasks.

During small fires the observer may not fly and instead spends the time in the field to create a plot by manual mapping techniques. During normal fire behaviour, observers may spend 2–3 h per day collecting intelligence. During extreme conditions it may be 6–8 h a day and require a dedicated aircraft to ensure information flow. At times, fire behaviour can escalate to a point where intelligence collected would not assist the planning or coordination of the operation and thus becomes a recording exercise to assist future research and inquiry.

Digital Hand-Held Cameras

Digital cameras have been another useful advance in technology that aids in the capture of bushfire intelligence information. Images can be taken while engaged in other tasks and if pointed at the right place at the right time can capture highly useful images and information. Images were captured from the scanner aircraft, helicopters, and vehicles or on foot and in January 2003, even from the international space station. The images provide a record of the events from many perspectives

Fig. 5 Spot fire in river bank vegetation. Uriarra Crossing ACT, 18 January 2003



and scales. It is often said that a picture paints a thousand words. Analysis of such pictures may also provide an insight into future events.

GPS mapping produced at control centres would typically involve an early morning and early evening (last light) flight. This allows planners to assess whether the fire's overnight travel had or was likely to compromise the planned strategies or to check the efficacy of the day's operation and determine a last light perimeter plot. Hand held digital images are most useful when metadata is captured with them such as date, location, time etc.

A digital image such as the one shown in Fig. 5 can convey a wealth of information to an experienced bushfire response planner. This spot fire started on the river bank less than a minute before the image was captured. Within a few minutes it had impacted the buildings lower middle and middle right. The smoke colour and flame height at the head shows how serious this situation is. This spotfire claimed three buildings despite having three helicopters at the scene including the sky crane water bombing aircraft. Adequately conveying this data by word is a challenge in itself. Images can be transmitted digitally with the map to the control centre. This scene was also captured on video and was used to estimate that the fire's forward rate of spread was faster than a fire tanker could negotiate the same terrain.

Such imagery can be a very valuable source of historical data in addition to displaying fire behaviour to the planning team. With adequate metadata they can be valuable in recording timeframes during periods when memories become clouded or overwhelmed. During the January 2003 firestorm, digital imagery from many sources was valuable in reconstructing time sequences.

FLIR

Forward Looking (thermal) InfraRed (FLIR) is a tool used to see through smoke and locate non smoking hot spots for mop-up of apparently extinguished fire edges. Used with GPS and GIS systems it can provide enhanced vision allowing hand mapping of



Fig. 6 This image taken 5 Dec 2002 near Borowra shows the difference FLIR can make to critical intelligence collection. (Top image is TIR and bottom image is the visual bands). Without FLIR the bottom view is all the crew can see

critical, operationally significant information such as determining breach of control lines through smoke.

This is valuable during extreme fire weather conditions as it allows operations staff to develop a better picture of the progress of the fire incident and provides a more efficient and safer operating environment with improved vision for air attack supervisors. Hand held and fixed front mounted TIR cameras were also used at various sites and research is required to assess each of these techniques for the purpose of mop-up quality assessment.

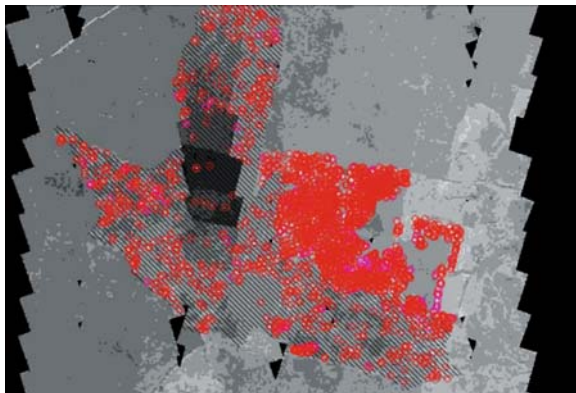
Figure 6 (above) is a screen capture from a video FLIR system operated by Gyrovision Pty Ltd during the Baulkham Hills fire on 5th December 2002. This system was used to video fire activity and to detect hotspots. It is clear that without the FLIR, observation of the rapidly moving fire front would be impossible. Its importance to air operations during major fire runs is underestimated as a tool for Air Attack Supervisors engaged in property protection.

TIR Camera System

A thermal infrared system (FireSearch Pty Ltd) was used to detect hotspot activity as a planning and quality control tool for mopping up operations. It also served as backup for the line scan aircraft during aircraft maintenance periods.

The system captured and classified thermal imagery to indicate fire activity and perimeter. It produced a mosaic of tiles sent in real time to output a single image

Fig. 7 This thermal composite image of a fire shows the density of hotspot around the fire. Denser areas (red) show recent fire activity and back burning. Less dense hotspot activity indicates declining persistence of hotspot against time to a point where a much smaller number of potential sources of reignition are likely to survive to the next cycle of hotter dryer weather in the near future



that was processed to a layer of points with temperature attributes. Figure 7 is an example of georectified and mosaiced data from this system. The system is most efficiently used to capture georectified hotspot temperature data indicating the likely success and effectiveness of the deployment of remote area crews for the mop-up of extinguished fire edges.

In bushland regions, conditions can often occur where reignition sources are masked by cooler and moister ground cover conditions and thus lay undetected using conventional ground-based surveillance means. This situation can remain undetected until (atmospheric) conditions deteriorate causing multiple reignitions to ruin much good work already carried out. This is particularly so during very dry periods and becomes evident during response scale down. There is little point deploying a Remote Area Fire Team (RAFT) with insufficient resources for them to mop up for hours together with expensive air support only to fail to contain the fire due to the task being much larger than was understood by incident controllers.

If the amount of containment work can be estimated by incident controllers early in the morning using airborne surveillance techniques, the most appropriate course of action can be implemented saving financial and human resources. Each failed attempt at suppression leaves the Incident Management Team (IMT) with a much larger perimeter to contain and fewer resources with which to carry the out work.

This equipment also captures an acceptable additional or alternative thermal edge plot at high altitude. This tool was used flexibly to improve data product delivery when other methods were unavailable or less efficient.

There are also times when a fire can be contained with a RAFT but is not attempted due to insufficient information on the actual hotspot activity. Hotspot density and persistence information adds a new dimension to resource planning and increases safety in the workplace. It does, however, require a calibration study to determine the percentage of actual hotspots detected that are relevant to reignition concerns.

Discussion

During the period reported in this paper (2001–2006), many different though complementary techniques were deployed across NSW and the ACT that were coordinated and tasked by a fledgling NSW RFS GIS unit (formed in 2001). The operational parameters of the techniques overlapped sufficiently to provide contingency cover maintaining product supply that could not be met by one technique alone. All of the techniques used provided useful information to one or more aspects of operational planning, post-fire event evidence and study.

The airborne intelligence tasking represented less than 1% of the aviation expenditure during the 2002–2003 fire season (NSW RFS figures). The information collected enabled better use of resources and reduced the amount of preventable errors. A lost spot fire (and fires can spot 15+ km ahead of a main front as measured from Daedalus scanner data over the Blue Mountains (west of Sydney)) on a severe weather day can cause a breakaway fire that can undo millions of dollars worth of suppression and weeks of volunteers' work based on ground and airborne fire fighting costs (NSW RFS). The relatively minor amount of money required for airborne intelligence is a small price to pay for increased fire management efficiency and the prevention of possible disasters and loss or damage to property.

Williams (2005) suggested that from a study of fire management over ten years of wildfires in the USA, 1% of all fires caused 95% of the damage sustained and 85% of the total budget for fire management in suppression cost. Williams proposed that at the extreme end of the scale, fire managers need to re-think the familiar paradigm of throwing ever increasing amounts of resources at 'mega fires' and that they should develop new strategies to deal with such situations that are likely to become more prevalent, especially given global climate change predictions. It is proposed here that the first step is to find better ways of identifying such wildfire events through the gathering of more relevant real time data.

The many techniques introduced in this paper, while individually very useful tools for the fire planner, when combined through an intelligent operations system can be deployed to provide data at many levels of resolution. This creates an operations system with great power to assist in the coordination of fire suppression planning and when properly archived, for future research. Such information can only enlighten and assist incident management teams to form better plans and contingencies once the data is understood in terms of its strengths and limitations. Airborne fire suppression costs are a significant component of the total fire suppression cost and are especially so with fires that occur throughout much of Australia's native vegetation that has evolved to maintain fire.

Also of great importance is the need for Australia-wide GIS mapping standards for the use by all emergency services to be designed, implemented and adhered to. Both the NSW RFS and ACT ESA (Emergency Services Authority) have already adopted standards of their own. GIS mapping standards should include not just GIS system methodologies, mapping techniques and equipment technical specifications, but also cartographic and display elements (including metadata) that can be used across all GIS platforms and that will be plainly visible and correctly interpreted

even when transmitted as a facsimile. Standards already exist for topographic, geologic, geophysical and oceanographic mapping and so should also exist for natural disaster mapping.

There is an enormous quantity of data and information that has been captured as part of normal fire operations and through research over the past twenty five years or more throughout Australia. Much of this has not been properly archived and much less fully analysed. It is imperative that all emergency management data from throughout Australia be permanently archived in preferably a national repository where it can be made readily and easily accessible to all parties with a need to investigate fire behaviour, property damage, etc.

Since 2003, the airborne scanner system under contract to the NSW RFS has also been deployed elsewhere in Australia to assist other jurisdictions with fire control efforts. Also since putting in place the airborne scanner system as described above and as a compliment to it, the Victorian Department of Sustainability and Environment has upgraded their TIR Daedalus airborne scanner with an attitude correction system to bring it more-or-less in line with the system used by the NSW RFS.

Conclusion

The strategies of throwing more resources at a fire when it is clear that this action is not providing the desired results need to be tempered by unbiased, relevant intelligence data to improve the chances of matching resources to the need for a more efficient outcome. A small percentage of the resource pool being used to provide a better perspective locally and across jurisdictions is seen as effort well spent considering the benefits of adequate amounts of timely, accurate and relevant data to facilitate more effective coordination and deployment of fire fighting resources.

The authors consider the work performed during the 2001–2003 period that saw the development of a holistic system to provide support to incident decision making to be very successful. Incorporation of field situation reports and other important data such as current weather data is needed.

‘Fires know no boundaries’. This saying refers to all natural and man made boundaries such as rivers and roads, National Park and State Forest boundaries and state and territory borders, etc. While this saying is becoming part of our everyday lexicon when talking about natural disasters, and co-operation between state and territory governments is increasing, more work is required to foster the importance and real meaning of it to those in positions of authority in all state and territory governments and relevant departments. This will become increasingly important where airborne surveillance is concerned and as overall fire suppression costs increase.

Eventually, a National approach may be warranted for airborne surveillance of natural disasters. Indeed, the authors recommend that a National airborne surveillance system be set up, possibly run by the Federal Government with proportional funding (in relation to area and population) provided by the state and territory

governments. It is believed given the cost associated with providing airborne surveillance (even though it is considerably less than air and ground based fire fighting costs) that such a national scheme would be considerably more affordable for the states and territories than going it alone.

With advances in communications, it is feasible for the airborne scanner and other system data to be transmitted to operation centres by satellites such that the data (in the case of airborne scanner data) can be rectified and displayed on large screens in near real time. Such data can also be draped over digital terrain models providing a further 3D enhancement for fire and other operations staff so that they are able to view a fire's progress not just in near real time but also in relation to topography.

Also of course, an airborne surveillance system can be put to a variety of uses for monitoring of natural disasters apart from active bush fires including floods, and oil spills and for man-made disasters, for post-disaster investigations to survey and map damage to property and the environment, on-shore and off-shore search and rescue and for general homeland security requirements.

Acknowledgements Robert Norman, Air Affairs Australia Pty Ltd, Nowra, NSW, Australia. Chris Humphries, FireSearch Pty Ltd, Moree, NSW, Australia. Will Stein, Gyrovision Pty Ltd, Granville, NSW, Australia

References

- McRae R, Walker A, 2001: "Community Mapping—an aid to emergency management" *The Australian Journal of Emergency Management* v 15 No 4 pp. 22–27.
- Williams J, 2005: Bushfire CRC and AFAC workshop on Mega-fires; 29 August 2006, Canberra.

Give Me the Dirt: Detection of Gully Extent and Volume Using High-Resolution Lidar

Alisa Eustace, Matthew Pringle, and Christian Witte

Abstract The Fitzroy catchment drains into the Great Barrier Reef lagoon. It is the largest catchment on the east coast of Australia, with an area of over 140,000 km². To ascertain point-sources of erosion, and to quantify the volume of sediment lost from gullies, within the Fitzroy catchment is a major challenge for land-management; despite this, gully locations and volumes have never been thoroughly investigated. This study aims to develop a semi-automated method to detect and map gully extent and volume, using aircraft-mounted Light Detection and Ranging (LiDAR) technology within the Fitzroy catchment. Twenty LiDAR transects were acquired in 2007 (5000 × 275 m). The average distance between points of the LiDAR data was 0.3 m on the ground, with a height accuracy of within 0.1 m. Digital Elevation Models were derived for the transects, with a 0.5-m spatial resolution. We delineated gullies using terrain attributes and the backscatter intensity of the LiDAR returns. Transects were classified as ‘gully’ or ‘non-gully’ using objected-oriented classification. Gully volume was estimated for each pixel of the twenty transects. For four transects, we used a random forest algorithm to model the relation between gully presence and a set of readily available ancillary variables. We also modelled the relation between gully volume and the ancillary variables. These models were used to predict gully presence and volume at unsampled locations. We considered the extrapolation a success. The products generated from this study will be used to inform water-quality models, to assess land condition, and to improve our understanding of the dynamics of gully erosion under different climate and land-management regimes.

Introduction

The sediment eroded from gullies deteriorates land condition and the quality of water in rivers. These can have dramatic long-term ecological effects. To ascertain

A. Eustace (✉)

Queensland Department of Natural Resources and Water, Remote Sensing Centre, Indooroopilly, QLD 4068, Australia
e-mail: alisa.eustace@qld.gov.au

point-sources of erosion, and quantify the volume of sediment lost from gullies, are major challenges for land-management in a catchment. The Fitzroy River catchment drains into the Great Barrier Reef lagoon, and is the largest catchment on the east coast of Australia covering over 140,000 km². Previous hydrological studies in the catchment have used the SedNet model to examine sediment-generation and water-quality (Hughes et al. 2001, Dougall et al. 2005, Joo et al. 2005); however, the uncertainty of the model was substantial (Dougall et al. 2006). Initially, the model assumed that gully volume was constant across the whole catchment, while the gully information used as input to the model was based on averages for studies outside Queensland (Hughes et al. 2001). To address these issues, a study was undertaken to refine the SedNet model for the Fitzroy catchment (Dougall et al. 2007). The refined model used spatially variable gully lengths, derived from high-resolution Quickbird imagery, to estimate gully volume (Trevithick et al. 2008). Unfortunately, the cross-sectional area used to convert gully length to volume was assumed constant at 10 m². This assumption signified the need for spatially variable information on gully volume: a layer such as this could be incorporated directly as an input to the SedNet model and may help to reduce the uncertainty of the model predictions for the Fitzroy catchment. Furthermore, the establishment of a high-resolution baseline of gully extent and volume information is crucial to the ability to monitor temporal change in the catchment.

Light Detection and Ranging (LiDAR) has been used in to identify and quantify temporal changes in topography due to erosion (Young and Ashford 2006, Thoma et al. 2005, Lane et al. 2003). This study uses LiDAR to establish a synoptic baseline of gully locations, extents, and volumes, based on a semi-automated procedure. Extrapolation of these data outside the bounds of the LiDAR transects will be vital if they are to be useful for modelling. Extrapolation can be facilitated with an ensemble decision-tree, known as a random forest (Breiman 2001, Liaw and Weiner 2002). A random forest can be used for classification and regression (depending on whether the predictor variable is categorical or continuous, respectively). The principle of random forests is that, rather than use just one decision-tree, we grow many trees, where each tree is based on a bootstrap sample of the data. The individual trees in a forest require no pruning, and the forest as a whole does not over-fit (Breiman 2001).

In this study we used a random forest classification of LiDAR data to determine the probability of finding a gully within the landscape. We also used a random forest regression analysis of LiDAR data to estimate the volume of gullies within the landscape. Extrapolation of the models' predictions to large areas will provide information that can be integrated into water-quality models, and also used to assess land-condition in the Fitzroy catchment.

Methods

Study Sites and Creation of a Baseline of Gully Information

Ten sites were selected within the Fitzroy catchment, Queensland (Fig. 1), where topography would be measured using a LiDAR sensor, mounted on an aircraft. The

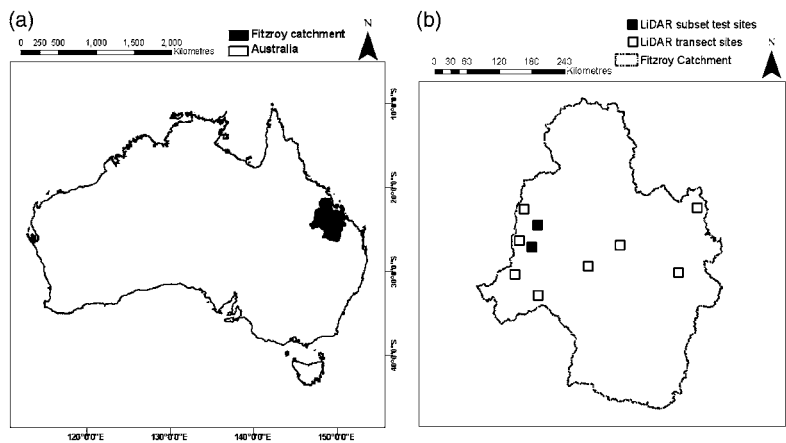


Fig. 1 (a) The location of the Fitzroy Catchment, Queensland; (b) the ten sites selected for LiDAR acquisition within the Fitzroy catchment. Filled in black squares represent the sites selected for testing extrapolation methods

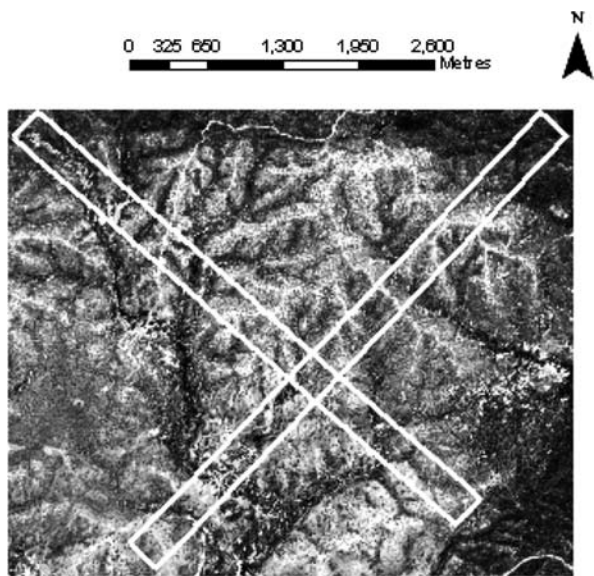


Fig. 2 The outline of a pair of transects (thick white line) obtained for one LiDAR site, placed over a grey-scaled Quickbird image. Light areas represent the tops of ridges; dark areas represent forested regions

study sites were selected on the basis that they encompassed a variety of landscape attributes. At each site, two transects were acquired (Fig. 2).

Ten transects were acquired between February 3rd–5th, 2007, with an Optech ALS ALT3100 Enhanced Accuracy LiDAR scanner. A further ten transects were acquired on July 27, 2007, using a Leica ALS50 scanner. The dimensions of each

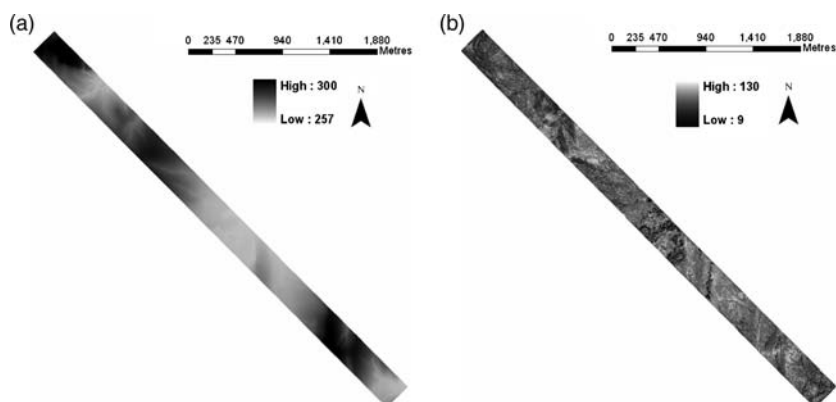


Fig. 3 (a) A 0.5-m raster DEM (units of metres) for one transect, derived from LiDAR; (b) the same transect displaying 0.5-m raster LiDAR backscatter intensity images (dimensionless)

transect were $5000 \times \sim 275$ m (there was a small variation in the width that depended on the sensor used). The data were supplied in a ‘cloud-point’ configuration that consisted of eastings and northings, height (metres above sea-level) and backscatter intensity (relative strength of the returning signal). A classification of the cloud points as either ‘ground’ or ‘non-ground’ was also provided with the data. The twenty cloud-point files were converted to Digital Elevation Models (DEMs) with a 0.5-m raster, using an inverse-distance weighted interpolation algorithm (Fig. 3a). The backscatter intensity was also processed to a 0.5-m resolution (Fig. 3b).

Object-Oriented Classification of Gullies

We used Definiens 5.0 Object-Oriented Classification software (Definiens 2006) to classify the DEMs into two classes: ‘gully’ and ‘non-gully’. Each of the twenty transects were processed separately. For every transect, the input images used in the classification comprised the DEM, backscatter intensity, slope of the DEM, standard deviation of the slope, and the texture of the DEM. Objects were created using the image-segmentation dialogue in the Definiens software package. The image-segmentation parameters included a scale factor, a colour factor, and a shape factor.

We used the multiresolution segmentation mode of the software (Definiens 2006). The objects of a segmented image (the ‘image-objects’) were classified as gully or non-gully based on shape and image attributes. Combinations of attributes of the image-objects (i.e., slope, texture, standard deviation of the slope, the length of longest edge of the object, length-to-width ratio, rectangular fit, asymmetry, and the relation to neighbours) were tested to determine the best thresholds and the attributes that most accurately classified gullies.

Gully Volume

Following segmentation, we removed from the cloud-point data those points that corresponded to the location of the ‘gully’ class. The elevation values associated with the remaining (‘non-gully’) locations were interpolated across the voids using a nearest-neighbour algorithm. This created a ‘non-gully plane’. For each transect, we then clipped the non-gully plane and the DEM to the extent of the gully class. The clipped DEM was subtracted from the non-gully plane to create an image of gully depth. The values at each pixel of the gully-depth image were multiplied by the area of the LiDAR raster pixel (2.5 m^2) to yield a volume (m^3).

Models of Gully Information

We selected four LiDAR transects for further analysis (Fig. 1b). Our intention was to investigate whether, in these transects, the relation between gully information and various ancillary variables could be modelled accurately. If so, these ancillary variables could be used to extrapolate the gully information at unsampled locations within a subset of the catchment. All modelling was done using the R statistical package (R Development Core team 2008).

Ancillary Variables

There was a combined total of approximately 24,000,000 pixels within the four LiDAR transects. We matched the LiDAR-derived data for each pixel (i.e., the spatial coordinate of the pixel centre, an indicator variable for gully presence/absence, and the gully volume) with a set of ancillary variables that were readily available for the extent of the entire catchment. These variables were:

- DEM estimated by Shuttle Radar Topographic Mapper (SRTM) and derivatives of the DEM such as
 - slope (degrees);
 - aspect (degrees from North);
 - shaded relief;
 - focal statistics (3×3 window) of the SRTM-DEM and slope images including minimum, maximum, non-directional edge and variance;
 - flow direction and accumulation, stream order, down-stream length;
- Landsat-derived products such as
 - 2006 Foliage Projective Cover (FPC) (Armston et al. 2004) and Bare Ground Index (BGI) (Scarth et al. 2006);
 - timeseries (1988–2006) FPC minimum (including and excluding outliers) and standard error and
 - timeseries (1987–2006) BGI minimum, maximum, mean, median and standard error;

- categorical products derived for the National Action Plan for Salinity and Water Quality (Brough et al. 2006) including discharge, drainage, recharge, salinity hazard risk map, permeability class, and Australian Soil Resource Information System soils classification;
- land-type class;
- pre-clearing Regional Ecosystem class.

The ancillary variables were available at spatial resolutions coarser (at least 50 times greater) than the 0.5-m LiDAR pixels. This meant that it was inefficient to attempt direct modelling of the 24-million-row data array, due to redundant information. We circumvented this issue through the use of conditioned Latin Hypercube Sampling (Minasny and McBratney 2006). Conditioned Latin Hypercube Sampling (cLHS) is an algorithm for optimum stratified random sampling, applicable to situations where one has ‘complete information’ consisting of numerous continuous and categorical variables. We used cLHS to extract a representative sample (optimised across all variables) of 5% of the pixels. Half of these sampled pixels were used to build a model of gully presence; the other half of the pixels were used for model validation. We used a random forest (Breiman 2001, Liaw and Wiener 2002) to model the relation between gully presence and the ancillary variables. For a categorical variable such as gully presence, the random forest out-of-bag error rate is a proportion analogous to the inadequacy of the model, where zero indicates a perfect fit. The random forest was used to predict the presence (or absence) of a gully in the pixels of the validation data. We denote this forest as Model 1. The agreement between observed ‘gully’ and ‘non-gully’ classes and those predicted by Model 1 was described with an error matrix (Congalton and Green 1999). We then calculated statistics associated with the error matrix such as the overall accuracy, and Kappa (Congalton and Green 1999).

The cLHS algorithm was used again to extract another representative sample of 5% of those pixels with a gully volume $> 0 \text{ m}^3$. Half of these sampled pixels were used to build a model of gully volume; the other half of the pixels were used for model validation. We used a random forest to model the relationship between gully volume and the ancillary variables. This random forest was used to predict the gully volume for the pixels of the validation data. We denote this forest as Model 2.

Extrapolation of Gully Volume at Unsampled Locations

Our objective was to establish whether the gully information in the LiDAR transects could be extrapolated at unsampled locations. We investigated this issue in a small subset region (250,000 ha) that encompassed four transects of interest (Fig. 1b). All ancillary variables were recorded at the nodes of a 25-m grid across this region.

The extrapolation of gully volume at unsampled locations was a two-step process: first, the ancillary variables required by Model 1 were used to calculate the probability of finding a gully at each unsampled location; and second, the ancillary variables required by Model 2 were used to calculate the volume of a gully at each

unsampled location. The predicted gully volumes were based on a 0.5-m raster, and thus required scaling to correspond to the 25-m pixel grid. The predictions of Model 2 were qualified by the predictions of Model 1, i.e., it was only appropriate to report predicted gully volumes for those pixels where we had reasonable confidence in the presence of a gully (a probability of 0.6 was used as a threshold).

Results

Object-Oriented Classification of Gullies

We achieved the optimum segmentation of the gullies through a heuristic process. A segmentation scale-factor of 50 provided well-defined gully boundaries that were associated with relatively few image-objects (Fig. 4a). A scale factor of 200 did not delineate gullies with enough detail (Fig. 4b), while a scale factor of 20 segmented the gullies excessively and created too many image-objects for efficient classification (Fig. 4c). The rules required to classify the image-objects as ‘gully’ or ‘non-gully’ are described in Table 1. The resulting classification identified ‘gully’ image-objects to create a map of the extent of the gullies (Fig. 5).

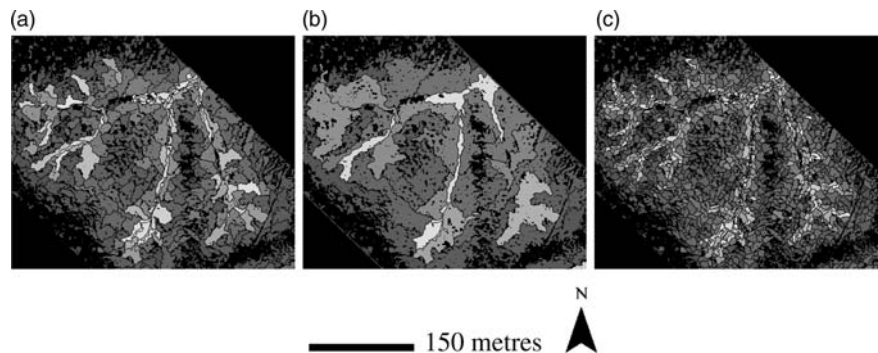
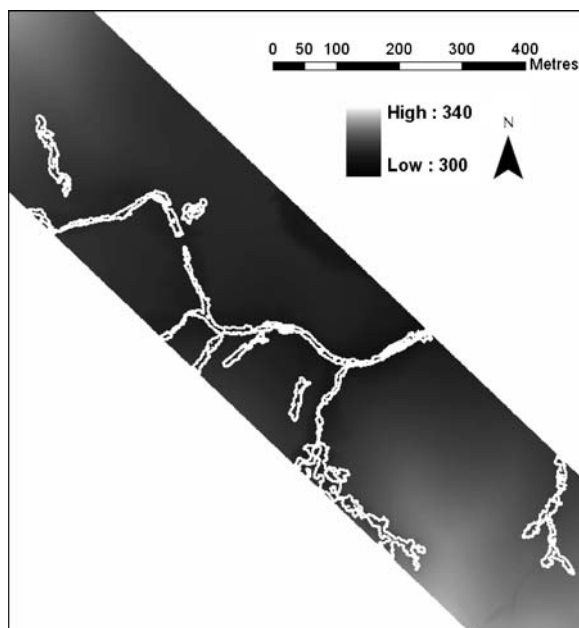


Fig. 4 Delineation of gully boundaries using multiresolution segmentation at different scale parameters: (a) 50; (b) 200; (c) 20

| Table 1 The rules required to classify image-objects as either ‘gully’ or ‘non-gully’ | |
|---|--|
| Class | Rule |
| Gully | Mean slope $\geq 15^{\circ}$ |
| | Mean DEM texture ≥ 50 (variance of digital number) |
| | Mean standard deviation of slope $\geq 6^{\circ}$ |
| | Length of longest edge of a polygon ≥ 18 m |
| Non-gully | Mean standard deviation of slope $\leq 7^{\circ}$ and mean slope $\geq 15^{\circ}$ |
| | Rectangular fit ≥ 0.9 (proportion between 0 and 1) |
| | Length-to-width ratio ≥ 1.5 and rectangular fit ≥ 0.9 (proportion between 0 and 1) |

Fig. 5 The classified extent of gullies map over a DEM (units of metres)



Gully Volume

Gully volumes were calculated for all twenty transects. An example of the gully volumes from one transect is shown in Fig. 6.

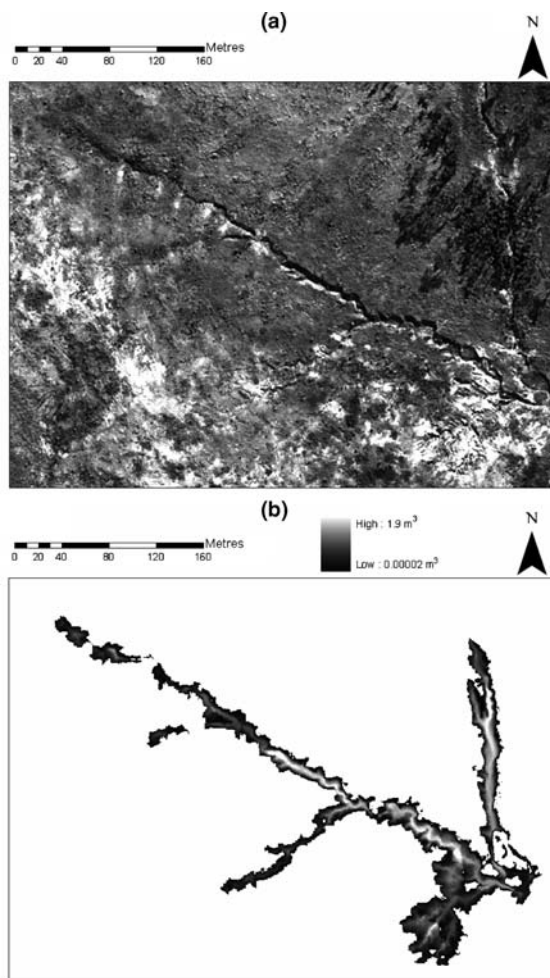
Summary statistics for gully volume suggested that volume varies substantially across the landscape (Table 2). Transect 3 had the most pixels classified as a gully (i.e., the largest surface area of gully extent). Transect 9 had the deepest gully pixel. Transect 14 had the smallest maximum and median volume and the smallest variance.

There was not a strong visual relationship between median gully volume and total gully volume for a given transect (Fig. 7). This indicated that different sites may have different gully morphologies and we cannot assume a proportional relation between the two quantities; one site may have many shallow gullies, while another may have few deep gullies.

Extrapolation of Gully Information

The out-of-bag error for Model 1 was 19.4%. When applied to the validation data, Model 1 predicted gully presence and absence with an overall accuracy of 75% and Kappa = 0.52. The most-important variables used to predict the presence of a gully were (in decreasing importance): the standard error of the Foliage Projective Cover (FPC) timeseries; the Bare Ground Index (BGI) timeseries standard deviation; the

Fig. 6 (a) Quickbird image displaying an area where gully volumes were mapped; (b) Gully volume (m^3) estimated for a subset within one LiDAR transect



FPC timeseries minimum (excluding outliers); the BGI timeseries maximum; the BGI timeseries median; and the FPC timeseries minimum (including outliers).

Model 2 has not been subjected to a formal accuracy assessment, but a cursory examination of the validation results suggested that the correlation of model-predicted gully volume with observed gully volume was $r = 0.58$, with a root-mean-square-error of 0.1 m^3 . Preliminary analysis also suggested that Model 2 predicted gully volume better at an aggregated spatial scale than at the native 0.5-m resolution. Further testing may confirm this. The most-important variables used to predict the volume of a gully were similar to those for Model 1, i.e. (in decreasing importance): the minimum (including outliers) of the FPC timeseries; the BGI 2006 value; the BGI timeseries minimum; the BGI timeseries mean; the BGI timeseries maximum and the SRTM-DEM.

Table 2 Summary statistics of gully volume for each LiDAR transect

| Transect | <i>N</i> | Max. (m ³) | Median (m ³) | Total volume (m ³) | Variance (m ³) ² |
|----------|---------------|------------------------|--------------------------|--------------------------------|---|
| 1 | 532823 | 1.99 | 0.10 | 115835 | 0.07 |
| 2 | 484286 | 1.97 | 0.23 | 164898 | 0.10 |
| 3 | 662963 | 0.93 | 0.07 | 73102 | 0.01 |
| 4 | 465156 | 0.87 | 0.07 | 51794 | 0.01 |
| 5 | 255654 | 0.73 | 0.09 | 31482 | 0.01 |
| 6 | 258649 | 0.99 | 0.07 | 31379 | 0.02 |
| 7 | 296614 | 0.85 | 0.07 | 29732 | 0.01 |
| 8 | 388281 | 1.28 | 0.13 | 67179 | 0.02 |
| 9 | 506556 | 2.31 | 0.10 | 89039 | 0.05 |
| 10 | 206757 | 1.09 | 0.09 | 30300 | 0.02 |
| 11 | 133167 | 2.23 | 0.25 | 52185 | 0.16 |
| 12 | 74513 | 2.01 | 0.21 | 24093 | 0.10 |
| 13 | <u>64238</u> | 1.25 | 0.09 | 12465 | 0.07 |
| 14 | 125168 | <u>0.53</u> | <u>0.06</u> | 11244 | <u>0.01</u> |
| 15 | 208570 | 1.45 | 0.17 | 48459 | 0.04 |
| 16 | 265356 | 1.42 | 0.13 | 48537 | 0.03 |
| 17 | 87276 | 1.02 | 0.07 | <u>10145</u> | 0.02 |
| 18 | 199238 | 1.29 | 0.13 | 37963 | 0.03 |
| 19 | 401180 | 1.38 | 0.07 | 49719 | 0.02 |
| 20 | 351976 | 1.15 | 0.07 | 42456 | 0.02 |

Bold indicates the maximum value of each statistic; the underline indicates the minimum. The number of pixels classified as ‘gully’ is denoted *N*.

Fig. 7 The relation between median and total gully volume, by transect. A larger total volume does not necessarily mean a larger median

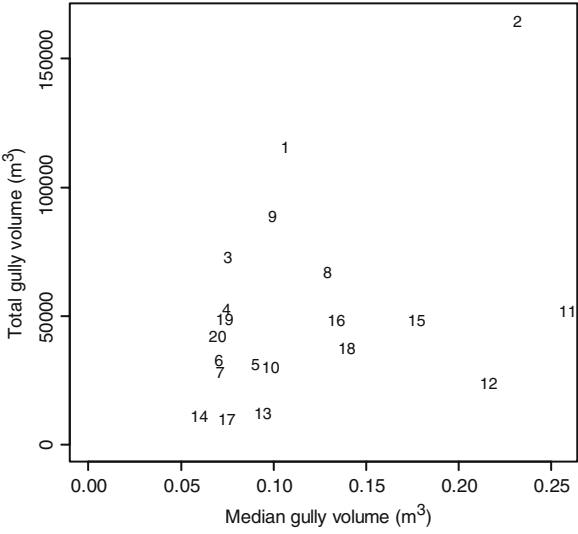
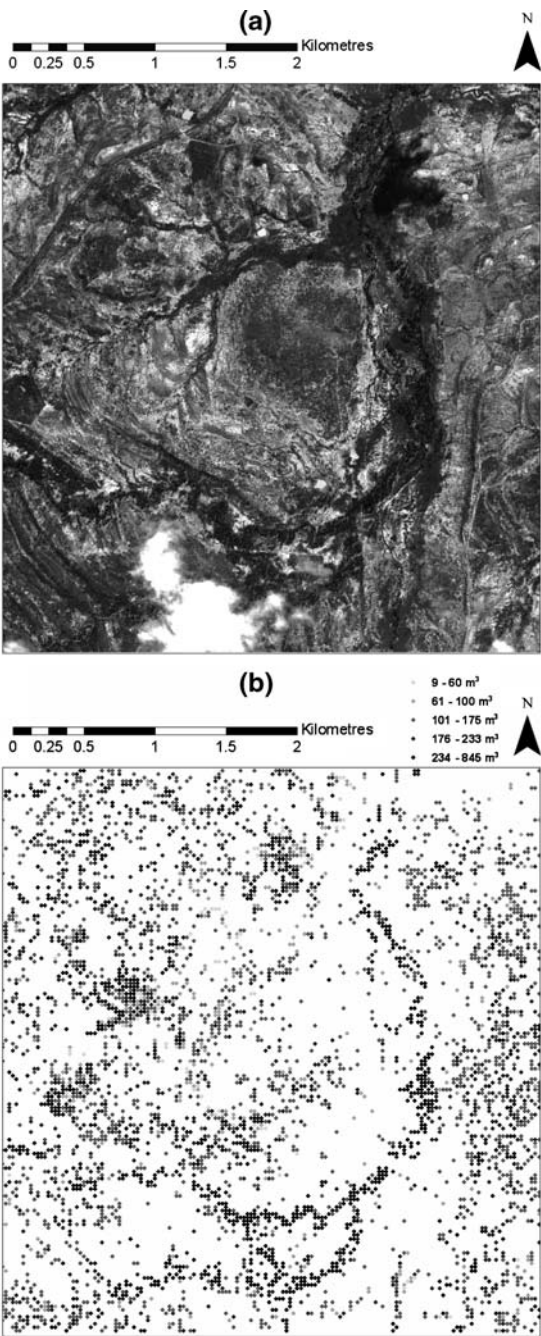


Figure 8 shows an example of the predictions of Model 1 and Model 2 at unsampled locations. Figure 8 integrates both variables into one layer, i.e., gully volume where the probability of finding a gully exceeds a probability of 0.6. Despite the spatial ‘noise’ in the predictions, we were encouraged to observe, running from the

Fig. 8 (a) Area on a Quickbird image where gully presence and volume have been predicted at unsampled locations; (b) Gully volume (m^3) estimate where the probability of finding a gully exceeds a probability of 0.6



lower-left of the image to the upper right, relatively large volumes predicted in an area that the Quickbird image suggests is a drainage depression. The linearity of the predicted feature was encouraging also, as this corresponded with the results of the object-oriented classification. We examined other parts of the region and found similar results.

Discussion

LiDAR Transects as a Baseline of Gully Information

Through the acquisition of twenty LiDAR transects, we have established a baseline of gully information for sampled areas in the Fitzroy catchment. This baseline can be used to detect and monitor change in gully morphologies. This will assist in identification of ‘active’ gullies in the landscape, and therefore, those areas most at risk of erosion. Future research into sedimentation rates and changes in gully morphology can be quantified using this baseline. This will contribute to our understanding of sediment movement throughout the Fitzroy catchment, to the quantification of rates of change in land-condition, and as an aid for land-management decisions. The gully-volume information can be used to improve the certainty of the gully-related inputs required by the SedNet model. The power of the baseline will be recognised if another LiDAR acquisition for the twenty transects is completed and shows that the volumes of some gullies have changed since the original acquisition, following the major flood event which occurred in the Fitzroy catchment in February 2008. Hotspots of gully activity may also be identified so that management of gullies can be targeted to regions where sediment is generated under the existing land management and climate conditions.

Object-Oriented Classification of Gullies

This study produced a semi-automated classification of LiDAR-derived products to map gully extent based on an object-oriented approach. The number of input attributes, the spectral and shape properties within the attributes, and combinations and permutations of each, created a multitude of options for determining how the image-objects can be allocated to classes. Initial testing that used slope as the sole rule for classification of gullies found that many areas with long hill slopes were allocated incorrectly to the ‘gully’ class. An additional rule that classified areas of steep, though relatively uniform, slope as ‘non-gully’ was able to reduce this error of commission. Texture-based rules were able to account for objects whose constituent pixels were relatively heterogeneous. Many ‘gully’ objects were highly variable in regard to slope and topography (DEM), which led to large values of texture, and an improved ability to distinguish ‘gully’ from ‘non-gully’ attributes. Shape-based attributes were also important factors for the classification of gullies. The length of

the longest edge of a polygon, the length-to-width ratio and rectangular fit criterion were able to discriminate thin objects from round or wide objects, as many gullies consisted of long and/or linear objects at a scale factor of 50.

Transect Gully Volume

The volume per pixel for each of the twenty transects provided an accurate and precise baseline measurement of sediment loss due to gully erosion. The lack of a correlation between total gully volume and the median gully volume (Fig. 7) indicated that areas of deep gullies do not necessarily occur in local regions where there are many gullies present. This has implications for modelling as it is possible that the many shallow gullies detected could contribute more sediment to the catchment's rivers than the few deep gullies that were found.

Extrapolation of Gully Information

The presence of gullies appeared to follow environmental boundaries identified in the Quickbird imagery. The six most-important ancillary variables out of the thirty-eight tested are noteworthy as they arise from three sources: the Landsat timeseries-derived FPC and BGI, and the SRTM-DEM. This has favourable implications for the extrapolation of gully information, as these sources are independently derived and are acquired at a relatively fine spatial resolution.

The extrapolation methods we have described will be carried out for the entire Fitzroy catchment, contributing to enhanced information on gully locations and volumes within the Fitzroy catchment. Further analysis will be carried out to validate the extrapolation results. The gully volume maps can be used to improve the spatial variability and uncertainty concerning gully locations and volumes within the Fitzroy. The products from this study can also be used to modify water quality models to include spatially variable data based on remotely sensed Queensland information.

Conclusions

This study developed a semi-automated method to map gully extent and volume using aircraft-mounted Light Detection and Ranging (LiDAR) technology within the Fitzroy catchment. We derived baseline Digital Elevation Models for the twenty LiDAR transects with a 0.5-m spatial resolution. Gullies were delineated and classified using an objected-oriented approach. Gully volume was also derived for the twenty transects. We carried out random forest classification and regression analysis to predict both the probability of finding a gully and also gully volume across a 250,000-ha subset of the Fitzroy catchment. This information produced a map

of gully volume where the probability of finding a gully exceeded a probability of 0.6. We consider that there is potential to extrapolate successfully gully information across the extent of the catchment. The products generated from this study will be used to inform water-quality models, to assess land condition under different climate and land-management regimes.

Acknowledgements We would like to thank Dr Robert Denham for his statistical and programming advice.

References

- Armstrong JA, Danaher TJ, Collett LJ (2004) A regression approach for mapping woody foliage projected cover in Queensland with Landsat data. In: Proceedings of the 12th Australasian Remote Sensing and Photogrammetry Conference, Fremantle, Australia, October 2004.
- Breiman L (2001) Random forests. *Machine Learning* 45:5–32.
- Brough DM, Claridge J, Grundy MJ (2006) Soil and Landscape Attributes: A Report on the Creation of a Soil and Landscape Information System for Queensland. Natural Resources, Mines & Water, Brisbane, Australia. QNRM06186.
- Congalton RG, Green K (1999) Assessing the Accuracy of Remotely Sensed Data: Principles and Practices. Lewis Publishers, Boca Raton, FL.
- Definiens, (2006) Definiens Professional 5: User Guide. Document version 5.0.6.2, Definiens AG, Munich, Germany.
- Dougall C, Packett R, Carroll C (2005) Application of the SedNet model in partnership with the Fitzroy Basin community. In: Zenger A and Argent RM (eds.) MODSIM 2005 International Congress on Modelling and Simulation. Modelling and Simulation Society of Australia and New Zealand, December 2005, pp. 1119–1125
- Dougall C, Packett R, Carroll C, Sherman BS, Read A, Chen Y, Brodie J (2006) Sediment and nutrient modelling in the Fitzroy NRM region. Volume 5 In: Cogle AL, Carroll C and Sherman BS (eds.) The Use of SedNet and ANNEX Models to Guide GBR Catchment Sediment and Nutrient Target Setting. Department of Natural Resources, Mines and Water, Brisbane, pp. 1–27.
- Dougall C, Carroll C, Herring M, Trevithick R (2007) Sednet modelling in the Fitzroy Basin 2007; spatially variable ground cover and revised gully layers can potentially generate significant changes in erosion sources and patterns. In: Oxley L and Kulasiri D (eds.) MODSIM 2007, International Congress on Modelling and Simulation. Modelling and Simulation Society of Australia and New Zealand, December 2007, pp. 881–887.
- Hughes AO, Prosser IP, Stevenson J, Scott A, Lu H, Gallant J, Moran CJ (2001) Gully Erosion Mapping for the National Land and Water Resources Audit, CSIRO Land and Water Technical Report, 26/01, August 2001.
- Joo M, Yu B, Carroll C, Fentie B (2005) Estimating and modelling suspended sediment loads using rating curves in the Fitzroy River catchment Australia. In: Zenger A. and Argent R.M. (eds) MODSIM 2005 International Congress on Modelling and Simulation. Modelling and Simulation Society of Australia and New Zealand December 2005 pp. 1161–1167.
- Lane SN, Westaway RM, Hicks M (2003) Estimation of erosion and deposition volumes in a large, gravel-bed, braided river using synoptic remote sensing. *Earth Surface Processes and Landforms* 28(3):249–271.
- Liaw A, Wiener M (2002) Classification and regression by random-Forest. *R News* 2(3). pp. 18–22.
- Minasny B, McBratney AB (2006) A conditioned Latin hypercube method for sampling in the presence of ancillary information. *Computers and Geosciences* 32:1378–1388.
- R Development Core Team (2008) R: A Language and Environment for Statistical Computing. (Vienna: R Foundation for Statistical Computing. ISBN 3-900051-07-0. URL: <http://www.R-project.org> ; last accessed 13.6.2008).

- Scarth P, Byrne M, Danaher T, Henry B, Hassett R, Carter J, Timmers P (2006) State of the paddock: monitoring condition and trend in groundcover across Queensland. In: Proceedings of the 13th Australasian Remote Sensing Conference, November 2006, Canberra.
- Thoma DP, Gupta SC, Bauer ME, Kirchoff CE (2005) Airborne laser scanning for riverbank erosion assessment. *Remote Sensing of Environment* 95:493–501.
- Trevithick R, Herring M, Dougall C (2008) Development of gully length density layer for the Fitzroy Basin, Queensland through gully mapping and extrapolation using Cubist. Proceedings of the 14th Australasian Remote Sensing and Photogrammetry Conference, Darwin, 29th September–3rd October, 2008.
- Young AP, Ashford SA (2006) Application of Airborne LiDAR for Seacliff Volumetric Change and Beach-Sediment Budget Contributions. *J Coastal Research* 22:307–318.

Integrating Mineralogical Interpretation of HyLogger Data with HyMap Mineral Mapping, Mount Painter, South Australia

A.J. Mauger and S. Hore

Abstract HyLogger, HyMap and PIMA II are three hyperspectral spectrometers variously sampling the electromagnetic spectrum between 450 and 2500 nm. At Blue Mine in the Mount Painter Province of South Australia, the opportunity arose to make a direct comparison of the three instruments. Drill hole BM5, an inclined diamond drill hole, intersected steeply dipping stratigraphy which outcrops in the steeply sloping, scree covered hills immediately above. HyMap data flown over the same district presented 5×5 m pixels each carrying spectra defined by 128 channel reflectance data from along the surface projected line of BM5.

This project has demonstrated that the three hyperspectral instruments provide mutually corroborative datasets in their ability to map mineralogy. It is clear that there remain significant differences between spectral datasets even after pre-processing. These differences limit the opportunity for automated mineral identification. In spite of those differences key common spectral features were identified in each dataset and mineralogical boundaries delineated.

A new subunit within the Wortupa Quartzite, identified mineralogically with these instruments, potentially offers better targeting of mineralisation in this part of the stratigraphy.

Keywords HyLogger · HyMap · Hyperspectral · Spectroscopy · Mineralogy · Mount painter · Ground validation

Introduction

The Mount Painter region has been a test bed of hyperspectral datasets used to map mineralogy for some years (Denniss et al., 1999, Hewson et al., 2001, Hewson et al., 2003). With the advent of HyLoggerTM technology (Huntington et al., 2004) an opportunity arose to use high resolution hyperspectral data to inform the analysis of airborne hyperspectral HyMap data in a geological context. An inclined diamond

A.J. Mauger (✉)

CRCLEME, Geological Survey Branch, PIRSA, Adelaide, SA 5000, Australia

e-mail: mauger.alan@saugov.sa.gov.au

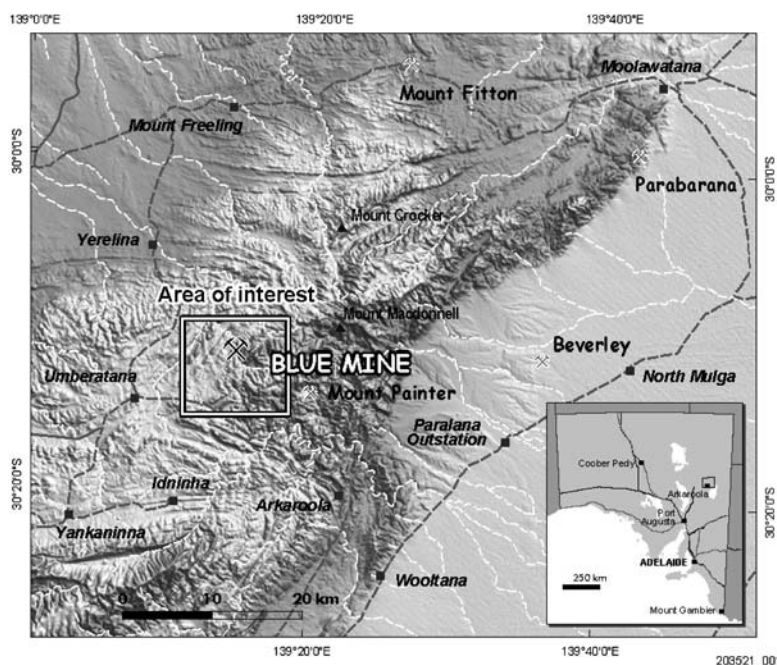


Fig. 1 Regional location diagram

drill hole in the vicinity of Blue Mine in the Mount Painter inlier intersected the stratigraphy orthogonal to dip (Elliot, 1972).

The Mount Painter Province (MPP) (Coats and Blissett 1971) is a geological province in the northern Flinders Ranges in the vicinity of Arkaroola (Fig. 1). Blue Mine is an abandoned Cu mine approximately 20 km north west of Arkaroola.

Geological Context

The Blue Mine Creek area is located at lat $30^{\circ}11'37''$ S long $139^{\circ}14'35''$ E GDA94 in the southwestern MPP an area where Mesoproterozoic basement rocks of the Mount Painter Inlier (MPI) are unconformably overlain by Neoproterozoic Adelaidean metasediments.

The Adelaidean sequences bordering the MPI have historically been a minor source of base metals, principally Cu, and some Pb–Ag. Bismuth has been recorded from a number of localities near the western contact with the MPI. The Cu occurs predominantly as small, high-grade secondary bodies consisting of malachite, azurite, cuprite and some chalcopyrite. Mines are predominantly sited on shears and faults or adjacent to faults, with mineralisation mainly occurring within carbonate-rich rocks (Anderson 1990).

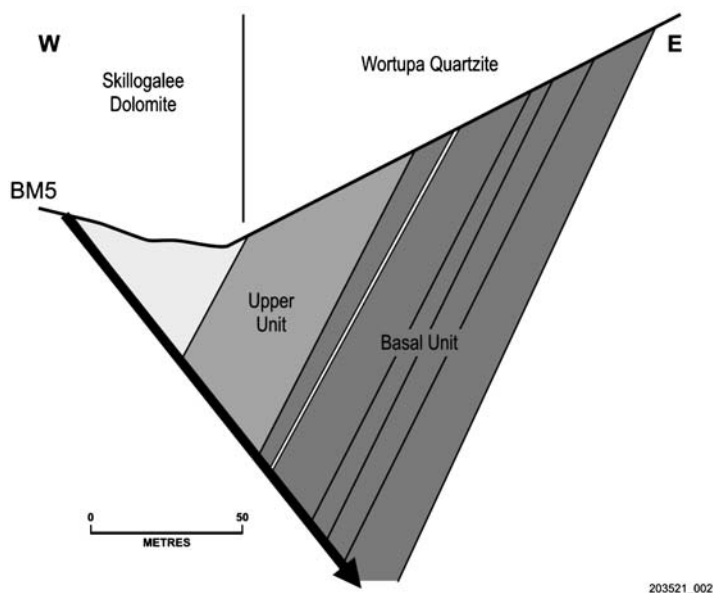


Fig. 2 Cross section of drill hole BM5 (after Elliot, 1972)

The Blue Mine was first prospected in 1891 and work ceased in 1910 and during this period 40 tons of ore was sold, averaging 18% copper. The workings were concentrated on small but high grade occurrences of secondary Cu ores (azurite, malachite, chrysocolla) within the Adelaidean Callanna Group (Elliot, 1972).

Drill-hole BM5 was drilled by Aquitaine Australia to investigate a geochemical anomaly, with an almost coincident IP anomaly, proximal to the main Blue Mine workings in the historic mining field. These workings are situated on a faulted section of the Wortupa Quartzite. The drillhole was spudded in the overlying Skillogalee Dolomite with interceptions of pyrite and chalcopyrite within the Wortupa Quartzite (Fig. 2), which were interpreted by Aquitaine to be stratiform with Cu values up to 0.95% over 1.5 m reported (Elliot 1972). The pyritic and chalcopyritic generation was sedimentary in origin and reconcentrated through folding and faulting and associated general metamorphism (Elliot 1972).

Reconnaissance exploration work by Marathon Petroleum Australia Ltd targeted the Au potential in the upper section of the Wortupa Quartzite. Samples include the Blue Mine Creek area and assays returned anomalous values averaging 1 ppm Au, which was associated with secondary Cu localised in veins and shears (Yates 1982).

The Wortupa Quartzite presents itself as resistant ridges formed by weathering of the underlying and overlying carbonate horizons, it is a continuous unit providing an excellent marker. It is often arkosic and becomes increasingly gritty towards the top. This is overlain by the calcareous muds of the Skillogalee Dolomite, which consists of siltstones, greywackes and magnesite horizons (Preiss, 1987).

The basement and Adelaidean rocks of the MPP were deformed and metamorphosed to mostly lower amphibolite facies during the Cambro-Ordovician Delamarian Orogeny (Preiss, 1987).

Methods

Surface sampling the units as projected to the surface and correlating the spectral responses from drill hole (1 × 1 cm) to surface sample to HyMap pixel (5 × 5 m) enabled the derivation of spectral signatures which were propagated further within the HyMap data.

HyMap

Nine runs of HyMapTM were flown over the Mount Painter inlier on 27 March 1998 between 30° 20' 09" S, 139° 11' 32" E and 29° 49' 44" S, 134° 46' 25" E at 2 000 m altitude on a 047° heading generating 2.5 km wide, 50 km strips of imagery at 5 m resolution. HyMap recorded 128 bands across the reflective solar wavelength region of 450–2500 nm with contiguous spectral coverage (except in the atmospheric water vapour bands) and band widths between 15–20 nm. The imagery was calibrated and corrected for atmospheric effects using ACORN 4TM software. Technical specifications for HyMap are available from HyVista's web site (HyVista Corporation, 2008).

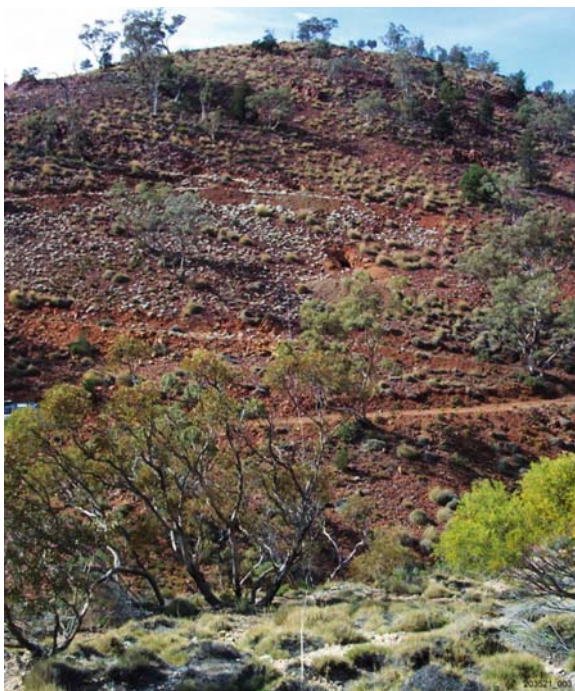
CSIRO HyLogger

In January 2005 Blue Mine diamond drill core was scanned by the CSIRO core scanning HyLoggerTM system (Huntington et al., 2004) at PIRSA's Glenside Core Library. The HyLoggerTM has three instruments installed on a support frame: a hyperspectral spectroradiometer (450–2500 nm); a three band, high resolution linescan camera; and a laser profilometer. The core scanner provides a rapid means of gathering semi-quantitative statistical distributions of minerals down hole. When linked with assay data, this provides a powerful tool for understanding drilling results in the context of deposit paragenesis.

Ground Validation

Figure 3 shows the topography and ground cover in the vicinity of Blue Mine. Samples collected every 5 m along the line of the surface projection of drill hole BM5, identified and described in Elliot (1972) and shown by the tape in Fig. 3, were measured with the PIMA II (1300–2500 nm). Spectra were then compared to those obtained from HyLogger and HyMap. Although the common spectral range shared by the three instruments is in the short wave infrared (SWIR) analysis was not constrained to SWIR active mineralogy. When comparing HyLogger and HyMap the visible-near infrared (VNIR) responses were compared as well.

Fig. 3 View of the Blue Mine workings from the collar of BM5 looking along the projected line of the hole



Data

HyMap

Thirty three pixels, identified by comparison to the Digital Globe Quick Bird imagery (Fig. 4), had their spectra extracted and stored in a separate library. In order to extract spectra from the HyMap data for comparison to both the HyLogger and

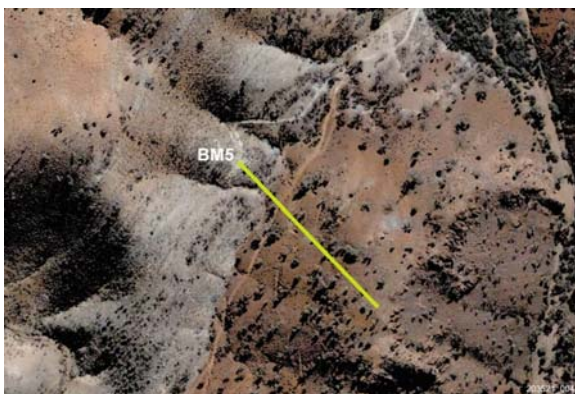


Fig. 4 Quickbird imagery over Blue Mine showing the surface projected line of drill hole BM5 (green line)

Fig. 5 HyMap imagery (1268,816,543:RGB) over Blue Mine showing the surface projected line of drill hole BM5



the PIMA results, several bad bands had to be removed. These bands display inconsistent spectral responses compared to adjacent bands. These effects are usually encountered either at the edges of the spectra or where the four sets of detectors that comprise the full 400–2500 nm range join or overlap in their response curves. In this case the dataset was reduced to 110 bands from the original 128 bands. The data were then scaled from an original response range of 0–475 to a range 0–1 for approximate comparison with the other instruments. Finally the band passes were resampled to match the HyLogger band passes using a ‘Spectral Library Resampling’ tool within ENVI software which employs a gaussian resampling model (Envi, 1999). This process enabled the spectra to be imported directly into TSG-Core.

The outcome was a spectral library with relatively subdued dynamic range for key absorption features in the shortwave infrared. Comparing PIMA and HyMap the results were not dissimilar to those achieved by Denniss et al. (1999).

For visual interpretation purposes the band combination of HyMap data employed in Fig. 5 highlighted the contact between the Skillogalee Dolomite (cyan colour) and the Wortupa Quartzite (reds and browns). It also sought to maximise the differences between hematite and goethite Fe oxide species within the quartzite unit. The green pixels are trees.

CSIRO HyLogger

With one spectra recorded every 0.8 cm along the core tray (Huntington et al., 2004) a certain degree of filtering is required before comparisons can be drawn with other datasets. First there is a process where extraneous pixels are masked from the analysis eg depth markers, tray ends, gaps that see the bottom of tray etc. Then the data was down sampled by depth and output as a new dataset. This has the effect of removing the noise and enhancing the signal by averaging adjacent spectra. By

selecting a 5 m interval the resultant spectra potentially average out the mineral signatures contributing to the equivalent HyMap pixels.

Ground Validation

The distance from the collar of BM5 along the ground was measured by tape. At the start, 1 m samples were collected but given the invariant nature of the samples and the 5 m resolution of the HyMap data it was decided to measure samples every 5 m. At some points multiple readings were taken to record the variety of materials observed. Once loaded into TSG-Core with their measured distances from the collar appended as a scalar it proved possible to downsample back to an even 5 m interval for the entire hole. Due to the nature of the topography it was necessary to collect over a longer surface distance than the vertical plan view indicated on the Quick Bird imagery. Final locations were checked by visual context on the imagery rather than relying on the GPS in averaging mode.

Results

The output from the three separate instruments are presented in Figs. 6, 7 and 8. Each horizontal line is a separate spectrum where red indicates an absorption feature and blue is a reflection peak. For this presentation the wavelength range along the x- axis has been subset to match the PIMA wavelengths 1300–2500 nm. Each plot

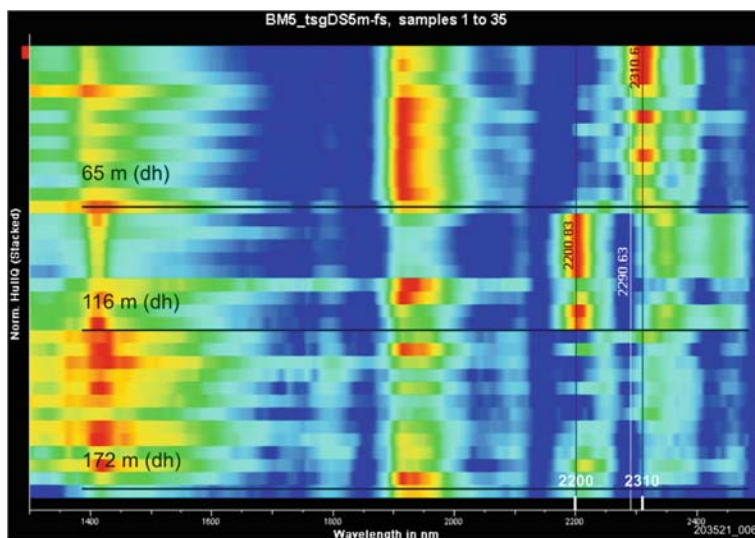


Fig. 6 Stacked spectra from HyLogger 1300–2500 nm

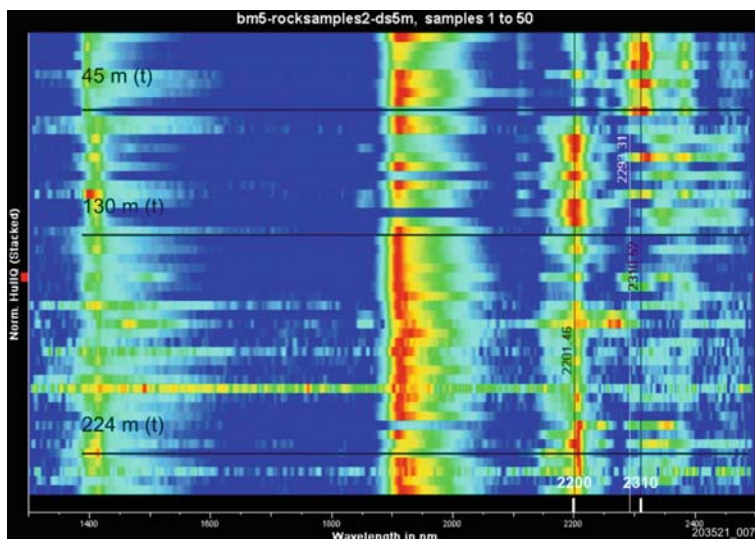


Fig. 7 Stacked spectra from PIMA II 1300–2500 nm

is arranged such that the collar of the hole is at the top of the diagram. In order to compare positions in each plot a calculation needed to accommodate the topography, the dip of the drill hole and the dip of the beds. The common point of the creek occurred at 65 m down the drill hole(dh), 45 m measured by tape (t) over the ground and 43 m by measure pixel (p) on the HyMap image. The end of the hole was respectively 172 m (dh), 224 m (t) and 200 m (p).

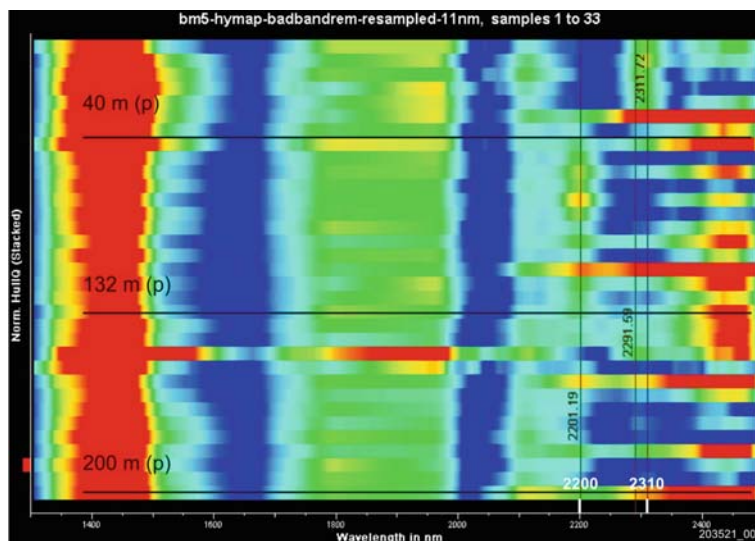


Fig. 8 Stacked spectra from HyMap 1300–2500 nm

In subdividing the stratigraphy by spectral response the key wavelengths to observe are 2310 and 2200 nm. The 2290 nm feature is also of interest. From the collar of the hole to the creek, the spectral response is dominated by tremolite/actinolite characterised by 2310 nm absorption. After the creek a strong illite/muscovite signal focussing on 2200 nm dominates to approximately 116 m (dh), 130 m (t), 132 m (p). Nontronite or talc registers at 2290 nm in the HyMap image after this boundary and this is supported by the HyLogger data. For the remainder of the hole the spectral response is dominated by kaolinite or aspectral material. Aspectral material does not imply lack of a signature rather the signature is not contained in the software library. This can be because the material has no recognised SWIR response. In this case magnetite and quartz would be regarded as aspectral and these tend to dominate the surface scree. What remains, sometimes as a minor component, is the kaolinite.

PIMA II is ill equipped to measure the presence of Fe oxide and is unable to identify species of Fe oxide. HyLogger identifies zones in the deeper part of the hole where Fe^{2+} dominates Fe^{3+} especially between 116 and 150 m (dh). By choosing bands to highlight variance in Fe oxide response the HyMap data shows stratification within the Wortupa Quartzite (Fig. 5).

Discussion

Three major units have been characterised at three scales of hyperspectral observation. The upper unit is the Skillogalee Dolomite. The two lower units, defined mineralogically, are part of the Wortupa Quartzite, the basal unit of which is associated with Cu mineralisation. The basal unit also has a higher Fe oxide content. Using bands that enhance the Fe oxide spectral response this unit can be traced on the HyMap imagery over considerable distances allowing better exploration targeting of mineralisation.

The low dynamic range of the final HyMap spectra limited the ability of TSG Core to provide automated mineral identification. However the PIMA interpretation of surface samples allowed the modification of the spectral library for HyLogger and this refinement enabled the logging of tremolite in the core.

The presence of kaolinite in a largely aspectral section of the stratigraphy was unexpected but, as noted above, this may not be an indication of absolute abundance, rather simply the only SWIR responsive mineral in the section. Jarosite was also noted in this section.

Conclusions

This project has demonstrated that the three hyperspectral instruments: HyMap, PIMA II and HyLogger, provide mutually corroborative datasets in their ability to map mineralogy. It is clear that there remain significant differences between

spectral datasets even after pre-processing. These differences limit the capacity for automated mineral identification using a program like TSG Core. In spite of those differences key common spectral features can be identified in each dataset and mineralogical boundaries delineated. In this instance the 2310 and 2200 nm absorption features highlighted changes from tremolite/actinolite dominated mineralogy of the Skilloogalee Dolomite to a white mica dominated upper unit of the Wortupa Quartzite. The third or basal unit of the Wortupa Quartzite, dominated by quartz, magnetite and kaolinite, was logged largely as aspectral but had sufficient spectral character to be mappable using HyMap imagery.

Acknowledgements Anglo American provided the HyMap data for analysis. AMIRA Project P685 was an essential precursor spectral logging campaigns at PIRSA's Glenside Core Storage Facility. CSIRO Detection Technologies Group provided the HyLogging system and supported the instrument and post-processing during the campaigns. Georgina Gordon and staff at Glenside Core Storage Facility were responsible for logistics and provided efficient core handling and data collection. HyLoggerTM and TSG CoreTM are registered trademarks of CSIRO.

References

- Anderson BE (1990) Annual report. Pan Australian Mining Ltd. South Australia. Department of Primary Industries and Resources. Open file Envelope, 3976 (unpublished)
- Coats RP, Blissett AH (1971) Regional and economic geology of the Mount Painter Province. Geological Survey of South Australia. Bulletin, 43
- Denniss, A, Huntington, J, Hore S (1999) Mount Fitton hyperspectral mineral mapping collaborative project. MESA Journal, Quarterly Earth Resources Journal of Primary Industries and Resources South Australia. 15: 12–14.
- Elliot P (1972) Department of Primary Industries and Resources. Open file Envelope, 1883 (unpublished)
- Envi (1999) ENVI User's Guide version 3.2, 864 pp.
- Hewson R, Hausknecht P, Cudahy T, Batty S, Stamoulis V, Mauger A (2001) Geophysically integrated profiling airborne mineral mapping – Mount Fitton. MESA Journal. 23:16–19.
- Hewson RD, Cudahy TJ, Quigley M, Huntington JH, Whitbourn LB, Hausknecht P. (2003) Mapping talc mineralisation and associated alteration using airborne and satellite-borne spectrometry: a case study at Mount Fitton, South Australia. In: Dentith MC. (ed). Geophysical signatures of South Australian Mineral Deposits. Centre for Global Metallogeny, University of Western Australia. Publication 31. Australian Society of Exploration Geophysics. Special Publication 12: 213–221
- Huntington J, Mauger A, Skirrow R, Bastrakov E, Connor P, Mason P, Keeling J, Coward D, Berman M, Phillips R, Whitbourn L, Heithersay P, (2004) Automated mineralogical logging of core from the Emmie Bluff iron oxide copper-gold prospect, South Australia. PACRIM 2004 Congress, 19-22 September 2004, Adelaide, South Australia. AUSIMM Pub 5/2004
- HyVista Corporation (2008) <http://www.hyvista.com> .
- Preiss, WV, (compiler), 1987. The Adelaide Geosyncline – late Proterozoic stratigraphy, sedimentation, palaeontology and tectonics. South Australian Geological Survey Bulletin 53: 438.
- Yates M (1982) A Review of Strataform Gold within the Adelaidean Sediments, Mount Painter Province, EL 871 and 627, South Australia. Open File Envelope 3976 (unpublished)

A Preliminary Study of Mapping Biomass and Cover in NZ Grasslands Using Multispectral Narrow-Band Data

L. Vescovo, M. Tuohy, and D. Gianelle

Abstract Mapping biophysical parameters (LAI, nitrogen content, biomass, Green herbage ratio) is fundamental to understanding ecosystem functioning. Considerable time and expense are commonly spent measuring these variables which can be scaled up from ecosystem to landscape level to monitor productivity, carbon stocks and fluxes. In a scaling up approach, remote sensing techniques can be used at ground, airborne and satellite levels, and different Spectral Vegetation Indices (SVI) can be compared with data collected by direct harvesting. Four main grassland classes (improved pastures, unimproved pastures, New Zealand native tussock grassland and depleted grasslands) were identified on Landsat ETM+ images. ASDI spectroradiometer and Landsat ETM+ data were examined at ground and satellite level (3×3 pixels), respectively. In January 2004, in New Zealand's South Island, ground observations (Leaf Area Index, biomass, necromass and spectral measurements with 170° diffusor optics) were performed at 12 sites belonging to the four grassland classes. Spectral signatures were determined at the two levels and spectral vegetation indices were calculated for the different grassland canopies investigated. The range of biomass levels within the different canopies was wide (from 10 to 667 g/m^2 of dry matter). Necromass rate was high in tussock grasslands which also showed high levels of biomass. However, tussock spectral signatures are similar to depleted areas. NDVI calculated for improved pastures, unimproved pastures, and depleted grasslands is correlated with dry biomass levels both at ground ($R^2=0,76$) and at Landsat ETM+ level ($R^2=0,74$). Most of the tussock NDVI values do not follow a typically logarithmic trend. Saturation of NDVI occurs above biomasses of 100 g/m^2 .

The preliminary results of the present study confirm the potential of upscaling the biophysical parameters estimation from ecosystem to landscape level. Tussock spectral response is shown to be different from the other grasslands, because of the particular structure and the influence of bare soil.

L. Vescovo (✉)

Centre for Alpine Ecology, Viote del Monte Bondone, Trento 38040, Italy
e-mail: vescovo@cealp.it

Materials and Methods

New Zealand Grasslands

New Zealand grasslands can be divided into 'native' and 'exotic'. Native grasslands are endemic to New Zealand, while the 'exotic' derive from seeding European species and consequent natural diffusion after the European colonization started the 18th century (Scott 1979). Tussocks are predominantly native grasslands. Because of their inability to cope with competition, they are often put under conservation by New Zealand Department of Conservation. However, replacement of native grasslands by introduced agricultural species is still continuing.

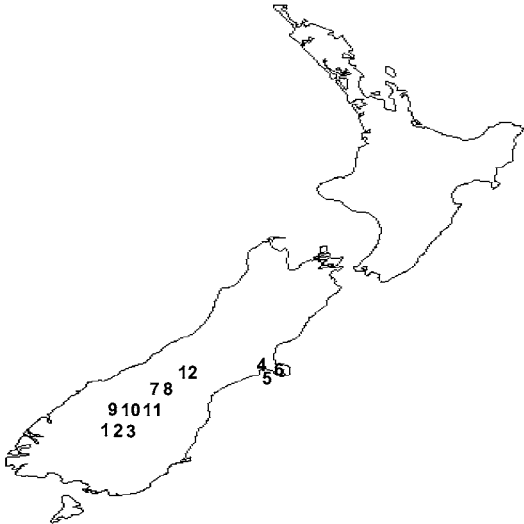
A field campaign started in early January 2004 with the identification of 12 New Zealand grassland areas (Fig. 1) for ground-truth measurements based on an existing classification project (Land Cover Data Base 2, LCDB2; finished in 2004; NZ Ministry for the Environment, Christchurch).

LCDB2 used Landsat 7 ETM+ imagery as primary data for thematic classification. Grassland was included into the seven 'first order' classes, and grasslands were further divided into several 'target' classes. In this study, most common grassland ecosystems such as improved pastures, unimproved pastures, tall/short tussock grasslands and depleted tussock grasslands were identified on the ETM+ 4, 5, 3 false-colour images (Fig. 2) and during the field campaign, locations were confirmed using a GPS system. Field sampling was done in the South Island (Banks Peninsula, Mackenzie Basin, and Central Otago), in collaboration with Steve Thompson and Ingrid Gruner, both working on the LCDB2 project as remote sensing and ecology specialists. During the field work, ground truth-areas for biophysical and spectral measurements were selected according to their location, topography, homogeneity, and similar management in the summers of 2003 and 2004.

Improved pastures (orange-red in the false colour visualisation, because of their high reflectance in the near-infrared band) are intensively managed exotic grasslands either cut for hay or rotationally grazed for wool, fat-lamb, beef, dairy, and deer production. Improved pastures are generally vigorous reflecting high levels of inherent soil fertility, typical of the plains and down-lands. In some dry areas of the Mackenzie basin, improved pastures are irrigated. Dominant species are clovers and ryegrass. Non-pasture species are inconspicuous.

Unimproved pastures (visualised as yellow, because of their lower reflectance in the near-infrared band) are extensively managed exotic grasslands grazed for wool, sheep-meat and beef production. A class typically found on steep hill and high country throughout New Zealand. Plant growth is usually less vigorous than in improved pasture reflecting lower levels of soil fertility, lower fertiliser application, seasonal drought or a shorter growing season, especially in the South Island. Dominant species are less productive exotic grasses, such as browntop and sweet vernal, usually mixed with indigenous short tussock species. Areas of unimproved pasture show a tendency to 'brown off' during summer months.

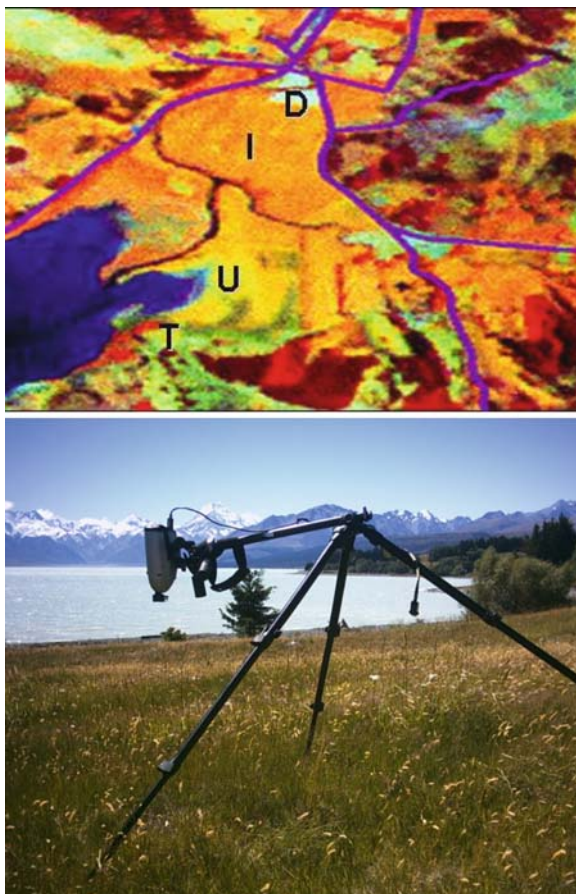
Short tussock grassland (visualised as greenish-brown, because of the high reflectance of the red and medium-infrared bands) include areas of grassland



| Name | Location | Grassland class | Ecosystem | VF (%) | Altitude (m) |
|--------------|-----------------|--------------------|-------------------------|--------|--------------|
| 1-Waikaia | Central Otago | Unimproved pasture | Pasture | 100 | 650 |
| 2-Waikaia | Central Otago | Tussock grassland | Tall tussock grassland | 70 | 600 |
| 3-Waikaia | Central Otago | Uninproved pasture | Abandoned pasture | 100 | 180 |
| 4-Sumner | Banks Peninsula | Depleted tussock | Depleted Pasture | 90 | 200 |
| 5-Sumner | Banks Peninsula | Tussock grassland | Tall tussock grassland | 80 | 180 |
| 6-Bossu road | Banks Peninsula | Uninproved pasture | Pasture (rare tussocks) | 90 | 750 |
| 7-Tara Hills | Mc Kenzie basin | Tussock grassland | Tall tussock grassland | 40 | 1400 |
| 8-Tara Hills | Mc Kenzie basin | Uninproved pasture | Pasture | 100 | 900 |
| 9-Simpson | Mc Kenzie basin | Improved pasture | Hay paddock | 100 | 100 |
| 10-Simpson | Mc Kenzie basin | Depleted tussock | Depleted pasture | 45 | 100 |
| 11-Simpson | Mc Kenzie basin | Improved pasture | Hay paddock | 100 | 100 |
| 12-Pukaki | Mc Kenzie basin | Uninproved pasture | Pasture | 95 | 500 |

Fig. 1 Location and description (grassland class, ecosystem, estimated Vegetation Fraction and altitude) of the 12 grassland ground truth areas in the New Zealand South Island. VF= vegetation fraction

Fig. 2 Upper Landsat ETM+ 4,5,3 false-colour visualisation of a Banks peninsula grassland area. I, U, D, T: Improved pastures, Unimproved pastures, Depleted tussocks, Tussock grasslands. Lower: Spectral measurements on an unimproved pasture in the Mackenzie basin



characterised by the presence of hard tussock (*Festuca novae-zelandiae*), blue tussock (*Poa colensoi*), and/or silver tussock (*Poa cita*). Short tussock grassland is typically over-sown with exotic pasture species to improve pastoral production, or exotic grasses have invaded from neighbouring areas. *Tall tussock grassland* (also greenish-brown) can be typically found at higher altitudes in the South Island high country with limited presence in the North Island main ranges. *Chionochloa* species dominate, usually accompanied by short tussock grassland species and a number of herbs, in particular, *Celmisia* species. Both short and tall tussock ecosystems can show low vegetation fraction (VF) values.

Depleted tussock grasslands (visualised as light blue, because of the very high reflectance in the red band) are areas of very low, herbal vegetation with a general grassland/herbfield character. They are common in dry areas and heavily-grazed areas, where some invasive species can find a most favourable habitat. Short tussock grassland species are usually present, but display less than 10% cover. *Hieracium* species, thyme and/or exotic grasses are conspicuous, as is the bare

ground component. Plant vigour and biomass are significantly lower than in short tussock.

In this work, 2 improved pastures, 5 unimproved pastures, 3 tussock grasslands and 2 depleted tussock grasslands were investigated.

Spectral and Biophysical Measurements

All field samples were collected during January 2004. Using the LCDB2 classification, improved pastures, non improved pastures, tussock grassland and depleted tussock areas were identified on Landsat ETM+ satellite imagery acquired in January 2003. With the colour composite of bands 4, 5, 3 (RGB) providing a good visualisation of the different classes, 12 ground-truth areas (100×100 m) were selected, consistent with the 3×3 pixel selected ROIs (pixel size 30 m, ROI size 90×90 m). The Landsat imagery was registered and atmospherically corrected at the New Zealand Centre for Precision Agriculture, Massey University, Palmerston North.

Spectral measurements have been carried out between 10.00 and 14.00 on clear sky conditions. Ground spectra were collected at the 12 sites using an Analytical Spectral Devices (ASD) Hand Held spectroradiometer. The ASD Hand Held wavelength range is 325–1075 nm. Cosine diffuser foreoptics were used during the field campaigns; 12 spectra were measured at each ground-truth area. Each spectrum was automatically calculated and stored by the spectroradiometer as an average of 20 readings. Spectra were exported and spectral vegetation indices were calculated from both ground measurements and from the Landsat 7 ETM+ reflectance values (used bands were red: 630–690 nm and Near-Infrared 750–900) obtained in 3×3 pixel ROIs (Regions of Interest indicated by the 12 GPS positions). For the Vegetation Indices calculation, ground data were matched to the ETM+ satellite band ranges.

Biophysical measurements were also carried out in the ground-truth areas. Investigated parameters were biomass, necromass, Leaf Area Index, nitrogen leaf concentration, biomass/necromass ratio (%) and biomass/phytomass ratio (Green Ratio (GR), %). GR is the proportion of green material in a grassland— in simple terms, it is the percentage of grass that is green, while the degree of curing (also used in the literature) represents the correspondent proportion of dead material. Phytomass was divided manually into biomass and necromass components. Samples were dried for 48 h at 80°C and then weighed. Biomass nitrogen content (%) was determined in the laboratory. Vegetation fraction (VF) was also estimated on a visual basis.

Results

Biophysical Measurements

The biophysical parameters range was very wide, as the research campaign included very different vegetation types, from very productive and green improved grasslands

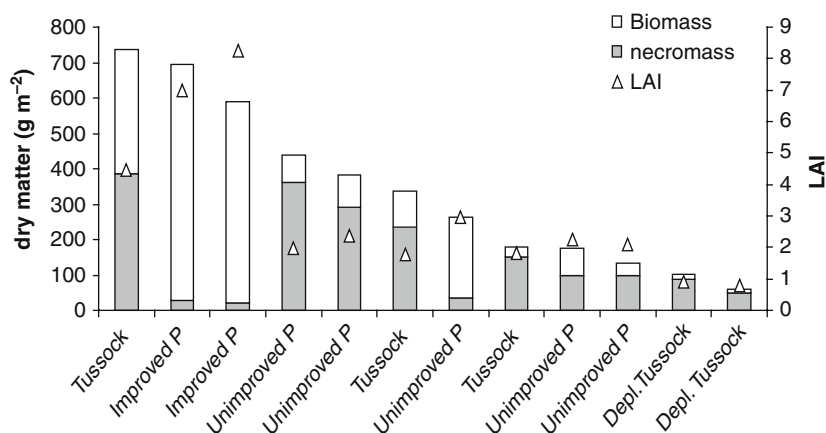


Fig. 3 Biomass, necromass and Leaf Area Index of the investigated grasslands

to dry unimproved pastures and tussocks (Fig. 3). Biomass values varied from 10 (depleted tussock) to 667 g m^{-2} (improved pasture) while necromass maximum values reached 386 g m^{-2} (tussock grassland). Vegetation necromass was generally high in most of the grassland ecosystems due to the dry conditions of the austral summer of 2004 in the Canterbury and Mackenzie Basin area. In fact, due to the dry climatic trend, it was possible to observe that in 9 of the 12 study areas the GR value was lower than 50%. The native grassland tussocks structure also generally includes many old leaves, so in all these grasslands the observed necromass was always high.

For this reason, the tussock grasslands look brownish especially in summer even if they show high biomass levels and generally discrete GR values. This is because of their tussock structure, where high rates of biomass are concentrated and 'hidden' within the sparse tussocks, while the ground in between the tussocks is poorly vegetated or sometimes even bare.

LAI range was also very high, being between 0.8 (depleted area) and 8.2 (intensively managed meadow). Observing the infrared reflectance (Fig. 4) it is possible to distinguish, in the near-infrared wavelength range (760–900 nm), improved pastures (with a biomass range between 400 and 700 g m^{-2}) from unimproved ones ($100\text{--}400 \text{ g m}^{-2}$). Improved pastures (grassland areas with high biomass) generate high reflectances in the near infrared (higher than 0.5 in the 825–900 nm range). With high biomass, the near infrared (NIR) reflectance continues to respond significantly to changes in moderate-to-high vegetation density in canopies. On the other hand, this higher sensitivity of the NIR reflectance has little effect on NDVI values once the NIR reflectance exceeds 0.3, as shown by Gitelson (2004). This different reflectance in the NIR still allows a different visualisation of improved (red-orange) and unimproved (yellow) pastures in the 4,5,3 ETM+ false-colour imagery. Blue colour in the false colour visualisation is typical of areas with high reflectance in the red wavelengths such as depleted tussocks (see Fig. 4). On the other hand, short and tall tussock areas look dark green or brownish according to

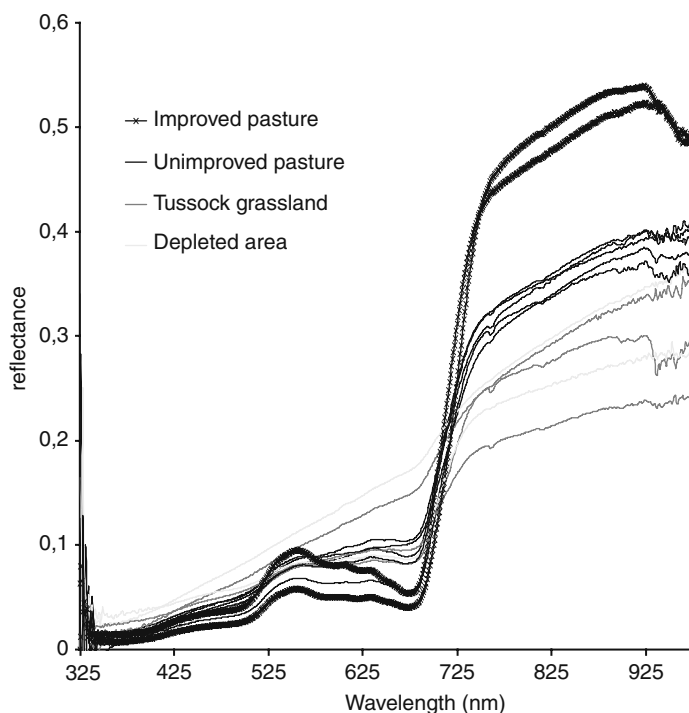


Fig. 4 Spectral signatures of the 12 investigated New Zealand grasslands

their reflectance in the red and especially in the mid-infrared wavelengths (band 5). New Zealand tussock grassland signatures are very similar to depleted, unproductive areas, despite the higher biomass content. This can be related to the particular structure of such canopies where biomass is concentrated into the dense tussocks and partially 'shaded' by both biomass and necromass elements. Also, there is a strong background effect due to the bare ground reflectance (low VF values). No significant differences could be found between tussocks and non-tussocks biomass nitrogen (%) content (data not shown). Figure 5 shows that correlation coefficient R , in the visible region, is negative for phytomass, biomass and necromass. Minimum value for LAI correlation is -0.75 at 500 nm, while in the infrared region R is positive, reaching a maximum value of 0.84 at 750 nm for LAI and a maximum of 0.82 at 740 nm for biomass. Also, biomass total nitrogen, biomass/necromass ratio and GR are negatively correlated in the visible and positively correlated in the NIR region. Necromass alone showed very low R values. These results seem to confirm the suitability of the hyperspectral approach for both in-situ and remote estimation of both quantity and quality of grass. Narrow-band reflectances and spectral vegetation indices can yield very good linear correlations with grassland biophysical parameters as demonstrated by Hansen and Schjoerring (2003) and Mutanga (2004).

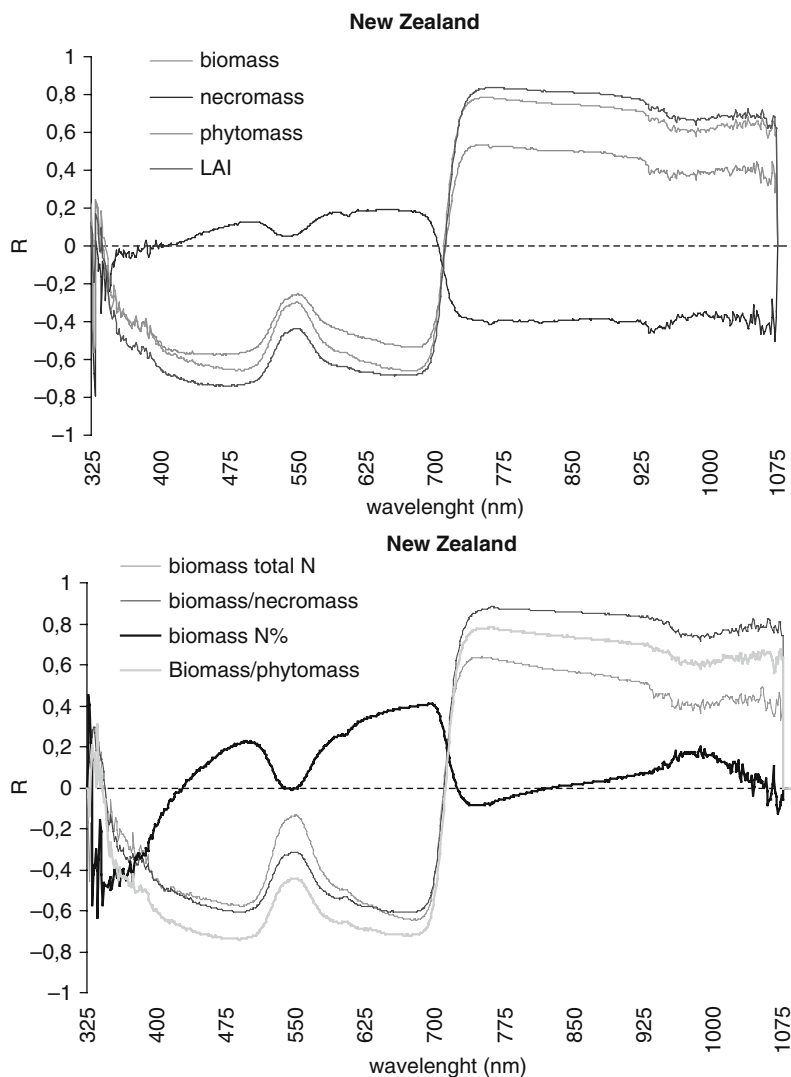
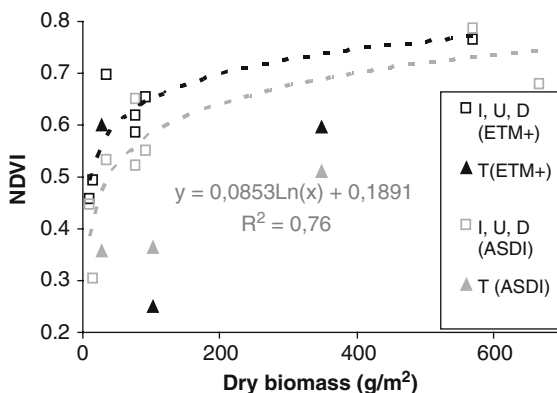


Fig. 5 Correlation between biophysical parameters and reflectance: R values at different wavelengths

GR (and consequently the curing rate) of grasslands is one of the most predictable parameters both in the visible and in the NIR bands. The multispectral approach still allows acceptable upscaling of the investigated parameters at regional scale. A good correlation between ground NDVI values (calculated from ETM+ simulated bands) and biomass was found ($R^2 = 0.76$, $RMS = 0.08$) see Fig. 6).

Fig. 6 NDVI and biomass regression for the 12 grassland sites. NDVI from ground spectral measurements (ASD spectroradiometer) and satellite ETM+ data. I, U, D, T: Improved/unimproved pastures and depleted tussocks. T: tussock grasslands



On the other hand, index saturation occurs above biomass rates of 150 g/m². A similar logarithmic trend could be found at ground and satellite level. Indices calculated from tussock reflectance data have to be considered separately as they show values which are not comparable to other grasslands, because of their canopy structure.

There is a good potential for monitoring grassland phenological properties, as the GR is highly correlated (see Fig. 7). with many vegetation indices, such as Green-NDVI, calculated as a normalised difference between the NIR and the green band. The correlation is mostly linear and do not perform well below 20–30% cover, as it typically happens for remote vegetation indices. The Prediction of GR (and then the curing rate of grasslands) seems to be possible according to the correlation coefficient found ($R^2 = 0.74$; RMS = 0.06), which can be considered sufficient for use in remote understanding grassland processes. Also in this case, tussock grasslands have to be considered separately because of their particular optical properties.

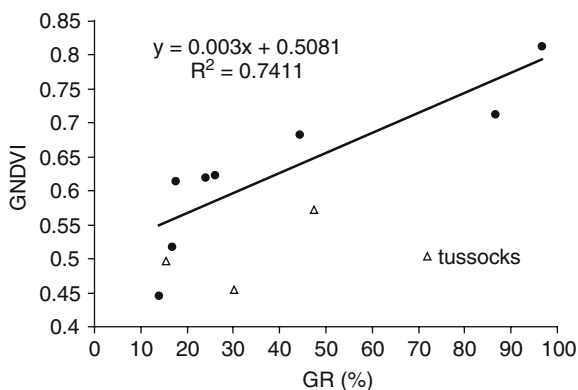


Fig. 7 Correlation between ground Green-NDVI (GNDVI) and GR

Conclusions

A marked variability of the investigated biophysical parameters was observed, according to the very different vegetation types and canopy structures which were observed.

Depending on their different biomass, improved and unimproved pastures showed very different spectral signatures in the NIR range. Despite this, NDVI-biomass regression is logarithmic as NDVI values saturate very early due to the index normalisation effect.

The native grassland tussocks signatures showed a spectral response very similar to depleted low-productive areas in the visible-NIR range. As these grasslands are visualised as green-brownish in the 4, 5, 3 false-colour ETM+ imagery, more studies are needed in order to investigate their the mid-infrared reflectance. These studies could also help to improve prediction of biophysical parameters and provide new information about the predictability of grassland water status.

Good correlations were found between narrow-band reflectances and biophysical parameters. Considering the curing monitoring need, necromass itself seems to be not predictable but biomass and GR showed good R values. All these results seem to confirm the suitability of the hyperspectral approach for both in-situ and remote estimation of both the quantity and quality of grass, using hyperspectral indices or a regression method exploiting several narrow bands.

On the other hand, depending on the spectral resolution available from the satellite platforms, multispectral vegetation indices allow the upscaling of the biophysical parameters. GR (and consequently the curing rate) of grasslands was one of the most predictable parameters and shows a linear correlation with Green NDVI. This kind of information is a key tool in grassland curing estimation for phenological monitoring and fire danger assessment.

Acknowledgements The authors would like to thank: Steve Thompson and Ingrid Gruner, from the NZ Ministry for the Environment (Christchurch), for their logistic and technical support during the field campaign. Alison Rutherford from the Tara Hills research centre for the precious help at Omarama Station. The farmers of the New Zealand South Island who allowed field work on their properties and gave very useful information during the campaign.

References

- Gitelson AA (2004) Wide Dynamic Range Vegetation Index for Remote Quantification of Biophysical Characteristics of Vegetation. *J Plant Physiol* 161:165–173
- Hansen PM, Schjoerring JK (2003) Reflectance measurement of canopy biomass and nitrogen status in wheat crops using normalized difference vegetation indexes and partial least squares regression. *Remote Sens Environ* 86: 542–553.
- Mutanga O (2004) Hyperspectral Remote Sensing of Tropical Grass Quality and Quantity. Phd thesis, Wageningen University, Netherlands.
- Scott D (1979) Use and conservation on New Zealand native grasslands in 2079. *N Z J Ecol* 2: 71–75.

Comparing Common Hyperspectral Vegetation Indices for Their Ability to Estimate Seasonal Nitrogen and Other Variables in Winter Wheat Across a Growing Season

J.G. Ferwerda, S.D. Jones, G. O'Leary, R. Belford, and G.J. Fitzgerald

Abstract Abstract Field spectroscopy was used to assess the nitrogen status and monitor crop growth and production of wheat (*Triticum aestivum* L, cv. Chara) under a range of nitrogen fertilizer treatments and two irrigation levels (rainfed and irrigated) throughout the growing season. The association between a range of commonly used vegetation indices for the detection of green biomass, nitrogen or chlorophyll concentration, and measured crop characteristics (nitrogen concentration, total nitrogen accumulated, dry weight, wet weight, relative foliar cover and moisture content) was determined for six moments in the growing season. At about 95–144 days after sowing, a strong correlation (r^2 between 0.7 and 0.99, $p < 0.01$) existed between vegetation indices and wheat biomass, relative foliar cover and total nitrogen load per square meter. However this association did not hold when multiple sample dates were combined. Changes in total biomass and/or foliar cover strongly affected the association between vegetation measures and the vegetation indices, making between-date comparisons difficult.

Introduction

Nitrogen is an important factor in environmental processes such as biomass decomposition (Recous et al., 1995), plant growth (Zhao et al., 2005) and herbivore foraging (Mattson, 1980). In agriculture it is one of the main fertilizers used to enhance crop productivity. Nitrogen status of a plant is linearly related to chlorophyll content (Zhao et al., 2005), and therefore to a plants photosynthetic capacity. Early detection of nitrogen shortages in crops may enhance fertilization schemes and improve crop production. It is therefore not surprising that many studies have tried to develop automated routines for the detection of foliar nitrogen concentration.

J. G. Ferwerda (✉)

Department of Mathematics and Geospatial Sciences, Royal Melbourne Institute of Technology, Melbourne, VIC 3000, Australia
e-mail: jelle@bio-vision.nl

A variety of remote sensing indices have been proposed to predict foliar nitrogen and chlorophyll concentration, as well as the relative foliar cover, such as Green Leaf Area Index, GLAI Ferwerda and Jones, 2006; Gong et al., 2002; Haboudane et al., 2004; Haboudane et al., 2002; Huete, 1988; Johnson, 2001; Yoder and Pettigrew-Crosby, 1995. Two distinct groups of indices can be distinguished. One group required a priori knowledge about the characteristic of the crop, such as biomass ranges, and foliar nitrogen content. An example is the Crop Canopy Chlorophyll Index (CCCI, (Fitzgerald et al., 2006)) which uses the Nitrogen Stress Index (NS Index (Rodriguez et al., 2006)) to determine the fertilisation status of crops. When tested on wheat, Rodriguez et al., (2006) found that the CCCI accounted for 68% of the variation in nitrogen status as early as Zadoc (growth stage) 33 (3rd node detectable). Although these indices work well, there is an obvious downside to the need of field data. The second group of indices is based solely on the reflectance signatures of the crop. These indices typically combine bands from chlorophyll absorption features in the visible light (around 450 nm or 680 nm) with one or more bands influenced by radiometric scattering by cell-wall material in the near infrared (primarily 700–900 nm) or short wave infrared light (primarily 1500–1750 nm). The main variation between these indices is the predicted sensitivity to the effects of soil reflectance under low canopy cover, and to variations in foliage cover. Common indices include the Transformed Chlorophyll Absorbed Reflectance Index (TCARI (Haboudane et al., 2002)), the Optimized Soil Adjusted Vegetation Index (OSAVI (Haboudane et al., 2002)), the Modified Soil Adjusted Vegetation Index (MSAVI (Qi et al., 1994)), and the Modified Simple Ratio index at 705 nm (MSR₇₀₅ (Sims and Gamon, 2002)).

In semi-arid production systems the balance between nitrogen availability and water availability strongly affects crop productivity. The effect of irrigation, besides increasing water availability and subsequent growth and cell-stretching (Munns et al., 2000), is an increased ability to absorb nitrogen, which further enhances growth. A shortage of available water therefore limits growth in two ways: Directly, through a reduced cell-extension, and at extreme levels, damage to cells and overheating of foliage, and indirectly, through a reduced ability to absorb nitrogen.

To test the effects of water and nitrogen availability on plant growth and wheat (*Triticum aestivum* L, cv. Chara) production, and the ability to detect these effects through remote sensing, a field experiment was performed. In particular the relationship between a variety of common vegetation indices (assumed to be related to biomass or foliar nitrogen (chlorophyll)) and the actual concentration of nitrogen, the GLAI and the standing crop biomass throughout the growing season for irrigated and rain-fed wheat on four different levels of fertilisation.

When vegetation indices are used to assess the fertilisation requirements and the growth of a crop at a specific moment in time, it is important to determine the spatial variation of a crop growing under similar conditions accurately, at that specific moment in time. However, when monitoring crop development throughout the season (for example for yield forecasting models), it is equally important that vegetation indices have a consistent relation with the measure of interest. Therefore the association between vegetation indices and measured vegetation characteristics

was analyzed for both individual sampling dates, as well as combined for the full growing season.

Methods

Field Setup

Wheat (*Triticum aestivum* L, cv. Chara) was grown during the 2004 growing season in Horsham, Victoria, Australia (Sowing date: June 17th; Date of emergence: June 22nd). As part of an ongoing experiment on the effects of nitrogen and water availability on the productivity of wheat in semi-arid systems (Rodriguez et al., 2006), wheat was grown on plots (soil type: Grey vertisol) with a variation of nitrogen applications and irrigation levels in a split-plot factorial design. The main treatments were Irrigated (390 mm; decile 9 for Horsham) and Rainfed (270 mm; decile 5 for Horsham) with four levels of nitrogen applied as urea (0, 16, 39, 163 kg N/ha) in subplots with three replications. Irrigated plots were irrigated six times with 25 mm each between September 6th and November 18th. Urea fertiliser was applied on the 28th of May. Rows were planted in a north to south orientation.

Hyperspectral Measurements

Spectral properties of the plots were recorded at eight sampling dates during the growing season (Table 1). The reflectance of approximately 1 m² of the canopy was recorded using an ASD (Analytical Spectral Devices, Inc, Boulder, USA) Fieldspec FR field spectrometer. This instrument combines three spectrometers to cover the 350–2500 nm range of the electromagnetic spectrum. The spectrometer is equipped with an optical fibre, which was placed in a pistol grip and mounted on a steel boom, 2.5 m above ground surface pointing downwards in a 90 degree angle to

Table 1 Sampling dates. Dates, and the number of days after sowing (17th of June 2004) at which samples were collected

| Date | Days after sowing |
|---------------|-------------------|
| 12 Aug 2004 | 56 |
| 27 Aug 2004 | 71 |
| 20 Sep 2004 | 95 |
| 06 Oct 2004 | 111 |
| 18 Oct 2004 * | 123 |
| 08 Nov 2004 | 144 |
| 22 Nov 2004 | 158 |
| 03 Dec 2004 | 169 |

* Spectrometer readings from the 18th of October displayed high levels of noise, and data from this date has been removed from analysis

measure the up-welling radiance of the wheat. Absolute reflectance was calculated using a calibrated Spectralon Reflectance Target (Labsphere, Inc, North Sutton, New Hampshire) as a reference. The above-ground biomass at the centre of each measured area was harvested (0.36 m^2) for further analysis (see below). All measurements took place between 2 h before and after solar noon on predominantly cloud-free days.

Sample Analysis

At eight sampling dates during the growing season above-ground biomass was harvested after spectral measurements were taken of the site. The following parameters were determined for the collected samples:

- Nitrogen concentration (N, g kg^{-1})
- Green Leaf Area Index (GLAI, $\text{m}^2 \text{ m}^{-2}$)
- Sample Moisture Content (SMC, g kg^{-1})
- Sample Dry Weight (SDW, gm^{-2})
- Sample Wet Weight (SWW, g m^{-2})

For the first two sampling dates (56 days after sowing (DAS⁵⁶) and DAS⁷¹) only N and SDW for rainfed plots were determined, as irrigation had not started yet. On the 13th of December two quadrates (4 rows by 1 meter; approximately 1 m^2) per treatment were harvested, and mean wheat production was determined.

Data Processing

Nitrogen concentration was converted to Nitrogen load per Square Meter paddock (NSM) by multiplying N with the SDW and dividing it by the sampled area. Since reflectance measurements were taken over a consistent area, it was expected that nitrogen per unit area would have a stronger relation to chlorophyll indices than nitrogen concentration. The effect of individual treatments on N, NSM, SDW, SWW, SMC and GLAI was tested using a factorial analysis of variance with nitrogen level ($n=4$), irrigation ($n=2$) and days after sowing, DAS ($n=8$) as interacting factors. For all variables the group distributions were slightly skewed, and a square-root transformation was applied to NSM, SDW, SWW, and GLAI, after which a Shapiro Wilks' W test indicated that group distributions did not seriously deviate from normality (Shapiro Wilks' W; $p > 0.05$). N and SMC were measured on a truncated scale (between 0 and 1000 g kg^{-1}), and their distribution is therefore by definition non-normal (Zar, 1999). An arcsine transformation was applied, after which these variables did not deviate from normality (Shapiro Wilks' W; $p < 0.05$). Analysis of Variance was performed using the transformed data.

Index Calculation

The hyperspectral readings for each plot were used to calculate a series of narrow-band vegetation indices related to crop chlorophyll content and biomass (See Table 2 for calculation details and literature from which the formulas' were derived) The IDL programming language (ITT Industries Inc., Boulder USA) was used to process the reflectance signatures and calculate the indices. The following indices were included, grouped by the biophysical parameters for which strong relations are expected.

Table 2 Overview of the vegetation indices used in this study, including the formula used to calculate them and the literature used to determine calculations. λ = Wavelength, R_λ = Reflectances of band with central wavelength closest to wavelength λ . See appendix 1 for an explanation of the indices

| Index | Calculation | Following |
|-------------------------|--|--------------------------|
| NDVI | $(R_{800} - R_{670}) / (R_{800} + R_{670})$ | Rouse et al. (1974) |
| MCARI | $[(R_{700} - R_{670}) - 0.2(R_{700} - R_{550})] / (R_{700} / T_{670})$ | Daughtry et al. (1992) |
| mSR ₇₀₅ | $(R_{750} - R_{445}) / (R_{705} - R_{445})$ | Sims and Gamon (2002) |
| MSAVI | $\frac{1}{2} [2R_{800} + 1 - \sqrt{2(R_{800} + 1)^2 - 8(R_{800} - R_{670})}]$ | Qi et al. (1994) |
| OSAVI | $(1 + 0.16)(R_{800} - R_{670}) / (R_{800} + R_{670} + 0.16)$ | Haboudane et al. (2002) |
| TCARI | $3[(R_{700} - R_{670}) - 0.2(R_{700} - R_{550})(R_{700} / R_{670})]$ | Haboudane et al. (2002) |
| LAIVI | TCARI/OSAVI | Haboudane et al. (2002) |
| mND705 | $(R_{750} - R_{705}) / (R_{750} + R_{705} - 2R_{445})$ | Sims and Gamon (2002) |
| RDVI | $(R_{800} - R_{670}) / \sqrt{R_{800} + R_{670}}$ | Haboudane et al. (2004) |
| TVI | $0.5[120(R_{750} - R_{550}) - 200(R_{670} - R_{550})]$ | Broge and Leblanc (2000) |
| NRI _{693,1559} | $(R_{693} - R_{1559}) / (R_{693} + R_{1559})$ | Ferwerda et al. (2005) |
| NRI _{693,1770} | $(R_{693} - R_{1770}) / (R_{693} + R_{1770})$ | Ferwerda et al. (2005) |
| PRE | λ where $dR/d\lambda$ is Max $650 \text{ nm} < \lambda < 780 \text{ nm}$ | Gong et al. (2002) |
| PYE | λ where $dR/d\lambda$ is Max $550 \text{ nm} < \lambda < 582 \text{ nm}$ | Gong et al. (2002) |
| PIRE | λ where $dR/d\lambda$ is Max $1300 \text{ nm} < \lambda < 1460 \text{ nm}$ | Gong et al. (2002) |

Relation Between Indices and Vegetation Characteristics

Pearson correlation coefficients were calculated between the 16 vegetation indices and N, NSM, SWW, SDW, SWW, SMC and GLAI. This was done for all samples collected in the study together, for these samples grouped by sampling date (seven groups), and for the samples grouped by sampling date and irrigation treatment (fourteen groups).

Results

Treatment Effects

All vegetation measures changed as the season progressed, and all measures were affected by the nitrogen and the irrigation treatments (Table 3, Fig. 1). For N, NSM and SWW the effects of the nitrogen treatment were dependent on the sampling

Table 3 Analysis of variance results testing for the effect of nitrogen and irrigation treatments of winter wheat vegetation characteristics throughout the growing season

| | N | NSM | SDW | SWW | SMC | GLAI | Yield |
|-------------|------|------|------|------|------|------|-------|
| DAS | *** | *** | *** | *** | *** | *** | — |
| N | *** | *** | *** | *** | *** | *** | *** |
| Irrigation | *** | *** | *** | *** | *** | *** | *** |
| DAS* N | *** | *** | n.s. | * | n.s. | n.s. | — |
| DAS* Irr | *** | n.s. | *** | *** | *** | *** | — |
| N* Irr | n.s. | ** | n.s. | *** | n.s. | *** | * |
| DAS* N* Irr | n.s. | n.s. | n.s. | n.s. | n.s. | n.s. | — |

*, P<0.05; ** P<0.01, *** p<0.001, n.s.: not significant

date (Table 3) with higher N, NSM and SWW on plots with higher fertilisation levels. For all measures, except NSM, the effect of irrigation was dependent on sampling date. A significant interaction occurred between nitrogen and irrigation treatments for NSM, SWW, Yield and GLAI (Table 3). In other words, the effect

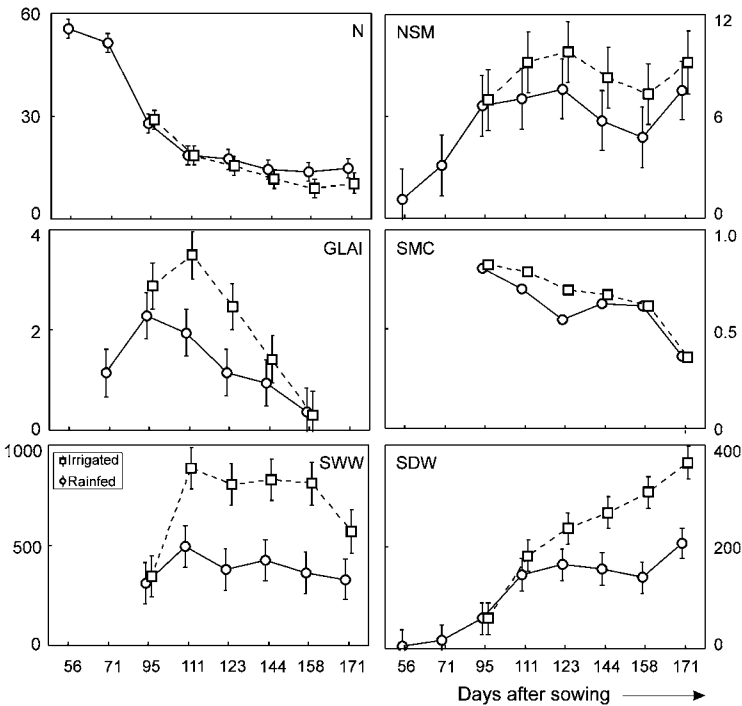


Fig. 1 Vegetation characteristics for wheat grown on irrigated versus rainfed plots over the growing season. Characteristics: Aboveground nitrogen concentration (N, in g kg^{-1}); Nitrogen loading per Square Meter (NSM, in g m^{-2}); Green Leaf Area Index (GLAI, in $\text{m}^2 \text{m}^{-2}$); Sample Moisture Content (SMC in g g^{-1}); Sample Wet Weight (SWW in g m^{-2}), Sample Dry Weight (SDW in g m^{-2})

of irrigation was dependent on levels of nitrogen fertilisation. These measures were higher on irrigated than rainfed plots, and the difference was more pronounced with increasing nitrogen levels. On rainfed plots GLAI levelled off for the highest two nitrogen treatments and even decreased with the highest nitrogen level for Yield. The interaction between nitrogen treatment, irrigation and days after sowing was not significant for any variable, indicating that the interactive effects of nitrogen and water availability on the measured vegetation variables did not vary throughout the growing season.

Relation Between Indices and Vegetation Characteristics

The correlation (r) between vegetation indices and vegetation characteristics as measured across growing stages was generally moderate to poor (Table 4). Only for GLAI and SMC correlations with vegetation indices were consistently high (Table 4). Two indices (NRI_{1770} and NRI_{1559}) showed a strong association with foliar nitrogen. No vegetation index showed a strong correlation with NSM, SDW or SWW.

When data were grouped by growth stage, stronger associations were found. Figure 2 gives an overview of the correlation between individual vegetation indices, and N, NSM, Yield, SDW, SWW and GLAI. For all plots combined, coefficients of determination were significant ($p \leq 0.05$) for r^2 values > 0.4 from DAS⁹⁵.

Table 4 Whole-season correlation (r) values between vegetation indices, and foliar nitrogen concentration (N, g kg⁻¹), Nitrogen load per square meter (NSM, g m⁻²), leaf area index (GLAI, m² m⁻²), sample dry weight (SDW g m⁻²), sample wet weight (SWW g m⁻²) and sample moisture content (SMC, g kg⁻¹) for all samples combined. Strong linear correlations ($|r| > 0.75$) are displayed in bold

| | N | NSM | GLAI | SDW | SWW | SMC |
|---------------------|-----------------|-----------------------|-----------------------|-----------------------|-----------------------|-----------------|
| LAIVI | -0.47*** | -0.42*** | -0.61*** | 0.15 ^{n.s.} | -0.31** | -0.42*** |
| MCARI | 0.72*** | 0.44*** | 0.82*** | -0.37*** | 0.39*** | 0.92*** |
| MSAVI | 0.73*** | 0.59*** | 0.88*** | -0.26* | 0.53*** | 0.88*** |
| MSR | 0.73*** | 0.56*** | 0.85*** | -0.28** | 0.51*** | 0.88*** |
| MSR ₇₀₅ | 0.73*** | 0.59*** | 0.86** | -0.26* | 0.55*** | 0.86*** |
| ND ₇₀₅ | 0.67*** | 0.48*** | 0.89*** | -0.29** | 0.48*** | 0.86*** |
| NDVI | 0.64*** | 0.45*** | 0.86** | -0.28** | 0.46*** | 0.86*** |
| NRI ₁₅₅₉ | -0.80*** | -0.37*** | -0.87*** | 0.50*** | -0.33*** | -0.91*** |
| NRI ₁₇₇₀ | 0.78*** | 0.37*** | 0.88*** | -0.50*** | 0.33*** | 0.91*** |
| OSAVI | 0.68*** | 0.51*** | 0.88*** | -0.27** | 0.50*** | 0.88*** |
| PIRE | -0.25* | -0.09 ^{n.s.} | -0.05 ^{n.s.} | 0.15 ^{n.s.} | -0.07 ^{n.s.} | -0.28*** |
| PRE | 0.64*** | 0.70*** | 0.86*** | -0.07 ^{n.s.} | 0.63*** | 0.73*** |
| PYE | -0.52*** | -0.28** | -0.65*** | 0.32*** | -0.17 ^{n.s.} | -0.56*** |
| RDVI | 0.71*** | 0.55*** | 0.88*** | -0.26* | 0.52*** | 0.88*** |
| TCARI | 0.60*** | 0.35*** | 0.77*** | -0.31** | 0.37*** | 0.85*** |
| TVI | 0.74*** | 0.55*** | 0.88*** | -0.29** | 0.49*** | 0.89*** |

*: $P < 0.05$; **: $P < 0.01$; *** $p < 0.001$

For DAS⁵⁶ and DAS⁷¹ coefficients of determination were significant ($p \leq 0.05$) for r^2 values > 0.6 . For rainfed and irrigated plots separately, significant relations occurred, independent of date or treatment, for r^2 values > 0.6 . Figure 3 show the best performing indices for the individual vegetation characteristics.

The relation between vegetation indices and the measures they try to predict varied throughout the growing season. The relation between individual indices and vegetation measures was strongest for NSM and SWW, with r^2 values over 0.90. Strong relations occurred with SDW and GLAI ($r^2 > 0.8$), and relationships with Yield and N were relatively poor ($r^2 < 0.8$). Overall, the strongest relations between vegetation parameters and vegetation indices occurred mid-growing season, around DAS95, DAS111 and DAS144.

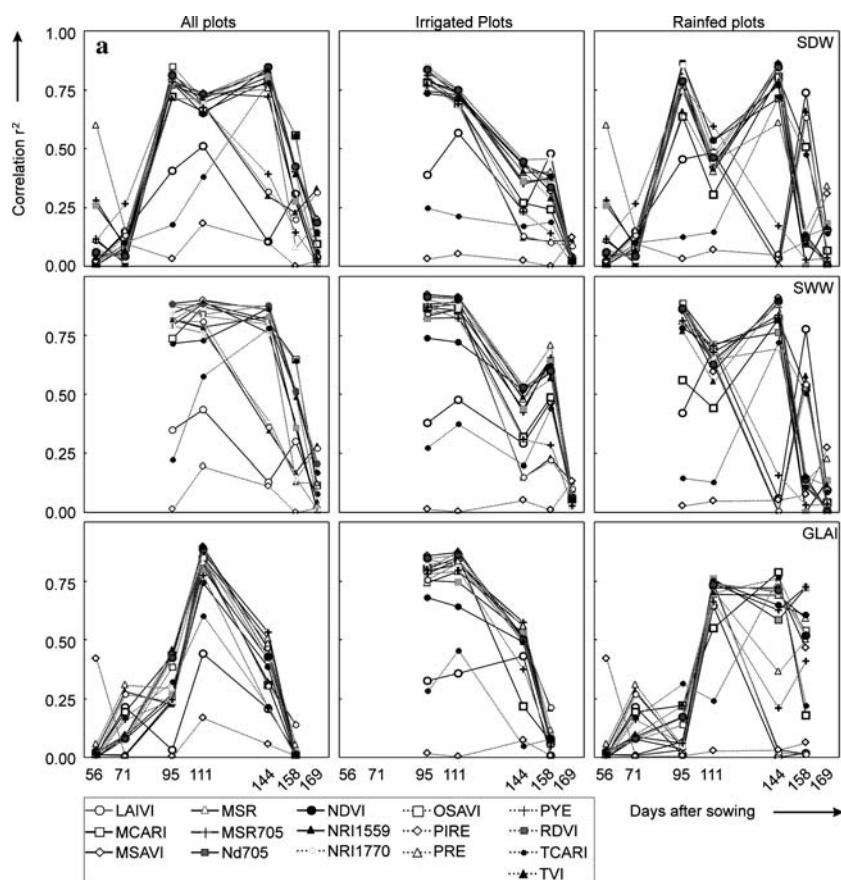


Fig. 2 Correlation r^2 between remotely sensed vegetation indices and: **a**: Sample dry weight (SDW), sample wet weight (SWW) and green leaf area index (GLAI). **b**: Nitrogen load per square meter (NSM), nitrogen concentration (N) and plot yield (Yield)

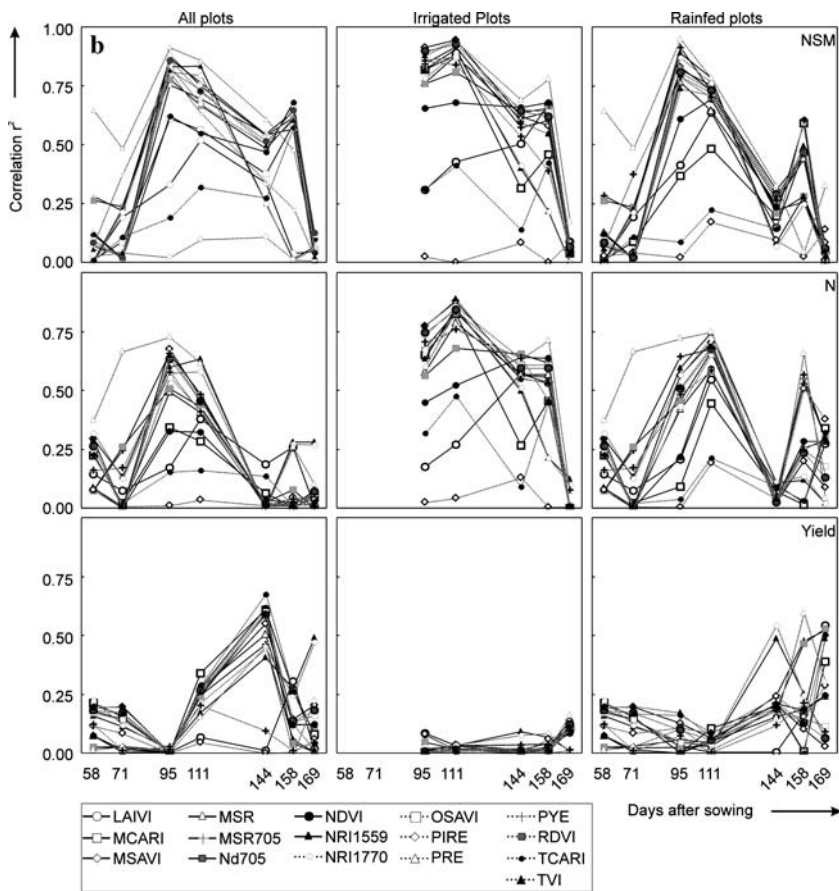


Fig. 2 (continued)

Sample Dry Weight

Maximum correlation ($p < 0.05$) between mean dry weight and an individual index across treatments occurred with OSAVI (DAS^{95} , $r^2 = 0.85$; DAS^{144} , $r^2 = 0.85$) and RDVI (DAS^{95} , $r^2 = 0.81$; DAS^{144} , $r^2 = 0.84$). When data was separated in irrigated and rainfed plots, maximum correlation occurred with OSAVI (DAS^{95} , $r^2 = 0.85$), RDVI (DAS^{95} , $r^2 = 0.84$) and PRE (DAS^{95} , $r^2 = 0.82$). Maximum correlation on rainfed plots occurred for NDVI, TVI and OSAVI (DAS^{95} , $r^2 = 0.86$), and MSAVI (DAS^{144} , $r^2 = 0.86$).

Sample Wet Weight

The correlation ($p < 0.05$) between mean wet biomass and the vegetation indices was the strongest of all vegetation measures. Correlation r^2 values peaked across treatments from DAS^{95} to DAS^{144} . Maximum correlations for all indices, except for

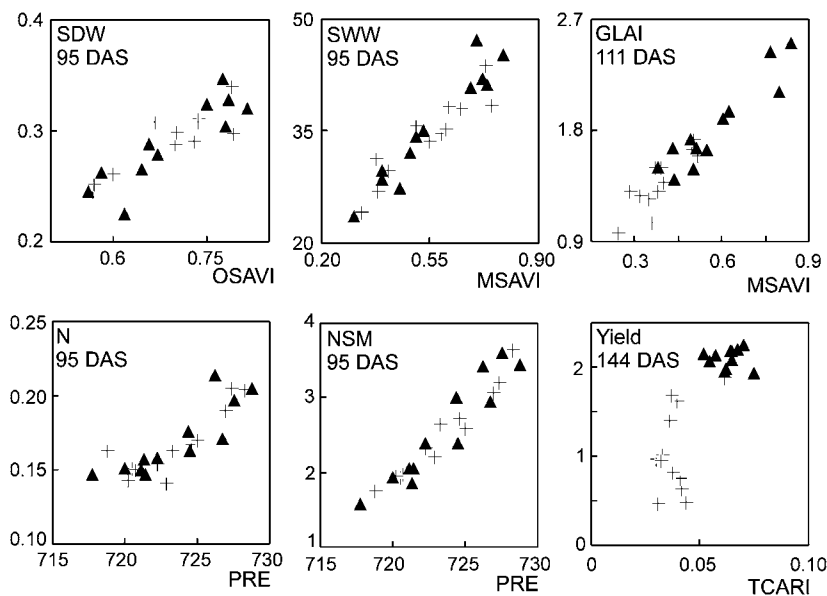


Fig. 3 Scatterplot of the strongest observed relations between an individual vegetation index and vegetation characteristics, with: Triangles = Irrigated plots, Plusses = Rainfed plots. Variables on the Y-axis were transformed for normality, and represent sample dry weight (SDW, g m⁻²), sample wet weight (SWW, g m⁻²), green leaf area index (GLAI, m² m⁻²), Nitrogen load per square meter (NSM, g m⁻²), nitrogen concentration (N, g g⁻¹) and plot yield (Yield, 1000 kg ha⁻¹)

LAIVI, PIRE, TCARI and NDVI, ranged between 0.78 and 0.92. For all plots combined the best relation occurred with MSAVI (DAS⁹⁵, $r^2=0.90$) and mSR₇₀₅ and TVI (DAS¹¹¹, $r^2=0.89$). For irrigated plots the peak r^2 values were observed for MSAVI (DAS⁹⁵, $r^2=0.92$ and DAS¹¹¹, $r^2=0.91$), PRE and RDVI (DAS⁹⁵, $r^2=0.91$ and DAS¹¹¹, $r^2=0.91$). On rainfed plots, peak correlations occurred for MSAVI, RDVI ($r^2=0.91$) and TVI ($r^2=0.90$) at DAS¹⁴⁴, and ND₇₀₅, OSAVI ($r^2=0.89$) and NRI₁₅₅₉ ($r^2=0.88$) at DAS⁹⁵.

Green Leaf Area Index

The correlation ($p<0.05$) between GLAI and the vegetation indices is generally not strong. Peak correlation occurred around DAS¹¹¹ for all plots and irrigated plots. For rainfed plots this was at DAS¹¹¹ and DAS¹⁴⁴. The maximum correlation for all plots was with MSAVI, RDVI and TVI (DAS¹¹¹, $r^2=0.89$). For irrigated plots peak correlations were observed for TVI ($r^2=0.88$, DAS¹¹¹) and MSAVI ($r^2=0.87$, DAS⁹⁵). For rainfed plots this occurred for MCARI ($r^2=0.78$, DAS¹⁴⁴), TCARI and TVI (DAS¹⁴⁴, $r^2=0.76$).

Nitrogen Concentration

Correlations ($p < 0.05$) between vegetation indices and N were relatively poor, with r^2 values above 0.75 only occurring on irrigated plots. For all plots combined the position of the red edge (PRE) was the best predictor of N ($r^2 = 0.72$, DAS⁹⁵), followed by MSAVI (DAS⁹⁵, $r^2 = 0.67$) and TVI (DAS⁹⁵, $r^2 = 0.65$). For irrigated plots the best prediction of N occurred at 111 days after sowing, with correlations between N and MCARI, MSAVI, MSR705, NRI1559, NRI1770, PRE, RDVI all above $r^2 = 0.80$. On irrigated plots maximum r^2 values occurred for NRI1559 (DAS¹¹¹, $r^2 = 0.75$) and PRE (DAS¹¹¹, $r^2 = 0.75$).

Nitrogen Per Square Meter

Correlations ($p < 0.05$) between NSM and the vegetation indices were generally strong. For all plots combined, maximum correlation between NSM and vegetation indices occurred for PRE (DAS⁹⁵, $r^2 = 0.91$), RDVI (DAS⁹⁵, $r^2 = 0.86$) and MSR₇₀₅ (DAS⁹⁵, $r^2 = 0.87$). On Irrigated plots maximum correlations occurred for MSAVI (DAS¹¹¹, $r^2 = 0.94$) PRE (DAS¹¹¹, $r^2 = 0.94$) and TVI (DAS¹¹¹, $r^2 = 0.94$). On rain-fed plots, the best indices were PRE (DAS⁹⁵, $r^2 = 0.95$), MSR705 (DAS⁹⁵, $r^2 = 0.91$) and NRI₁₅₅₉ (DAS⁹⁵, $r^2 = 0.89$).

Yield

Correlation ($p < 0.05$) between grain yield and the vegetation indices was poor. Only in the late growing season (DAS¹⁴⁴) the coefficient of determination was significant, with values of over $r^2 = 0.6$ for TCARI ($r^2 = 0.67$), NDVI ($r^2 = 0.61$), OSAVI ($r^2 = 0.60$) and MCARI ($r^2 = 0.61$).

Discussion

The correlations between individual indices and the vegetation characteristics all showed a similar trend in time and between irrigation treatments. There was no 'best' index for the prediction of any of the vegetation characteristics, and accuracies across the growing season were fairly similar. Considering that most indices are derived from the same wavebands this is not unexpected.

One of the main interests for a production farmer is the fertiliser needs of the crop. A big increase in the detectability of nitrogen occurs between 71 days after sowing (Corresponding to Zodiac stage 30; start of stem erection) and 95 days after sowing (Corresponding to Zodiac stage 33; third node detectable). Correlation r^2 between a number of vegetation indices and nitrogen concentration reached 0.8–0.9 at Zodiac stage 33, which is well within the time window for additional fertilisation. These correlation levels are slightly higher than those found by Rodriguez et al. (2006).

The poor overall association between vegetation indices and the vegetation characteristics across the growing season illustrates the effect of plant development on the vegetation indices. The relation between the index and the measure of interest

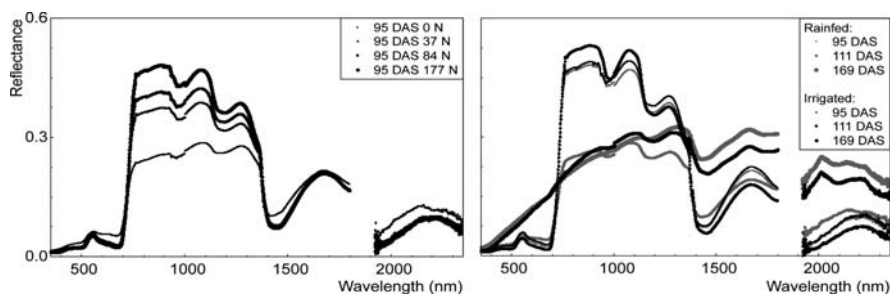


Fig. 4 Reflectance signatures of winterwheat: (a) 95 days after sowing, for wheat growing at full density, on irrigated sites with no fertilisation and 16, 39 or 163 kg N/ha (0 N, 16 N, 39 N, and 163 N respectively). (b) Difference between rainfed and irrigated wheat growing on plots fertilised with 163 kg N/ha, 95, 111 and 169 days after sowing (95 DAS, 111 DAS and 169 DAS respectively)

may change throughout the season, as a result of changes in the reflectance due to increased biomass and changes in water content or redistribution of nitrogen in the plant. Although for rainfed plots the sample dry weight increases throughout the growing season, a peak in green leaf area is already reached at DAS⁹⁵, a point clearly reflected in the difference in reflectance between irrigated and rainfed plots (Fig. 4b). If indices designed to detect vegetation characteristics are not properly calibrated against variation in green leaf area, this may affect across-season validity of the index. OSAVI for instance, has a strong relation with dry biomass: at 95 days after sowing, OSAVI explains 85% of the variation in biomass across

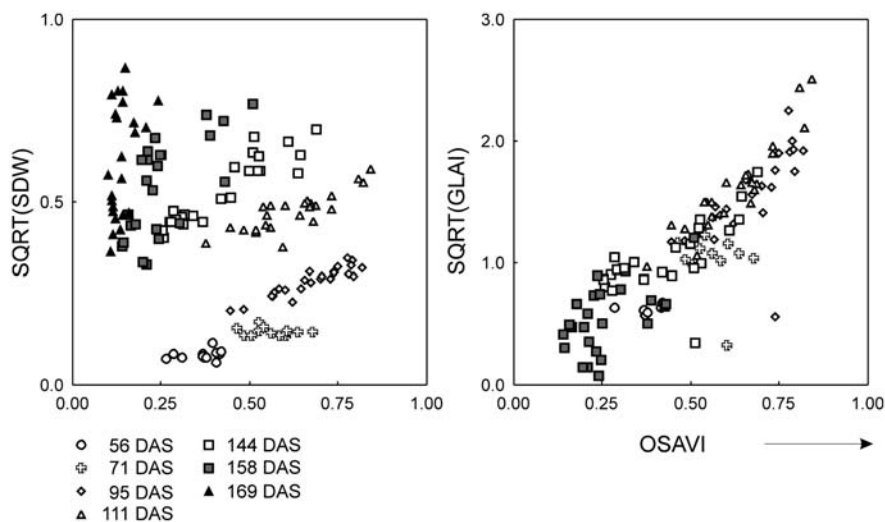


Fig. 5 OSAVI versus leaf area index and sample dry weight, categorized by DAS

treatments (Fig. 2). However, when the data from the whole growing season is combined, only 27% of the variation in biomass can be predicted (Table 4). Plotting dry weight as a function of OSAVI shows why the relation across the growing season is poor (Fig. 5). As the season progresses, and biomass increases, the regression line between dry weight and OSAVI becomes steeper. At the onset of the growing season (DAS⁵⁶) an increase of OSAVI corresponds to only a limited change in biomass. At the end of the growing season, this is inverted: A slight increase of OSAVI corresponds to a steep increase in biomass. For all other indices the same relation between dry biomass and vegetation index occurs. This gives rise to the idea that not biomass, but a proxy is detected by the vegetation index. When GLAI is plotted as a function of OSAVI for the full growing season (Fig. 2a) there is a clear relation between GLAI and OSAVI. Higher levels of OSAVI predict higher GLAI. Figure 1 shows that GLAI increases until about 111 days after sowing, and then gradually decreases, even though biomass increases to the end of the growing season, which is in line with the decrease in predictive capability of vegetation indices trying to predict biomass.

Yield Forecasting

Reasonable correlations occur at DAS¹⁴⁴ across plots, but this mainly represents a difference in yield between rainfed and irrigated plots (Fig. 3f). Previous work on wheat has shown similar poor relations between final grain yield, and early season vegetation indices. Aparicia et al. (2000) concluded that although under rainfed conditions a significant correlation occurs between grain yield and vegetation indices, these indices saturate when GLAI reaches values of over 3, which occurs in the more favourable irrigation environment. The current study seems to confirm this conclusion. Previous studies have shown promising results for yield forecasting using an accumulated NDVI (Hochheim et al., 1996). The rational behind this is that end of season grain yield is an integrated measure of all growing conditions encountered over the duration of the growing season. Therefore the accumulated NDVI was calculated over the last 6 sampling dates, and the correlation coefficient with total grain yield was calculated. This resulted in a poor overall correlation ($r^2=0.05$; $p<0.1$). When data is categorized by irrigated versus rainfed, these become $r^2=0.00$ ($p<0.76$) and $r^2=0.33$ ($p<0.003$) respectively.

Data Acquisition and Accuracy

Spectral readings from measurement 5 (October 18th, 123 DAS) were noisy, with a number of spikes in the visible/near infrared part of the electromagnetic spectrum for most signatures, and all measurements from that date were therefore excluded from analysis. When visually analyzing Fig. 2, a slight drop in correlations between the indices and vegetation characteristics for measurement 6 (November 8th, 144 DAS) can be observed, with a subsequent increase correlation for the next acquisition date. In theory this could be the result of variation in plant-water status

between plots. However, irrigation of irrigated plots occurred every time at least five days before spectral readings were taken, making this less likely. Growing conditions during the week following irrigation were no different then on other dates. Therefore it is assumed that the noise in the spectra is a result of the data-acquisition setup. For each plot, one spectral signature was acquired at each acquisition date. This may have resulted in a decreased signal-to-noise ratio. For future studies, a higher number of spectral readings per plot, and a reduction in setup times should be aimed for.

Conclusions

At about 95–144 days after sowing, a good correlation (r^2 between 0.7 and 0.99) existed between vegetation indices and wheat biomass, relative foliar cover and total nitrogen load per square meter. A reasonable correlation (r^2 between $0.5 < r^2$ and 0.75) occurred with foliar nitrogen concentration. This difference is likely the result of the inability of these basic indices to separate the effect of total biomass on the nitrogen signal: The total amount of N per square meter can be more accurately predicted than the concentration of N in foliage. Since the relation between vegetation measures and the indices changed throughout the growing season, these indices seem to be suitable for site-specific analysis of underperforming regions, but require continuous calibration against field data in order to make between-date comparisons realistic. To improve between-date relationships, other methodologies, that better remove the effect of increased biomass/leaf area on absolute reflectance, should be explored, such as continuum removal (Clark and Roush, 1984), derivative analysis (Tsai and Philpot, 1998) and principal component analysis (Thenkabail et al., 2004).

Acknowledgements The authors would like to thank the Victorian Department of Primary Industries Australia in Horsham, Australia for generously sharing their data. The field site and experimental data used in the analysis in this paper were derived from an ‘Our Rural Landscape’ project. We thank Daniel Rodriguez and Lene Christensen for project leadership and data acquisition and Russel Argall for conduct of the field experiment. The project was financially supported by a post doctoral grant for Dr. Ferwerda by RMIT, Mathematical and Geospatial Sciences.

Appendix: Summary of the Indices Used in this Study

Indices Typically Used for Biomass (Green Leaf Area)

NDVI (Normalized difference vegetation index). Commonly used to assess the amount of green biomass, uses the difference between reflectance around 800 nm, which is influenced by cell-wall scattering, and reflectance around 670 nm, which is influenced by chlorophyll absorption.

OSAVI (Optimized Soil Adjusted Vegetation Index (Haboudane et al., 2002)). This index is based on the Soil Adjusted Vegetation Index (Huete, 1988). Effectively chlorophyll absorption around 670 nm is used as an index, which is stabilized for soil background using reflectance in the NIR (800 nm).

MSAVI (Modified Soil Adjusted Vegetation Index (Qi et al., 1994)). This is another index based on SAVI. MSAVI minimizes the effect of soil-background on vegetation signals using a soil-background adjustment function, which has been empirically derived from NDVI and WDV. Effectively chlorophyll absorption around 670 nm is used as an index, which is stabilized for soil background using linear and quadratic reflectance in the NIR (800 nm).

RDVI (Re-normalized Difference Vegetation Index (Haboudane et al., 2004)). Similar to the NDVI, this index uses the ratio between the sum and the difference of a band in a chlorophyll absorption feature (670 nm) and a band in cell-wall scattering region (800 nm) to predict biomass. To reduce saturation effects at higher biomass levels, the square root is taken of the nominator.

Indices Typically Used for Chlorophyll/Foliar N

LAIVI (Leaf Area Insensitive Vegetation Index (Haboudane et al., 2002)) (TCARI/OSAVI). In order to reduce the effects of non-closed canopies and soil-reflectance on TCARI, TCARI is divided by OSAVI, which results in LAIVI.

MCARI (Modified Chlorophyll Absorption index (Daughtry et al., 1992)). A measure of the depth of chlorophyll absorption at 670 nm relative to the reflectance at 550 and 700 nm,

mSR₇₀₅. (Modified simple ratio index around 705 nm (Sims and Gamon, 2002)). Based on a simple ratio index. Reflectance is normalized by subtracting a stable reflectance (e.g., reflectance at a saturated absorption feature 445 nm) from a reference index (750 nm) and dividing it by the difference between the stable reflectance and an index wavelength (705 nm).

mND₇₀₅ (Modified Normalized Difference Vegetation Index (Sims and Gamon, 2002)). Based on normalised ratio indices such as NDVI. The index is based on the difference between two bands, and normalized for shifts in overall intensity by dividing by the sum of the index and reference bands. To further reduce the effect of surface reflectance, the reflectance of a saturated absorption feature is subtracted from the nominator.

NRI_{693,1559} (Normalized ratio index at 1559 (Ferwerda et al., 2005)). A variation on the NDVI, this index uses the less-saturated part of chlorophyll absorption at 693 nm as an index, and a foliar water absorption feature around 1559 nm as reference.

NR_{693,1770} (Normalized ratio index at 1770 (Ferwerda et al., 2005)). A variation on the NDVI, this index uses the less-saturated part of chlorophyll absorption at 693 nm as an index, and a carbon-hydrogen absorption feature as reference.

PRE (Position of the red edge (Gong et al., 2002)). The wavelength where the first derivative reaches a maximum, within the spectral region of the red edge 670–740 nm.

PYE (Position of the yellow edge (Gong et al., 2002)). The wavelength where the first derivative reaches a maximum, within the spectral region of the yellow edge (550–582 nm).

PIRE (Position of the infrared edge (Gong et al., 2002)). The wavelength where the first derivative reaches a maximum, within the spectral region of the infrared edge (1300–1460 nm).

TCARI (Transformed Chlorophyll Absorption Index (Haboudane et al., 2002)). A transformed variant of the chlorophyll index MCARI, which is more sensitive to low chlorophyll values and more resistant to vegetation non-photosynthetic materials.

TVI (Triangular Vegetation Index (Broge and Leblanc, 2000)). Promoted as a general vegetation index, it uses an absorption ‘triangle’ to quantify the depth of the chlorophyll absorption feature between 550 and 750 nm, centred at 670 nm.

References

- Aparicio, N., Villegas, D., Casadesus, J., Araus, J.L. and Royo, C., 2000. Spectral Vegetation Indices as Nondestructive Tools for Determining Durum Wheat Yield. *Agronomy Journal*, 92(1), 83–91.
- Broge, N.H. and Leblanc, E., 2000. Comparing prediction power and stability of broadband and hyperspectral vegetation indices for estimation of green leaf area index and canopy chlorophyll density. *Remote Sensing of Environment*, 76, 156–172.
- Clark, R.N. and Roush, T.L., 1984. Reflectance Spectroscopy: Quantative Analysis Techniques for Remote Sensing Applications. *Journal of Geophysical Research*, 89(B7), 6329–6340.
- Daughtry, C.T.T., Gallo, K.P., Goward, S.N., Prince, S.D. and Kustas, W.P., 1992. Spectral estimates of absorbed radiation and phytomass production in Corn and Soybean canopies. *Remote Sensing of Environment*, 39, 141–152.
- Ferwerda, J.G. and Jones, S.D., 2006. Continuous wavelet transformations for hyperspectral feature detection. In: W. Kainz, A. Riedl and G. Elmes (Editors), *Progress in Spatial Data Handling, 12th International Symposium on Spatial Data Handling*. Springer-Verlag, Vienna, pp. 167–178.
- Ferwerda, J.G., Skidmore, A.K. and Mutanga, O., 2005. Nitrogen detection with hyperspectral normalized ratio indices across multiple plant species. *International Journal of Remote Sensing*, 26(18), 4083–4095.
- Fitzgerald, G.J., Rodriguez, D., Christensen, L.K., Belford, R., Sadras, V.O. and Clarke, T.R., 2006. Spectral and thermal sensing for nitrogen and water status in rainfed and irrigated wheat environments. *Precision Agriculture*, 7(4), 233–248.
- Gong, P., Pu, R. and Heald, R.C., 2002. Analysis of in situ hyperspectral data for nutrient estimation of giant sequoia. *International Journal of Remote Sensing*, 23(9), 1827–1850.
- Haboudane, D., Miller, J.R., Pattey, E., Zarco-Tejada, P.J. and Strachan, I.B., 2004. Hyperspectral vegetation indices and novel algorithms for predicting green LAI of crop canopies: Modelling and validation in the context of precision agriculture. *Remote Sensing of Environment*, 90, 337–352.
- Haboudane, D., Miller, J.R., Tremblay, N., Zarco-Tejada, P.J. and Dextraze, L., 2002. Integrated narrow-band vegetation indices for prediction of crop chlorophyll content for application to precision agriculture. *Remote Sensing of Environment*, 81, 416–426.
- Hochheim, K.P., Barber, D.G. and Bullock, P.R., 1996. Spring wheat yield prediction for Western Canada using weekly NOAA AVHRR composites, *Geoscience and Remote Sensing Symposium, 1996. IGARSS '96. 'Remote Sensing for a Sustainable Future.'*, International, 4, 1992–1994.
- Huete, A.R., 1988. A soil adjusted vegetation index (SAVI). *Remote Sensing of Environment*, 25, 295–309.
- Johnson, L.F., 2001. Nitrogen influence on fresh-leaf NIR spectra. *Remote Sensing of Environment*, 78, 314–320.

- Mattson, W.J., 1980. Herbivory in relation to plant nitrogen content. *Annual Review of Ecology and Systematics*, 11, 119–161.
- Munns, R., Passioura, J.B., Guo, J., Chazen, O. and Cramer, G.R., 2000. Water relations and leaf expansion: importance of time scale. *Journal of Experimental Botany*, 51(350), 1495–1504.
- Qi, J., Chehbouni, A., Huete, A.R., Kerr, Y.H. and Sorooshian, S., 1994. A modified soil adjusted vegetation index. *Remote Sensing of Environment*, 48(2), 119–126.
- Recous, S., Robin, D., Darwis, D. and Mary, B., 1995. Soil inorganic N availability: Effect on maize residue decomposition. *Soil Biology and Biochemistry*, 27(12), 1529–1538.
- Rodriguez, D., Fitzgerald, G.J. and Belford, R., 2006. Detection of nitrogen deficiency in wheat from spectral reflectance indices and basic crop eco-physiological concepts. *Australian Journal of Agricultural Research*, 57(7), 781–789.
- Rouse, J.W., Haas, R.H., Schell, J.A., Deering, D.W. and Harlan, J.C., 1974. Monitoring the Vernal Advancements and Retrogradation (Greenwave Effect) of Nature Vegetation, NASA/GSFC, Greenbelt, MD.
- Sims, D.A. and Gamon, J.A., 2002. Relationships between leaf pigment content and spectral reflectance across a wide range of species, leaf structures and developmental stages. *Remote Sensing of Environment*, 81, 337–354.
- Thenkabail, P.S., Enclona, E.A., Ashton, M.S. and Van der Meer, B., 2004. Accuracy assessments of hyperspectral waveband performance for vegetation analysis applications. *Remote Sensing of Environment*, 91(3–4), 354–376.
- Tsai, F. and Philpot, W., 1998. Derivative analysis of hyperspectral data. *Remote Sensing of Environment*, 51, 66–41.
- Yoder, B.J. and Pettigrew-Crosby, R.E., 1995. Predicting nitrogen and chlorophyll content and concentrations from reflectance spectra (400–2500 nm) at leaf and canopy scales. *Remote Sensing of Environment*, 53(3), 199–211.
- Zar, J.H., 1999. Biostatistical Analysis. Prentice-Hall, London.
- Zhao, D., Reddy, K.R., Kakani, V.G. and Reddy, V.R., 2005. Nitrogen deficiency effects on plant growth, leaf photosynthesis, and hyperspectral reflectance properties of sorghum. *European Journal of Agronomy*, 22(4), 391–403.

The Spectral Response of Pastures in an Intensively Managed Dairy System

R.N. Handcock, G. Mata, G.E. Donald, A. Edirisinghe,
D. Henry and S.G. Gherardi

Abstract All grazing-based industries require information on their feed resources in order to manage them optimally. Gathering this information through traditional methods for measuring pasture biomass is time-consuming and error-prone, resulting in increased interest in remotely-sensed methods. Remote sensing used to monitor feed resources in farming systems differs from remote sensing of systems such as forestry because of how the time-scale of management practices impacts on the growth rate and accumulation patterns of biomass. Also, in operational systems, designed for near real-time delivery to end-users of quantitative pasture measurements, we are restricted to the commercially available broad-band high-resolution sensors. The goal of this paper is to understand how remotely-sensed observations of pastures in an intensively managed dairy system change in relation to intensive management practices, so that better image analysis and ground-validation methods can be developed for measuring and monitoring such systems. At two dates in the growing season we examined high-resolution (SPOT-5 and Ikonos) images of an intensively managed perennial dairy farm in Victoria (Australia). We showed that the observed spectral response in the images varied with the length of time since the paddock was grazed, consistent with the re-growth of pastures post-grazing. The operational remote sensing of pastures is often restricted by the range of spectral bands that are available on broad-band sensors. However, these results suggest that when choosing a vegetation index for intensively managed dairy pastures it should incorporate the short-wave infrared (SWIR) band to improve observations of recently grazed pastures and tune analyses based on the spectral response.

Introduction

The goal of this paper is to understand how remotely-sensed observations of pastures in an intensively managed (rotationally grazed) dairy system change in relation to intensive management practices, so that better image analysis and ground-validation

R.N. Handcock (✉)

Commonwealth Scientific and Industrial Research Organization, Floreat, WA 6014, Australia
e-mail: Rebecca.Handcock@csiro.au

methods can be developed for measuring and monitoring such systems. In this dynamic system, quantitative measurements of pasture biomass (kg DM ha^{-1}) and pasture growth rate ($\text{kg DM ha}^{-1} \text{ day}^{-1}$) are required frequently (\sim weekly) at the scale of dairy paddocks ($< 1 \text{ ha}$) which therefore restricts images to commercial broad-band sensors such as SPOT and Ikonos.

The remote sensing of pastures in an intensively managed dairy system differs from vegetation systems such as forests because of the impact of management practices such as grazing on the growth patterns and accumulation of pasture over short-time periods. In non-pasture systems, vegetation biomass and growth rates are closely related. However, in pasture systems management practices such as the interval between, and number of, grazing events or the addition of fertilizers change the pasture biomass that otherwise would result from a typical phenological cycle. Also, grazing a pasture is not the same as clear-cutting in a forest because the grazing pressure may vary and the re-growth occurs on top of a pasture residue which increases with repeat grazing events (Fig. 1).

All grazing-based industries require information on their feed resources in order to manage them optimally. Gathering this information through traditional methods for measuring pasture biomass (e.g. pasture cuts, visual assessments and plate meters) (Sanderson et al. 2001) are time-consuming and error-prone, resulting in increased interest in remotely-sensed methods which are spatially-extensive, labor-saving, and reliable. The chosen sensors and analysis methods for the remote sensing of pastures is complicated by the image pixel-resolution, paddock size, and edge effects due to mixed pixels on the fence-line. Issues with the collection of on-farm validation/calibration data include the growth of pastures between the time of the image and the time of sampling, and problems with accurately geo-locating measurements.

Farm management practices will impact the remote sensing of pastures, both in the observed spectral response and the logistics of ground sampling and timing images, and should be recorded as part of collecting validation data. As well as grazing, cultivation, and conservation (e.g. for silage or hay), farm-management practices include harvesting, nutrient inputs, and standing water from irrigation. Repeat grazing events will result in changes in the amount of background soil that is exposed, both across the season, but also across the farm, which will alter the spectral response. Unlike a cropping system, at any point in time intensively managed

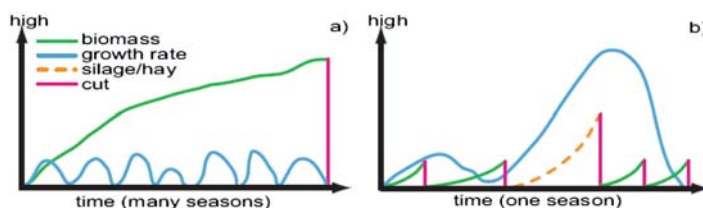


Fig. 1 Schematic illustrating vegetation growth for (a) forested, and (b) intensively managed systems. The x-axis represents biomass or growth (not to scale)

pastures may be at different stages of growth depending on where they sit in the grazing rotation. Repeat grazing events will also affect the proportion of green and dead material in the pasture, as seen by the gradual build-up of senesced leaves (Moore et al. 1991) in the pasture residue through repeat grazing. The animals themselves can have an impact on ground and remote observations, through pugging, that is where stock intensely trample wet soil, affecting soil and sward structure. Also, there are the logistics of choosing paddocks for sampling which do not have management practices being actively applied over part of the paddock during image acquisition.

Conceptually, the remote sensing of a farm is different from regional remote sensing due to the discrete spatial partitions created by fences which define each paddock. As well as observing pastures at individual pixels it is possible to study the farm on a paddock by paddock basis. Aggregating data to the paddock-scale has the benefit of giving a fixed spatial unit for further analysis and comparison of the remotely-sensed values with farm management practices that typically occur at the paddock-scale. However, activities such as strip-grazing (using temporary electric fences to control animal access) can also occur are the sub-paddock-scale (Fig. 2).

While there is extensive work on the remote sensing of agriculture (Dorigo et al. 2007), this has tended to focus on crops (Seelan, et al. 2003) which do not experience the cycle of grazing and re-growth, or on rangeland remote sensing (Todd et al. 1998). There are studies that look at the relationship between vegetation indices and pasture biomass (Edirisinghe et al. 2000) or growth rate (Hill et al. 2004) within extensive grazing systems, but none that examine the impact on remotely-sensed images of intensive farming practices such as exist within a rotationally grazed dairy system.

In this paper we examine the remote sensing of pastures across the full spectrum of pasture re-growth stages that are encountered in a commercial dairy system. At two dates in the growing season we examine high-resolution (SPOT-5 and Ikonos) images of an intensively managed dairy farm in Victoria (Australia). We compare characteristics such as the number and interval between grazing events and ground measurements of biomass with remotely-sensed observations of pastures.

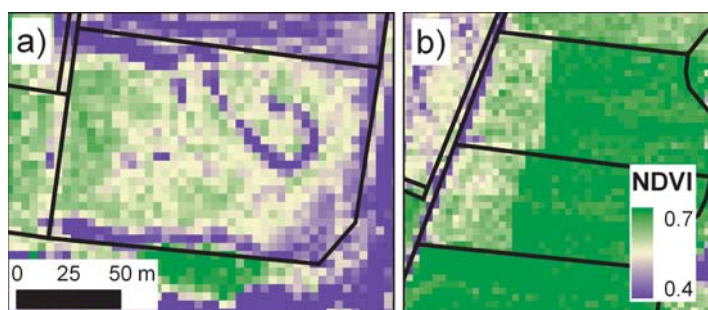


Fig. 2 Three example paddocks from Ikonos July showing (a) the remains of uneaten hay, and (b) strip grazing

The image-analysis and ground-validation methods we use are a case-study for measuring and monitoring an intensively managed dairy system, which differs from other agricultural systems due to the dynamics of repeat grazing and re-growth.

Approach

Study Site

Image and ground data were collected in July and September 2005 at the Ellinbank Research Institute, situated in West Gippsland, Victoria, Australia (latitude 38° 16'S, longitude 145° 59'E). Ellinbank is a 217 ha research farm with a median paddock size at the time of the study of 0.4 ha. Ellinbank has a temperate climate. Total annual precipitation is 1093 mm, and the average annual temperature minimum is 8.7°C and the maximum is 18.2°C (Australian Bureau of Meteorology 2006).

The pastures at Ellinbank are based on perennial ryegrass (*Lolium perenne*) with some white clover (*Trifolium repens*) and the soils are predominantly clay-loam. Remnant vegetation is characterized by tall tree wind-breaks on the edges of paddocks. Unlike an annual pasture system where the growing season has a well-defined start (initialized by plant germination) and finish (defined by plant senescence), the perennial pastures found at Ellinbank are characterized by changes in growth rate, and not by distinct changes in vegetation condition.

Image Data

Three high-resolution satellite images were acquired from both the SPOT-5 (10 m pixels) (CNES SPOT Image 1989) and the Ikonos (4 m pixels) (Peterson et al. 2001) broad-band sensors. The Ikonos sensor has four bands (blue, green, red, near-infrared (NIR)), and the SPOT-5 sensor has 4 bands (green, red, NIR, short-wave infrared (SWIR)). Two data collections were made approximately two months apart. In September the SPOT-5 and Ikonos images were only two days apart (Table 1).

Satellite images were obtained from Raytheon Australia, calibrated, processed to top of atmosphere (TOA) reflectance, and geo-referenced to base-data by Landgate. The Ikonos and SPOT-5 images in September had different viewing geometries,

Table 1 Details of image and ground data at Ellinbank

| Image Date | 22nd July 2005 | 4th September 2005 | 6th September 2005 |
|---|----------------|--------------------|--------------------|
| Sensor | Ikonos | Ikonos | SPOT-5 |
| # paddocks sampled | 8 | 14 | 15 |
| Paddock-average range of biomass cuts [kg DM ha ⁻¹] | 469–2623 | 1205–2583 | 1205–2583 |

which resulted in differences in the TOA reflectance for each image. While a Bidirectional Reflectance Distribution Function (BRDF) correction is generally necessary to adjust for different viewing geometries before inter-image comparison is attempted (Bacour et al. 2006), suitable data to model the BRDF were not available. This was not an issue for comparing the two Ikonos images because the images had similar viewing geometries, and the SPOT data was analyzed separately. For a within-image analysis of an individual image we assume a negligible effect on the imagery from not correcting for the BRDF.

For each image the Normalized Vegetation Index (NDVI) (Tucker, 1979) was determined from the red and near infrared (NIR) reflectance NDVI is widely-used to capture the 'vigour' of plant greenness, although many broad-band vegetation metrics can be calculated (Elvidge and Chen, 1995).

Ground Measurements

We made measurements of pastures biomass on selected paddocks and collected additional information on when pastures were grazed and other farm-management practices occurring at the time of image acquisition. Grazing data is used to examine the relationship between the number of days since the paddock was grazed and the resulting spectral response, and with biomass. Biomass measurements can also be used to develop empirical calibrations between the image and ground-data to predict pasture biomass, but this is not the focus of the present study.

Surrogates for Paddock Biomass

Paddocks were rotationally grazed in a sequential manner, such that all paddocks in the rotation can be ranked according to their paddock biomass. As biomass information for all paddocks on the farm is usually not available, NDVI, or alternate vegetation indices sensitive to green vegetation, can be used as a surrogate for ranking paddock-average biomass. Alternatively, as the biomass in a paddock is a function of pasture growth rates and the time since grazing, and we can assume that pasture growth rate only changes slowly within the cycle of a grazing rotation, the number of days since the paddock was grazed can be used as a surrogate for paddock-average biomass.

Timing Ground-Measurements

Ground sampling on the same day as image acquisition was not always possible due to practicalities of weather and human resources. The timing of the ground sampling in relation to the image acquisition will impact on the accuracy of any comparison between the remotely-sensed data and ground-observations such as pasture biomass because of pasture growth in the intervening period. This is worst in spring when growth rates are high. Ground sampling was completed within 3–4 days of image acquisition.

Paddock Selection

Paddocks were chosen to provide a range of biomass (Table 1) within the range of what is to be expected under normal commercial practice which optimizes pasture quality (1000–1200 to 3400–3600 kg DM ha⁻¹) (Fulkerson et al. 1997). To focus sampling on this optimum biomass range, excluded from the selection were paddocks that had been grazed within the five previous days, or undergoing active farm management. Where possible large, regularly shaped, paddocks were selected, to maximize the number of ‘pure’ pixels contained entirely within a paddock. Steeply sloping paddocks were avoided to minimize BRDF differences among sampled paddocks.

Laying Out the Sample Grid Within the Paddock

A 3 × 3 grid (nine locations) was laid out within each paddock with a 20 m grid spacing for the July sampling and a 4 m grid spacing for the September sampling. Grids were located in a representative area of ‘uniform pasture’, and at least 10 m from the fence line. Areas of pugging and bare ground were avoided. Locations where pasture measurements were made were geo-referenced using a GPS (Garmin Model #72, ± 5–7 m).

Making Pasture Cuts

Pasture biomass at each grid location was determined by pasture cuts made to ground level using electric hand shears within a 0.22 m² quadrat (Cayley and Bird 1996). This was laid out so that the pasture inside the quadrat was uniform in composition and quantity. For the July sampling five cuts were made at the corners and centre locations of each grid. For the September sampling cuts were made at all 9 grid locations. All cuts were photographed from above at a 45° angle so that pasture height was visible. Where necessary the cut pasture was washed, dried and weighed to determine pasture biomass (kg DM ha⁻¹).

Data Analysis

Paddock Masks

Paddocks in dairy farms are typically small in comparison to the size of pixels, and may not be regular in shape. Pixels on the edges of the paddocks are typically mixed with the fence line, roads or neighboring paddocks. This can impact on any analysis which uses all of the pixels within a paddock, particularly when the pixel size is large or the paddock is surrounded by spectrally contrasting material.

To avoid any issues with geo-registration of the image to the fence-lines or unusual ground conditions near the paddock gate, each paddock was first masked with a 10 m buffer in from the fence line. Masking of non-pasture vegetation within the paddocks, such as individual trees or tall-windbreaks along the fence lines,

was also necessary so that pixels identified as pasture were as pure as possible. Remaining variation in the paddock-scale spectral response can be interpreted as farm management practices, such as half-grazed paddocks, or bare-soil exposed through cultivation.

Within-Paddock and within-Grid Statistics

Analyses of image and ground data were made at two spatial scales. Firstly, the image pixels were analyzed at the spatial scale of entire paddocks (within-paddock statistics), and secondly, the ground measurements made at grids within a paddock were examined.

Within-paddock statistics (mean, and standard deviation) were calculated from the pixel values of each image band and the NDVI by overlaying the masked image in the GIS with the paddock boundaries. These statistics were collated with the farm management practices on the image data, such as the number of days since grazing.

For the purpose of analyzing an individual pasture cut, the image and ground data from each paddock measurement grid was considered representative of more 'operational' scale image data (20 m pixels) as distinct from the high resolution images used in the present study. This is because an individual pasture cut can not capture the fine-scale spatial heterogeneity in pasture observed within an individual pixel, or across the paddock. All ground data were therefore aggregated within a 20×20 m area, resulting in each paddock being represented by a single aggregated ground measurement and its corresponding image pixels.

Results

Figure 3 shows the range of standing green biomass exhibited in a typical managed dairy farm, as captured by the NDVI. Across the farm the NDVI tends to be higher in July than in September. At the sub-paddock level we see strip-grazing practices (Fig. 2b) and the remains of uneaten hay put out on the paddock during supplementary feeding of cattle (Figs. 2a and 3).

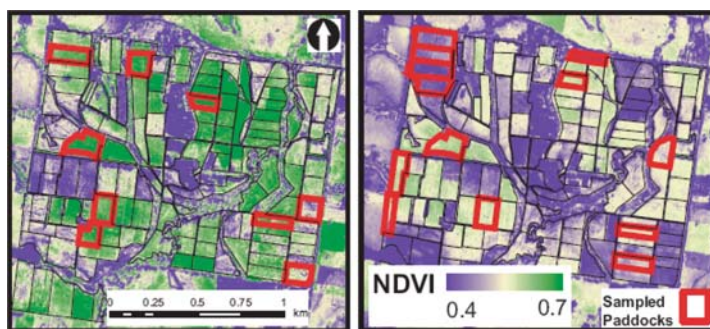


Fig. 3 Range of Ikonos-NDVI representing standing green biomass exhibited on a typical managed dairy farm, for (a) July, and (b) September. *Thick lines* indicate sampled paddocks

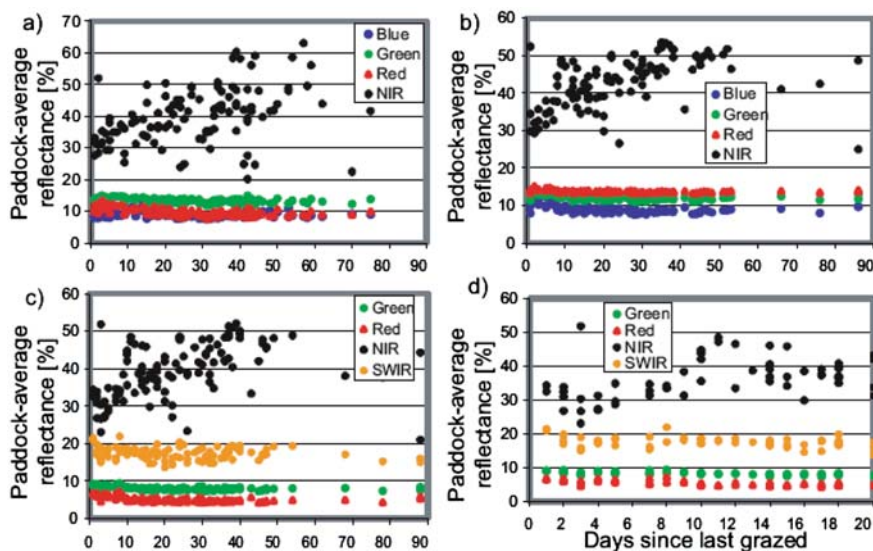


Fig. 4 Paddock-average reflectance (%) vs. the number of days since grazing for, (a) Ikonos, July, (b) Ikonos, September, and (c) SPOT-5 September images, (d) SPOT-5 detail

Figure 4 shows the spectral reflectance (%) of the individual paddocks compared to the number of days since the pasture was grazed. We see the expected spectral differences between bands as is typical for vegetation, with little variation in the red, blue, or green, and the maximum response in the NIR bands. For paddocks in the first few days after grazing the SWIR band of the SPOT-5 image exhibits a different response compared to paddocks that have been out of grazing for longer (Fig. 4d).

Figure 5a shows the variation in paddock-average NDVI, from the July and September Ikonos images with the number of days since grazing. NDVI increases with time since grazing, and tended to be higher in July than in September. NDVI values are very variable soon after grazing, before increasing to an asymptote, and then decreasing.

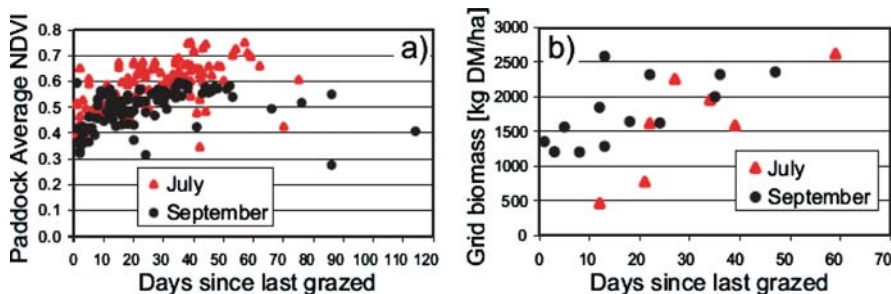


Fig. 5 (a) Paddock-average NDVI from Ikonos data for July and September 2005 vs. the number of days since grazing, (b) grid-average biomass derived from pasture cuts vs. days since grazing

Figure 5b shows the relationship between the biomass cuts made in each paddock and the number of days since grazing. Paddocks sampled in this range were at the 1 to 2.5 leaf stage as is expected from a pasture system with grazing management which targets paddocks at the 2 to 3.5 leaf stage (Fulkerson et al. 1997). Each point on Fig. 5b corresponds to a sub-paddock area designed to represent the operational scale of currently available image sensors. These ground results are all from paddocks that were at least five days post-grazing, so do not cover the full range of paddocks presented in Figs. 4 and 5a.

Discussion

The Impact of Time Since Grazing on Remotely-Sensed Observations

These results illustrate the effect of the grazing practices on the spectral response of dairy pastures as seen in remotely-sensed images. In Figs. 4 and 5 the number of days since grazing represents the re-growth period of the pasture in each paddock. Typically, the longer the time since grazing the greater the standing biomass (Fig. 5b), and the greater the corresponding NIR reflectance (Fig. 4) and NDVI (Fig. 5a).

The active growing period is defined from when new leaf tissue appears (~3 days after defoliation). The standing biomass in a paddock at any point will be the result of many factors. These include environmental factors such as weather, the availability of solar irradiance and aspect, but also management factors such as time since grazing, the ability to recover from hard grazing, the cultivar, and the input of nutrients in the form of fertilizers. The image captures the compound effect of these factors at a single instant in time.

Plant characteristics such as the number of tillers (which will increase across the growing season), leaves, seed heads, and lodging (falling sideways) impact on the magnitude and variability of the spectral response. Other factors are the amount of exposed soil background and the build-up of senesced leaves in the pasture residue (Moore et al. 1991) with repeat grazing. These factors will also vary with the composition of the pasture sward. While the pastures in the present study were predominantly ryegrass, they contained small proportions of other species such as clover and cape weed which have different spectral characteristics, particularly as larger leaves have greater reflective surface area. The exact state of the pasture post-grazing is also influenced by how hard the paddock was grazed, although most farms try to graze down to a uniform pasture residue.

Spectral Response Soon After Grazing

In the first few days after grazing there is a different spectral response of pastures, as is seen in the difference in both the SWIR reflectance and NDVI in paddocks soon after grazing (Figs. 4d and 5a) compared to paddocks that have been out of

grazing for a period of time (Figs. 4c and 5a). This difference in spectral response is similar to that reported for non-intensely managed mown grasslands observed using Landsat multi-spectral data (Mino et al. 1998).

For the purpose of developing quantitative measurements from the remotely-sensed images it is necessary to manage this different spectral response from paddocks soon after grazing. While a variety of metrics of vegetation greenness and vigor can be determined (Elvidge and Chen 1995), and refined for different conditions of soil background, leaf-area, dry matter and atmospheric conditions, Ikonos and SPOT-5 do not have suitable bands for complex metrics. However, the SWIR region is more sensitive to dry vegetation and soils, although the specific response depends on the soil type and brightness (Todd et al. 1998). When choosing a vegetation index for intensively managed dairy pastures it is best to select one which incorporates the SWIR band, so that it is more robust to changes in the proportion of exposed soil post first leaf emergence and prior to canopy closure.

Spectral Response Across the Optimum Grazing Range

Across the optimum grazing range the spectral response of the pasture (Fig. 4) and the NDVI (Fig. 5a), both relative to the days since grazing, behaves as would be expected with actively growing pastures. During this period the impact of the amount of soil background becomes less significant as the pasture re-grows and canopy closure is reached.

In July NDVI reaches a plateau around day 40 while in September the plateau is reached between 25–30 days after grazing (Fig. 5a) before declining. This decline in response with time is likely to be associated with higher pasture growth rates resulting in the pasture canopy reaching full closure and the pasture sward approximating the 3 leaf stage of development. Also, the saturation of vegetation indices for high biomass is well established, particularly for NDVI (Sellers 1985).

The difference in relationships between NDVI and the number of days since grazing for July and September are not unexpected due to the across-season changes typical in perennial pastures (Fig. 5a). These differences are due to factors such as dilution in chlorophyll levels, lower nitrogen status of the plant during rapid growth in spring or morphological changes as the plant shifts from a vegetative to a reproductive state in preparation for head emergence and seed production.

Ground Sampling Logistics

Ground sampling of pastures for comparison with remotely-sensed images also needs to be tailored to account for variations in pasture conditions. If paddocks are only sampled during the optimum pasture growth period then this may limit the range of any calibration relationships made from the image data due to physiological or morphological differences in the pasture which result in a different spectral response.

Additionally, because the amount of exposed soil background prior to canopy closure will impact on the remotely-sensed observations, a useful measurement to

make would be the proportion of pasture coverage at different re-growth stages post-grazing. This could be achieved through photos which distinguish pasture coverage from background material (soil, dead vegetation) (Rotz et al. 2008), allowing the change in the amount and spatial pattern of pasture vs. background material to be determined.

Implications of These Results

These results enhance our understanding of how remotely-sensed observations of pastures within a intensively managed dairy system change in relation to on-farm management practices. While the use of hyper-spectral data to observe pasture canopies would provide extensive spectral information that could be compared to the plants growth and physiology (Thenkabail et al. 2000), for the practical remote sensing of intensively managed dairy systems users are currently restricted to commercially available satellite-based broad-band sensors such as SPOT. Tailoring image analysis and ground-validation methods based on knowledge of how farm-management affects the spectral response of pastures will allow the refinement of quantitative measurements of pasture characteristics such as pasture biomass or growth rate. For example by using different relationships for pastures that are early, middle and late in the growing period, since these pastures may behave differently.

Although the present study does not discuss these in detail, potential on-farm applications of remote measurements of pasture characteristics include pasture management tools to optimize pasture utilization. This includes the setting of target rotation speed, feed allowances calculated on a per-cow basis and supplementation required, based on the amount of available biomass and pasture growth rate, and the animal requirements. In extensive grazing systems (e.g. sheep, and large pad-docks) such tools are currently available through the Pastures from SpaceTM project (www.pasturesfromspace.csiro.au), but are too-coarse for paddock-scale delivery on dairy farms. The project derives moderate-resolution weekly pasture growth rate using a light-use efficiency model, and moderate resolution satellite images (Hill et al. 2004).

As the growing season progresses the combination of grazing and management practices will change the proportion of pasture and exposed soil and hence its spectral response. More research is needed on this changing spectral response of pastures over time, as seen in recent work using a time-series of SPOT images (Handcock et al. 2008).

Conclusions

By understanding how remotely-sensed observations of pastures changed in relation to intensive management practices, better remote sensing applications can be developed for measuring and monitoring such systems. Tailoring image analysis and ground-validation methods, based on knowledge of how the farm-management

affects the spectral response of pastures, will allow the refinement of relationships to predict quantitative measurements of pasture characteristics such as pasture biomass or growth rate from remotely-sensed data. For example, by using different relationships for pastures early, middle and late in the growing period, since these pastures may behave differently.

The observed spectral response in the images was shown to vary with the length of time since the paddock was grazed, consistent with the re-growth of pastures post-grazing. The operational remote sensing of pastures is often restricted by the range of spectral bands that are available, however these results suggest that when choosing a vegetation index for intensively managed dairy pastures it should incorporate the SWIR band (if available) as this should improve observations of pastures that have recently been grazed.

We showed that broad-band multi-spectral sensors with frequent revisit times can be used for the operational remote sensing of pasture characteristics, such as biomass, on dairy farms which have small paddocks and which require frequent (~weekly) data. These results enhance our understanding of how remotely-sensed observations of pastures within a intensively managed dairy system change in relation to on-farm management practices.

Acknowledgements This research has been funded in part by the Dairy Australia. We gratefully acknowledge field and technical assistance from personel from the Ellinbank Research Institute (DPI, Vic.), and CSIRO Livestock Industries (Elizabeth Hulm), as well as image pre-processing from Landgate (WA).

References

- Australian Bureau of Meteorology (2006), <http://www.bom.gov.au/weather/>
- Australian Commonwealth Scientific and Research Organisation (2006) Pastures from Space. Available <http://www.pasturesfromspace.csiro.au> [accessed December 2008].
- Bacour C, Breon FM, Maignan F (2006) Normalization of the directional effects in NOAA-AVHRR reflectance measurements for an improved monitoring of vegetation cycle. *Remote Sens of Environ* 102:402–413
- Cayley JWD, Bird PR (1996) Techniques for measuring pastures. Report, Agriculture Australia, p. 55
- CNES SPOT Image (1989) SPOT User's Handbook. Centre National d'Etudes Spatiales and SPOT Image Corporation. Toulouse, France pp 285
- Dorigo WA, Zurita-Milla R, de Wit AJW, Brazile J, Singh R, Schaepman ME (2007) A review on reflective remote sensing and data assimilation techniques for enhanced agroecosystem modeling. *Int J Appl Earth Ob* 9:165–193
- Edirisinghe A, Hill MJ, Donald GE, Hyder MW, Warren B, Wheaton GA, Smith RCG (2000) Estimating Feed-On-Offer and pasture growth rate using remote sensing. 10th Australasian Remote Sensing and Photogrammetry Conference, Adelaide, Fremantle, Oct 18–22nd 2004
- Elvidge CD, Chen Z (1995) Comparison of broad-band and narrow-band red and near-infrared vegetation indices. *Remote Sens of Environ* 54:38–48
- Fulkerson W, Blacklock M, Nelson N (1997) Managing Pastures. Report, Dairylink, NSW Agriculture, Australia
- Handcock RN, Mata G, Gherardi SG (2008) Combining spectral information aggregated to the paddock-scale with knowledge of on-farm practices will enhance remote sensing methods

- for intensively managed dairy pastures. Conference. 14th Australasian Remote Sensing & Photogrammetry Conference, Darwin, Sep 29th–Oct 3rd 2008
- Hill MJ, Donald GE, Hyder MW, Smith RCG (2004) Estimation of pasture growth rate in south western australia from NOAA AVHRR NDVI and climate data. *Remote Sens of Environ* 93:528–545
- Mino N, Saito G, Ogawa S (1998) Satellite monitoring of changes in improved grassland management. *Int J Remote Sens* 19:439–452
- Moore KJ, Moser LE, Vogel KP, Waller SS, Johnson BE, Pedersen JF (1991) Describing and quantifying growth stages of perennial forage grasses. *Agron J* 83:1073–1077
- Peterson B, Gerlach F, Hutchins K (2001) IKONOS Relative Spectral Response and Radiometric Calibration Coefficients. Report, Thorton: Space Imaging
- Rotz JD, Abaye AO, Wynne RH, Rayburn EB, Scaglia G, Phillips RD (2008) Classification of Digital Photography for Measuring Productive Ground Cover. *Rangeland Ecology Management* 61:245–248
- Sanderson MA, Rotz CA, Fultz SW, Rayburn EB (2001) Estimating forage mass with a commercial capacitance meter, rising plate meter, and pasture ruler. *Agron J* 93:1281–1286
- Seelan SK, Laguette S, Casady GM, Seielstad GA (2003) Remote Sensing applications for precision agriculture: A learning community approach. *Remote Sens of Environ* 88:157–169
- Sellers PJ (1985) Canopy reflectance, photosynthesis and transpiration. *Int J Remote Sens* 6: 1335–1372
- Thenkabail PS, Smith RB, De Pauw E (2000) Hyperspectral vegetation indices and their relationships with agricultural crop characteristics. *Remote Sens of Environ* 71:158–182
- Todd SW, Hoffer RM, Milchunas DG (1998) Biomass estimation on grazed and ungrazed rangelands using spectral indices. *Int J Remote Sens* 19:427–438
- Tucker CJ (1979) Red and photographic infrared linear combinations for monitoring vegetation. *Remote Sens of Environ* 8:127–150

Using Pasture Growth Rate Data in a National Agricultural Drought Assessment Monitoring Tool

R.G.H. Stovold, M. Adams, S.W. Maier, G. Donald,
S. Gherardi, and M. Broomhall

Abstract Pastures from Space (PFS) provides rural enterprises across Australia with a unique ‘Australian first’ – it is a pasture management tool that utilizes satellite images from the MODIS sensor to determine pasture growth rates (PGR) and assist farmers adjust stocking levels.

PGR data have been selected for inclusion in the National Agricultural Monitoring System (NAMS) to streamline the Exceptional Circumstance (EC) drought relief application and assessment process.

PFS is a collaborative project between Landgate, Department of Agriculture and Food Western Australia, CSIRO Livestock Industries and commercial partner Fairport Technologies. It uses primarily the Normalised Difference Vegetation Index (NDVI) and climate data in a model developed by CSIRO.

The NAMS web-based tool is using the following quantitative pasture growth rate data in whole or part:

1. Monthly standard PGR data for the southern region of Australia at one kilometre resolution.
2. Monthly PGR data for the southern region of Australia derived from the deviation of the median value of the last 12 year PGR historical archive.
3. Monthly PGR time series graphs for all shires in the southern region of Australia. The graphs are based on the comparison of the current season to the previous three seasons.

The purpose and use of the information is for inclusion in the National Agricultural Monitoring System (NAMS), a web based data delivery tool being developed on behalf of the Primary Industries Ministerial Council, to assist proponents and jurisdictions in the development and assessment of Exceptional Circumstances (drought relief to rural producers) application and assessment

R.G.H. Stovold (✉)

Landgate, Satellite Remote Sensing Services, Leeuwin Centre, Floreat, WA 6014, Australia
e-mail: Richard.Stovold@dli.wa.gov.au

processes. The data is web enabled ready for producers and land managers interpretation and compiled into reports for immediate use.

This paper outlines the acquisition and processed outputs of the PGR data to provide close to real time maps and graphs, using NAMS, for interpretation by rural producers and drought assessment authorities.

Introduction

The Satellite Remote Sensing Services (SRSS) section within Landgate has been routinely acquiring satellite data for farmers and rural consultants and building operational processing and internet delivery systems based on the Normalised Difference Vegetation Index (NDVI) (Tucker, Sellers, 1986)

Some of the agricultural products that are being generated routinely from this data and delivered to farmers, consultants and corporate users include:

- Spatial assessment of predicted and forecasted *Pasture Growth Rate* (PGR) (Donald et al., 2004; Hill and Donald 2004) on a weekly time step for the Mediterranean annual pasture zone of southern Australia, PGR®
- Estimates of *Feed On Offer* (FOO) at paddock level in southwest Western Australia only, FOO®
- and Agimage, a single Landsat image acquired during the crop growing season which is converted to biomass and targeted at the cropping sector.

SRSS produce the pasture growth rate information from MODIS satellite data combined with weather data obtained from the Bureau of Meteorology utilising the CSIRO model for PGR. PGR values are calculated weekly on a per paddock basis for subscribers, which can then be mapped or displayed in PastureWatch (Fairport Technologies, South Perth, WA), a proprietary software program.

PGR information can be accessed and viewed graphically through an internet web service developed at SRSS as well as in PastureWatch®. The PGR data can be automatically downloaded from the SRSS web server to the PastureWatch® software. The PGR model is run weekly covering the previous week's estimated PGR. Some of this information is available freely at regional scale from <http://www.pasturesfromspace.csiro.au>. Paddock level information is available as an annual subscription service.

The PGR data is included in the National Agricultural Monitoring System (NAMS) to assist assessment of Exceptional Circumstances or drought conditions over rural Australia. NAMS is web enabled and delivers data to land managers for interpretation and reporting.

The Nams Project

Project Objectives

The primary purpose of NAMS is to streamline the Exceptional Circumstances (drought assistance) application and assessment process.

Development on the NAMS was instigated by Primary Industries Ministerial Council, and the project is funded by all Australian, State and Territory governments.

The objectives of the project are:

- To contain relevant and comprehensive data that is user friendly and client focused;
- To provide a centralised access point for that data;
- To provide quicker and cheaper access to data than existing sources;
- To enhance the timely identification of an emerging Exceptional Circumstances event;
- That data can be applied to areas equivalent to local government areas; and
- To identify the longer term uses for other applications, for example more objective state drought declarations, improved approaches to risk management.

What Is the NAMS?

The National Agricultural Monitoring System (NAMS) is a website that contains maps, graphs and reports that demonstrate the production situation for major agricultural systems, and their climatic drivers. It has been primarily developed to streamline the Exceptional Circumstances (drought relief) application and assessment processes. However, producers can use the NAMS to assist in management decisions by improving their ability to judge and assess the risks posed by climate variability.

Presently the scope of the NAMS covers dryland and broadacre industries. It is envisaged that the NAMS will be extended to other industries, such as irrigated agriculture and horticulture.

Reports

NAMS can produce four different reports designed to present agricultural production and climatic information at the National, State/Territory and Regional level. These reports are:

- The National Report which presents the recent climatic and agricultural production situation across Australia;

- The State/Territory Report which presents the recent climatic and agricultural production situation across the selected State/Territory;
- The Regional Profile Report, which presents background information on the selected region, such as population, agricultural statistics and climatic averages; and,
- The EC Report, which presents the core set of analyses for the selected region required for an EC application. This report provides contextual information and information on the climatic, agricultural production and economic condition of the region.

Method of Data Acquisition, Processing and Analysis of PGR Data for use in NAMS

Acquisition

One of the key datasets for calculating PGR is NDVI acquired from the National Aeronautics and Space Administration (NASA) MODIS sensor. MODIS data is acquired daily by the Western Australian Satellite Technology and Applications Consortium (WASTAC) receiving stations from the Aqua and Terra satellite platforms. Weekly composites of cloud free pixels provide the base data for the calculation of the NDVI. Maximum value NDVI pixels are then combined with climate data supplied from the Bureau of Meteorology in a model (Hill and Donald, 2004) initially developed by CSIRO to calculate PGR values on a weekly time basis.

Processed Outputs

Processed data is split into two broad regions, southwest Western Australia, and the southern, Mediterranean climate regions of South Australia, Victoria and New South Wales.

For the NAMS project, the weekly PGR data is summarized into mean monthly data and resampled to 1 km from the original 250 m grid cells. (Fig. 1).

Two additional products are calculated. First is the PGR anomaly map (Fig. 2), which is a comparison of the respective month's mean PGR compared to the 12 year median value on a pixel by pixel basis. Cut-offs in the legend are for 15, 30, and 60% greater or less than the long term median for each pixel. The 12 year PGR median value is based on the available supply of MODIS data from 1993 to the present.

Fig. 2 PGR Anomaly map of eastern Australia for August 2006 showing lower PGR values in brown and pale blue colours when compared with the long term 12 year median value. Due to severe drought conditions in 2006 there are few areas of green indicating higher than the median PGR value

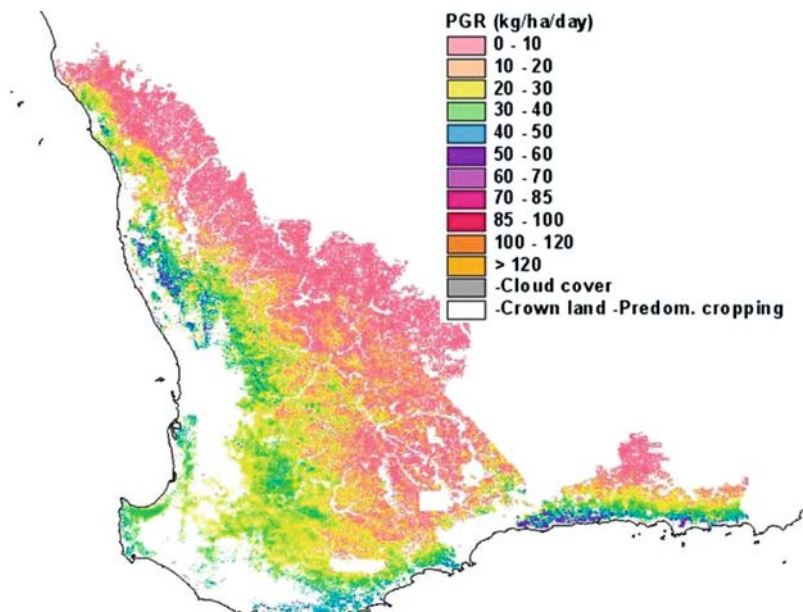


Fig. 1 An example of mean monthly PGR data for August 2006 resampled to 1 km covering the South Western agricultural area of Western Australia. These maps are also produced for eastern Australia. Area of lowest PGR values is shown in pink and high PGR in blue and purple

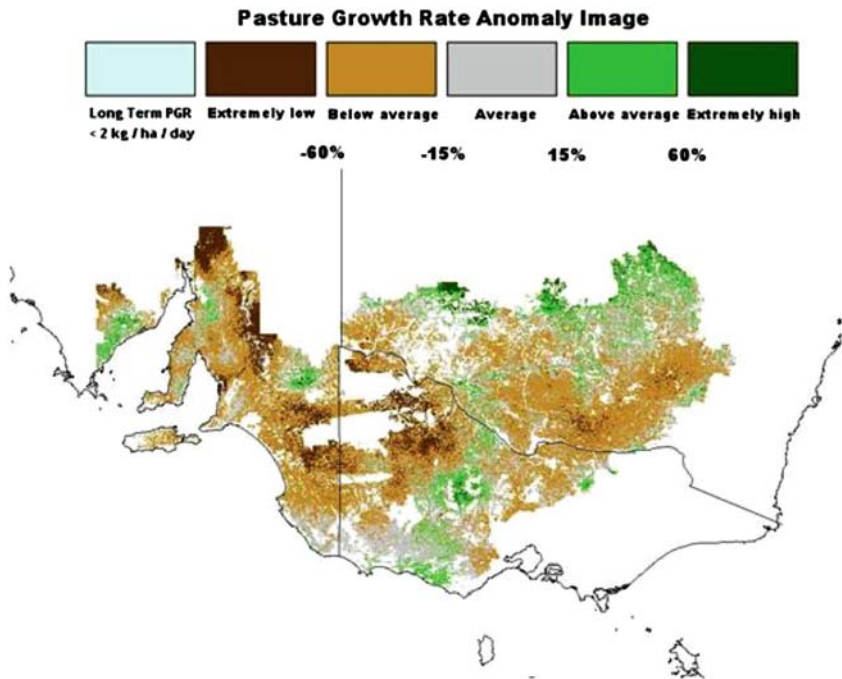


Fig. 2 (continued)

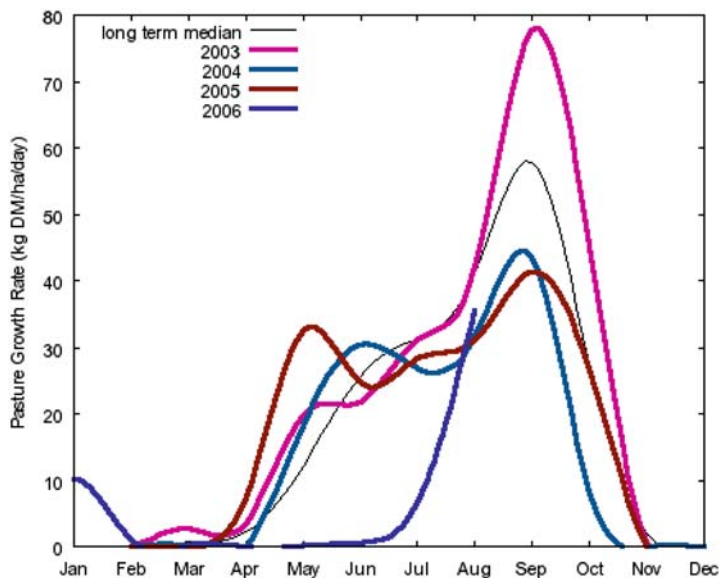


Fig. 3 Monthly PGR time series graphs for a SLA or shire in Western Australia. The graphs are based on the comparison of the current season to the previous three years

Secondly, monthly PGR is summarized on a Statistical Local Area (SLA) basis, and automatically graphed. The SLA graph includes the monthly mean PGR measured in the current year, the past three years, and the long term median (Fig. 3).

Discussion

Spatial assessment of accumulative PGR data can be used to provide decision support information suitable for farm, catchment, regional and shire applications. Figure 4 as an example shows the yearly pattern of gross Dry Matter (DM) of biomass produced for a Western Australian shire for selected years. For these years 6.9, 4.9 and 9.0 tonnes of DM were produced for 1995, 2000 and 2005 respectively with an average of seven tonnes for all years 1994–2005. This shire is located in the south-west of Western Australia with a seasonal break usually occurring in late March–April. These data currently could be provided across the southern districts of Australia.

The monthly PGR time series graphs available within NAMS covers all SLA's and provides land managers and farmers with monthly growth trends and gives an insight into seasonal patterns of growth, hence productivity, which then gives a clear picture of the climatic trends through the season.

Comparison of the long term median PGR base with previous years' graphed data provides land managers with a tool to estimate the productivity of their current season to other seasons.

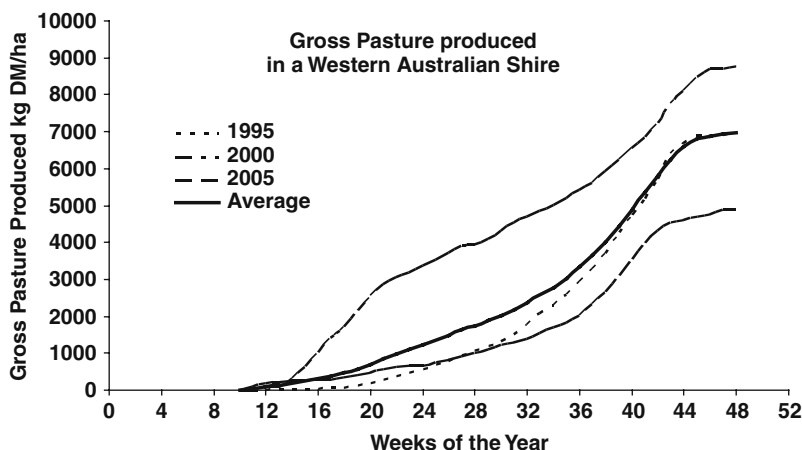


Fig. 4 Accumulative PGR graph representing gross pasture produced for a Western Australia shire (average – meaned over all years 1994–2005)

Conclusions

The Pastures From Space project run by partners from Landgate, CSIRO and Department of Agriculture and Food is delivering current and 12 years of quantitative historical PGR data on modelled pasture production for every rural property in the southern Mediterranean agricultural zone in Australia.

The PGR data is potentially a valuable input to the NAMS website for viewing and assessment of the extent and severity of drought by rural producers and Exceptional Circumstance managers.

The three products currently delivered to NAMS include:

- Monthly standard PGR data for the southern region of Australia resampled to one kilometre resolution.
- Monthly PGR data for the southern region of Australia derived from the deviation of the median value of the last 12 year PGR historical archive.
- Monthly PGR time series graphs for all shires in the southern region of Australia. The graphs are based on the comparison of the current season to the previous three years.

The NAMS project is providing a valuable service to the rural community by allowing easier and wider access to climatic, agronomic and production based analysed information on a publicly viewable website. This will allow producers to more efficiently manage their properties and streamline the reporting mechanisms for Exceptional Circumstance drought applications.

Improvements to the currently supplied PfS data would be an accumulative PGR graph to represent gross pasture production. This would more clearly represent PGR anomalies at a local and regional scale.

References

- Donald, G.E., Edirisinghe, A., Henry, D.A., Mata, G., Gherardi, S.G., Oldham, C.M., Gittins, S.P. and Smith, R.C.G (2004). "Pastures from Space – Validation of Predictions of Pasture Growth Rates." *Animal Production in Australia* **25**: 232.
- Hill, M., G. Donald, (2004). "Estimation of Pasture Growth Rate in South Western Australia from NOAA AVHRR NDVI and Climate Data." *Remote Sensing of Environment* **93**(4): 528–545.
- Tucker, C.J. and Sellers, PJ (1986). Satellite Remote Sensing of Primary Production. *International Journal of Remote Sensing*, 7, 1395–1416.
- Smith RCG, Allen A, Stovold R, and Wiese R (2004) Pastures from Space® Delivering the Information to Farmers. *Proceedings of the 25th Biennial Conference of the Australian Society of Animal Production*. p. 317

Investigating the Potential for Mapping Fallow Management Practises Using MODIS Image Data

Ralf-D. Schroers, Robert Denham, and Christian Witte

Abstract The objective of this study was to investigate the potential for mapping fallow land management practices on local farm scale in Southern Queensland, Australia, using high temporal frequency satellite remote sensing over a period of six years. The Moderate Resolution Imaging Spectroradiometer (MODIS) was chosen as it provides a temporal resolution fine enough to detect ground cover change within cropping cycles (fallow periods). Previous studies have successfully employed MODIS data detecting cropping patterns in Kansas, North America and Northern Kazakhstan.

Multivariate logistic regression examined the relationship between fallow management practices and image data. A binary response was formed by classifying observations during fallow periods as either cultivated (ploughed) or non-cultivated (zero-tillage).

Explanatory data represented 8-day 500 m as well as 16-day 250 m MODIS composite imagery, and derived vegetation indices (Normalized Difference Vegetation Index, Enhanced Vegetation Index, Normalized Cellulose Absorption Index and Normalized Difference Tillage Index). The combination of bands and indices characterized a broad explanatory source and showed high predictive ability (area under the receiver operating curve: 0.788) distinguishing between cultivated and non-cultivated fallow periods.

The ability to discriminate sprayed and non-sprayed areas using immediate pre and post event imagery during fallow times was also investigated. Reasonable predictive power (0.724 area under the receiver operating curve) was achieved based on the MODIS 8-day 500 m composite data.

The results were promising and suggest that there is considerable potential for differentiating land management practices during fallows periods. This information is valuable for modelling erosion risk, understanding potential on-farm impacts on productivity and off-farm impacts on water quality.

R.-D. Schroers (✉)
Spatial Diversity Pty Ltd, Karalee, Qld 4306, Australia
e-mail: ralf@spatialdiversity.com.au

Introduction

The objective of this study was to investigate the potential to map fallow land management practises on local farm scale using high temporal frequency satellite remote sensing. The Moderate Resolution Imaging Spectroradiometer (MODIS) has been chosen as a tool to identify agricultural tillage practises and detect ground cover changes during fallow periods providing high temporal resolution data. Previous studies have successfully employed MODIS data in order to detect cropping patterns in Kansas, North America and Northern Kazakhstan (Wardlow and Egbert 2002; Muratova and Terekhov 2004; Sultangazin, Muratova et al. 2004).

Monitoring crop residue cover of agricultural land during fallow periods requires continuous observation data in order to determine detailed characteristics of ground cover over time between cropping periods. Remotely sensed data, frequently captured over selected broad-acre farms, offered the opportunity to recognize events of fallow management activities and consecutive changes of fallow land cover.

Overview of Study Area

Four properties in South Central Queensland, Australia were selected as study area (Fig. 1).

Data

Investigating the spectral response of fallow areas required the acquisition of detailed ground information. The collection of field records for this study was conducted in cooperation with land holders who provided detailed information on fallow management activities. Spectral responses for these farm areas were acquired during fallow periods using remotely sensed imagery.

Field Records

Local field records at farm or paddock level were obtained in Southern Queensland, Australia. Cropping history over the past six years for 21 paddocks was collected. The average paddock size of selected farm areas was 122 ha, ranging between 35 and 320 ha. The data included information on crop types, planting and harvesting times and methods, tillage and other fallow management practises to control weeds. Records of fallow management practises such as ploughing, cultivating or spraying were available with given dates. The dates for farm applications of other paddocks were estimated if land manager's data referred to monthly recordings.

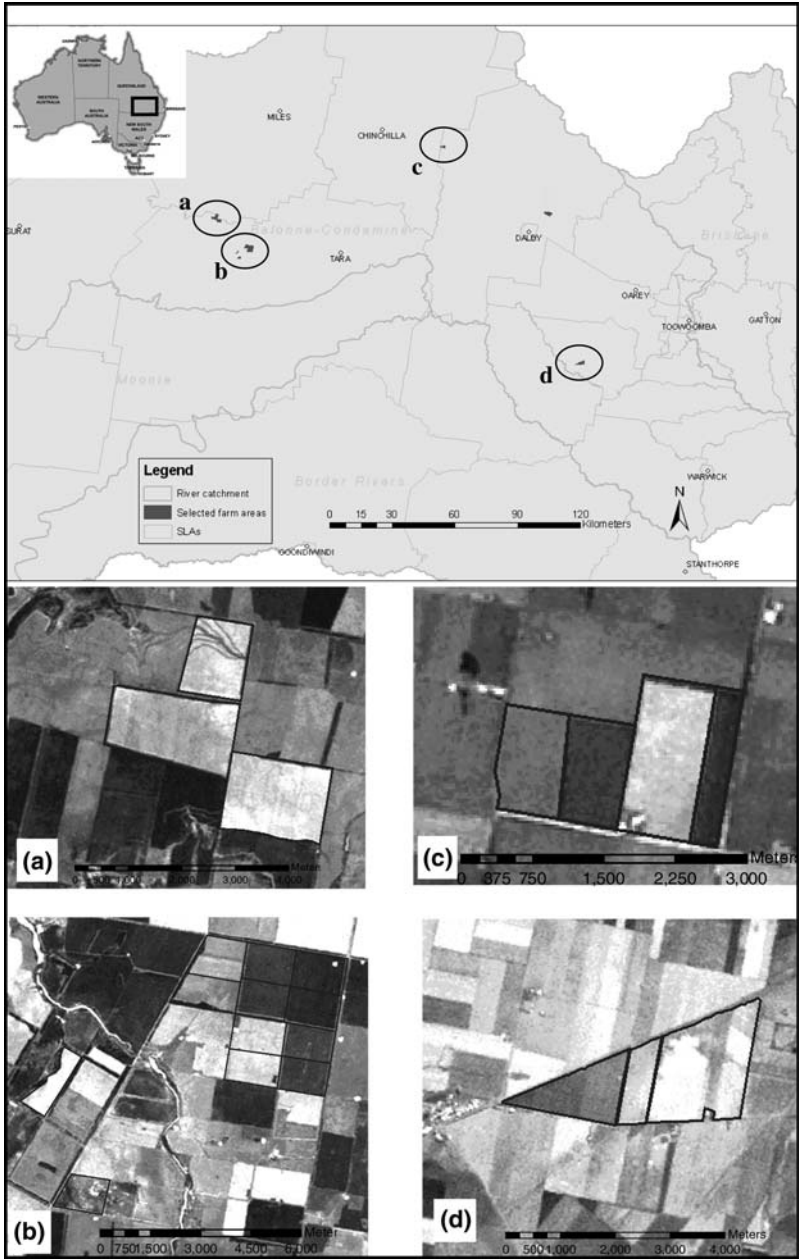


Fig. 1 Overview of Study Area (eastern Balonne-Condamine catchment and Stat. Local Areas); enlarged are farm sites where ground information was used (a, b, c, d). The background shows a true colour LANDSAT image (July/August 2005)

Image Data

MODIS Bands and Indices

MODIS products used for this study included 16 day composite data of the MODIS product MOD13Q1 (250 m spatial resolution) and eight day composite data of the MODIS product MOD09A1 (500 m spatial resolution). The time series data comprised a period from April 2000 until end of 2005. Each year was represented by 46 layers of the 8-day 500 m composite data and 24 layers of MODIS 16-day 250 m composite data.

The 16-day 250 m composites provided index data of NDVI and Enhanced Vegetation Index (EVI) and spectral reflectance in the RED (620–670 nm, band 1) and NIR (841–876 nm, band 2). The EVI data derived from band 1, 2 and 3, with band 3 being resampled to a spatial resolution of 250 m.

MODIS 8-day 500 m composites included surface reflectance data such as Band 1 (RED, 620–670 nm), 2 (NIR, 841–876 nm), 3 (blue, 459–479 nm), 4 (green, 545–565 nm), 5 (1230–1250 nm), 6 (1628–1652 nm), 7 (middle infrared, MIR, 2105–2155 nm). These bands were 8-day-composite interval reflectances and were used to calculate of spectral indices NDVI, EVI, Normalized Cellulose Absorption Index (NCAI) and Normalized Difference Tillage Index (NDTI).

The NCAI was computed as

$$\frac{Band7 - Band6}{Band7 + Band6},$$

and the NDTI resulted from

$$\frac{Band2 - Band7}{Band2 + Band7}.$$

NDVI and EVI index data served as a measure of vitality and amount of active vegetation (Jensen 2005; NRM 2005). Crop-residue sensitive bands 6 and 7 of MODIS 8-day 500 m composite data were used to calculate a cellulose lignin absorption index, and band 2 and 7 were selected to compute a tillage index. Further calculations using band 1 and 2 allowed the calculation of NDVI and band 1, 2 and 3 delivered the EVI.

Methodology

The relationship between paddock-level information on fallow management and corresponding spectral response based on MODIS composite time series was analysed. This required grouping the field data into specified classes, extracting the various MODIS band values for each of the paddocks and undertaking statistical analysis. The following sections describe each of these components of the methodology.

Formatting Field Observations

Field data provided by farmers describing the cropping history were classified based on two approaches. Fallow classes initially were clustered as cultivated and non-cultivated. Fallows with mechanical impact on the surface such as ploughing, cultivating or harrowing were considered as cultivated. Fallows being sprayed, grazed or burnt were classified as non-cultivated. If only harrowing occurred in conjunction with spraying activities, corresponding fallows were identified as non-cultivated, since no stronger physical impact had happened (Fig. 2). Fallow here refers to the time from harvesting of the previous crop to planting of the next crop. If any cultivation occurred during this time then the fallow is classed as cultivated.

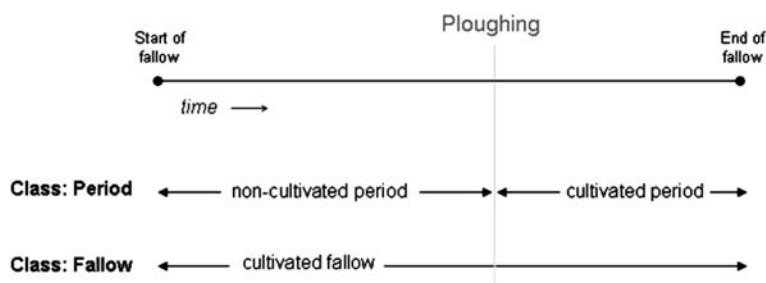


Fig. 2 Two approaches used for classifying fallow period observations, the first approach established periods of cultivation and non-cultivation depending on ploughing operations, *the second approach classified whole fallow times as either cultivated or non-cultivated irrespective of the point in time the ploughing operations occurred*

A second approach was classifying observations into periods. The period leading up to a cultivation event is classed as non-cultivated. The period following is classed as cultivated. This effectively divided some fallows, as defined above, into a non-cultivated and cultivated period.

Image Analysis

LANDSAT Thematic Mapper (TM) imagery was used to georeference the selected paddocks and thereby the detailed cropping information. MODIS data provided band and index variables describing spectral response of observed paddock areas.

Extraction and Classification of Spectral Reflectances

Each paddock area was digitized, and the derived polygon shapes were used to retrieve MODIS image data in form of spectral reflectance or vegetative indices values. Given the considerable number of MODIS products analysed and the large number of images used for this study, Python scripting was used to automate the majority of the processing (Python 2001). Records of farm activities were used to mask out time intervals of MODIS imagery. These time series were then classed according to ground information into the categories ‘cultivated’ and ‘non-cultivated’ fallow, and served as the response in later developed logistic regression models.

Statistical Analysis

Univariate analysis of MODIS bands and indices showed the ability of each band and index variable to discriminate between cultivated and non-cultivated fallows, as well as cultivated and non-cultivated periods (see Fig. 2).

Multivariate logistic regression explored the relationship of MODIS spectral band and index combinations to dichotomous class establishments such as cultivated versus non-cultivated fallow, cultivated versus non-cultivated periods as well as spraying versus non-spraying events.

Both univariate comparisons and multivariate modelling employed 8-day 500 m and 16-day 250 m MODIS composite data.

Model predictions of fallow type classes were conducted for paddocks where cropping information had not been collected. The accuracy was assessed by asking landholders for feedbacks on the predictions

Univariate Analysis of Band and Index Variables

The analysis of single bands and indices provided a measure of how separable the different fallow types were. Boxplots were descriptive measures depicting distribution patterns, variability, median, lower and upper quartiles of spectral values of two established fallow classes. Median and inter-quartile ranges were a measure of how distinctive a classification was observed within a band or index. The statistical means of the two established classes were examined conducting a t test using the software R (Crawley 2002; R 2006). That revealed whether the means of two groups were statistically different from each other, and described the performance of each band or index as a classifier.

Multivariate Logistic Regression Employing Band and Index Variables

Cultivation vs Non-cultivation

Model development was based on spectral response of both cultivated/non-cultivated fallows and cultivated/non-cultivated periods.

Relating a number of MODIS bands and indices to a binary response in the form of two classes, such as cultivated and non-cultivated fallow, could be approached by logistic regression.

A multivariable logistic regression model was designed describing potential associations between the two fallow classes and MODIS band reflectance values and indices. The logistic model employed was equivalent to

$$P = \frac{1}{1 + e^{-(z)}},$$

where P denoted the probability for model estimations being assigned to either one of the two established classes (Kleinbaum 1994). The probability was ranging between values of 0 and 1, and represented the probability that a paddock was non-cultivated. The value z is the linear predictor consisting of a combination of MODIS band and index variables (Kleinbaum 1994).

Regressions were developed for both 8-day 500 m and 16-day 250 m MODIS composites. Stepwise regression was conducted using the AKAIKE Information criteria (AIC) to minimize the number of explanatory band and index variables. The prediction performance was analysed using the statistical method of receiver operating characteristic (ROC), representing the tradeoffs between sensitivity and specificity of a model estimation (van Schalkwyk and van Schalkwyk 2001).

Spraying Events and Non-spraying Events

Fallow management events were differentiated according to their physical impact on agricultural fields. Two classes were established, spraying operations, not disturbing the soil, and non-spraying operations where events disturbed the soil surface. Ploughing, lighter ploughing operations (using secondary tillage equipment) and harrowing were categorized to a class 'non-spraying'. The probability that observations referred to spraying events was ranging between 0 and 1. Further analyses using the ROC approach were investigating the probability that the classifier could accurately predict observed discriminations.

Each event could be described by two image composites. The earlier image representing reflectances of land cover when the farm operation was carried out (cause), and the consecutive image characterizing the spectral response of the impact. This analysis employed ground information of twelve paddocks providing precise dates for farm operations.

Predicting Non-cultivation or Cultivation During Fallow Times

Firstly, predictions were based on data from the study site that were used for model development. In this way model performance could be assessed by comparing predictions against observations. Based on 8-day 500 m data, two models provided probabilities for observed areas being not cultivated at a point in time, ranging between 0 and 1. Low probabilities indicated a cultivation. Boxplot analysis provided information on how separable predicted classes were and delivered a threshold level representing a probability value separating between cultivated for non-cultivated classes. One model was employing data from cultivated and non-cultivated fallows and the second model was based on cultivated and non-cultivated periods.

Secondly, predictions were made for ten new selected paddock areas outside the observation data frame, of which five were cropped agricultural land. The two models delivered each prediction probabilities for areas being cultivated or non-cultivated. The results were validated through ground information provided by land holders.

Predictions based on 8-day 500 m data delivered estimations for every 8th day. A polynomial was fit using least squares to predicted probability values for pixels of each paddock. Hence, the local regression fit computed one probability value for each paddock over time.

Results

The discrimination of spectral response between cultivated/non-cultivated fallow and cultivated/non-cultivated periods was analysed. The performance of each MODIS band and index as individual classifier was examined. Multivariate regression revealed how well a band or index combination could account for class discrimination. It was also investigated whether four different fallow management practices (spraying, ploughing, lighter ploughing and harrowing) could be discriminated based on their spectral response using two image dates, one before and one after the event.

Cultivated vs Non-cultivated Fallows

A fallow was defined as the period from the harvest of the last crop to the planting of the next one and is classed as either cultivated or non-cultivated. 8-day 500 m data and 16-day 250 m MODIS data were investigated as tools for differentiating these two classes.

Eight-Day 500 m Data

Univariate Analysis

The class establishment based on spectral response of cultivated and non-cultivated fallow through individual bands and indices did not reveal large difference between class medians (Fig. 3). However, the differences of class means were

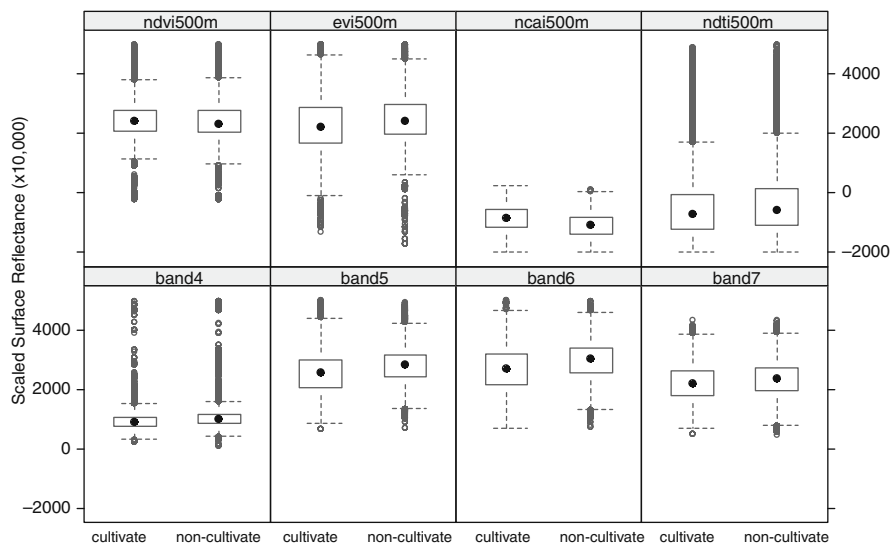


Fig. 3 Boxplots for classified spectral response of all farm areas for the years 2000–2005. The data employed derived from MODIS 8-day 500 m composites, based on observations cultivated and non-cultivated fallows; Band 6 provided maximum discrimination

statistically significant at the 5% level. Best discrimination was achieved by Band 6 (1628–1652 nm), followed by NCAI, Band 5 (1230–1250 nm) and EVI. The NDTI could not strongly discriminate between spectral responses of cultivated and non-cultivated fallows. As individual classifier, the NCAI had some potential to establish cultivation classes.

Multivariate Regression

Ten spectral variables were used as explanatory source in a logistic regression accounting for fallows being cultivated or non-cultivated. The model was composed of MODIS bands 1, 2, 3, 4, 6, and 7 and indices EVI, NCAI, NDTI and NDVI. Correct classifications were represented by true positive fractions, matching non-cultivated observations with a non-cultivated prediction class. A ROC curve plotted true positive against false positive results that depicted wrong class assignment of non-cultivated fallow observations. The derived area under ROC of 0.742 showed that the model had some predictive power to distinguish between the two classes (Fig. 4).

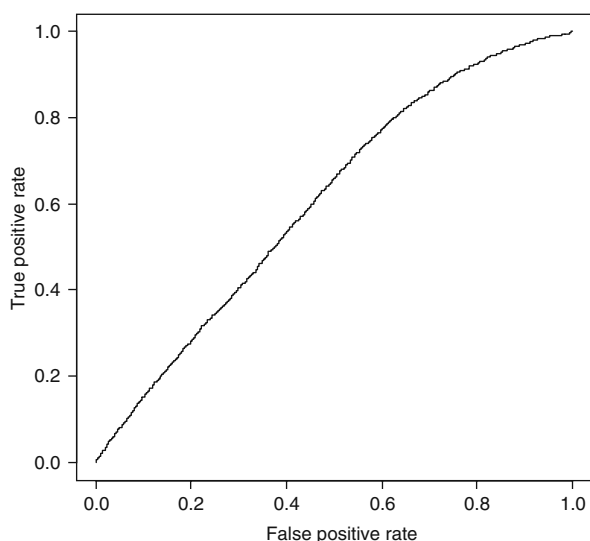


Fig. 4 Prediction of cultivation/non-cultivation based on fallow observations and 8-day 500 m composite data; area under the ROC curve: 0.742

Sixteen-Day 250 m Data

Univariate Analysis

None of the image band or index variables was particularly suitable for representing the cultivation status of farm fallows. Both EVI and NDVI resulted in lower differences of mean values as discrimination criterion for spectral class establishment than their respective composite parts, RED (620–670 nm) and NIR

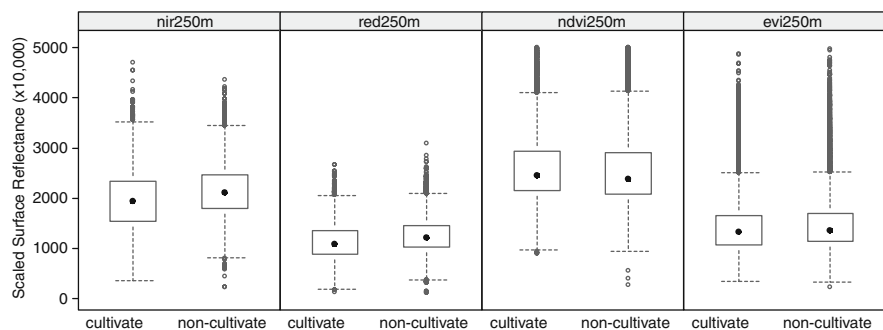


Fig. 5 Boxplots for classified spectral response of all farm areas for the years 2000–2005. The data employed derived from MODIS 16-day 250 m composites, based on observations cultivated and non-cultivated fallows

(841–876 nm) (Fig. 5). Differences of class means for the latter were statistically significant at the 5% level.

Multivariate Regression

Discriminations of fallows based on 16-day 250 m composite data employed a three variable model. The variables comprised EVI, NIR, and RED. Corresponding predictions could not distinguish between cultivated and non-cultivated fallow periods very well as the ROC curve was close to the graph of a random prediction model (Fig. 6). The area under the ROC curve was 0.608.

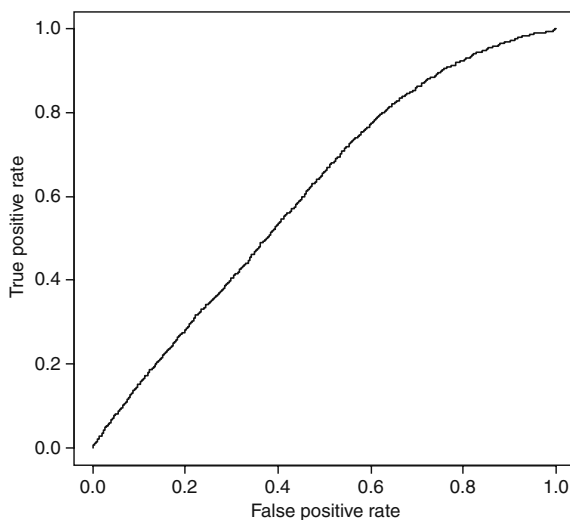


Fig. 6 Prediction of cultivation/non-cultivation based on fallow observations and 16-day 500 m composite data; area under the ROC curve: 0.608

Cultivated and Non-cultivated Periods

Observations in form of spectral response of cultivated and non-cultivated periods served as explanatory source. In contrast to fallows, periods were considering ploughing or lighter ploughing operations during fallow times (Fig. 2). Periods were classed as uncultivated unless soil disturbing operations occurred.

Period data of the 8-day 500 m composites generally better distinguished between cultivation and non-cultivation than 8-day 500 m fallow data (see Chap. 6.1).

Eight-Day 500 m Data

Univariate Analysis

Band 6 (1628–1652 nm) provided maximum discrimination followed by EVI and band 5 (1230–1250 nm). The NCAI composed of band 6 (1628–1652 nm) and band 7 (2105–2155 nm) computed low differentiations between fallow classes (Fig. 7). Band 7 showed low potential for class discrimination. All class means were statistically different at the 5% level.

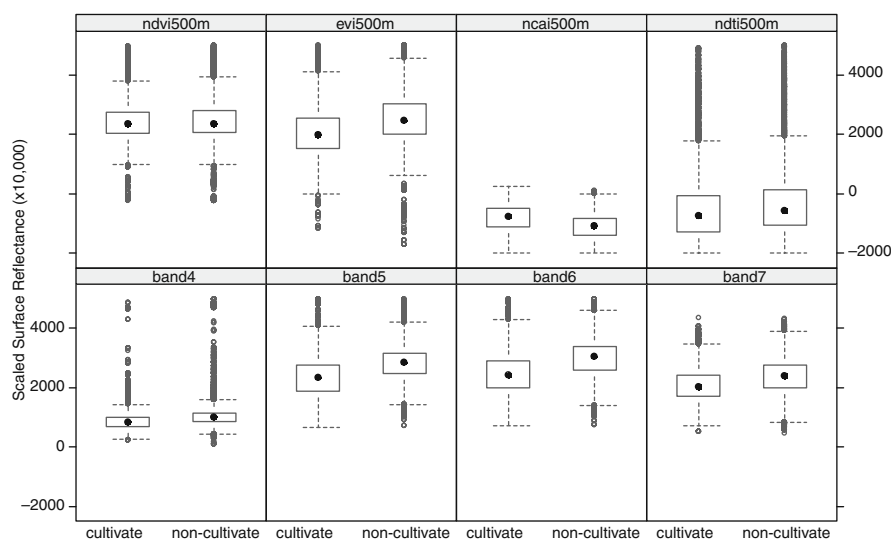
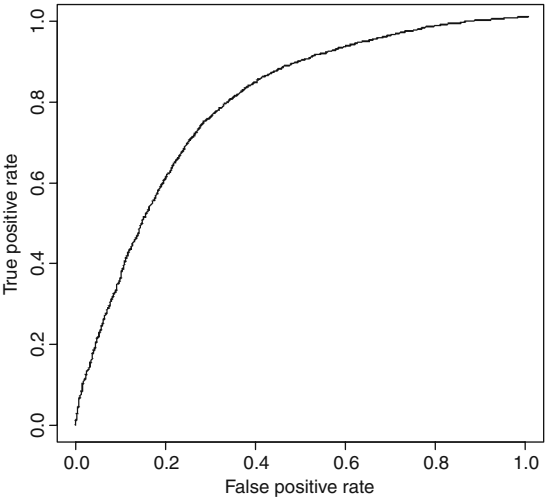


Fig. 7 Boxplots for classified spectral response of all farm areas for the years 2000 to 2005. The data employed derived from MODIS 8-day 500 m composites, based on observations cultivated and non-cultivated periods; Band 6 provided maximum discrimination

Multivariate Regression

A ten variable model predicting fallow type classes was developed composed of MODIS bands 1, 2, 3, 4, 6, and 7 as well as indices EVI, NCAI, NDTI and NDVI. The model performance was analysed by plotting the ROC curve (Fig. 8). It

Fig. 8 Prediction of cultivation/non-cultivation based on period observations and 8-day 500 m composite data; area under the ROC curve: 0.788



provided a measure for accuracy of true class assignment describing the sensitivity of the model to correctly identify observations non-cultivated periods. The measure of predictive ability represented by the area under the ROC curve was 0.788 (Fig. 8). This model promised to deliver fairly good predictions of cultivated vs. non-cultivated periods.

Sixteen-Day 250 m Data

Univariate Analysis

A higher variation of class medians of EVI could be observed in the boxplot shown in (Fig. 9). NIR band data (841–876 nm) showed highest variation in the position

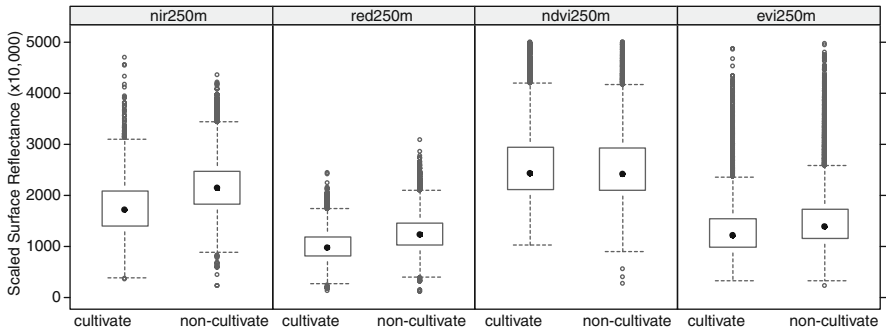


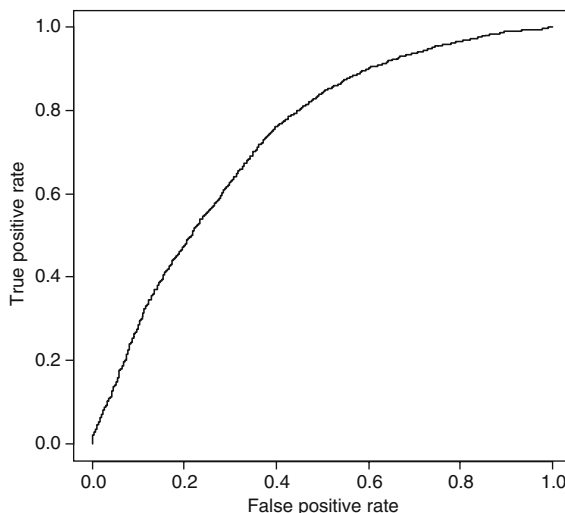
Fig. 9 Boxplots for classified spectral response of all farm areas for the years 2000–2005. The data employed derived from MODIS 16-day 250 m composites, based on observations cultivated and non-cultivated periods

of class medians (Fig. 9). Also the RED band (620–670 nm) provided noticeable difference in class discrimination. Only the NDVI class means were not significantly different at the 5% level.

Multivariate Regression

Model predictions based on 16-day 250 m data employed the variables EVI, NIR and NDVI. This model was a fairly good predictor, the area under the ROC curve was computed as 0.731 (Fig. 10).

Fig. 10 Prediction of cultivation/non-cultivation based on period observations and 16-day 250 m composite data; area under the ROC curve: 0.731



Comparing 16-Day 250 m and 8-day 500 m Data Using Same Variables

Model comparison between the 8-day 500 m composite time series and the 16-day 250 m imagery was conducted based on period observations. Both models employed the same independent variables (NIR, NDVI and EVI) explaining cultivation and non-cultivation. The model based on 8-day 500 m composite data produced an area under ROC curve of 0.696. This result was lower than the predictive ability of the 16-day 250 m composite series (area under ROC curve: 0.731). Here, prediction performance improved with higher spatial but lower temporal resolution.

Spraying vs. Non-spraying Events

A model was developed based on spectral response of land cover changes induced by spraying and non-spraying events. An event class was created, aggregating the spectral response of ploughing, lighter ploughing and harrowing events each

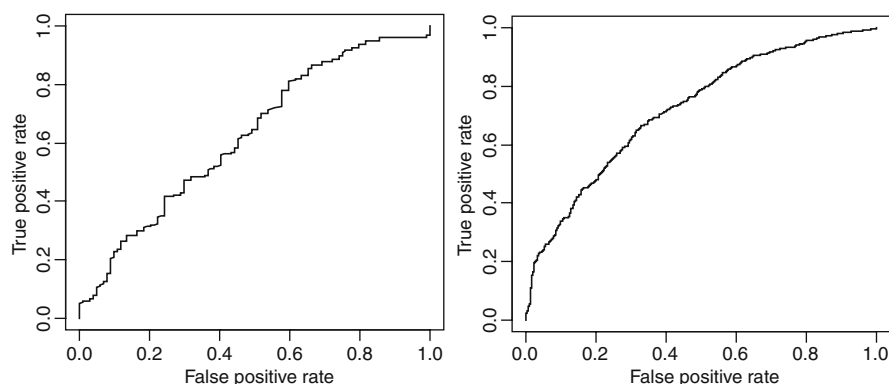


Fig. 11 ROC curves for models predicting spraying events (true positive fraction) vs. non-spraying events (false positive fraction) for twelve selected paddocks during 2000 and 2005; *left: 16 day 250 m data, area under the ROC curve: 0.624; right: 8-day 500 m time series, area under the ROC curve: 0.724*

described by a series of two images. Non-spraying events were considered to have a higher physical impact on the surface, than spraying operations. A binary response was defined as ‘spraying’ and ‘non-spraying’ events.

The ROC curve corresponding to the probability of prediction achieved an area of 0.624 and 0.724 based on the 16-day 250 m and 8-day 500 m time series, respectively (Fig. 11). The models employed 10 variables, bands 1–7, NDVI, EVI and NCAI.

The 8-day 500 m series computed higher predictive ability as the area under the ROC curve was 0.724, compared to 0.624 of the 16-day 250 m dataset.

Model predictions based on the 8-day 500 m composite data were validated. Corresponding error matrix showed that a high number of spraying events were predicted as non-spraying operations (20.6%). The overall accuracy resulted in 78%.

Predicting Non-cultivation or Cultivation During Fallow Times

Predictions using data from the study site permitted an analysis of model performance. The model outcomes represented probabilities of areas being non-cultivated at a point in time. Field observations were then taken for comparison against models’ predictions. This permitted defining a probability threshold level for class separation. Predicted probabilities ranged between 0 and 1, lower probabilities below the derived threshold level indicated that farm sites were cultivated. One model employing data from cultivated and non-cultivated fallows showed a threshold value of 0.69. The second model was based on cultivated and non-cultivated periods and separation threshold was 0.84.

As a further step, predictions were computed for ten new paddock areas outside the observation data frame. Based on the two models’ specific probability thresholds

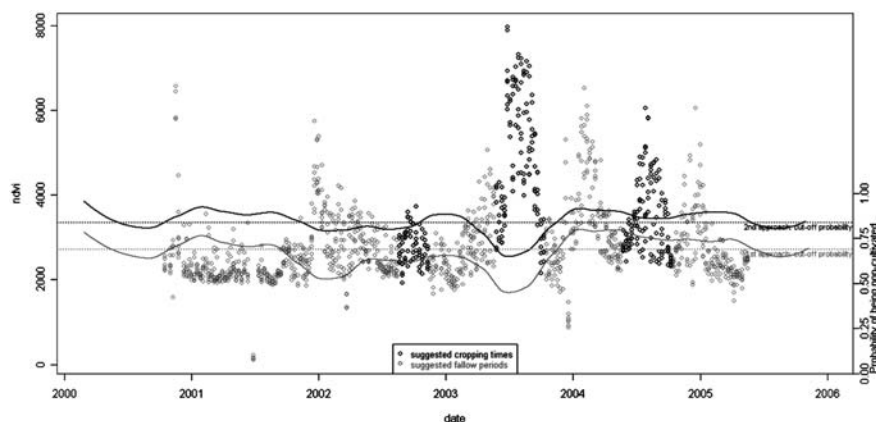


Fig. 12 Prediction probability as colour coded lines (local regression fit); predictions based on either fallow observations (light line) or period observation (dark line); Colour coded cut-off levels symbolize probability thresholds dividing cultivation classes; NDVI reflectance of corresponding paddock areas are represented by data points: assumed fallow times (light dots) and assumed cropping times (dark dots)

predictions indicated either cultivation (above threshold) or non-cultivation (below threshold). Most of the predicted fallows and periods did match with ground information provided by corresponding landholders. 25 fallow periods were predicted for five selected farm sites. Over a period of from spring 2002 onwards, fallows were estimated each for spring and autumn. Out of 30 fallow cycles the validation was conducted for 25 fallows. Nine fallow cycles were identified correctly as non-cultivated, thirteen as correctly classed as cultivated.

The achieved overall accuracy of predictions was 88%. Both models achieved same classification results. Figure 12 shows an overlay of prediction probabilities over a sequence of NDVI reflectances of a selected paddock. Two predictions were based on fallow and period observations, respectively. Both prediction outcomes followed almost similar trends indicating either cultivation or non-cultivation.

Discussion and Conclusion

Four different types of observation data were employed for investigating the potential to map cultivation during fallow times. Field information was formatted either as fallow or period, and each of the latter employed spectral reflectances of two image series. One image set was of 8-day 500 m composites consisting of the 11 layers MODIS band 1–7, NDVI, EVI, NCAI and NDTI. The second image set was of 16-day 250 m composites comprising the four layers MODIS band 1 and 2 as well as MODIS NDVI and EVI. Band 1 and 2 of both data sets represented the RED and NIR region, respectively. Figure 13 provides an overview for results of univariate comparisons and multivariate regression.

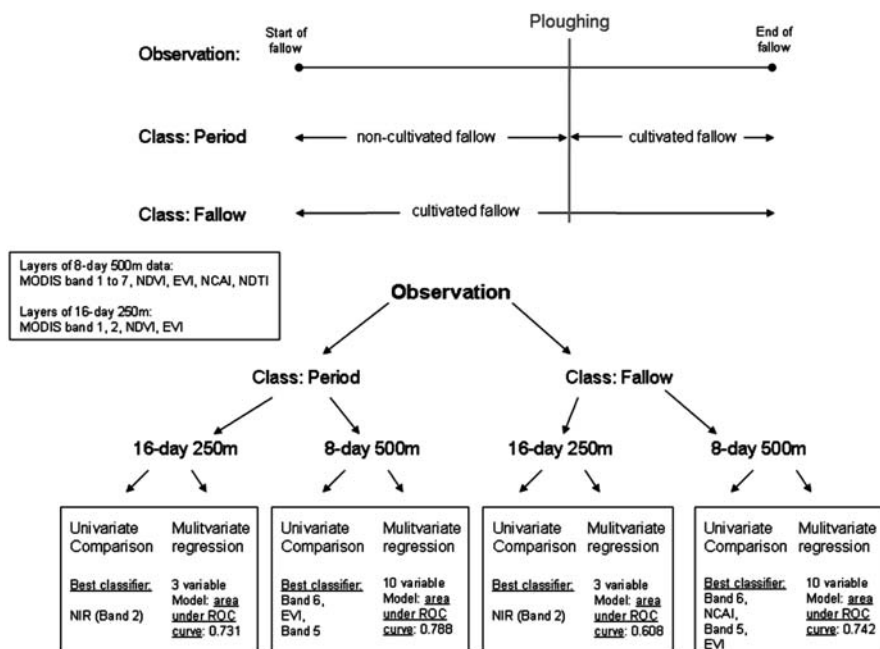


Fig. 13 Overview explanatory sources and results for identifying cultivation and non-cultivation during fallow times using univariate comparison and multivariate regression. Observations were classed as either fallows or periods

Generally, better discriminations were achieved through 8-day 500 m data than 16-day 250 m data.

In decreasing order of performance, Band 6 (1628–1652 nm), EVI and band 5 (1230–1250 nm) achieved best discrimination of classes of periods and the 8-day 500 m data. Band 6, NCAI, band 5 and EVI best distinguished classes of fallows and the 8-day 500 m composites. Best classifier for classes of period and fallow based on 16-day 250 m composites was NIR (841–876 nm), followed by RED (841–876 nm) and EVI.

Multivariate modelling revealed fairly strong predictive power regarding the estimation of cultivation and non-cultivation. Best predictions were achieved for period rather than fallow observations and were based on a 10 variable model based on MODIS 8-day 500 m composites (area under the ROC curve of 0.788). Also a three variable model achieved good prediction accuracy based on MODIS 16-day 250 m data (area under the ROC curve of 0.731).

The role of temporal and spatial resolution was explored regarding predictive ability of cultivation and non-cultivation. Two models were investigated using 8-day 500 m data and 16-day 250 m data with the same explanatory variables (NIR, NDVI and EVI) of periods. The results showed that higher temporal resolution did not compensate for lower spatial resolution. The model based on 8-day 500

m composites produced an area under ROC curve of 0.696 compared to the better predictive ability of the 16-day 250 m composites with an area under ROC curve of 0.731.

The discrimination of spraying and non-spraying event classes showed considerable potential. The best results were achieved through a 10 variable multivariate model using the MODIS 8-day 500 m composites (area under the ROC curve of 0.724). The predictive ability of the model based on period observations and 16-day 250 m data was considerably weaker (area under ROC curve of 0.624).

The regression models using periods and 8-day 500 m data were used to predict cultivation in a number of paddocks which were not included in the study so far. The results were given to the corresponding land managers and feedback on each paddock was provided. The overall accuracy of predictions for cultivation or non-cultivation was 88%. 22 out of 25 fallow types were correctly classed as either cultivated or non-cultivated.

As an indicator for crop residue quantities Band 7 (2105–2155 nm) could not clearly distinguish between cultivation classes (Daughtry et al. 2005). Slightly higher reflectance values for non-cultivated fallows were discernable and could explain higher residue cover levels throughout these phases. Cultivated fallows might have also been covered with plant litter (to a lower extent), preventing a detection of bare soil via band 7.

The NCAI sensitivity to plant cellulose showed reasonable potential for discrimination of cultivation classes for fallow observations.

The discrimination between spraying and non-spraying events was successful. An explanation for differences in spectral response could be the stronger physical impact on the surface left by ploughing, lighter ploughing or harrowing activities. Best prediction results were achieved by the 8-day 500 m data. The predictive ability based on 16-day 250 m data was weak. 8-day 500 m models employing higher temporal resolution were performing better and seemed to compensate for the lower spatial resolution.

References

- Crawley, M. J. (2002). *Statistical Computing, An Introduction to Data Analysis using S-Plus*. West Sussex, John Wiley and Sons.
- Daughtry, C. S. T., E. R. Hunt Jr., D. P.C. and J. E. McMurtrey III (2005). "Remote Sensing the Spatial Distribution of Crop Residues." *Agronomy Journal* **97**: 864–871.
- Jensen, J. R. (2005). *Introductory Digital Image Processing, A Remote Sensing Perspective*. Upper Saddle River, USA, Prentice Hall.
- Kleinbaum, D. G. (1994). *Logistic Regression*. New York, Springer Verlag.
- Muratova, N. and A. Terekhov (2004). "Estimation of Spring Crops Sowing Calendar Dates using MODIS in Northern Kazakhstan." *IEEE* **2/04(c)**: 4019–4020.
- NRM (2005). Development of Methodology to Map Land Use Change and Application to the Fitzroy River Catchment. Brisbane, Queensland Land Use Mapping Program, Land & Environment Assessment, Department of Natural Resources & Mines.
- Python (2001). Python Language. <http://www.python.org>.
- R (2006). R 2.3, A Language and Environment for statistical computing. R. D. C. Team. Vienna, R Foundation for Statistical Computing. www.R-project.org.

- Sultangazin, U., N. Muratova, P. Doraiswamy and A. Terekhov (2004). "Monitoring of crop rotation and weed infestation estimation using MODIS 2004." *IEEE* **6**: 4036–4069.
- van Schalkwyk, L. and J. van Schalkwyk (2001). The worldwide anaesthetist. *The magnificent Receiver Operating Characteristic curve*. <http://www.anaesthetist.com/mnm/stats/roc>, accessed on 14th April 2006.
- Wardlow, B. D. and S. L. Egbert (2002). *Discriminating cropping patterns in the U.S. Central Great Plains region using time-series MODIS 250-meter NDVI data - Preliminary Results*. Pecora 15 and Land Satellite Information IV Conference.

Spectral Mixture Analysis for Ground-Cover Mapping

Michael Schmidt and Peter Scarth

Abstract Monitoring of ground-cover is an important task for land management since it has been linked to indicators of soil loss, biodiversity, and pasture production. Ground-cover is an indicator adopted by Queensland natural resource and catchment management groups. However, accurate spatial estimation of ground-cover is confounded by varying cover types, cover greenness and soil colour.

This research reports on ground-cover mapping based on spectral mixture analysis (SMA) of LANDSAT satellite imagery. Estimates of green and senescent vegetation and soil fractions are derived from iterative SMA. Correlations with field data are from SMA iterations are discussed with r^2 values of 0.78 and 0.69 respectively for bare ground estimates over black soils.

Introduction

Land- and ground-cover data of the earth surface is of strong interest for studies of terrestrial and atmospheric processes of energy fluxes and feedback mechanisms from regional to global scale (Cihlar 2000). Ground cover data is a key source of information for various scientific questions and natural resource management (Jensen 1996). Major drivers for ground cover are understood to be climate and land management (Scarth et al. 2006); sustainable land management is a priority for the State of Queensland. Approximately 65% of Queensland is covered by state rural leasehold land (more than 40 million hectares). The Queensland government has initiated a review process for renewal of leases which require estimates of bare-ground for the assessment of the land condition (Karfs et al. 2007).

Scarth et al. (2006) used Landsat data Thematic Mapper (TM) and Enhanced Thematic Mapper (ETM+) over Queensland with a regression based approach to estimate bare ground as a state-wide product using 450 field estimates as training data. The product is the best available data source for ground-cover, but has

M. Schmidt (✉)

Department of Natural Resources and Water, Indooroopilly, QLD 4068, Australia
e-mail: michael.schmidt@nrw.qld.gov.au

some shortcomings particularly on regional scales. Black soils are known to pose difficulties in this state-wide regression based approach (Scarth et al. 2006). Gill and Phinn (2008) evaluated short wave infrared data from the ASTER satellite sensor over specific study sites in Queensland for bare-ground estimates via a spectral mixture analysis.

The dry vegetation component is a crucial parameter in estimating bare-ground fractions. It is one of the elements of the total cover, important in carbon accounting, infiltration, runoff, water and wind erosion modelling (Van Leeuwen and Huete 1996). Since this component can not be detected easily by greenness based vegetation indices from satellite data over different soil types there is the need to develop and apply other methods (García-Haro et al. 1996).

This study aims to derive ground-cover and vegetation fraction estimates over a study site with a variety of soil types, focussing on black soils. Fraction estimates of certain constituents under the spectral unmixing paradigm provide physically based estimates of soil or vegetation coverage (Hill 2000; Hurcom and Harrison 1998; Smith et al. 1996). Spectral unmixing describes spectral data in terms of membership grades to a cluster or a reference spectrum on sub-pixel scale (Roberts et al. 1998).

We apply a spectral mixture analysis (SMA) of LANDSAT data over a test area of $80 \times 120 \text{ km}^2$ with a large proportion of black soils (see Fig. 1). The aim is to investigate the SMA paradigm to reliably estimate fractions of cover, green and dry vegetation for the study area and to potentially apply an SMA approach for the state of Queensland.

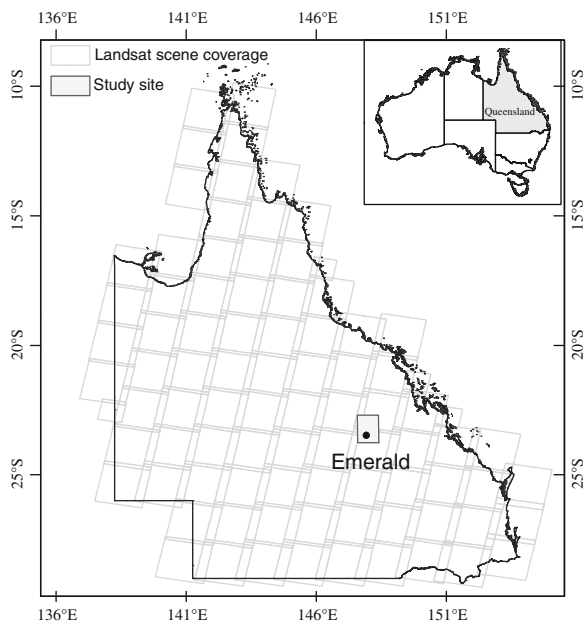


Fig. 1 Location of the study area near Emerald, Queensland

Data

Satellite Images

Two adjacent LANDSAT TM5 images from the same satellite overpass over a region surrounding Emerald (10th June 2007) were geometrically corrected (Armston et al. 2002), radiometrically corrected (Danaher 2002; de Vries et al. 2007), mosaiced and subsetting. The images are part of the Department of Natural Resources and Water (NRW) satellite image archive over Queensland. The image subset was chosen to represent a variety of soil and cover types.

Field Data

Fieldwork was conducted from May 15 to 19, 2007 during a dry period to minimise cloud contamination of the satellite data (Fig. 2).

Field measurements were acquired via a modified discrete point sampling method (Brady et al. 1995) along three star shaped 100 m transects, the first laid in the north-south direction with 60 degree angles clockwise to the next transect (Scarth et al. 2006). Ground layer data (bare, rock, dead leaf attached, litter, green leaf and cryptogram), mid-storey and over-storey strata attributes were recorded at each metre along each transect and subsequently entered into a palmtop computer in-situ. A running mean was calculated on 20 point blocks and provides an indication of stability (i.e. homogeneity) of the plot. The data points were compared with the respective location of the Landsat data analysis extracted from a 3×3 pixel area around GPS the location.

In addition to transects, visual estimates of biomass and cover were recorded for different soil types and stored in a geospatial database as polygons (Fig. 3). It is important to note that visual estimates were taken over a range of soil types.



Fig. 2 Photos of two field sites (M. Schmidt 16.05.2007)

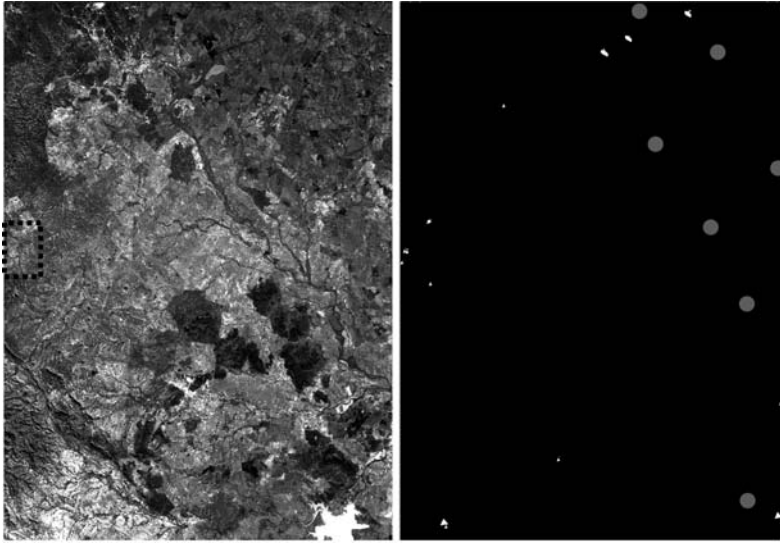


Fig. 3 Landsat Channel 1 image of the study area (*left*), the *grey* points (on the *right*) indicate the location of the standard ground-cover sampling sites; in white are the visual estimation polygons displayed. (The *dotted line* refers to a zoom region of Fig. 9.)

Methods

The term ‘mixed pixels’ describes an effect that occurs when different surface materials or land cover types comprise the spectrum measured within a satellite’s IFOV (Instantaneous Field of View). Spectral mixture analysis is based on the assumption that the spectrum recorded from the satellite is a linear or non-linear combination of each of those components (Adams et al. 1986). The decomposition of a surface area within the IFOV or a pixel, into proportional abundance of a finite number of endmembers assumes that most of the spectral variation in a multispectral image can be described, in a first approximation, by additive (linear) spectral mixtures (Adams et al. 1995; Schmidt and Schoettker 2004). A mixed spectrum P_λ of a given pixel can thus be modelled by the sum of the fractions f of the n endmembers E_i in the IFOV:

$$P_\lambda = \sum_{i=1}^n f_i E_{i\lambda} + \varepsilon_\lambda \quad (1)$$

where λ represents a spectral band, n the number of endmembers and ε the residual term. The model fit is expressed either as error in the fractions f or ε_λ at each wavelength or across all bands as global RMSE (Roberts et al. 1998):

$$RMSE = \frac{1}{m} \sqrt{\sum_{i=1}^m (\varepsilon_{i\lambda})^2} \quad (2)$$

where m is the number of bands. The process of SMA creates the endmember fractions for every pixel in the image and each endmember, referred to as endmember abundance (Hill 2000). The identification of endmembers such that the spectra of most pixels are explained properly, is the key issue in spectral unmixing (Hill 2000) with the best results obtained by choosing extreme spectra.

Candidate endmembers were chosen to be green vegetation (GV), non photosynthetic vegetation (NPV), soil and shade. A set of potential NPV endmember spectra were derived from spectral libraries (Gill and Phinn 2008), US geologic survey and jet propulsion laboratory as implemented in ENVI (RSI 2007) and endmember spectra derived from the imagery itself. The candidate endmember spectra used in this study are shown in Fig. 4 as scatter plots of different bands as a 2D histogram.

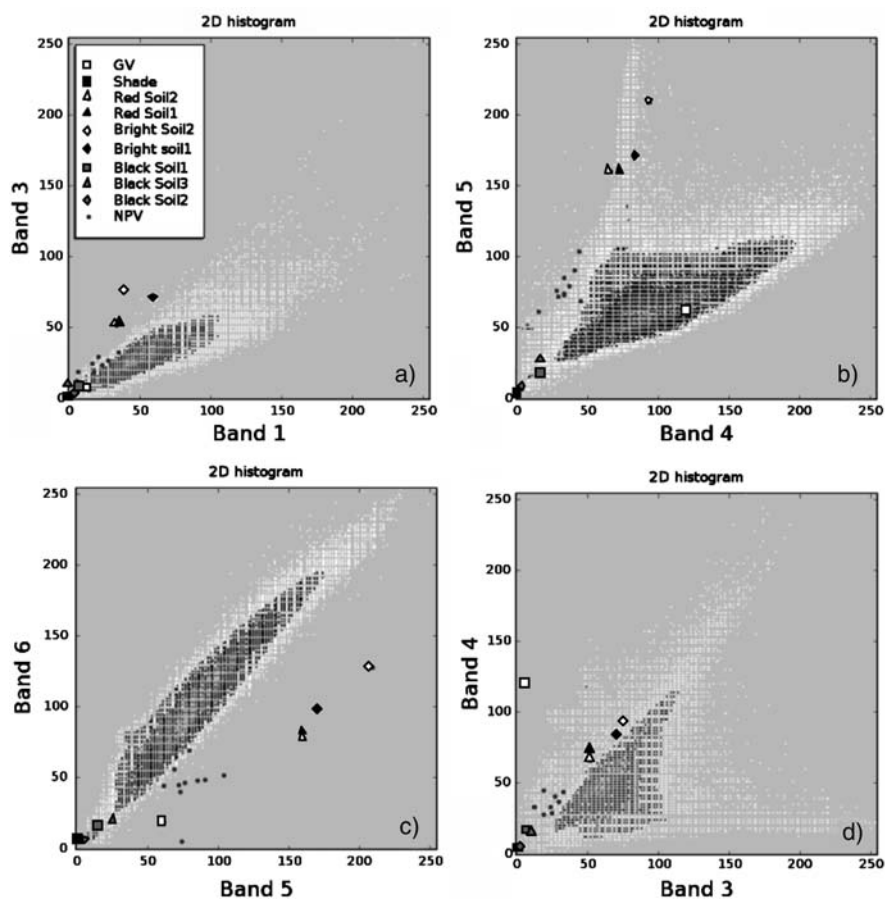


Fig. 4 2D histogram of the imagery with candidate endmembers for some band combinations (the 9 NPV spectra used are shown in the same symbol)

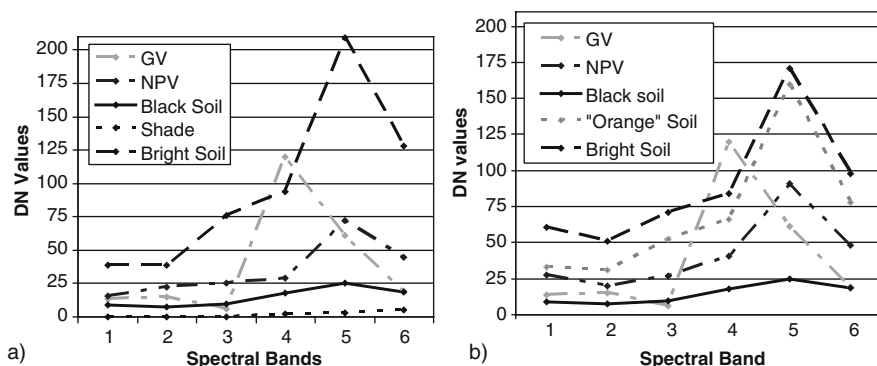


Fig. 5 Two examples of spectra used in the SMA iterations as extracted from the spectral library of candidate endmembers

The GV spectrum was taken from pixels with the highest NDVI (Normalized Difference Vegetation Index (see (Tucker 1979) for more details) values in the image while pure soil spectra were obtained from polygons obtained during field work.

SMA results of a 4 (not shown) and 5 endmember model were tested and iterated - the 5 endmember model seemed to perform better overall. All combinations of several candidate endmembers: 1 GV spectrum, 9 NPV, 3 soil type 1 (dark soil), 2 soil type 2 (bright soil) and 2 shade/soil type 3 (red soil) were iterated, resulting in 108 SMA runs; Fig. 5 shows two examples of endmember spectra used in the iterations.

Bare-ground, or percent bareness, is in this approach defined as 1-NPV-GV on a per pixel basis.

Results

Figure 6 shows plots for the two example SMA runs described in Fig. 5 including the correlation coefficients and regression lines: mean values for the transect measurements of both NPV and ground cover were plotted with means of the SMA runs over the respective area (Fig. 6a, b). Figure 6c incorporates the RMSE (in DN values) to indicate the quality of the SMA solution. The visual estimates of cover over a variety of soil types are included to indicate the quality of the SMA for different soil types (see Fig. 6d).

The percent dry cover NPV relationship in (Fig. 6a) shows a good relationship, especially in the case of Example 1 with an $r^2 = 0.78$ and a slight offset from the 1:1 line. The p values from the F-test of significance are indicated in Fig. 6 and show that all datasets pass the 5% significance test of a correlation.

The percent bare field measurements show good correlations for the two Examples, but the total of 7 observations with only one data point in high bare conditions (or low cover) make the need for more field data obvious in order to obtain

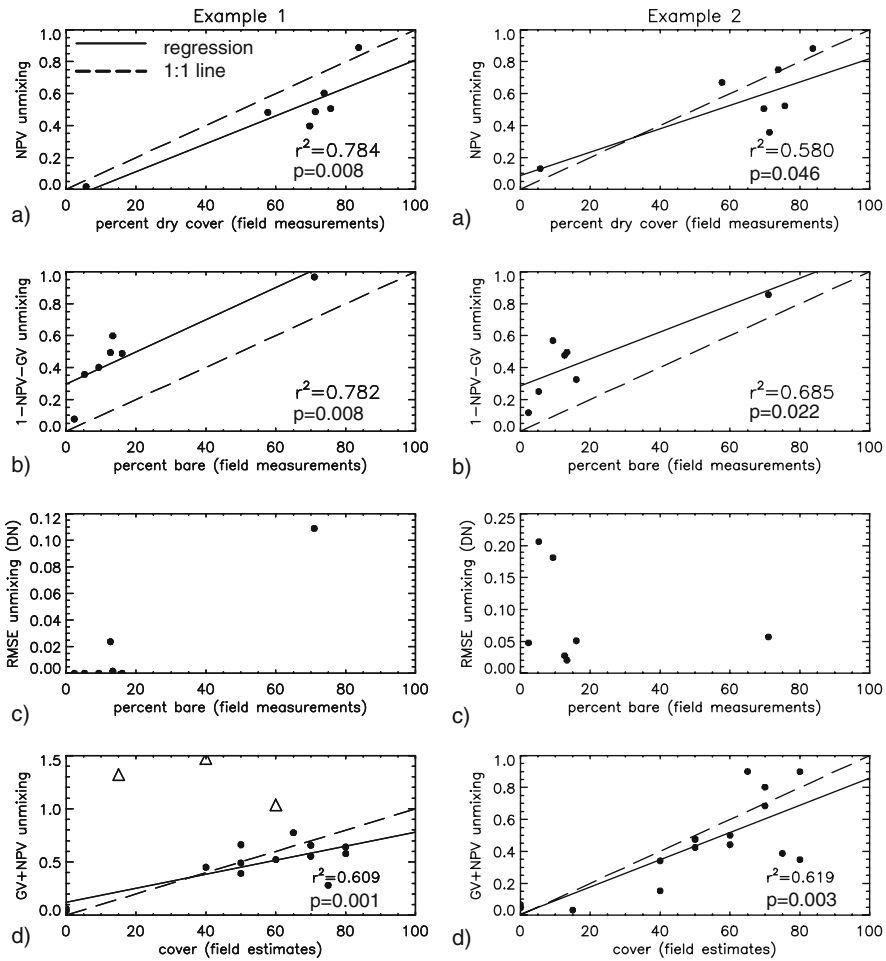


Fig. 6 Regression plots of the field data and SMA results for two examples as shown in Fig. 5 (see text for more details). The triangles in the Example 1 (d) represent polygons where $NPV + GV > 1$ indicating that the spectral mixture was insufficient and thus were these points left out of the regression

more reliable estimates. However, the correlations and point distributions are very promising, however there is a common bias for each example in the bare-ground estimates ($1-NPV-GV$).

The RMSE values are low for both plots and show that the SMA is working well for both Examples over the 7 black soil field sites.

Visual cover estimates, performed over different soil types, were used to establish an indication of robustness of the SMA results over the whole study area as shown in (Fig. 6d) – the field measurement sites were not included. Example 1 shows the higher r^2 values (Fig. 6a) for field measurements, but Example 2 shows higher

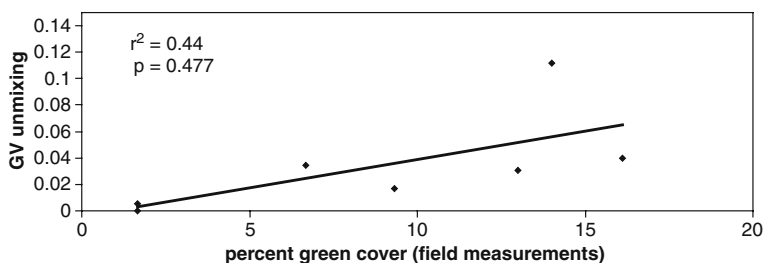


Fig. 7 Regression plot of the field estimates in green cover and the GV estimates from SMA (SMA Example 1)

correlations for the visual estimates (Fig. 6d). One physical explanation might be that in Example 1 a shade endmember was used, which seems to be beneficial in the SMA, particularly over black soils, while in Example 2 this spectrum was replaced with a red soil spectrum to better represent different soil conditions, especially where there were red soils. In the SMA result for Example 2 none of the sites were modelled with $NPV + GV > 1$ (see Fig. 5d) which indicates a better overall solution. The visual estimates can only be seen as a proxy for true ground cover and inherit potential (human) errors.

The green vegetation component is important for ground cover estimation. Figure 7 shows a regression plot for the field measured percent of green cover against GV from the SMA (Example 1). The relatively low correlation for GV with 6 of the 7 data points being below 4% is expected, as the mapped signal is weak given a low signal to noise ratio (see also Fig. 2).

More GV measurements are needed in the higher greenness range and more cover values need to be obtained in further field campaigns, possibly during a wet season, as the current field data were obtained in pastoral areas during a dry period with very little greenness (i.e. the representation in Fig. 7 is relatively accurate).

The bare-ground plots from Fig. 6 were also plotted for the current state wide bare-ground product, as described in (Scarth et al. 2006), as shown in Fig. 8.

The existing NRW bare ground product (Bi3) product does not perform well with the field data, but black soils have not been represented adequately in the training

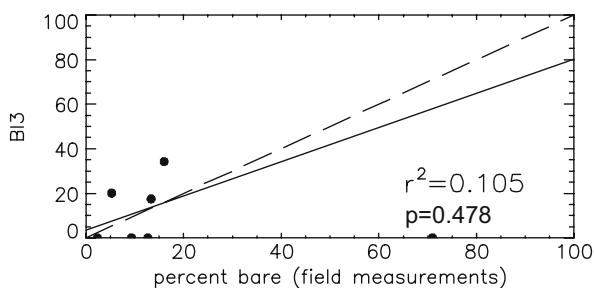


Fig. 8 Same as above for the existing NRW bare-ground product Bi3 (Scarth et al. 2006) generated as a state-wide product

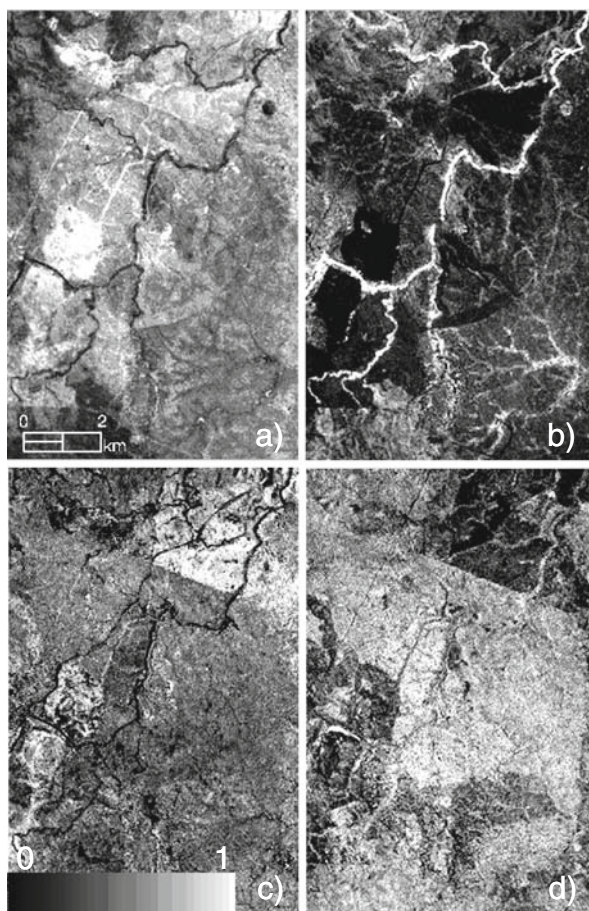


Fig. 9 (a) Landsat Channel 1 and the abundance channels for (b) GV, (c) NPV and (d) 'red' soil for the image subset of the study area as indicated in Fig. 3 of an SMA result (Example 2)

dataset for the current regression based approach of bare-ground mapping (Scarath, 2008 pers. comm.). The field data shown here are not yet included in the Bi3 dataset, but will be included in an attempt to improve the model performance in black soil areas.

Figure 9 displays a map of GV, NPV and a soil abundance for the study region (see Fig. 3 in comparison). The grayscale values represent the percentages of each cover fraction per pixel (see Eq. (1)).

Discussion and Conclusion

The SMA runs show high correlation coefficients for bare-ground estimates and field transect measurements with $r^2=0.78$ and 0.69 . The results need confirmation with more field data as only 7 field measurements were used in the data validation;

all of which were obtained over black soils. The bare-ground and dry cover information over these sites seems to be relatively reliable, but needs further examination over other soil types. The study area of $\sim 80 \times 120 \text{ km}^2$ is large enough to represent certain heterogeneity, but the transferability of this approach to a state-wide product needs to be further evaluated. This will be done in conjunction with existing regression based approaches to evaluate the best representation of bare-ground for the state-wide product.

SMA layers provide physically based information for different abundance channels, which are a rich source for further analysis (e.g. a land cover classification or soil mapping).

Techniques to optimise the computing time and to find the 'ideal' set of endmembers in e.g. a sphere around 'good spectra' from which endmembers for a second iteration could be extracted might improve the overall performance and efficiency.

Only one GV spectrum was used in all iterations, which was image derived from densely vegetated agricultural areas. The question of scaling arises for such a spectrum to be representative of Australian native vegetation. A pure vegetation endmember (e.g. 100% greenness) needs to be defined in this environment.

Future work will include the use of a Landsat time series from the NRW satellite archive to monitor changes in ground-cover over time.

Acknowledgements The authors would like to thank Jeff Milne (formerly with NRW, Indooroopilly), Gorge Bourne and Cameron Dougall (NRW, Emerald) for their help and useful comment during the fieldwork and thereafter.

References

- Adams, J.B., Sabol, D.E., Kapos, V., Filho, R.A., Roberts, D.A., Smith, M.O., and Gillspie, A.R. (1995). Classification of Multispectral Images Based on Fractions of Endmembers: Application to Land-Cover Change in the Brazilian Amazon. *Remote Sensing of Environment*, 52, 137–154
- Adams, J.B., Smith, M.O., and Johnson, P.E. (1986). Spectral Mixture Modelling: A New Analysis of rock and Soil Types at the Viking Lander 1 Site. *Journal of Geophysical Research*, 91, 8098–8112
- Armston, J.D., Danaher, T.J., Goulevitch, B.M., and Byrne, M.I. (2002). Geometric correction of LANDSAT MSS, TM, and ETM+ imagery for mapping of woody vegetation cover and change detection in Queensland. In, *11th ARSPC conference*. Brisbane
- Brady, W.W., Mitchell, J. E., Bonham, C.D., and Cook, J.W. (1995). Assessing the Power of the Point-Line Transect to Monitor Changes in Plant Basal Cover. *Journal of Range Management*, 48, 187–190
- Cihlar, J. (2000). Land cover mapping of large areas from satellites: status and research priorities. *International Journal of Remote Sensing*, 21, 1093–1114
- Danaher, T. (2002). An empirical BRDF correction for LANDSAT TM and ETM+ imagery. In, *11th Australasian Remote Sensing and Photogrammetry conference*. Brisbane: ARSPC
- de Vries, C., T., D., Denham, R., Scarth, P., and Phinn, S. (2007). An operational radiometric calibration procedure for the Landsat sensors based on pseudo-invariant target sites. *Remote Sensing of Environment*, 107, 414–429
- García-Haro, F., Gilabert, M., and Meliá, J. (1996). Linear spectral mixture modelling to estimate vegetation amount from optical spectral data. *International Journal of Remote Sensing*, 17, 3373–3400

- Gill, T., and Phinn, S. (2008). Estimates of bare ground and vegetation cover from Advanced Spaceborne Thermal Emission and Reflection Radiometer (ASTER) short-wave-infrared reflectance imagery. *Journal of Applied Remote Sensing*, 2, 023511
- Hill, J. (2000). Assessment of Semiarid Lands: Monitoring Dryland Ecosystems through Remote Sensing. In R.A. Meyers (Ed.), *Encyclopedia of Analytical chemistry - Instrumentation and Applications*. Encyclopedia of Analytical chemistry, Chichester (pp. 8769–8794)
- Hurcom, S.J., and Harrison, A.R. (1998). The NDVI and spectral decomposition for semi-arid vegetation abundance estimation. *International Journal of Remote Sensing*, 19, 3109–3125
- Jensen, J.R. (1996) Introductory Digital Image Processing: A Remote Sensing Perspective. 2nd Edition. New Jersey. Prentice-Hall
- Karfs, R., Chilcott, C., and Scarth, P. (2007). Land monitoring information for grazing management. In, *Northern Beef Research Update Conference*
- Roberts, D.A., Batista, G.T., Pereira, J.L.G., Waller, E.K., and Nelson, B.W. (1998). Change Identification Using Multitemporal Spectral Mixture Analysis: Eastern Amazonia. In, *Remote Sensing Change Detection: Environmental Monitoring, Methods and Applications*, Ann Arbor Press, Chelsea, MI (pp. 137–161)
- RSI (2007). ENVI Online Help, Version 4.3.
- Scarth, P., Byrne, M., Danaher, T., Henry, B., Hassett, R., Carter, J., and Timmers, P. (2006). State of the paddock: monitoring condition and trend in groundcover across Queensland. In, *13th Australasian Remote Sensing Conference, November 2006.*. Canberra
- Schmidt, M., and Schoettker, B. (2004). Sub-pixel analysis in combination with knowledge based decision rules to optimise a land cover classification. In R. Goossens (Ed.), *Remote Sensing in Transition* (pp. 53–59). Rotterdam: Millpress
- Smith, M.O., Ustin, S., Adams, J.B., and Gillespie, A.R. (1996). Vegetation in deserts I: A regional Measure of Abundance from Multispectral Images. *International Journal of Remote Sensing*, 17, 1031–1058
- Tucker, C.J. (1979). Red and photographic infrared linear combinations for monitoring vegetation. *Remote Sensing of Environment*, 8, 127–150
- Van Leeuwen, W., and Huete, A.R. (1996). Effects of Standing Litter on the Biophysical Interpretation of Plant Canopies with Spectral Indices. *Remote Sensing of Environment*, 55, 123–138

Vineclipper: A Proximal Search Algorithm to Tie Gps Field Locations to High Resolution Grapevine Imagery

A. Hall and J. Louis

Abstract Grapevine canopy characteristics as determined from remotely sensed imagery have been shown to be effective in forecasting grape composition parameters that can be used to estimate the quality of wine made from those grapevines. Maps of canopy characteristics are therefore valuable tools for precision viticulture practice. In a case of extracting reflectance data at the scale of individual vines from vineyard imagery with a pixel resolution of ca. 0.5 m, simple use of sample point location data provided by a GPS (the GPS points) projected onto a georectified image proved too inaccurate for the desired analysis. At the individual vine scale, the spatial error between the GPS point and the corresponding location in a georectified image was great enough to result in clearly incorrect pixels being identified as representative of the sample grapevine canopy. The sample GPS point locations were, however, sufficiently close to the correct vine canopy in the georectified image to act as a seed point for a computer search algorithm.

The VineClipper algorithm was developed to identify a more representative set of vine pixels using the sample GPS points as seed points in a proximal spatial search. The procedure automatically recognises vine rows in an image close to each GPS point and then determines the local central line of the vine row closest to the GPS point location. The central point of the canopy pixels selected to correspond to the GPS field data point was selected as the point on the centre line closest to the GPS point. Reflectance data of the pixels surrounding this point were then extracted from inside a rectangle (equivalent to the area of one vine) aligned with the row direction. The methodology and the novel algorithm that was developed to automatically perform this procedure are presented.

Interested readers may obtain a copy of the algorithm code or further details by contacting Andrew Hall (email: ahall@csu.edu.au).

A. Hall (✉)

National Wine and Grape Industry Centre, School of Environmental Sciences,
Charles Sturt University, Wagga, NSW 2678, Australia
e-mail: ahall@csu.edu.au

Introduction

High levels of spatial variability in fruit composition and yield are common to many vineyard blocks, presenting management challenges to viticulturists (Bramley and Proffitt 1999, Bramley 2001, 2005). The use of spatial technologies in viticulture research and industry is now common (Proffitt et al. 2006, Reynolds et al. 2007, Tisseyre et al. 2007). Similarly, significant within-block spatial variability in canopy vigour, as quantified by leaf area index (LAI), calculated as leaf area per unit ground area, has been observed (for example Sommer and Lang 1994, Nemani et al. 2001, Hall et al. 2008). Due to the modification of the light and temperature microclimate in the fruiting zone, vine canopy vigour is a major variable influencing grape composition and yield (e.g. Smart 1985, Smart et al. 1988, Dry 2000, Bergqvist et al. 2001, Spayd et al. 2002). It follows therefore that the spatial pattern of variability of canopy vegetation should correlate to the spatial pattern of variability in fruit composition and yield. Quantitatively assessing grapevine canopy characteristics on the ground is time consuming and unlikely to result in producing information that is more valuable than the cost of its procurement. Remote sensing technologies, on the other hand, offer rapid assessment of vegetative characteristics of large vineyard areas (Lamb et al. 2001, Hall et al. 2002, Johnson et al. 2003), enabling the opportunity to produce inferred maps of grape quality at a relatively low expense. The key to enabling such inferences is developing an understanding of the link between remotely sensed imagery of vineyards and actual vine canopy characteristics.

Recent work has shown that differences in vine performance can be identified from remotely sensed data from which normalised difference vegetation index (NDVI) images have been calculated. The possibility of determining prospective wine quality for vineyard regions based on remotely sensed data through the relationship between canopy and fruit composition has been indicated by Johnson et al. (1998, 2001). More attention is now being paid to the relationship between NDVI imagery and measures of vine canopy vigour such as LAI. Using 4-m resolution IKONOS satellite imagery, significant correlations have been achieved between NDVI and both canopy LAI and leaf area per vine (m^2 per vine) in multiple vineyards (Johnson et al. 2001, 2003, Johnson 2003). As well as the 4-m resolution employed by IKONOS, Dobrowski et al. (2003) used 6-m resolution NDVI imagery to estimate dormant pruning weights over consecutive growing seasons. Lamb et al. (2004) used NDVI imagery (initially 1-m resolution but sub-sampled to 5-m resolution) to estimate phenolics and colour levels in red winegrapes. Common to all the above-mentioned work is the fact that the pixel size is much larger than individual vines. If high spatial resolution imagery, where the pixel size is smaller than the individual grape vine canopies, is used then a number of pixels can be identified to determine the canopy characteristics. The higher degree of accuracy in describing canopy characteristics potentially allows more accurate forecasts of fruit quality and yield down to the individual vine scale.

For studies in precision viticulture at the individual vine scale, identifying the location of a sample vine in a remotely sensed image is necessary if an accurate analysis of the influence of canopy density on fruit quality is to proceed. The Vinecrawler algorithm (Hall et al., 2003) was developed to assess vine canopy

characteristics for individual grapevines from high spatial resolution imagery. The use of this algorithm was limited for use in relatively small uniformly straight vineyards. In larger vineyards, in which there are many thousands of vines or where the rows are not uniformly straight, the mechanism of Vincrawler becomes unwieldy and requires a high degree of user intervention. Vincrawler also produces data for the whole vineyard, using unnecessary processing time when only a small proportion of sample vines may be required. This paper presents the methodology used in a focused approach to collect canopy data from images, delivering increased efficiency and results that could be validated with a greater degree of confidence. VineClipper has been developed in response to a specific research problem, and its use is intended for research purposes where there are a number of sample vines within a vineyard for which information from imagery is required. Nevertheless, the algorithm can be applied to whole vineyards if all vine locations are included in the input GPS vine location file. An automated or semi-automated procedure for estimating the locations of all vines in a vineyard block based on the coordinates of a few corner locations could rapidly provide the vine location data. With all individual vine canopies characterised, commercial precision viticulture practice can potentially be applied to whole vineyard blocks.

GPS locations collected with a modern real-time kinematic differential GPS system is accurate in 3 dimensions to within 0.02 m (Proffitt et al. 2006). The spatial error in data collected with a modern GPS is therefore negligible when working with imagery that has a spatial resolution of 0.5 m. The main cause of error between GPS locations and corresponding locations in imagery is due to geometric error introduced by the remote sensing system. Geo-rectification of the imagery is usually performed using polynomial models to warp the imagery to minimise this spatial distortion (Jensen 2005). Polynomial models are calculated using a number of ground control points (GCPs), the coordinates of the GCPs are acquired using an accurate surveying method, and the locations of the GCPs are chosen so that they can be easily identified in imagery. Although image warping decreases spatial distortion and provides map coordinates for imagery, it does not produce perfect results in all locations within an image. Differences between the map coordinates in the image and actual coordinates on the ground remain (e.g. Hughes et al. 2006, Tisseyre et al. 1999). Having optimised a geo-rectification procedure on imagery with a spatial resolution of 1 m, Zhou and Li (2000) achieved an average accuracy of 3 m for checkpoints (not GCPs) used to assess the geo-rectification accuracy across whole images. In the case of imagery with a 0.5 m spatial resolution (as used in this paper), average geo-rectification accuracy can be reasonable assumed to be no better than 1.5 m. With a row spacing of 3.6 m in the study vineyard, a 1.5 m spatial error is great enough to place GPS points well away from the grapevine canopy in an image. Figure 1 illustrates the mismatch that can occur between sample sites and vine locations. Extraction of pixels at these locations delivers a set of pixel values that do not represent the vegetative characteristics of the vines in the vicinity. To produce a more representative set of pixels for each sample location, a procedure was developed whereby the central line of the vine row closest to the GPS point was identified. The central point of the pixels to be extracted to represent the vine for each GPS point in the image was selected as the point on the central line

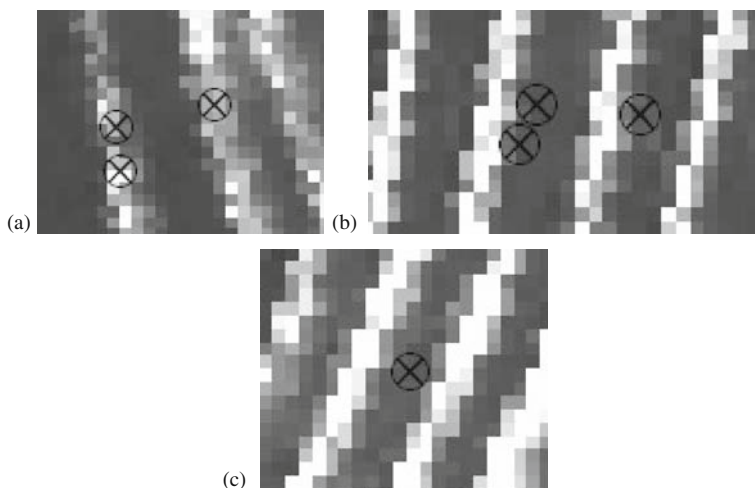


Fig. 1 Georectified NDVI image of vineyard sections with vine sample locations (at the point of the intersection of the crosses). (a) Sample locations at vine row centre. (b) Sample locations at vine row edges. (c) Sample location in between two adjacent vine rows

closest to the GPS point. Reflectance data of the pixels surrounding this point were then extracted from inside a rectangle aligned with the row direction equivalent to the size of one vine. This paper describes the method developed to perform these operations.

Methods

Spatial Data Collection

This work formed part of a large precision viticulture study involving a remote sensing component to quantitatively characterise the canopy characteristics of grapevines. Multispectral images of an area of a commercial vineyard in the Eden Valley of South Australia were acquired between 2003 and 2006. Figure 2 contains an NDVI image of the vineyard. The site is a machine-pruned block of Riesling on a single wire trellis system planted in 1972. The vines are arranged in several smaller sub blocks on topographically varied terrain. Generally, there is a space of 3.6 m between rows, and individual vines are separated by 2.1 m along the row, although the irregular nature of the vineyard means that this is not always the case. Trellises follow the contours of the topography resulting in an irregular winding pattern of vine rows.

Steps of the VineClipper Algorithm

While reading the text, it will be useful to refer to the diagram containing the geometry (Fig. 3). The major steps of the VineClipper algorithm are presented in Fig. 4.

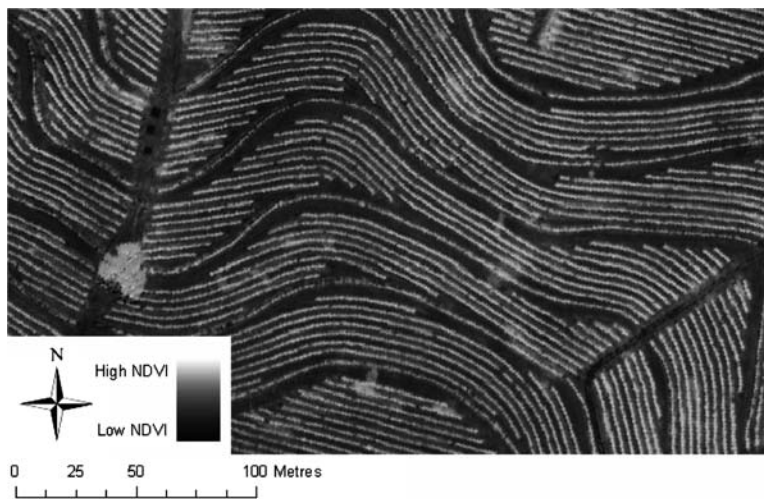


Fig. 2 Section of NDVI image of study site

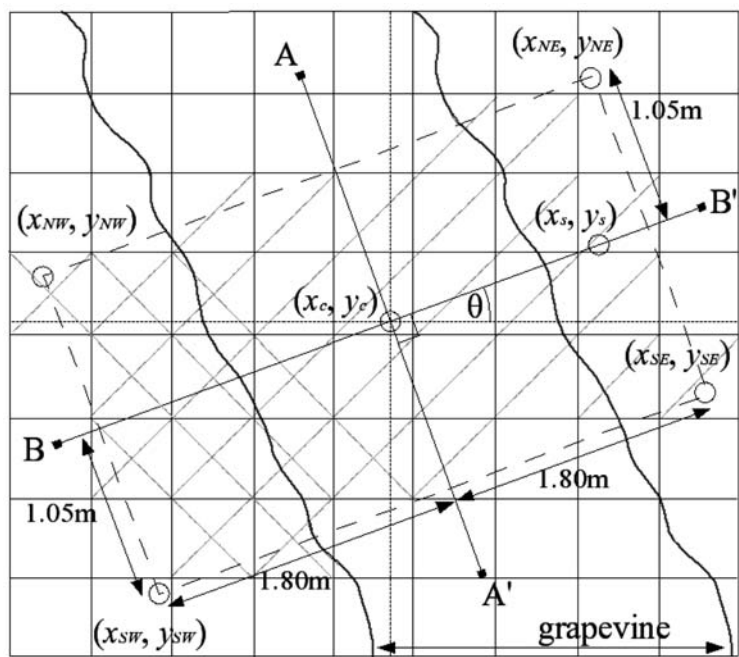


Fig. 3 Identification of sample vine pixels and related geometry. Line A–A' is the centre line of the vine row and line B is perpendicular to line A and intersects the centre point (x_c, y_c) . The grid represents image pixels. If the centre point of a pixel lies within the dashed rectangle and has an NDVI value of that pixel is greater than the threshold NDVI, then the pixel is designated as being a representative member of the sample vine

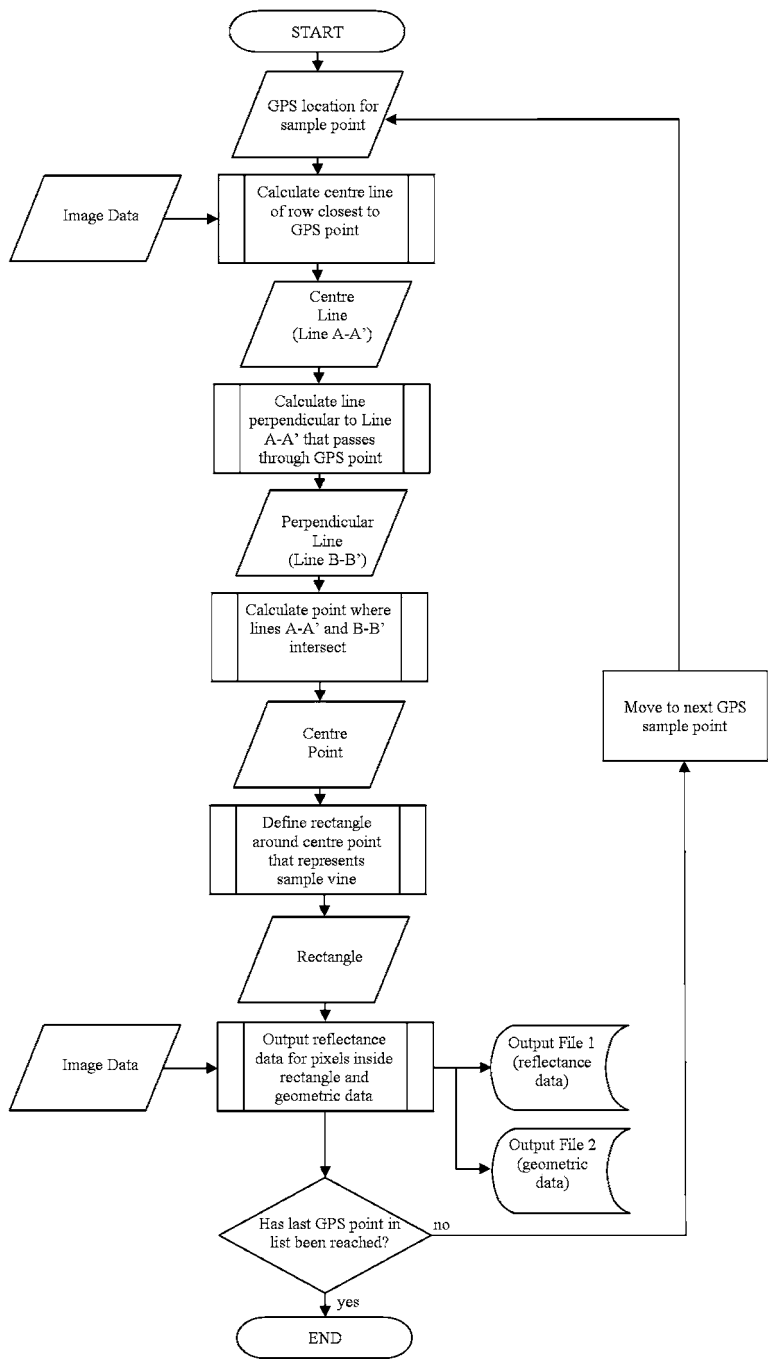


Fig. 4 Flow chart of the major steps of the VineClipper algorithm

Each of the pre-defined process boxes (the boxes bound by two vertical lines) in the flow chart are explained in detail in the following section.

Calculate Centre Line of Row Closest to GPS Point (Line A–A')

1. The pixels with coordinates within a 5.4 m (1.5 times the vine row spacing) by 5.4 m square centred on the starting coordinate (x_s, y_s) are extracted.
2. The extracted pixels' NDVI values are interpolated to a 40 by 40 grid using linear interpolation (Fig. 5 (Left)).
3. The interpolated grid is then converted to a binary image: the highest 20% of NDVI values within the grid are given the value 0; the remaining pixels within the grid are given the value 1 (Fig. 5 (Right)).
4. All vine pixels within a 0.9 m (one quarter the vine separation) radius of the starting coordinate (x_s, y_s) are identified. A region growing algorithm continues to locate further vine pixels that lie within a 0.9 m radius of any of the previously identified vine pixels.
5. The spatial range in the x and y directions of the pixels identified in step 4 are determined.
6. A linear regression model is applied to the x location values and the y location values. If the range is greater in the x direction, then the model used is

$$y = m_A x + c_A. \quad (1)$$

Equation (1) represents line A–A', and can be defined as the centre line of the vine row closest to the given point, oriented in the direction of the row in the region of pixels determined in step 4. If the range is greater in the y direction, the equation representing line A–A' is determined with a method that uses the model,

$$x = m_m y + c_m. \quad (2)$$

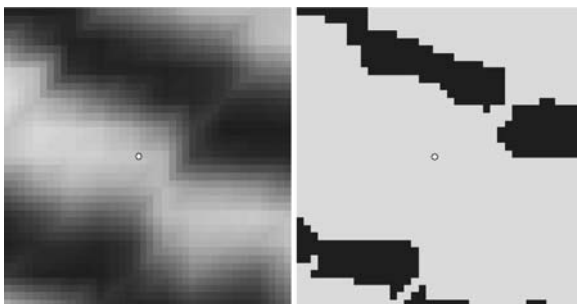


Fig. 5 (Left) Linear interpolation to a 40 by 40 grid using of the extracted pixels' NDVI values. (Result after Step 2.) The sample point (x_s, y_s) is represented by the circle at the centre of the image. (Right) Binary version of image in Fig. 5 (Left). The highest 20% of NDVI values have been assigned the value 1; the remaining pixels have been assigned the value 0. (Result after Step 3.) The sample point (x_s, y_s) is represented by the circle at the centre of the image

To produce a model similar to Eq. (1) m_A and c_A are calculated using

$$m_A = \frac{1}{m_m} \quad (3)$$

and

$$c_A = \bar{y} - m_A \bar{x}, \quad (4)$$

where (\bar{x}, \bar{y}) = the centroid of pixels identified in step 4.

Closest Point on the Centre Line of a Vine Row to a Given Coordinate (Vine Centre Point) is Located

Line B–B' is defined as the line perpendicular to A–A' that intersects the sample point (x_s, y_s) , i.e.

$$y = m_B x + c_B, \quad (5)$$

where

$$m_B = \frac{-1}{m_A} \quad (6)$$

and

$$c_B = y_s - m_B x_s. \quad (7)$$

Where Lines A–A' and B–B' intersect is the vine centre point (x_c, y_c) , where

$$x_c = \frac{c_A - c_B}{m_B - m_A} \quad (8)$$

and

$$y_c = m_A x_c + c_A. \quad (9)$$

The Pixels to be Used Around the Vine Centre (Sample Vine Pixels) are Identified

The centre points of the pixels extracted to describe the characteristics of the canopy of the vine are contained within a polygon centred at (x_c, y_c) . The rectangle is oriented in the cross-vine direction of B–B' (θ), i.e.

$$\theta = \tan^{-1} m_B \quad (10)$$

The four nodes of the rectangle are calculated using the following four equations.

$$(x_{NE}, y_{NE}) = (x_c + 1.8 \cos \theta - 1.05 \sin \theta, y_c + 1.8 \sin \theta + 1.05 \cos \theta) \quad (11)$$

$$(x_{SE}, y_{SE}) = (x_c + 1.8 \cos \theta + 1.05 \sin \theta, y_c + 1.8 \sin \theta - 1.05 \cos \theta) \quad (12)$$

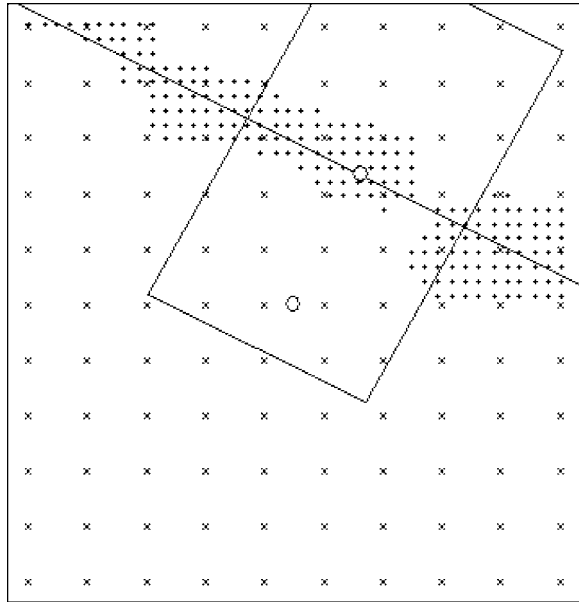
$$(x_{NW}, y_{NW}) = (x_c - 1.8 \cos \theta - 1.05 \sin \theta, y_c - 1.8 \sin \theta + 1.05 \cos \theta) \quad (13)$$

$$(x_{SW}, y_{SW}) = (x_c - 1.8 \cos \theta + 1.05 \sin \theta, y_c - 1.8 \sin \theta - 1.05 \cos \theta) \quad (14)$$

The numerical parameters in Eqs. (11–14) are derived from the row and vine spacing. The area identified is a rectangle 2.1 m by 3.6 m, which is the mean distance between vines and the mean distance between rows, respectively. Figure 6 illustrates the rectangle calculated for the image region shown in Fig. 5.

Once the rectangle has been defined, all pixels that lie within the rectangle are identified from the image and recorded in a table that forms the main output file. The main output file (1) contains information about each pixel within each rectangle identified by VineClipper. A second output file (2) contains data on the new coordinates for each sample vine as well as geometric information used in the calculations.

Fig. 6 Rectangle calculated for the binary image region shown in Fig. 5 (Right). The centre points of the interpolated pixels are shown as +. The centre points of the original pixels of the NDVI image are shown as ×. The sample point (x_s, y_s) is represented by the circle at the centre of the Fig. The corrected sample point (x_c, y_c) is represented by the circle at the centre of the rectangle. Each NDVI pixel of the original image that lies within the rectangle is recorded as being part of the sample vine



VineClipper Output Data

The data in Output File 2 is used to check the algorithm function, provides the corrected coordinates of the sample location, and includes data that can be used in further analyses concerning the effects of row direction (i.e. orientation to the Sun) on vine performance. An r^2 value for the goodness of fit obtained for Line A–A' to the interpolated local image in Step A6 is also recorded to provide an indication of how well this step was executed. A low r^2 value indicates a possible problem with the line fitting procedure, requiring a visual check.

The data in Output File 1 contains the reflectance values for each of the pixels identified as being in the rectangles defined for each sample vine. There are, on average, 23 pixels returned per sample vine. At this point, canopy descriptors can be calculated. Hall et al. (2003) calculated six different canopy descriptors using the output of their VineCrawler algorithm. Although the output of VineClipper is subtly different, similar descriptors to those calculated for VineCrawler can be calculated. Simple algorithms have been developed to read Output File 1 and return a number of vine canopy descriptors. For example, the mean of the NDVI values is calculated for the pixels that have identical Vine IDs, resulting in single NDVI values for each sample vine.

Conclusions

A procedure for tying GPS field location data to grapevine sample locations in high spatial resolution imagery has been developed. Imagery is first converted into a single number vegetation index (the NDVI). Around the local area of each GPS field location the NDVI pixels are re-sampled to a higher spatial resolution. A thresholding procedure is used to separate non-vine and vine re-sampled pixels. The re-sampled vine pixel closest to the GPS field location is identified, and a region grow technique is applied to identify all re-sampled pixels that are likely to be part of the same vine row as the first re-sampled vine pixel identified.

The closest centre point to the GPS field location of a vine row is then located, and this is used as the basis for defining a rectangle that encompasses the area of the image of the sample vine intended to be recorded by the GPS operator. The reflectance values of the image pixels within the rectangles defined for the sample vines are returned by the algorithm in an output file. Geometric information about the row direction is additionally returned that provides data for use in analyses involving vine – sunlight interactions.

Preliminary comparisons of the extracted NDVI data with viticultural data collected on the ground reveal some significant correlations consistent with those outlined by Smart (1985) and suggested by Hall et al. (2002). These correlations go some way to demonstrating the ability of the algorithm to extract the pixels that do correspond with the sample vines. A full analysis of these data is underway. In addition to the application of VineClipper to the purpose described in this paper,

the algorithm, or variations of the algorithm, could be used where similar automatic pixel extraction is required. If particular objects can be identified in a similar way to how grapevine canopy can be identified from a background of senesced or sparse vegetation, then VineClipper (or a modified version VineClipper) can be used to extract reflectance information of objects in georectified imagery that does not match up exactly with the location coordinates of those objects. Reflectance information from linear image features that can be split into discrete elements such as rivers, roads or geological features may be extracted with VineClipper. In addition, by using a slightly modified version of VineClipper, objects that are not part of linear features may be identified, and the pixels of those object extracted for analysis, such as individual trees in an orchard or forestry plantation.

Acknowledgements This work was supported by Australia's grapegrowers and winemakers through their investment body the Grape and Wine Research and Development Corporation, with matching funds from the Federal government, and by the Commonwealth Cooperative Research Centre Program. The work was conducted by the National Wine and Grape Industry Centre, Charles Sturt University, and forms part of the research program of the Cooperative Research Centre for Viticulture. The authors appreciate ongoing support provided by Charles Sturt University's Spatial Analysis Unit (CSU-SPAN).

References

- Bergqvist, J., Dokoozlian, N., Ebisuda, N., 2001. Sunlight exposure and temperature effects on berry growth and composition of Cabernet Sauvignon and Grenache in the central San Joaquin Valley of California. *American Journal of Enology and Viticulture*, 52(1), 1–7.
- Bramley, R., Proffitt, A.P.B., 1999. Managing variability in viticultural production. *The Australian Grapegrower and Winemaker*, 427, 11–16.
- Bramley, R., 2001. Progress in the development of precision viticulture – Variation in yield, quality and soil properties in contrasting Australian vineyards. In: *Precision tools for improving land management*. Currie, L.D. and Loganathan, P (Eds). Occasional report No. 14. (Fertiliser and Lime Research Centre, Massey University, Palmerston North), pp. 25–43.
- Bramley, R.G.V., 2005. Understanding variability in winegrape production systems – 2. Within vineyard variation in quality over several vintages. *Australian Journal of Grape and Wine Research* 11(1), 33–42.
- Dobrowski, S.Z., Ustin, S.L., Wolpert, J.A., 2003. Grapevine dormant pruning weight prediction using remotely sensed data. *Australian Journal of Grape and Wine Research*, 9(3), 177–182.
- Dry, P.R., 2000. Canopy management for fruitfulness. *Australian Journal of Grape and Wine Research*, 6, 109–115.
- Hall, A., Lamb, D.W., Louis J., Holzapfel, B., 2002. Optical remote sensing applications in viticulture – A review. *Australian Journal of Grape and Wine Research*, 8(1), 37–47.
- Hall, A., Louis, J.P., Lamb, D.W., 2003. A method for vineyard attribute mapping from high resolution multispectral images. *Computers and GeoSciences*, 29(7), 813–822.
- Hall, A., Louis, J., Lamb, D.W., 2008. Low resolution remotely sensed images of winegrape vineyards map spatial variability in planimetric canopy area instead of LAI. *Australian Journal of Grape and Wine Research*. 14(1), 9–17.
- Hughes, M.L., McDowell, P.F., Marcus, W.A., 2006. Accuracy assessment of georectified aerial photographs: Implications for measuring lateral channel movement in a GIS. *Geomorphology*, 74, 1–16.
- Jensen, J.R., 2005. *Introductory Digital Image Processing: A Remote Sensing Perspective*. (Pearson Prentice Hall, Upper Saddle River, New York.), 526 pp.

- Johnson, L.F., 2003. Temporal stability of an NDVI-LAI relationship in a Napa Valley vineyard. *Australian Journal of Grape and Wine Research*, 9(2), 96–101.
- Johnson, L.F., Bosch, D.F., Williams, D.C., Lobitz, B.M., 2001. Remote sensing of vineyard management zones: Implications for wine quality. *Applied Engineering in Agriculture*, 17(4), 557–560.
- Johnson, L., Lobitz, B., Bosch, D., Wiechers, S., Williams, D., Skinner, D., 1998. Of pixels and palates: can geospatial technologies help produce a better wine? *Proceedings, 1st International Conference on Geospatial Information in Agriculture & Forestry*, Lake Buena Vista, Florida, 2, pp. 469–476.
- Johnson, L.F., Roczen, D.E., Youkhana, S.K., Nemani, R.R., Bosch, D.F., 2003. Mapping vineyard leaf area with multispectral satellite imagery. *Computers and Electronics in Agriculture*, 38(1), 33–44.
- Lamb, D.W., Hall, A., Louis, J., 2001. Airborne remote sensing of vines for canopy variability and productivity. *Australian Grapegrower and Winemaker*, 449a, 89–92.
- Lamb, D.W., Weedon, M.M., Bramley, R.G.V., 2004. Using remote sensing to predict grape phenolics and colour at harvest in a Cabernet Sauvignon vineyard: Timing observations against vine phenology and optimising image resolution. *Australian Journal of Grape and Wine Research*, 10(1), 46–54.
- Nemani, R., Johnson, L., White, M., 2001. Adding science to intuition: Application of remote sensing and ecosystem modelling to vineyard management. *Australian Grapegrower and Winemaker*, 449a, 45–47.
- Proffitt, T., Bramley, R., Lamb, D., Winter, E. (2006) *Precision Viticulture: A new era in vineyard management and wine production*. (Winetitles, Ashford, South Australia), 90 pp.
- Reynolds, A.G., Senchuk, I.V., van der Reest, C., de Savigny C., 2007. Use of GPS and GIS for elucidation of the basis for terroir: Spatial variation in an Ontario Riesling vineyard. *American Journal of Enology and Viticulture*, 58(2), 145–162.
- Smart, R.E., 1985. Principles of vine canopy microclimate manipulation with implications for yield and quality. A review. *American Journal of Enology and Viticulture*, 36(3), 230–239.
- Smart, R.E., Smith, S.M., Winchester, R.V., 1988. Light quality and quantity of fruit ripening for Cabernet Sauvignon. *American Journal of Enology and Viticulture*, 39, 250–258.
- Sommer, K.J., Lang, A.R.G., 1994. Comparative analysis of two indirect methods of measuring leaf area index as applied to minimal and spur pruned grape vines. *Australian Journal of Plant Physiology*, 21, 197–206.
- Spayd, S.E., Tarara, J.M., Mee, D.L., Ferguson, J.C., 2002. Separation of sunlight and temperature effects on the composition of *Vitis vinifera* cv. Merlot berries. *American Journal of Enology and Viticulture*, 53(3), 171–182.
- Tisseyre, B., Ardoin, N., Sevila, F. (1999). Precision viticulture: Precise location and vigour mapping aspects. In: *Precision Agriculture '99: Papers presented at the 2nd European Conference on Precision Agriculture*. Stafford, J.V. (Ed.). (Sheffield Academic Press, Sheffield) vol. 1, pp. 319–330.
- Tisseyre, B., Ojeda, H., Taylor, J., 2007. New technologies and methodologies for site-specific viticulture. *Journal International des Sciences de la Vigne et du Vin*, 41(2), 63–76.
- Zhou, G.Q., Li, R., 2000. Accuracy evaluation of ground points from IKONOS high-resolution satellite imagery. *Photogrammetric Engineering and Remote Sensing*, 66, 1103–1112.

Modelling Weed Distribution Across the Northern Australia Using Very Extensive Transects

C. Hempel, N. Preece, K. Harvey, and J.C.Z. Woinarski

Abstract A Generalised Additive Modelling (GAM) approach is used to predict weed occurrence across the Top End of the Northern Territory, Australia. The availability of new toolsets such as GRASP (Generalised Regression Analysis and Spatial Predictions) and the application of novel GIS variables, including remotely sensed Radiometric data, Infrastructure density (roads and fences) mapping and Climate layers, provide a useful framework for mapping regions at high risk of infestation. An independent set of weed locations provides support for the regional accuracy of the modelling. Infrastructure density is a significant factor in the prediction of weed occurrence in this study. Coastal areas with high levels of infrastructure appear most susceptible to weed infestation, although 8 Biogeographic Regions are considered currently at risk.

Introduction

Relatively small and isolated human populations in the Northern Territory's savannas has allowed for the persistence of very extensive tracts of intact environments. These vast landscapes, however, are subject to increasing infrastructure developments and the related incursion of exotic weeds. Weed data from a very long transect survey have been modelled against GIS derived landscape and climate variables to predict the likely distribution of weeds throughout the Top End. Topics discussed include relating spatial data to weed distribution, alternative modelling techniques, field validation using an independent data set and implications for regional weed management strategies.

The focus of this study is to describe the characteristics of the predicted invaded environments and assess which regions are more susceptible to these weeds to help set broad scale management priorities for habitat protection and invasion control in the Top End (Hobbs and Humphries 1995).

C. Hempel (✉)

Environmental Protection Agency, Queensland Government, Queensland, QLD, Australia
e-mail: craig.hempel@epa.qld.gov.au

Modern regression techniques such as generalised linear models (GLM) and generalised additive models (GAM) are used extensively in all types of ecological research. This popularity is due to their ability to relate the complex, often non-linear, relationships between a species and its environment (Guisan et al. 2002). The integration of such regression analysis with Geographic Information Systems (GIS) helps describe the spatial relationships of species and their environments.

Generalised linear modelling has been used in the Northern Territory to map rare plant distributions in the Victoria River Region (Crane et al. 2006), improve the management of Buffel Grass in Watarrka National Park (Puckey et al. 2007) and develop habitat models for a suite of microchiropteran bat species (Milne et al. 2006).

Current research favours the use of GAM, a semi-parametric version of GLM, with its proven ability to handle highly non-linear and 'non-monotonic' relationships. Using this technique the data themselves determine the nature of the relationship between response and explanatory variables and can be described as data-driven models (Guisan et al. 2002).

A major criticism of this technique is its computational overhead and cumbersome nature in generating predictions from datasets in a GIS environment (Leathwick et al. 2006). Recently software packages designed specifically for GLM and GAM modelling have become available to ecologists, such as GRASP which has been developed in Splus (Lehmann et al. 2004) and R (<http://www.r-project.org/>). In this study we utilise the tools available through the Splus version of GRASP to examine a set of environmental layers which best describe the ecological niche of introduced plants over a region of Northern Australia.

Methods

Study Area

This study comprises the Northern Territory savanna lands north of 18° South latitude, including major coastal Islands. This 'Top End' landscape (~520,000 Km²) is dominated by Eucalypt open woodlands with a dense grassy understorey. The monsoonal climate produces distinct wet and dry seasons, with 90% of annual rainfall occurring between December and March, although the timing and onset of the monsoon season is highly variable (Taylor and Tulloch 1985). There is a marked decline in average annual rainfall from 1900 mm on the Tiwi Islands in the North West to 500 mm in the Southern interior.

Land tenure in this region is predominantly Pastoral leasehold (50%) with large areas of Aboriginal freehold lands (35%). This Top End region remains largely intact, with less than 5% of its area subject to significant landscape modification, although human-caused disturbance is widespread. About 10% of this region is protected under public and private conservation estate. The prevalence and long history of pastoralism has lead to the introduction of exotic plants considered palatable by stock. Extensive burning is a common land management practice during the dry seasons throughout this landscape.

Transect Sampling

Sampling over three extensive transects was undertaken during the late dry season for the years 2001–2004 inclusive. This allowed for the most optimal access along the entire route but did mean that some areas surveyed were previously burnt. Four-wheel drive vehicles were used to traverse pre-determined pathways, often far removed from existing roads or tracks. In some cases transects became discontinuous due to physical and cultural reasons. Over this four year period a total of 1,900 km was surveyed, with the major routes being North-South from Darwin to Mataranka and West-East from Wadeye to Nhulunbuy (Fig. 10).

Track logs and individual weed occurrences were recorded using hand-held GPS. Flora species data were recorded at an average spacing of 2 kilometres over all transects. Records were spaced further apart in uniform environments, but where a weed occurrence was observed or where there was a sharp change in habitat, records were placed closer together.

Plants known to have been introduced to the Top End since pastoralism began are considered weeds. Table 1 lists the names of all weed species recorded in the

Table 1 Weeds observed in Transect Surveys

| Weed species | Common name | Records | Weed classification |
|-----------------------------------|-----------------------|---------|---|
| <i>Acacia nilotica</i> | Prickly Acacia | 4 | Schedule 1 |
| <i>Achyranthes aspera</i> | Chaff Flower | 4 | |
| <i>Andropogon gayanus</i> | Gamba Grass | 3 | Schedule 1 outside and Schedule 2 inside 'Management Zone'. |
| <i>Bidens pilosa</i> | Cobbler's Peg | 1 | |
| <i>Brachiaria mutica</i> | Para Grass | 1 | |
| <i>Calopogonium mucunoides</i> | Calopo | 1 | |
| <i>Calotropis procera</i> | Rubber Bush | 13 | Schedule 2 – south of 16° 30' |
| <i>Centrosema pubescens</i> | Centro | 1 | |
| <i>Hyptis suaveolens</i> | Hyptis | 106 | Schedule 2 |
| <i>Jatropha gossypifolia</i> | Bellyache Bush | 1 | Schedule 2 |
| <i>Macroptilium atropurpureum</i> | Atro | 1 | |
| <i>Mimosa pigra</i> | Giant Sensitive Plant | 10 | Schedule 1 – south of 14° |
| <i>Parkinsonia aculeate</i> | Parkinsonia | 2 | Schedule 2 |
| <i>Passiflora foetida</i> | Wild Passionfruit | 25 | |
| <i>Pennisetum polystachion</i> | Mission Grass | 6 | |
| <i>Senna obtusifolia</i> | Sicklepod | 10 | Schedule 2 |
| <i>Sida acuta</i> | Spiny Head Sida | 1 | Schedule 2 |
| <i>Sida cordifolia</i> | Flannel Weed | 1 | Schedule 2 |
| <i>Sida</i> sp. | | 2 | Schedule 2 |
| <i>Stachytarpheta</i> spp. | Snake Weed | 2 | Schedule 2 – outside town areas |
| <i>Themeda quadrivalvis</i> | Grader Grass | 11 | Schedule 2 |
| <i>Xanthium strumarium</i> | Noogoora Burr | 5 | Schedule 3 |
| | TOTAL | 211 | |

transect surveys. Seventeen of the species identified in the transects are declared as weeds under the Northern Territory's *Weeds Management Act* (Northern Territory Government, 2006). The other species listed are considered to be 'environmental' weeds. From here on these weeds will be referred to collectively as 'savanna weeds'.

Predictor Variable Selection

The selection of an appropriate set of predictor variables requires an understanding of the ecological principles that determine the occurrence of savanna weeds across the Top End landscape. 'Resource' predictors such as rainfall and soil type, 'direct' predictors including temperature variation and 'indirect' predictors such as elevation, population and infrastructure density are all involved in the spread of weeds throughout the Top End.

A total of 21 environmental and anthropogenic variables were used as inputs into the modelling process, these are listed in Table 2. BIOCLIM (Houlder, 2000) was used to create mean annual rainfall, rainfall seasonality, mean annual temperature, minimum temperature (coldest quarter) and maximum temperature (warmest quarter) climate layers. Distance from Drainage/Floodplain and Drainage/Floodplain density were mapped from Series 3 GEODATA hydrography layers (Geoscience Australia 2006). A digital elevation model (DEM) was provided by the Shuttle Radar Topography Mission (Farr and Kobrick 2000). Radiometric thorium, potassium and total count data were sourced from the Northern Territory Geological Survey (Clifton 2004) and used as surrogates for soil fertility.

Continental scale maps of vegetation (Wilson et al. 1990), which was grouped into five broad categories, surface geology (Bureau of Rural Sciences after Australian Geological Survey Organisation 1991) and soil texture (Bureau of Rural Sciences after Commonwealth Scientific and Industrial Research Organisation 1991) were also included as predictor variables. These thematic maps were also used to create an additional composite layer, habitat complexity, which is described as an index calculated from the total number of different soil, geology and vegetation types occurring within a 10 by 10 km neighbourhood (Milne et al. 2006).

Both Distance from population centre and population density were calculated from 2001 Census data (Australian Bureau of Statistics 2002). Distance from infrastructure and infrastructure density were mapped from the combination of fence and road features available in the Series 3 GEODATA infrastructure layers (Geoscience Australia 2006). Broad tenure was created by dissolving the digital cadastral database (DCDB) of the Northern Territory by tenure type and reclassing the output into 4 categories. Distance from coastline was calculated from the Series 3 GEODATA coastline framework.

All predictor variables were resampled using cubic convolution to coincide with a grid representation of the Series 3 GEODATA outline of the Northern

Table 2 Environmental Variables used in Modelling Weed Distribution

| Predictor variables | Acronym | Units |
|---------------------------------------|----------|---|
| Climate and hydrology | | |
| Mean annual rainfall | P12ANNR | millimetres |
| Rainfall seasonality | P15SEAS | Coefficient of variation |
| Minimum Temperature Warmest Period | P05MAXT | Degree celsius |
| Maximum temperature coldest period | P06MINT | Degree celsius |
| Mean annual temperature | P01MNTM | Degree celsius |
| Distance from drainage/floodplain | WATDST | Metres |
| Drainage/floodplain density | WATD25 | Metres within 25 km radius |
| Land and vegetation | | |
| Elevation | ELEV | Metres above sea level |
| Radiometric total count | TC | Scaled 8-bit |
| Radiometric thorium | TH | Scaled 8-bit |
| Radiometric potassium | K | Scaled 8-bit |
| Surface geology | SUFGEOL | Categorical (bedrock; quartz sand; sand, silt, clay and gravel; limestone; duricrust; clay, silt and minor sand) |
| Soil texture | SOIL | Categorical (coarse; medium; fine; cracking; gradational; duplex) |
| Vegetation type | VEG | Categorical (non-eucalypt forest; eucalypt forests and woodlands; low woodlands with tussock grass understorey; low woodlands with hummock grass understorey and grasslands; littoral and floodplain) |
| Habitat complexity | COMPLEX | Index (1–53) |
| Distance from coast | COASTDST | Metres |
| Population and infrastructure | | |
| Broad tenure | TEN4 | Categorical (Built-up; Pastoral; Aboriginal; Reserve) |
| Distance from populated place | POPST | Metres |
| Population density | POP25 | Localities within 25 km radius |
| Distance from infrastructure | INFST | Metres |
| Infrastructure density | INF25 | Metres within 25 km radius |

Territory (clipped to 18° latitude), with a 2 km cell size and a lamberts conformal projection.

GIS was used to attribute all savanna weed locations with values from the 21 predictor variables. Grid cell values with multiple weed sites were included only once as ‘presence’ sites if any one location contained weeds or ‘absent’ if all sites contained no weeds, to reduce the effects of auto-correlation. A site density grid was also created in the GIS to test for auto-correlation in the modelling process.

Univariate Analysis of Spatial Data

A set of histograms presented in Fig. 1 shows the distribution of savanna weeds for each predictor variable or environmental gradient. Weed presence is represented in

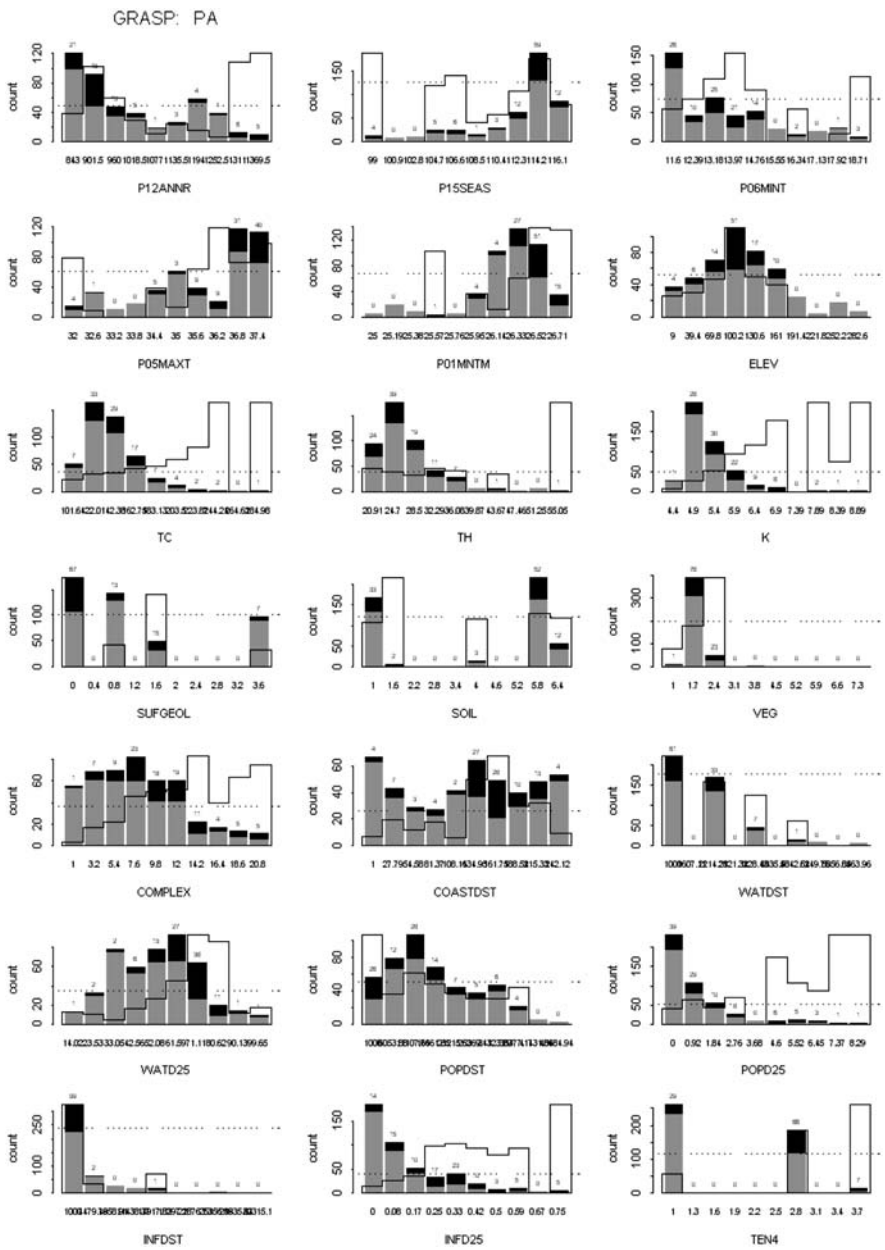


Fig. 1 Histograms showing the distribution of savanna weeds across each predictor variable

dark grey with a number above each bar. Absence observations are represented in light grey. The dashed line gives the overall average proportion of observations, with the solid line representing the proportion of presence observations in comparison to the total.

Multivariate Analysis of Spatial Data

Multivariate statistics such as Principal Component Analysis (PCA) and Cluster Analysis (CA) can be used to tease out relationships between environmental layers using information from presence observations (van Strien 2007). Results from PCA show those environmental gradients with high information content. CA results can be described using a dendrogram in which related environmental gradients are grouped together into clusters. Figure 2 shows outputs from both PCA and CA analysis of selected input variables.

Generalised Additive Modelling Trials using GRASP

The GRASP method contains many functions exploring, modelling and interpreting spatial predictions of species/environment relationships. The following parameters were set for all modelling runs:

- A maximum acceptable correlation between any pair of input variables set to 0.8 (See Fig. 3)
- P limit for tests set to 0.05.
- Stepwise model selection in both directions.
- 4 degrees of freedom.
- Minimum model contribution of 5%.

GRASP offers six different statistical tests for selection of model parameters:

1. AIC: Akaike Information Criteria.
2. BIC: Bayesian Information Criteria.
3. F: An f test is used to test whether predictors are significant.
4. CHI: A Chi Squared test is used.
5. CROSS: A cross validation method is used at each step of a BIC model. Parameters that present the highest cross-validation statistics are kept.
6. BRUTO: An adaptive back-fitting procedure that optimises the degree of smoothing for each variable (Leathwick et al. 2006).

Spatial models predicting savanna weed occurrence across the Top End were run using all 6 statistical tests. All models were evaluated according to goodness of fit as described using the proportion of explained deviance (Crawley 1993) and by plotting random subsets of model predictions against observed data using receiver operating characteristic (ROC) analysis and measuring the area under the curve (Fielding and Bell 1997).

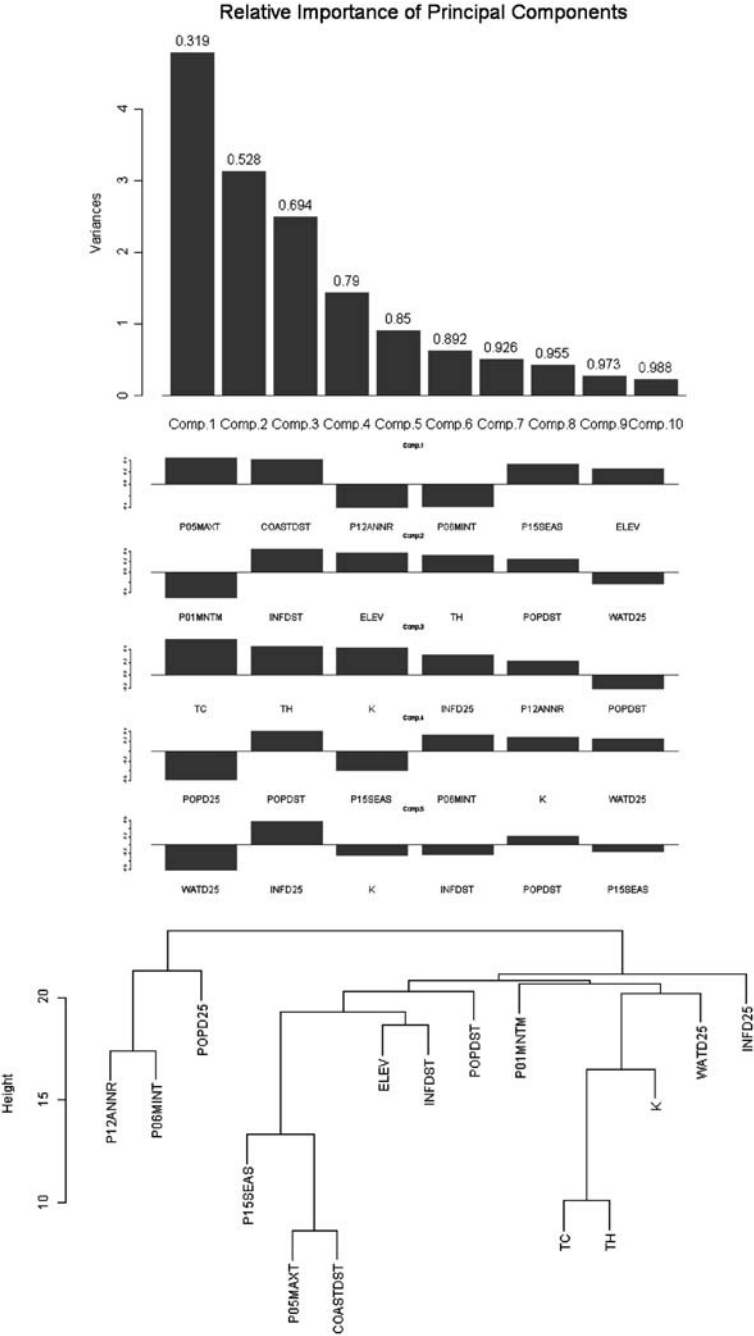


Fig. 2 Principal Component and Cluster Analysis of selected predictor variables

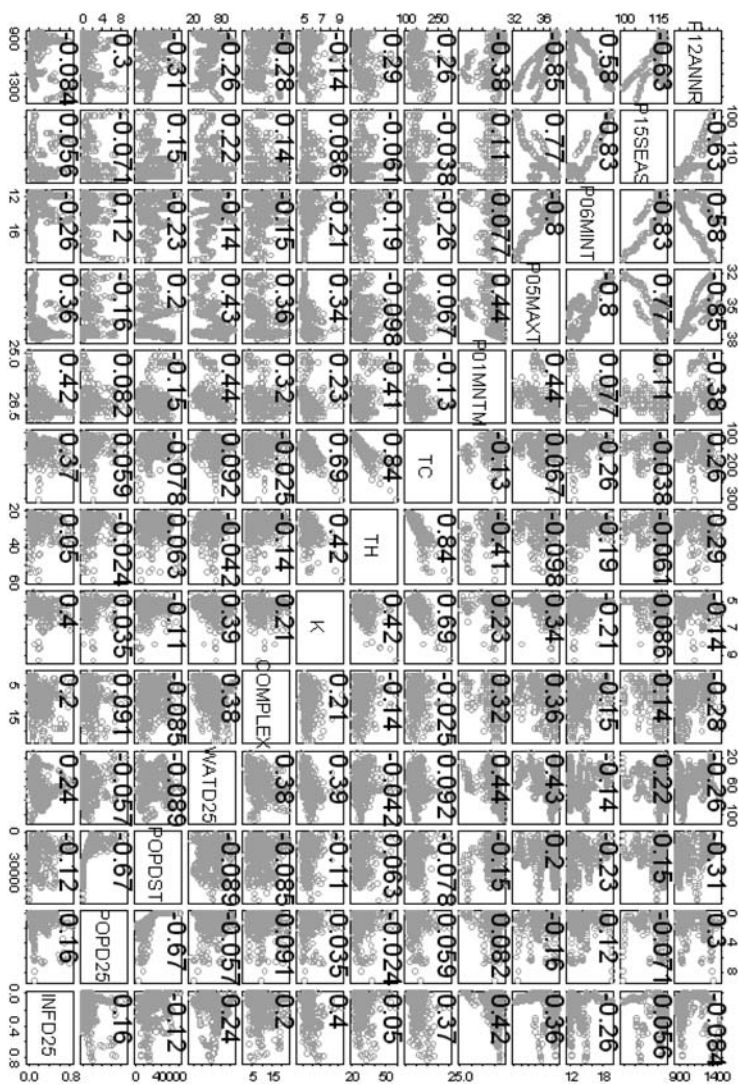


Fig. 3 Correlation co-efficient biplots for all predictor variables

Results

Models

Table 3 shows robust internal model performances, with explained deviance ranging from 0.25 to 0.41 and the area under the ROC curve not moving below 0.8. Three of the models (AIC, CHI and F TEST) selected identical predictor variables and shared an explained deviance of 0.4. The BIC selected model was able to predict 25%

Table 3 Internal Model Performance

| Model | n | null.dev | resid.dev | expl.dev | df.residual | ROC | cvROC | COR | cvCOR |
|--------|-----|----------|-----------|----------|-------------|------|-------|------|-------|
| AIC | 461 | 487.27 | 292.25 | 0.40 | 436.30 | 0.90 | 0.85 | 0.67 | 0.56 |
| BIC | 461 | 487.27 | 365.87 | 0.25 | 452.08 | 0.84 | 0.82 | 0.52 | 0.48 |
| BRUTO | 461 | 487.27 | 326.43 | 0.33 | 450.77 | 0.87 | 0.84 | 0.60 | 0.52 |
| CHI | 461 | 487.27 | 292.25 | 0.40 | 436.30 | 0.90 | 0.85 | 0.67 | 0.57 |
| CROSS | 461 | 487.27 | 290.30 | 0.41 | 428.10 | 0.90 | 0.86 | 0.67 | 0.57 |
| F TEST | 461 | 487.27 | 292.25 | 0.40 | 436.30 | 0.90 | 0.85 | 0.67 | 0.57 |

of the variance using only Radiometric Potassium and Average Annual Rainfall. The BRUTO model was the only one to use the Complexity Index as a predictor variable. The CROSS validation model was the least parsimonious, requiring 8 input variables.

Each model was run with the GRASP autocorrelation function using a local density map of transect site locations. The autocorrelation term was found not significant in all 6 models. Figures 4, 5, 6, and 7 give an output map, graphs showing predictor variable contributions and response curves for all models. An averaged map representing the probability of weed occurrence for the Top End was computed from the 6 input models in a GIS and used in further analysis (Fig. 8).

Comparisons of the 'probable' locations of weed infestations with maps of land tenure and Biogeographic subregions can now be presented. As we are attempting to predict the occurrence of environmental weeds that are yet to invade suitable environments, these results need to be taken with caution. To facilitate this comparison the averaged savanna weed map was separated into 4 probability classes (<0.1 or low; 0.1–0.5 or medium; 0.5–0.75 or high and >0.75 or very high).

Testing the Model with Independent Data

A database of weed distribution North of 18° (n = 4523, Fig. 9), provided by the weeds branch (NRETA 2008), was used to test the efficacy of the savanna weed map. The four probability classes were compared against a random set of points (n = 1000); all species present in the independent dataset; the same species recorded as in the transect surveys and individual weed Genera distribution.

According to Fig. 10 the random points are poorly represented in high probability classes (<12%). 60% of all weeds branch records fall within the high to very high classes. *Andropogon*, *Mimosa*, *Pennisetum* and *Sida* spp. records occur predominantly in the high to very high classes, although there were only a small number (19) of *Andropogon* records. The location of *Parkinsonia* and *Passiflora* spp. records are poorly predicted by our composite weeds model. About 40% of the Weeds Branch *Parkinsonia* spp. records are found south of 18° latitude and hence this genus's environmental envelope falls largely outside that described by our modelling.

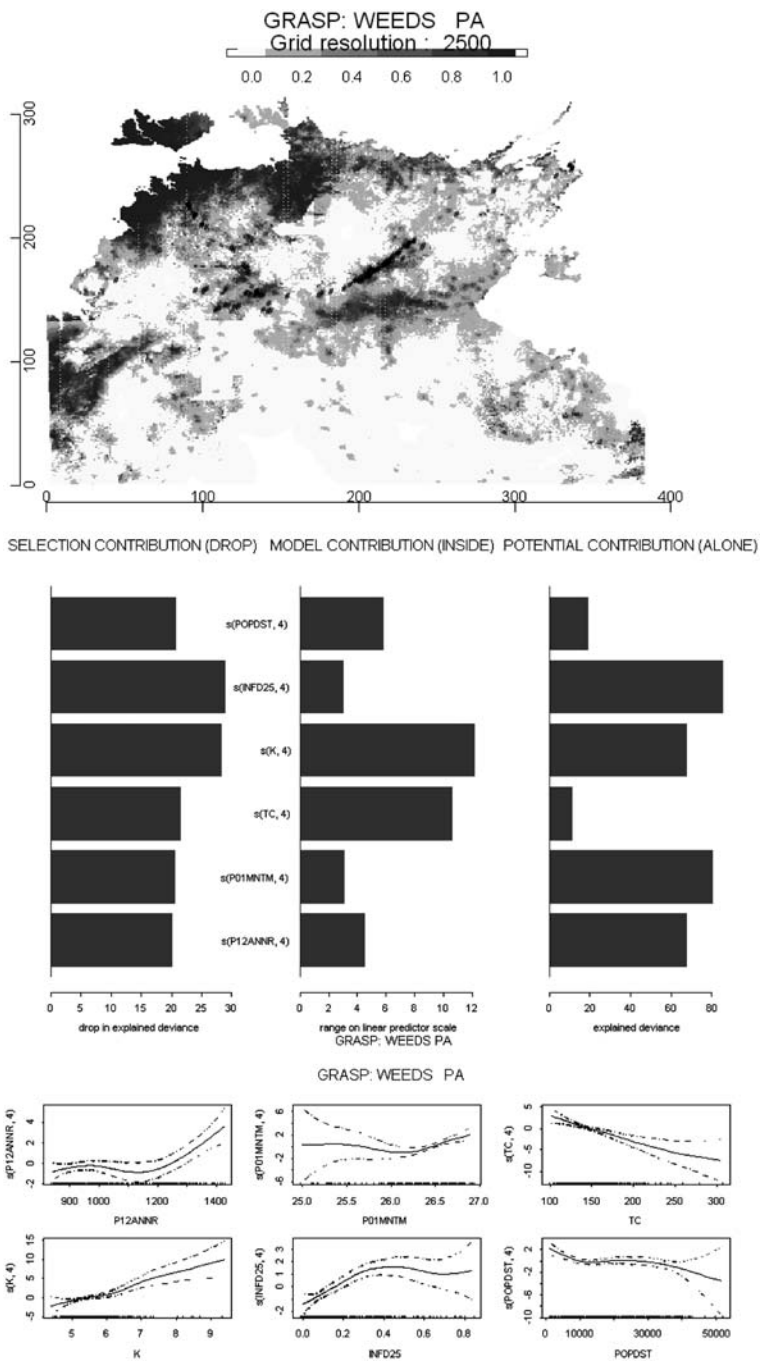
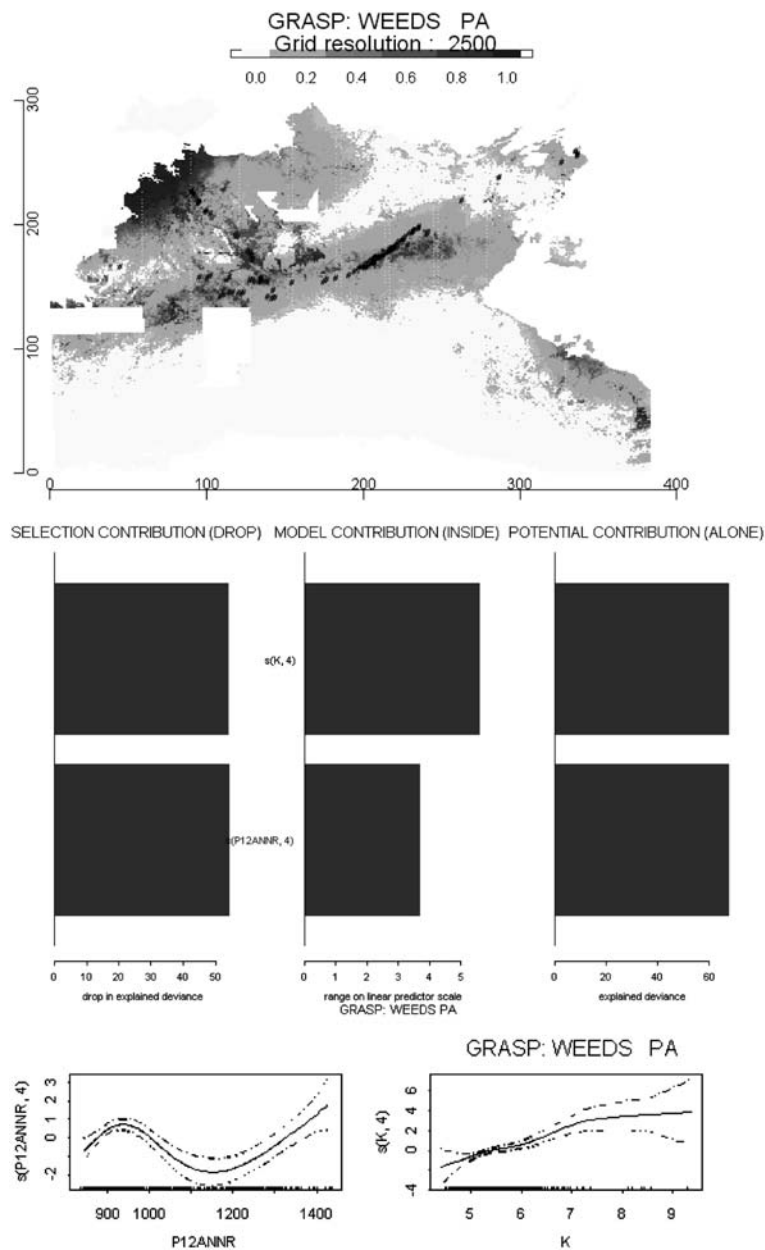


Fig. 4 Average Probability Map of Weed Occurrence



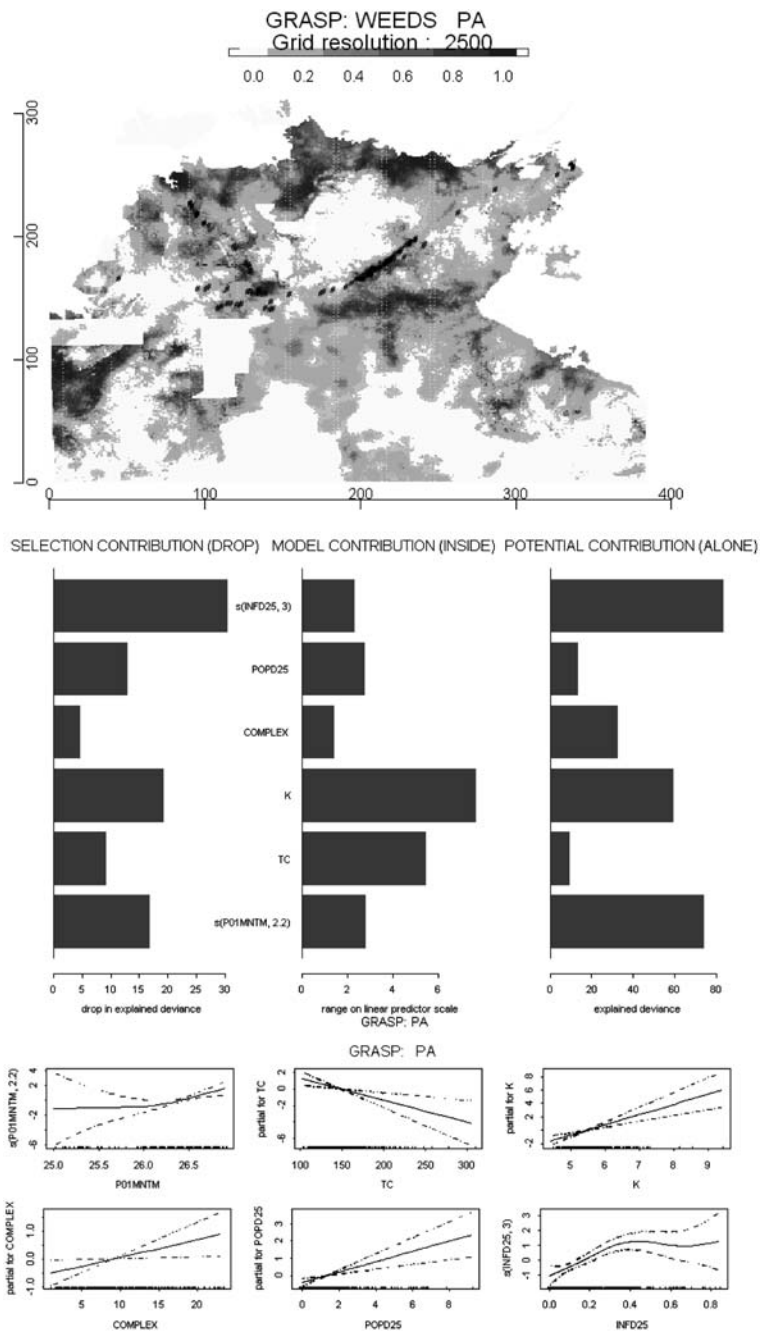


Fig. 6 Model output for the BIC test

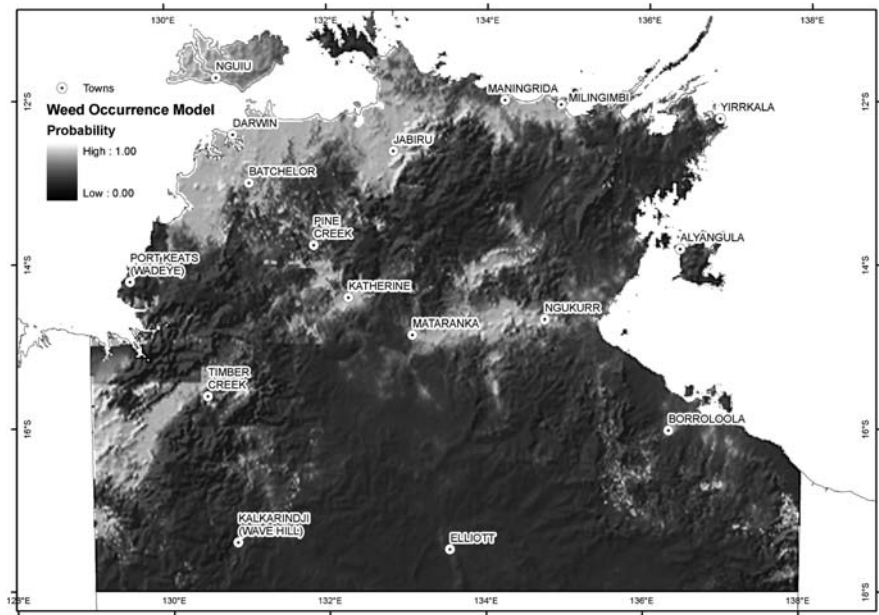


Fig. 8 Model output for CROSS Validation test

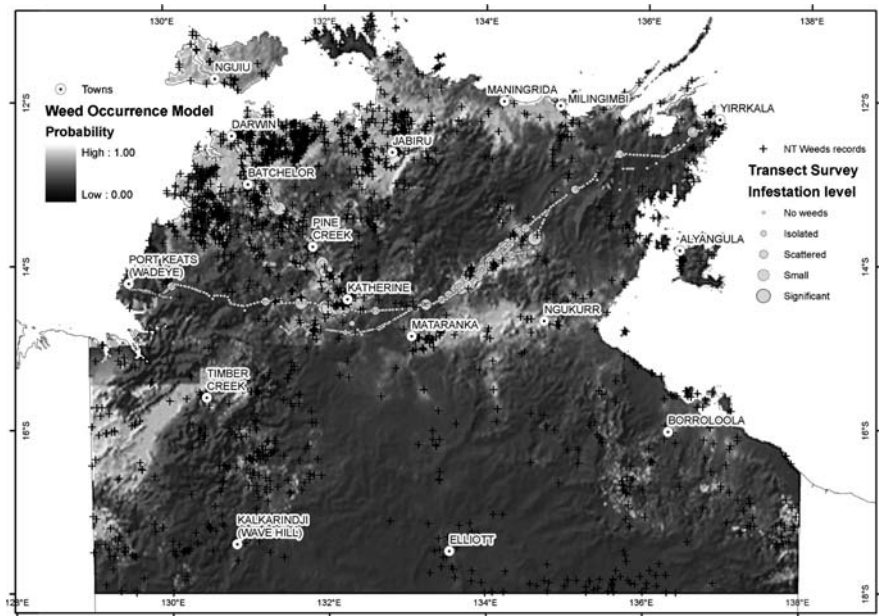


Fig. 9 Comparison of model probability classes with random observations and independent weed records

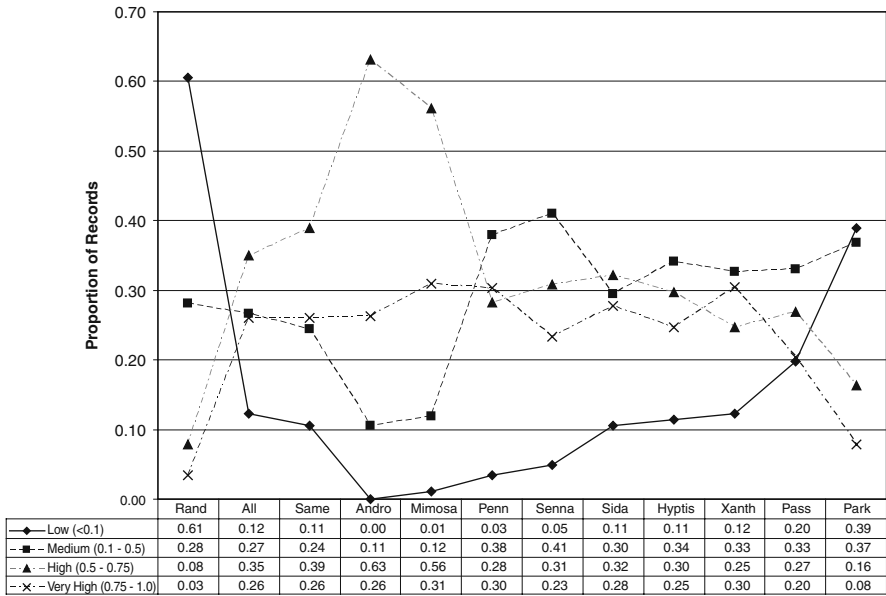


Fig. 10 Location of Transect Surveys and Weeds Branch data

Comparisons with Land Tenure

Broad Land Tenure was not selected as a predictor variable by any of the models. When comparing the savanna weed map with a 4 category map of land Tenure (built-up areas; Pastoral land; Aboriginal land and Conservation Reserves), built-up areas are faced with the greatest risk of complete infestation, with over 70% of their extent in the very high class (Fig. 11). Conservation Reserves have over 20% of their extent falling in the high to very high risk classes. Aboriginal and Pastoral lands appear to be at less risk of infestation, with values of around 10% in the high to very high class, but this remains a significant problem as these are the dominant land tenures in this region.

Comparisons with Biogeographic Subregions

Comparison of the savanna weed map with Biogeographic Subregions (Department of the Environment, Water, Heritage and the Arts 2004) provides a finer scale picture of which environments face greater peril from weed invasion. Fig. 12 shows 8 Biogeographic Sub-Regions which are considered to have large areas at a high to very high risk of invasion. As expected, the Darwin Coastal Subregion faces the greatest challenge with over 60% of its extent most vulnerable. The risk to the

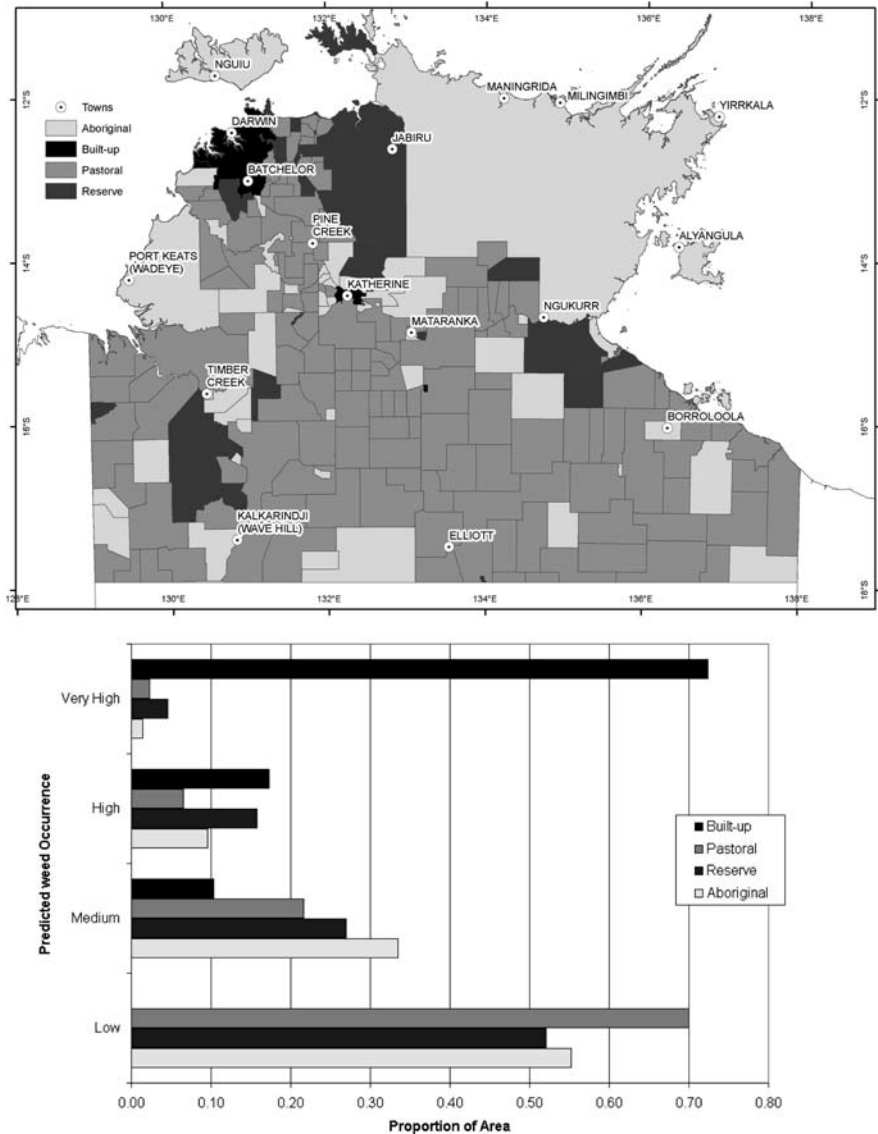


Fig. 11 Predicted weed occurrence across 4 dominant Land Tenure Types

Tiwi-Coburg Subregion, with 50% in the high class, is of concern considering the large scale forestry developments underway on Melville Island. Victoria-Bonaparte; Ord-Victoria Plains; Arnhem-Coast; Pine Creek; Gulf Falls and Uplands and the Daly Basin Subregions are all considered to be at high risk of savanna weed incursion.

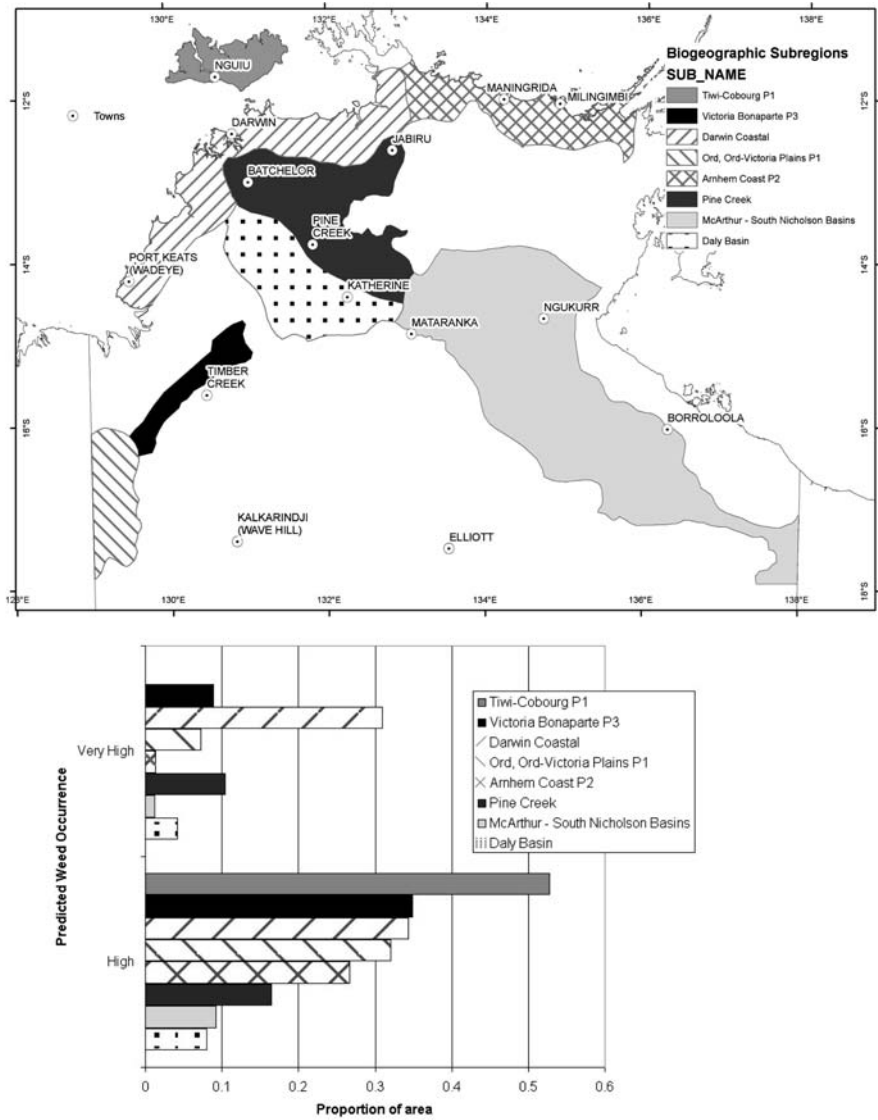


Fig. 12 Predicted Weed Occurrence across 8 Biogeographic Subregions

Discussion

With any regression modelling of species distribution there is an implicit assumption of pseudo-equilibrium between the species and its environment. This can often lead to poorly performing models or the prediction of presence in areas the species is yet to occupy (Guisan et al. 2002, Franklin 1995). Many of these weed species have

been present in more populated parts of the Top End for decades (Cook and Dias 2006), but may still venture further into remote areas as development of Northern Australia continues. We caution the use of these weed models as maps of current distribution, but rather regionally indicative of environments at greater risk of weed incursion in the Top End.

Few studies of predictive species modelling incorporate field validation. In this exercise we have used an independent set of weed observations to 'test' the field validity of our predictions. 65% of records for the same species recorded in the transect surveys occurred in high to very high probability classes. This does provide confidence in the magnitude of threat depicted in these weed models. However, the poor prediction for the location of *Parkinsonia sp.* records, suggests this modelling does not adequately represent weed risk in the Rangeland environments of the Sturt Plateau.

As with similar studies, this scale of modelling areas at risk of weed infestation and the related understanding of broad environmental processes favouring exotic plants is a useful tool for planning the long-term management of these environments (Collingham et al. 2000, Puckey et al. 2007), although the control of weeds will always be managed at a finer spatial scale and these predictive models will not necessarily aid in the planning of field work (Kean and Price 2003).

Across all the statistical tests used in this study there is a consistent theme of high rainfall, suitable surface lithology (from the Radiometric data) and proximity to populated places and/or human infrastructure in predicting infestations of weeds. However these spatially static models take no account of dispersal factors, rates of spread or neighbouring spatial context. Incorporating these factors into the modelling process should be the focus of future work in predicting weed incursions in Northern Australia.

Acknowledgements The authors would like to thank Frances Perrett, Greg Wallis, Tom Vigilante and Ron Firth for their tireless efforts in the field and Woodside and Epic Energy for funding the field work. Keith Ferdinands provided useful comments and staff from the Biodiversity North Unit of NRETAS provided access to GIS layers.

References

- Australian Bureau of Statistics (2002) Census 2001. <http://www.abs.gov.au/>.
- Bureau of Rural Sciences after Australian Geological Survey Organisation (1991) Digital Version of the 1976 Edition of Geology of Australia, 1:2,500,000 Scale. <http://www.brs.gov.au/datasets>.
- Bureau of Rural Sciences after Commonwealth Scientific and Industrial Research Organisation (1991) Digital Atlas of Australian Soils. <http://www.brs.gov.au/datasets>.
- Crawley MJ (1993) GLIM for Ecologists. Blackwell Scientific Publications, Oxford, England.
- Clifton R (2004) Radiometric map of the Northern Territory. Northern Territory Geological Survey. http://www.dme.nt.gov.au/ntgs/ecw/NT_wide.htm
- Cook GD and Dias L (2006) It was no accident: deliberate plant introductions by Australian government agencies during the 20th century. *Aust. J. Bot.* 54: 601–625.
- Crane B, Cowie ID and Michell CR (2006) Distribution and conservation status of the rare plants *Melaleuca triumphalis* and *Stenostegia congesta* (Myrtaceae), Victoria River District, northern Australia. *Aust. J. Botany.* 54: 641–653.

- Collingham YC, Wadsworth RA, Huntley B and Hulme PE (2000) Predicting the spatial distribution of non-indigenous riparian weeds: issues of spatial scale and extent. *J. App. Ecology*. 37(Suppl. 1), 13–27.
- Department of the Environment, Water, Heritage and the Arts (2004) Interim Biogeographic Regionalisation for Australia (IBRA), Version 6.1 (Sub-regions). <http://www.environment.gov.au/parks/nrs/science/bioregion-framework/ibra/index.html>.
- Farr TG and Kobrick M (2000) Shuttle Radar Topography Mission produces a wealth of data. *Amer. Geophys. Union Eos*. 81:583–585. <http://www2.jpl.nasa.gov/srtm/>.
- Fielding AH and Bell JF (1997) A review of the methods for the assessment of prediction measures in conservation presence/absence models. *Env. Cons.* 24: 28–49.
- Franklin J (1995) Predictive Vegetation Mapping: geographic modelling of biospatial patterns in relation to environmental gradients. *Prog. Physic. Geog.* 19: 474–499.
- Geoscience Australia (2006) GEODATA TOPO 250 k Series 3 Topographic Data. http://www.ga.gov.au/nmd/products/digidat/250_k.jsp
- Guisan A, Edwards TC and Hastie T (2002) Generalized linear and generalized additive models in studies of species distributions: setting the scene. *Ecol. Model.* 157: 89–100.
- Hobbs RJ and Humphries SE (1995) An integrated approach to the ecology and management of plant invasions. *Cons. Biol.* 9: 761–770.
- Houlder DJ (2000) ANUCLIM (Version 5.1). Centre for Resource and Environmental Studies, Australian National University.
- Kean L and Price O (2003) The extent of Mission grasses and Gamba Grass in the Darwin region of Australia's Northern Territory. *Pacific Cons. Biol.* 8: 281–290.
- Leathwick JR, Elith J and Hastie T (2006) Comparative performance of generalized additive models and multivariate adaptive regression splines for statistical modelling of species distributions. *Ecol. Model.* 199: 188–196.
- Lehman A, Leathwick JR and Overton JMcC (2004) GRASP v.3.0 User's Manual. Swiss Centre for Faunal Cartography, Switzerland. <http://www.cscf.ch/grasp/grasp-s/welcome.html>.
- Milne DJ, Fisher A and Pavey CR (2006) Models of the habitat associations and distributions of insectivorous bats of the Top End of the Northern Territory, Australia. *Bio. Cons.* 130:370–385.
- NRETAS (2008) The Department of Natural Resources, Environment, the Arts and Sports. Northern Territory Government. <http://www.nt.gov.au/nreta/>.
- The Northern Territory Government (2006) Government Gazettal of the declared weeds list. The Northern Territory Government Gazette No. G51, 20 December 2006. http://www.nt.gov.au/nreta/natres/weeds/pdf/weeds_gazette.pdf
- Puckey H, Brock C and Yates C (2007) Improving the landscape scale management of Buffel Grass (*Cenchrus ciliaris*) using aerial survey, predictive modelling, and a Geographic Information System. *Pacific Cons. Biol.* 13(4), 264–273.
- Taylor JA and Tulloch D (1985) Rainfall in the wet-dry tropics: extreme events at Darwin and similarities between years during the period 1870–1983. *Aust. J. Ecol.* 10: 281–295.
- Van Strien M (2007) Modelling the influence of climate change on vegetation communities in Queensland, Australia: A manual for the modelling process. Queensland Herbarium, Environmental Protection Agency of Queensland.
- Wilson BA, Brocklehurst PS, Clark MJ and Dickinson KJM (1990) Vegetation Survey of the Northern Territory, Australia. Conservation Commission of the Northern Territory, Technical Report no. 49.

Automated Reconstruction of Buildings Using a Hand Held Video Camera

J.R. Fulton and C.S. Fraser

Abstract Abstract This work looks at the automation of the reconstruction of buildings using a handheld consumer grade video camera. We discuss our progress to date which includes: deinterlacing the video footage, automated selection of non-blurred key frames, registration of key frames using a Fast Fourier Transformation technique and tracking of points and features to be used in the bundle adjustment.

Introduction

The automatic reconstruction of buildings from image sequences is currently an active area of research, as indicated by the work of Faugeras et al. (1998), Zisserman et al. (1999) and Pollefeys et al. (2000), for example. A recent review of image based 3D modelling, which encompasses 3D object reconstruction from sequences of imagery acquired using handheld video cameras, has been presented by Remondino and El-Hakim (2006). The automated image measurement and matching, along with the subsequent orientation and object point triangulation phases, invariably involves selected images only from the sequence, and thus the question arises as to which images are optimal for this process. Obviously, geometric factors are important here as the images used need to form a network exhibiting sufficient geometric strength and redundancy in order to achieve a reliable reconstruction. Another important factor is the quality of the imagery and specifically the amount of blur within each image. Image blur can degrade feature extraction and also the matching and orientation, so it is important that the automatic process adopted to select the appropriate images from a sequence takes account of the extent of blurring so that images with

J.R. Fulton (✉)

Air Operations Division, Defence Science and Technology Organisation, Fishermans Bend, VIC 3207, Australia

e-mail: John.Fulton@dsto.defence.gov.au

excessive blur are avoided. In order to achieve this, a metric is needed to enable blur to be quantified and the development of such a metric forms the subject of this paper.

After deinterlacing video footage many of the video frames may be blurred due to camera motion. The blur metric to be introduced allows the automated selection of non-blurred key frames. Registration of these key frames is then performed using a fast Fourier transformation based technique called phase correlation. A new metric that indicates when robust matches have occurred in the tracking of points and features via a modification of the phase correlation technique has also been developed.

Methodology

In this section we will give a brief overview of the methodology before we look more closely at each stage.

The methodology used in conducting this research was firstly to video the building of interest. The video sequence was then transferred to the computer and saved as individual JPEG frames. The images in PAL format were then interpolated into their odd and even fields. A metric is then run on every field in the sequence to see how blurred it is. Key frames with the least amount of blurring within a window of up to 4 s of video are then selected. The selected key frames are then registered using phase correlation. Feature extraction on the registered frames is then performed using either Harris and Stephens (1988) or Canny (1986). These detected features are then searched for using phase correlation of smaller windows in the subsequent images. At the end of this process the top 60 tracked points or features are then output so that the exterior orientation of the sequence may be recovered. For the remainder of this section we will look in more detail at each step of the process.

Image Sequence

While a number of image sequences have been used for this research, for this paper we will report results on one sequence called 'building 47'. The building is surrounded by plants and trees. The first frame of video from the sequence is shown in Fig. 1.

The video camera employed was a Sony MiniDV Digital Handycam DCR-PC1e. This camera records in PAL format. This sequence was transferred to a computer initially using Apple Quicktime Pro, and later the open source program 'kino'. For each PAL image the odd and even fields were extracted, with interpolation being employed to fill pixels in the missing lines. Individual fields were 720×576 pixels with 24-bit colour. The sequence is made up of 3300 individual images – that is 6600 fields of odd and even video.



Fig. 1 First frame of b47 sequence and its Fourier transform

Blur Metric

Initial inspection of the video showed that some frames are in focus while others are badly distorted by motion blur. The blurring was due to motion caused by the camera being hand held while encircling the building. Tracking of features would fail on the badly blurred images so a blur metric was then developed to automatically select the least blurred images.

Motion blur occurs when a camera moves too fast for the image sensor to accurately record the light coming from a single 3D point. Thus the light from one 3D world point ends up being detected by multiple sensors. Incorrect focusing of the image on the image plane causes focal blur.

There has been much work related to the removal of motion blur from single images in the literature with Rosenfeld (1969), Gonzalez and Woods (1992) and Reiter (2000) providing overviews of the application of Fast Fourier Transform (FFT) techniques for this purpose. Rekleitis (1996) uses the FFT and a cepstral analysis based technique to recover optical flow when motion blur exceeds a few pixels, while Kang et al. (2001) recover motion and focal blur using a spatially adaptive regularisation algorithm. Trussell and Fogel (1992) present a non-FFT image sequence method which finds the velocity vectors (Fogel, 1991) between frames of the sequence and then uses a modified Landweber iteration method to correct the image based on the frame rate of the camera, with interlaced video not being considered. Rooms et al. (2001) use wavelets with a Lipschitz exponent to estimate the amount of Gaussian blurring on vertical lines in the image, whereas Elder and Zucker (1998) use a scale space technique to estimate the amount of focal blurring on lines.

Marziliano et al. (2002) provide a perceptual blur metric based on vertical edges in the image, whereas Marichal et al. (1999) give a blur metric based on a histogram of the Discrete Cosine Transform data present in MPEG and JPEG images. Mayntz et al. (1999) estimate the amount of blur by first determining its direction from the eigenvalues of a matrix with elements made up of summation of different

components of the FFT. The extent of blurring is then estimated by finding the zeroes in either the power spectrum or bispectrum. Finally, Devčić and Lončarić (2000) have used a Singular Value Decomposition method to estimate the amount of blur.

We developed two methods of classifying the amount of blur that both involve taking the FFT of the image. The power spectrum $PS(x,y)$ of an image scaled between 0 and 1 is calculated as:

$$PS(x,y) = \log \left(1 + |F(x,y)|^2 \right) / \log \left(1 + |F(0,0)|^2 \right) \quad (1)$$

where F is the 2D FFT of the image. The first blur metric is defined as:

$$ThresholdBlurMetric = \sum_{x=1}^{(N-1)/2} \sum_{y=1}^{M-1} \begin{cases} 1 & PS(x,y) \leq \alpha \\ 0 & otherwise \end{cases} \quad (2)$$

where α is a threshold and N and M are the dimensions of the image in the x and y directions. Eq. (2) provides a metric for the amount of blur in an image. Zero hertz frequency components (when $x = 0$ or $y = 1$) are ignored as they do not improve the measure. x is only summed to $(N - 1)/2$ due to Hermitian symmetry (Frigo and Johnson, 1999). This metric is invariant with respect to blur direction because the frequencies in both x and y directions are considered. A trough detector will therefore find the images with least motion blur when applied to an image sequence.

The second blur metric uses the mean of the normalised power spectrum:

$$MeanBlurMetric = \frac{-2}{(M - 1)(N - 1)} \sum_{x=1}^{(N-1)/2} \sum_{y=1}^{M-1} PS(x,y) \quad (3)$$

Here the negative sign is used to make more blurred images have higher peaks. Again the 0 Hz components have been ignored.

When comparing these blur metrics to Marichal et al. (1999), Marziliano et al. (2002), and Yoshida et al. (1993) with an image which has been increasingly artificially blurred we can see that both metrics work well. Figure 2 shows the image from Fig. 1 artificially motion blurred by 20 pixels and its resulting Fourier Transform. Note that the nulls in the power spectrum are lines perpendicular to the direction of motion blur and in the case of focal blur are concentric circles about the origin (Cannon, 1976). Figure 3(a) shows a plot of the results for increasingly blurred images for all the metrics between 0 and 20 pixels of blur.

A brief summary of our results on the blur metrics is that we favour the mean blur metric of Eq. (3) because it does not need any parameters to be specified and has good precision even for minor blurs. Marziliano should be avoided as it fails when the blur is larger than the response of the Sobel (1970) Operator. If the task is time critical but less precision is required then Marichal is a good choice due to it using the already existing frequency components of the discrete cosine transform.



Fig. 2 Image from Fig. 1 artificially blurred by 20 pixels and its Fourier transform

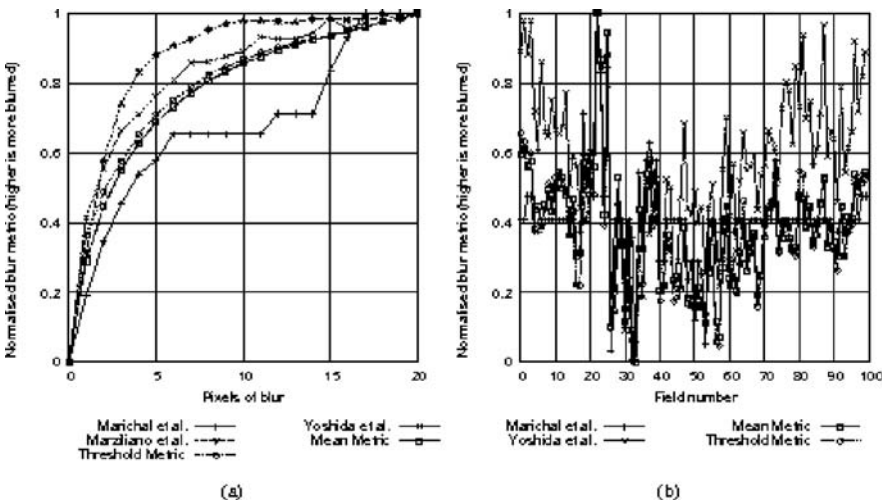


Fig. 3 Plot of various blur metrics for (a) increasingly blurred images and (b) for first 100 odd and even fields of the building 47 image sequence. The higher the value the more blurred the image.

A plot of the first 100 fields of the building 47 sequence for the Marichal, Yoshida, Mean and Threshold metrics is shown in Fig. 3(b). Manual verification showed that the peaks of the mean and threshold metrics corresponded to the most blurred images.

Registration of Key Frames

Once the blur metric has identified the frames of least blurring, we register the images using a phase correlation technique which recovers scale, rotation and x and y translations between two images. The original frequency domain technique, known as Phase Correlation (Kuglin and Hines, 1975), is based on the translation property of the Fourier transform. This property (also called the shift theorem) states

that if two images f_1 and f_2 are related by a translation (x_0, y_0) :

$$f_2(x, y) = f_1(x - x_0, y - y_0) \quad (4)$$

then their Fourier transforms (F_1 and F_1) will be related by

$$F_2(\xi, \eta) = e^{-j2\pi(\xi x_0 + \eta y_0)} F_1(\xi, \eta) \quad (3)$$

The cross-power spectrum of the two images is defined as

$$F_1(\xi, \eta) F_2^*(\xi, \eta) / |F_1(\xi, \eta) F_2(\xi, \eta)| = e^{-j2\pi(\xi x_0 + \eta y_0)} \quad (4)$$

Taking the inverse Fourier transform of the resultant exponential produces an impulse at the position of best registration.

The Fourier-Mellin transform converts the power spectrum of an image to log-polar coordinates. The reason for doing this is to recover rotation and scale. The polar transform converts changes in the rotation to a translation. Likewise the logarithmic transform converts changes in scale to a translation. With rotation and scale both represented as translations, phase correlation can be used to recover them. The use of the power (or magnitude) spectrum decouples the calculation from x and y translations in the image domain because these translations are encoded in the phase information of a Fourier transform.

Due to the processing efficiency of the FFT compared to the Fourier transform, in practice, these algorithms are implemented using the FFT.

Recovery of rotation and scale using the Fourier-Mellin transform was first demonstrated by Casasent and Psaltis (1976, 1977) using optical computing devices. Later Chen et al. (1994) and Reddy and Chatterji (1996) proposed similar computer algorithms which are summarised as follows:

1. For two images f_1 and f_2 , calculate their FFTs F_1 and F_2 .
2. Convert the magnitudes of F_1 and F_2 to the Fourier-Mellin (polar-log) equivalent so that:

$$F_2(\phi, \rho) = F_1(\phi - \phi_0, \rho - A) / a^2 \quad (5)$$

where rotation $\phi = \arctan(\eta/\xi)$ and scale α is recovered from $A = \log(a)$ where $\rho = \log(\sqrt{\xi^2 + \eta^2})$.

1. Use phase correlation on the newly created polar-log image to recover the rotation (ϕ) and scale (a).
2. Unscale f_2 by $1/a$.
3. Rotate the unscaled image by $-\phi$ and another copy of the unscaled image by $-\phi + 180^\circ$ (a 180° degree ambiguity is introduced by using the magnitude spectra).
4. Phase correlate both copies against f_1 and keep the translation solution which produces the highest correlated peak.

Published examples using this technique include Stricker (2001) and Xie et al. (2003) who both confirm the need for at least 30% overlap of image content for the method to work.

Notes on our implementation include;

- using Hamming windows on all data before the FFT is applied (steps 1, 3 and 6) which results in higher peak power in the inverse power spectra and the technique working for images that are further apart in the image sequence.
- The Fourier-Mellin image created in step 2 has dimensions of 720×720 which gives an angular resolution of 0.5° .
- Rotation of an image by 180° in the frequency domain can be achieved by multiplying imaginary components of the Fourier transform by -1 which allows partial combination of steps 5 and 6.

For images with the dimensions of a PAL image we can confirm the observation of Reddy and Chatterji (1996) that having the final peak greater than 0.03 always gives a satisfactory registration. We have however found that the final peak is highly dependent on the image dimensions which we will discuss in the following section. For recovery of the rotation and scale we insist that the peak be above 0.017 and when this fails assume no change in scale or rotation.

If an image pair fails to register then the next best image as determined by the blur metric is selected and registration attempted. We continue until we have key frames spanning the sequence registered to their neighbouring key frames.

Feature Registration

To find features to track in individual frames we use either the method of Harris and Stephens (1988) or Canny (1986) and note that many studies such as Trajković and Hedley (1998) and Cooke and Whatmough (2005) find the Harris detector to be the most stable corner detector. We also use the features matched in the previous frame.

To find the match to an individual feature we take the original image and the next key image in the sequence. The next key image is unscaled, unrotated and untranslated using the values found by the previous stage. We then take a patch of the image centred on the feature and find the best phase correlation for this patch in the next image. This is only for translation as scale and rotation were corrected in the previous step.

Choice of window size involves a trade off between size, processing time and inclusion of the target point. Larger sizes take longer to process and are more affected by changes in the 3D geometry of the scene. While small windows need to be large enough to include the required point. Figure 4(a) show the number of correct points this technique finds regardless of the height of the peak. The smaller

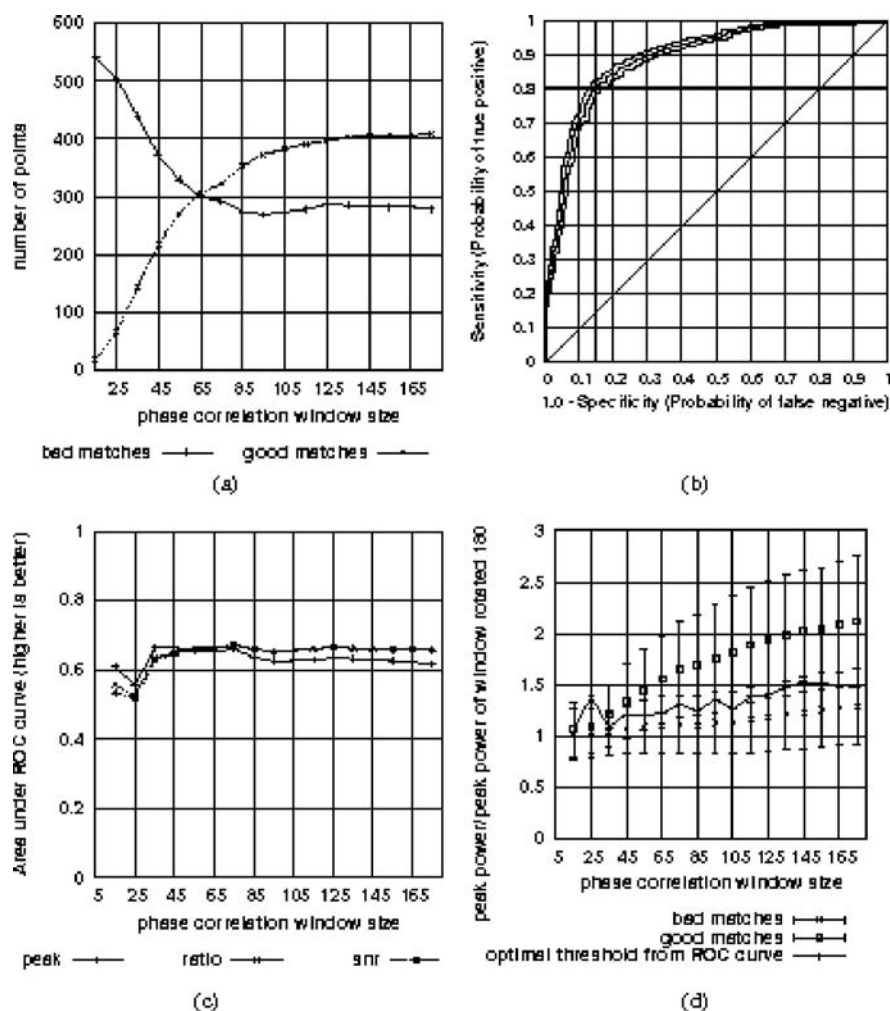


Fig. 4 (a) Plot of correctly found points using phase correlation for various window sizes regardless of peak. Data were taken from matches between even fields of frames 17 and 96. (b) ROC curve of the ratio classifier with 0.95 confidence intervals for the 135×135 window. The cross hairs show the Optimal Operating Point. (c) Area under the ROC curves versus window size for the ratio, SNR and peak classifiers. (d) The mean values for good and bad matches versus window sizes with the 'peak ratio' classifier. Error bars are shown at 1 standard deviation. The optimal threshold to decide between a good and bad match from the ROC curve is also shown.

window sizes performed poorly because they were too small to include the target points.

While Reddy and Chatterji (1996) use a peak in inverse power spectra greater than 0.03 to classify a good registration, we have found that this value is highly correlated to the window size. This method also shows no indication of when a badly localised match occurs for near identical windows. For example when presented

with two patches of sky, a high correlation peak results, but the location of the peak is highly susceptible to noise and its position is essentially random.

We have found a more accurate and stable test of correctness is the peak of the correctly oriented window divided by the peak of the window which is rotated by 180° .

$$peakratio = peak/peak_{180^\circ} \quad (6)$$

We will call this method the 'peak ratio' classifier. The Signal to Noise Ratio (SNR) of the peak is defined as

$$SNR = (peak - \mu)/\sigma \quad (7)$$

where μ and σ are the mean and standard deviation respectively of the inverse power spectrum not including the peak. We can define a third classification of a good match as

$$SNR_{ratio} = SNR/SNR_{180^\circ} \quad (8)$$

where SNR is the SNR of the correctly oriented window and SNR_{180° is the SNR of the window rotated by 180° .

Both the peak ratio and SNR ratio methods are more stable over a larger window range with an optimal threshold near 1.5. More importantly when presented with near identical patches of sky they both give results of near 1.0 indicating a bad localisation match.

To compare the 3 methods we plotted the Receiver Operator Characteristic (ROC) curves for the 3 methods using various window sizes. Figure 4(b) shows the ROC curve for the peak ratio classifier. The area under a ROC curve indicates how good a method performs as a classifier. Using numerical integration we calculated the areas under all the ROC curves and presented them in Fig. 4(c). We see that, for the window sizes 55×55 and larger, the peak ratio and SNR ratio classifiers outperform the peak classifier.

More data will be required to separate the performance of the peak ratio and SNR ratio classifiers. When faced with a choice between the two, we favour the peak ratio classifier because of its simpler implementation (the SNR requires the mean and standard deviation of the inverse power spectra). We have noted that the peak ratio and SNR ratio classifiers often only differ in the second decimal place.

The test points we have used in this paper were found with the Harris corner detector, so that there are no uniform patches of sky or tarmac which would have shown even stronger results in favour of the peak ratio and SNR ratio methods.

While there are a number of ways of determining the Optimal Operating Point (OOP) on a ROC curve (Gallop et al. 2003), we use the maximum of the simple metric

$$OOP = Se + Sp \quad (9)$$

where Sp is the specificity (probability of a true negative) and Se is the sensitivity (probability of a true positive).

To find the optimal threshold for the different classifiers we take the OOP for the sensitivity (y -axis) off the ROC curve. We then sort our inliers and select the threshold which includes this percent of the inliers. Figure 4(d) shows the optimal thresholds as defined from the ROC plots.



Fig. 5 (a) Using phase correlation for matching can sometimes give incorrect results. A crop of two consecutive frames with a point on the pole incorrectly matched to the position which was behind the pole in the previous frame. (b) A feature point tracked through multiple frames. Only the 20 pixels above and below the feature are shown from each frame.

Discussion

While the phase correlation method works well to find matches for many of the points, there are times when it fails. For example it can some times match the background image features and ignore the foreground. For example Fig. 5(a) shows a point on a pole in one frame which is matched to the scenery that was behind the pole in the next frame, further more the peak in the inverse power spectra is very strong. In order to detect these errors we currently check the pixel colour values of the matches and fail any match that does not have all red, green and blue values within 25–30% of each other.

Using the described method we have managed to track a number of features of the building for around 400 frames. Figure 5(b) shows one such corner.

Conclusions and Future Work

Using a combination of a blur metric and registration with phase correlation we have been able to automatically select key frames for further processing. We have investigated using phase correlation for tracking feature points and have identified a new classification metric for deciding if we have found a good match.

Further work is need to extend these matched feature points to larger angular separations to get a more robust geometry for the bundle adjustment phase of 3D object reconstruction.

References

- Cannon M. (1976) Blind deconvolution of spatially invariant images blurs with phase. *IEEE Transactions on Acoustics, Speech and Signal Processing*, 24(1):58–63
- Canny J. (1986) A computational approach to edge detection. *IEEE Transactions on Pattern Analysis and Machine Intelligence* 8(6): 679–698
- Casasent D, Psaltis D (1976) Position, rotation, and scale invariant optical correlation. *Applied Optics* 15(7):1795–1799
- Casasent D, Psaltis D (1977) New optical transforms for pattern recognition. *Proceedings IEEE* 65:77–84
- Chen Q, Defrise M, Deconinck F (1994) Symmetric phase-only matched filtering of fourier-mellin transforms for image registration and recognition. *IEEE Transactions on Pattern Analysis and Machine Intelligence* 16(12):1156–1168.
- Cooke T, Whatmough R (2005) Detection and tracking of corner points for structure from motion. Technical Report DSTO-TR-1759, Defence Science and Technology Organisation.
- Devčić Z, Lončarić S (2000) Blur identification using averaged spectra of degraded image singular vectors. In: *IEEE International Conference on Acoustics, Speech, and Signal Processing*, pp. 2195–2198.
- Elder JH, Zucker SW (1998) Local scale control for edge detection and blur estimation. *IEEE Transactions on Pattern Analysis and Machine Intelligence* 20(7):699–716
- Faugeras O, Robert L, Laveau S, Scurka G, Zeller C, Gauclin C, Zoghلامي I(1998) 3-D Reconstruction of Urban Scenes from Image Sequences. *Computer Vision and Image Understanding*. 69(3):292–309.
- Fogel S (1991) The estimation of velocity vector fields from time-varying image sequences. *Computer Vision, Graphics and Image Processing: Image Understanding* 53(3):253–287
- Frigo M, Johnson SG (1999) *FFTW User's Manual*. Massachusetts Institute of Technology.

- Gallop RJ, Crits-Christoph P, Muenz LR, Tu X M (2003) Determination and interpretation of the optimal operating point for ROC curves derived through generalized linear models. *Understanding Statistics* 2(4):219–242
- Gonzalez RC, Woods RE (1992) *Digital Image Processing*. Addison-Wesley, New York.
- Harris C, Stephens M (1988) A combined corner and edge detector. In: 4th Alvey Vision Conference, pp. 147–151
- Kang SK, Hong MJ, Paik JK (2001) Simultaneous digital focusing and motion blur removal using segmentation-based adaptive regularization. In: *Visual Communications and Image Processing 2001*, SPIE, pp. 776–786.
- Kuglin CD, Hines DC (1975) The phase correlation image alignment method. In: *IEEE 1975 International Conference Cybernetics and Society*, pp. 163–175.
- Marichal X, Ma W-Y, Zhang H (1999) Blur determination in the compressed domain using DCT information. In: *1999 International Conference on Image Processing 2*, pp. 386–390.
- Marziliano P, Dufaux F, Wionkler S, Ebrahimi T (2002) A no-referenced perceptual blur metric. In: *2002 International Conference on Image Processing*, pp. 57–60.
- Mayntz C, Aach T, Kunz D (1999) Blur identification using a spectral inertia tensor and spectral zeros. In: *1999 International Conference on Image Processing 2*, pp. 885–889.
- Pollefeys M., Koch R. Vergauwen M., Van Gool L. (2000) Automated reconstruction of 3D scenes from sequences of images. *ISPRS Journal of Photogrammetry and Remote Sensing*, 55(4): 251–267
- Reddy BS, Chatterji BN (1996) An fft-based technique for translation, rotation and scale-invariant image registration. *IEEE Transactions on Image Processing* 5(8):1266–1271
- Reiter C (2000) With j: Fast Fourier transforms and removing motion blur. *ACM SIGAPL APL Quote Quad* 31(1):16–17
- Rekleitis IM (1996) Steerable filters and cepstral analysis for optical flow calculation from a single blurred image. In: *Vision Interface*, Toronto, pp. 159–166.
- Remondino F, El-Hakim S (2006) Image-based 3D Modelling: A Review. *The Photogrammetric Record* 21(115): 269–291.
- Rooms F, Pizurica A, Philips W (2001) Estimating image blur in the wavelet domain. In: *Proceedings ProRISC 2001 (12th annual Workshop on Circuits, Systems and Signal Processing)*, pp. 568–573.
- Rosenfeld A (1969) Picture processing by computer. *ACM Computing Surveys (CSUR)* 1(3): 147–176
- Sobel I (1970) Camera models and machine perception. *Stanford AI Memo* 121
- Stricker D (2001) Tracking with reference images: a real-time and markerless tracking solution for out-door augmented reality applications. *Proceedings of the 2001 conference on virtual reality, archeology, and cultural heritage*, ACM Press, New York, NY, USA: pp. 77–82.
- Trajković M, Hedley M (1998) Fast corner detection. *Image and Vision Computing* 16:75–85
- Trussell HJ, Fogel S, (1992) Identification and restoration of spatially variant motion blurs in sequential images. *IEEE Transactions on Image Processing* 1(1):123–126
- Xie H, Hicks, N, Keller, GR, Huang H, Kreinovich V (2003) An IDL/ENVI implementation of the FFT based algorithm for automatic image registration. *Computers and Geosciences* 29: 1045–1055
- Yoshida Y, Horiike K, Fujita K (1993) Parameter estimation of uniform image blur using dct. *IEICE Trans. Fundamentals* E76-A(7):1154–1157.
- Zisserman A, Fitzgibbon A, Cross G (1999) VHS to VRML: 3D Graphical Models from Video Sequences. *Proceedings IEEE International Conference on Multimedia*.

Mapping Seagrass Biomass with Photo-Library Method

Tiit Kutser, Ele Vahtmäe, Chris Roelfsema, and Liisa Metsamaa

Abstract Validation of benthic habitat maps produced from remote sensing imagery is quite time consuming and expensive. Validating maps of seagrass biomass is even more sophisticated and time consuming as the seagrass has to be collected, dried and weighed in the laboratory. We developed a method for estimating the dry weight of the seagrass based on photo transect data and a photo library of quadrats with known seagrass biomass. For seagrass biomass estimation we selected 13 different bottom classes. A photo of each 25×25 cm quadrat was taken prior to collecting the samples for each class. Seagrass (and macroalgae, if present) dry weight for each class was measured in the laboratory. These photos were then used to estimate seagrass biomass in 100 m long geolocated photo transects. Seagrass dry weight estimated from the photo transects using the photo-library method was compared with QuickBird satellite radiances. Preliminary results show that QuickBird imagery may be used for mapping seagrass biomass even in highly variable environment such as the Ngederrak Reef in Palau.

Introduction

Seagrass habitats have a valuable role in marine ecosystems since they function as nursery grounds, a natural resource, and provide biodiversity and coastal protection (Waycott et al. 2005). Therefore, for conservation and management purposes one needs appropriate monitoring methods for the biophysical characteristic of seagrass species, cover and biomass (McKenzie et al. 2001; Short and Coles 2001).

A variety of methods have been developed to measure seagrass biomass, sampling designs will continue to be modified and improved. The most appropriate sampling method for estimating biomass depends on the size of the area to be assessed, resource and time limitations, the accuracy required, the structure of the vegetation complex and vegetation components of interest (Catchpole and Wheeler, 1992).

T. Kutser (✉)

Estonian Marine Institute, Tartu University, Tallinn 12618, Estonia
e-mail: tiit.kutser@sea.ee

The most widely used method for estimating seagrass biomass is the manual harvesting of macrophytic tissue within quadrats (Downing and Anderson, 1985). Biomass is measured by harvesting either the above-ground or the total biomass within the sampling frame (Krause-Jensen et al., 2004). Samples may be collected by sampling randomly (Hossain, 2005; Boer, 2000; Phillips et al., 2006) or by applying point samples on a line transect (Lin and Shao, 1998; Tolan et al., 1997). To determine the patterns of seagrass abundance over a gradient of water depth, a transect method is recommended. The aim of random sampling is to estimate the real biomass of the meadow (Duarte and Kirkman, 2002). The manual harvesting method provides a relatively precise measure of seagrass abundance, but has the disadvantage of being destructive, time consuming and expensive.

If biomass estimation studies are carried out in marine protected areas, priority should be given to less destructive sampling methods. Mellors (1991) designed a non-destructive visual assessment method for estimating above-ground seagrass biomass which allows repeated monitoring, is less damaging to the environment and is generally faster than destructive methods.

Mellors (1991) visual assessment method uses a linear scale of 5 biomass categories (1–5), which are assigned to seagrass samples in 0.25 m² quadrats. Five calibration quadrats are chosen so that the first quadrat is placed in the seagrass bed with the highest biomass (referred to as category 5). A second quadrat is placed in an area with the lowest biomass (referred to as category 1). Quadrats for categories 2, 3 and 4 are placed by estimating biomass differences between categories 1 and 5. Each quadrat is photographed and harvested as a biomass sample. Using the photographs of the calibration quadrats as a guide, observers proceed to visually estimate seagrass biomass at the study site. Mumby et al. (1997) extended the range of reference quadrates from five to six, as it was hypothesised that surveyors were tempted to place a disproportionate number of quadrats in the middle category.

In Palau, the research study area seagrass beds are included in marine protected areas, because they are important feeding areas for dugongs. Consequently the maximum number of destructive samples the authors allowed to collect was limited to fifteen. The variability of habitats in the Ngederrak Reef is very high: varying from dense seagrass beds to almost bare sand and from dense macroalgal cover with some seagrass to dense coral cover with some seagrass. We were not able to use the methods which require the training of observers by taking multiple biomass samples of each class (Mellors, 1991; Mumby et al., 1997). Also classification with just six seagrass density classes would have been insufficient in such a complex environment. As a result we had to modify the sampling strategy and rely on photo transect data which we classified visually using photos of the fifteen sample quadrats with known biomass.

Method

Study Area

The study was carried out in the Republic of Palau at the Ngederrak Conservation Area in April 2006. The Ngederrak Reef contains several habitats including seagrass

beds, which are known to be important feeding grounds for dugongs. The seagrass beds situated on sandy substrates vary between sparse to dense cover and consist of several seagrass species: *Cymodocea rotundata*, *Halodule uninervis*, *Halophila ovalis*, *Thalassia hemprichii*, *Syringodium isoetifolium* and *Enhalus acoroides*. The canopy height of these beds can vary from a few centimetres for *Halophila ovalis*, to less than 20 cm for *Enhalis accroides* and over 30 cm for *Thalassia hemprichii* (Waycott et al., 2005). *Thalassia hemprichii* and *Enhalis accroides* were the most frequently occurring seagrass species.

The Ngederrak seagrass habitats are mixed with algae and coral species. The algae species are mainly; *Laurencia*, *Caulerpa*, *Sargassum*, *Turbinaria*, *Dictyota* and *Padina*. In the fieldwork area *Laurencia* was the most abundant species mixed with the seagrass often forming dense and continuous cover below the seagrass canopy. Dense *Padina* beds were also present in some of the studied areas. The seagrass/algae cover was mixed with mainly branching *Acropora spp.* and massive and branching *Porites spp.* Some of the habitats were covered in cyanobacterial mats overgrowing sand, seagrass, algae and coral.

Photo-Transect Method

The photo-transect method for creating benthic habitat maps for the calibration and validation of satellite imagery was developed in the Centre for Remote sensing & Spatial Information in the University of Queensland (Roelfsema et al., 2006). Bottom types are identified based on still images taken along a 100 m tape geolocated and fixed to the seafloor. The photos are captured at a 2 m interval. A Sony PC10 camera in Marine Pack UW housing and external wide angle lens were used in the Ngederrak Reef. A plumb line attached to the camera was used to determine the right distance from the bottom to capture 1 × 1 m area in each photo. A Garmin 72 GPS was towed by the photographer to geolocate the photo transect data. The time stamp of the GPS position and of the photo allowed the geolocation of each photo taken along the transects.

Biomass Samples

The Ngederrak reef area was visually inspected prior to the survey work to identify the range of seagrass biomass. Fifteen sampling sites were chosen in the study area to cover the diversity of habitats from dense seagrass beds to almost bare sand and from dense macroalgal cover with some seagrass to dense coral cover with some seagrass. Biomass samples of seagrass standing crop and algae were collected from 0.25 m² quadrats after a photo record of the quadrat was taken. The contents of the quadrats were carefully and completely removed and placed into mesh bags.

At the laboratory samples were cleaned of remaining sediments. Cleaned samples were separated into seagrass and macroalgae. Epiphytes on the seagrass leaves were removed by soaking in hydrochloric acid. Each biomass sample was dried

in an oven at 60°C for approximately 24 h. Dried samples were weighed immediately after removal from the oven since they reabsorb moisture quickly. Dry weights of seagrass and macroalgae (if present) were measured for each quadrat. The dry weight of macroalgae was not used in this study.

Photos of the sorted biomass samples were taken in the laboratory. The biomass was sorted according to major seagrass and macroalgae species. A measuring tape was included in the frame to enable a rough estimate of seagrass leaf length. Thus, the photo library used in further estimation of seagrass biomass consisted of two photos: one taken in situ before removing the biomass and one taken in the laboratory after biomass sorting but prior to drying. The latter proved useful in seagrass biomass estimation as the measuring tape gave more detailed information about the height of the seagrass canopy than some of the in situ photos. The relative amount of macroalgae was also more clearly visible in the laboratory photos than in situ photos.

Satellite Imagery

We used a QuickBird satellite imagery acquired on March 6th, 2006. QuickBird is a high spatial resolution instrument (2.4 m), with 4 bands in the visible and near-infrared part of the spectrum. Wavelength ranges of the QuickBird bands are: blue: 450–520 nm, green: 520–600 nm, red: 630–690, and near-infrared: 760–900 nm. The dynamic range of the instrument is 11 bits. In this preliminary stage we used a QuickBird top of the atmosphere radiance image (without atmospheric correction).

Photo-Library Method

Seagrass biomass estimations were performed by visual assessment comparing transect photos to the photos of the quadrats with known biomass (photo-library). As mentioned above the photo library consisted of two photos for each class: one taken in situ and one after sample sorting in laboratory. The transect photographs (1×1 m in size) were divided into 16 squares (0.25×0.25 m). Each of the 16 squares were visually compared with the photo library photos. Seagrass biomass estimates were given for each sixteenths of the transect photo. The total biomass in each 1×1 m transect photo was then calculated as the sum of biomasses in the 16 squares.

Results and Discussion

Three of the quadrats had similar biomass values (see Table 1) and bottom types (seagrass on sand) despite our attempt to create a photo-library of as many differing bottom types as possible. Therefore, the actual number of classes used in estimating biomass along the photo transects was reduced to 13. Table 1 illustrates that there are some other classes with similar seagrass dry weights. However, these classes were different in their bottom type composition.

Table 1 Biomass values (dry weight) of the 0.25 m² cm calibration quadrates

| Sample no | Seagrass dry weight (g) | Algae dry weight (g) | Substrate |
|-----------|-------------------------|----------------------|------------|
| #15 | 0,56 | 5,33 | Sand |
| #5 | 0,62 | 5,43 | Sand/Coral |
| #10 | 0,68 | — | Sand |
| #9 | 1,72 | 21,47 | Coral |
| #16 | 1,96 | — | Sand |
| #8 | 3,75 | 20,96 | Coral |
| #13 | 4,15 | — | Sand |
| #2 | 4,22 | — | Sand |
| #1 | 4,23 | — | Sand |
| #7 | 7,62 | 11,34 | Sand/Coral |
| #11 | 7,64 | 10,24 | Sand |
| #4 | 12,83 | 46,62 | Sand |
| #3 | 13,82 | 1,32 | Sand |
| #6 | 13,91 | — | Coral |
| #14 | 17,31 | 4,08 | Sand |
| #12 | 24,98 | 0,75 | Sand |

Seagrass dry weight estimates along a photo transect by three observers are shown in Fig. 1. The correlation between the results obtained by the observers was good as seen in Figs. 1 and 2. It must be noted that two of the observers participated in the fieldwork, but the observer #3 did not have any previous experience with the seagrasses and did not participate in the fieldwork. This explains why the results of observers #1 and #2 are more consistent. Bigger discrepancies between the results of observer #3 and the other two observers occur at higher biomass values. This

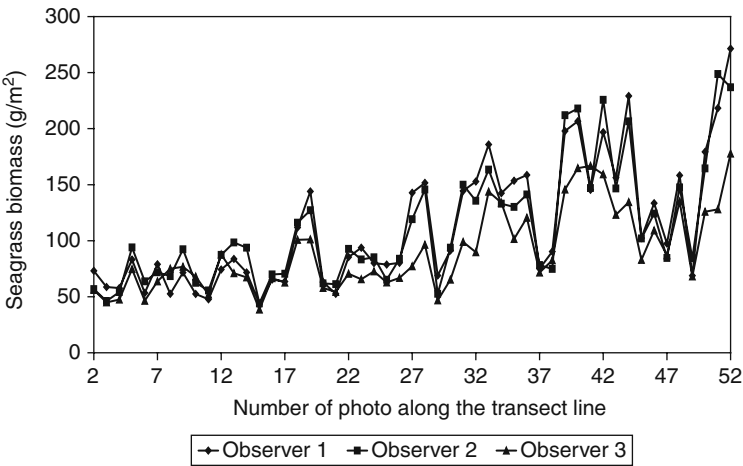


Fig. 1 Seagrass dry weight (in g/m²) along a photo transect estimated by three different observers using the photo-library of quadrats with known biomass

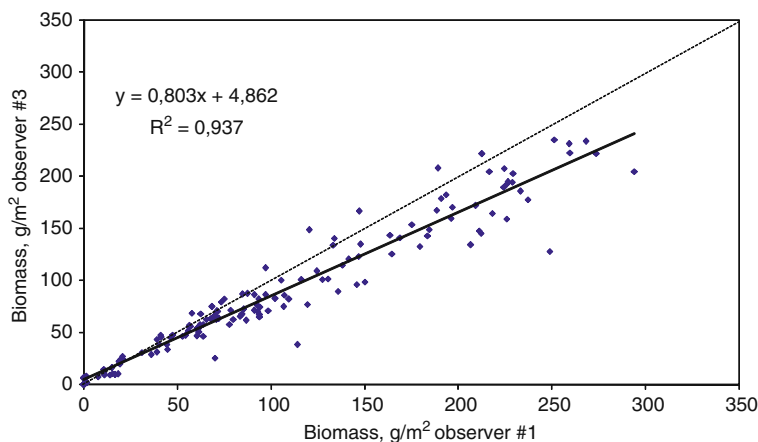


Fig. 2 Correlation between seagrass dry weight estimates (in g/m²) obtained by two observers along the same photo transect. One-to-one line is indicated with dashed line

result is explained by the 3D structure of the canopy, which Observer #3 had never observed. It is theoretically easier to get larger discrepancies in biomass estimates in the case of higher biomass values. The reason behind this is larger between-class differences (see Table 1) in biomass in the case of more dense canopies. The most extreme example would be if one observer decides that all sixteen quadrats in a transect photo belong to a class with the seagrass dry weight of 17.31 g (second highest biomass class) but another observer classifies all as belonging to the highest biomass class (24.98 g). In this example the results of seagrass dry weight estimates per square metre would be 276.96 and 399.68 respectively. This kind of discrepancies did not happen. It must be noted that the transect shown in Fig. 1 was the first all observers classified. The results became more consistent in subsequent transects. Figure 2 illustrates the correlation between biomass estimates of the observer with previous seagrass and in situ fieldwork experience (observer #1) and the observer without previous seagrass experience (observer #3) obtained for four different transects.

The photo-library method can be used as a fast in situ method for the mapping of seagrass biomass. All diving time can be used to take bottom photos either along transects or as point measurements as there is no need to train staff under water or to write down visual biomass estimates. However, our final aim is to estimate seagrass biomass from satellite data. This part of study is still in very preliminary phases. We used a QuickBird top-of-atmosphere radiance image without atmospheric or water column removal. This assumed that the atmosphere did not change within the small area of the Ngederrak Reef and water depth was stable along the photo transects under investigation (as it was).

Correlation between the estimated seagrass dry weight and QuickBird band 1 radiance is shown in Fig. 3. Bottom types along the 100 m transect were variable. There were patches of almost bare sand, areas with almost 100% live coral

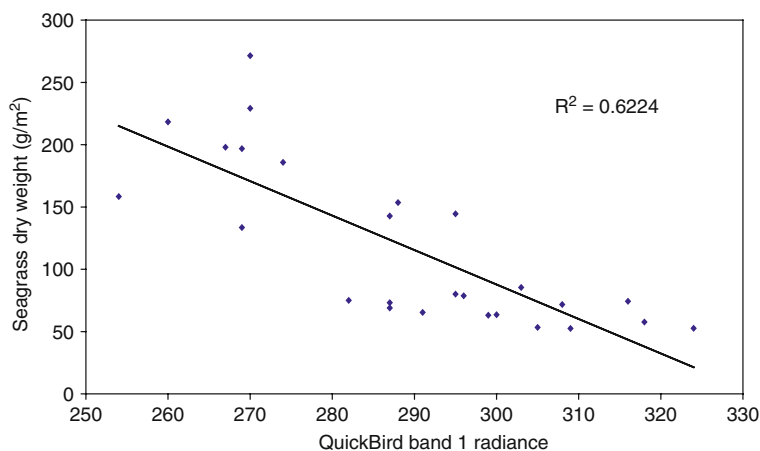


Fig. 3 Correlation between seagrass dry-weight estimated along a photo transect using the photo-library method and QuickBird radiance values along the same transect

cover with sparse seagrass and areas with dense *Thalassia* beds. The variability was often high even within the 1×1 m areas seen in each transect photo. For example 1×1 m scenes could contain live branching and massive coral colonies, bare sand, dense macroalgal cover and different species of seagrasses with variable density. Therefore, the correlation between estimated seagrass dry weight and QuickBird radiance was surprisingly good. This correlation was similar the same when based upon the other two QuickBird visible bands.

There is a general tendency of decreasing seagrass biomass with increasing radiance values (Fig. 3), bare sand pixels being the brightest. However, the pixels with no seagrass may be covered with bright coral sand, relatively dark live coral or rubble covered with turfing algae of different densities. This means that pixels with no seagrass may have very variable brightness values. Variable water depth across the reef also causes variability in radiance values. The later can be removed to a certain extent as demonstrated by Lyzenga (1978). It has been shown that seagrass density can be mapped from satellites (Dierssen et al., 2003) in optically simple situations like seagrass beds on sand substrate. Nevertheless, more studies are needed before one can conclude whether it is possible to map seagrass biomass with QuickBird imagery in such highly variable environment as experienced by the Ngederrak Reef in Palau.

Conclusions

The photo-library method provides an opportunity to map seagrass biomass across a larger area than in the case of other methods as all the diving time is used for collecting photo samples (transect or point) as opposed to training or any other activities.

The biomass samples and photo library have to be collected once. This also saves valuable diving time. Biomass sample collection for the photo-library can also be conducted in non-protected areas

Low variation in results obtained by observers, with different level of experience with seagrasses, suggests that the method is easy to learn in office situations and there is no need to spend diving time on the training of staff.

A first test of using the photo-library method for determining seagrass biomass from space gave promising results even in such a highly variable environment like the Ngederrak Reef in Palau. Further studies are needed to conclude on what types of background (e.g. sand, coral, rubble) seagrass biomass can be estimated from space and determine in which type of backgrounds (dense macroalgal cover?) it may be difficult or impossible.

Acknowledgements The research for this paper was possible through funding through World Bank GEF Coral Reefs Project, Coral Remote Sensing and the field support of the Palau International Coral Reef Center and Dr. Karen Brady. Tiit Kutser's and Ele Vahtmäe's participation in the fieldwork was funded by the Estonian Science Foundation grant 6051 and Estonian Basic Research grant 0712699s05.

References

- Boer, W.F. (2000). Biomass dynamics of seagrasses and the role of mangrove and seagrass vegetation as different nutrient sources for an intertidal ecosystem. *Aquatic Botany* 66: 225–239.
- Catchpole, W.R., Wheeler, C. J. (1992). Estimating plant biomass: a review of techniques. *Australian J Ecol* 17: 121–131.
- Dierssen, H.M., Zimmerman, R.C., Leathers, R.A., Downes, T.V., Davis, C.O. (2003). Ocean color sensing of seagrass and bathymetry in the Bahamas Banks by high-resolution airborne imagery. *Limnol. Oceanogr* 48: 444–455
- Downing, J.A., Anderson, M.R. (1985). Estimating the standing biomass of aquatic macrophytes. *Canadian J Fish and Aquat Sci* 42: 1860–1869
- Duarte, C.M., Kirkman, H. (2002). Methods for the measurement of seagrass abundance and depth distribution. In: Short FT, Coles RG (eds.) *Global Seagrass Research Methods*. Elsevier Science B.V., Amsterdam.
- Hossain, M.K. (2005). An examination of seagrass monitoring protocols as applied to two New South Wales estuarine settings. MSc Thesis. Australian Catholic University.
- Krause-Jensen, D., Quaresma, A.L., Cunha, A.H., Greve, T.M. (2004). How are seagrass distribution and abundance monitored? In: Borum J, Duarte CM, Krause-Jensen D, Greve TM (eds.) *European seagrasses: an introduction to monitoring and management*. The M&MS Project, European Union.
- Lin, H., Shao, K. (1998). Temporal changes in the abundance and growth of intertidal *Thalassia hemprichii* seagrass beds in southern Taiwan. *Botanical Bulletin of Academia Sinica* 39: 191–198
- Lyzenga, D.R. (1978). Passive remote sensing techniques for mapping water depth and bottom features. *Applied Optics* 17: 379–383
- Mellors, J.E. (1991). An evaluation of a rapid visual technique for estimating seagrass biomass. *Aquat. Bot* 42: 67–73
- McKenzie, L., Finkbeiner, J.M.A., Kirkman, H. (2001). Seagrass Mapping Methods. In: F.T. Short and R.G. Coles (eds.) *Global Seagrass Research Methods*. Amsterdam, Elsevier, pp. 101–122.

- Mumby, P.J., Edwards, A.J., Green, E.P., Anderson, C.W., Ellis, A.C., Clark, C.D. (1997). A visual assessment technique for estimating seagrass standing crop. *Aquatic Conservation: Marine and Freshwater Ecosystems* 7: 239–251
- Phillips, R.C., Milchakova, N.A., Alexandrov, V.V. (2006). Growth dynamics of *Zostera* in Sevastopol Bay (Crimea, Black Sea). *Aquatic Botany* 85: 244–248
- Roelfsema, C., Phinn, S., Joyce, K. (2006). Benthic validation photo transect method. University of Queensland, Brisbane. http://www.gpa.uq.edu.au/CRSSIS/publications/GPS_Photo_Transects_for_Benthic_Cover_Manual.pdf
- Short, F.T., Coles, R.G. (2001). *Global Seagrass Research Methods*. Amsterdam, Elsevier.
- Tolan, J.M., Holt, S.A., Onuf, C.P. (1997). Distribution and community structure of ichthyoplankton in Laguna Madre seagrass meadows: potential impact of seagrass species change. *Estuaries*, 20: 450–464
- Waycott, M., Longstaff, B.J., Mellors, J. (2005). Seagrass population dynamics and water quality in the Great Barrier Reef region: A review and future research directions. *Marine Pollution Bulletin* 51: 343–350

A Comparison of Bathymetric Signatures Observed on ERS SAR and LANDSAT TM Images Over the Timor Sea

Medhavy Thankappan and Craig J.H. Smith

Abstract Modulation of surface capillary waves by tidal current flow over submarine relief features causes roughness variations on the ocean surface that are detected by Synthetic Aperture Radar (SAR). Previous studies have demonstrated the presence of features in SAR images that correspond with submarine topography under appropriate sea-state and imaging conditions. In this study, bathymetric signatures observed on two European Remote Sensing Satellite (ERS) SAR images and a near-coincident Landsat Thematic Mapper (TM) image over an area west of Melville Island in the Timor Sea were investigated. Bathymetric features visible on the SAR and optical satellite images correspond well with isobaths of the study area. Submarine relief features seen on the satellite images of the study area were analysed in conjunction with wind and sea-state data. Based on the analysis, we highlight some factors governing the expression of submarine relief features seen in satellite images of the study area. Submarine relief signatures are sensed by optical and SAR sensors through different mechanisms, however similarities in signatures observed in the near-coincident optical and SAR images indicate that the underlying mechanism is common to optical and SAR imaging. Sun glint resulting from specular reflection and modulated by ocean surface roughness is the predominant mechanism producing features on the Landsat TM image that correspond with bathymetric signatures seen on the ERS SAR images. This study demonstrates the potential to extract information on sea bottom topography from sun glint in optical images under specific sun-sensor-target geometries and sea-state conditions, to complement similar information derived from SAR.

Introduction

Satellite based Synthetic Aperture Radar (SAR) sensors have been used to observe various ocean related phenomena. Internal waves, currents, eddies, fronts and bathymetric features have been identified on SAR images in previous studies

M. Thankappan (✉)

Geospatial and Earth Monitoring Division, Geoscience Australia, Canberra, ACT 2601, Australia
e-mail: medhavy.thankappan@ga.gov.au

(Johannessen et al. 1993, Alpers and Hennings 1984, Lyzenga and Marmorino 1998, Shuchman et al. 1985, Jones et al. 2006). The potential of temporally coincident SAR and optical images for studying ocean dynamics has been demonstrated by Gagliardini and Clemente-Colon (2004); they compared thermal fronts detected on European Remote Sensing Satellite (ERS) SAR and Landsat Thematic Mapper (TM) images, by analysing sun glint, upwelling radiance and SAR backscatter.

Studies by Alpers and Hennings (1984), Shuchman et al. (1985), Hennings et al. (1994), Gagliardini and Clemente-Colon (2004), and Jones et al. (2006) have shown that the interaction of tidal currents with bottom topography produces surface signatures that express the bathymetry on SAR images. Hennings et al. (1988) compared satellite images acquired by optical and SAR sensors for a shallow ocean area with submarine relief features; they concluded that brightness variations in both radar and optical images are due to surface effects resulting from the tidal flow over submarine relief.

Chust and Sagarminaga (2007) showed that for two optical satellite images examined under sun glint conditions, the Multi-angle Imaging Spectroradiometer (MISR) sensor provided better detection of capillary wave damping by oil, compared to the single-view Moderate Resolution Imaging Spectroradiometer (MODIS) sensor. Adamo et al. (2006), have proposed the use of MODIS images acquired in sun-glint conditions to complement SAR based detection of oil slicks. The physical principle for retrieving bathymetric information from satellite images over optically shallow water is based on measuring the sunlight reflected off the bottom in conjunction with scattering and attenuation of sunlight in the water column. Several well known approaches model these processes to derive depth information from optical images.

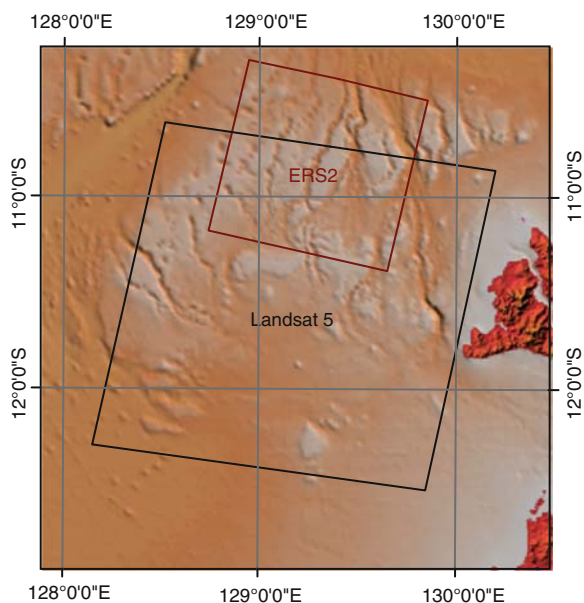
Bathymetric features observed on near-coincident SAR and optical images over the Timor Sea, Australia, are compared in this study. The motivation for this work was to understand various mechanisms that generate low-backscatter signatures on SAR in order to increase the confidence of natural hydrocarbon seep identification in the region. Similarities and differences in the SAR and optical imaging mechanisms and the influence of sun glint are discussed. This study demonstrates the potential for deriving information about submarine relief from sun glint in optical images to complement similar information from near-coincident SAR images.

Methods

Study Area

The study area is located within 10.5° S, 129° E and 11.5° S 130° E. This area of the Timor Sea west of Melville Island, Australia has a shallow and variable bathymetry and is in the vicinity of a region with petroleum potential (Fig. 1). Natural hydrocarbon seeps have previously been observed in SAR images over this region (O'Brien

Fig. 1 Study area showing footprints of the ERS SAR and Landsat TM images on the regional bathymetry grid



et al. 2002). The study area is also located in one of the world's largest macro-tidal shelf environments with large tidal amplitudes that generate strong currents. Shallow, variable bathymetry can interact with the significant tidal flows to produce features on SAR images that resemble natural hydrocarbon seeps.

Satellite and Ancillary Data

Satellite Data

An ERS-1 SAR image acquired on 10 December 1995 at 1:35 UTC and an ERS-2 SAR image acquired on 26 October 1998 at 1:35 UTC were used in this study. The two SAR images were spatially co-located. A Landsat TM image acquired 28 min before (1:07 UTC) the ERS SAR image of 26 October 1998 was also used in this study. Overlap between the footprints of ERS SAR and Landsat TM images is shown in Fig. 1.

Wind Fields

Wind field data close to the time of ERS SAR and Landsat TM imaging was acquired from QuikScat and the Defense Meteorological Satellites Program (DMSP) series of satellites. Wind data in gridded binary format from Remote Sensing Systems (2004), based on the algorithm by Wentz (1992) was used.

Bathymetry

The Geoscience Australia regional bathymetry grid with 0.01 degree cell size (Petkovic and Buchanan, 2002) and hydrographic charts, published by the Australian Hydrographic Service were used.

Tides and Currents

Tide heights coincident with the time of satellite data acquisition were obtained using tide prediction software developed by Flater (2008). Tidal current data modelled for Geoscience Australia's sediment transport studies by Porter-Smith et al. (2004), was used.

Observations

The SAR and Landsat images were analysed in conjunction with ancillary data to understand the mechanisms generating features identified on the images. Archived images were also examined to determine specific conditions under which these features could be identified on the optical images.

ERS SAR and Landsat TM

Similar features, oriented north-east to south-west can be seen on the ERS SAR images acquired on 10 December 1995 (Fig. 2), and 26 October 1998 (Fig. 3). The patterns visible on the 1995 ERS-1 SAR image are less distinct compared to patterns on the 1998 ERS-2 SAR image.

The near-coincident Landsat-5 TM image acquired 28 min before the ERS-2 SAR image also shows similar patterns that correspond to features seen on both the ERS-1 and ERS-2 SAR images (Fig. 4). This is unexpected because the mechanism for SAR imaging is based on Bragg wave resonance and that for optical imaging is based on Fresnel's law which describes the behaviour of light in media with different refractive indices.

Hydrographic charts of the area show a series of submarine valleys approximately 2–4 km wide and up to 80 m deep, in water depths ranging from 25 to 100 m. The regional bathymetry of the study area is shown in Fig. 5. Following a combined analysis of the images from ERS SAR, Landsat TM and the regional bathymetry within a GIS, we found that features in all the images were co-located and corresponded well with the shoals and valleys observed in the regional bathymetry. Figure 6 shows a section of the composite ERS SAR and Landsat TM image (Red: ERS-1 SAR Green: ERS-2 SAR Blue: Landsat TM) with isobaths from the hydrographic charts overlaid. Isobaths from the hydrographic charts coincide with the bathymetric features observed on the ERS SAR and Landsat TM images.

Fig. 2 ERS-1 SAR acquired on 10 December 1995 at 1:35 UTC © ESA 1995

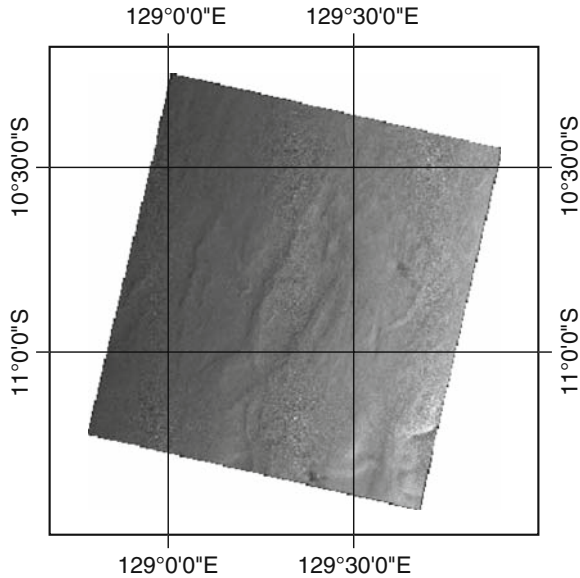
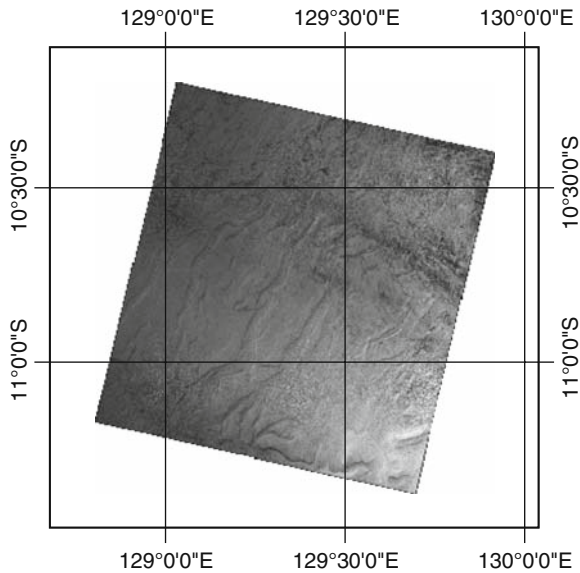


Fig. 3 ERS-2 SAR acquired on 26 October 1998 at 1:35 UTC © ESA 1998



Wind speeds between 3 and 12 m/s provide the roughness elements required for observation of capillary waves (of the order of centimetres) by SAR; within this range the distinct signatures produced by the modulation of capillary waves by wind are most evident. At lower wind speeds, a smoother sea surface reflects radiation away from the sensor to produce dark features on the image. At higher

Fig. 4 Landsat-5 TM image acquired on 26 October 1998 at 1:07 UTC

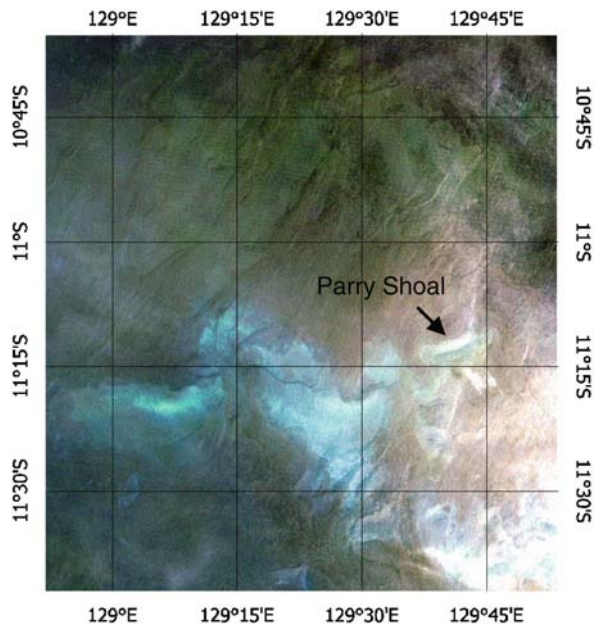
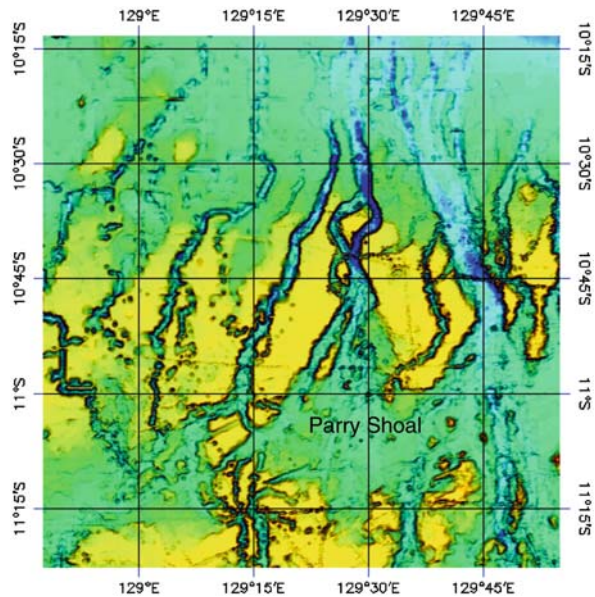


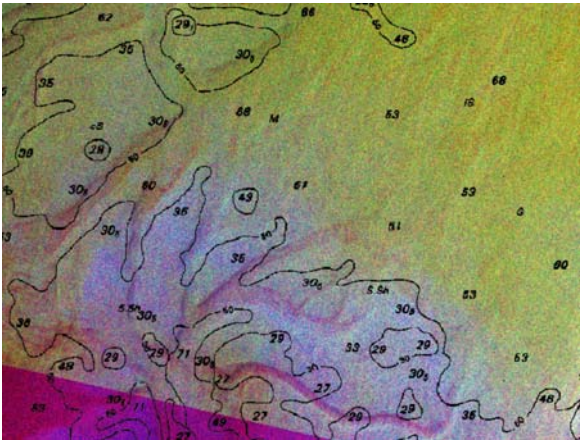
Fig. 5 Regional bathymetry showing valleys and shoals in the study area (yellow = shallow, blue = deep)



wind speeds, increased SAR backscatter diminishes contrast of the observed ocean features (Gagliardini and Clemente-Colon, 2004).

According to Alpers and Hennings (1984), bottom topography is expressed on SAR images in the presence of moderate winds of 3–5 m/s and tidal current speeds

Fig. 6 A section of the ERS SAR and Landsat TM composite image with isobaths from hydrographic chart



of about 0.5 m/s. Imaging of bottom topography by SAR is based on the effect of tidal current on the radar backscatter. The interaction between tidal current and bottom topography results in modulation of the surface current velocity; the modulation of surface current velocity generates variations in the wave spectra intensity; the variations in the wave spectra intensity modulate the level of radar backscatter. A schematic representation of the theory of SAR imaging of bottom topography is shown in Fig. 7.

To understand the mechanism involved in imaging of the bathymetric features seen on the Landsat TM image while comparing it with the ERS SAR images, the condition of wind, tide and currents at the time of image acquisition were examined. Wind and tide condition at the time of satellite image acquisition is presented in Table 1.

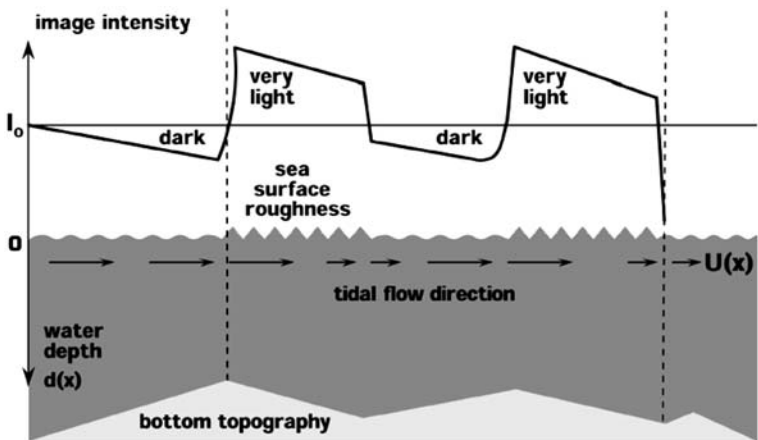


Fig. 7 Relationship between SAR image intensity, sea surface roughness, tidal flow and bottom topography (Alpers and Hennings, 1984)

Table 1 Wind speed and tide height at the time of SAR and TM image acquisition

| Satellite and sensor | Date time (UTC) | Wind speed (m/s) | Tide height (m) (hours to low tide) |
|----------------------|--------------------------|------------------|--|
| ERS-1 SAR | 10 December 1995 (01:35) | 7.5 | 0.74 Ebb (1.1) |
| ERS-2 SAR | 26 October 1998 (01:35) | 3.5 | 1.5 Ebb (2.4) |
| Landsat-5 TM | 26 October 1998 (1:07) | 3.5 | 1.9 Ebb (3.0) |

The wind speed at the time of acquiring the 1995 SAR image was 7.5 m/s compared to 3.5 m/s in the 1998 SAR and Landsat TM images. The time of imaging of the SAR and optical images coincided with ebb tide with time to low tide varying from 0.74 to 1.9 h.

Tidal currents of the study area modelled for GEOMAT, Geoscience Australia's sediment transport model (Porter-Smith et al., 2004) indicated strong semi-diurnal tidal currents measuring 0.5 m/s directed east-west in the study area. Typical monthly current time-series plots indicated strong east-west currents, with speeds of approximately 0.5 m/s during spring tides and approximately 0.2–0.3 m/s during neap tides.

Figure 8(a) and (b) shows bathymetry of a part of the study area with convergent channels and the corresponding section of the ERS-2 SAR image. Depth of the convergent channels range from 25 to 75 m. From analysis of the wind speed, tide height, current speed and bathymetry of the study area in the context of the SAR imaging theory (Alpers and Hennings, 1984), features seen on the ERS SAR images can be adequately explained by the variations in the sea surface roughness caused by tidal flow over variable bottom topography. The reduced contrast in the 1995 ERS-1 image (Fig. 2) compared to the 1998 ERS-2 image (Fig. 3) can be explained by the higher wind speed of 7.5 m/s at the time of ERS-1 imaging which has increased the average SAR backscatter and diminished the overall contrast of features observed in the image.

Sun glint seen in satellite images results from specular reflection of solar radiation and its existence is well documented (Cox and Munk, 1954). Sun glint is seen on satellite images when the sun-sensor-target geometry is such that the law of reflection is satisfied. The Landsat TM image in Fig. 4 shows the presence of sun glint, identified by increased brightness on the lower right side of the image which

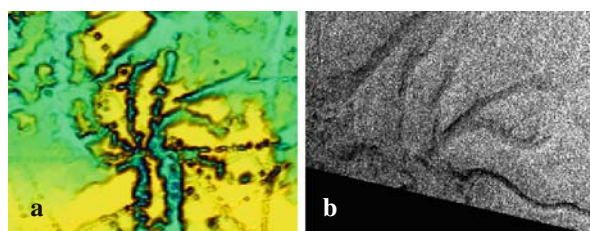


Fig. 8 (a) Bathymetry showing convergent channels (b) same bathymetric features on ERS-2 SAR © ESA 1998

progressively decreases towards the left of the image. The presence of sun glint in the image is consistent with the illumination geometry at the time of Landsat overpass; the sun elevation angle was 60.8° and sun azimuth angle was 94.6° . In their study using aerial photographs of sun glint to determine the statistical occurrence of capillary wave slopes, Cox and Munk (1954) showed that wave-slope statistics are governed by wind speed; they showed that the mean square wave slope increased linearly with wind speed. Their study revealed that capillary and locally induced gravity waves were the main contributors to sun glint.

Hennings et al. (1988) showed that the interaction of tidal flow and bottom relief increases the mean slope of the waves, which causes an increase in the number of wave facets imaged by the optical sensor. Hennings et al. (1988) suggested that the Cox-Munk model alone may not adequately explain increased brightness observed in optical images over shallow water and that the effects due to tidal interaction with bottom relief need to be considered as well.

We examined the visibility of bathymetric features as a function of TM wavelength bands in order to understand the influence of sun glint. Figure 9 shows the area of convergent channels as it appears in the TM Visible (Blue, Green, and

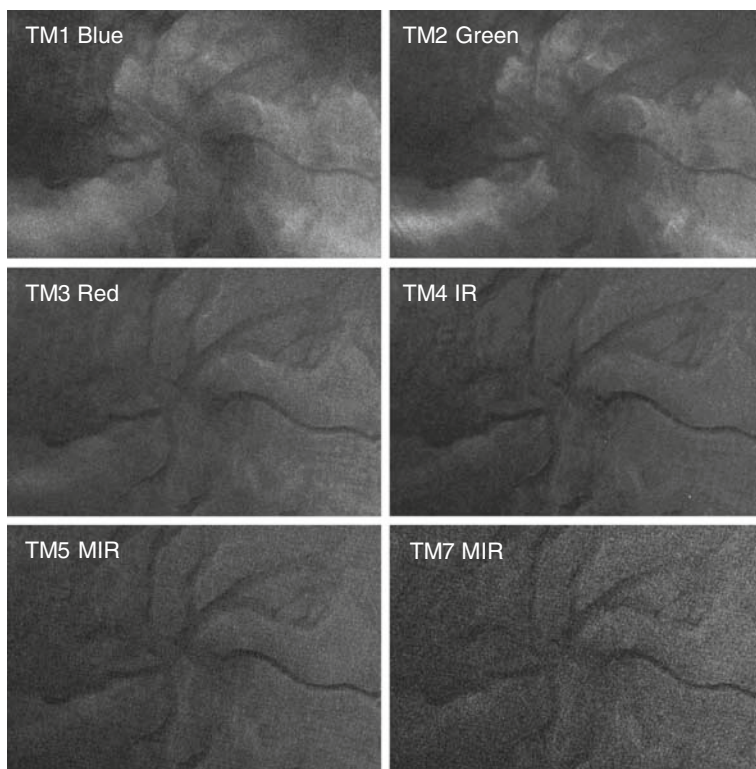


Fig. 9 Bathymetric feature visibility as a function of wavelength on Landsat TM image of 26 October 1998

Red), Infrared (IR) and Middle Infrared (MIR) wavelength bands. The bright areas around the convergent channels in TM bands 1 and 2 could be a result of water constituents associated with ocean colour or the circulation of distinctive water masses (Fig. 4). It is interesting to note that the same convergent channels are also visible in the TM near infrared (NIR) and middle infrared (MIR) wavelength bands; this is somewhat unexpected, as water absorbs strongly in the NIR and MIR wavelength region.

The visibility of these features on the Landsat TM image has a weak dependence on wavelength, as seen in Fig. 9, indicating that the features are the result of surface phenomena. This raises the question of whether the features in the Landsat TM image are caused by the same mechanism as in the case of the SAR images.

Our interpretation of the above finding is that the sun glint is being modulated by the interaction of the tidal current and bottom topography. Based on the observations of the features in the Landsat TM NIR and MIR bands, the only possible mechanism that could adequately explain the correlation between submarine topography and brightness in the image is specular reflection of the sunlight from the sea surface with variable roughness where the roughness is based on bottom-current interaction effects described above. Therefore, sun glint modulated by ocean surface roughness is the predominant mechanism generating the expression of bathymetric features on the Landsat TM image.

Archived Landsat Images

Surface expressions of bathymetric features resulting from sun-glint have not been observed on optical images of the study area very frequently. Therefore, 284 Landsat Thematic Mapper and 127 Enhanced Thematic Mapper (ETM) archived quick look images acquired at the Australian Centre for Remote Sensing (ACRES) between 1986 and 2005, were examined to determine if detection of bathymetric features was related to specific sun-sensor-target geometries. The images were examined to determine if Parry Shoal, a prominent feature below 20 and 30 m of water, could be identified. The location of Parry Shoal is indicated on images shown in Figs. 4 and 5. A similar exercise was not attempted for the SAR images as the only two images available in the archive that show Parry Shoal, are used in this study.

Table 2 lists all Landsat TM and ETM images from the ACRES archive in which Parry Shoal could be unambiguously identified. Table 2 also shows the illumination conditions described by sun elevation and azimuth angles, and the wind speeds and tide heights at the time of imaging; it is clear that only certain combinations of the sun-sensor-target geometry, wind and tide conditions favour the identification of Parry Shoal. Sun elevation angles ranging from 52° to 63° and sun azimuth angles from 57° to 111° in conjunction with low to moderate wind speed of 3–7 m/s at low tide seem to be favour generation of bathymetric signatures on Landsat images of the study area. To select glint-free satellite images for bathymetry mapping, Sagar

Table 2 Wind, tide and illumination conditions for archived Landsat TM and ETM images in which Parry Shoal can be identified (ETM images shown in bold)

| Date time (UTC) | Sun elevation | Sun azimuth | Wind speed (m/s) | Tide height (m) (hours to low tide) |
|-----------------------------|---------------|---------------|------------------|-------------------------------------|
| 12 Oct 1987 00:56:23 | 56.7° | 85.3° | 3 | 1.7 Ebb (2.9) |
| 17 Oct 1989 00:54:02 | 56.8° | 89.1° | 3 | 0.3 Ebb (1.6) |
| 4 Oct 1990 00:48:32 | 53.7° | 81.2° | 3 | 0.6 Ebb (0.4) |
| 8 Nov 1991 00:53:09 | 57.1° | 102.3° | 4 | 0.4 Ebb (1.2) |
| 7 Oct 1997 01:02:00 | 57.5° | 81.9° | 5 | 1.80 Ebb (3.0) |
| 8 Sep 1998 01:07:40 | 52.5° | 64.1° | 7 | 1.0 Ebb (1.5) |
| 14 Jan 2005 01:15:04 | 55.7° | 111.0° | 5 | 1.6 Ebb (2.6) |
| 29 Oct 2002 01:16:45 | 62.9° | 88.7° | 3 | 2.2 Ebb (4.1) |
| 2 Feb 2003 01:17:33 | 55.8° | 103.2° | 3 | 0.6 Ebb (0.9) |
| 22 Mar 2003 01:17:38 | 54.9° | 72.3° | 3 | 2.6 Ebb (2.7) |
| 29 Aug 2003 01:17:20 | 52.0° | 57.6° | 3 | 1.4 Ebb (1.4) |
| 18 Oct 2004 01:17:38 | 62.7° | 88.7° | 3 | 1.0 Ebb (2.2) |
| 21 Oct 2005 01:18:11 | 63.0° | 90.8° | 3 | 0.8 Ebb (2.0) |

et al. (2008) applied a tool that uses the sun elevation and azimuth angles for predicting the sun glint potential. We used the sun elevation and azimuth angle ranges identified above in the glint prediction tool and found that the sun glint potential for these values was moderate to high. The wind speed and tidal current speed threshold requirements specified by Alpers and Hennings (1984) for expression of bathymetry on SAR images were also met in the study area at the time of Landsat image acquisition.

The prevalence of low tide in all instances of imaging where Parry Shoal could be identified on the Landsat images is a significant finding. The average tide height at high tide for all observations is 3.8 m compared to an average tide height of 1.2 m at the time of imaging. The time to low tide, shown within parentheses in the last column of Table 2, identifies the point in the tidal cycle corresponding to the time of imaging; this provides a measure of the hydrodynamic flow. While these observations apply only to Parry Shoal and not the larger study area, it is reasonable to assume that other submarine features across the study area which were identified on the SAR images are likely to be identified on the Landsat images if similar illumination and sea-state conditions prevail at the time of imaging; further investigation into this is required.

Figures 10 and 11 show two Landsat TM images where Parry Shoal is not apparent. The image in Fig. 10 was acquired on 12 October 1993 at 00:51 UTC; the sun elevation angle was 55.5° and the sun azimuth angle was 86.1°; the illumination conditions are within the optimum ranges outlined in Table 2. At the time of image acquisition however, it was flood tide and 95 minutes after occurrence of low tide at 23:16 UTC. The wind speed at the time of image acquisition was 4 m/s.

The image in Fig. 11 was acquired on 3 May 2004 at 01:09 UTC; the sun elevation angle was 47.6° and the sun azimuth angle was 50.6°; illumination conditions are outside the optimum ranges identified earlier. Low tide occurred at 00:40 UTC;

Fig. 10 Landsat TM image of 12 October 1993 over Parry Shoal (bathymetric feature not apparent)

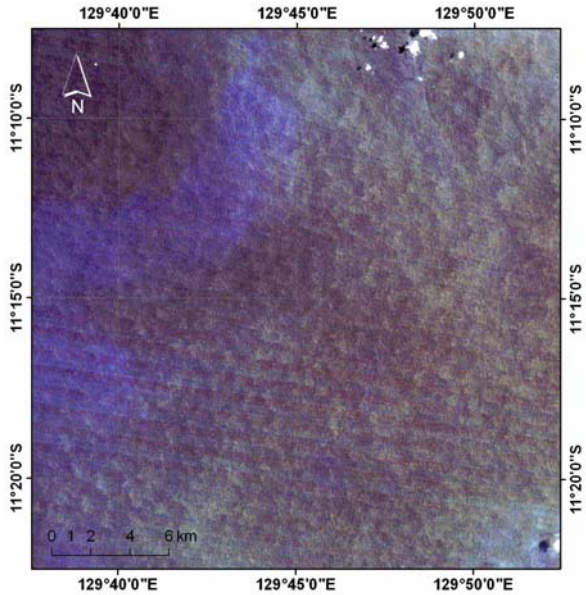
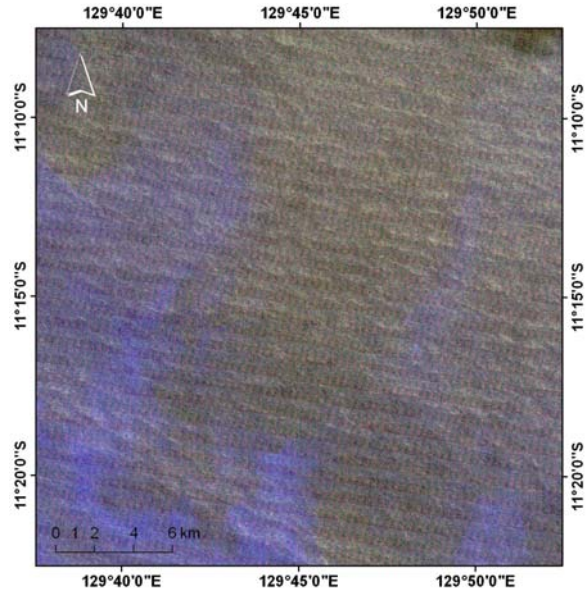


Fig. 11 Landsat TM image of 3 May 2004 over Parry Shoal (bathymetric feature not apparent)



at the time of image acquisition it was 29 min after low tide(flood tide) and wind speed was 7 m/s. The two images illustrate the need for appropriate illumination conditions to occur in conjunction with the hydrodynamic flows during ebb tide for expression of bathymetric features in optical images over the study area.

Discussion

The prevalence of ebb tide in all cases where bathymetric features have been imaged by the SAR and optical sensors indicates that interaction of tidal currents and variable bottom topography is a dominant factor. A shallower water column over the submarine bathymetric features during low ebb tide is likely to result in stronger expression of bathymetry at the sea surface enabling imaging of the features by both SAR and optical sensors.

When solar illumination geometry favours the observation of upwelled radiance over sun glint (low solar elevation and azimuth angles), TM channel 1 can provide information related to ocean colour and water quality. The relatively weak intensity of water leaving radiance is strongly dependent on wavelength, with an absorption minimum corresponding to the blue-green region.

When illumination conditions favour sun glint, it dominates the water leaving radiance detected by the optical sensor. As detection of sun glint has weak dependence on wavelength, sun glint can be observed in all the optical bands. The features observed on the Landsat TM image of 26 October 1998 correspond to the reflective effects of sun glint resulting from sea surface roughness modulated by tidal current flow over variable bathymetry.

In the case of ERS SAR the antenna position with respect to the illuminated area of the sea surface remains the same for each spatially co-located image footprint; this means under optimal wind and tide conditions when hydrodynamic modulation of sea surface roughness occurs, bottom topography in the study area is more likely to be imaged by SAR.

Optical imaging with Landsat however is different as the sun's position changes during the day and throughout the year. The illumination geometry for the presence of sun glint is generally satisfied only around the time of summer solstice in the study area when the combination of sun elevation and sun azimuth angles is optimal. In addition to the presence of sun glint, wind and sea-state conditions also need to be optimal for imaging bathymetric features in the study area.

Conclusions

Ocean features associated with bathymetry of the study area are imaged by both SAR and optical sensors with striking similarities. Moderate winds, strong currents and low tide prevailed at the time of imaging in all cases where bathymetric features are identifiable. This indicates the prominent role of tidal flow in hydrodynamic modulation of capillary waves enabling surface expression of bathymetry.

In the case of ERS SAR, bathymetric feature imaging is enabled primarily through modulation of sea surface roughness by tidal flow over variable bottom topography. In the case of Landsat TM, imaging of the same bathymetric features is enabled primarily through the modulation of sun glint by sea surface roughness resulting from interaction of tidal flow and bottom topography.

ERS SAR and Landsat TM images with sun glint represent to a first approximation the sea surface roughness conditions in the study area. For optical imaging, illumination conditions change and therefore bathymetric feature detection through sun glint is achieved only under very specific sun-sensor-target geometries

When sun glint prevails in the study area, optical sensors can image bathymetric features through their response to sea surface roughness modulated by tidal currents and bathymetry. Under optimum conditions, sun glint in optical satellite images could provide useful information on ocean features which complement the use of SAR.

Acknowledgement The authors would like to thank Mark Hemer for providing the modelled tidal current data for the study area.

References

- Adamo M, DeCarolis G, De Pasquale V, and Pasquariello G (2006) On the combined use of sun glint MODIS and MERIS signatures and SAR data to detect oil slicks. In: Bostater CR, Neyt X, Mertikas SP and Velez-Reyes M (eds) *Remote Sensing of the Ocean, Sea Ice and Large Water Regions 2006*, Proceedings of SPIE Vol. 6360, 63600G
- Alpers W, and Hennings I (1984) A theory of the imaging mechanism of underwater bottom topography by real and Synthetic Aperture Radar. *Journal of Geophysical Research*, 89–6: 10529–10546
- Chust G, and Sagarminaga Y (2007) The multi-angle view of MISR detects oil slicks under sun-glitter conditions. *Remote Sensing of Environment* 107: 232–239
- Cox C, and Munk WH (1954) The measurement of the roughness of the sea surface from photographs of the sun's glitter. *Journal of the Optical Society of America*, 44: 838–850
- Flater D (2008) XTide Tide and Current Predictor, <http://tbone.biol.sc.edu/tide/> accessed on 4-07-2007
- Gagliardini DA, and Clemente-Colón P (2004) A comparative assessment on the use of SAR and high resolution optical images in ocean dynamics studies. *International Journal of Remote Sensing*, 25: 1271–1275
- Hennings I, Doerffer R, and Alpers W (1988). Comparison of submarine relief features on a radar satellite image and a Skylab satellite photograph. *International Journal of Remote Sensing*, 9: 45–67
- Hennings I, Matthews J, and Metzner M (1994) Sun glitter radiance and radar cross section modulations of the sea bed. *Journal of Geophysical Research*, 99–8: 16303–16326
- Johannessen JA, Røed LP, and Wahl T (1993) Eddies detected in ERS-1 SAR images and simulated in reduced gravity model. *International Journal of Remote Sensing*, 14: 2203–2213
- Jones AT, Thankappan M, Logan GA, Kennard JM, Smith CJ, Williams AK, and Lawrence GM (2006) Coral spawn and bathymetric slicks in Synthetic Aperture Radar (SAR) data from the Timor Sea, northwest Australia. *International Journal of Remote Sensing* 27: 2063–2069
- Lyzena DR, and Marmorino G (1998) Measurement of surface currents using sequential Synthetic Aperture Radar images of slick patterns near the edge of the Gulf Stream. *Journal of Geophysical Research*, 103–9: 18769–18777
- O'Brien GW, Glenn K, Lawrence G, Williams AK, Webster M, Burns S, and Cowley R (2002) Influence of hydrocarbon migration and seepage on benthic communities in the Timor Sea, Australia. *APPEA Journal*, 42: 225–239
- Petkovic P, and Buchanan C (2002) Australian bathymetry and topography grid. [CDROM]. Canberra: Geoscience Australia

- Porter-Smith RP, Harris PT, Anderson O, Coleman R, and Greenslade D (2004) Classification of the Australian continental shelf based on predicted sediment threshold exceedance due to tidal currents and swell waves. *Marine Geology*, 211: 1–20
- Remote Sensing Systems (2004) SSM/I and QuikScat data <http://www.remss.com/> accessed on 10-11-2008.
- Sagar S, Wettle M, Damlamian H (2008) Shallow water bathymetry mapping using a physics-based remote sensing approach for tsunami inundation modelling in the south-west Pacific. *Proceedings of the 14th Australasian Remote Sensing and Photogrammetry Conference*, Darwin, 29 September–3 October
- Shuchman R, Lyzenga DR, and Meadows G (1985) Synthetic Aperture Radar imaging of ocean-bottom topography via tidal current interactions: Theory and observations. *International Journal of Remote Sensing*, 6–7: 1179–1200.
- Wentz FJ (1992) Measurement of oceanic wind vector using satellite microwave radiometers. *IEEE Transactions on Geoscience and Remote Sensing*, 30: 960–972

Optical Properties of Water Bodies in the Torres Strait, Australia, from Above-Water Reflectance

L.J. Majewski, W.M. Klonowski, and M.M. Slivkoff

Abstract The marine environment in the shallow waters to the north of Australia is poorly characterised. Vast areas have never been surveyed and relatively little is known about the composition of the water mass, the properties of the seabed and the bathymetry of the shallowest areas. Satellite-based optical remote sensing has potential to provide wide-ranging, inexpensive and frequent coverage of the region, but techniques for the estimation of environmental parameters from satellite data are dependent on robust inversion algorithms and a high level of knowledge about the prevalent environmental conditions. In November 2005 a suite of physical, optical and biological measurements were collected in the Torres Strait (near Thursday Island, Australia) and in the Gulf of Carpentaria. Above-water reflectance measurements were made along the cruise track using a 3-channel continuous sampling spectroradiometer. A semianalytic model was applied to the reflectance measurements to estimate water column depth and in-water optical properties. Model retrieved backscattering compared favourably, both in terms of spectral slope and magnitude, with in-water measurements. The model retrieved phytoplankton absorption compared favourably with laboratory measurements where these were available. Model retrieved depth values were within 10% of sounded depths at 10 of 11 measurement sites where the bottom contribution to the measured above water reflectance exceeded 15%.

Introduction

Accurate, high spatial resolution, bathymetric data are required for a multitude of purposes. Foremost among these are navigation, physical oceanography and benthic ecology. Consequently determination of bathymetry has prompted many hydrographic, oceanographic and ecological surveys to be undertaken. Passive remote sensing of shallow water bathymetry has long been suggested as a method for

L.J. Majewski (✉)

Department of Imaging and Applied Physics, Curtin University of Technology, Perth, WA 6845, Australia

rapidly obtaining high-resolution bathymetric data (Lyzenga, 1978). Satellite-based optical remote sensing has potential to provide wide-ranging, inexpensive and frequent coverage of a particular region of interest (Robinson et al., 2000).

Ratio-based methods have been devised (Lyzena, 1978) and applied to multi-spectral data sets with high spatial resolution (Dierssen et al., 2003). These ratio-based methods often require regional tuning that inherently accounts for, or obscures, variations in the optical properties of the overlying water column. Accounting for these water column properties has been shown to improve the accuracy of retrieved depth (Philpot, 1989) and benthic cover information (Mumby et al., 1998). The increased availability of hyperspectral data, often with high-spatial resolution, has enabled the development and application of more robust coastal water algorithms that address the problem of separating contributions from benthic signals and water column properties from above water remotely sensed reflectance, R_{rs} , (Lee et al., 1999).

Relatively little is known about the properties of the seabed and the bathymetry of the shallow waters to the north of Australia. Still less is known regarding the magnitude and variability of in-water optical properties. As an example, the NASA bio-Optical Marine Algorithm Data set (NOMAD, Werdell and Bailey, 2005) currently holds no measurements of optical properties in the Torres Strait. The Torres Strait is a submerged land bridge between Australia and Papua New Guinea linking the tropical Arafura and Coral Seas; it is shallow and dotted with numerous reef systems and over 200 islands. Narrow channels between the reef systems experience strong tidal currents that influence the structure of the sea floor (Harris, 1991) and change in-water optical properties substantially over relatively small distances (this study).

In November 2005 a suite of physical, optical and biological measurements were collected in Torres Strait and the Gulf of Carpentaria (Fig. 1). The primary objective of the field program was to obtain a baseline characterisation of the inherent

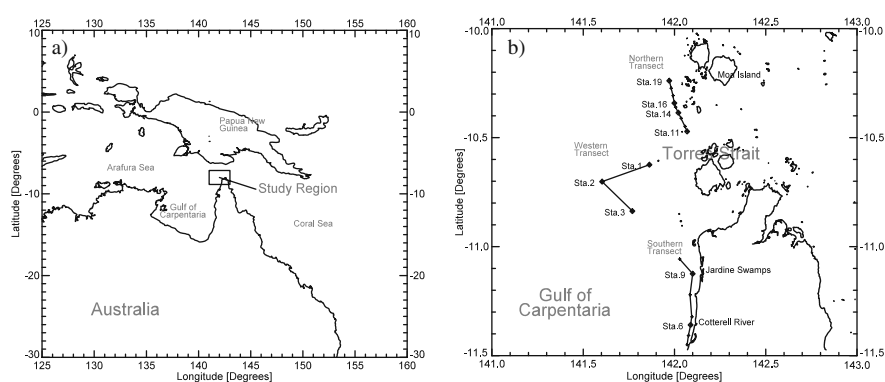


Fig. 1 Location of the study region and field operations. (a) Regional map indicating the location of the study region. (b) Location of sampling sites within the study region. In-water optical properties were measured at Sta. 1–19. Water samples were collected at Sta. 1, 2, 3, 6, 9, 11, 14, 16 and 19 for laboratory analysis

optical properties of the waters in and around Torres Strait. The secondary aim was to assess the accuracy and validity of depth and optical property retrievals obtained through application of a semianalytic model to measurements of R_{rs} collected along horizontal transects.

Method

To address the aims of the research program, simultaneous measurements of temperature, salinity, beam attenuation at 660 nm, $c_{pg}(660)$, and chlorophyll fluorescence were measured along horizontal transect lines using a ferry-box system (composed of a SeaBird SBE-43 μ TSG, WET Labs Wetstar and c-star). Profiles of in-water optical properties were obtained at a series of 19 locations along the cruise track and water samples were collected at nine locations for laboratory analysis (see Fig. 1b). Stations 1–3 (western transect, 23/11/2005) were sampled to the west of Torres Strait, Stations 4–10 (southern transect, 24/11/2005) were sampled in the coastal waters of the Gulf of Carpentaria while Stations 11–19 (northern transect, 25/11/2005) were conducted in Torres Strait, northwest of Thursday Island (10.35°S, 142.13°E). R_{rs} was measured along the cruise track using a 3-channel continuous sampling spectroradiometer (DALEC: downwelling above water radiance (L) and irradiance (E) collector).

In Water Backscattering

Profiles of the volume scattering function in the direction of 140°, $\beta(140^\circ)$, were measured at six wavelengths with a HOBILabs HydroScat-6 at all profiling stations. Estimates of the particulate backscattering coefficient at depth z , $b_{bp}(z)$, were obtained using the method of Maffione and Dana (1998),

$$b_{bp}(z, \lambda) = 2\pi \chi \left(\beta(z, \lambda, 140^\circ) - \beta_w(z, \lambda, 140^\circ) \right), \quad (1)$$

where β_w is the volume scattering function for water at a given temperature and salinity (Morel, 1974). χ is known to be dependent upon the volume scattering function of the observed water column, but was given the wavelength independent value of 1.18 following Boss and Pegau (2001).

The path length of the HydroScat-6 varies with the amount of absorbing and scattering material present within the water column. In highly attenuating water, a small portion of the backscattered light will be selectively absorbed before reaching the detector. Measured optical properties were used with the HydroSoft (HobiLabs) processing software to correct for path length amplification. A spectral shape parameter, Y (unitless), may be used to approximate b_{bp} at any wavelength in the range 200–800 nm (Smith and Baker, 1981),

$$b_{bp}(\lambda) = b_{bp}(\lambda_0) \left(\lambda_0 / \lambda \right)^Y, \quad (2)$$

where λ_0 is a reference wavelength. For $\lambda_0 = 400$ nm, values of Y derived from field measurements generally range between 0 and 2.5 (Lee et al 1999). Y varies with the size of backscattering particles. If the particles are small (e.g. oligotrophic regions where nanophytoplankton and picophytoplankton may dominate the particle assemblage) then the value of Y is large and vice versa (Carder et al, 1999).

Absorption, Suspended Matter and Chlorophyll

Laboratory based measurements of in-water properties are used as the bench mark against which bio-optical measurements are compared. Sub-samples of the collected water were strained through glass fibre filters (Whatmann GF/F) and stored in liquid nitrogen for subsequent laboratory determination of particulate absorption, a_p .

The optical density of each particulate absorption sample was measured following the protocol (Mitchell et al., 2003). Pathlength amplification was accounted for using the coefficients of Cleveland and Weidemann (1993), to yield a_p (m^{-1}). The filter pads were then treated with bleach to remove any algal pigments present and re-examined, yielding absorption due to non-algal particles, a_{nap} , and absorption due to phytoplankton, a_ϕ , since $a_\phi = a_p - a_{nap}$.

Other sub-samples were obtained for the determination of Total Suspended Matter (TSM) and the fluorometric determination of the phytoplankton pigment chlorophyll-a (*TChl-a*). Due to the remote location and operational constraints, measurements of chromophoric dissolved organic matter (CDOM) absorption, a_g , were not made.

Above Water Surface Reflectance

Above-water remote sensing reflectance, R_{rs} , was measured along the cruise track using the DALEC. The DALEC consists of three optical channels, which permit simultaneous recordings of above water downwelling irradiance, E_d , total upwelling radiance, L_t , and downwelling sky radiance, L_{sky} . The E_d and L_t channels record light into 256 channels, from 350 to 1100 nm, with a nominal bandwidth of 3.3 nm. The L_{sky} sensor incorporates 2048 spectral channels, covering the wavelength range 350–800 nm, and has a nominal bandwidth of 0.3 nm per spectral channel.

Radiometric calibration of the DALEC was performed a week prior to the field campaign.

Dark current measurements were recorded just before and/or just after the collection of underway transect field measurements. The dark current measurements were subtracted from each spectrum collected along transects, after which the lab-determined calibration responsivity coefficients were employed to yield E_d , L_t and L_{sky} .

R_{rs} is calculated as the ratio of L_w/E_d , where L_w is the water leaving radiance. An above water, downward-looking, radiance detector will measure the total radiance

incident upon the detector, L_t , where L_t is the sum of L_w , the sky glint reflected by the sea surface, L_r , and the reflected sun light or glint, L_g .

In practice, when L_g is significant the water-leaving radiance is impossible to estimate and these contaminated spectra are discarded. The L_t sensor was orientated to view the surface 135° away from the solar plane and 40° from nadir to minimise the occurrence of L_g contamination. Additionally, the L_{sky} sensor was orientated to view 40° off zenith and 135° off the solar plane. The DALEC was mounted on the bow of the vessel using a gimballed mounting structure, allowing for pitch, yaw and roll movement, minimising deviations in view geometry caused by vessel motion.

A number of methods, differing in complexity, are available to estimate L_r (Mobley, 1999). During this particular field experiment the wind speed was on the order of 5–10 m/s and the sky was often overcast. These conditions allow the use of the simplistic model $L_r(\lambda) = \rho L_{sky}(\lambda)$, where ρ is a reflectance factor given the value 0.028 (Mobley, 1999). Thus, R_{rs} for each set of measurements may be determined using

$$R_{rs}(\lambda) = (L_t(\lambda) - 0.028L_{sky}(\lambda))/E_d(\lambda). \quad (3)$$

During DALEC deployments the vessel speed was maintained between 6 and 12 kt. The system captured over 10,000 quality controlled spectra during the 4–5 h it was deployed each day.

Reflectance Model

R_{rs} is a function of in-water properties, solar geometry and viewing geometry. When operating in shallow water, the influence of the substrate must also be accounted for. This relationship can be formulated as,

$$R_{rs}(\lambda) = f[a(\lambda), \beta(\lambda), \rho_{benthos}(\lambda), H, \theta_w, \theta_v, \varphi], \quad (4)$$

where $\rho_{benthos}$ is the reflectance of the substrate, H is the depth of the water column, θ_v is the subsurface sensor view-angle, θ_w is the subsurface solar zenith angle and φ is the viewing azimuth angle from the solar angle.

R_{rs} and the radiance reflectance just below the surface, r_{rs} , are related by accounting for transmission/reflectance at the air-sea interface using $R_{rs} = \zeta r_{rs}/(1 - \Gamma r_{rs})$, where ζ represents the water-to-air radiance divergence factor and the denominator accounts for the internal reflection from water to air (Lee et al., 1998; 1999).

Numerous researchers have developed bio-optical models relating in-water properties to r_{rs} for an optically deep water column, r_{rs}^{dp} , (e.g. Gordon et al., 1988). In shallow water, the contribution to r_{rs} from the benthos, r_{rs}^b , may not be negligible. Lee et al. (1999) developed a semianalytic model which accounts for water column and benthic contributions to the measured reflectance.

A Levenberg-Marquardt optimisation scheme was used to alter the parameters of the semianalytic model to match measured values of R_{rs} , after accounting for air-water interface effects (Lee et al., 1998; Klonowski et al., 2006).

Results

The vertical profiles of temperature, salinity and $\beta(140^\circ)$ indicated that the water column at each measurement site was well mixed. Thus, near surface and depth averaged parameters may be used to characterise the optical properties of these sites. Figure 2 displays the surface $TChl-a$, TSS , $a_\phi(440)$, $a_{nap}(440)$ and the depth averaged values of $b_{bp}(400)$ at sites where in-water measurements were made.

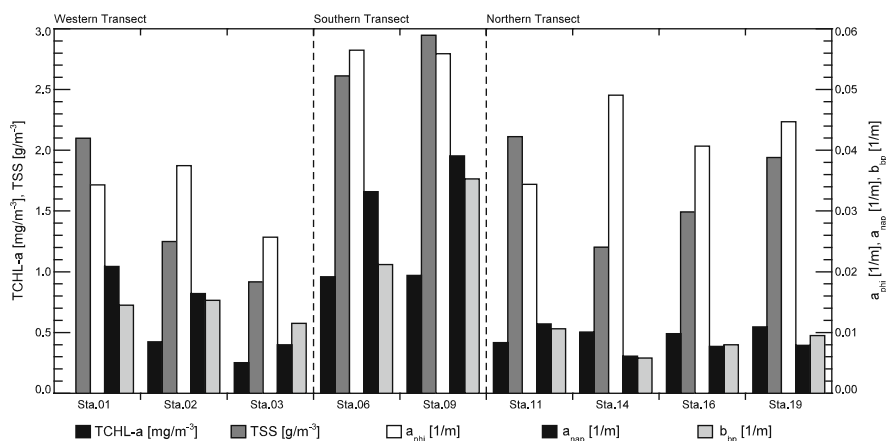


Fig. 2 Selected bio-optical properties from sites where in-water optical measurements were made

The spectral properties of coefficients are required to solve the inverse problem. The average, normalised, a_ϕ spectra measured during the experiment was input directly to the semianalytic model since there was no NOMAD data available. The spectral slope (S) of a_{CDOM} was set to the global mean of 0.015 (Twardowski et al., 2004), Y was determined using the empirical relationship of Lee et al. (1999) and the reflectance spectra of coral sand, as measured by Maritorena et al. (1994), were used.

The predictions of the inversion scheme from reflectance measurements made at the profiling stations were compared to in-water measurements. The retrieved $b_{bp}(400)$ was compared to station averaged $b_{bp}(400)$ estimated from HydroScat-6 measurements (Fig. 3a). The normalised root mean square error (RMSE) of the direct comparison was 10%, with a small bias. The RMSE for $a_\phi(440)$ retrievals was 17%, with all points within 25% of in-laboratory-based measurements (not shown).

Depth retrievals were considered to be invalid if the contribution of the bottom component to $r_{rs}(500)$ was $< 15\%$ ($N=7$). At each of these sites the depth was

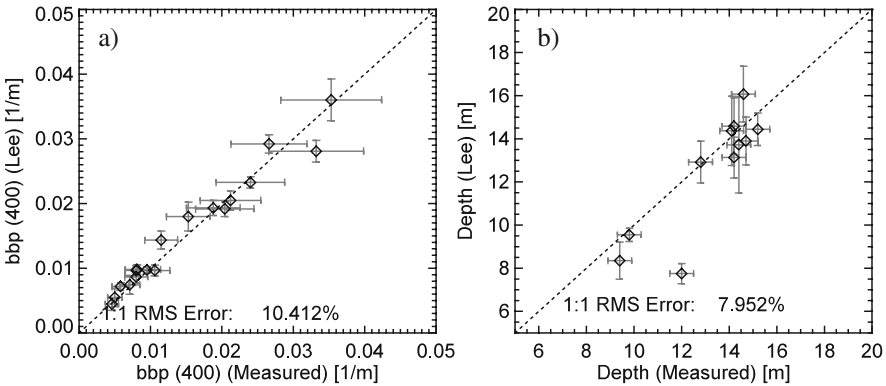


Fig. 3 Comparison between measured and retrieved parameters. (a) $b_{bp}(400)$ and (b) depth at measurement stations compared with the parameters retrieved from DALEC measurements

> 9.5m and > 5.5 m deeper than the Secchi depth. The valid depth retrievals ($N=11$) were compared to the depth measured by the ships echo sounder (Fig. 3b) and had a RMSE of 8%. The RMSE may not be an accurate description of the performance of the depth retrievals, as there were two clusters of echo sounder measurements (around 9 and 15 m).

The low RMSE of the $b_{bp}(400)$ retrieval when compared to Hydroscat-6 measurements suggests that the backscattering component of the retrieval system is robust. For further verification, $b_{bp}(660)$ retrieved from DALEC measurements was compared with the ferry box measured $c_{pg}(660)$, which can vary significantly along the cruise track. Figure 4 displays an example of this variation along part of the northern transect (note the different scales). There were local $c_{pg}(660)$ maxima at 10.51°S, 10.47°S and 10.43°S. These local maxima are also displayed in the $b_{bp}(400)$ and $b_{bp}(600)$ retrievals (Fig. 4, note the different scale).

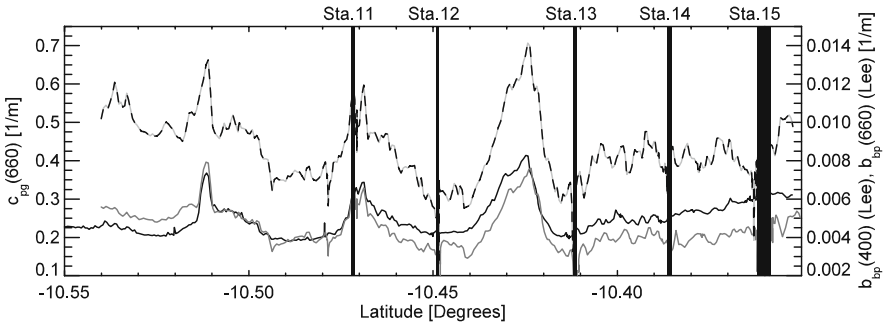


Fig. 4 Spatial variation in measured $c_{pg}(660)$ (black), retrieved $b_{bp}(660)$ (gray) and retrieved $b_{bp}(400)$ (dashed line). Black bars indicate station locations

The magnitude of $c_{pg}(660)$ is primarily influenced by particulate scattering and backscattering; the contribution of $a_g(660)$ to $c_{pg}(660)$ is generally less than 1%. Performing a correlation between $c_{pg}(660)$ and $b_{bp}(660)$ along each transect yielded correlation coefficients, r^2 , of 0.82, 0.90 and 0.66 respectively.

Conclusion

In order to develop a baseline characterisation of the inherent optical properties of the Torres Strait and Gulf of Carpentaria measurements of biological, physical and optical properties were obtained along a series of horizontal transects over the course of three days (23–25/11/2005). The set of measurements included discrete samples, high-resolution vertical profiles and underway measurements.

Measured values of $b_{bp}(z)$ were relatively low throughout the experiment and displayed limited vertical structure, with the majority of sites being well approximated by near-surface values. The hyperbolic slope of back scattering, Y , varied from 0.75 to 1.22, with the greatest values (steepest slope) occurring in shallow coastal waters on 24/11.

The semianalytic model developed by Lee et al. (1999) was applied to the horizontal transects of R_{rs} collected using the DALEC. At stations where in-water measurements were available, the model retrieved $b_{bp}(400)$ ($N=18$) and $a_{\varphi}(440)$ ($N=9$) compare well to in-water measurements (RMSE of 10 and 18% respectively). Valid depth retrievals were obtained at 11 of 18 sites with a RMSE of 8%.

Along track in-water measurements depicted large differences in optical properties over a relatively small distance (Fig. 4). Some of these sharp gradients could not be resolved using the discrete optical profiles, showing the value of along track measurement systems. The model retrieved $b_{bp}(660)$ and in-water measurements of $c_{pg}(660)$ showed a high degree of spatial correlation along each of the three transects. These results indicate that it is possible to obtain in-water inherent optical properties to within stated uncertainties from hyperspectral measurements of R_{rs} .

Additional field surveys, conducted during different seasons and over a greater spatial extent, are required to characterise the optical properties of the Torres Strait. The use of the semianalytic model with atmospherically corrected hyperspectral data from air-borne and/or space-borne sensors would greatly speed up the process.

References

- Boss E, Pegau WS (2001) Relationship of light scattering at an angle in the backward direction to the backscattering coefficient. *Appl Opt*, 40:5503–5507.
- Carder KL, Chen FR, Lee ZP, Hawes SK, Kamykowski D (1999) Semiabalytic moderate-resolution imaging spectrometer algorithms for chlorophyll a and absorption with bio-optical domains based on nitrate-depletion temperatures. *J Geophys Res*, 104:5403–5421.
- Cleveland JS, Weidemann AD (1993) Quantifying absorption by aquatic particles: A multiple scattering correction for glass-fiber filters. *Limnol Oceanogr*, 38:1321–1327.

- Dierssen HM, Zimmerman RC, Leathers RA, Downes TV, Davis CO (2003) Ocean color remote sensing of seagrass and bathymetry in the Bahamas Banks by high-resolution airborne imagery. *Limnol Oceanogr*, 48:444–455.
- Gordon HR, Brown OB, Evans RH, Brown JW, Smith RC, Baker KS, Clark DK (1988) A semianalytic radiance model of ocean color. *J Geophys Res*, 93:10909–10924.
- Harris PT (1991) Reversal of subtidal dune asymmetries caused by seasonally reversing wind-driven currents in Torres Strait, northeastern Australia. *Cont Shelf Res*, 11:655–662.
- Klonowski WM, Lynch MJ, Majewski LJ, Fearn PRCS (2006) Bottom type and depth determination from hyperspectral imagery, 2006 Ocean Sciences Meeting. *Eos Trans. AGU*, Honolulu.
- Lee Z, Carder KL, Mobley CD, Steward RG, Patch JS (1998) Hyperspectral remote sensing for shallow waters. I. A semianalytical model. *Appl Opt*, 37:6329.
- Lee Z, Carder KL, Mobley CD, Steward RG, Patch JS (1999) Hyperspectral remote sensing for shallow waters: 2. Deriving bottom depths and water properties by optimization. *Appl Opt*, 38:3831–3843.
- Lyzenga D (1978) Passive remote sensing techniques for mapping water depth and bottom features. *Appl Opt*, 17:379–383.
- Maffione RA, Dana DR (1998) Instruments and methods for measuring the backward-scattering coefficient of ocean waters. *Appl Opt*, 36:6057–6067.
- Maritorena S, Morel A, Gentili B (1994) Diffuse reflectance of oceanic shallow waters: influence of water depth and bottom albedo. *Limnol Oceanogr*, 39:1689.
- Mitchell BG, Kahru M, Wieland J, Stramska M, 2003. Determination of spectral absorption coefficients of particles, dissolved material and phytoplankton for discrete water samples. NASA/TM-2003-211621/Rev4-Vol. IV.
- Mobley CD (1999) Estimation of the remote-sensing reflectance from above-surface measurements. *Appl Opt*, 38:7442–7455.
- Morel A (1974) Optical properties of pure water and pure seawater. In: Jerlov NG, Steeman Nielsen E (eds), *Optical Aspects of Oceanography*. Academic, San Diego, Calif., pp. 1–24.
- Mumby PJ, Clark CD, Green EP, Edwards AJ (1998) Benefits of water column correction and contextual editing for mapping coral reefs. *Int J Remote Sens*, 19:203–210.
- Philpot WD (1989) Bathymetric mapping with passive multispectral imagery. *Appl Opt*, 28:1569–1578.
- Robinson JA, Feldman GC, Kuring N, Franz B, Green E, Noordeloos M, Stumpf RP (2000) Data fusion in coral reef mapping: working at multiple scales with SeaWiFS and astronaut photography, 6th International Conference on Remote Sensing for Marine and Coastal Environments, pp. 473–483.
- Smith RC, Baker KS (1981) Optical properties of the clearest natural waters (200–800 nm). *Appl Opt*, 20: 177–184.
- Twardowski MS, Boss E, Sullivan JM, Donaghay PL (2004) Modeling the spectral shape of absorption by chromophoric dissolved organic matter. *Mar Chem*, 89:69–88.
- Werdell PJ, Bailey SW (2005) An improved bio-optical data set for ocean color algorithm development and satellite data product validation. *Remote Sensing of Environment*, 98:122–140.

Accordance of MERIS Standard Products over the Gulf of Finland to the Parameters Measured Under Regular Monitoring Program

L. Metsamaa, A. Reinart, K. Alikas, T. Kutser, and A. Jaanus

Abstract The Medium Resolution Imaging Spectrometer (MERIS/Envisat) was launched in March 2002 to provide a dedicated mission of coastal zone monitoring. A full reprocessing of the MERIS products using the latest set of algorithms was finished in March 2006. The main objective of the present study was to evaluate performance of the new MERIS Level 2 products in such optically complex waters like those found in the Gulf of Finland, the Baltic Sea. Large temporal and spatial variability in the concentrations of chlorophyll and suspended sediments is characteristic of these waters. Potentially toxic cyanobacterial blooms occur every year in the middle of summer in the Baltic Sea. Aggregations of cyanobacteria often form dense subsurface blooms or even surface scum, which are spatially extremely patchy. Coloured dissolved organic matter has a significant influence on the optical properties of the Baltic Sea and is the major contributor to the optical properties of coastal waters. MERIS products are compared with available in situ data obtained regularly by an Estonian monitoring programme. Our results indicate that the satellite sensors give consistent results, which are in the same range as in situ data. Chlorophyll concentrations may exceed standard processing limits during heavy bloom conditions.

Introduction

The Baltic Sea is one of the largest brackish water areas on Earth, with a drainage basin that is four times larger than its surface area. The Baltic Sea is extremely vulnerable to anthropogenic disturbance due to its special hydrographical conditions, simple ecosystem structures and poor water exchange with the North Sea (Voipio 1981).

Reliable and cost-efficient monitoring techniques of coastal waters that are able to resolve spatial patterns in high resolution are growing in importance

L. Metsamaa (✉)

Estonian Marine Institute, Tartu University, Tallinn 12618, Estonia
e-mail: liisa.metsamaa@sea.ee

as a consequence of increasing symptoms of on-going eutrophication processes. Phytoplankton blooms are extremely patchy, both temporally and spatially (Reinart and Kutser, 2006). Consequently, they often remain unobserved using the traditional sampling methods based on temporally sparse sampling at fixed monitoring stations (Härmä et al. 2001).

Unattended flow-through systems on ships-of-opportunity (Leppänen et al. 1995; Lindfors et al. 2005), airborne (Dekker et al. 1992; Jupp et al. 1994) and satellite-based remote sensing (Kahru et al. 1993, 2000; Kutser 2004) have been frequently used methods to provide greater spatial information about the distribution of water quality characteristics (e.g. chlorophyll *a* concentrations) than the conventional monitoring programs can provide. Easiest and fastest availability of satellite data is provided by NASA (MODIS images). However, standard algorithms developed for MODIS overestimate chlorophyll concentrations in the Baltic Sea by 150–200 % even in non-bloom conditions (Darecki and Stramski 2004). MODIS standard algorithms were designed primarily for Case 1 waters, where the concentrations of optically active substances in seawater are assumed to co vary with the chlorophyll concentration (Gordon and Morel 1983; Morel and Prieur 1977). The Baltic Sea waters do not satisfy this assumption and can be classified as Case 2 waters. High variation in phytoplankton biomass is accompanied with relatively high dissolved organic matter and suspended sediments concentration (values for Gulf of Finland $a_{CDOM}(440)=0.41\pm0.27\text{ m}^{-1}$ and $C_{TSS}=1.1\text{--}11\text{ g m}^{-3}$ accordingly). However these two parameters are not included into regular monitoring programme, which hampers the application of remote sensing methods. Thus the overall poor performance of Case 1 water algorithms in the Baltic is not surprising (Darecki et al. 2003).

The prospects of better remote sensing of Case 2 waters are improving with technological advances in ocean color sensors and the scientific efforts underway to gain an in-depth understanding of optics in Case 2 waters (Darecki and Stramski 2004). MERIS has been providing a new opportunity to map phytoplankton biomass (Gower and Borstad 2004). MERIS offers a combination of several narrow wavebands to target both chlorophyll *a* and accessory pigment absorption in the red spectral region (at 620 and 709 nm), at a spatial resolution sufficient for medium sized water bodies and coastal areas, with a satisfactory signal-to-noise ratio (Doerffer and Schiller 2007).

It have been shown that during the spring bloom ship-of-opportunity data together with satellite data can provide a practical tool for operative determination of chlorophyll *a* concentrations in the Baltic Sea. Further investigation is still needed because during the different phases of the same bloom the chlorophyll *a* concentrations vary a wide range even within a local area (Vepsäläinen et al. 2005; Koponen et al. 2007).

The aim of the present paper is to study the possible usage of MERIS standard products for chlorophyll concentration (algal_1 and algal_2) in the Gulf of Finland, the Baltic Sea. We compared MERIS chlorophyll concentration products with the available field data to clarify, whether this sensor is capable of detecting the high variability in chlorophyll values in the Baltic Sea.

Material and Methods

Study Area and Chlorophyll *a* in Situ Data

The study area is located in the northern part of Europe, in the Baltic Sea (Fig. 1). The Gulf of Finland has one of the busiest shipping routes in the world.

Potential negative environmental impacts are also conditioned by runoff enters from a large catchments area. Active monitoring is very important for this area. Operative in situ chlorophyll *a* measurements are provided by the continuous flow-through fluorometer system on board a passenger ferry travelling in the across the Gulf of Finland between Tallinn (Estonia) and Helsinki (Finland) (Fig. 1). Regular monitoring in the Gulf is carried out in the frame of Estonian and Finnish National Monitoring Programs according to HELCOM convention recommendations. Main aim is to secure the Baltic Sea ecosystem preservation and biodiversity.

Chlorophyll *a* fluorescence, salinity and temperature were measured continuously along the Tallinn-Helsinki transect and water samples for nutrients and chlorophyll *a* were taken weekly by automatic water samplers included in the flow-through system. Onboard the ship-of-opportunity, chlorophyll *a* fluorescence was measured semi-continuously at an interval of 20 s using Turner 10-AU fluorometer. Once a week chlorophyll samples were collected to calibrate fluorescence values into chlorophyll concentrations (Chl). An automatic refrigerated water sampler (Teledyne ISCO) conducted water sampling for chlorophyll *a* analysis. The sampling depth was ~5 m, but the sampling water was assumed to represent mixed surface water due to the mixing caused by the ferry. We used these samples to validate the MERIS algorithms performance.

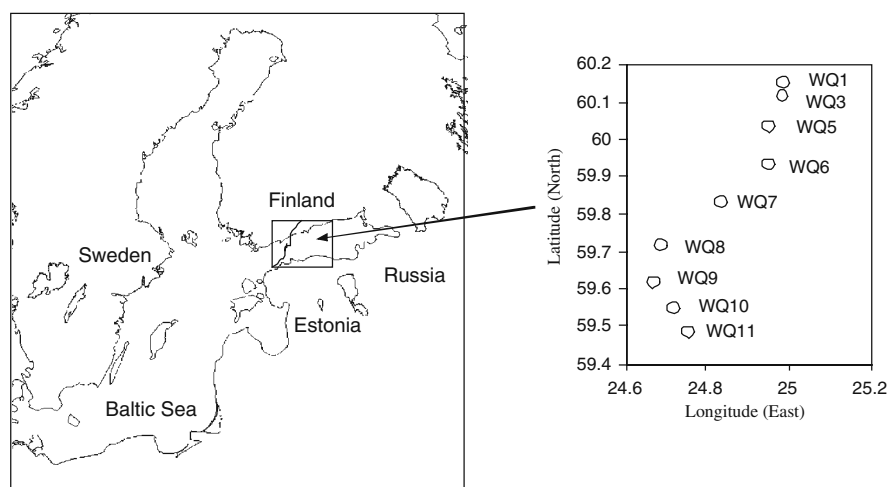


Fig. 1 Locations of the ferry line between Tallinn and Helsinki in the Baltic Sea, where the study was carried out. Sampling points are indicated by labelled circles in box

The samples of chlorophyll *a* were filtered through Millipore GF/F filters, extracted in 96% ethanol for 24 h at room temperature and measured spectrophotometrically (Jenway 6400). Typically there are two periods in Baltic Sea, when phytoplankton blooms occur. The first one starts early in the spring before ice totally melts. This bloom is dominated by diatoms and dinoflagellates. The second bloom occurs later in the summer and is dominated by cyanobacteria. Extent and duration of the bloom varies between years and depends significantly from local climatic conditions. We used in situ data describing three different conditions of the phytoplankton development in the Gulf of Finland: 12/05/2003 (spring bloom), 17/06/2003 (non-bloom) and 29/07/2003 (summer bloom) (Table 1).

Table 1 Dates of the satellite overpass and the operative monitoring with dominating species on the last column

| Date of the satellite overpass | Date of the in situ measurements | Dominating species ($\mu\text{g/l}$ -average for the ship rout) |
|--------------------------------|----------------------------------|--|
| 10/05/2003 | 12/05/2003 | Dinoflagellates (4118) Diatoms (1885) |
| 17/06/2003 | 17/05/2003 | Dinoflagellates (220) |
| 31/07/2003 | 29/07/2003 | Cyanobacteria (845) |

MERIS Chlorophyll Retrieval Algorithms and Image Analyses

The MERIS Level 2 standard products include two chlorophyll retrieval algorithms: *algal_1* and *algal_2*. *Algal_1* is an estimate of the chlorophyll concentration in oceanic waters, where the concentration is derived from empirically developed relationship between the ratio of the blue and green signal leaving the water surface and the concentration of algal pigments. *Algal_2* is derived by inverting a model of the optical properties of the water through the use of a neural network and may be more suited to optically complex waters (Doerffer and Schiller 2007). The algorithm used in the latest reprocessing (MEGS 7.4.(1)) uses the output of the neural network (absorption by phytoplankton pigments) with an empirical relationships (Eq. 1) to form an estimate of chlorophyll concentration (MERIS 2006):

$$\text{algal_2} = 21 * \text{apigment}(443)1.04, \quad (1)$$

Concentrations of non-absorbing suspended matter and the CDOM absorption at 443 nm is also output by this algorithm.

Frequent cloud cover over the Baltic Sea makes it difficult to obtain an extensive set of cloud-free satellite images for inter-comparison with in situ data. Remote sensing and in situ measurements were in general not carried out at the same time. We used meteorological and wave measurements supplied by the Finnish Environmental Institute (SYKE) to estimate drift of the water masses and chose the most suitable images in order to compare the remote sensing data and the

in situ measurements. For describing different ecological conditions in the Gulf of Finland three cloud free MERIS/ENVISAT reduced resolution image were used: 10/05/2003, 17/06/2003 and 31/07/2003 (<http://envsat.esa.int>.) (Table 1). Images were visualized and analyzed using software BEAM 3.2 and ENVI 4.1 (ResearchSystemsInc.).

In situ measurement points were marked with a pin in the MERIS L2 images and a 3 x 3 pixel area around the pin was examined. Average concentrations and standard deviations were calculated at every measurement point for every date based on nine pixel values in *algal_1*, *algal_2*. If some pixel value around exceeded pinned value more than 30%, this pixel was not used in further analyses. The total number of data points was 85 (10/05/2003), 58 (17/06/2003) and 93 (31/07/2003).

Results and Discussion

First step was to study the fluorescence and measured chlorophyll match-ups. Correlation between laboratory measured chlorophyll and in situ measured fluorescence on 12/05/2003 was strong ($R^2=0.81$), but root mean square error was very high (RMSE=25.6). However, we have used these relationships to calculate chlorophyll from measured fluorescence data to describe horizontal variability as this is the common method in our monitoring system for such kind of data.

During non-bloom conditions in 17/06/2003 dinoflagellates dominate in water but biomass of phytoplankton was much lower compared with spring and summer bloom conditions. There was weak correlation ($R^2=0.37$; RMSE= 2.4) between the laboratory measured chlorophyll and in situ measured fluorescence. The correlation is disturbed by one outlier, where concentration of the dinoflagellates is the highest. If the outlier is excluded from this comparison we get a perfect correlation ($R^2=0.95$; RMSE=5.5, Fig. 2). Excluding this station does not affect the comparison with the satellite data. Station is located in the harbor and is left out from the satellite data processing because of land adjacency effect.

In 2003 only medium cyanobacterial bloom occurred close to the Finnish coast in the end of July and beginning of August. The laboratory measured chlorophyll and

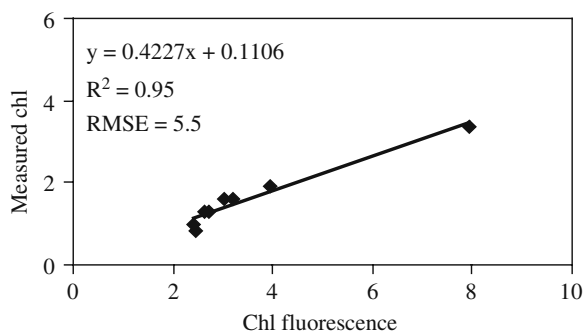


Fig. 2 Correlation between laboratory measured chlorophyll (Chl) and in situ measured fluorescence for 17/06/2003

in situ measured fluorescence at 29/07/2003 were in perfect correlation ($R^2=0.98$; RMSE=7.2).

Figure 3a is describing the situation on 10/05/2003, typical time for spring bloom. Dinoflagellates and diatoms occur in bloom conditions in the Northern regions of the Baltic Sea, every year. These species lack the ability to govern their motion within the water column and are therefore distributed equally in the upper mixed layer. Consequently there should be better correlation between the chlorophyll values measured at the depth of 5 m and estimated by satellite based sensors. It is also seen in Fig. 3a that chlorophyll calculated from fluorescence data and algal_2 product coincide relatively well. Algal_1 results are much higher (around 20 mg m^{-3}) and noisier than algal_2 and only few pixels are processed, but the numerical values are closer to measured ones, while algal_2 are too low.

The MERIS image from 17/06/2003 was cloudy near Helsinki. Thus, comparisons could not be made for about one third of transect (Fig. 3b). The algal_2 values showed a rapid decrease from Tallinn towards the open sea, similar to the fluorescence values. However, as seen in Fig. 3b, between 59.6°N and 60.1°N the chlorophyll values obtained from the flow-through fluorescence values stayed around 2 mg m^{-3} , while MERIS algal_2 values varied around $4\text{--}8 \text{ mg m}^{-3}$. In this case the product algal_1 showed even closer values to the fluorescence chlorophyll than algal_2.

Medium cyanobacterial bloom conditions were noticed close to the Finnish coast in the end of July and beginning of August. Figure 3c shows typical cyanobacterial situation in the Baltic Sea, where fluorescence gives almost the straight line, however correlation between chlorophyll and fluorescence was perfect ($R^2=0.98$; RMSE=7.2). This effect is probably caused by picoplankton. Seppälä et al. (2007) have shown that chlorophyll fluorometers, commonly used in the flow-through systems, cannot provide information about the amount of cyanobacteria in the water as most of chlorophyll *a* in cyanobacteria is in non-fluorescing photosystem. They suggest that flow-through measurements have to be done parallel with phycocyanin fluorescence measurements. MERIS algal_2 high chlorophyll values are shown close to the Finnish coast, which are not supported by measured fluorescence data. This may be caused by the accumulation of cyanobacteria in upper water layers (above 5 m where is intake of flow-through system). The algal_1 and algal_2 values coincide rather well with measured fluorescence profiles towards the Estonian coast, where the bloom is not so pronounced.

MERIS products include set of flags showing various steps in processing or problems. In all cases the flag showing uncertainties in estimates of water leaving radiance (PCD_1_13) were raised over the entire transect. This is typical of MERIS images over Baltic Sea and shows that problems in processing start already during atmospheric correction, which means that further products can not be trusted as well. Another important flag showing high level of dissolved organic matter in water have not been activated yet in MERIS processing, but probably will in the next reprocessing.

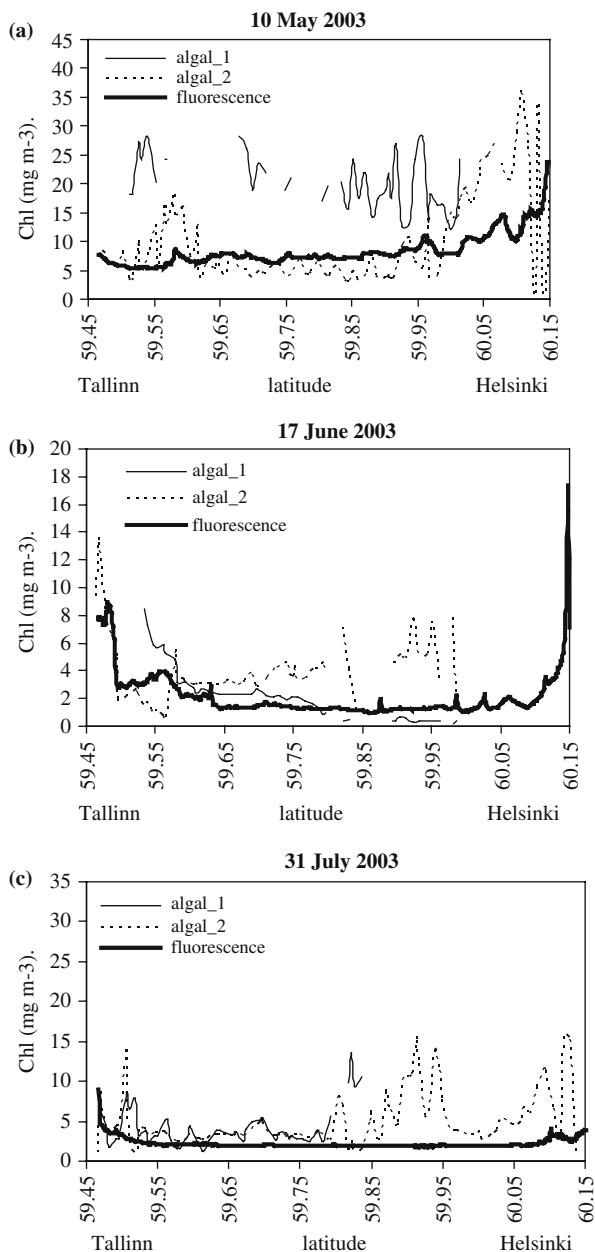
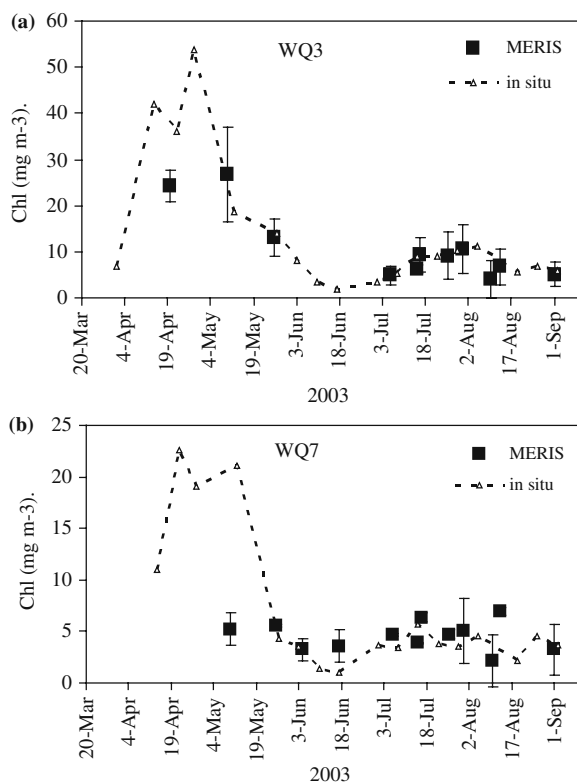


Fig. 3 Comparison of MERIS derived chlorophyll products with in situ measured chlorophyll (Chl) by fluorescence, (a) 10–12/05/2003, when spring bloom (diatoms and dinoflagellates) was present; (b) 17/06/2003, when non-bloom situation was present (c) 29–31/07/2003, when summer bloom (cyanobacteria) was present

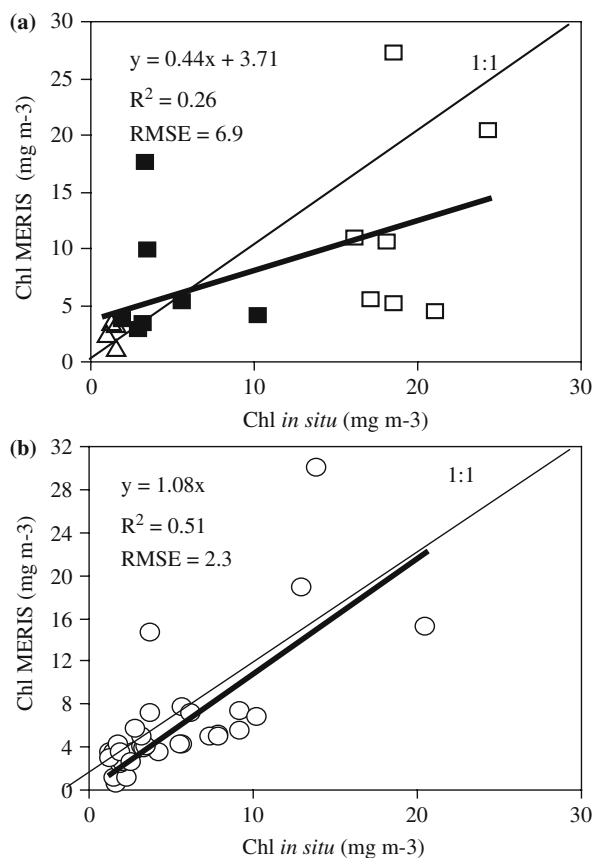
Fig.4 Seasonal variation of chlorophyll (Chl) concentration by in situ measurements and MERIS algal_2 product (average and standard deviation of 9 pixel values) (a) near Finnish coast – point WQ3; (b) in the central region of the Gulf of Finland – point WQ7



MERIS algal_2 product shows rather well the seasonal variation of chlorophyll (Fig. 4a, b), having significantly higher values in the spring bloom and lower values later in the summer period. It also conforms to the increase of measured chlorophyll in July–August, when cyanobacterial bloom occurs. In 2003 the in situ measurements show that bloom was more pronounced in coastal regions than in the open waters, and the same difference can be noticed also by satellite data. However, MERIS estimates rise up to 39.2 mg m^{-3} and do not reach to the highest values measured in situ (58.1 mg m^{-3}).

Comparison for the three selected cases shows, that MERIS algal_2 is capable to detect relative distribution of chlorophyll rather well (Fig. 5a) and highest values accord to the spring bloom, while lowest are for the non-bloom conditions. When all available data collected at same day with satellite overpass (all together 33 points) are plotted against MERIS algal_2, then R^2 was 0.51 and RMSE was 2.3 mg m^{-3} , points are close to 1:1 line (Fig. 5b). For algal_1 there were less points available (28) and even the R^2 value was slightly higher (0.6) RMSE was very high – 21.8 mg m^{-3} and algal_1 values are about two-times higher than the in situ measured chlorophyll.

Fig. 5 Comparison of MERIS algal_2 and in situ chlorophyll (Chl) values (a) measured in points WQ3-WQ10 during spring bloom (10–12/05/2003; unfilled quadrate), cyanobacterial bloom (29–31/07/2003; filled quadrate) and non-bloom conditions (17/06/2003; unfilled trigon); (b) all data in 2003, when satellite image and sampling data were available for the same day



Use of chlorophyll values derived from fluorescence measurements for comparisons with satellite data could increase the data points but in reality does not give any better results. When fluorescence measurements and MERIS algal_2 at the same day (17/06/2003) were compared pixel-by-pixel bases, then R^2 value was only 0.16, and linear regression rather similar to that shown in Fig. 5a. ($y=0.49x+2.9$, $RMSE=4.4$).

It was surprising that MERIS data and flow-trough measurements are so weakly comparable even in conditions when there were no extensive surface accumulations of cyanobacteria in the Northern part of the Baltic Sea. The cyanobacterial situation in the Gulf of Finland, where the bloom is usually most dense, was relatively good. Only medium bloom conditions were noticed close to the Finnish coast in the end of July and beginning of August. This situation was caused by the cold weather in the summer of 2003. A basic requirement for the development of an algal bloom is high enough temperature within the euphotic zone. We assume that in surface bloom conditions there is hardly any connection between the bloom near or on the water surface satellites are detecting and the bloom flow-through systems are

detecting. Further investigations are needed about the vertical distributions of the phytoplankton species and the other optically active substances in water column.

Conclusions

Results of this study suggest the performance of the MERIS standard algorithm *algal_1* is un-stable and therefore not suitable for use in the Gulf of Finland. It could give some valuable estimates when chlorophyll values are low (below 4 mg m⁻³). The additional effect caused by the dissolved organic and suspended matter, *algal_1* may be applicable only in limited regions of the open water and short period when non-bloom conditions occur.

As expected the MERIS *algal_2* product is performing better. It gives more consistent chlorophyll values. However, depending on local conditions it underestimates lower values and overestimates higher chlorophyll values. It is also important to understand, that fluorescence and flow-through data collected during cyanobacterial blooms is often not suitable for validation of satellite products. First of all concentration of chlorophyll and chlorophyll *a* fluorescence are not in correlation during cyanobacterial blooms. On the other hand concentration of chlorophyll at the depth of 5 m and concentration of chlorophyll near the water surface, that satellites are detecting, are not correlated during the phytoplankton blooms capable of migrating in the water column (like cyanobacteria). This makes it very difficult to develop remote sensing algorithms for quantitative mapping of cyanobacteria. More reliable information about vertical distribution as well as optical properties of the dominating phytoplankton species and the accompanying optically active substances are needed. In the mean time remote sensing is a very valuable tool to estimate relative abundance of phytoplankton and to study occurrence and dynamics of blooms.

Acknowledgements The authors thank all colleagues from the Estonian Marine Institute for performing the in situ data. The study was funded by the Estonian National Monitoring Program, Estonian target financed project 0712699s05 and Estonian Science Foundations grant 6814. Thanks also to the two anonymous referees for their valuable comments on this paper.

References

- Arnone RA, Martinolich P, Gould RW, Sydor M, Stumpf RP (1998) Coastal optical properties using SeaWiFS. Ocean Optics XIV Conference, Kailua-Kona, Hawaii, 10–13 November 1998, Ocean Optics XIV CD ROM Washington, DC: Office of Naval Research.
- Darecki M, Weeks A, Sagan S, Kowalczyk P, Kaczmarek S (2003) Optical characteristics of two contrasting Case 2 waters and their influence on remote sensing algorithms. *Cont Shelf Res* 23: 237–250
- Darecki M, Stramski D (2004) An evaluation of MODIS and SeaWiFS bio-optical algorithms in the Baltic Sea. *Remote Sens Environ* 89:326–350
- Dekker AG, Malthus TJ, Goddijn LM (1992) Monitoring cyanobacteria in eutrophic waters using airborne imaging spectroscopy and multispectral remote sensing systems. In: *Proceedings of Sixth Australasian Remote Sensing Conference* 1: 204–214

- Doerffer R, Schiller H (2007) The MERIS Case 2 water algorithm. *Int J Remote Sens* 28(3/4): 517–535
- Gordon HR, Morel A (1983) Remote assessment of ocean color for interpretation of satellite visible imagery—A review. In: Barber RT, Bowman MJ, Mooers CNK, Zetschel B (eds) *Lecture notes on coastal and estuarine studies*. Springer-Verlag, New York.
- Gower JFR, Borstad GA (2004) On the potential of MODIS and MERIS for imaging chlorophyll fluorescence from space. *Int J Remote Sens* 25 (7–8): 1459–1464
- Härmä P, Vepsäläinen J, Hannonen T, Pyhälähti T, Kämäri J, Kallio K, Eloheimo K, Koponen S (2001) Detection of water quality using simulated satellite data and semi-empirical algorithms in Finland. *Sci Total Environ* 268: 107–121
- Jupp DLB, Kirk JTO, Harris GP (1994) Detection, identification and mapping of cyanobacteria using remote sensing to measure the optical quality of turbid inland waters. *Aust J Mar Fresh Res* 45: 801–828
- Kahru M, Leppänen J-M, Rud O (1993) Cyanobacterial blooms cause heating of the sea surface. *Mar Ecol-Prog Ser* 101:1–7
- Kahru M, Leppänen J-M, Rud O, Savchuk OP (2000) Cyanobacteria blooms in the Gulf of Finland triggered by saltwater inflow into the Baltic Sea. *Mar Ecol-Prog Ser* 207: 13–18
- Koponen S, Attila J, Pulliainen J, Kallio K, Pyhälähti T, Lindfors A, Rasmus K, Hallikainen M (2007) A case study of airborne and satellite remote sensing of a spring bloom event in the Gulf of Finland. *Cont Shelf Res* 27: 228–244
- Kutser T (2004) Quantitative detection of chlorophyll in cyanobacterial blooms by satellite remote sensing. *Limnol Oceanogr* 49: 2179–2189
- Leppänen J-M, Rantajarvi E, Hällfors S, Kruskopf M, Laine V (1995) Unattended monitoring of potentially toxic phytoplankton species in the Baltic Sea in 1993. *J Plankton Res* 17: 891–902
- Lindfors A, Rasmus K, Strömbec N (2005) Point or pointless – quality of ground data. *Int J Remote Sens* 26 (2): 415–423
- MERIS (2006) Products Quality Status Report MEGS7.4 and IPF 5, MERIS Product Quality Status Report, 14.03.2006. (<http://earth.esa.int/pcs/envisat/meris/documentation/>)
- Morel A, Prieur L, (1977) Analysis of variations in ocean colour. *Limnol Ogenogr* 22: 709–722
- Rateoja M, Seppälä J, Ylöstalo P (2004) Fast repetition rate fluorometry is not applicable to studies of filamentous cyanobacteria from the Baltic Sea. *Limnol Oceanogr* 49 (4): 1006–1012
- Reinart A, Kutser T (2006) Comparison of different satellite sensors in detecting cyanobacterial bloom events in the Baltic Sea. *Remote Sens Environ* 102: 74–85
- Sathyendranath S (ed) (2000) Remote sensing of ocean colour in coastal, and other optically-complex, waters. IOCCG Report 3, Nova Scotia: IOCCG Project Office, Dartmouth
- Seppälä J, Ylöstalo P, Kaitala S, Hällfors S, Raateoja M, Maunula P (2007) Ship-of-opportunity based phycocyanin fluorescence monitoring of the filamentous cyanobacteria bloom dynamics in the Baltic Sea. *Estuar Coast Shelf S* 73: 489–500
- Siegel DA, Wang MH, Maritorena S, Robinson W (2000) Atmospheric correction of satellite ocean color imagery: the black pixel assumption. *Appl Optics* 39: 3582–3591
- Vepsäläinen J, Pyhälähti T, Rantajarvi E, Kallio K, Pertola S, Stipa T, Kiirikki M, Pulliainen J, Seppälä J (2005) The combined use of optical remote sensing data and unattended flow-through fluorometer measurements in the Baltic Sea. *Int J Rem Sens* 26(2): 261–282
- Voipio A (1981) The Baltic Sea. Elsevier Oceanogr Ser 30: 41